WARWICK
THE UNIVERSITY OF WARWICK

A Thesis Submitted for the Degree of PhD at the University of Warwick

Permanent WRAP URL:
http://wrap.warwick.ac.uk/79313

Copyright and reuse:
This thesis is made available online and is protected by original copyright.
Please scroll down to view the document itself.
Please refer to the repository record for this item for information to help you to cite it.
Our policy information is available from the repository home page.

For more information, please contact the WRAP Team at: wrap@warwick.ac.uk

warwick.ac.uk/lib-publications

The Synthesis and Characterisation of Hexagonal Ferrite Fibres

Volume One of Two

Robert Carlyle Pullar

University of Warwick
School of Engineering

December 1999

A thesis submitted in canditure for the degree of Doctor of Philosophy

Abstract

Hexagonal ferrites are a family of magnetic oxides which include M ferrite, the most commonly used magnetic material in the world today. They also have more specialist potential applications, such as microwave absorption and catalysis. They are highly complex crystal structures which usually require high temperatures to form a well sintered product, at the expense of grain growth, which in turn affects the magnetic properties of the material. They all exhibit magnetocrystalline anisotropy; depending upon the ferrite they can have a preferred direction of magnetisation along the c axis of the hexagonal crystal (uniaxial), or in the hexagonal plane or in a cone at an angle to the plane (ferroxplana).

A material made in a fibrous form has many properties; firstly it can be incorporated into a matrix to form a composite material, imparting any special properties into the whole composite. Provided their microstructure is sufficiently fine, fibres tend to be stronger than the bulk ceramic form, and if fine enough they can even be woven into a cloth. It has also been suggested that some properties, such as magnetisation, will be enhanced when the material is an aligned fibre, although this specific case has never been proven previously.

This thesis presents the manufacture of a range of hexagonal ferrite fine fibres from an inorganic aqueous sol-gel precursor, and their subsequent characterisation both physically and magnetically. The fibres were blow spun from a viscous solution using a modified commercial process, and they were collected in both random and aligned forms. The sols were made from the peptisation of a precipitated iron(III)hydroxide with a mineral acid, and various combinations of iron(III) salt and acid were investigated using PCS. The best results were found to come from iron(III)chloride precipitated by ammonia and peptised with HBr, with totally nitrate and chloride based systems proving inferior. Chloride was found to add structuring to the sol, aiding spinning but resulting in a thixotropic gel if too much was present. The stoichiometric ferrite sols were made by doping the iron(III) sol with solution of metal salts, and these were found to be critical to the stability of the sol, with barium causing particular problems, and titania was added as a second colloidal species. Stoichiometric sols of BaM, SrM, $BaCo_xTi_xFe_{12-2x}O_{19}$, $SrCo_xTi_xFe_{12-2x}O_{19}$, Co_2Y, Co_2Z, Co_2W, Co_2X and Co_2U ferrites were made, among others, and all were successfully spun as fibres. They typically had diameters of 4 – 6 μm and an alignment of over 90% within +/- 20° of the axis of alignment, comparable to commercially developed fibres.

The sol-gel process typically produces ceramic materials at lower temperatures and with smaller grain sizes than standard ceramic techniques, and this proved to be the case. SrM and BaM began to form at 800 °C and had become the pure phase product by 1000 °C, being 98% sintered at this stage and with a submicron grain size. Co_2Y ferrite was also the sole phase at a low temperature of 1000 °C, although it consisted of hexagonal platelets up to 3 μm wide and 0.2 μm thick. Substituted M ferrites also formed the M phase at similar temperatures, but were more porous and did not have the greatly reduced grain size reported previously. None of these ferrites underwent the sudden, exaggerated grain growth seen in many hexagonal ferrites, even at 1200 °C. However, both the Co_2Z and Co_2W ferrite fibres underwent this process concurrently with the formation of these phases, and it appears to be an unavoidable step under normal conditions, although steam firing or doping with CaO enabled the formation of a majority-Z product without this growth. It was found that halide retained in the fibre inhibited the formation of the hexagonal ferrite phase, as it was retained up to 1000 °C. When the fibres were treated to remove halides or made from a halide free precursor they formed M ferrites ~200 °C lower, and with a reduced grain size below 0.1 μm. The fibres were characterised by XRD, XRF, XPS and SEM.

The samples were characterised magnetically by VSM, and while the M ferrites proved to have typical M_s values and high coercivities for polycrystalline samples, the ferroxplana ferrites all had M_s equal to or better than the previously reported maximum values. It was also found that there were definite alignment effects on M_s in all fibres except those which had under gone the exaggerated grain growth, with an enhancement in M_S of up to +40% along the axis of alignment when parallel to the applied field compared to values for random fibre. This is the first time that the effect of fibre alignment upon magnetic properties has been demonstrated.

Declaration

The research described in this thesis was carried out at the University of Warwick between October 1995 and June 1999. This thesis is the original work of the author except where acknowledged by reference, and no part has been submitted for any other degree in this or any other University.

The copyright of this thesis rests with the author. No quotation from it should be published without the prior written consent of the author, and any information derived from it should be fully acknowledged.

Acknowledgements

Many thanks to my supervisors, Ashok Bhattacharya and David Taylor, for their help and patience whilst I was writing this thesis, and for their support over the last few years. Thanks also to my fellow workers at Warwick and elsewhere who have given me their advice and assistance: Gavin Walker, M. G. Krishna, Marappa Rajendran, Richard Reynolds, Kajal Mallick, Martin Lees, Steve Appleton and Ellen Williams. I wish to thank the Process Technology Group, University of Warwick, and DERA for funding my work over the previous years. And finally thank you to Clara for being patient with me over the last few months – sono stanco morto, ma finalmente è finito!

This thesis is dedicated to my parents and Clara.

List of Abbreviations

DGG	discontinuous grain growth
EM	electromagnetic
rf	radio frequency
1D	one dimensional
2D	two dimensional
3D	three dimensional
PZC	point of zero charge
CMC	ceramic matrix composite
MMC	metal matrix composite
RMC	resin matrix composite
IEP	iso-electric point
n/a	results not avaliable
mol	moles
M	moles litre^{-1}
MW	molecular weight
PEO	polyethylene oxide
IPA	iso-propyl alcohol
PCS	photon correlation spectroscopy
RI	refractive index
DTA	differential thermal analysis
TGA	thermo-gravimetric analysis
XRD	x-ray diffraction
XRF	x-ray fluorescence spectroscopy
XPS	x-ray photo-electron spectrscopy
SEM	scanning electron microscopy
ASAP	analysis of surface area and porosity
VSM	vibrating sample magnetometer
MCA	magneto-crystalline anisotropy
T	Tesla (= 1 x 10^4 Gauss = 795.77 kA m^{-1})
emu	electromagnetic unit (= 10^3 A m^2)
emu g^{-1}	mass magnetisation (= 10^3 A m^2 g^{-1})
M_s	saturation magnetisation
M_r	remanent magnetisation
H_c	coercivity
T_c	Curie point or temperature
H	magnetic field
$\parallel$	aligned parallel to H
$\perp$	aligned perpendicular to H
FMR	ferromagnetic resonance

Contents

Volume One

Chapter Four
The Solid State Reactions, Crystallisation, Sintering and Microstructure of Hexagonal Ferrite Fibres

Volume two

Introduction and Thesis Overview

This thesis describes work undertaken to synthesise polycrystalline fine fibres of a series of hexagonal ferrites, and characterise their physical and magnetic properties, particularly in comparison to non-fibrous forms of these materials. The hexagonal ferrites are a family of iron-based ceramic magnetic compounds of enormous commercial and technological importance, ranging from the most common magnetic material used today found in a host of everyday objects, to high-technology and specialist applications. However, they have never been produced as a continuous fine fibre previously, despite the potential advantages and unique applications of a material in this form. Many properties, such as magnetic moment, could be enhanced in an aligned fibrous ferrite, and they could also be incorporated into a composite material. This introduction briefly details an overview of the research carried out and the structure of the following chapters, and a scheme of the steps involved, and the chapters in which they are discussed, is shown in the scheme below.

The aims of the research contained within this thesis were:

- To make a stable multicomponent sol-gel system from which gel fibres can be spun to produce a range of hexagonal ferrite ceramic fibres.

- To blow spin stoichiometric sols to make precursor gel fibres, which could then be fired to give ceramic fibres consisting of the desired hexagonal ferrite phases.

- To characterise the morphology and physical and magnetic properties of these hexagonal ferrite fibres.

- To investigate the effects of process parameters on the formation, morphology, and magnetic properties of the fibres.

- To investigate the effects of non stoichiometric additions and substitutions, and variations in the characteristics of the sol precursor on the ceramic fibres.

- To determine if the magnetic properties of the hexagonal ferrites are enhanced in fibrous form compared to bulk materials, and in aligned versus random fibres.

This thesis is in two volumes; Volume One contains chapters 1 – 5 and a summary, while Volume Two contains the figures, references and appendices. The first chapter contains in part A a review of the history, structure, synthesis and commercial and industrial applications of the hexagonal ferrites. Part B is a review of the general properties of fibres and the advantages possible from the use of materials in fibrous form, the methods of manufacture of polycrystalline fibres, and their use in composite, refractory and structural materials and other niche applications. A survey of polycrystalline ceramic fibres previously produced can be found in appendix B.

Chapter two concerns the creation of a stable multicomponent sol-gel system capable of producing a range of hexagonal ferrite fibres, and begins with a review of the sol-gel process, the structure of sols and their advantages and applications. It was important that the entire series of ferrites could be produced from a single precursor, with variations in doping or additives to obtain the desired stoichiometry, and that the sols were sufficiently stable to be spinnable. The structure and particle size of the sol has an effect on the following processes of spinning, crystallisation and sintering, and the sols were characterised and optimised using PCS. This technique, the nature of the properties it can determine, and the syntheses of the sols produced are detailed in the experimental section.

In chapter three the blow spinning of the gel fibres from the sol precursor is discussed. The sol must remain stable whilst being concentrated to a higher degree than is usual in sol-gel processing. The blow spinning process and the apparatus used are also described in this section, and the relative qualities of the amorphous gel fibres thus produced are assessed. The fibres were collected as both random staple and aligned blankets.

Chapter four concerns the crystallisation of the gel fibres to the polycrystalline ceramic product with heating, and the sintering and microstructural processes associated with this. The solid state chemistry and characteristics of hexagonal ferrites previously produced from a

variety of methods are reviewed for comparison, and the compositions, crystalline phases and microstructures of the fibres are characterised and compared by a variety of techniques including XRD, SEM and XRF. Variations in the microstructure and sintering of the hexagonal ferrite fibres are investigated, influenced by changing either a process parameter such as the initial sol particle size, firing regime or atmosphere, or by non-stoichiometric doping of the ferrite sol with additives.

The magnetic properties of the ceramic fibres are investigated in chapter five, derived from the magnetic hysteresis loop measured by VSM. The nature of magnetism in hexagonal ferrites is reviewed, along with the previously published work on the effects of variations in synthetic method employed, and both substitution and non-stoichiometric doping, on the magnetic properties. The principles of the magnetic phenomena discussed are explained in appendix A, and the VSM technique and sample preparation are detailed in the experimental section. Microstructure is known to have a major influence upon the magnetic characteristics of ferrites, and variations influenced by changing either a process parameter or by non-stoichiometric doping of the ferrite sol with additives known to improve magnetic properties were investigated. The effect of the fibrous nature of the materials on their magnetic properties, particularly with respect to alignment, was also investigated and compared to both random fibre and bulk samples.

Fianlly the conclusions drawn from the previous chapters are summarised and commented upon, and future avenues of investigation are briefly discussed.

Scheme of the content and structure of this thesis

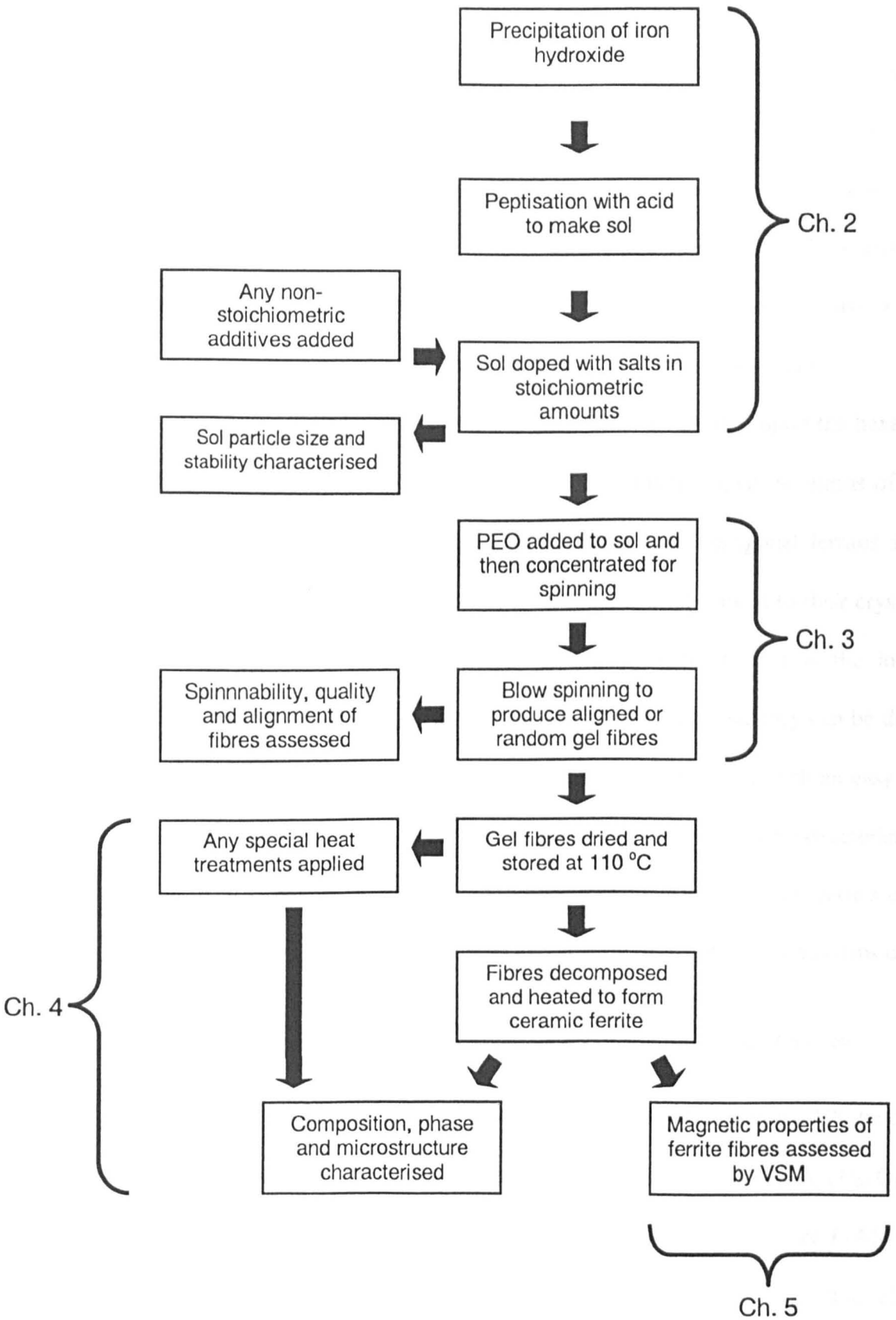

Chapter One

Part A: Hexagonal Ferrites

Ever since Neolithic man used a piece of suspended lodestone to navigate, mankind has used magnetic materials of various kinds. However, it was not until the advent of electricity that the magnetic processes began to be understood. It is now known that lodestone is an iron ore, magnetite, which is one of a wide range of magnetic ceramics based on iron(III)oxide, called the ferrites. Magnetite, Fe_3O_4, is in a structural class of compounds known as the spinels with the composition $MeFe_2O_4$ where Me is a divalent cation. These compounds have a cubic structure, but there are also a group of ferrites with a hexagonal crystal structure.

For the purposes of this investigation the interest shall be focused upon the hexagonal ferrites containing barium and cobalt as divalent cations, although doped variations of these and ferrites containing other cations will also be discussed. The hexagonal ferrites are all ferrimagnetic materials, and their magnetic properties are intrinsically linked to their crystalline structures. They all have a magnetocrystalline anisotropy (MCA), that is the induced magnetisation has a preferred orientation within the crystal structure, and they can be divided into two main groups, those with an easy axis of magnetisation, and those with an easy plane of magnetisation, known as the ferroxplana ferrites. Although some magnetic characteristics of the ferrites shall be discussed here, further details regarding their magnetic properties can be found in chapter five, and appendix A contains an explanation of the theories and terms used.

1. The discovery, composition and characteristics of the hexagonal ferrites

The magnetic mineral magnetoplumbite was first described in 1925 [1], and in 1938 the crystal structure was deduced as being hexagonal with the composition $PbFe_{7.5}Mn_{3.5}Al_{0.5}Ti_{0.5}O_{19}$ [2]. The synthetic form of magnetoplumbite was found to be $PbFe_{12}O_{19}$, or pure PbM, and a number of isomorphous compounds were suggested including $BaFe_{12}O_{19}$, although this material was not structurally investigated until after the Second World War. This material is known by many names, including barium ferrite, hexaferrite, barium hexaferrite, ferroxdure,

M ferrite and BaM, and was also shown to consist of a hexagonal structure [3]. Investigations of the $BaO\text{-}Fe_2O_3$ system then produced more complex hexagonal compounds, in which there were both divalent and trivalent iron species, and further compounds were also discovered when the ternary $BaO\text{-}Fe_2O_3\text{-}MeO$ system was heated at 1200 - 1400 °C, where Me = a small divalent cation [4]. BaM and the cubic $MeFe_2O_4$ spinel appear as the end members of this system, with zero populations of Me and Ba respectively. The physical characteristics of the hexagonal ferrites discussed in this thesis are shown in table 1.1.

Ferrite	Formula	MW / g	ϱ / g cm^{-3}	c / Å	Magnetisation
BaM	$BaFe_{12}O_{19}$	1112	5.28	23.18	uniaxial
SrM	$SrFe_{12}O_{19}$	1062	5.11	23.03	uniaxial
Co_2Y	$Ba_2Co_2Fe_{12}O_{22}$	1410	5.40	43.56	in cone
Co_2Z	$Ba_3Co_2Fe_{24}O_{41}$	2522	5.35	52.30	in plane
Co_2W	$BaCo_2Fe_{16}O_{27}$	1577	5.31	32.84	in plane
Co_2X	$Ba_2Co_2Fe_{28}O_{46}$	2688	5.29	84.11	in cone
Co_2U	$Ba_4Co_2Fe_{36}O_{60}$	3624	5.31	38.16	in plane

Table 1.1 The physical characteristics of some hexagonal ferrites at room temperature.

All of these compounds were found to have a hexagonal crystal structure, with two crystalline lattice parameters: a, the width of the hexagonal plane, and c, the height of the of the crystal (fig. 1). All had a preferred direction of magnetisation when placed in a magnetic field, giving them an MCA, which was usually parallel to the c-axis, coming out of the basal plane of the hexagonal crystal. This uniaxial anisotropy in effect fixes the magnetisation in the direction of the c-axis, and the magnetisation can only be moved out of this direction at the expense of the high anisotropic energy.

However, some compounds containing a divalent cation, especially those containing cobalt, were found to have a plane of spontaneous magnetisation in the basal plane, perpendicular to the c-axis. These compounds were named the ferroxplana ferrites, and are now known also to include compounds which have a cone of magnetisation at an angle $0 < \theta < 90°$ to the c-axis. While the direction of magnetisation can easily rotate within the plane or

cone through an angle of 360°, the magnetisation is still locked in this plane or cone by a high magnetic anisotropy energy.

1.1 The M ferrites

The compound BaM, $BaFe_{12}O_{19}$, was known to exist for many years, with a melting point of 1390 °C confirmed in 1936 [5]. However, the structure was not confirmed as being isomorphous with the hexagonal magnetoplumbite until it was first studied and characterised magnetically in the early 1950's by Philips [3]. BaM was initially named ferroxdure, to distinguish it from the spinel ferrite which was called ferroxcube at the time [6]. At the time it was considered an unusual ferrite as it contained no cobalt or nickel, yet it was magnetically hard, with a coercivity of 0.2 - 0.32 T. Although it had a lower saturation magnetisation than the existing alloy magnets, it was much cheaper to produce, had a high electrical resistivity of 10^8 Ω cm and the high magnetic uniaxial anisotropy along the c-axis. The molecular weight of BaM is 1112 g and the maximum density is 5.28 g cm^{-3} [7], although in reality the ceramic material often has a density only 90% of theoretical density .

SrM, in which the barium has been replaced by the smaller strontium atom, has a density of 5.11 g cm^{-3} and molecular weight of 1062 g, but resembles BaM in most other physical properties [8]. The Pb^{2+} ion is sized in between Ba and Sr, but lead is a much heavier atom than barium, and so PbM has a molecular weight of 1181 g and a density of 5.65 g cm^{-3} [2]. CaM has never been seen as a pure phase, but it has been formed in glass by the glass crystallisation method [9].

1.2 The W ferrites

W ferrites have the formula $BaMe_2Fe_{16}O_{27}$, where Me is usually a first row transition metal or some other divalent cation, and the barium can be substituted by another group two metal. The first reported W ferrite was Fe_2W ($BaFe_2Fe_{16}O_{27}$) [3], but it was initially only made as a mixed phase with M and X ferrites. Single phase Fe_2W was found to have an easy axis of magnetisation in the c-axis of the hexagonal crystal structure, but had a much higher

electrical conductivity than BaM due to the Fe^{2+} ions.

All of the W ferrites have uniaxial anisotropy, except Co_2W ferrite ($BaCo_2Fe_{16}O_{27}$) [4], which has a molecular weight of 1581 g and a density of 5.31 g cm^{-3} [7]. This has a cone of easy magnetisation at a constant angle of 70° to the c-axis from -273 °C to 180 °C, at which point this anisotropy rotates towards the c-axis with increasing temperature until it becomes uniaxial at 280 °C, and the magnetisation remains in the c-axis with a further rise in temperature [10].

1.3 The X ferrites

The X ferrites were first reported in 1952 as a mixed phase with M or W ferrite, and have the chemical formula $Ba_2Me_2Fe_{28}O_{46}$, where Me is a divalent first row transition metal or some other divalent cation. The first reported X ferrite was Fe_2X, in which Me = Fe^{2+} [11], and this was also found to have a uniaxial magnetic anisotropy along the c-axis and density of 5.29 g cm^{-3} [7]. All the X ferrites have this uniaxial anisotropy at room temperature, except for Co_2X (molecular weight = 2688 g), which has a cone of magnetisation at an angle of 74° to the c-axis [12]. Like the W ferrite it resembles, this cone changes to adopt an orientation parallel to the c-axis at a higher temperature, in this case 143 °C [13].

1.4 The Y ferrites

The Y ferrites were the first ferroxplana ferrites to be discovered, and it is now known that nearly all Y ferrites have a preferred plane of magnetisation perpendicular to the c-axis at room temperature [4]. The formula of the Y ferrites is $Ba_2Me_2Fe_{12}O_{22}$, where Me is a small divalent cation, and the first two to be made were Zn_2Y and Co_2Y. The molecular weight of Co_2Y is 1410 g, and it has a density of 5.40 g cm^{-3} [7].

Co_2Y has a planar magnetic anisotropy at room temperature, but this changes to a cone of magnetisation below -58 °C. From this temperature to the Curie point the anisotropy remains in the preferred plane [4]. Cu_2Y is the only Y ferrite that has been found to have a preferred uniaxial direction of magnetisation [14].

1.5 The Z ferrites

The Z ferrites have the composition $Ba_3Me_2Fe_{24}O_{41}$, and they were discovered at the same time as the ferroxplana Y ferrites [4]. Co_2Z has a molecular weight of = 2522 g and a maximum density of 5.35 g cm^{-3} [7]. The Z ferrites all have a uniaxial anisotropy parallel to the c-axis, except for Co_2Z, which is planar at room temperature but has a complex magnetic anisotropy, with at least four different anisotropic states.

At low temperatures Co_2Z has an easy cone of magnetisation, at an angle of 65° to the c-axis, and this remains constant up to -103 °C. Between this temperature and -53 °C the angle increases to 90°, and the preferred magnetisation remains in the basal plane until it switches to the c-axis at some temperature between 207 and 242 °C [7;15].

1.6 The U ferrites

The U ferrites, $Ba_4Me_2Fe_{36}O_{60}$, although identified at the same time as the other hexagonal ferrites mentioned here, have not been characterised much either structurally or magnetically, but the density of Zn_2U has been calculated as 5.31 g cm^{-3} [7]. They all have uniaxial anisotropy except Co_2U, which has planar anisotropy at room temperature [16], and a molecular weight of 3622 g.

1.7 Other hexagonal ferrites

At least 61 distinctive members of the hexagonal ferrites family have been discovered, related to either the W or Z ferrites. Most of these are extremely large and complex compounds, and the largest so far discovered has the formula $Ba_{70}Me_{86}Fe_{444}O_{802}$ and a molecular weight of 52,450 g [17].

2. The structure of the hexagonal ferrites

All of the hexagonal ferrites have closely related, highly complex crystal structures [11], which can be interpreted in various ways as summarised in table 1.2. At a simple level, they can all be

seen as molecular combinations of the three ferrite compounds S (spinel, $MeFe_2O_4$), M ($BaFe_{12}O_{19}$) and Y ($Ba_2Me_2Fe_{12}O_{22}$). W ferrite, $BaMe_2Fe_{16}O_{27}$, can be considered as M + 2S, X ferrite ($Ba_2Me_2Fe_{28}O_{46}$) = W + M = 2M + 2S, Z ferrite ($Ba_3Me_2Fe_{24}O_{41}$) = M + Y, and U ferrite ($Ba_4Me_2Fe_{36}O_{60}$) = Z + M = 2M + Y. The other larger hexagonal ferrites are similarly composed. The Ba^{2+} ion is large, as is the O^{2-} ion, and the barium always replaces an oxygen atom somewhere in the oxygen lattice. As the barium ion is slightly smaller than the oxygen ion, it distorts the lattice in its immediate vicinity. The barium ion can be substituted by another divalent metal provided it is of sufficient size, such as strontium or lead, to maintain the structure without too much distortion. Fe^{3+} and Me^{2+} are much smaller ions and insert themselves in interstices between the oxygen positions, and as in inverse spinels, both divalent and trivalent ions inhabit both octahedral and tetrahedral sites in the oxygen framework. The ionic radii of various ions are compared in table 1.3.

Ferrite	Molecular formula	Molecular units	Spinel plates and hexagonal layers	Hexagonal blocks
S	$CoFe_2O_4$	S	S_1	1/2 S
M	$BaFe_{12}O_{19}$	M	$M_5 = B_1S_4$	SR
W	$BaCo_2Fe_{16}O_{27}$	M + 2S	$W_7 = M_5S_2 = B_1S_6$	SSR
X	$Ba_2Co_2Fe_{28}O_{46}$	2M + 2S	$X_{12} = M_5S_2M_5 = B_1S_4B_1S_6$	SRS*S*R*
Y	$Ba_2Co_2Fe_{12}O_{22}$	Y	$Y_6 = B_2S_4$	ST
Z	$Ba_3Co_2Fe_{24}O_{41}$	Y + M	$Z_{11} = Y_6M_5 = B_2S_4B_1S_4$	STSR
U	$Ba_4Co_2Fe_{36}O_{60}$	Y + 2M	$U_{16} = M_5Y_6M_5 = B_1S_4B_2S_4B_1S_4$	SRS*R*S*T

Table 1.2 Comparison of various descriptions of the molecular units of hexagonal ferrites. * = 180° rotation of that block around the c-axis.

To describe a hexagonal crystal four Miller indices h, j, k and l are needed. The principal axis is in the (0001) direction along the length of the crystal, and the three other axes are across the basal (0001) plane of the hexagonal polyhedron at angles of 120° to each other. The principal axis is named the c-axis and its length is the c lattice parameter. In the ferrites the three axes of the hexagonal plane are all equal, and so only one other parameter, a, is

required to describe a regular hexagonal crystal, which is the length of one of the sides of this plane. Therefore, only two lattice parameters, c and a, are needed to give the dimensions of the crystal.

Ion	Radius	Ion	Radius	Ion	Radius
Ba^{2+}	1.35	Co^{2+}	0.72	Fe^{3+}	0.64
Sr^{2+}	1.18	Ni^{2+}	0.69	Fe^{2+}	0.74
Pb^{2+}	1.20	Zn^{2+}	0.74	La^{3+}	1.15
Ca^{2+}	0.99	Mn^{2+}	0.80	In^{3+}	0.81
Mg^{2+}	0.65	Cu^{2+}	0.72	Al^{3+}	0.50
Li^{+}	0.60	Sc^{3+}	0.75	Ga^{3+}	0.62
Na^{+}	0.95	Cr^{3+}	0.62	Zr^{4+}	0.80
Cl^{-}	1.88	Si^{4+}	0.40	Sn^{4+}	0.71
Br^{-}	1.96	V^{5+}	0.59	Ti^{4+}	0.68
O^{2-}	1.40	Nb^{5+}	0.70	Ir^{4+}	0.68

Table 1.3 Ionic radii of various ions in Å [210;211].

2.1 The spinel-based model

The structures can also be thought of as plates of cubic close packed oxygens with smaller metal ions in octahedral and tetrahedral interstices, in the same arrangement as the spinel structure. The spinel is a close-packed cubic structure, in which the positions of the layers of four oxygen atoms repeat every three vertical layers to form an ABCABC lattice, these layers being approximately 2.30 Å apart. In the spinel structure, the interstices between these cubic layers are alternatively filled with three octahedral sites and one octahedral and two tetrahedral sites per four oxygen atoms, as shown in figure 2. The spinel layers form plates either four or six oxygen layers thick, and between the outer two layers at both ends of the plates only octahedral sites are occupied by the metal atoms. The W structure contains only six-layer plates (S_6), the X structure consists of alternating six- and four-layer plates (S_6 and S_4) and M, Y, Z and U of only S_4 plates [11].

These spinel plates are joined together by two possible barium containing layers, which

both have a hexagonal close-packed structure which repeats every two vertical layers forming an ABAB lattice. The B_1 layer is a single hexagonal close-packed layer with 3-fold symmetry between two spinel plates, in which one of the four oxygen atoms is replaced by a barium atom, with the remaining oxygen atoms grouped in two sets of triangles. The metal atoms are in plane in the centre of one triangle and out of plane at about half the layer distance above and below the centres of the other sets of triangles (fig. 3). These layers hold spinel plates so they always contain a mirror plane in the B_1 layer, giving rise to a sequence of hexagonal close packed layers. The B_1 layer appears in M, W and Z ferrites, where the mirror plane reflects the entire structure, and in X ferrite where it only reflects a limited number of adjacent layers [11].

The B_2 layer consists of two hexagonal close-packed layers between two spinel plates, in which one of the four oxygen atoms in each layer is replaced by a barium atom, giving two barium atoms in the B_2 layer. The barium atom in one layer is in contact with the three oxygen atoms of the other layer, and the octahedral sites between the oxygen atoms contain the small metal ions. There are other metal ions sites at one layer distance above and below, and there are more just out of the plane opposite each barium atom (fig. 4). These B_2 layers form a hexagonal close packed array with the adjacent spinel layers only. They occur in Y ferrite, which contains only B_2 layers, and Z ferrite, in which they alternate with the B_1 layers [11].

This rather confusing representation describes the structures of the hexagonal ferrites in terms of mostly cubic plates separated by hexagonal layers. The relationships between the structures are better demonstrated by combining the S and B layers into three distinct units which can be used to make any of the hexagonal ferrites, S_2 = two spinel layers, M_5 = a B_1 layer sandwiched between four spinel layers (M ferrite), and Y_6 = two B_2 layers sandwiched between four spinel layers (Y ferrite), as depicted in figure 5.

A superior way to describe the hexagonal structures is as being made out of three distinct blocks, related to the units above, which better relate to their unit cells and chemical compositions [7]. The blocks also have discrete magnetic characteristics that can be summed to give the saturation magnetisations of the whole ferrite, and these are discussed in chapter

five. The structures of the blocks and each ferrite are discussed separately in the following sections.

2.2 The S, R and T blocks

The S block consists of two spinel units and therefore has the unit formula $Me_2Fe_4O_8$, where Me = a divalent metal ion, and is equivalent to the S_2 unit (fig. 6). Therefore, each S block consists of two layers of four oxygen atoms with three metal atoms between each layer, in four octahedral sites where the cation is surrounded by six oxygen anions and two tetrahedral sites where four oxygen anions surround the cation. The S block is shown in cross section through the diagonal mirror plane of the cubic structure in figure 7, and it can be seen that this gives the S block a threefold symmetry.

The R block consists of three hexagonally packed layers of four oxygen atoms each, but one of the oxygen atoms in the centre layer is replaced by a similarly sized barium atom to give the unit formula $BaFe_6O_{11}$. This is equivalent to the M_5 unit with the top and bottom layers removed. The single barium atom in the block creates an asymmetry in some of the cation sites, resulting in five octahedral sites, no tetrahedral sites as they are pushed into octahedral sites by the bulky barium atom, and a five-coordinate trigonal bipyramidal site in which the cation is surrounded by five oxygen anions, a unique position only found in the R block (fig. 6).

The T block is made of four oxygen layers, with a barium atom replacing an oxygen atom in the middle two layers, to give the unit formula $Ba_2Fe_8O_{14}$ (fig. 6), and again this is the Y_6 unit with the top and bottom layers removed. Because there are two large barium atoms opposite each other in adjacent layers, both the barium and cations which would have been in the five coordinate sites are pushed away in opposite directions. This reduces the five-coordinate trigonal bipyramidal sites to four-coordinate tetrahedral sites, resulting in two tetrahedral and six octahedral sites.

The actual unit cells of most hexagonal ferrites consist of multiples of the molecular

ferrite, two molecular units for M, W and Z ferrite, and three molecular units for X and Y ferrite, but only one molecular unit for U ferrite. Due to the complex nature and large size of the unit cells, individual crystals of these ferrites can be very large. The various depictions of the unit cell are summarised in table 1.4.

Ferrite	Unit cell	Spinel plates and hexagonal layers	Hexagonal blocks
M	2M	$2M_5 = B_1S_4B_1S_4$	SRS*R*
W	2W	$2W_7 = 2(M_5S_2) = B_1S_6B_1S_6$	SSRS*S*R*
X	3X	$3X_{12} = 3(M_5S_2M_5) = B_1S_4B_1S_6B_1S_4B_1S_6B_1S_4B_1S_6$	3(SRS*S*R*)
Y	3Y	$3Y_6 = B_2S_4B_2S_4B_2S_4$	3(ST)
Z	2Z	$2Z_{11} = 2(Y_6M_5) = B_2S_4B_1S_4B_2S_4B_1S_4$	STSRS*T*S*R*
U	U	$U_{16} = (M_5Y_6M_5) = B_1S_4B_2S_4B_1S_4$	SRS*R*S*T

Table 1.4 Comparison of various descriptions of the unit cells of hexagonal ferrites. * = 180° rotation of that block around the c-axis

2.3 The M structure

The molecular unit of M ferrite is made of one S and one R block, with an overlap of hexagonally and cubically packed layers. The basal plane containing the barium atom is a mirror plane, and the two S blocks above and below the R block are therefore 180° rotations around the c-axis of each other. A mirror R block, R*, is then required to continue the structure, and it is for this reason that the unit cell requires two molecular M units, giving the unit cell formula SRS*R*, where * = a rotation of the block through 180° around the c-axis (fig. 8) The lattice parameters of BaM are 23.17 Å for the c-axis length and 5.89 Å for a, the width of the basal plane, and this a-parameter is constant for all the barium hexagonal ferrites [11]. The ratio of height to width is 3.94, so BaM has a large crystalline anisotropy, which becomes even higher for the other hexagonal ferrites. A perspective view of the structure is shown in figure 9.

SrM has smaller lattice constants due to the smaller size of the Sr^{2+} ion, giving the parameters c = 23.03 Å and a = 5.86 Å. Otherwise it has the same structure and unit cell

ordering as BaM [8]. The Pb^{2+} ion is also smaller than Ba^{2+}, and the lattice parameters for PbM are c = 23.02 Å, a = 5.88 Å [2].

2.4 The W structure

The molecular unit of W ferrite is composed of two S blocks and one R block, so it is similar to the M structure but not identical. There are now two S blocks above and below the R block, but again there is a mirror plane in the R block and the unit cell consists of two molecular W units to give SSRS*S*R*. The cell length of Fe_2W is 32.84 Å, it is a member of the space group $P6_3/mmc$, and the structure is shown in figures 10 and 11 [11].

2.5 The X structure

The X structure is very similar to that of W, being composed of one M and one W molecular units (fig. 12), to give the structure SRS*S*R*, with the blocks of the W section rotated through 180° relative to the M section . The unit cell is constructed from three identical units to give the crystal structure 3(SRS*S*R*), c = 84.11 Å, and it is a member of the R_3M space group [11].

2.6 The Y structure

The molecular unit of Y ferrite is one S and one T unit, with a total of six layers, the unit cell consists of three of these units, with the length of the c-axis being 43.56 Å, and is a member of the space group R_3m [11]. The T block does not have a mirror plane, and therefore a series of three T blocks is required to accommodate the overlap of hexagonal and cubic close packed layers, with the relative positions of the barium atoms repeating every three T blocks. This gives the unit cell formula as simply 3(ST), and the structure is shown in figure 13. The structure is shown in perspective in figure 14.

2.7 The Z structure

The Z unit is composed of Y + M, and therefore consists of ST + SR, with a mirror plane in

the R block and a repeat distance of 11 oxygen layers. Therefore, two molecular units are required to form a single unit cell of Z ferrite, one rotated 180° around the c-axis relative to the other, to give STSRS*T*S*R*, with a c axis length of 52.30 Å (fig. 15), and it is a member of the space group $P6_3/mmc$ [11]. A perspective view of the structure is shown in figure 16.

2.8 The U structure

The U ferrite structure has been found to consist of the molecular units Z + M, or M + Y + M, to give the block structure SRS*R*S*T (fig. 17). Unusually the unit cell consists of only one molecular unit, where c = 38.16 Å [17], in which the R and S blocks of the Z section are rotated through 180° relative to the M section.

2.9 The structures of higher hexagonal ferrites

The structures of 61 hexagonal ferrites have so far been established, including the ferrites mentioned above. These are divided into two groups, and in the higher hexagonal ferrites the molecular unit and unit cell are equivalent, as with Co_2U. The M-S series has five members, basic M ferrite without an S unit, and four others of the formula M_nS, where n = 1, 2, 4 and 6. When n = 1 W ferrite is formed and n = 2 is X ferrite. The end member of this group, M_6S, has a molecular formula of $Ba_6Me_2Fe_{76}O_{122}$ and a unit cell length of 223.4 Å. The other series is M_nY_p, in which n = 1, 2, 4, 6, or 8 and p = up to 33, and there are 56 members of this group including Y (n = 0, p = 1), Z (n = p = 1) and U (n = 2, p = 1). The highest ferrite so far reported is the enormous $Ba_{70}Me_{86}Fe_{444}O_{802}$ with the unit formula M_4Y_{33}, in which the units are in the sequence $MY_6MY_{10}MY_7MY_{10}$, and this has the largest inorganic unit cell ever seen at c = 1577 Å (0.158 μm!). The smaller $Ba_{62}Me_{54}Fe_{420}O_{746}$ is the most structurally complex ferrite, with over 400,000 possible grt permutations for the sequence of the M_8Y_{27} units. They occur in the sequence $MMMY_4MY_7MYMYMY_6MY_8$ and c = 1455 Å [17].

2.10 Electrical conductivity of ferrites

Although the hexagonal ferrites are good electrical resistors, if the bivalent ferrous ion is associated with the ferric ion, even in small amounts, it lowers the resistance greatly as an interchange of electrons can occur very readily, generating a current [18]. This is why magnetite is such a good electrical conductor for an oxide. There are two possible conduction mechanisms, n-type electron conduction and p-type hole conduction. In high resistance materials, if one cation is replaced by another that seeks a lower valency level then p-type conduction occurs, if the cation prefers a higher valency then it results in n-type. In ferrites excess iron promotes Fe^{2+} formation and n-type conduction results, but an iron deficiency results in p-type conduction which is very poor in ferrites [19]. Therefore, an excess of iron should be avoided if the material is to have any electrical applications. Unfortunately, the high sintering temperatures needed to promote a dense product also increase the proportion of Fe^{2+} in the ferrite, although an addition of manganese or cobalt in amounts as small as 0.02% lowers resistance by several orders of magnitude [20].

2.11 Iron oxides

The common forms of iron(III) oxide are haematite (α-Fe_2O_3) and maghemite (γ-Fe_2O_3). Haematite is a hexagonal crystal based on hexagonal close packing of O^{2-} with $^2/_3$ of the interstices filled with Fe^{3+}, each cation being surrounded by 6 0^{2-} ions, and it can act as a nucleation site for the growth of other hexagonal species such as α-FeOOH or α-Al_2O_3 [21]. The similar oxyhydroxide goethite (α-FeOOH) has the Fe^{3+} ion occupying $^1/_2$ of the sites, with each cation surrounded by 3 O^{2-} and 3 OH^- ions.

Maghemite resembles the cubic magnetite (Fe_3O_4), which is an inverse spinel with Fe^{3+} ions occupying some of the tetrahedral sites normally only inhabited by M^{2+} ions, but in maghemite cation vacancies compensate for the oxidation state of the missing Fe^{2+} ions. This leaves the Fe^{3+} randomly distributed over a mixture of tetrahedral and octahedral sites with only octahedral vacancies [22]. The compound could better be thought of as $Fe_{2.67}\square_{0.33}O_4$,

where □ = a vacancy, and it is really a solid solution with a variable cell parameter [23]. In the iron oxides the Fe^{3+} ion is always in the high spin d^5 state with all electrons unpaired, and has no preference for octahedral or tetrahedral sites [21].

3. Synthesis of ferrites

The formation of the hexagonal ferrites is an extremely complicated process, and the mechanisms involved are not fully understood despite having been investigated by many researchers for over 40 years [14;24;223;264;267]. If a non stoichiometric mixture of $BaO.Fe_2O_3.CoO$ is heated the following products generally form and decompose in this order:

	Major Products	Minor Products
500 °C	α-Fe_2O_3, Co_3O_4, BaO	
600 °C	α-Fe_2O_3, Co_3O_4, BaO	$CoFe_2O_4$, $BaFe_2O_4$
700 °C	α-Fe_2O_3, $CoFe_2O_4$, $BaFe_2O_4$	BaM, BaO
800 °C	BaM, $BaFe_2O_4$	α-Fe_2O_3, $CoFe_2O_4$
900 °C	BaM, Y	$BaFe_2O_4$, $CoFe_2O_4$
1000 °C	BaM, Y	$BaFe_2O_4$, $CoFe_2O_4$
1100 °C	Y, BaM	$BaFe_2O_4$
1200 °C	Z,Y, BaM	W
1300 °C	Z	Y, W
1400 °C	W, Z	

As can be seen (fig. 18), the different hexagonal phases all overlap, and except for the M ferrites they all need high temperatures of at least 1000 °C to become the major phase. This makes it extremely hard to obtain single phase specimens of some of these ferrites, and their particle size tends to be large due to the high temperatures required. At temperatures over 1200 °C an exaggerated grown pattern is seen, in which some particles grow to a much greater extent and at a greater rate than their neighbours, even in a single phase material. This morphology, containing a wide spread of particle diameters ranging up to many tens or even hundreds of μm, is named discontinuous grain growth (DGG), and individual hexagonal grains

up to 1 mm in diameter can occur. The solid state reactions are examined in more depth in chapter four.

3.1 Laboratory methods for the synthesis of ferrites

Standard ceramic techniques used to prepare the hexagonal ferrites involve heating a mixture of oxide and barium carbonate powders to produce the desired phase. The ceramic product then usually has to be milled and powdered to produce a finer material, and then sintered to increase density. The high temperatures and long firing times required usually result in a coarse grain product, with average grain sizes between 1 and 10 μm for the M ferrites, and up to 50 μm for the higher hexagonal phases, such as Y, Z and W. However, if the starting materials are intimately mixed at the atomic or ionic level before reaction, crystallisation occurs at lower temperature resulting in smaller particles and lower sintering temperatures, and the fully densified material can often be produced in one step [25]. Most of the following methods are based on precipitation of a ferrite precursor, and achieve this to varying degrees of success.

3.2 Coprecipitation

The chemical coprecipitation of salts with a base, resulting in a precipitate containing all the components mixed at an ionic level, has been used to produce ferrites since the early 1960's [26]. It has often been found that an iron deficient non-stoichiometric mixture must be used, for example with an Fe:Ba ratio of 10 - 11 for BaM, instead of the correct ratio of 12 [27]. SrM from coprecipitates needs an even lower Fe:Ba ratio of less than 9 to give pure M [28]. Using this process BaM can be formed at temperatures between 750 - 900 °C with a submicron grain size, and the density of the product can be increased if it is washed by centrifuge as opposed to decantation [29].

To improve homogeneity, a wet chemical process was developed in which an aqueous solution of metal salts was precipitated with a strong base, and the resultant hydroxide

oxidised by bubbling air through the suspension to give a homogenous fine grained ferrite product [30]. In more recent work a non-stoichiometric solution of iron(II) salts and barium salts are coprecipitated with NaOH at pH 14, and the resultant hydroxides are oxidised with hydrogen peroxide (H_2O_2) and then washed to pH 7. The dried hydroxides are then heated, producing pure BaM at the very low temperature of 600 °C and with a grain size below 0.1 μm [31]. Sodium hypochlorite (NaClO) has also been employed for a similar purpose to produce BaM [31]. Co_2Z has been made from the coprecipitation of very dilute solutions of barium and cobalt chlorides and iron nitrate, the precipitates being reacted together with acetic acid and an organic stabiliser, filtered, and then processed by normal ceramic routes to form Co_2Z [32].

3.3 Salt-melt method

In this technique a solution of metal chlorides is coprecipitated by NaOH, Na_2CO_3 or $NaHCO_3$ and then the salts NaCl and / or KCl are added to this mixture, which is then dried and heated to a flux between 600 and 1100 °C to give a mixture of the ferrite material and the alkaline metal salts on cooling [33]. The original process was less sophisticated, involving just a mixture of the standard ceramic precursors $BaCO_3$ and Fe_2O_3 heated in a flux of a NaCl-KCl mixture [34], but the coprecipitation stage results in a superior product. The sodium and potassium salts can be easily removed from the ferrite by washing with water or dilute acid, although there is inevitably some contamination of the ferrite product with the alkaline metals. BaM with good magnetic properties has been made by this process in a non-stoichiometric mixture with an Fe:Ba ratio of 10, and the submicron grain size and magnetic properties can be varied by changing the compositions of the fluxing components [35]. The highly insoluble sulphates are the cheapest and most abundant minerals of barium and strontium, and a salt-melt consisting of these sulphates, Fe_2O_3 waste from steel pickling and Na_2CO_3 with the Fe:Ba ratio of 11 has been used to make pure SrM and BaM over 860 °C [36].

A variation on this method is melt-flux precipitation, in which less fluxing material is

added, so that instead of a true liquid phase system forming there are only microregions of slightly melted salt in which the crystallisation occurs. This has been employed to make BaCoTiM from mixtures of γ-Fe_2O_3, $BaCO_3$, $CoCO_3$, TiO_2 and the fluxing agents $7BaCl_2.3B_2O_3$ [37]. When the melt-flux was heated radiothermally by an electron beam instead of normal thermal heating, the pure ferrite was formed at a lower temperature and with a grain size one third of the size at under 100 nm [38].

3.4 Ion exchange

The compound $KFe_{11}O_{17}$, or β-ferrite, is isomorphous with the M ferrites, but has no magnetic moment [11]. A cobalt doped BaM with the formula $BaFe_{11.5}Co_{0.5}O_{19}$ was made from the ion exchange of Ba^{2+} for K^+ in the compound β''-ferrite, $KFe_{10.5}Co_{0.5}O_{17}$, which was first synthesised from a stoichiometric mixture of metal chlorides heated to 700 °C. This compound was then added to a salt-melt of $BaCl_2$ and KCl at 750 °C for 24 hours, at the end of which a total substitution of Ba^{2+} for K^+ had occurred in 75% of the material, the rest remaining as β''-ferrite. After annealing at 900 °C the grain size of the M phase was 200 nm, and despite being 25% impure the magnetic properties were acceptable as the β''-ferrite is non-magnetic [39]. When the same synthesis was attempted in an aqueous solution of nitrates instead of a salt-melt only a partially substituted M compound resulted, containing both Ba^{2+} and K^+ ions, which had poor magnetic properties [40]. SrM single crystals have also been produced from the ion exchange of β''-ferrite single crystals [41].

3.5 Sol-gel

The sol-gel process mixes precursor particles, which can be inorganic or metaloorganic, on the colloidal scale, this mixing being retained when the material is condensed to a gel, and fine grained polycrystalline ferrites have been prepared by this method with a narrow size distribution. In aqueous sol-gel synthesis, an aqueous solution of metal salts is coprecipitated by a base, but instead of then drying and firing the precipitates are treated to form a colloidal

sol, which can then be concentrated to a gel and subsequently fired to give the ferrite [42]. The sol must be very basic if it contains precipitated $Ba(OH)_2$ as this compound is only stable at a high pH, and such a sol cannot therefore be formed by acid digestion and peptisation. An organic coordinating agent such as ethylene glycol is often added to the hydroxide solution to produce a sol, which forms a gel structure upon evaporation of the water. When BaM was made from a sol-gel route involving the evaporation of glycol containing coprecipitated salts to give a homogenous gel, it was still found that a non-stoichiometric mixture was needed, and a ratio of Fe:Ba of 10.5 gave M ferrite at 900 °C / 1hr with a grain size of only 200 nm [43]. Only the barium rich precursor yielded pure M without any α-Fe_2O_3 as a second phase, but with a ratio of less than nine $BaFe_2O_4$ appeared as a secondary phase instead [44], indicating that there is only a narrow compositional window for the formation of BaM by this method. An acid sol was produced by dissolving precipitated and washed iron(III) hydroxide in a citric acid solution at 60 °C, to which $BaCO_3$ was added in the ratio Fe:Ba = 11.6, and evaporated to form a viscous residue which formed a gel at 170 °C. After prefiring to remove the organic components this produced single phase BaM at 750 °C which consisted of hexagonal crystals in a narrow diameter range of 90 - 110 nm, and subsequent annealing had little effect on the grain size [45].

In the synthesis of BaM from an organic sol-gel precursor, crystallisation occurs from 680 °C as the iron oxide phases decompose, until single phase BaM is left at 1000 °C [46]. Using ethanol as the solvent, iron(III) nitrate and barium metal were heated at 80 °C under N_2 to make a sol, which when heated to between 800 and 900 °C gave 150 - 200 nm BaM. Pure BaM could be formed with stoichiometric mixtures, but the barium had to be between 0.72 - 0.95 wt% of the precursor sol [47]. SrM has been manufactured by the sol-gel process as a combusted foam and a spray roasted aerosol [48].

3.6 Stearic acid gel method

This is a sol gel method which avoids both coprecipitation and metaloorganic compounds. A

stoichiometric mixture of salts are dissolved in melted Stearic acid and heated at 80 - 120 °C / 2hr to form a clear sol, which upon cooling forms a homogenous gel intermixed at the atomic level. After combustion of the organic component at 450 °C this results in the formation of nanocrystalline products at low temperatures. $BaCo_xTi_xFe_{12-2x}O_{19}$, x = 0.6 with a grain size of 10 - 20 nm at 750 °C by this process [49].

3.7 Citrate synthesis

Ultrafine particles can be synthesised at low temperatures from decomposed citrates, the decomposition reaction being violently exothermic, in which generation of CO_2 results in a very porous product with a high surface area. To make BaM, a stoichiometric solution of metal salts was mixed with citric acid in a ratio of cation:citrate = 1, and ammonia added to raise the pH and form a homogenous solution. This was heated to 80 °C to drive off any ammonia remaining and added to ethanol to form an iron / barium / citrate complex which precipitated out due to alcohol dehydration, and this was then dried and decomposed at 425 - 470 °C / 48hr. This amorphous product, with a very small grain size of under 10 nm, was then heated to 600 °C to give BaM, although a temperature of over 700 °C was required to obtain a fully crystalline sample with good magnetic properties and a grain size of 60 - 80 nm [50]. Nanocrystalline SrM particles with a diameter of 42 nm have also been made from this technique at 800 °C [51].

3.8 Hydrothermal synthesis

In hydrothermal synthesis a solution of metal salts and a base are autoclaved under pressure to give the product. BaM was made by autoclaving mixtures of the metal nitrates and NaOH at 332 °C / 5hr, which was then annealed at 900 °C to give the pure crystalline product. It was found that an Fe:Ba ratio of 10 - 12 and an alkali ratio of $OH^-:NO_3^-$ = 2.5 - 4 was needed to give single phase BaM. Therefore, although this is also a coprecipitation technique the pure phase of BaM can be made from stoichiometric mixtures of barium and iron [52].

3.9 Glass crystallisation

In the glass crystallisation method the ferrite is produced from raw materials mixed with a glass flux, which is then cooled and heated to a temperature below the melting point of the glass to produce the ferrite. A small grain is attainable with this process, as the ferrite is contained within an amorphous glassy matrix, which is then removed with acid to leave the polycrystalline ferrite product [53]. BaM particles made from the glass crystallisation method using fine filaments of B_2O_3 glass produced hexagonal platelets less than 0.1 μm at 800 °C which grew to over 1 μm at 1000 °C. [54].

$BaCo_{0.77}Ti_{0.77}Fe_{10.46}O_{19}$ was made from a mixture based on 34 mol% ferrite and 66 mol% glass made from silica or boria. The mixture was melted at 1500 °C and quenched between rollers to give 30 mm flakes, which were then heated at 500 - 900 °C to produce the ferrite and leached in acid to remove the glass phase. B_2O_3 was found to be the superior glass, with M ferrite crystallising at 642 °C and giving a pure phase product with a grain size of 57 nm, compared to 260 nm at 800 °C with silica [55].

3.10 The combustion method

In a variation on the citrate process, the solution of salts, ammonia and citric acid at pH 7 was evaporated to dryness on a hot plate, at which point a self propagating decomposition occurred. A foamy mass swelled up and ignited in a violent exothermic reaction that propagated through the entire sample in 20 seconds, as the citric acid polymerised and evolved CO_2 and the cations were completely converted to α-Fe_2O_3 and $BaCO_3$. The driving force of this extreme exothermic reaction was the combustion of NH_4NO_3 formed in the neutralisation of the solution, and it produced a reaction temperature of 227 °C [56]. The speed of the reaction ensured that homogeneity was maintained and the evolution of gas produced a very porous foam structure that yielded a loose agglomeration when powdered. After firing to 700 °C the sample was mostly BaM with some a-Fe_2O_3 present, and it had formed pure BaM at 1000 °C, but the material has poor magnetic properties, probably because of the small grain

size causing superparamagnetic effects [57]. Other organic reducing agents have also been used, such as tetraformaltrisazine (TFTA, $C_4H_{12}N_6$) and oxalic acid dihydride (ODH, $C_2H_6N_4O_2$), which spontaneously ignite on dehydration and produce higher temperatures over 300 °C, to yield BaM with a grain size of 0.2 μm and good magnetic properties at 850 °C [58].

3.11 Self-propagating high temperature synthesis (SHS)

In this method once the reaction has been started, usually by a hot filament, the reaction enthalpy drives the self-energetic reaction to completion. A propagation wave spreads out through the material away from the initiation point at a velocity of 2 mm s^{-1}, causing rapid heating and cooling. SrM was formed from a mixture of SrO_2, which acted as the internal oxidising agent propagating the reaction, and Fe_2O_3 which absorbs some of the energy of the reaction, reducing the synthesis temperature from 2110 °C to 950 °C and preventing the explosive ejection of material from the reaction sites. The pure SrM was then annealed at 1200 °C to give a 1 - 2 μm product which had mediocre magnetic properties [59].

3.12 Spray drying

Fine hollow spheres of BaM have been made from the aerosolisation of a solution of metal nitrates, which was atomised and sprayed in a N_2 gas flow into a heated zone for only one second, after which the mainly amorphous spheres were collected [61]. These hollow spheres were under 0.1 μm in diameter, and they formed pure BaM with further annealing but had poor magnetic properties [62]. An industrial method of manufacture is from the freeze drying of iron(III)oxalate and barium acetate in cold pentane [60].

3.13 Water-in-oil microemulsions

A microemulsion is a dispersion of two immiscible liquids stabilised by an interfacial film of surfactant molecules, resulting in 5 - 10 nm domains of one liquid in the other. In this case aqueous droplets are dispersed in an organic solvent, and they continuously collide, coalesce

and then break apart again, mixing and exchanging their solute contents. If two microemulsions are mixed which are identical except that they carry different reactants in each aqueous phase, upon collision and mixing the reaction can take place to give nanoparticles, and the morphology can usually be controlled better than in normal coprecipitation [63].

This elegant method of controlled precipitation has been applied to BaM by using a stoichiometric metal salt solution and ammonium carbonate / sodium hydroxide solution as the two aqueous phases, to give a nanosized iron-barium-carbonate / hydroxide precipitate which was then separated, washed and dried. BaM forms over 600 °C and is single phase at 925 °C, with control of grain size over the range 120 - 170 nm. [64].

3.14 Thin films

The standard way of producing a polycrystalline ferrite thin film is via the rf sputtering of a ferrite target onto a substrate to give an amorphous film between 100 - 300 nm thick, which must then be annealed typically at 800 °C to form the ceramic phase. SrM [65], BaM and $BaCo_xTi_xFe_{12-2x}O_{19}$ films are the most commonly produced thin film ferrites by this process. BaM and SrM up to 200 nm thick have also been produced from the reactive evaporation method, in which iron and barium targets are heated by an electron beam in a vacuum to coat an α-alumina substrate. Although the pure ferrite films produced by this method had poor magnetic properties, a mixed Ba/SrM material approached bulk properties and all had the c-axis perpendicular to the surface [66], and oriented SrM thin films have also been produced from by pulsed laser deposition [67]. If using separate barium and iron targets they must be non stoichiometric, with an Fe:Ba ratio of no more than 8.

BaM films have been made from non-stoichiometric sol-gel precursors, by either dip coating [68] or spin coating [69] the sol on to a substrate, giving a crystalline product upon annealing with a submicron grain size and high magnetic values. To reduce the grain size to levels suitable for high density recording applications, additives such as Cr_2O_3 [70] and cobalt and titanium [71] have been added to the sol, and such films have the c-axis parallel to the

film. $BaCo_xTi_xFe_{12-2x}O_{19}$ films have also been made by dip coating with the c-axis perpendicular to the film [72], and a range of M ferrites doped with Me^{2+} / A^{4+} ions have been produced by rf sputtering for potential use as recording media [73;74]

A novel organic process for producing thin hexagonal ferrites films involved dissolving solid organic compounds of barium and iron in 1,2-dimethoxyethane under an inert argon atmosphere. This was injected a few microlitres at a time and heated to produce a film by CVD, 250 nm thick and magnetically oriented, on a hot sapphire substrate [75]. Magnetite films have been produced from the precipitation of an aqueous solution, which was then autoclaved with an organic chelating agent at 200 °C, and other spinel ferrites such as Co, Ni and Mn were made at only 100 °C by the same process [76] . This would enable the plating of substrates with a low heat tolerance such as plastic or biomedical products, and the system is compatible with both aqueous and organic compounds [77].

3.15 Industrial manufacture of ferrites

The raw materials used to manufacture commercial M ferrites are α-Fe_2O_3, either natural or synthesised from iron pyrite (FeS_2), iron chloride or organometallic pigments, and barium or strontium carbonates. Ferrites can be made from iron oxides recovered from waste steel pickling liquors, a cheap source of raw material in a sulphuric acid liquor with a high Fe^{2+} content. Goethite, haematite and magnetite have all been recovered successfully [78], and BaM with very good magnetic properties has been manufactured from the iron oxide recycled materials [79;80]. The iron oxides are granulated, mixed and presintered to form the M phase, milled again to improved homogeneity, pressed to increase density and sintered at up to 1400 °C [81].

In the dry milling of BaM, M_s and H_c are decreased with milling time because of two factors, an increase in lattice distortions from the induced stress and the formation of the magnetically weak BaO and α-Fe_2O_3 phases. Milling the material in a low oxygen pressure or a vacuum can reduce the second effect. Wet milling lowers the energy and gives a stress free

powder, removing the source of lattice distortions and preserving the structure of the M ferrite, but it also increases the rate of particle size decrease and after 60 hours M decomposes to the oxides. With increasing milling time H_c increases and M_s and M_r decrease as the particle size is reduced, but if surfactants are added to the liquid a large H_c value is still obtained but the decrease of M_r is lessened and a material with a square loop and higher energy results [82]. The ball milling of hydrated $Ba(OH)_2$ and Fe_2O_3 in a hydrophilic solvent encouraged the formation of micro-agglomerates enhanced the homogeneity and reactivity of the components, which sintered easily [83].

Ferrites can be granulated by the vacuum hot steam process, which gives a drier, denser, more homogeneous and more abrasion resistant material than other granulation processes. The ceramic is first homogenised and mixed in a high speed mixer by shearing forces, and then granulated by drying under vacuum as superheated steam is passed through the material [84]. In rubber isostatic pressing M ferrite with a small addition of calcium stearate is pressed in an external magnetic field and then sintered. This gives a highly dense (~5 g cm^{-3}) material with improved magnetic orientation, and if a fine grained ferrite is used both M_r and H_c can be optimised. For a high M_r material, 0.7μm SrM with 1 wt% calcium stearate is fired to 1240 °C to give a 99% oriented material with a coercivity of 0.300 T, and for a high H_c ferrite 0.3 mm SrM powder has 2 wt% stearate added, and the ferrite fired at 1200 °C to give a 96% oriented material with a coercivity of 0.400 T [85]. The optimum mixture, to make a 71% SrM plastoferrite with 99% orientation by injection moulding, was found to be 95 - 98% 2 - 3 μm grains with 2 - 5% 100 - 600 nm grains [86].

A simple method of making small grain, high coercivity ferrites is mechano-chemical processing, in which mixtures of iron and barium chlorides, in a non-stoichiometric ratio of Fe:Ba = 10, and a large excess of NaOH are milled together. A chemical reaction is induced giving a homogeneous mixture of metal oxides / hydroxides and NaCl, which can be washed out after the powder has been annealed at 800 °C to give BaM grains 100 nm wide and 20 nm thick [87]. Ferrites with a high length to diameter ratio are usually made by extrusion or

isostatic pressing [88] . Flat bars and sheets of pure BaM are made by pressing the dense pre-sintered ferrite perpendicular to the direction of extrusion, to give a material with a grain size of 0.5 - 1.3 μm [89], and monodisperse powders are produced by spray drying [90].

4. Applications of hexagonal ferrites

Magnets are used in a multitude of applications, for example motors, generators, transformers, actuators and sensors, information storage, diagnostic devices and to focus electron beams. The most used magnetic materials are ferromagnetic metals and alloys or ferrimagnetic ceramics, and a further explanation of these terms can be found in chapter five.

4.1 Permanent magnets

Magnetic materials for good permanent magnets need to be hard magnetically, resistant to demagnetisation. Therefore, they need to have stable domains, and must have a large remanence and coercivity. A large, square loop with a high energy product is also preferable, so more energy is needed to demagnetise the material. The M ferrites are ideally suited to such applications

In 1970 hard ferrites took the lead over alloys in world production, with 80,000 tonnes manufactured in 1977 [91]. Common uses of ceramic M ferrite magnets are in loudspeakers, windscreen wiper motors and other small electric motors, relays, clocks, magnetic separators, correction magnets in cathode ray tubes, dynamos and holding magnets. In 1974 65% of permanent magnets were used in the communications industry (and 70% of those as loudspeaker magnets), 20% for brake coupling and sealing devices and 15% in dynamos and motors. Communications uses include loud speaker magnets (70%), centring rings to focus cathode rays tubes, and magnetrons, used to direct electrons into a spiral path and generate microwaves.

4.2 Electrical devices

Usually the ferrite is expected to do work, enhancing the magnetic field as an electrical current

is passed through them. Such devices include the cores of electromagnets, motors, transformers, and generators, using AC currents. As the magnet must be cycled through the hysteresis loop continually and rapidly, so the energy product of the loop should be as low as possible. Hence a small coercivity and remanence is desirable, but the material must also have a high magnetic saturation and permeability to generate a sufficient induced magnetisation. Therefore, the ferroxplana ferrites are ideally suited for such applications, as despite being soft magnets from the rotation of the anisotropy within the plane or cone of magnetisation, they also have high magnetic permeabilities.

The material must also have a high electrical resistivity and a rapid realignment of domains in response to high frequency magnetic fields to minimise the energy losses. If the frequency of the applied field is too high the domains cannot realign each cycle causing the device to overheat due to dipole friction. At higher frequencies there is also more heating due to the completion of more cycles per second, resulting in the loss of more energy. Most hexagonal ferrites have a high resistance and therefore very low eddy current losses, so they are well suited for high frequency applications, at radio and microwave frequencies, especially if the remanence is raised. Films several μm thick are often used in microwave devices such as circulators and antennas, so a high deposition rate is required, usually sputtered by rf from a single non-stoichiometric target onto a silica or alumina substrate [92].

4.3 Data storage and recording

In digital memories a bit is stored as either 0 or 1, so a square loop with a big remanence is required to ensure the data remains stored and is not lost accidentally, and a high signal to noise ratio is required to reduce error rates. However, in re-recordable memories low saturation magnetisation and coercivity are required so small fields can be used to overwrite the data. In both cases chemical stability and longevity of the magnetisation is vital [93]. Commercial products include various makes of VCR tape, Professional Hi-8mm data tape, Sony DAT tape, Toshiba 4 MB floppy disks, and rigid or hard disks.

BaM and SrM are used for high density magnetic recording and magneto-optical recording, being chemically stable and mechanically strong, and with high saturation magnetisations. Oriented ferrites are used in both longitudinal and perpendicular recording, in which the magnetic anisotropy of the material is aligned respectively parallel or perpendicular to the recording media. In longitudinal recording the magnetic media is usually an acicular particulate of single domain size, with the longer axis aligned parallel with the direction of motion past the recording head, whereas perpendicular media consist of a polycrystalline thin film with the grains aligned parallel to the direction of motion of the disk, and not the head. The coercivity of M ferrites is too high for many recording applications, because a large magnetic field would be required to record and re-record data, but it was found that in doped M ferrites these properties could be tailored with varying substitution [94].

Cobalt-titanium doped M ferrites were first developed for recording by Toshiba in 1982, and they are particularly suited for use in recording media such as magnetic tape when coated as a thin film on to a substrate, as the grain size and coercivity can be lowered considerably but without much loss of magnetisation in the ferrite [95]. It is important that such materials have low switching fields, low magnetic losses and high signal-to-noise ratios, and all of these criteria are satisfied by the range of CoTiM ferrites. The ideal substitution level for longitudinal recording in $BaCo_xTi_xFe_{12-x}O_{19}$ was found to be $x = 0.7$, with a coercivity of 0.110 T [96], which is the lower limit for this kind of application [92].

Ideal high density recording devices need an information density of over 2 GB cm^{-2} and a high coercivity, but the grains should be as small as possible to increase signal-to-noise ratio and bit density, and magnetically isolated from each other to minimise transition noise [92]. BaM thin film recording media are promising, but they cannot have a protective coat for wear or erosion resistance, as these devices need a very low flying height for the recording head. Particulate media magnets are better than thin films in so far that they can have a better wear resistance, but they also tend to have lower magnetisations. One way around this is to make a composite ferrite consisting of two phases, such as BaM coated with nanocrystalline γ-

Fe_2O_3 or $CoFe_2O_4$.

The magnetic bubble memory is a recording device which was first studied in BaM single crystals [97]. If a polycrystalline sample of BaM was arranged so the c-axis is perpendicular to the hexagonal plane, and it had a small enough particle size, each grain carried a single bit of information in a cylindrical "bubble" domain. This kind of memory still has potential for use in computing, if a small enough grain size can be achieved to maximise the information density.

4.4 Plastoferrites

Plastoferrites, or bonded magnets, are magnetic composite materials in which a powder of a ceramic ferrites is incorporated into a resin or thermoplastic matrix. These have diluted magnetic qualities due to their composite nature, but the products are not brittle and fragile, and are hard to break or crack. They can be cut, stamped and shaped, in a highly mass productive and therefore cheap process, and complex shapes are possible with a high degree of dimensional precision. These include flexible sheets, very long or thin shapes and radially oriented materials, and many electrical components are manufactured in this way [91]. In the preparation of resin encapsulated ferrites compressive stress can be induced as the resin sets, and if the material has a negative magnetorestriction M_r will increase at the expense of H_c. Therefore, resins which shrink a lot or harden unevenly should be avoided, and some resins also generate extreme localised heat as they set, which could affect the magnetic properties [81]. Plastoferrites are most familiar as refrigerator door magnets, both the decorative type on the outside and the magnetic sealing strips inside the rim of the door.

4.5 Other applications

Various designs for sensors incorporating ferrites have been proposed, including a humidity sensor based upon the change of resistance in a copper-zinc ferrite [98]. A device has been proposed, consisting of a uniaxial hard ferrite wire or fibre, made with the anisotropy along the wire's axis, with a conducting coil wound around it and a BaM magnet at each end, which

could detect 0.7 mV per turn of wire in the coil [99].

A highly porous BaM was made by the citrate process at 900 °C, doped with 1 - 5 wt% Ir^{3+}, which stabilised the high surface area up to 1200 °C. The material was found to be a god catalyst for the clean combustion of methane [100].

Part B: Polycrystalline Ceramic Fibres

Ceramics are one of the oldest classes of man-made materials, with evidence of pottery dating back many thousands of years. They are hard, brittle compounds with complex crystalline structures formed from ionic or covalent bonding, and that break easily when subjected to mechanical or thermal shock. They also tend to contain many irregularities and defects in their crystalline structure, resulting in a wide scatter in their properties.

These features seem incompatible with transformation to a flexible, fine fibre of less than 10 μm diameter. However, the selection of precursor, a successful fibre production method and control of microstructure in the ceramic product can result in a fibre that has greater strength, toughness and flexibility than the bulk ceramic material. First developed commercially as refractory materials, ceramic fibres are now often used in composite form to reinforce other materials, extend their use to higher temperatures and reduce their scatter in mechanical properties of the composite, as well as many other more specialised high technology applications, and the range of ceramic fibres is reviewed in appendix B.

5. Properties of fibres

5.1 Aspect ratio

A fibre is a long, fine filament of matter that has a large aspect ratio. The aspect ratio is the fibre's length divided by the diameter of the fibre, and this can range from 10^1- 10^2 for short discontinuous fibres or thick fibres to near infinity for continuous fine fibres. There is no strict definition of what qualifies as a fibre, although the author would not consider a filament with an aspect ratio of less than 50 to constitute a fibre, and a fine fibre should have a diameter of < 30 μm. Examples of fine continuous aligned fibres produced by the author are shown in figure 19, and the early carbon, boron and silicon carbide fibres had diameters several times in excess of this, rendering them inflexible. By comparison a human hair is around 100 - 200 μm in diameter.

Not only is a continuous fibre better for many reinforcing and structural applications, but it can be collected in an aligned form either as a tow or a blanket, and if flexible and strong enough subsequently manufactured in a textile form. Some properties can also be enhanced in an aligned fibre as the aspect ratio increases, as is shown in figure 20 [101]. For a composite with a particle volume fraction of 10%, the magnetic permeability of the composite increases as the aspect ratio, A, increases, for a ferrite with a given magnetic permeability. As can be seen, the difference in the composite permeability for two fibres with aspect ratios of 50 and 100 becomes more pronounced as the magnetic permeability of the pure fibre increases. It was also found that in an array of lead zirconium titanate (PZT) rods with a diameter of 25 mm, electromechanical coupling effects increased with aspect ratio due an increase in the piezoelectric coefficient of the material [102].

5.2 Scatter of properties in fibres

In any population of fibres there will be a difference in diameter, defects, and mechanical properties between individual fibres. Therefore, while it is possible to give a value for the strength or size of a single fibre, this is not applicable to the fibrous material as a whole, as there will be a spread of such values throughout it. This inherent scatter of fibre properties ensures that a statistical approach is necessary to accurately describe the properties of a single fibre. As in any section of a blanket of fibres or a composite there will be hundreds or thousands of fibres such materials are well suited to such an approach, the results being most easily interpreted in the form of a histogram, reported as a mean or median value, or as a Weibull modulus. The Weibull modulus is approximately the reciprocal of the fractional standard deviation in fibre strength at constant fibre diameter. This gives a "bath tub" curve, with most of the fibres having values close to the mean, and a high Weibull modulus indicates a small deviation from this mean [103]. Unless otherwise stated, all values quoted for fibre dimensions in this thesis are either mean values, or the range of values is indicated. However, the properties of a section of a composite or a blanket can be measured and given for that

whole unit.

5.3 Strength of fibres

The stress-strain curve of a material passes through a maximum, and this point is the tensile strength of that material, so the stress-strain relationship can be used to describe the deformation and failure mechanism of a material. A ductile material is one which can deform plastically, becoming permanently deformed without breaking, and in such materials failure occurs below the maximum stress after necking has reduced the cross sectional area supporting the load. Ceramics are brittle, and so they behave largely as elastic bodies, that is they recover deformation when the applied load is removed, but in a brittle ceramic catastrophic failure occurs at the maximum load, as no plastic flow occurs. Therefore, the maximum load = breaking strength = tensile strength. This means that the tensile strength of a ceramic fibre is easy to measure using a simple technique such as the bend test detailed in chapter 4, although surface flaws can impede such a measurement, and any porosity in a fibre will decrease the cross sectional area on which a load is applied, serving as a stress concentrator and weakening the fibre [104]. Flaws also concentrate the stress in ceramic materials, with a fracture occurring when the stress at a flaw reaches a critical value, causing a crack to form. Other useful properties of a material are toughness (the ability to resist failure by impact) and hardness (the resistance of a material to penetration by a sharp object).

The scatter of the mechanical properties within a polycrystalline ceramic fibre is related to the grain size in the microstructure and the distribution of defects within its volume. A longer, finer filament demands a finer control of microstructure than that usually found in bulk ceramics, with upper limit of grain size obviously being the fibre diameter, although a grain size one tenth of this is required for a reasonably strong fibre. Also as the diameter is reduced the ratio of surface area to volume increases, reducing the importance of flaws within the volume [105]. In a study on the relationship of the tensile strength and diameter of glass fibre it was found that the strength increased from 0.7 GPa to 1.3 GPa, 2.8 GPa and 6.0 GPa as the diameter was decreased from 19 μm to 10 μm, 5 μm and 2.5 μm respectively [106].

Therefore, well sintered ceramic fibres tend to be intrinsically superior to the bulk ceramic, and are often incorporated into a metal or ceramic matrix to impart their properties to the composite as a whole.

5.4 Flexibility and stiffness

Handleability, due to flexibility, is an important feature for many applications of ceramic fibres, and is essential for textile operations. If flexibility is taken as a measure of the critical buckling load on a column with one end fixed, then the flexibility of a fibre is inversely proportional to the cross sectional modulus of that fibre, Ed_f^4, where E = elastic modulus and d_f = fibre diameter [107]. Therefore, the flexibility of a fibre is inversely proportional to the diameter^4. In investigations into the knotting of fibres between 3.6 and 9 μm in diameter it was also shown that, when allowance was made for the increased tensile strength of the finer fibres, knot strength is inversely proportional to the $d_f^{2.65}$ [107]. The strength of a woven fabric made of ceramic fibres is often less than that of the individual filaments it is made from due to poor abrasion resistance and lack of flexibility. However, the careful selection of the type of weave used can improve this, as in the case of carbon cloths [108].

As the flexibility of a fault-free fibre is determined solely by its diameter, so materials which appear virtually inflexible in their bulk form can behave like textile fibres as a fine filament. The flexibility of a fibre is quite different from its stiffness, measured by the elastic modulus, or Young's modulus, of the material, which is taken from the slope of the stress-strain curve in the elastic region. For example, glass is as stiff as aluminium with an elastic modulus of 70 GPa [109], but glass fibre with a diameter of 14 μm can be bent back on itself into a tight loop and woven into a cloth similar to a synthetic organic textile fibre, such as nylon which has an elastic modulus of around 4 GPa. Steel has an elastic modulus of 210 GPa, diamond (the stiffest material known) of 1200 GPa, fine carbon graphite fibre up to 800 GPa and the best polycrystalline α-alumina fibre of around 400 GPa [110].

5.5 Creep

At room temperature ceramics deform only as brittle elastic bodies. However, at high temperatures, usually over 1000 °C, they deform plastically or even super plastically, by a mechanism defined by their microstructure. Therefore, a ceramic heated over this threshold and put under stress will undergo a plastic deformation which is retained once the body has cooled down. This relaxation process is known as creep, and is obviously of great importance in ceramic used at high temperature, for instance as jet engine turbine blades. An established solution to this problem is the use of continuous fibre reinforcement in the ceramic matrix. Ceramic oxide fibres are a suitable candidate due to their high thermo-mechanical stability and resistance to oxidising atmospheres at high temperatures [111].

The creep process progresses through a mixture of grain lattice diffusion and grain boundary sliding/dislocation processes [112]. To best resist creep a fibre must be chemically and structurally stable at high temperatures, with as few random grain boundaries as possible to minimise easy diffusion. Therefore, a single crystal fibre possesses the best creep resistance, but for a polycrystalline fibre optimum flexibility and strength are enhanced by as small a grain size as possible. The best material to resist creep would be a stable, high melting point oxide with a complex crystal structure ordered over a long distance, as simple crystal structures have an easier potential for slip dislocation. From estimated creep behaviour the most resistant materials should be mullite ($3Al_2O_3.2SiO_2$, MP = 1850 °C, chrysoberyl ($BeO.Al_2O_3$, MP = 1870 °C) and yttrium aluminium garnet (YAG, $5Al_2O_3.3Y_2O_3$, MP = 1970 °C). The creep strength of these, defined as the tensile stress needed to produce a creep rate of 10^{-9} S^{-1} at 1600 °C, is respectively 480, 280 and 140 MPa - by comparison α-alumina (MP = 2000 C) is only 60 MPa [113]. These compounds still all have rather low melting points, so investigations are currently underway to produce higher melting point analogues of these compounds containing yttria, germania, zirconia and lanthanide oxides.

5.6 Health issues

Due to the many issues involved in research in the area and vested commercial interests, the damaging effects of ceramic fibres on humans are not well quantified. It is known that particles below 5 μm and fibres below 3 μm can be respired into the lung cavities. The diameter of a ceramic fibre has a major bearing on its carcinogenic properties, as while very small particles will pass straight into the blood stream, fine fibres with a diameter of 0.1 - 1 μm are carcinogens, probably due to their fibrous shape. In particular these cause the fatal disease mesothelioma, where the fibre is absorbed into body tissue from the lungs and intestines, and causes lesions which may turn malignant. However, fibres up to 3 μm may still have health effects, dependent upon their aspect ratio. Inorganic fibres with a diameter smaller than 1.5 μm and a length of over 8 μm exhibited carcinogenicity when implanted in to the respiratory system of rats [114].

Some mineral fibres, such as asbestos and the natural zeolite erionite, have a wide range of diameters going well into the submicron level, are extremely toxic at extremely small levels in the environment, either as airborne fibres or contamination in soil, rocks and water. These cause diseases such as silicosis and asbestosis, and the less serious but nevertheless debilitating fibrosis leading to severe tissue inflammation, as well as mesothelioma at extremely low fibre levels [115]. However, chemically inert aluminosilicate fibres with diameters below 1 μm are now acknowledged by the industry to be carcinogenic, and recent European legislation will restrict the use of ceramic fibres below 3 μm in diameter.

6. Manufacture of polycrystalline ceramic fibres

There are several basic types of polycrystalline ceramic fibre:

- Extruded or blown fibres from a melt of the ceramic material
- Composite fibres, either made by the core-sheath method, or boron and silicon

carbide fibres produced from chemical vapour deposition onto a core filament.

- Carbon, carbides, borides and nitrides produced from the pyrolysis of an organic polymer precursor fibre.

- Metal oxide fibres produced from the calcination of a precursor fibre material, which is itself spun, extruded or drawn from a precursor solution.

6.1 Melt derived fibres

As early as 1935 a process for air-drag spinning mineral fibres from a melt of waste mining products using a pressurised blast of air was patented [116], and in modern melt spinning kaolin is fiberised by blowing a thin stream of it with compressed air or steam. This rapid quenching results in discontinuous amorphous fibres less than 3 μm in diameter and several cm long, but as they are made from an elongated droplet the product maintains a very large droplet on the end of the fibre, and so can consist of up to 50% shot. Despite this, even today most commercial aluminosilicate fibres are made by melt spinning.

Vitreous continuous phase glass fibres have been extruded from a melt since the 1940's. Thompson Fibre Glass produced a fine grained polycrystalline fibre in a continuous form by conventional extrusion methods, with an organic binder and grain growth inhibitors added to limit the grain size to below 20% of the fibre diameter [104]. In 1941 Corning patented a method of mechanically drawing and collecting on a rotating drum fine glass fibres 0.5 - 2 μm in diameter from a platinum-rhodium orifice [117]. Glass fibres are amorphous silica, sometimes with other additives, in which the molecules are oriented along the fibre axis as the fibre is cooled rapidly to prevent crystallisation. Standard E-Glass fibre is made by Hoechst Celanese from the melt spinning of a mixture of 75% SiO_2 and 25% Na_2O, which then has the sodium leached away with acid to leave a 99% silica fibre 1.5 - 10 μm in diameter. The fused silica *Astroquartz* fibre is made by the same method.

In the recent melt-jetting method an alumina-rich melt is jetted into a reactive atmosphere of $CaCl_2$ and solidified to produce coarse filaments [118]. In metal melt jetting the

solution viscosity is extremely low, so a very high feed rate is required to produce a large enough stable jet length to reach the gas which then forms a stabilising surface. Due to this the method is limited to the manufacture of very coarse filaments and wires. In kaolin melt jetting the melt viscosity is much higher, enabling the production of much finer fibres.

6.2 Core sheath method

Perhaps the oldest way of making a core-sheath composite filament is the Taylor wire. A glass tube full of molten metal is drawn into a fine filament as small as 70 μm in diameter. In a variation on the process developed by the Narmco R & D division of Whittacker Corp., a tube of fused silica is filled with the core material, the end is melted in a flame and pulled to give a fibre 25 - 200 μm in diameter [119]. This combines the formability of vitreous fibres with the high elastic modulus of polycrystalline fibres by making a composite fibre. A fused silica sheath material is used because it has a high tensile strength and heat resistance, and will draw over a wide temperature range, and the core is usually composed of alumina based systems to exploit their stiffness.

6.3 Chemical vapour deposition (CVD)

The fibres made by this method are deposited on a metal or graphite core filament. The substrate must be electrically conducting so it can be resistance heated up to 1200 °C, and the resulting fibres are actually therefore composites themselves, with diameters of 100 μm or more.

6.4 Pyrolysis of an organic precursor fibre

This method is based on the PAN method of manufacturing fine carbon fibre from polyacrylonitrile, which is pyrolysed under tension to remove nitrogen and water and then heated to over 2200 °C to produced the graphite form. Now used to make ceramic silicon carbide and nitride fibres amongst others. The organic polymer precursor is melt spun as a fibre, then oxidised on the surface for stability, pyrolysed in a nitrogen atmosphere to produce

the amorphous form at 800 °C or β-SiC at 1200 °C.

6.5 Extrusion and spinning

Ceramic fibres were first spun from an adaptation of the process used to make *Rayon* organic textile fibres, spinning 60 continuous fibres at a time from a spinneret [120]. Discontinuous fibres can be either drawn by aerial drag in staple blow spinners [121] or drawn on centrifugal spinners and deposited as staple fibre on a collection drum or belt [122]. In centrifugal spinning a cup or vane measuring only 10 cm in diameter rotates at up to 10,000 RPM. Inertial forces dominate the discharge of the fibre which has a high spinning rate, but any disturbances due to particulates cause it to be ejected from the spinner and appear in the fibre as shot. The spinning must be protected with cool humidified air as the fibres are blown from a high speed rotating cup by a circumferential ring of hot air into a chamber at an intermediate temperature. Continuous centrifugal spinners have a high feed rate per site, and so need a very long jet length to allow the fibre time to dry, and have a correspondingly slow wind up rate.

Most commercial alumina fibres are now produced by dry spinning, where continuous fibres are produced as a jet from a solution through spinning holes, or spinnerets, and the gel fibre is formed by evaporation of the solvent. The fibres can be extruded from a viscous polymeric solution, where the fibres are spun relatively slowly, initially in air at ambient temperature to avoid premature drying and skinning of the solution surface before the fibre is fully drawn and subsequently dried [123]. Alternatively the fibres can be blow spun from a less viscous solution with jets of humid air, and then dried quickly with secondary hot air to form a gel fibre which can be mechanically collected on a belt or rotating drum as an aligned blanket, as in the ICI *Saffil* and *Safimax* processes [124;125]. A modified ICI blow spinning process is described in further detail in chapter three. In wet spinning, the spinning solution is coagulated in a liquid medium, and in extrusion spinning very viscous sols and polymers are extruded through spinnerets and passed through heated chambers to form the ceramic fibre.

A viscous suspension spinning process has now been developed to make continuous

fine filaments of any powdered ceramic over 1 km in length, but of only moderate mechanical strength [126]. It should be noted that many developmental fibres claimed to have been produced from a spinnable sol precursor are never actually spun. They are often just pulled by hand from a viscous sol, usually made from hydrolysed alkoxides, with a glass rod or some other such implement, to give a single gel fibre which must then be gathered by hand and dried before further processing.

6.6 Sol-gel

In traditional ceramic manufacturing processes the particles are sized over 1 μm, and precursor materials must be heated to extreme temperatures to produce a spinnable or extrudible melt. In the sol-gel process a high temperature ceramic fibre can be produced from the firing of a low temperature fibre precursor whose particles are dispersed on a colloidal or molecular scale. The advantages of the sol-gel process are described more fully later in chapter 2; the increased homogeneity allows crystallisation and sintering of the ceramic at a lower temperature and higher rate, reducing grain size and flaws in the fibre product. As the fibre has much smaller dimensions than the bulk ceramic, this fine scale homogeneity enables features such as surface roughness to be kept within viable limits.

All the polycrystalline alumina fibres commercially manufactured are produced from a stabilised alumina sol, or an alumina / silica mixed sol produced from either a solution of polyions (such as aluminium chlorohydrate), an organic polymer or a hydrolysed and condensed metal alkoxide solution. High purity quartz fibres, consisting of 99.999% SiO_2 and resistant up to 1000 °C, have also been made from an alkoxide precursor spun as a gel fibre and fired to 1000 °C [127].

The sol-gel fibre production process consists of these five steps:

- Synthesis of a stable stoichiometric sol
- Preparation of the sol for spinning
- Spinning of the sol and some drying to produce a gel fibre

- Further drying and decomposition to make a porous precursor fibre
- Heating to crystallise and sinter the ceramic

This process will be examined more closely in chapters 2 to 4.

This thesis is part of a wider, ongoing inorganic fibres development programme, in which a range of structural, magnetic and electronic ceramic fibres have been produced from an aqueous sol-gel based process. The advantage of using an aqueous precursor is that it can be made from air-stable starting materials, and contains only small amounts of organic compounds in the gel fibres to be removed during firing.

An extremely rudimentary method for making a so-called "fibre" from by a sol-gel method was proposed by Horizons Inc. USA, in the early 1960's. A film of a colloidal oxide suspension would be spread out upon a flat surface, which was heated strongly leading to rapid evaporation of the solvent, "fibres" forming from the cracking of the film along the radii of the deposit [128]. This was used to produce polycrystalline filaments of a range of ceramic oxides including alumina and silica. A similar process is observed if one of the author's sols is placed in a furnace at over 200 °C on a curved watch glass.

A similar, though much superior, method now used is the directional freezing of sol-gels. The sol is freeze-dried at low temperatures, increasing the viscosity and concentration to form a gel, and in which process the water forms ice crystals. The gel flows into the spaces between these ice crystals, and if the freezing is directional then the gel forms as filaments between columns of ice crystals, which can then be dried at 150 °C to leave oxy-hydroxide fibres. This process has been used to make amorphous silica fibres of 50 μm diameter and 200 mm length [129], but finer fibres can be produced by using more dilute sols and faster freezing rates.

6.7 Other methods of fibre manufacture

Workers at MIT first proposed using an electrostatic field and air blast to propel a molten liquid towards a charged collection target in 1936, producing a fibre during this travel [130].

Now, in electrostatic spinning, solutions can be discharged from a charged needle and thrown as fibre on to an earthed collection belt [131]. Babcock and Wilcox described tack spinning, where a roller is used to pull fibres from a sticky solution smeared on a belt [132].

Polycrystalline fibres with grains smaller than 0.25 μm can be made from the crystallisation method, although they are always low density, hollow filaments 2 - 100 μm in diameter. A good wicking material such as cotton or rayon is impregnated with a concentrated solution which is then heated so the solvent is flash evaporated giving rapid crystallisation. The core material is then pyrolysed leaving a hollow skeleton of the oxide behind.

In the normal cutting of a ceramic a problem called chatter vibration sometimes makes the tool vibrate at a constant frequency, chipping off small filaments with constant lengths in the region of 0.5 - 250 mm. The diameter can be varied from 20 - 500 μm by changing the cutting speed and feed rate, and up to 20,000 filaments can be produced a second. These filaments are triangular in cross section, but their rough surface can aid bonding in some applications.

7. Applications of polycrystalline ceramic fibres

Typically while being brittle and mechanically fragile to mechanical shock, bulk ceramics are hard, high melting point materials with high compressive and low tensile strengths, which have low electrical and thermal conductivity and good chemical and thermal stability. Ceramic fibres are mostly used for refractory and insulating materials, although other applications could include high temperature structural materials and reinforcements, electronics, magnetics, catalysis and use in sensors and abrasives. However, there is potential to modify almost any property of a ceramic material by manipulation of the microstructure, morphology, stoichiometry, density and processing conditions, so ceramics exist which are tough, ductile or super-plastic, good thermal conductors, electrical semi-conductors or even super conductors.

Ceramic fibres are more expensive than glass fibre and most polymer fibres. For example, E glass costs \$7 kg^{-1} and *Kevlar* costs \$44 kg^{-1}, compared to around \$66 kg^{-1} for

spun alumina, \$220 kg^{-1} for pyrolysed Silicon carbide and over \$700 kg^{-1} for boron fibres [105]. However, the advantages, higher quality products and high technology applications gained from ceramic fibres can still allow them to be an economically viable option, and even the most exepnsive inorganic fibre is still ten times cheaper than superalloys [133]. When the product is a top of the range golf club costing \$700, a passenger jet costing \$50m, a formula one racing car costing £100m, a B2 stealth bomber costing \$2bn or the astronomically expensive space shuttle, the higher cost of the ceramic fibres used becomes less significant. Therefore, the main impetus for high performance inorganic fibres has come from the aerospace and motor sport industries, where high strength, light weight and heat resistant fibres can increase range and payload or reduce weight and fuel consumption.

7.1 Composites

Brittle ceramics demonstrate higher strength in fibrous form, and can also add toughness to a composite through crack deflection. Ceramic fibres can be embedded in a matrix to reinforce and strengthen the composite material by increasing the elastic modulus and hindering crack propagation, or extend the use to higher temperatures by controlling creep. The strength and modulus of the composite can also be tailored to meet specific loading conditions. Alternatively the matrix can be used to support the brittle fibre and increase its toughness, or to complement the special properties of an effect fibre. A fibre composite can consist of short, discontinuous fibres in either random orientation or aligned in the same direction, or continuous aligned fibres. If the fibres are aligned, the composite can either be unidirectional, in which all the fibres are aligned within the same axis, or cross-plied, in which successive layers, or plies, of aligned fibres rotate through an angle, usually 90° or 45° (fig. 21), although multilayer unidirectional composites are also often manufactured from stacks of aligned sheets or tapes. Multidirectional composites can also be made containing fibres in a two- or three-dimensional weave, giving alignment in two or three axes simultaneously throughout the material (fig. 22).

The micromechanical stress is the local stress on distinct continuous phases of fibre, matrix or sometimes interfaces and voids, but in a composite it is often more useful to measure the total composite stress. In a multilayer composite this can measured as the ply stress, assuming homogeneity within each ply but where the properties of the fibre and matrix are smeared and no longer act as distinct phases throughout that ply, or as laminate stress which is the average of all the ply stresses across the thickness of the composite, in which the stresses of the individual plies are smeared [134].

7.1.1 Effect of fibre alignment on properties in composites

It has been shown that properties such as thermal and electrical conductivity, and magnetic, electrical, and optical behaviour can be enhanced in fibrous form [135]. The dielectric constant ε^* of a fibre composite material depends not only on the ε of the two composite components, but also on their geometry. The composite's ε^* can only be estimated, but if the geometry of the components is known the estimate approaches the true value, and this rule is also applicable to other properties, such as magnetic moment [136]. Some properties are independent of the particle size or crystalline anisotropy of the fibre material, but for other properties such as magnetisation this magnetocrystalline anisotropy must also be accounted for.

If the fibres are continuous and unidirectional, purely independent and isotropic material properties such as ε, thermal conductivity and density can be calculated from the rule of mixtures as purely additive parallel to the fibre axis. That is, the composite density, ϱ_c, can be written as

$$\varrho_c = V_m \varrho_m + V_f \varrho_f \qquad \text{Eqn. 1.1}$$

where ϱ_c = composite density, ϱ_m and ϱ_f = matrix and fibre densities and V_m and V_f = matrix and fibre volume fractions of the composite. A property such as thermal or electrical conductivity would approach the value of the most conductive material of the two, for

example the metal in a metal-ceramic composite or the ceramic in a resin-ceramic composite [105].

Similarly, if a stress was applied parallel to the continuously aligned fibres the elastic modulus, E, will also behave in a purely additive fashion, unless the applied load is so large that the matrix deforms and a non-linear stress-strain curve develops [137]. In this case the less stiff composite component contributes little to the elastic modulus of the composite, E_c , so for a fibre reinforced composite

$$E_c \cong V_f E_f \qquad \text{Eqn. 1.2}$$

On the other hand, if the load is applied perpendicularly to the fibre alignment, each matrix component acts independently, so in this case

$$\frac{1}{E_c} = \frac{V_m}{E_m} + \frac{V_f}{E_f} \qquad \text{Eqn. 1.3}$$

Therefore, continuously aligned unidirectional fibres produce anisotropic effects in directionally affected properties, with the strength and stiffness being highest parallel to the axis of alignment [105].

This has also been proved true for the magnetic permeability, μ, of an aligned fibre, provided any demagnetising effects between individual fibres are ignored, as it can be for a composite with a volume fraction below the percolation threshold (less than 15 - 30%) [101]. The permeability, μ_{eff}, of a fibre aligned parallel to an incident magnetic field can be calculated from

$$(\mu - 1)_{eff} = V_f (\mu - 1) \qquad \text{Eqn. 1.4}$$

Whereas for a fibre aligned perpendicular to the incident field,

$$(\mu - 1)_{eff} = \frac{V_f (\mu - 1)}{[1 + (\mu - 1)]/2} \qquad \text{Eqn. 1.5}$$

The change in the magnitude of the property at a varying angle between parallel and

perpendicular to the axis of alignment is not a linear one, as can be seen in the varying strength of the layers in a 0°/30°/60°/90° pile E glass reinforced epoxy composite, where each successive layer of aligned fibre is rotated by an angle of 30°. The tensile strength in the 0° pile (parallel) is 7 times that of the 90° pile (perpendicular), but the 30° pile is only 2.5 times as strong and the 60° pile only 1.2 times stronger when the load is applied parallel to the 0° pile (fig. 23) [105]. In the case of magnetic permeability, to get a good estimate of the total effective permeability contributions from all alignments of the fibre must be added. If a fibre is at an angle to the field it can be resolved into parallel and perpendicular components and the effective permeability will be the sum of these components. It is clear that in a fibre at an angle of 45° degrees to the incident field the contribution of the parallel component will be greater than that of the perpendicular component, so the effective permeability at 45° will have a value closer to that for the parallel fibre [101].

Fibres randomly oriented in a plane, where the plane = xy, are a more complicated case, but it has been shown [138] that ε can be given, in the plane and perpendicular to it in the axis z, as:

$$\varepsilon_z = \varepsilon_m + \frac{2V_f \varepsilon_z (\varepsilon_f - \varepsilon_m)}{\varepsilon_z + \varepsilon_f} \qquad \text{Eqn. 1.6}$$

and

$$\varepsilon_x = \varepsilon_y = \varepsilon_m + \frac{V_f (\varepsilon_f - \varepsilon_m)(\varepsilon_f + 3\varepsilon_x)}{2(\varepsilon_x + \varepsilon_f)} \qquad \text{Eqn. 1.7}$$

7.1.2 Metal matrix composites (MMCs)

Synthetic ceramic fibres have been available for the reinforcement of light alloys since the early 1960's, produced by CVD on a substrate core. The first materials so produced were boron fibres and silicon carbide fibres. Carbon fibres were also produced at around the same time and were used to reinforce aluminium and magnesium structures, and now alumina based fibres are most commonly used for this purpose.

MMCs exploit the lower rigidity of the matrix to deform plastically. The greater rigidity of the fibre reinforcements allows stresses to be transferred to the fibres through the matrix, conferring their strength to the composite as a whole. The mechanism of reinforcement is the transfer of a load applied to the composite to the reinforcing fibres by plastic deformation of the matrix around the fibres. A good bond between the fibre and matrix is vital, as the matrix is constrained by the rigidity of the fibres and suffers a shear, which determines the structural properties of the composite, a process described by the Cox Model [139]. This demonstrates that long, thin continuous fibres provide the best reinforcement, as they give the best transfer of load to the matrix.

7.1.3 Ceramic matrix composites (CMCs)

On the other hand CMCs have a very stiff matrix in which less rigid fibres are embedded. These fibres stop crack propagation throughout the composite material, and thus reducing brittleness, by a process involving debonding of the fibre matrix interface. The bridging of cracks by fibres and their subsequent pull-out means that the interfacial bond is of primary importance in structural CMCs, as described by the ACK model [140]. Firstly the fibres should be aligned parallel to one another. If the matrix cracks the fibres must not, so that the crack may propagate around the fibres, but the only way the crack can open further is by either the fibre breaking or the fibres pulling out of the matrix. If the bond between the fibre and matrix is strong the cracks either stop at the fibre-matrix interface or they deviate along that interface, so the fibre does not break, and the fibre pull-out mechanism determines the overall failure toughness of the composite. In fibres used to reinforce CMCs a poor interface bond is often ensured by coating the fibre surface in carbon or adding silica to the fibres.

7.1.4 Resin matrix composites (RMCs)

RMCs can be reinforced by the addition of ceramic fibres, in a similar fashion to MMCs. More typically however, the resin matrix is used to support a ceramic effect fibre; that is one which is desired for other than structural reasons, such as magnetic, electrical or optical properties.

7.1.5 Composite manufacture

In MMCs the matrix is usually a light metal or an alloy made from aluminium, magnesium or titanium, the metal being injected into a fibre preform itself made rigid with an inorganic sol binder. For CMCs the ceramic can be added to the fibre as a powder and the composite formed from a pressurised press moulding or physically squashed together in a squeeze casting. The fibre can also be infiltrated by a sol which is then dried to a gel and calcined to form the ceramic composite, or by chemical vapour infiltration forming. In an aligned composite the maximum possible volume fraction is 50%, as after this loading there is insufficient matrix to separate the individual fibres. For random fibre composites a lower aspect ratio allows the volume fraction to be increased. With an aspect ratio of over 100 fibres readily tangle, between 100 - 30 they bundle and clump together, and below 30 they flow like a powder. An aspect ratio of less than 20 is needed for a volume fraction of over 50%, and the maximum achievable is 80% [141]

The RMC matrix is usually made from a thermosetting resin or a thermoplastic, although rubber is also sometimes used. The resins are usually based on epoxides, which have good creep and environmental resistance up to 160 °C, or polyamides and phenolics which can go up to 320 and 250 °C respectively. Thermoplastics such as PEEK and PET have a much higher viscosity than the resins, so the fibre infiltration is difficult, but the resulting composite can be heated and reshaped. The plastic is impregnated either by dissolving in a solvent which is then evaporated after the fibres have been added, or by a melt / pressure process.

7.2 High temperature applications

Standard refractory fibre products are formed from the so-called acid refractories based on alumina and aluminosilicates. These consist of either a blanket of fibre, a brick composed of compacted fibres containing a large amount of porosity in the bulk to reduce weight and improve thermal insulation, or a mat or sheet made of a mixture of fibres, one component of which melts to a glassy phase at a lower temperature to act as a binder. An aluminosilicate

blanket resistant to 1350 °C has been fabricated by mixing aluminosilicate fibres with powdered bentonite and a resin binder [142], and silica sols are commonly used as binders for high temperature fibre boards.

Fibres are being developed which are stable at high temperatures in oxidising atmospheres – in the absence of O_2 carbon fibres would be best for most high temperature reinforcement applications, but above 400 °C they suffer from oxidation. Carbon fibres can resist at 300 °C for short durations but the material wears out quickly, as can be seen by its short life span in high temperature applications such as brakes and re-entry shields.

Silicon carbide demonstrates an outstanding resistance to oxidation resistance, and CVD boron fibres are used in aerospace frames such as the Space Shuttle. SiC fibres based on a titanium core are the only way of reinforcing titanium, and such MMCs are stable up to 600 °C. At present nickel based alloys are used in jet engines, but they can only tolerate temperatures up to 1100 °C, whereas engine temperatures can exceed 1600 °C. The alloy must be coated with a ceramic material and cooled with air channels to survive. Present ceramic materials used are stable at 1400 °C, and alumina and zirconia can be stable up to 1550 and 1650 °C respectively. However, an ideal fibre for jet engine use would be chemically and microstructurally stable at 1600 °C for 60,000 hours of use, less than 20 μm in diameter for flexibility, possess an elastic modulus of 200 GPa and a tensile strength of over 2 GPa at room temperature, and also be affordable!

In the early 1980's Japanese researchers produced small diameter fibres based on SiC from the conversion of an organosilicon precursor. This generated interest in the possibility of producing ceramic composites capable of surviving for long periods in air at temperatures over 1000 °C, although above this temperature the fibres strength fails as the surface pits. These fibres are non stoichiometric and their mechanical properties are not those of bulk SiC. The most recent generation of this type of fibre, which now include nitrides and borides, have a modified microstructure giving them long term stability at 1300 – 1400 °C. Above this temperature existing oxide fibres must be used, either with controlled polycrystalline

microstructures to avoid grain boundary sliding and dislocation, or as oriented single crystal filaments or whiskers. Silicon carbide is also used to coat other less heat resistant fibres, and has been bonded with aluminosilicate fibres to form a refractory mat or sheet [143].

7.3 Structural applications

Reinforced composite materials have been used since ancient Egypt when straw was used to strengthen mud bricks, to steel-reinforced concrete last century, to materials reinforced with ceramics, carbon, glass and polymers today.

Since *Saffil* was first produced in the early 1970's it has become the most widely used fibre reinforcement for light magnesium and aluminium alloys, and is also deployed in aluminium matrices to give abrasion resistance [144]. Also used are the 3M *Nextel* range of fibres, dating from the same time and composed of a mixture of amorphous mullite and γ-alumina. In the late 1970's duPont incorporated small-diameter alumina fibres into MMCs. All such materials exhibited improved stiffness and creep resistance compared to unreinforced aluminium, but their high costs limited their use. Discontinuous fibres are presently used in automotive engine applications, where long term durability and resistance to thermal fatigue and wear are of great importance. *Saffil* is used by Toyota to reinforce aluminium piston crowns for instance [145].

A wide range of non-oxide ceramic fibres have structural applications, especially as lightweight reinforcement. The high strength of boron and SiC has already been mentioned, but even stronger are silicon nitride, Si_3N_4 and boron carbide, B_4C. These materials are not as good as SiC at high temperatures but are both stronger and are used in lightweight structural composites. B_4C finds use as nuclear shielding, and with titanium boride, TiB_2, is also very hard and these are used in bullet proof armour and abrasion resistance. In *Sialon* fibres aluminium and oxygen are substituted into Si_3N_4 to give a fibre with the composition $Si_{6-x}Al_xO_xN_{8-x}$. This is used to produce a light weight ceramic fibre which is very tough and strong with a low thermal expansion coefficient, with applications in engine components [105].

7.4 Other specialist applications

Some non-oxide fibres such as TiB_2 are good thermal conductors and may be used as heat sinks, and TiB_2 is also a good electrical conductor [105]. The author has manufactured aligned conductive magnetite fine fibres which could be used as sensors to detect damage in a composite material [146]. Superconducting Bi-Pb-Sr-Ca-CuO fibres have been produced, spun from a sol gel precursor and heated to 850 °C, which become magnetic below 110 K and have zero electrical resistance below 98 K [147].

As well as a refractory and structural material, alumina is used as an electrical insulator in spark plugs and to support electronic circuits, and in dental and orthopaedic applications due to its low reactivity. *Saffil Ecoflex* mats are flexible and resilient up to 1200 °C, and their excellent recovery from compression and the exertion of engine pressures makes them suitable as automotive catalyst support materials. Titania based fibres also have potential applications in the manufacture of artificial replacement joints and bones. Titania based fibres can also be piezoelectric, that is they change in length when an electrical current is passed through them and generate a current when stressed, in an analogous process to magnetorestriction. Such fibres could be used as sensors, artificial muscles, vibration dampers and ultrasonic generators. With longitudinally aligned fibres produced form a sol-gel process, a damping loss factor of 12% has been obtained in a composite at a fibre volume fraction of 30% [148]. Although these materials only extend a few μm for every cm of length, a woven or braided fibre material can contain very long lengths of material in a small volume, with a fibre volume fraction of 25%. Such a material would be a much more efficient vibration damper or generator than a bulk ceramic [149].

Magnetic fibres have a host of potential uses, from hard magnetic materials, transformers, inductors, switching elements and magnetorestrictive devices, to storage memories, recording devices and EM wave absorbing and shielding materials. For the latter applications a high permeability nickel-zinc spinel composite fibre was produced, for use at frequencies up to 1000 MHz [101]. These short discontinuous fibres could be incorporated in

a matrix in either an oriented or random manner, with either an accompanying dielectric filler material, or another dielectric fibre such as PZT aligned at an angle to the ferrites, as plies or as a weave, to minimise the demagnetising effects (Fig. 24). Continuous fibres are also used in composites where microwave transparency is combined with durability at high temperatures, such as radomes. Glass fibre is more suitable at lower temperatures because of its low dielectric constant, but at high temperature microwave applications alumina fibre is preferred despite its higher dielectric constant (low conductivity).

Chapter Two

Sol-Gel Precursors

1. The sol-gel process

A sol is a colloidal suspension of solid particles in a liquid, which upon condensation or concentration will form a continuous amorphous structure known as a gel. Other kinds of colloidal dispersion include aerosols (particles or droplets in a gas, to give a smoke or a fog respectively) and emulsions (droplets in a liquid medium, both being immiscible). The two types of sol are particulate sols made from inorganic precursors, or polymeric sols, made from either totally organic or metaloorganic compounds, such as the alkoxides which consist of an element with alkoxy (RO^-) ligands attached.

Sols are formed from the creation of colloidally-sized particles in a hydrolysis / condensation reaction. In hydrolysis a hydroxyl (OH^-) ion is attached to the metal (M) with a corresponding loss of ligand (L), and varying the amount of water used, catalyst used or time allowed can determine the degree of hydrolysis. For example;

$$ML_4 + H_2O \longrightarrow HO\text{-}ML_3 + LH$$

and condensation occurs by the linking together of hydrolysed molecules:

$$M\text{-}OH + HO\text{-}M \longrightarrow M\text{-}O\text{-}M + H_2O$$

However, the reactions involved are rarely as simple as this.

Polymeric sols made from silicon alkoxides were first used to make glasses by the Schott Glass Company in Germany in the early 1930's, and the particulate silica sol system has been the most thoroughly investigated since then [150], with particular interest in the homogeneity attainable from the intimate mixing of the sol-gel process. Polymeric sols are used to produce most commercial alumina-based fibres. Inorganic sols were not really investigated until the 1950's [151], when the nuclear industry developed techniques for

manufacturing ceramic microspheres from a wet process, avoiding the generation of radioactive dusts. Inorganic transition metal sols are now used to produce the TiO_2 coatings on toughened glass, semiconducting films, ferroelectric and superconducting ceramics, and magnetic ferrite films and particles.

1.1 The structure and stability of sols

A colloid is a suspension in which the dispersed phase is so small (1 - 1000 nm) that gravity forces are negated by short range forces such as Van der Waals attraction, surface charges and Brownian motion. This last process is the "random walk" diffusion driven by momentum from collisions between the sol particles and the molecules of solvent. The other forces are discussed in more detail below.

Van der Waals forces originate from the non-uniformity of electron distribution in two atoms creating a dipole, which is inversely proportional to separation[6]. They are created by three types of interaction, between permanent-permanent dipoles (Keesom forces), permanent-induced dipoles (Debye forces) and transitory-transitory dipoles (London forces). It is the last of these, London forces, which are responsible for the short range attraction between colloidal particles. As two identical atoms move closer together their electrons redistribute so as to minimise the total energy of the system. The transitory dipoles formed in this process have a net attraction, although the net permanent dipole moment remains at zero, and they fluctuate with a period of 1×10^{-16} s. This means that if the particles are more than 30 nm apart, by the time the EM wave has passed between them the distributions will have changed, and this effect is called retardation. It reduces the attraction, and in colloids retarded forces are reduced so much as to be negligible beyond this distance [152].

The attractive London forces are additive, resulting in flocculation of colloids if unopposed, and therefore a barrier must be extended in the nm range between particles. This can be achieved either by electrostatic repulsion in particulate sols known as the DLVO (Derjaguin, Landau, Verwey, Overbeek) theory of stability, or by steric repulsion. In steric

repulsion a thick organic layer is absorbed on to particles, which physically prevents close approach and agglomeration, and it must be over 3 nm deep to overcome the van der Waals forces. The large organic groups must mix together as two particles approach, but the chains entangle and restrict movement, and squeeze out solvent from between them, both processes raising the energy of the system [153]. In DLVO theory the net force between particles is a sum of van der Waals attraction, and electrostatic repulsion created by charges absorbed on the surface of the particles. This repulsive barrier relies on two kinds of ions forming a double layer of charge determining ions directly on the surface, and a cloud of counterions in solution around the particle to screen the charges of the charge determining ions [154].

In hydrous oxides the charge determining ions are either H^+ or OH^-, depending on the acidity of the M-OH bond in the particle, and this in turn is determined by the point of zero charge (ZPC). ZPC is the pH value at which the sol particle is neutral, being typically between 6 and 11 for M_2O_3 oxides. For Fe_2O_3 it is 8.6, for FeOOH it is 6.7 and for TiO_2 it is 6.0 [155]. Above this pH value the negative surface charge dominates, below it the positive dominates, and the magnitude of the surface potential increases with variation from the ZPC. Hydrous metal oxides are hydrophilic, so layers of water also adsorb strongly at the surface, bound by hydrogen bonding and dipole-dipole forces.

Counterions are strongly attracted by both the electrostatic potential of the charge determining ions and van der Waals forces, attraction increasing with polarisability of the counterion, which in turn increases with charge and size. A diagram of the double layer is shown in figure 25, in which the curved line represents the variation of the electrostatic potential, ϕ, with distance from the particle surface. This potential drops linearly from the maximum at the surface, ϕ_0, as it passes through a tightly bound layer of water and counterions known as the Stern layer, until the counterions are able to diffuse freely. At this point the potential decreases by a lesser and non-linear rate, according to Debye-Huckel theory, as the diffuse double layer (or Gouy layer) begins, the point of change being named the Helmholtz plane, with the potential ϕ_H. The more counterions present, the quicker the

potential drops in the Gouy layer and repulsion can be increased with only a small addition of counterions. If too many counterions are added however, the double layer can collapse, resulting in no repulsion and causing the flocculation of the sol.

If an electric field is applied to a sol, the charged sol particles move to the opposite electrode in a process called electrophoresis. These particles will carry along the Stern layer and part of the Gouy layer with them, up to a point known as the slip plane, where the potential is ϕ_Z, while the remainder of the counterions will move toward the other electrode. The rate of this movement depends on ϕ_Z, which is called the zeta potential, ζ, which is much smaller than the surface potential ϕ_0 because of counterion screening effects. The pH at which $\zeta = 0$ is the isoelectric point (IEP), which is usually not the same as the ZPC. To be stable, a colloid needs a repulsive ζ of at least 30 - 50 mV [156].

These attractive van de Waals forces and repulsive electrostatic forces can be summed by DLVO theory to give a net potential energy of the sol with distance from the surface of the particle, as shown in figure 26. Very close to the particle there is a very deep energy minimum at which point the repulsive forces are vastly out weighed by the attractive forces, but as the distance from the particle is increased the repulsive forces become more important because of double layer repulsion, giving an energy maximum V_{max}. As ϕ falls rapidly beyond the Stern layer there is a second small energy minimum, but this is too small to attract particles. If the counterion concentration is increased the volume needed for the shielding and reduction of ϕ by the double layer is reduced, and if the distance of the Helmholtz plane from the particle gets too small the net potential becomes attractive and falls in to the deep primary energy well, causing the colloid to rapidly coagulate. This explains why an addition of too many counter ions will collapse the double layer.

According to DLVO theory agglomeration happens by reduction of double layer repulsion, either through decreasing the surface potential of the particle by moving pH towards the ZPC or by increasing the number of counterions to over the critical concentration,

which depends on the valency of the counterion. The Schulze-Hardy rule states that the concentration needed to cause flocculation is inversely proportional to (charge of the counterion)^6, although this is only an approximate rule, and cannot be applied to chemisorbed or reactive ions. For two sol particles with the same surface potential, the repulsive barrier will be greater for the larger particle because of the influence of radius on van der Waals forces, and once a certain size has been achieved further growth is prevented by this barrier. In a polydisperse sol consisting of two distinctly sized species, they may aggregate together even if in individual monodisperse sols both would be stable, and the attraction is increased by a greater size differential between the two components [153].

The process of dispersal or redispersal of a colloid is called peptisation. Flocculated sols can often be redispersed by either washing out counterions if there are too many of them, or by re-adsorbing charge determining ions on to the surface by adding an acid or a base, to re-establish the double layer. However, if the potential energy has fallen over the potential barrier in to the primary potential minimum well the sol will be irreversibly coagulated. If enough charge determining ions are absorbed onto the surface of a particle it can result in charge reversal, reversing the signs of the ZPC, IEP and ζ. Some polyvalent cations can reverse charge in this way, giving electrostatic stability over a wide range of pH, but it is a process mainly seen in organic sols. It is not seen in unhydrolysed cations, and in divalent metal ions the high pH needed for hydrolysis to occur causes insoluble precipitates to form [157].

1.2 Particulate sols

These consist of dispersed, dense particles, such as oxides, hydroxides and hydrous oxides, and although they may be polymeric in nature, they are much denser than the linear polymers discussed in section 1.3. The particulate is partially soluble in the solvent, usually with the aid of an acid or base catalyst, and the hydroxides can dissolve and reprecipitate, with reversible condensation reactions occurring until an equilibrium state is reached. At this equilibrium a

denser structure than the single hydroxide will have formed by condensation, probably consisting on a oxide core with a hydroxide skin. As a minimum surface area is energetically preferred such particles can be thought of as Euclidean solid spheres of radius r, in which the mass is proportional to r^3 and surface area is proportional to r^2 [153]. The easiest method of making an inorganic sol is to spray a metal salt solution into base to precipitate the hydroxide, and then if necessary then peptise it to produce the sol, although it must be remembered when selecting the base that the ammonium ion will complex with some metals and alkali metals will remain in the product.

1.2.1 Hydrolysis and condensation of transition metals

Before hydrolysis the metal salt is dissolved in water, and it exists as an ion, M^{z+}, solvated by the water. A partial charge transfer occurs from the lone pairs on the oxygen atoms in the water to the empty d orbitals of the metal ion, and this in turn induces a partial positive charge on the hydrogen atoms in the water, making the water more acidic:

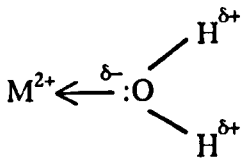

Assuming that no complexes are formed with the anion from the salt, this gives the hydrated species $[MO_nH_{2n-m}]^{(z-m)+}$, where n = coordination number of water and m = molar ratio of hydrolysis, and changing the water acidity, and therefore m, determines the form of this ion. One of the following ions will form:

$m = 0$	aquo ion	$[MO_nH_{2n}]^{z+}$	
$0 < m < n$	hydroxy-aquo ion	$[M(OH)_x(OH_2)_{n-x}]^{(z-x)+}$	
$m = n$	hydroxy ion	$[M(OH)_n]^{(n-z)-}$	pH
$n < m < 2$	oxo-hydroxy ion	$[MO_x(OH)_{n-x}]^{(n+x-z)-}$	
$m = 2n$	oxy ion	$[MO_n]^{(2n-z)-}$	

When m is an integer then a simple ion forms, but when m is not an integer one of the two complex ions form, and precipitated hydroxides are often really one of these [158]. The nature

and charge of the resulting ion depend upon the charge, coordination number and electronegativity of the metal, and the pH of the solution. At low pH cations with a valency of 4^+ or less give only the first three species in solution, with the hydroxy and oxo-hydroxy ions becoming more favoured as the pH rises. Pure oxo ions are only encountered with either very high pH or highly charged cations.

Hydrolysis is facilitated by an increase in charge density on the metal ion, the bridging of metals by oxo or hydroxo ligands, and ligands containing more protons, but it is inhibited as the number of hydroxo ligands coordinated to the metal ion increases. Using the partial charge model, when two atoms react charge transfer occurs from the most negative atom so that the electronegativity of each atom is equal to the average electronegativity. As the hydrolysis and condensation reactions occur through nucleophilic substitution and addition respectively, the substituent with the highest negative partial charge, δ^-, is the nucleophile and that with the largest positive partial charge, δ^+, is the leaving group in substitution reactions, and such reactions stop when there are no remaining nucleophiles with a negative partial charge. Both Fe^{3+} and Ti^{4+} form oxy-hydroxy complex ions when hydrolysed with a base.

The condensation reaction often has to be catalysed by the addition of an acid or a base, and proceeds by either nucleophilic substitution if the metal is already fully coordinated:

$$M_1\text{-}OX + M_2\text{-}OY \longrightarrow M_1\text{-}\overset{\displaystyle X}{\underset{|}{O}}\text{-}M_2 + OY$$

or by nucleophilic addition if the metal is not coordinately saturated, in this case increasing the coordination number of M_2:

$$M_1\text{-}OX + M_2\text{-}OY \longrightarrow M_1\text{-}\overset{\displaystyle X}{\underset{|}{O}}\text{-}M_2\text{-}OY$$

The oxo ion, predominant in very high pH solutions and high valency cations, although being a powerful nucleophile, can only be condensed by addition when one of the species is coordinately unsaturated, as the oxo ligand is a poor leaving group. Conversely the aquo ion,

which is predominant at very low pH solutions or with low valency cations, is a good leaving group but a bad nucleophile, and so condensation only occurs with the presence of an attacking nucleophile. Hydroxo ions and the complex hydroxy-aquo and oxo-hydroxy ions contain both good leaving groups (H_2O or OH) and good nucleophiles (O or OH), and condensation can occur as soon as one OH ligand is coordinated to the metal. The condensed species are called polyions, to distinguish them from the fractal polymeric species made from organic precursors.

Olation is the process in which condensation occurs by substitution, forming a hydroxy bridge between two metals:

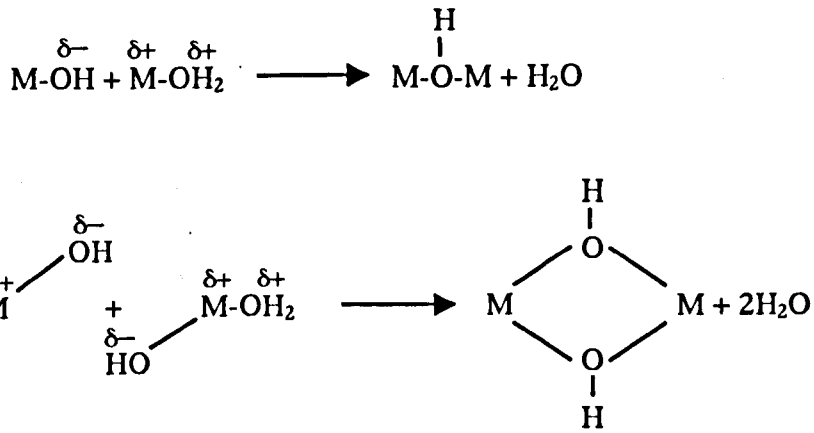

As the leaving group is H_2O, the lability is dependent upon the metal, and a larger size and smaller charge favour the dissociation of the aquo ligand, meaning that the Fe^{3+} aquo ion is much less labile than Fe^{2+}, Co^{2+} or the extremely labile Ba^{2+} aquo ions. As the electron donating aquo ligands are removed, any hydroxl ligands sharing the same metal become less δ^- favouring the formation of small oligomers in a narrow pH range [153].

Oxolation is the process where an oxo bridge is formed between two metals, and this can happen by either nucleophilic addition or substitution. With coordinately unsaturated ligands this happens by simple addition reactions:

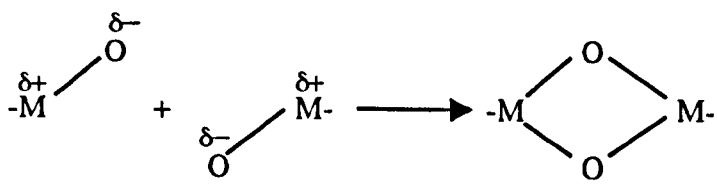

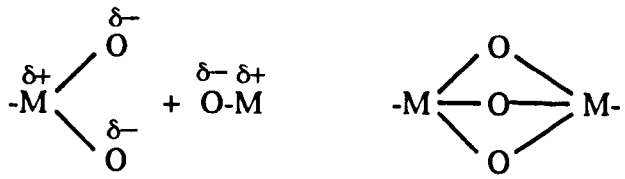

In coordinately unsaturated metals this happens in a two step substitution, catalysed by a base and an acid for each step respectively:

$$M\text{-}OH + M\text{-}OH \xrightarrow{OH^-} M\text{-}O(H)\text{-}M\text{-}OH \xrightarrow{H_3O^+} M\text{-}O\text{-}M + H_2O$$

Near their IEP neutral particles can condense virtually indefinitely via olation and / or oxolation reactions to form extended hydroxide / oxyhydroxide products, and this can result in either precipitation or gelation.

1.3 Polymeric sols

These are the most extensively researched form of sol, and are a suspension of colloidal polymers, with no oxides or other dense particles above 1 nm in diameter, the lower limit for a colloid. Unlike particulate sols, the solid hydrolysed phase is insoluble in the organic liquid phase and so the condensation reactions are irreversible. This means that the polymers usually form as 3D branched structures, with a dendritic or fractal pattern, as bonds form at random between the molecules, and these fractal patterns are non-Euclidian and less dense than particulate sols. Due to their branched structure, as radius increases so density decreases and surface area increases, compared to a solid sphere of the same radius. Therefore, polymeric sols consist of less dense and more porous particles than particulate sols. A 3D fractal polymer is unlike a crystalline structure in that it contains random branching out from a central point, and any closed loops that occur are well over the atomic scale in size.

1.3.1 Hydrolysis and condensation of alkoxides

The most studied polymeric sol systems are those of the group IV elements, such as silica sol made from the alkoxide tetraethoxy silane (TEOS, $Si(OCH_2CH_3)_4$). Alkoxides are either a liquid or can be dissolved in an anhydrous organic solvent to make a solution of the monomeric alkoxide, $M(OR)_4$. This is then hydrolysed by reacting 1 mol with n mol of water, and if $n < 4$ then the alkoxide is only partially hydrolysed:

$$M(OR)_4 + nH_2O \longrightarrow M(OR)_{4-n}(OH)_n + nROH$$

The hydrolysis step follows this general nucleophilic substitution reaction:

$$H_2O + M\text{-}OR \longrightarrow HO{:}\!\rightarrow\!M\text{-}OR \longrightarrow HO\text{-}M\!\leftarrow\!{:}OR \longrightarrow M\text{-}OH + ROH$$
(H under HO: and under :OR)

A partially hydrolysed monomer can then react with another monomer, either hydrolysed or unhydrolysed, as the -OH ligand is much more labile than the -OR ligand, and condensation occurs through a series of polymerisation reactions:

$$(OR)_3M\text{-}OH + HO\text{-}M(OR)_3 \longrightarrow (OR)_3M\text{-}O\text{-}M(OR)_3 + H_2O$$

$$(OR)_3M\text{-}OH + M(OR)_4 \longrightarrow (OR)_3M\text{-}O\text{-}M(OR)_3 + ROH$$

This occurs through nucleophilic addition:

$$M\text{-}OH + M\text{-}OR \longrightarrow M\text{-}O{:}\!\rightarrow\!M\text{-}OR \longrightarrow M\text{-}O\text{-}M\!\leftarrow\!{:}OR \longrightarrow M\text{-}O\text{-}M + ROH$$
(H under M-O: and under :OR)

The extent of the polymerisation reactions depends on the degree of hydrolysis, and the number of labile groups is given by the functionality, f, of the alkoxide. If f = 1, then molecules without any reactive -OH groups remaining will tend to form, resulting in short chains of 2 - 100 monomer units called oligomers, molecules which are between monomers and true polymers. If f = 2 then only linear structures or closed loops can result, leading to 2D networks, and this is often exploited to produce polymers suitable for spinning as fibres:

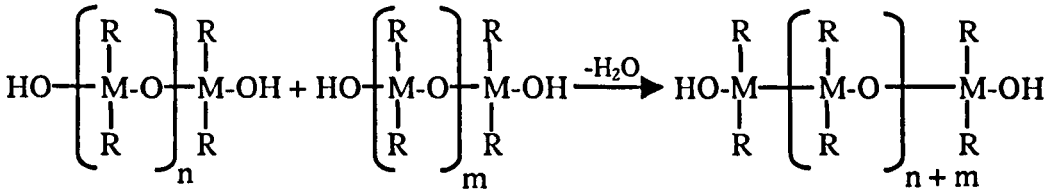

However, if f > 2 then side branching can occur, and this leads to a 3D structure:

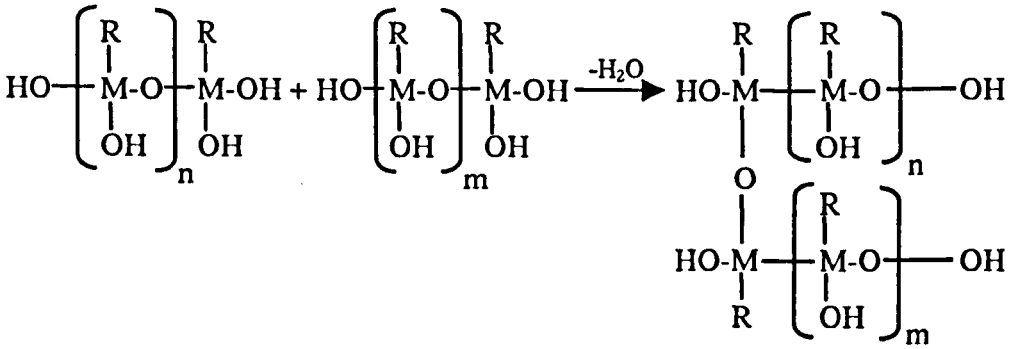

So it can be seen that the nature of the polymeric sol can be controlled by the hydrolysis step, with more 3D structures resulting from fuller hydrolysis of the alkoxide.

1.3.2 Metal alkoxides

These are metaloorganic compounds, in which a metal is attached to an organic ligand by a metal - oxygen (M-O) bond, as opposed to the metal - carbon (M-C) bond which exists in organometallic compounds. As the alkoxide group, RO^-, is an alcohol with the proton removed, these highly electronegative groups are very reactive, stabilising transition metals in high oxidation states but also leaving them open to nucleophilic attack.

Transition metal alkoxides differ from those of group IV, as the lower electronegativity of the metal makes the alkoxide more electrophilic and less stable towards the nucleophilic hydrolysis / condensation reactions. However, they are more reactive with moisture, and so they must be stored carefully, and careful control of the hydrolysis conditions is essential to obtain a homogenous gel, as opposed to a non-dispersible precipitate. Reaction times of transition metal alkoxides are very rapid and difficult to study, occurring within seconds as opposed to the hours needed to hydrolyse TEOS. They often have several stable coordinations, and when coordinately unsaturated they can expand coordination by either

olation, oxolation, or alkoxy-bridging, which occurs in polar solvents such as alcohols to form oligomers:

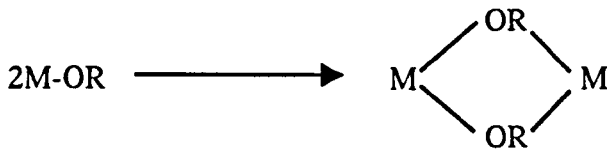

1.4 Gelation and ageing

Gelation occurs when the condensation or structuring between sol particles has reached such a point that it forms a 3D network, consisting of a continuous solid skeleton enclosing a continuous liquid phase. This means that it is possible to travel from one side of the gel to the other either entirely in the liquid or solid phases, but travel in a straight line will pass from phase to phase over distances on the colloidal scale. Fast transport of ions can also occur through the continuous aqueous phase, at a rate only slightly slower than in pure water [159]. This structuring is formed by van der Waals attraction and hydrogen bonding in inorganic sols, or covalent polymeric cross linking or steric entanglement in organic sols. The continuity of the solid phase gives the gel elasticity, but the bonds formed in gelation are sometimes reversible and can be broken up with an input of energy, and for this reason heating or shaking a gel can redisperse the sol particles. Many inorganic gels are thixotropic, that is they will flow as a thick fluid after agitation but will gel reversibly again with time, as seen in tomato ketchup, whereas most organic sols gel irreversibly. In inorganic sols the gelation rate also increases to a maximum as the IEP is approached [153].

In gelation the distance between particles decreases uniformly with change from sol to gel, without any change in the arrangement of the particles, but with changes in property. The clusters grow by coordination of polymers or aggregation of particulate until clusters collide with each other, forming a gel when a structure reaches across from one side to the other of a container to form a spanning cluster, which will not pour when tipped. Initially many smaller clusters will not be attached to the spanning cluster, but over time they will eventually all link together to form one giant single cluster, with an increase in stiffness. This gel point, when the

spanning cluster is first formed, is not accompanied by a latent heat, but there is a corresponding rapid increase in viscosity and the material becomes elastic. The time needed to gel an aqueous sol can be decreased by increasing the condensation rate using an acid catalyst, decreasing water concentration, increasing temperature, or decreasing the size of any alkoxy groups in an alkoxide precursor. For example 1 M TEOS has a gel time of 1000 hr at a pH of 5, whereas this can be reduced by the addition of 0.05M acid to 400 hr at pH = 0.3 with HI, 285 hr at pH = 0.2 for HBr, 100 hr at pH = 0.05 with HNO_3 and 92 hr at pH = 0.05 for HCl [153].

Classical gelation theory assumes that the polymers or agglomerates form as branches, without any closed loops, to form a dendritic Bethe lattice. The average cluster MW will increase and give a broad distribution of MWs, until the gel point is reached, when the average MW decreases as larger polymers attach themselves to the spanning cluster, leaving only smaller clusters free. This branching causes crowding at the periphery of the cluster, with the increase in density being proportional to the increase in radius, an impossibility as density can not increase indefinitely as the radius grows [160]. Therefore, classical theory is incomplete as it does not account for closed loops forming a less dendritic structure. In Percolation theory, which does not exclude the formation of closed loops, fractal aggregates grow until they impinge on each other, and link together with bonds formed between sites at random. As the number of sites bonded to another increases there is a broad range of cluster sizes, until a spanning cluster forms at the percolation threshold extending through the sol as a 3D network. The smaller solid phase clusters will then attach to this network to produce a single continuous structure [161].

When a sol is dried normally by surface evaporation, capillary pressure causes shrinkage of the gel network, resulting in a xerogel with volume reduced by a factor of up to 10. Alternatively if a gel is dried in an autoclave under supercritical conditions there is no interface between the liquid and vapour phases, and therefore no capillary pressure and little shrinkage. This results in an aerogel, a very porous and undense product which may be as little

as 1% solid by volume, and such materials are often still reactive with many labile sites [162]. The rapid evaporation of a solvent can also lead to the formation of a gel, as used in thin film preparation. Monodisperse sols of varying particle size can be made by adding a quantity of surfactant to an aqueous sol, which will then extract water from the sol when it is added to an organic solvent. If droplets of the sol are passed through an ammonia atmosphere to form a skin before they enter the organic solvent and surfactant mixture, almost perfectly spherical sol particles can be produced. Such sols have a lower repulsive barrier and ordered, almost crystalline structures, and improved density when dried to a gel. Gels made from ordinary aggregated sols have a porosity of ~70% and never become fully dense upon sintering, whereas gels from unaggregated spherical sols were only ~40% porous when dried and sintered at low temperatures. Gels of spinel and garnet ferrites have been made with a porosity of ~50% by this process.[153]. When the smallest dimension of the gel is several mm it is called a monolith, and such materials are frequently used as ceramic precursors.

Once the gel has formed, gelation reactions and condensation can still occur well beyond the gel point, permitting the flow and movement of segments of the network, and producing gradual changes in structure [163]. Other bond forming processes can also occur such as dissolution and reprecipitation, evaporation of solvent or phase transformations, and these changes after initial gelation are known as ageing. Therefore, ageing can improve a dried product, and improve crystallisation, densification and sintering.

Dissolution and reprecipitation in gels is driven by the differences in solubility between surfaces with differing radii of curvature. Particles have positive radii and are more soluble than a flat surface, and so smaller particles are more soluble than larger ones and reprecipitate onto them. Meanwhile crevices and necks have negative radii and so are less soluble and material tends to accumulate in them. These processes reduce the net curvature and surface area of the particulate, with small particles being adsorbed and small pores being filled, but this increases average pore size and strengthens and stiffens the gel (Fig. 27). No shrinkage occurs in this coarsening and ripening process, as the centres of the large particles do not move

relative to one another, but the growth of neck width gives strength to the network, and variations in temperature, pH, concentration and solvent affect the extent. The capillary pressure when drying a gel is proportional to the interfacial area, so coarsening also reduces this giving stiffer and stronger gels which can withstand this pressure, with less shrinkage and cracking in subsequent drying as a result.

Shrinkage can occur as a result of solvent evaporating from the surface of the gel, drying and deforming the network. Another process is syneresis, in which bonds or attractive forces between particles spontaneously shrink the gel, expelling liquid from the pores as a result, which can then crystallise on the surface of the gel as it loses solvent in turn [164]. In aqueous inorganic sols the amount of electrolyte, and therefore counterions present, can determine the rate of contraction of a gel through syneresis by reducing the double layer, and this rate reaches a minimum when at the IEP [165]. Phase transformation can also occur through microsyneresis, the localised segregation into solid and liquid phases, or the separation of the liquid phase into two components such as water and unreacted alkoxide. Nitrate salts are prone to crystallise and amorphous hydrous oxides precipitate out, and amorphous gels can become crystalline over time by dissolution and reprecipitation, as with hydrous alumina sols which slowly become crystalline aluminium hydroxide on standing [166].

1.5 Advantages and applications of sol-gel

There are many advantages to the sol-gel process [167]. Fibres, monoliths, films and monosized powders are obtainable from a uniform and reproducible process, with more precise compositional and microstructural control than is possible in standard ceramic methods. Gels are more porous than traditional ceramics, and this porosity, with high surface area and small pore diameter, can be maintained in the final product if desired by the lower processing temperatures used, as the small grain sizes involved lead to lower crystallisation temperatures. On the other hand the products can also be sintered and densified at lower temperatures, and it is even possible to sometimes sinter an amorphous product to give a

dense glass. The homogeneity is better because of the small scale intimate mixing of the components from the very beginning, and the lower firing temperatures required save energy [168]. The possible disadvantages include the relatively high costs of the raw materials, the high shrinkage and porosity intrinsic to the gelation process and the existence of residual fines pores trapped within the final ceramic body. If using an organic based route many of the solutions and solvents used are toxic and residual carbon can also be retained in the end product, affecting properties such as conductivity, and the process is generally longer and more complex than simple solid state reactions of oxides and powders, although much shorter firing times are usually required [169)].

Inorganic sol-gel was first developed to avoid the dangerous dusts produced in the processing of radioactive oxide fuels, which were made by a dry standard ceramic process. However it was found that sol particles 5 - 50 nm could be gelled into highly monodisperse, free flowing spheres with diameters ranging from 10 μm - 1 mm [170]. In turn these can be fired into extremely homogeneous ceramics, and if a mixture of three sizes of particle differing in diameter by increments of a factor of seven was mixed together by vibration a packing density of over 90% could be achieved [171]. This was used to make dense nuclear fuel rods, with less risk of contamination.

Fibres and filaments are made from either the spinning of viscous sols or the unidirectional freezing of gels. Commercial continuous fibres are mostly spun from sols made by the acid catalysed hydrolysis of a metal alkoxide using low H_2O:metal ratios, or organometallic precursors. The resulting gel fibres are microporous with a high amount of residual organic matter. The use of inorganic solutions of polyions or particulate sols to produce fibres is often overlooked, even though 3M, ICI, Denki and Matsui have all used particulate sol precursors. Unidirectional freezing gives non-continuous filaments with polygonal cross sections and high surface areas, and they are therefore good catalysts and enzyme supports. The highly porous aerogels are also used to make free-standing filters, membranes and catalytic substrates because of their large surface areas. Sols are used to make

polycrystalline thin films for optical, electrical, magnetic and protective applications, as well as porous films and coatings. Monodisperse powders grains and spheres made by sol-gel are used for ceramic precursor products, and homogeneous single components for optical, electronic and insulation uses and made from monoliths, bulk cast from a gel and dried without cracking. Sol-gel derived dense and hollow spheres are used to manufacture abrasives, high temperature superconductors, refractory materials, beads and waste immobilisation materials. Gels are also used to make the matrices for many fibre, whisker or particulate reinforced composites, or for the matrix of organic and metallic phases in CMCs.

1.6 The behaviour of aqueous iron(III) species

There are five polymorphs of FeOOH; Goethite (α-FeOOH), Lepidoctrite (γ-FeOOH), Akaganite (β-FeOOH), Feroxyhyte (δ-FeOOH) and Ferrihydrite ($Fe_5(OH)_8.4H_2O$) [172]. When precipitated with an excess of base, iron(III) solutions form brown gelatinous precipitates which have a composition between that of α-FeOOH and α-Fe_2O_3. The precipitate consists of needles of oxy-hydroxide 2 - 4 nm wide, and it is the ordering of these into rods which causes the gelatinous nature of the precipitate. With the removal of OH^-, catalysed by the addition of an acid during peptisation, a red polyionic species will form as spheres between 2 - 4 nm in diameter, containing approximately 100 Fe^{3+} ions, and with further removal of OH^- to a ratio of 1:1 with Fe^{3+} the dimeric $[Fe_2(OH)_2(OH_2)_8]^{4+}$ polyion will result through olation, which can nucleate γ-FeOOH [153]. ICI work on Fe^{3+} sols indicated that they are less stable than Al^{3+} or Cr^{3+} sols, and that the hydroxide sol is easily dehydrated to precipitate α-FeOOH [173]. This precipitates as long, thin needles [21], which can join together to form a tactoid agglomerates [153], and giving structuring and gelling the sol causing mudding and gelation rather than precipitation out of solution. Acidic iron(III)hydroxide sols made from $Fe(NO_3)_3$ with a particle size of 5 nm have been observed to flocculate with ageing, both by formation of crystalline goethite and aggregation of the amorphous sol particles [174].

It should be remembered that the anions used in solution will compete with the aquo ions for coordination to the metal, and a change in counterion can affect the particle morphology. Even when the metal is fully coordinately saturated complexation can occur by substitution reactions. While still being a nucleophile, the substituting ligand should have a lower electronegativity than aquo ion, to form a more covalent bond less likely to suffer ionic dissociation [153], and the new bond should be more resistant to hydrolysis if it is to remain in the particle. It has also been shown that ζ varies with changes in pH and anion in iron(III) sols [175].

2. Results and discussion

The initial aim of this research was to develop a stable multicomponent sol precursor, which would be suitable for blow spinning to produce the hexagonal ferrite fibres. Therefore, the system had to be able to contain up to four different metal species in varying proportions whilst maintaining the stoichiometry, homogeneity and stability of the sol, and capable of withstanding concentration up to a point where fiberisation was feasible. The only previous sol-gel fibre process to contain even three components is the *Nextel* range, containing aluminium and boron salts in a silica sol [123]. It is known that addition of over 10% M^{2+} ions to basic aluminium and zirconium salts cause gelation, and prevent spinning [176].

If gel fibres could be successfully spun then their conversion to a ceramic and the physical and magnetic characterisation of that product could progress. The possibility of adapting an existing method for synthesising a stable and spinnable iron sol, initially developed by ICI in 1979, was first investigated, although it had never been applied to compounds as complex as the hexagonal ferrites. Alternative methods of sol preparation were also investigated and compared, such as coprecipitation and metaloorganic based precursors. The solubilities of various relevant inorganic compounds are shown in table 2.1.

The sol-gel technique has always been considered a black art, and the processes involved in well established and studied single component systems are still not fully

understood after many years of study. The chemical interactions of ions in solution and sol particles in complex systems with up to four main components, as required to produce the hexagonal ferrites, are unpredictable and highly dependent upon the conditions and methods employed. Even the order in which components are added can have an effect upon sol stabilities, and a successful system is often developed by a process of simple trial and error, varying one element at a time and gauging the effect.

It was beyond the scope of this thesis to fully characterise and understand the structures of the sols produced. Therefore, only those properties directly relevant to the spinning of ferrites fibres, such as sol particle size, stoichiometry, stability, concentration and viscosity, were investigated. While a narrow particle size distribution would be preferable, it is known that a minimum polydispersity of 6% is required to prevent crystallisation from a sol composed of spherical particles [177]. The volume distribution of the sol particles has a direct effect on the spinning process, and even a small number of large particles can severely impede or even nullify the spinnability of the sol, as well as having stability effects Therefore, volume distribution was considered a more relevant measure than the number distribution or Z average, and the nature of the various values obtained from PCS measurements are explained in section 4.

2.1 Attempted use of the ICI iron(III) sol process

In previous work carried out by ICI for DERA, a method of synthesising a stable iron sol suitable for spinning from aqueous inorganic precursors had been developed [178]. This process involved the peptisation of an iron(III)oxy-hydroxide precipitate (Fe = 0.044 mol, 2.46 g) with HNO_3 in the ratio acid:Fe = 1:2, and simultaneous concentration to give a sol which was stable for several months. Lactic acid was hydrolysed in hot water and added to the sol as a stabilising agent, and the sol rendered spinnable by the addition of polyethylene oxide and concentration to around 15% Fe. This was successfully repeated and a reddish-brown sol formed after 30 minutes of digestion / peptisation on a rotary evaporator at 50 °C and under a

vacuum of 95 kPa. This sol had a viscosity of 0.6 poise, which did not increase with further peptisation, and a concentration of 17.7% Fe (3.17 M), which was stable with further concentration only up to 20% Fe, at which point the sol still only had a viscosity of 1 poise.

Compound	Solubility	Compound	Solubility
$Fe(NO_3)_3.9H_2O$	150 g 100 ml^{-1}	$Ba(NO_3)_2$	8.7 g 100 ml^{-1}
$FeCl_3.6H_2O$	91.9 g 100 ml^{-1}	$Ba(ac)_2$	58.8 g 100 ml^{-1}
$FeBr_3.6H_20$	Very soluble	$BaBr_2.2H_2O$	151 g 100 ml^{-1}
$Co(NO_3)_2.6H_2O$	133.8 g 100 ml^{-1}	$BaCl_2$	37.5 g 100 ml^{-1}
$Co(Ac)_2.4H_2O$	Slightly soluble	BaI_2	170 g 100 ml^{-1}
$CoCl_2$	45 g 100 ml^{-1}	$BaSO_4$	0.0002 g 100 ml^{-1}
$CoBr_2$	66.7 g 100 ml^{-1}	NH_4HCO_3	11.9 g 100 ml^{-1}
$CoBr_2.6H_2O$	Soluble	$NaHCO_3$	6.9 g 100 ml^{-1}
$CoI_2.2H_2O$	376.2 g 100 ml^{-1}	Na_2CO_3	7.1 g 100 ml^{-1}
$CaBr_2$	142 g 100 ml^{-1}	$Ba(NO_2)_2$	67.5 g 100 ml^{-1}
$LaCl_3.7H_2O$	Very soluble	$Sr(NO_3)_2$	70.9 g 100 ml^{-1}
$GdCl_3.6H_2O$	Soluble	$SrBr_2..6H_2O$	204 g 100 ml^{-1}
$YCl_3.6H_2O$	217 g 100 ml^{-1}	$SrCl_2$	53.8 g 100 ml^{-1}
$ZnBr_2$	447 g 100 ml^{-1}	$TiCl_4$	Soluble
$MnBr_2.4H_2O$	296.7 g 100 ml^{-1}	$TiBr_4$	Decomposes
$MgBr_2.6H_2O$	316 g 100 ml^{-1}	$NiBr_2.3H_2O$	199 g 100 ml^{-1}

Table 2.1 The solubilities at room temperature of various inorganic compounds [212].

Attempts were then made to dope the iron(III) sol with stoichiometric amounts of metal salts to form the hexagonal ferrites. As can be seen in table 2.1, the solubility of $Ba(NO_3)_2$ is relatively low at 87 g l^{-1}, and therefore a saturated solution of $Ba(NO_3)_2$ (261.33 g mol^{-1}) is quite dilute at only 0.33 M (4.57% Ba). A saturated solution of 0.96 g of $Ba(NO_3)_2$, the stoichiometric amount needed for the BaM composition (Fe:Ba = 12), nearly doubled the volume of the sol, reducing its concentration to only 9.8% Fe (1.75 M). While the stability of the sol appeared unaffected by the barium addition, upon concentration of the sol colourless needles crystallised out of the solution as the solubility limit of the barium nitrate was passed. This occurred below the minimum concentration of 13% that is required for a spinnable sol,

and this precipitation of $Ba(NO_3)_2$ at higher concentrations rendered the sol unspinnable, as well as upsetting the stoichiometry of any product and promoting flocculation of the sol over time.

As the cause of this problematic solid phase was deemed to be the low solubility of $Ba(NO_3)_2$, the sol was doped with stoichiometric amounts of more soluble barium salts such as $Ba(ac)_2$, $BaCl_2$ and $BaBr_2$. While some improvement was observed, the crystals still appeared at a sol concentration of over 13% Fe, caused by the presence of NO_3^- ions in the iron sol. The sol must be concentrated to at least 13% Fe for spinning, or else the distance between individual particles is too great resulting in a weak and dangerously thin fibre, which also contains too much water and becomes damaged upon drying. Although this was on the limit of spinnability, BaM has a lower barium content than all hexagonal ferrites except W. As the aim was to produce an aqueous, inorganic system capable of producing fibres of all the hexagonal ferrites, nitrate-free systems using alternative counterions were investigated.

2.2 Nitrate-free sol systems

To synthesise a totally nitrate-free sol based on the inorganic aqueous precipitation / peptisation process, both the iron(III) salt and peptising acid used had to be changed, as a small amount of nitrate could be retained within the precipitate. The sulphate ion had to be avoided because of the great insolubility of $BaSO_4$, so the halides were investigated. Iron(III)chloride hexahydrate was used as the iron(III) salt, as it has a very high solubility, and unlike iron(III)bromide is a cheap and plentiful compound. It was precipitated over 15 minutes to pH 5 with 4% ammonia solution added dropwise from a burette. The change of solution pH with addition of ammonia solution is shown in figure 28, clearly showing that the bulk of the addition occurred over a pH between 2 and 3 as the solution was buffered. Although a small amount of precipitate was formed from the beginning of addition, this steadily redissolved back into the solution, and the main precipitation commenced at pH 3 as the pH began to increase more rapidly. By pH 4 the precipitate had become very thick and the stirring speed

had to be increased to ensure mixing, but at around pH 4.3 the mixture became more fluid again, and remained so until the end point was reached. The acids HCl and HBr were used as the peptising agents in varying amounts, and other parameters in the ICI process were varied to gauge their effect. HI and iodide solutions are known to be photosensitive, so these were not used.

Firstly the halide sols were more temperature sensitive, and an irreversible flocculation occurred if the sol was heated to 40 °C. Therefore, the digestion / peptisation process was carried out at a temperature of 35 °C and the acid mixture was not heated before addition to the precipitate. The lactic acid stabiliser was also found to be unnecessary, and was omitted from the preparation. An acid:Fe ratio of 1:5, considerably smaller than that used previously, was sufficient with both HBr and HCl to supply enough counterions to form a stable sol, but the behaviour of that sol was found to be quite different in each case.

The chloride stabilised sol became a thixotropic gel at 7.8% Fe and was therefore unspinnable, due to cross linking between the chlorides. It was more sensitive to temperature than the bromide stabilised sol too, gelling reversibly at over 30 °C. The chloride ion has a slightly lower electronegativity (2.40) than the aquo ion (2.49), and therefore can attach to the metal ion in a sol particle as a ligand [153]. Chloride is also known to act as a bridging ligand between metal centres, and the thixotropy effects seen to some degree in all sols containing the Cl^- ion have been attributed to the extra structuring caused by this, which was sometimes beneficial to spinning in very small amounts. By comparison, the electronegativity of the NO_3^- ion (2.76) is higher than water, so it was lost to the iron in solution by ionic dissociation. The addition of $MgCl_2$ to aluminium chlorohydrate has been found to promote slow flocculation and enhance gelation [176].

The bromide stabilised sol was spinnable at over 31.4% Fe, an extremely high concentration for a sol to survive at, and HBr could be used to make a sol in ratios of HBr:Fe as low as 1:7, although the optimum was 1:5. Therefore, the bromide ions appeared to add stability to the sol, and this had to be considered in any non-bromide stabilised sols that were

attempted. This was predicted by DLVO theory, which states that of two counterions of equal charge, the larger will be attracted more strongly. Not only does this mean that the attraction of Br^- will be greater than Cl^- as a counter ion, but it also suggests that the even larger I^- ion would be more effective still.

The *B* coefficient is a way of representing the ion-solvent interaction of an ion, and the amount of order or disorder introduced into a solution by that ion, and is a measure of how strongly water molecules bind to that ion compared to each other . A negative value reduces structuring and a positive value enhances structuring, and the effect is known to be additive. OH^- has a positive value of 0.112, thus contributing to structure within the sol, and it also has an inverse viscosity-temperature dependence, perhaps partially explaining why the sols are so temperature dependent. The NH_4^+ and Cl^- ions both have slightly negative *B* values of -0.007, but Br^- has a higher value of -0.042, lessening structural effects between sol particles [179].

2.3 Nitrate-based sol system

It was thought that the halide ions may restrict the formation of the ferrite phases as they remained in the fibre until 1000 °C. As a stable sol could be made from halides with much less acid than was used in the original ICI preparation, it was decided to make a nitrate analogue of the Fe/Br sol, using HNO_3 in a ratio of 1:5 to iron. A nitrate sol was successfully produced which was stable up to 23.5% Fe, beyond which point it started to precipitate, and at which point it had a viscosity of 16 poise. Not only was this lower than the Fe/Br sol, but the sol was much more viscous and muddy looking than the Fe/Br sol at equivalent concentrations, adding further evidence that the Br^- ions actually help to stabilise the sol more than other counterions.

2.4 Sol particle size and behaviour

Particles in the 1 - 5 nm range tend to redissolve and the reprecipitate on larger particles in an Ostwald ripening type process, and this process has been seen to double the size of 4 nm silica sol particles [153]. Therefore, even a small number of larger particles can be detrimental to the stability of a sol, as well as causing problems later during spinning. Also if two distinct sizes of

particle coexist in an otherwise stable sol they can agglomerate, an event which becomes more likely with an increase in size differential, or as the sol is concentrated and temporary clusters can form.

While the counterion in the sol (Br^- or Cl^-) had an important effect on the interaction between sol particles, it made little difference to the particle size of the sol. Therefore, a series of experiments were undertaken to examine the effects of various parameters in sol preparation in the bromide system. Using PCS the average size and upper limit in size of the sol particles was measured after variations in both time and pH of precipitation.

The iron was usually precipitated to pH = 5, but a variation in pH between 4 and 6 was found to have little effect on the size of the sol particles, and the results are summarised in table 2.2. As the end pH decreased from 6 to 4 the volume average and upper limit decreased only slightly from 4.7 and 18.4 nm with 99.4% within 3.4 - 11.0 nm at pH 6, to 3.8 and 17.7 nm with 99.3% within 2.7 - 10.6 nm at pH 4. A larger differential was seen in the number averages, with 99.6% being within 2.3 - 7.3 nm at pH 6 and 99.3% within 2.7 - 4.5 nm at pH 4, as shown in figure 29. The very small change in volume distributions indicated that any changes would be insignificant regarding spinning concentrations, and this was found to be the case. Therefore, all sols were made by precipitation to an end pH of 5.

pH	Z Av. /nm	Vol Av. / nm	Vol upper/ nm	No. Av. / nm	No. upper / nm	Range / nm	Poly.
4	3.0	3.8	17.7	3.5	7.5	1.0 - 9.0	0.500
5	3.3	4.6	18.3	4.0	9.3	1.1 - 11.5	0.571
6	3.7	4.7	18.4	4.4	11.6	1.2 - 12.4	0.530

Table 2.2 PCS results for Fe/Br sols made from 15 min precipitations to various end pHs.

However, the duration of precipitation did have a major effect as shown in figure 30 and table 2.3, and any sols with an initial volume average of over 7 nm proved difficult to spin with the addition of other metals.

Precipitation	Instant	Mixer	3 min	15 min	30 min	60 min
Z Av. / nm	14.1	21.2	5.7	4.7	4.5	8.0
Vol Av. / nm	15.7	8.1	6.1	6.0	4.4	7.4
Vol upper / nm	49.9	94.8	25.2	20.0	20.2	28.3
No. Av. / nm	12.7	7.6	4.7	5.1	3.2	5.9
No. upper / nm	31.5	11.9	16.1	14.2	10.1	17.9
Range / nm	4.0 - 50.0	6.9 - 64.7	1.7 - 19.5	1.2 - 18.7	1.4 - 14.6	2.5 - 25.8
Polydispersity	0.643	0.499	0.605	0.760	0.550	0.551

Table 2.3 Effect of variation in precipitation time of iron(III)chloride on characteristics of Fe/Br sol.

For the instant precipitation samples 70 ml of ammonia solution was poured into the stirred iron solution in one go, resulting in a thick and uneven precipitate, and this clearly gave the sol with the largest size averages. In an attempt to produce a more even, but still rapid, precipitation, a mixer consisting of twin chambers which could be simultaneously emptied into a syringe consisting of a series of opposing blades to mix the two components before the precipitate suspension exited the syringe. A more dilute iron solution was required so the volumes of the two components was equal, and the entire addition and mixing process took 30 seconds. This resulted in a sol with smaller distributions averages, but they were still prohibitively high for spinning, and even worse although 99.7% of the volume distribution was within a small range of 4.7 - 11.9 nm, the remainder was as high as 95 nm. For addition times of 3 min and over, the ammonia solution was added through a burette at a uniform rate, whilst the solution and precipitate was stirred. An optimum precipitation time was found to be between 10 and 30 minutes, resulting in a sol with a volume average of 6.0 - 4.4 and an upper limit of 20 nm, and a number average of 5.1 - 3.2 nm and an upper limit <15 nm. The volume average distributions over the range or precipitation times are shown in figure 31*I*, and without the 60 min sample in figure 31*II* for clarity.

A slight improvement was also noticed if the solutions were all chilled in ice before and during the precipitation, and it was found that the iron(III)chloride decomposed slightly over a period of one year, giving an insoluble oxidised component that although very minor,

influenced the particle size. This decomposition could be observed by eye in the crystalline yellow iron(III)oxide as buff-coloured pock marks on the surface. When sols were made by the standard 15 min precipitation using a fresh supply of iron(III)chloride, all the particle sizes were found to be reduced slightly, as can be seen in the Fe/Br precursor sol used to make the CoTiM ferrite fibre detailed in section 2.9. This had a volume average of 4.7 nm with an upper limit of 20.6 nm, and a number average of 4.2 nm with an upper limit of 12.3 nm. It is known that any recrystallisation of the precipitate with ageing before peptisation hinders sol formation and increases particle size [180], and any crystalline oxide present would have the same effect. Other factors found to increase the average size distributions and upper limits were to use the minimum amount of HBr possible (1:7 HBr:Fe) and the retention of more chloride ions in the cake by less washing (shown by a higher conductivity of the washings), as shown in figure 32.

2.4.1 Bromide sol characterisation and stability

The standard bromide sol used as a basis for all hexagonal ferrite fibres was made from iron(III)chloride precipitated to pH 5 over 15 - 20 minutes, peptised with HBr and left to stand for 24 hours before use at a concentration of 10.5% Fe, as detailed in the experimental. The general, but small, decrease with time in the size distributions and other properties, taken from the moment when a sol had been formed by the digestion / peptisation process, is shown in table 2.4. After 24 hr the PCS data indicated that the sol had stabilised, with no further change in properties. The Z average of the iron(III) sol was 4.7 nm, with a polydispersity of 0.760, and the volume average was found to be 6.0 nm, with an upper limit on particle size of 20 nm, although 99.6% was within 3.1 - 14.2 nm. 99.2% of the number distribution was within 3.1 - 8.5 nm, and the number average was 5.1 nm with an upper limit of 14.2 nm (fig. 33). This agreed well with previous work giving the average particle size for FeOOH sols as 2 - 4 nm [153] and 3.5 nm [180].

Time / hr	0	1	2	3	4	5	7	8	20
Z Av. / nm	5.3	6.1	6.4	4.6	7.1	4.9	4.8	4.9	4.8
Vol Av. / nm	6.9	6.3	7.3	7.2	6.2	6.7	6.4	5.6	5.5
Vol upper / nm	31.3	34.5	29.1	25.0	31.6	27.1	24.3	23.2	22.4
No. Av. / nm	6.3	4.5	7.2	7.1	5.0	6.1	5.9	4.1	4.1
No. upper / nm	15.3	17.3	16.5	17.8	15.8	14.8	14.6	13.2	12.9
Range / nm	1.5 - 18.6	1.7 - 22.7	1.8 - 22.5	1.7 - 20.8	2.1 - 23.5	1.3 - 18.5	1.2 - 19.4	1.8 - 18.9	1.9 - 17.9

Table 2.4 Changes in characteristics of Fe/Br sol, made from 15 minute precipitation, over time from peptisation.

The 10.5% Fe sol had a pH of around 3, this being well below the PZC, and the zeta potential was measured as 38.4 +/- 1.4, within the range expected for a stable sol. The sol was found to be stable for a period of at least 3 years at a concentration of 11% Fe by weight, and was also stable at increased concentrations up to around 36.5% Fe, after which the sol began to precipitate out causing a "mudding" (loss of transparency) of the sol. The PCS sample was too dilute to show structuring with an increase in temperature. A small increase in size was observed with an increase in temperature to 30 °C, which then decreased again to previous levels with further sample temperature rise, indicating that the flocculation of the real sol with temperature was due to inter-particle bonding processes, rather than destabilisation of the sol itself. The results shown in table 2.5 are for a BaM sol, explaining the slightly higher values.

Temp. / °C	20	30	40	50	60
Z Av. / nm	6.7	7.2	7.4	7.6	7.8
Vol Av. / nm	7.2	8.1	7.3	6.9	7.3
Vol upper / nm	28.1	35.0	33.0	34.1	35.2
No. Av. / nm	5.9	6.1	5.3	5.2	5.3
No. upper / nm	16.9	22.1	16.5	17.1	17.6
Range / nm	1.8 - 25.2	2.0 - 27.3	2.1 - 25.8	2.5 - 23.3	1.8 - 22.0
Polydispersity	0.395	0.701	0.626	0.497	0.632

Table 2.5 Changes in BaM sol properties with increase in ambient sample temperature, for 15 minute precipitation.

2.4.2 Nitrate sol characterisation and stability

As can be seen in table 2.6, the Fe/NO_3 sol initially had a much larger average particle size and upper limit than the Fe/Br sol upon formation, and it required a longer period of at least 36 hr to complete peptisation. The decrease in volume distribution is shown in figure 34. The resultant Fe/NO_3 sol had a larger average particle size than the Fe/Br sol, with a Z average of 6.8 nm and a polydispersity of 0.658, and the PCS plots are shown in figure 35. Although the volume average was only slightly larger at 7.8 nm, it had an upper limit more than 50% higher at 31.5 nm, and 2.5% was over 19 nm. The number distribution was closer to that of the Fe/Br sol, with an average of 6.4 nm and an upper limit of 15.7 nm, but the relatively larger amount of higher volume material accounts some of the differences observed in stability and spinnability of the nitrate sols. The Fe/NO_3 sol was stable at a concentration only up to 23.5% Fe, and was only stable for around a year when stored as 10.5% Fe. NO_3^- counterions have been found to elongate α-Fe_2O_3 sol particles to 100 - 200 nm, compared to spheres under 100 nm when using Cl^- counter ions [153], and clearly are less beneficial than Br^- counterions to iron(III)oxy-hydroxide sols.

Time / hr	1	2	5	10	20	30
Z Av. / nm	37.7	22.4	14.5	13.9	9.6	7.0
Vol Av. / nm	30.7	18.7	15.7	11.8	11.6	8.6
Vol upper / nm	267.2	126.2	102.9	78.6	27.5	23.2
No. Av. / nm	24.5	14.9	11.0	9.2	11.1	8.2
No. upper / nm	67.1	39.9	32.5	31.3	20.0	15.7
Range / nm	10.1 - 140.3	6.3 - 80.1	4.3 - 49.4	4.3 - 45.5	3.0 - 30.8	3.0 - 23.6

Table 2.6 Changes in Fe/NO_3 sol characteristics over time from peptisation

2.5 Doping of Fe/Br sols

To produce precursor sols for BaM, Co_2Y, Co_2Z, Co_2W, Co_2X and Co_2U, stoichiometric amounts of barium and cobalt salt were added to the iron sol. It was therefore essential that the addition of the two salts did not destabilise the sol, and that a sufficient concentration to

produce a spinnable sol could be obtained, even for the highly doped Co_2Y sol with a M^{2+}:Fe^{3+} ratio of 1:3. Because of the problems with the solubility of barium nitrate and sulphate, these salts were also avoided for any other additives to the nitrate-free bromide sols. Most metal ions have a positive *B* coefficient, and Ba^{2+} has a very high value of 0.220 and also has an inverse temperature-viscosity dependence, so the addition of metal ions would be expected to increase overall structuring of the sol [179].

Barium acetate, chloride and bromide were all added to make stoichiometric BaM sols without destabilising the sol. However, upon concentration the chloride ions again caused the sol to structure at spinnable concentrations, and so chlorides were abandoned. BaM sols containing both $Ba(ac)_2$ and $BaBr_2.2H_2O$ were stable at spinnable concentrations, with the acetate containing sol precipitating at 12.43% Fe and the bromide at 18.29% Fe. Strontium bromide was also compatible with the Fe/Br sol at sufficient levels to make a stoichiometric SrM sol.

However, with the addition of cobalt to form a ternary system matters became more complicated. Again chlorides were shown to induce structuring at low concentrations, with a Z sol mudding out by 9.9% Fe and becoming thixotropic before this, but acetate salts were also found to precipitate small orange crystals of cobalt acetate at concentrations over 12.2% Fe in all ternary sols. As seen in table 2.1, cobalt acetate is only sparingly soluble, and caused the sol to precipitate even when a mixture of $Ba(ac)_2$ and $CoBr_2$ was used. Therefore, the use of acetate salts was also abandoned.

Using the bromides $BaBr_2.H_2O$ and $CoBr_2$ there were no problems with solubility or incompatibility, and doped sols with a loading up to Z stoichiometry were produced with concentrations up to 14.4%. However, the Y precursor sol had a borderline stability for spinning, and all the sols except BaM muddied slightly on standing over night. This did not occur in sols containing only barium or cobalt bromides, and the stability and transparency of the doped sol was improved if the barium bromide was added before the cobalt, implying that the cobalt was in some way destabilising the Ba^{2+} ions in solution. Co^{2+} is known to form

association complexes with chloride ions, and there is evidence of cobalt-bromide association complexes forming in solutions of over 5M HBr [181], as well as the known existence of many simple cobalt(II)bromide complexes [182]. Various organic additives known to sometimes stabilise inorganic sols, such as lactic acid, ethylene glycol and dextran, were added with either no, or in the case of dextran harmful, effect, and all were found to promote thixotropic gelation. Anhydrous $CoBr_2$ was used in preference to the hydrated form, as a small amount was found to decompose to the insoluble oxide over time, which affected both the sol stability and subsequent spinning. For this reason a stock 1 M solution of cobalt bromide was made up from fresh anhydrous cobalt bromide, and used to dope the sols to avoid this problem.

It is known that macrocyclic organic compounds can bond as multidentate ligands to cations, when the central hole is of the correct size for the cation, and there is a particularly strong affinity between alkaline earth metal and crown ethers [183]. The macrocyclic group increases solubility in organic and / or aqueous media, depending if it is hydrophobic and / or hydrophilic [184], to the extent that cryptates can even render $BaSO_4$ soluble, and without removing the hydration sphere or preventing ionic interactions of the Ba^{2+} ion [185], so such compounds are still able to form alkali earth metal complexes [186]. Known organic chelating agents for Ba^{2+} are 18-crown-6-ether and various substituted versions [183], in which the large Ba^{2+} ion is held in the centre of a planar ring of six oxygen atoms, as shown in figure 36, with a coordination number of up to 11 in the $[Ba(NO_3)_2(H_2O)(18\text{-crown-}6)]$ complex [187]. As the unsubstituted crown ether is very soluble in water this was investigated as a possible chelating agent to enhance barium solubility in the presence of the Co^{2+} ions.

It was found that if 18-crown-6-ether was dissolved in the barium bromide solution prior to addition, in a ratio of crown ether:barium of 1:3, then the adverse effects of cobalt addition could be avoided, the stability and maximum concentration of the sol increased, and spinning was also improved. With further crown ether addition structuring was induced in the sol, resulting in thixotropy. This use of this additive solved the final solubility / compatibility

problem, and stoichiometric sol precursors of all the barium / cobalt hexaferrites could be synthesised at spinnable concentrations and viscosities using the Fe/Br sol doped with barium bromide, 18-crown-6-ether and cobalt bromide.

2.6 Doping of Fe/NO_3 sols

In the Ba/NO_3 sols peptised with less acid than the ICI sol, it was possible to use $Ba(NO_3)_2$ to make a BaM sol using 18-crown-6-ether to help stabilise the sol. However, these proved to be worse than the nitrate-free sols regarding both stability and spinning. Higher Ba doping levels still resulted in an unspinnable sol.

Barium nitrite, $Ba(NO_2)_2$, is much more soluble than the nitrate, but when this was added to an Fe/NO_3 sol, it violently reacted to form a frothy precipitate. After two weeks the precipitate had peptised to form a sol with BaM stoichiometry, and a spinnable concentration of 17.6% Fe with a viscosity of 1.3 poise was achieved. However, when a Co_2Z sol was evaporated to over 30% Fe and exposed to air an extremely sudden and exothermic reaction spontaneously occurred, generating clouds of a dense white, pungent smoke, with the solid glowing red hot with enough heat to damage the glass container and ignite combustible materials in contact with it. It has been reported that Co^{2+} forms the complex $[Co(NO)_2)_6]^{3-}$ ion in acidic conditions, which can explode upon heating [188]. Therefore, the use of nitrites was abandoned for safety reasons, although the extreme heat had caused an unidentified black crystalline magnetic product to form.

Strontium nitrate is much more soluble than barium nitrate, and a SrM precursor sol could be made without any stabilising additives needed. This also allowed the opportunity to synthesise ternary sols using an all nitrate system, but again these proved less effective than the halide based sols.

2.7 BaM sols

The BaM sol made from an Fe/Br sol could be concentrated to over 18% Fe without any flocculation, mudding or large increase in viscosity. Although a spinnable sol could be made

without adding any chelating agent to the sol, it was found that including 18-crown-6-ether resulted in a superior spinning solution and better fibres, and so it was used in most M sols. From the PCS data the Z average of the doped Fe/Br sol was 7.4 nm, with a polydispersity of 0.630. By volume distribution, the mean size was found to be 6.6 nm, with an upper limit of 33.2 nm and 99.5% was within 3.3 - 21.0 nm, significantly higher than the undoped sol. The number distribution more resembled the Fe/Br sol, 98.8% being within 3.3 - 8.3 nm, with an average of 5.1 nm an upper limit of 16.7 nm, and the number and volume distributions are shown in figure 37. The increased maximum particle size clearly accounted for differences in stability and spinnability, and were attributed to the addition of barium rather than the extra counterions added with the salt, as the sol system is capable of withstanding large amounts of bromide without loss of stability.

When a BaM sol was made from the halide free Fe/NO_3 sol, not unsurprisingly problems were encountered with stability and particle growth upon addition of barium, even with the crown ether. The volume distribution had an average of 53.8 nm with 99.0% between 36.0 - 142.8 nm and an upper limit of 281.9 nm, obviously rendering the sol totally unspinnable. The number average was similar at 48.9 nm, but both the range of 99.4 % within 36.6 - 72.3 nm and the upper limit of 120.4 nm were proportionately much lower, although still a massive increase, caused by the barium as can be seen when compared to the halide free SrM sol (fig. 38).

2.8 SrM sols

Similar to the BaM sol, the halide SrM sol could be concentrated to higher levels than the cobalt containing sols, in this case 19.7%, and no chelating agent was required. The PCS data was very similar, with a Z average of 6.4 nm and a polydispersity of 0.82. By volume distribution, the mean size was found to be 7.0 nm, and 99.6% was within 3.6 - 18.0 nm with an upper limit of 30 nm. The number average was 5.1 nm, with an upper limit of 18.0 nm and 99.2% was within 2.9 - 11.4 nm. These results are similar to the BaM sol, and the distributions are shown in figure 39.

A potential advantage of SrM was that it could be produced from a halide-free, nitrate stabilised sol, and then compared to the halide containing fibres. The nitrate based sol was almost identical to the halide sol without barium, and was stable to over 17% Fe. The volume average was 8.0 nm with an upper limit of 27.2 nm and 99.1% within 5.7 - 15.8 nm, while the number distribution was 99.3% within 5.7 - 11.2 nm, with an upper limit of 18.7 nm. The lack of very small particles below 5.7 nm gave the mean peaks a narrow distribution, and this sol is contrasted to the halide free BaM sol in figure 38.

2.9 $BaCo_xTi_xFe_{12-2x}O_{19}$ sols

Substitution of Fe^{3+} in BaM ceramics with Co^{2+} and Ti^{4+} ions has proved to enhance their microstructure and magnetic properties, and so the synthesis of a stable and spinnable four-metal-component sol system was investigated. The aqueous chemistry of titanium is quite different from the metals used so far, and the only easily soluble salts are the titanium(IV)halides (table 2.1), which require a strongly acidic environment of pH <1 if hydrolysis is to be avoided. Therefore, as a simple salt could not be added, another method had to found of adding titanium to the iron sol without destabilising it. However, it was known to be possible to make stable acidic Ti^{4+} sols [15;189], and so the synthesis of a titania sol with a sufficiently small particle size to be compatible with the Fe/Br sol was investigated. Previously in mixtures of α-FeOOH and titania ($TiO_x(OH)_{4-2x}$) sols, spherical titania particles have been shown to group around rod-shaped iron particles to form a single, slightly larger particle [153], so it was hoped that the two discrete sols would be compatible when mixed. The Fe/Br sol used for all the titania-doping experiments was made with fresh $FeCl_3$, and so had slightly smaller particle size distributions.

2.9.1 Completely aqueous titania sol

A standard Fe/Br sol was doped with stoichiometric amounts of barium and cobalt bromides was to be used, but due to the unavailability of titanium(IV)bromide, a solution of titanium(IV)chloride was used, which was highly acidic and existed as a mixed hydroxy-

chloride compound with the formula $TiCl_{2.8}(OH)_{1.2}$.

Following an existing method [189] the pure $TiCl_4$ solution was added dropwise to a 1 M ammonia solution with stirring in a reverse of the usual precipitation method so that the Ti^{4+} ions were rapidly and totally hydrolysed. The thick white precipitate was washed and centrifuged until the supernatant had a conductivity of <15 μS and a pH of <3, and the precipitate digested in a solution of HBr at a ratio to Ti of 1:5. A week was needed for total peptisation to occur, giving a sol with a Z average of 28.1 nm and a polydispersity of 0.490, and the daily decrease in volume distribution is shown in figure 40. The volume distribution was 99.6% between 12.6 - 63.0 nm, with an upper limit of 79.3 nm and an average of 24.8 nm, and a number distribution of 99.6% within 12.6 - 39.7 nm, an upper limit of 63.0 nm and an average of 19.5 nm. The sol continued to peptise and particle size decreased over a further six weeks, when it stabilised at a volume average of 16 nm and an upper limit of 50 nm (fig. 41), and the sol remained stable for over a year.

In an attempt to speed the process, one week after initial peptisation the sol was dried to a gel on a rotary evaporator and redispersed with water. When the sol was dried at ambient temperature it failed to become totally dry, forming a sticky gel which resembled the original sol upon redispersal with a volume average of 26.9 nm and an upper limit of 150 nm. When evaporated to dryness at 35°C and redispersed the particle size had increased drastically to a volume average of 125.4 nm with an upper limit <500 nm, and this was only improved to 76.5 nm and 350 nm when the sol was evaporated at 95°C. The volume distributions of the original and redispersed sols are shown in figure 42.

When the fully peptised titania sol was added to the Fe/Br sol it yielded an unspinnable sol due to the large volume average (13.8 nm) and upper limit (69.4 nm). This was unaffected by the addition of the metal bromide salts, but after standing for just one day the volume average and upper limit had increased to 16 nm and 80 nm respectively (fig. 43), indicating a lack of stability in the mixed sol, probably due to the mismatch in particle size between the two sols. Even with the lowered chloride content of $TiCl_4$ solution it would also add more Cl^-

ions to the combined sol, as some would be retained within the titania sol even after washing and peptisation of the cake, and this route was abandoned.

2.9.2 Alkoxide derived titania sols

Titanium(IV)alkoxides are the starting materials most commonly used to produce titania sols, and titanium(IV) n-propoxide was hydrolysed and peptised to produce a chloride free titania sol. When the propoxide was added directly to water a waxy solid instantly formed, with unhydrolysed alkoxide trapped within the mass, which became granular on standing in the water. When the washed granules were digested in a solution of HBr with a ratio to Ti^{4+} of 1:5 at 60°C, the sol had peptised after only 3 hr, but it was yellowish in colour and had a distinct organic smell, and still had a volume average of 26 nm and an upper limit of 90 nm.

When a dilute solution of 10% propoxide in dry IPA was hydrolysed by the dropwise addition over 30 min of an excess amount of water (Ti^{4+}:water = 1:12), also as a 10% solution in IPA, a fine milky precipitate was produced. However, when this was peptised with the same amount of acid as previously a sol was produced with a similar particle size as before. Even when the sol was peptised and vacuum evaporated to dryness at 95°C in an attempt to removed any remaining organic compounds, the redispersed sol had a volume average of 23 nm and an increased upper limit of 150 nm (fig. 43).

2.9.3 Peptisation of titanium(IV)alkoxide with iron solutions

The co-sol consisting of two discrete populations of iron(III)hydroxide and titanium(IV)hydroxide particles would appear the easiest option, but the sizes of the two components were too dissimilar resulting in instability. A single population of homogenous particles containing both iron and titanium could be produced, by coprecipitation or copeptisation, or a primary particle could be coated with an added secondary component hopefully without loss of stability, and so this method was investigated.

In an attempt at coprecipitation a stoichiometric amount of titanium(IV)n-propoxide was added as a 10% solution in dry IPA to a solution of iron(III)chloride (1.33 M) dropwise

with stirring. The alkoxide simultaneously precipitated and peptised to give a volume average of 26.2 nm and an upper limit of 160 nm, which continued to peptise over time until it had stabilised after 25 days with a volume average of 14.5 nm, an upper limit of 64.6 nm and a distribution of 99.5% between 8.1 - 40.7 nm. The iron was then precipitated with ammonia and a Fe/Br sol made by the standard method, but it was found that the average particle size had increased greatly compared to either the pure iron sol or the titania / $FeCl_3$ mixture (fig. 44). The volume distribution was now 99.8% within 33.2 - 209.9 nm, an upper limit of 264.3 nm and volume and number averages of 69.4 and 52.9 nm respectively.

However, when a 10% solution of titanium(IV)n-propoxide in IPA was added dropwise to the Fe/Br sol, the simultaneous precipitation and peptisation gave a stable iron / titania sol with a volume average <15 nm and an upper limit <50 nm for a maximum of x = 1.8 after 24 hr (fig. 45). However, it can clearly be seen that there is a second, if small, peak in volume distribution, with 95% centred around an average of 7.6 nm and 5% around an average of 20.3 nm with an upper limit of 37.3 nm. The iron sol, with a pH of 3, was less acidic than the iron(III)chloride solution, and therefore would hydrolyse the propoxide more slowly, and the small increase in particle size suggested that the titania particles were being adsorbed onto the surface of the existing sol particles, with a corresponding drop in pH to 1.7 as more counterions were removed from the solution.

Stoichiometric $BaCo_xTi_xFe_{12-2x}O_{19}$ sols were made for x = 0.5, 0.75, 1.0 and 1.1, and their properties are compared in table 2.7. The iron / titania sols took progressively longer to peptise fully with increasing substitution, with the particle size stabilising after only 1 hr for x = 0.5, 15 hr for x = 0.75, 24 hr for x = 1.0 and 48 hr for x = 1.1, giving final volume averages from 7.1 nm for x = 0.5 to 13 nm for x = 1.1 (fig. 47). It can be seen from a plot of the maximum stable concentration for the doped sols against x (fig. 46) that it drops with increasing substitution, and that the relationship is non-linear with the rate of decrease in stability rising with x. As the undoped iron / titania sol was stable up to concentrations of 13.59% Fe at values of x of at least 1.8, this instability must have been due to the effect of

cobalt on barium stability. The volume distributions of the sols are compared in figure 47, and again it can be seen that the upper limits become disproportionately higher with increasing x, leading to destabilisation at lower concentrations. The volume distributions were 99.0% within 4.8 - 18.0 nm for x = 0.5, 99.6% within 5.5 - 18.6 nm for x = 0.75, 99.8 % within 7.2 - 21.0 nm for x = 1.0 and 99.7% within 9.8 - 34.6 nm for x = 1.1, and the sol became unspinnable at substitution levels over this. Ti^{4+} has a lower IEP than Fe^{3+}, 4 compared to 6.7 [153], and this would lower the ζ of the sol, and as the surface of the sol is coated with Ti^{4+}, it would also reduce the surface charge of the sol particles, thus reducing stability.

x	Fe sol	0	0.5	0.75	1.0	1.1
Z Av. / nm	3.5	7.1	5.2	6.0	10.3	12.3
Vol Av. / nm	4.7	6.3	7.1	7.9	12.3	13.1
Vol upper / nm	20.6	23.1	22.0	25.3	32.6	43.5
No. Av. / nm	4.2	4.7	6.4	7.2	10.1	12.3
No. upper / nm	12.3	16.0	13.2	18.0	26.7	34.6
Range / nm	0.9 - 13.1	2.2 - 23.4	1.5 - 18.4	1.5 - 23.7	2.5 - 41.9	3.5 - 43.3
Polydispersity	0.712	0.565	0.640	0.761	0.785	0.636
Max. Conc. / %Fe	33.97	23.51	20.90	18.29	13.97	13.07

Table 2.7 Comparison of stoichiometric $BaCo_xTi_xFe_{12-2x}O_{19}$ sols for x = 0, 0.5, 0.75, 1.0 and 1.1, and the undoped Fe/Br sol, all at 10.5% iron concentration. The x = 0 sample was not made from a sol using fresh $FeCl_3$, and hence has disproportionately large size values to a small degree

2.10 $SrCo_xTi_xFe_{12-2x}O_{19}$ sols

Barium was substituted with strontium to compare a series of both strontium-doped and halide-free strontium-doped sols analogous to the BaCoTiM sols, with x = 0.5 and 1.0. In the halide Fe/Br sol based systems, a titania sol made from ultrasonic peptisation was added to the iron sol. The titania sol was made in a manner similar to the ultrasonic iron sols described in section 2.17.3, using titanium(IV)n-propoxide and a ratio of HBr:Ti of 1:1 in a large excess of water. The titania sol had a very high z average of 49.6 nm, but this was due to a very small amount of larger material. As can be seen from the intensity distribution in figure 48, a proportion of particles were present between 65 - 255 nm, but these were so few in number as

to have no effect on the volume and number distributions, and it was hoped they would not affect the spinnability of the sol. The volume average was a low 5.3 nm, with 99.5% between 3.0 and 11.8 nm and an upper limit of 16 nm, and the number distribution was also similar to the Fe/Br sol, with 99.6% being between 3.0 - 8.7 nm, and average of 4.1 nm and an upper limit of 11.8 nm.

It was hoped that despite the presence of the small proportion larger particles, the similarities between the two sols would lead to a stable mixture, and this indeed proved to be the case. The PCS volume distributions of the two sols after addition of stoichiometric amounts for x = 0.5 and 1.0 are shown in figure 49, and it can be seen that the addition of the ultrasonic titania sol actually seemed to reduce particle size slightly. For x = 0.5 the Z average was 11.5 nm, with a volume average of 4.4 nm, an upper limit of 13.8 nm and 99.1% between 3.0 - 8.7 nm, and the number distribution was 9.3% between 3.0 - 6.4 nm with an upper limit of 8.7 nm and a number average of 3.7 nm. The Z average for the x = 1.0 sol was only 6.7 nm, with a lower volume distribution of 95.5% between 3.0 and 7.5 nm, an upper limit of 10.2 nm and an average of 4.1 nm, and a number average of 3.6 nm, a small upper limit of 7.5 nm and a distribution of 99.8% within 3.0 - 6.4 nm. Both sols were stable up to a concentration of 16.2% Fe, and this is in contrast to the substituted BaM sols, suggesting less interaction between the strontium and cobalt ions.

A halide free sol with x = 0.5 was made using the ultrasonic titania sol peptised with HNO_3, the Fe/NO_3 sol and nitrate salts. However, this proved to have a much larger particle size, more like the BaM sols based on nitrates, with a volume average of 20.0 nm, 99.6% between 10.4 - 41.5 nm and an upper limit of 65.8 nm, and a number average of 16.1 nm up to a maximum of 41.5 nm. The volume distribution is compared to that of the undoped halide free SrM sol in figure 50. Despite this it did not began to precipitate until over concentrations of 16% Fe, again indicating that any strontium / cobalt interaction had a less detrimental effect upon sol stability, but the large particle size could still render it unspinnable.

2.11 Y ferrite sols

The stoichiometric mixture required to produce Co_2Y contains the highest proportion of simple metal salts as dopants, which not only contributed nothing to gel formation but actually destabilised the sol itself because of the interaction between cobalt and barium. The PCS data indicated that the Z average of the sol was 8.2 nm, with a polydispersity of 0.524. By volume distribution the mean size was found to be 7.5 nm, with an upper limit of 36.8 nm and 99.3% within 3.7 - 18.6 nm, not dissimilar to the M sols (fig. 51). The number distribution was almost identical with 99.6% being within 3.5 - 11.7 nm, an average of 5.9 nm and an upper limit of 17.4 nm. Despite having a large ratio of Fe^{3+}:M^{2+} = 3:1, the sol could withstand concentration to over 15.7% Fe without flocculation or increased structuring, and the slight lowering of maximum concentration of all the cobalt containing sols is attributed to increased structuring due to the cobalt ions.

Sol	Co_2Y	Ni_2Y	Mn_2Y	Zn_2Y
Z Av. / nm	8.2	9.4	9.4	7.8
Vol Av. / nm	6.5	8.7	8.5	8.9
Vol upper / nm	36.8	41.9	33.2	13.9
No. Av. / nm	5.4	6.7	7.0	8.9
No. upper / nm	14.7	21.0	20.9	13.9
Range / nm	2.5 - 27.0	3.5 - 28.1	3.5 - 25.0	6.0 - 110.1
Polydispersity	0.564	0.480	0.385	0.359

Table 2.8 Comparison of several stoichiometric Y ferrite doped Fe/Br sols at a concentration of 10.5% iron.

As Y ferrite had the highest loading of all the sols, several other Y ferrites were made simply by substituting the cobalt bromide for another divalent metal bromide to tests the limits of the system. The metals investigated were nickel, for it's magnetic properties, manganese because the many oxidation states possible could affect sol stability, and zinc because it is notorious for causing solubility and compatibility problems when in solution. The characteristics of the sols of the various Y ferrites are shown in table 2.8, and their

number distributions compared in figure 52. Instead of gelling as with cobalt, the Ni_2Y sol precipitated reversibly at 15.15% Fe, and redispersed in minutes when diluted to 10%, whereas the Mn_2Y sol became rapidly thixotropic at concentrations over12.5% Fe, without any sign of precipitation. It can be seen these two sols resemble one another, and have size distributions only slightly larger than Co_2Y ferrite.

As predicted, the addition of Zn^{2+} caused problems. Small colourless crystals began to precipitate out of solution at 10.6% Fe, and as these were thought to be barium because the solubility of $ZnBr_2$ is so high, a further amount of 18-crown-6-ether was added to the sol, after an addition of more HBr proved ineffective. This immediately triggered the precipitation of a large amount of the crystals, as much of the zinc appeared to precipitate out of solution, although they all dissolved back into solution with dilution. As the zinc ions appeared to be precipitated by the crown ether, a sol was made without the crown ether in. This did not precipitate or form a thixotropic gel, but what was a smooth sol at 12.9% Fe just appeared to dry out at 13.9%, a state that was fully reversible with dilution. PCS results gave identical and suspiciously symmetrical peaks for the number and volume distributions, and the results for this sol are not thought to be entirely reliable.

2.12 Z ferrite sols

The PCS data indicated that the average particle size of the Co_2Z precursor sol was slightly larger than for Co_2Y, with a Z average of 9.3 nm and a polydispersity of 0.690, despite having a lower level of dopants. The number distribution was also slightly larger with an average of 8.1 nm and 98.8% within 4.1 - 13.1 nm with an upper limit of 20.8 nm (fig. 53). The volume distribution was similar with 99.5% between 4.1 - 20.8 nm, an average of 8.1 nm and an upper limit of 33 nm, so it was concluded that these minor differences between the sol characteristics make little difference except for the upper volume limit, which appears to be a reliable determining factor for the stability and spinnability of the sols containing cobalt. This was demonstrated by the sol stability at concentrations up to 16.20% Fe, slightly higher than for the Co_2Y sol.

A halide free strontium substituted Co_2Z analogue was made from stoichiometric amounts of Fe/NO_3 sol and strontium and cobalt nitrates, without any crown ether. This demonstrated a very similar particle size to the halide free SrM sol, with a volume average of 10.0 nm and upper limit of 14.8 nm with 99.6% between 8.1 - 12.1 nm, and a similar number distribution of 99.9% between 8.1 - 12.1 nm, an average of 9.8 nm and an upper limit of 13.4 nm. This could be concentrated to over 15.68% Fe.

2.13 Co_2W ferrite sol

The stoichiometric mixture required to produce Co_2W also contained a relatively high proportion of simple metal salts as dopants, but it had the lowest proportion of Ba:Fe of any of the hexagonal ferrites, at a ratio of 1:16, whilst the Co:Fe ratio was high at 1:8. Despite the low barium content crown ether was added to ease spinning. The sol began to form a gel at 16.33% Fe. The PCS data indicates that the Z average was 6.8 nm, with a polydispersity of 0.648, and by volume distribution the mean size was found to be 6.6 nm, with an upper limit of 30.9 nm and 99.4% between 3.1 and 19.5 nm.. The number average was 5.2 nm with an upper limit of 15.5 nm and 99.6% being within 3.1 - 9.8 nm (fig. 54).

2.14 Co_2X ferrite sol

The sol gelled at a concentration of 16.22%. The Z average was 7.6 nm with a polydispersity of 0.574, and the volume distribution showed that 99.2% was within 3.4 - 21.5 nm with an average of 7.7 nm and an upper limit of 3.0 nm. The number distribution had an average 6.0 nm, an upper limit of 17.1 nm and 99.3% was within 3.4 - 10.8 nm (fig. 55).

2.15 Co_2U ferrite sol

The U sol had a much larger Z average of 16.3 and polydispersity of 0.380 than the other ferrite sols, and a larger volume average of 9.4 nm, although the upper limit of 32.6 nm was in line with the rest and 99.3% was within 5.6 - 22.5 nm. Similarly the number average was high at 7.5 nm and with 99.3% being between 5.6 - 14.1 nm, but the upper limit was a lower 18.7

nm (fig. 56). This sol appeared to lack the smaller sized fraction, thus raising the average values but not the more important upper limits, and therefore had no effect on spinning. The reasons for this difference are unknown, but may have been due to an older source of iron(III)chloride being used. The sol demonstrated problems in concentration too, becoming viscous at only 10.03% Fe and gelling at 12.54% Fe.

2.16 Sols with additives

For various reasons discussed in chapter four, additives with potential to control the microstructure of the ceramic fibre were added to sols of Z ferrite as it suffered greatly from DGG, and BaM as it was the most simple system to study.

2.16.1 Silica, boria and alumina doped Co_2Z sols

Stoichiometric amounts of a commercial silicone surfactant, DC193, were added to a standard Co_2Z sol, to produce 0.3% and 0.7% silica doped sols. The surfactant had no detrimental effects on particle size or spinnability, although great care had to be taken when evaporating the sol because of foaming. Stoichiometric amounts of DC193 and a 1% solution of *ortho*-boric acid, H_3BO_3 were added to a standard Co_2Z sol, to dope it with 1% of each to give 2% SiO_2-B_2O_3 doped Co_2Z. Again the sol appeared unaffected by this, but the same was not true of a sol identical to this but with 1% alumina added as well. The alumina source was an aluminium chlorohydrate solution used in the production of alumina fibres, but it became very viscous at low concentrations, and began to become slightly muddy and thixotropic at a barely spinnable concentration. The particle size of the alumina polyion solution, stated to be around 2 - 3 nm by ICI, was thought too small to account for this destabilisation, but it contained 1 mole of Cl^- for each mole of alumina and this was the suspected cause for the increased structuring seen in the sol. This was confirmed in a sol containing 1% each silica and alumina, which could be concentrated to over 14% but became very thixotropic. Finally a sol containing 1% $CaSiO_3$ and 0.3% alumina was made from the two commercial sols with

calcium bromide added as a 1% solution. While this was an improvement on the sol containing 1% alumina, the added Cl^- ions were still responsible for making the sol slightly thixotropic.

2.16.2 Metal salt doped Co_2Z sols

The addition of small amounts of bivalent or trivalent metal salts to a standard Z sol appeared to have little effect on particle size or behaviour. 1.93% La_2O_3, 2.15% Gd_2O_3 and 1.34% Y_2O_3 doped sols were made by adding 0.00125 mol of $LaCl_3.7H_2O$, $GdCl_3.H_2O$ and $YCl_3.6H_2O$ respectively to a Co_2Z sol containing 0.1 mol Fe with no observable change in sol behaviour. Similarly 0.67% CaO doped and 1.23% SrO doped Co_2Z fibres were made by adding 0.00125 mol of $SrCl_2.6H_2O$ and $CaBr_2$ respectively, and the Co^{2+} doped sol was studied by PCS. Compared to undoped Co_2Z, the 0.67% CaO doped Co_2Z precursor sol had a slightly higher volume average of 8.3 nm and an upper limit of 35 nm, but this appeared to be an insignificant difference that had no observable effect on stability.

Dopant / wt%	1% Y_2O_3	1% ZrO_2	1% Cr_2O_3	1% stab. ZrO_2	0.25% V_2O_5	0.06% Nb_2O_5
Z Av. / nm	46.4	34.4	33.1	31.5	20.8	19.0
Vol Av. / nm	45.1	31.4	31.9	29.6	19.3	17.0
Vol upper / nm	164.7	122.1	121.8	110.8	73.9	67.4
No. Av. / nm	34.4	26.0	26.1	23.5	15.8	13.5
No. upper / nm	103.9	77.0	66.8	70.5	46.6	42.5
Range / nm	13.5 - 159.7	12.6 - 94.3	11.2 - 98.2	10.9 - 91.0	7.9 - 55.0	7.2 - 50.2
Polydispersity	0.611	0.406	0.472	0.451	0.378	0.377
Max. Conc.	11.89%	13.29%	15.20%	13.64%	14.82%	18.29%

Table 2.9 Comparison of stoichiometric BaM sols doped with potential sintering aids at a concentration of 10.5% iron.

2.16.3 Doped BaM sols

These are quite different from the stoichiometrically substituted CoTiM sols, in that small amounts (<1%) were added to a stoichiometric BaM sol, to investigate effects on microstructure and magnetic properties. Additions of 0.83 mol% Gd^{3+} and La^{3+} as bromide

salts has absolutely no effect on the sol or spinning characteristics. Other dopants did have an effects on the sol, and their various characteristics are shown in table 2.9, and their volume distributions compared in figure 57. Despite the large volume distributions and upper limits all of these sols were spinnable, if only for short periods before holes blocked with particulate. One interesting, and as yet unexplained, feature is that the "stabilised zirconia" doped sol, in fact consisting of 1% $Zr_{0.84}Y_{0.16}O_{1.92}$, shows improved characteristics over the two individually doped sols. Also Cr^{3+} ions seemed to improve sol stability until precipitating out as crystals at over 19.30% Fe, and the fibre produced contained lumps of shot made of these crystals, despite the fact that Cr^{3+} was found by ICI to mix well with alumina sols and readily forms polyions [153]. $NbCl_5$ hydrolysed instantly to form an insoluble product in water, so it was dissolved in 5 drops of concentrated HCl first and then diluted and added.

2.17 Alternative preparative methods

2.17.1 Coprecipitation

An investigation was mounted into the possibilities of co-precipitating salts of iron(III), cobalt and barium simultaneously. Whilst iron(III) and cobalt(II) salts generally precipitate at a pH less than 7, barium requires a much higher pH to precipitate fully, and many barium salts are not particularly soluble. Because of the insolubility of $Ba(NO_3)_2$, the more soluble barium acetate was also used. Iron(III) and cobalt(II) nitrates were used in all cases. The experiments were carried out for a stoichiometric Z ferrite mixture, with Fe:Ba = 8 and Fe:Co = 12.

Four different bases, NH_3, NH_4HCO_3, $NaHCO_3$ and Na_2CO_3, were used to precipitate the metal salts, and these were added to give an end point over a range of pH values. In all cases a brown precipitate had formed by the lower end point of pH 5, as the iron precipitated. The precipitates were filtered to give a brown gelatinous cake which was washed with water, weighed and then fired, and examination of the ceramic products is discussed in chapter 4. All of the washed cakes weighed between 23 and 30 g. The filtrates had 2M H_2SO_4 added to them to precipitate any retained barium as a milky cloud, and this was approximately quantified by

nephelometry. The results are summarised in table 2.10.

Ba salt	Base	pH	Volume	% Ba lost	Filtrate colour
$Ba(ac)_2$	NH_3	6	29 ml	73.7	Pale pink
$Ba(ac)_2$	NH_3	7	33 ml	51.4	Very pale pink
$Ba(ac)_2$	NH_3	8	37 ml	53.3	Clear
$Ba(NO_3)_2$	NH_3	5	24 ml	54.2	Pink
$Ba(NO_3)_2$	NH_3	6	32 ml	46.3	Pink
$Ba(NO_3)_2$	NH_3	7	33 ml	43.8	Very pale pink
$Ba(NO_3)_2$	NH_3	8	35 ml	46.1	Clear
$Ba(ac)_2$	NH_4HCO_3	5	111 ml	39.4	Pale pink
$Ba(ac)_2$	NH_4HCO_3	6	130 ml	23.4	Pale pink
$Ba(ac)_2$	NH_4HCO_3	7	212 ml	7.5	Clear
$Ba(ac)_2$	NH_4HCO_3	8	306 ml	3.8	Clear
$Ba(NO_3)_2$	NH_4HCO_3	5	83 ml	23.6	Pink
$Ba(NO_3)_2$	NH_4HCO_3	6	92 ml	20.2	Pink
$Ba(NO_3)_2$	NH_4HCO_3	7	255 ml	4.9	Pale pink
$Ba(NO_3)_2$	NH_4HCO_3	7.5	487 ml	1.8	Lilac
$Ba(ac)_2$	$NaHCO_3$	5	53 ml	34.0	Pink
$Ba(ac)_2$	$NaHCO_3$	6	64 ml	16.6	Pale pink
$Ba(ac)_2$	$NaHCO_3$	7	94 ml	4.2	Very pale pink
$Ba(ac)_2$	$NaHCO_3$	8	298 ml	1.7	Clear
$Ba(NO_3)_2$	$NaHCO_3$	5	111 ml	33.0	Pink
$Ba(NO_3)_2$	$NaHCO_3$	6	127 ml	21.2	Pale pink
$Ba(NO_3)_2$	$NaHCO_3$	7	238 ml	7.7	Clear
$Ba(NO_3)_2$	$NaHCO_3$	7.5	400 ml	3.9	Clear
$Ba(ac)_2$	Na_2CO_3	7	69 ml	6.3	Clear
$Ba(ac)_2$	Na_2CO_3	8	77 ml	0.44	Clear
$Ba(ac)_2$	Na_2CO_3	9	127 ml	0.16	Clear
$Ba(NO_3)_2$	Na_2CO_3	7	62 ml	5.5	Very pale pink
$Ba(NO_3)_2$	Na_2CO_3	8	67 ml	0.37	Clear
$Ba(NO_3)_2$	Na_2CO_3	9	113 ml	0.16	Clear

Table 2.10 Summary of results for the coprecipitation of $Fe(NO_3)_3$, $Co(NO_3)_2$ and either $Ba(ac)_2$ or $Ba(NO_3)_2$ with various bases over a range of pH values.

With 4% ammonia solution at all pH values between 5 and 8 a large proportion of the barium, between 73% and 44% in all cases, was retained in the filtrate, and therefore was lost to the ceramic product. The filtrate also had a pink colour up to pH 7, indicating that there was also some retention of cobalt in the filtrate forming a complex ion, probably $[(NH_3)_6Co]^{2+}$, but the pale colour indicated this loss was relatively small. A small volume of around 35 - 37 ml of ammonia solution was required to reach a pH of 8.

When a 2.5 wt% solution of NH_4HCO_3 was added to the salt solutions an immediate effervescence was observed, and the solution appeared to buffer between pH 7 and 8, as over 300 ml of the base was required to reach the upper value. This resulted in a very dilute filtrate, which explained why although no milky precipitate was seen upon addition of H_2SO_4, a loss of barium was detected by nephelometry even at pH 8. This was much less than for the ammonia barium was detected by nephelometry even at pH 8. This was much less than for the precipitated products however, and this system showed the largest difference between the behaviour of the two barium salts. With $Ba(ac)_2$ 39.4% of the barium was lost at pH 5, decreasing to 3.8% at pH 8, compared to 23.6% and 1.8% at pH 5 and 7.5 respectively for $Ba(NO_3)_2$, and the nitrate system also retained cobalt in solution up to pH 8, as evidenced by the lilac colour. The reason for this differential has not been discovered so far, but the $Ba(NO_3)_2$ sample also seemed to buffer at a lower pH of 7.5.

A saturated 1.9 wt% solution of $NaHCO_3$ was used, again resulting in apparently clear filtrates at high pH due to the large volume of base needed, and again the $Ba(NO_3)_2$ containing solution buffered at a lower pH of 7.5. However, in this case the barium retention was reversed, with both being similar at low pH but with only 1.7% barium being lost with $Ba(ac)_2$ compared to 4.5% for $Ba(NO_3)_2$ at high pH. There was no cobalt apparent in the filtrate over pH 7 in either case.

Finally a 3 wt% Na_2CO_3 solution was used to precipitate the metal salts, and this enabled a higher end pH of 9 to be achieved with relatively small volumes of base. None of the filtrates above pH 7 indicated any cobalt species, and although they suffered similar barium

losses of several percent at lower pH values, both precipitates retained 99.84% of the barium at pH 9. This was enough to produce a product with a stoichiometric Z composition, but the problem of sodium contamination would remain after firing.

No sols or fibres were produced from coprecipitates due to the problems of barium loss at lower pH and sodium retention at higher pH.

2.17.2 Alkoxide derived sols.

Although the aim of this thesis was to produce hexagonal ferrite fibres from an inorganic aqueous sol-gel process, the synthesis of an alkoxide derived sol was briefly investigated, as an alternative method of coprecipitation, and possibly a more homogeneously mixed precursor. The methoxides $Fe(OMe)_3$ and $Co(OMe)_2$ were used, and barium ethoxide was made by dissolving barium metal in ethanol. The methoxides were contaminated with 5% and 3% LiCl respectively, an unavoidable feature on their manufacture. As alkoxides and barium metal react with atmospheric moisture, they were stored and solution prepared in a glove box with a positive atmosphere of blue spot nitrogen, and all reactions up to the hydrolysis stage were carried out under a nitrogen atmosphere. All solvents were anhydrous or distilled, dried with molecular sieve and degassed with nitrogen before use.

While $Fe(OMe)_3$ was sparingly soluble in ethanol (50 g l^{-1}), $Co(Me)_2$ was almost totally insoluble in ethanol even after refluxing for several hours, and cobalt alkoxides are known to be difficult to dissolve due to their polymeric nature. The highly toxic and teratogenic 2-methoxyethanol was found to be the only good solvent for $Co(OMe)_2$, and after refluxing for two hours a deep blue solution resulted. The solvent was also used to dissolve $Fe(OMe)_3$ and barium, which effervesced and released H_2 gas upon addition, but a total metals concentration of only 0.13 M was possible. After much experimentation it was found that a spinnable sol could only be produced if the barium was dissolved in the solvent before methoxide addition and refluxing, an excess of water was added as a 10% solution in ethanol, the solution then digested with HBr (in the high ratio acid:Fe = 2.5:1) as a 10% solution in

IPA on a rotary evaporator, and the sol then evaporated to near dryness, rediluted with IPA and re-evaporated again to remove all of the 2-methoxyethanol, and finally water added to give the mixed stoichiometric Co_2Z sol. However, the sol was completely unspinnable, with a Z average of 42.9 nm. As can be seen in figure 58, the number distribution was concentrated in a reasonably narrow peak around an average of 51.0 nm with a very small fraction as large as 129.6 nm, but the volume fraction was bimodal, with 93.4% centred around an average of 52.2 nm and 6.6% around 127.8 nm, with a high upper limit of 255.9 nm.

For a BaM alkoxide preparation anhydrous ethanol could be used as the solvent, which was again evaporated to near dryness and redispersed with water, to give a sol which was stable to 14.6% Fe. However, the sol prove to be even worse than the Z sol, showing clearly bimodal populations in both number and volume distributions (fig. 59). Both were centred around 185 and 420 nm averages, with 75% of the volume distribution being in the larger fraction with an upper limit of over 800 nm. The complexity and unreliability of this process, together with the limited size of the batches possible, the expense of the starting materials, difficulties in spinning and no improvement in end product, resulted in the abandonment of the alkoxide route.

2.17.3 Ultrasonic peptisation

An Fe/NO_3 sol was made by the ultrasonic peptisation of a mixture of precipitated iron(III)nitrate, made by the standard precipitation, and HNO_3 in a ratio of acid:Fe of 1:5. The precipitate was peptised in a large excess of water (0.65 M) in the ultrasonic bath at room temperature for 1 hr, to give a transparent red / brown sol. As can be seen in figure 60, although the averages were higher than for the normally peptised sols, the main peaks of the distributions were over a narrower range, with the number distribution being all between 9.7 - 16.0 nm with an average of 11.7 nm. However, although 98% of the volume distribution was centred in a tight peak around 12.1 nm, 2.5% formed a small secondary hump with an average of 24.8 nm and an upper limit of 60.5 nm, to the detriment of the spinnability. This had

improved to only 30 nm after a week, but after a month the volume average had increased to 13.1 %, still with a 2% fraction at 45.6 nm now, and an upper limit of 70 nm. HBr sols made by this suffered similar from similar size and stability problems, but this technique deserves further exploration.

2.17.4 Spinel sols

As spinels are one of the phases encountered in the hexagonal ferrite system, attempts were made to produce a spinel ferrite fibre so as to better understand the complex processes involved in the formation of the hexagonal ferrites. To this end a series of spinel ferrites were attempted, but with special attention to cobalt(II)spinel ferrite. However, it proved impossible to make a cobalt(II), copper(II), nickel(II), zinc(II) or manganese(II) sol that was stable at the high concentrations required for spinning, due to complexation and precipitation of the metal ions involved.

Attempts were made to dope an iron sol with salts of the divalent ions, but with the exception of cobalt all of the sols precipitated at around 8.5% Fe, a concentration far too low for spinning to succeed, because of the high ratio of M^{2+}:Fe^{3+} of 1:2. The cobalt spinel sol could be concentrated to a maximum concentration of around 10.97% Fe, and although the volume average was only 8.2 nm with 99.0 % between 4.8 - 19.1 nm, the upper limit was a high 60.5 nm. Cobalt spinel was spun at a concentration of 10.5% Fe, but the fibres were of poor quality, dangerously thin (~1 μm) and contained too much water to be of any use. Upon firing they behaved exactly as standard sol-gel specimens. An alkoxide route to cobalt ferrite was also tried but was unsuccessful.

3. Conclusions

A stable iron(III) sol was successfully made from the peptisation of a precipitated iron salt, precipitated to pH 5 with ammonia, with acid in a ratio of Fe:acid of 5:1. Two kinds of sol were investigated, a nitrate based system using $Fe(NO_3)_3$ and HNO_3 and a halide based system using $FeCl_3$ and HBr, and it was also found that a sol peptised with HCl became too

thixotropic at low concentrations due to structuring and destabilisation effects from the Cl^-. An optimum precipitation time of 15 - 30 min was found for the peptisation stage, and the sol was then peptised at 35 °C for the Fe/Br sol and 65°C for the Fe/NO_3 sol under a vacuum of 95 kPa on a rotary evaporator. The sols flocculated irreversibly at temperatures over these. Although a sol was formed in 30 - 60 min, the sols required at least 24 hr to stabilise and give a constant particle size, as shown in figure 61. It was also found that a smaller particle size could be obtained if fresh $FeCl_3$ was used to make the Fe/Br sol, as the $FeCl_3$ decomposed slightly over time.

Sol	standard Fe/Br	Fresh $FeCl_3$	Fe/NO_3
Z average / nm	4.7	3.5	6.8
Volume average / nm	6.0	4.7	7.8
Volume upper limit / nm	20.0	20.6	31.5
Number average / nm	5.1	4.2	6.4
Number upper limit / nm	14.2	12.3	15.7
Polydispersity	0.760	0.712	0.658
Range / nm	1.2 - 18.7	0.9 - 13.1	3.0 - 19.0

Table 2.11 Comparison of standard Fe/Br, Fe/Br from fresh $FeCl_3.6(H_2O)$ and Fe/NO_3 sols, all 15 min precipitation, at a concentration of 10.5% iron.

The Fe/Br and Fe/NO_3 sols are compared in table 2.11, and it can be seen that the Fe/Br sol had a smaller average particle size. Also very important for spinning was the existence of any large species, even in small numbers, and the degree to which the sol could be concentrated without flocculating or gelling. The number and volume distributions of the Fe/Br and Fe/NO_3 sols are compared in figures 62 and 63, and it could be seen that the upper limits of both were smaller in the Fe/Br sol. This had an average particle size of 4.2 - 5.1 nm, which compared well to previously reported FeOOH sols, but the volume distribution was more relevant for spinning, and the volume average was slightly higher at 4.7 - 6.0 nm. Because of added stability effects from the Br^- ion the Fe/Br sol could also be concentrated to

up to 36.5% Fe, compared to 23.5% for the NO_3 sol. It was found a sol with a volume distribution upper limit of < 50 nm and a concentration of at least 13% Fe was usually needed to be spinnable, so the requirements of the following sols were stricter than those normally needed in sol-gel work.

Sol	BaM	SrM
Z average / nm	7.4	6.4
Volume average / nm	6.6	7.0
Volume upper limit / nm	33.2	28.5
Number average / nm	5.1	5.1
Number upper limit / nm	16.7	18.0
Polydispersity	0.630	0.820
Range / nm	2.1 - 26.1	1.5 - 26.7

Table 2.12 Comparison of stoichiometric SrM and BaM doped Fe/Br sols at a concentration of 10.5% iron.

The stoichiometric ferrite precursor sols were made by doping the iron sols with metal salts. The existence of any NO_3^- ions in the sol tended to precipitate $Ba(NO_3)_2$, so nitrate sols were not used for the barium containing ferrite precursors, and nitrate salts could not be used to dope the sols either. Barium nitrite is much more soluble than nitrate, but the sol was not very stable, and produced an extremely exothermic reaction upon concentration and partial dehydration when containing Co^{2+}. For this reason the nitrites were abandoned, but this should be investigated in the future as a possible combustion method for producing BaM, as it resulted in a black, magnetic product. Chloride salts were avoided as the addition of more Cl^- to the sol resulted in gelation and thixotropy at low concentrations, and acetates were found to induce the precipitation of cobalt chloride, so bromide salts were used as extra bromide had no effect on stability, and all the metal bromides were very soluble. The number distributions of the Fe/Br, BaM and SrM sols are compared in figure 64, and it can be seen in table 2.12 that the addition of barium resulted in a slight increase of particle size, which was similar in

both BaM and SrM sols. $Sr(NO_3)_2$ is much more soluble than $Ba(NO_3)_2$, so a halide free SrM sol was also made for comparison, but this proved to be no better. It was known that a small amount of Cl^- was retained in the precipitate from $FeCl_3$, and this appeared to help sol stability and spinning in small quantities by adding a degree of structure to the sol, especially useful in the more dilute three and four component sols.

In the higher barium levels needed for the ferroxplana ferrites it was found that a chelating agent, 18-crown-6-ether, was needed to keep the barium in solution even with bromides. With the addition of cobalt there was also a harmful interaction between the two metals which reduced the stability of the sols slightly. The cobalt free M sols could be concentrated up to at least 18% Fe without any change in structure, whereas cobalt containing sols begin to gain structure, while remaining optically transparent, at around 14.6% Fe. Nevertheless stable and spinnable sols were made of all the hexagonal ferrites, and their characteristics are contrasted in table 2.13. There was a general further increase in particle size to a number average of 6 - 7 nm and volume average to 7 - 9 nm, but all remained within spinnable limits.

Sol	Y	Z	Ca-Z	W	X	U
Z Av. / nm	8.2	9.3	8.8	6.8	7.6	16.3
Vol Av. / nm	7.5	8.1	8.3	6.6	7.7	9.4
Vol upper / nm	36.8	33.0	35.0	30.9	33.0	32.6
No. Av. / nm	5.9	7.5	6.7	5.2	6.0	7.5
No. upper / nm	17.4	20.8	17.4	15.5	17.1	18.7
Range / nm	2.6 - 27.1	3.1 - 27.5	2.3 - 27.9	1.8 - 23.4	2.3 - 25.3	6.1 - 33.1
Polydispersity	0.524	0.470	0.562	0.648	0.574	0.380

Table 2.13 Comparison of stoichiometric Co_2Y, Co_2Z, 0.67% CaO-doped Co_2Z, , Co_2W, Co_2X and the Co_2U ferrite doped Fe/Br sols at a concentration of 10.5% iron

Although there was little difference between the particle sizes of the ferrite sols, there was a marked difference in their maximum stable concentrations, shown as a factor of iron content in the ceramic, in figure 65. This was found to be related to the content of M^{2+} ions, but there was a strange irregularity in the order, where the W sol, with the ratio $Fe^{3+}M^{2+} = 5.3$

had a lower maximum concentration than the Z sol with a ratio of only 4.8 (fig. 66). This was explained if the Fe^{3+}:Co^{2+} ratio was examined; as shown in figure 67 in which the W and Z positions are reversed, with a decrease in maximum concentration, and therefore stability, with increasing cobalt addition. The M ferrite, with no cobalt, should be at infinity but is placed arbitrarily at a ratio of 100 to indicate that stability is suddenly lost around the stoichiometric levels required for Z ferrite, and the spinning concentrations are shown to indicate that the same trends exist in the spinning solutions, discussed in chapter 3. If the reciprocal ratio is used, Co^{2+}:Fe^{3+}, it can be seen that there is a major stability drop from the undoped iron sol to the M sol due to barium addition, but then the effects from increasing cobalt levels dominate (fig. 68). The levels required for cobalt spinel (Fe:Co = 2), without any barium effects, render it unspinnable, and Y ferrite is approaching the limit of spinnability at a ratio of Fe:Co = 6.

Due to its aqueous chemistry, the direct addition of Ti^{4+} salts to make a series of $BaCo_xTi_xFe_{12-2x}O_{19}$ sols was not possible, so various attempts were made to produce a titania sol from $TiCl_4$ and alkoxides, which could then be added to the iron sol. However, these all had much larger particles than the Fe/Br sol, and upon mixing resulted in unstable and unspinnable mixed sols. In these mixtures of pre-prepared iron and titania sols much larger particle sizes were seen larger than either of the two individual components, suggesting that the smaller iron particles were coating the larger titania particles. Eventually a stable mixed sol was made by adding a dilute alkoxide solution slowly to the Fe/Br sol, simultaneously hydrolysing and peptising the titanium(IV)alkoxide to give a mixed sol which could be doped with cobalt and barium bromides as usual. As even at the higher substitution level the ratio of Ti:Fe was only 11%, it is probable that the hydrolysed titania was adsorbed onto the surface of the iron particles, leading to an increase in size dependent upon x. Longer peptisation times with x were indicative of dissolution / reprecipitation processes onto larger particles, giving secondary species with larger diameters, and increasing the upper limits of size correspondingly. The small but steady increase in volume average gave 13.1 nm at x = 1.1, but the upper size limit increased at a much greater rate, as shown in figure 69. The almost

bimodal nature of the iron / titania sols, divided into two neighbouring distinct populations of 95% and 5%, accounted for the difference in stability between these and the other cobalt-containing ferrite sols, with the larger sized 5% fraction combining with the cobalt / barium interactions to lower stability. As shown in figure 70, the addition of Ti^{4+}/Co^{2+} had a disproportionately large effect on stability, which increases rapidly beyond x = 0.75. and was not due purely to Co^{2+} content. The x = 0.5 sol (Fe:Co = 22) is equivalent to the Z sol (Fe:Co = 5.3), the x = 0.75 sol (Fe:Co =14) matches the W sol (Fe:Co = 4.8), and the x = 1.1 sol (Fe:Co = 8.9) is almost as bad as the unspinnable cobalt spinel sol (Fe:Co = 2). The surface coating of Ti^{4+}, which has a lower IEP than Fe^{3+}, would reduce the surface charge of the sol particles and lower ζ of the sol, thus reducing stability.

$SrCo_xTi_xFe_{12-2x}O_{19}$ sols did not show this trend, with no change in stability with x and an actual small decrease in particle size. This was attributed to two factors. Firstly, the nature of the titania sol used to make a co-sol in these precursors, in which neither the ultrasonically peptised titania sol nor the mixed iron / titania co-sol showed a secondary population, and had much lower size distributions. Secondly there was evidence that any strontium / cobalt interaction was a less harmful one than for barium, with all $SrCo_xTi_xFe_{12-2x}O_{19}$ sols (even the halide free sol unspinnable due to particle size) being stable up to 16% Fe, comparable to the undoped SrM sols. The larger particle size in the halide free sol could be due to an interaction between the trace amount of high diameter material seen in the ultrasonic titania sol and the inherently less stable Fe/NO_3 sol.

Alternative methods of sol preparation were also investigated. To produce a coprecipitate with a stoichiometric ferrite composition, a pH of 9 was required in the precipitation process, and to achieve this Na_2CO_3 had to be used as the base. This was predicted to result in later problems with sodium retention in the ceramic product, and this combined with the uncertain stoichiometry in lower pH precipitations led to the abandonment of this method. Alkoxide based sols and ultrasonically peptised sols were also made, but all proved inferior to the entirely aqueous doped iron(III) sols.

4. Experimental

4.1 Analytical techniques

4.1.1 Photon correlation spectroscopy (PCS)

PCS, otherwise known as dynamic light scattering (DLS), is a technique in which a beam of collimated and coherent light is shone into a sol, and the scattered light measured at an angle to the incident beam. The beam is polarised perpendicular to the scattering plane. A small amount of background scattering will occur from the solvent itself, but the bulk of scattering is observed from interfaces between differences of refractive index (RI), and for this reason it is best to have a large difference between the RIs of the solvent and particles. In Rayleigh scattering the intensity of light scattered is proportional to the ratio $(RI_{part.}:RI_{solv.})^4$, but it is also proportional to the particle radius^6 [190].

The particle sizes of the sols were measured on a Malvern Instruments Lo-C Autosizer and series 7132 multi-8 correlator at an angle of 90°, using a 4 mW diode laser, 670 nm wavelength. The sol was added to a transparent cuvette filled with filtered water, after filtering the sol through a 0.45 μm filter. The apparatus was capable of measuring samples at up to 60 °C, but unless otherwise stated all measurements were taken at 20 °C. The detector was a photomultiplier, giving an amplification of $>10^7$ electrons for each photon detected in 50 ns pulses, with a maximum count rate of 20 MHz, although for the dilute iron sols the count rate was usually ~20 KHz, an acceptable level provided the background was below 10% of the signal. The PCS had been certified by the manufacturers to measure inorganic colloidal species of 3 nm diameter and above, provided the difference between the RI of the solvent and particle was sufficiently large. This was the case with our samples, the RI used being 1.33 for the solvent (water) and 1.89 for FeOOH, 2.30 for $Ti(OH)_4$, 1.70 for $Zr(OH)_4$ and 1.73 for $Y(OH)_3$.

This piece of equipment conformed to the Methods of Particle Size Determination Standards ISO 13321, part 8 - PCS (1996) and BS3406, part 8 - PCS (1997) for

determination of the Z average and polydispersity, which were calculated from the monomodal cumulants analysis, which also provided the range values quoted. The cumulants were measured by counting the number of signals over periods of increasing time (0.1 - 100 μs) split into 128 channels using the correlator. The detector can track rapid changes of intensity to provide a "snapshot" of intensity for each sample time, adding the intensities together to form progressively longer channels, and the correlator also constantly monitors the strength of the signal received and accounts for statistical variations in it. Therefore, the Z average, polydispersity and range values are only initial estimates calculated from the distribution of accumulated intensities, and assumed the sol to be monomodal. As a doubling of particle diameter will lead to an increase of intensity by a factor of 64 (2^6), it can be seen that a small number of large particles will disproportionately influence the intensity distribution. The volume and number distribution particle sizes and ranges were calculated from the cumulants results using the Malvern PCS software version 1.32 with multimodal and contin algorithms, the latter being better suited for more monodisperse and bimodal samples. The volume distribution is a measure of the volume occupied by particles against their size, and the number distribution is a simple assessment of the particle size distribution, and these two values more accurately reflect the true nature of the sol.

It must be considered that as the PCS technique is unable to detect particles below the 3 nm threshold, these measurements may be higher than the actual true figures, as reflected in the (estimated) range values. Also the sols were much too concentrated to be measured undiluted, and samples were made up typically as 5 drops of 10.5% Fe filtered sol in 2 - 3 cm^3 of water filtered through a 0.7 μm filter. This dilution did not destabilise the sols, and they showed no change over 1 day after being diluted. When samples were measured at other than room temperature they were allowed to stabilise at the set temperature for 30 min before measurement. The samples were measured over 15 minutes, with 30 runs in each scan combined to give a mean result. This was repeated at least three times with each sample to ensure reproducibility of results, indicated by the Z average values all being within 2% of each

other, and all results quoted passed the Malvern quality test. Zeta potentials were measured at Malvern Instruments using a Malvern Zeta sizer.

4.1.2 Viscosity

Viscosity was measured on a cone-and-plate paint viscometer. This was calibrated with glycerol, known to have a viscosity of 8 poise. Measurements were made at a shear rate of 1000 s^{-1}, compared to shear rates in the spinning holes of 300 – 500 s^{-1}.

4.2 Preparation of iron sols

A comprehensive list of the compounds, solvents and reagents used in this work, their grades and manufacturers, can be found in appendix C. All reactions were carried out at ambient temperature and atmospheric pressure unless otherwise stated. All water used was distilled, and all NH_3 solutions used were 4 wt% solutions diluted from 35% ammonia with water.

4.2.1 ICI iron sol preparation

1.4 ml of lactic acid and 4.2 ml of distilled water were heated in a covered boiling tube for 2 hours in a water bath at 95 °C. Meanwhile 17.52 g $Fe(NO_3)_3$ was dissolved in 48 ml water and cooled in ice, as was a stock solution of 4% ammonia. The ammonia was added from a dropping funnel with stirring to the iron(III)nitrate solution until pH 5 was reached, and the precipitate was then filtered and washed with 2 x 50 ml water acidified to pH 5 with HNO_3. 1.4 ml of HNO_3 (acid: Fe = 1:2) was then added to the lactic acid solution, heated to 65 °C and this added to the precipitate in a 250 ml Bucchi rotary evaporator flask. The mixture was then digested on the rotary evaporator at 65 °C under a vacuum of 95 kPa, and the viscosity measured every 30 minutes until a viscosity of between 0.5 and 1.0 poise was achieved, with a smooth brown sol (17.6% Fe, 3.1 M) being formed in the process.

4.2.2 Standard synthesis of Fe/Br sol

The Fe/Br sols used to make all of the fibres discussed in this thesis were produced by this

standard preparation, unless otherwise detailed in the results section. Larger batches were made purely by scaling up the weights / volumes of the materials used, and using larger pieces of glassware where appropriate, but increasing the rate of ammonia addition to maintain the overall precipitation time. 13.52 g (0.05 mol, 2.79 g Fe) of iron(III)chloride hexahydrate was dissolved in 25 ml of distilled water in a 250 ml beaker, and cooled in an ice bath for at least 30 minutes. A solution of 4% NH_3 in distilled water was also cooled in ice for the same period. This was then added to the iron chloride solution drop-wise by burette over 15 - 20 minutes, at a rate of 4 - 6 ml min^{-1}, whilst the mixture was still cooled in an ice bath and stirred at 400 RPM by a 48 mm impeller blade, until the solution had reached a pH of 5.

The pH was measured by a freshly calibrated pH meter, which also acted as a baffle to improve the mixing during stirring. The $FeCl_3$ solution had a pH of around 1. A fine brown precipitate began to form immediately when the ammonia was first added, and the pH rapidly increased to approximately 2 after the addition of ~ 10 ml. The pH remained between 2 and 3 for the bulk of the reaction, as further iron was precipitated, until the pH began to rise rapidly again after addition of 65 ml of ammonia in total. At a pH of 3.5 the precipitate suddenly thickened and the stirring rate had to be increased to 600 RPM to maintain an even mixing of the solution, but the stirring rate could later be turned down at pH 4 as the mixture became more fluid again. For the last minute the rate of addition had to be reduced so as not to overshoot the pH 5 end point, as at this point one drop (~0.5 ml) was roughly approximate to a rise in pH of 0.05. Around 70 ml of ammonia solution was needed to reach a pH of 5.

The resulting thick brown precipitate was filtered in a buchner funnel and washed with 4 x 50 ml of water, also adjusted to pH 5 with HBr, and the weight of the washed precipitate cake was 37.5 g (7.4% Fe by weight). The final wash had a pH below 3 and a conductivity below 3 μS. The hydroxide cake was then transferred to a 500 ml Bucchi rotary evaporator flask, and a mixture of concentrated HBr (0.01 mol, 1.13 ml) in 20 ml water, so that there was an acid:Fe ratio of 1:5, was added to the flask, The cake was broken up and mashed into the solution for 30 seconds with a spatula, which was then washed with water to ensure all the

iron remained in the flask, and more water added if necessary so the total mixture had a weight of 70 g (3.9% Fe, 0.70 M). The flask was then immediately mounted on a rotary evaporator and the slurry digested and peptised for 30 minutes at a temperature of 35 °C and under a vacuum of 95 kPa. All of the hydroxide was digested within half an hour and a smooth brown sol had formed with a concentration of 16 - 21% Fe (2.86 - 3.76 M), but the sol continued to peptise for up to 24 hours, after which time there was no further significant decrease in the average sol particle size. Therefore, after initial peptisation the sol was diluted to 26.6 g (10.5% Fe, 1.88 M), and left to peptise further for 24 hours whilst rotating on the sealed rotary evaporator at 35 °C and atmospheric pressure.

4.2.3 Synthesis of Fe/NO_3 sol

This was made in a method similar to the of the Fe/Br sol, with the following differences. 19.8 g (0.05 mol) of iron(III)nitrate nonahydrate was dissolved in 25 ml of distilled water, and ml of ammonia solution was added until the mixture had reached a pH of 5. The resulting filtered and washed thick brown precipitate was peptised with concentrated nitric acid (0.61 ml, 0.01 mol) in a ratio of iron to acid of 5:1 which was added to 20 ml of distilled water. Again all of the hydroxide had been digested within half an hour and a sol had formed, but the sol continued to peptise for up to 24 hours, after which time there was no further significant decrease in the average sol particle size. The resulting sol had a concentration of 10.11% Fe by weight (1.8 M).

4.3 Stoichiometric doping of iron sols

The salts were added as individual solutions, with a minimum volume of 5 ml, to a sol with a concentration of 10.5% Fe. The diluted sol was then re-concentrated, and the stability range assessed.

4.3.1 BaM sol

The standard BaM sol was made by adding a solution of 2.78 g $BaBr_2.2H_2O$ (0.00833 mol),

without any crown ether, to a 0.1 mol Fe/Br sol (5.59 g Fe, 10.5% Fe). When made using a 0.1 mol Fe/NO_3 sol as a basis, a solution of 2.18 g $Ba(NO_3)_2$ (0.00833 mol) and 0.73 g 18-crown-6-ether (0.00278 mol) were dissolved in water and added to give the stoichiometric BaM sol.

4.3.2 SrM sol

The standard SrM sol was made by adding a solution of 2.96 g $SrBr_2.6H_2O$ (0.00833 mol), without any crown ether, to a 0.1 mol Fe/Br sol (5.59 g Fe, 10.5% Fe). When made using a 0.1 mol Fe/NO_3 sol as a basis, a solution of 2.18 g $Sr(NO_3)_2$ (0.00833 mol) was dissolved in water and added to give the stoichiometric SrM sol.

4.3.3 CoTiM sols

The $BaCo_xTi_xFe_{12-2x}O_{19}$ sols were made from a 10.5 % Fe sol coated with titania sol particles and then doped. To a 0.1 mol Fe/Br sol a stoichiometric amount of $Ti(n\text{-}OPr)_4$ as a 10% solution in dry IPA was added dropwise with stirring to the iron sol over five min. The titanium propoxides are much less reactive with atmospheric moisture than the other alkoxides used in sections 4.4.2 and 4.4.3, and a special protective atmosphere was not required. After stirring at room temperature for either 1 hr (x = 0.5), 15 hr (x = 0.75), 24 hr (x = 1.0) or 48 hr (x = 1.1), the mixed sol was doped with stoichiometric amounts of $BaBr_2.2H_2O$ and 18-crown-6-ether dissolved in water, followed by 1 M $CoBr_2$ solution. This was then reconcentrated to 10.5% Fe on a rotary evaporator at 35 °C and under a vacuum of 95 kPa

The $SrCo_xTi_xFe_{12-2x}O_{19}$ sols were made by mixing a Fe/Br sol with stoichiometric amounts of the titania sol made by ultrasonic peptisation, as detailed in section 4.4.4, and stoichiometric amounts of $BaBr_2.2H_2O$ dissolved in water, followed by 1 M $CoBr_2$ solution.

4.3.4 Co_2Y sol

A 0.1 mol Fe/Br sol (5.59 g Fe, 10.5% Fe) had a solution of 5.55 g $BaBr_2.2H_2O$ (0.0167 mol) and 1.47 g 18-crown-6-ether (0.00556 mol) dissolved in 20 ml water added to it, followed by

16.67 ml of a 1 M $CoBr_2$ solution. This was then reconcentrated to 10.5% Fe on a rotary evaporator at 35 °C and under a vacuum of 95 kPa.

4.3.5 Co_2Z sol

To a 0.1 mol Fe/Br sol (5.59 g Fe, 10.5% Fe) were added 4.16 g $BaBr_2.2H_2O$ (0.0125 mol) and 1.10 g 18-crown-6-ether (0.00417 mol) dissolved in 20 ml water, followed by 8.33 ml of a 1 M $CoBr_2$ solution. This was then reconcentrated to 10.5% Fe on a rotary evaporator at 35 °C and under a vacuum of 95 kPa.

4.3.6 Ca-doped Co_2Z sol

4.16 g $BaBr_2.2H_2O$ (0.0125 mol) and 1.10 g 18-crown-6-ether (0.00417 mol) were dissolved in 20 ml water and added to a 0.1 mol Fe/Br sol (5.59 g Fe, 10.5% Fe). 8.33 ml of a 1 M $CoBr_2$ solution and 1.25 ml of a 1 M $CaBr_2$ solution were also added to the sol, and it was then reconcentrated to 10.5% Fe on a rotary evaporator at 35 °C and under a vacuum of 95 kPa.

4.3.7 Co_2W sol

To a 0.1 mol Fe/Br sol (5.59 g Fe, 10.5% Fe) was added 2.08 g $BaBr_2.2H_2O$ (0.00625 mol) and 0.55 g 18-crown-6-ether (0.00208 mol) dissolved in 20 ml water, followed by 12.5 ml of a 1 M $CoBr_2$ solution. This was then reconcentrated to 10.5% Fe on a rotary evaporator at 35 °C and under a vacuum of 95 kPa.

4.3.8 Co_2X sol

A 20 ml solution of 2.38 g $BaBr_2.2H_2O$ (0.00714 mol) and 0.63 g 18-crown-6-ether (0.00238 mol) was added to a 0.1 mol Fe/Br sol (5.59 g Fe, 10.5% Fe), followed by 7.14 ml of a 1 M $CoBr_2$ solution. This was then reconcentrated to 10.5% Fe on a rotary evaporator at 35 °C and under a vacuum of 95 kPa.

4.3.9 Co_2U sol

To a 0.1 mol Fe/Br sol (5.59 g Fe, 10.5% Fe) was added 3.70 g $BaBr_2.2H_2O$ (0.0111 mol) and 0.98 g 18-crown-6-ether (0.00370 mol) dissolved in 20 ml water, followed by 5.56 ml of a 1 M $CoBr_2$ solution. This was then reconcentrated to 10.5% Fe on a rotary evaporator at 35 °C and under a vacuum of 95 kPa.

4.4 Alternative methods of preparation

4.4.1 Coprecipitation

Sufficient stoichiometric amounts to produce 10 g of Co_2Z ferrite were used. 8.76 g $Fe(NO_3)_3.9H_2O$, 0.53 g $Co(NO_3)_2.6H_2O$, and either 0.73 g $Ba(ac)_2$ or 0.71 g $Ba(NO_3)_2$ were dissolved in 25 g of water in a 500 ml conical flask. Quantities of the desired base were then added titrametrically with a burette, whilst the salt solution was stirred with a magnetic bead, to coprecipitate the metals until the desired pH was reached. The precipitate was then filtered to a gelatinous cake, washed with water and weighed. The combined filtrate and washings were also weighed and enough 2M H_2SO_4 was added to precipitate all of the barium originally in the solution, to precipitate any barium retained in the filtrate as a visible cloudy white precipitate.

This was then examined on a nephelometer, which estimates the amount of precipitate in a solution by the amount of light absorbed or reflected by the particles in suspension. This rather crude piece of apparatus was used only at the beginning of the experiments detailed here, before the PCS equipment was obtained, and is a only qualitative technique which requires quite dilute systems to operate. It was not used after the PCS apparatus was obtained. The equipment was calibrated using 10 g stock solutions of 0.005%, 0.0025% and 0.001% Ba^{2+} precipitated with 2M H_2SO_4, which gave readings of 121, 60 and 26, demonstrating a linear relationship. A sample of the filtrate with added sulphate, between 0.5 - 10 g depending on the concentration of the filtrate, was then made up to 10 g with water, and the comparative

amount of barium in the sample of filtrate estimated from this measurement. From this the total amount of Ba^{2+} ion remaining in the filtrate could be extrapolated, as a measure of the success of the coprecipitation.

4.4.2 Alkoxide derived Co_2Z sol

A 250 ml flask, flushed with N_2, was loaded with 5.31 g $Fe(OMe)_3.3MeOH$ (0.0222 mol), 0.28 g $Co(OMe)_2.MeOH$ (0.0018 mol) and 0.37 g barium metal (0.0027 mol) in a glovebox under an atmosphere of N_2. The flask was then mounted on to a condenser set up for reflux, which had been flushed with N_2 for 30 min, and maintained under a constant flow of N_2 until after hydrolysis, with the N_2 input being through a rubber septum at the top of the condenser. 200 ml of anhydrous 2-methoxyethanol was added to the flask, resulting in an instant effervescence as the barium metal dissolved. As this released H_2 gas, the second neck of the flask was left open until all of the barium had dissolved to let the gas escape, the flow of N_2 maintaining the atmosphere of the apparatus during this time. A closed dropping funnel was then mounted on this second neck, and the mixture refluxed for two hours whilst being stirred with a magnetic bead, to give a bluish-brown solution (0.2265 mol total metals, 1.13 M). This was allowed to cool to room temperature.

An excess of water (5 ml) was added as a 10% solution in IPA through the dropping funnel over 5 minutes with stirring, resulting in the instant formation of a light brown precipitate. This was then transferred to a 500 ml Bucchi flask and reduced to 50 ml on a rotary evaporator at 35 °C and a vacuum of 95 kPa. 0.7 ml of HBr in 50 ml water was added to the mixture it was kept under vacuum on the rotary evaporator for 2 hr, adding more water as required. After a dark brown sol had formed, the sol was transferred to a 250 ml flask and reduced to near dryness, the point at which it is beginning to mud out and stick to the walls of the flask (17.3% Fe). Then 100 ml IPA was added, the sol being maintained, and his was reduced in turn to near dryness. The sol was then diluted to 10.5% Fe with water.

4.4.3 Alkoxide derived BaM sol

This was made by the same method as the Co_2Z sol, except for the following differences. 200 ml anhydrous ethanol was used as the solvent to dissolve 5.31 g $Fe(OMe)_3.3MeOH$ (0.0222 mol) and 0.23 g barium metal (0.00169 mol), and this was refluxed and hydrolysed as above, but with 5 ml of water in ethanol. The mixture was then digested with 1 ml HBr in 50 ml water, evaporated to near dryness once, and redispersed with water to form the sol.

4.4.4 Ultrasonic peptisations

These reactions were carried out in a Decon Ultrasonics FS200 ultrasonic bath containing water at room temperature, with a frequency sweep of $^{+}/_{-}5$ KHz from a mean frequency of between 40 - 45 KHz.

The iron salt was precipitated and washed as in the standard preparations to give a cake (0.05 mol Fe), which was then mixed by hand briefly into 80 ml water containing 0.01 mol acid. This mixture was then placed in a crystallising dish, so that the solution was wide and shallow, and this in turn was placed in the ultrasonic bath for 1 hr at ambient temperature to form the sol, which could be concentrated further afterwards.

To make the titania sol, 0.32 g $Ti(n\text{-}OPr)_4$ (0.00114 mol) in 3 ml dry IPA was added to a large excess of water (10 ml) containing 0.13 ml HBr (0.00115 mol) dropwise with mixing, to give a clear solution with no visible precipitation. This was then placed in a crystallising dish in the ultrasonic bath for 30 minutes to form the sol.

Chapter Three

The Blow Spinning of Gel Fibres

1. Blow spinning

In a general spinning process fibres are formed from a liquid by discharging it from a spinning site, to give a fibre less than 10 - 20% of the original site dimension. The spinning liquid must be capable of forming stable jets which can be drawn to fine diameters and then transform smoothly to a gel fibre, at a rate which permits draw but suppresses the growth of disturbances in the jetting/draw operation. The transformation should be continuous, with the liquid viscosity increasing until a glassy gel is formed without phase change. This principle of continuous transformation was established in investigations of the spinning of polymers derived from the hydrolysis of silicon ethoxide [153]. This transformation from a viscous solution to a glassy gel is also a property of many aqueous inorganic sols, as discussed in chapter two, and of the basic salt solutions of Group III and IV metals which are used in the preparation of many commercial inorganic fibres. Blow spinning is a form of dry spinning in which the gel forms when the spinning solution loses solvent, and the fibre is drawn from the spinnerets by a flow of air.

1.1 Spinning solutions

There is much academic discussion on the molecular or colloidal constitution of a spinnable material, and it is beyond the remit of this thesis to explore the structure, rheology and spinning behaviour of the spinning solutions synthesised in any great depth. However, the spinning behaviour of the silica sol system produced from the hydrolysis of an alkoxide precursor has been investigated in some depth [191], and there is much knowledge within the fibre industry regarding the spinning of alumina sols made from aqueous aluminium chlorohydrate sols [192].

1.2 Rheology of sols

Generally fibres are formed from a spinning solution by discharging it from a spinning site of some kind. This could be a hole (or spinneret), a droplet on a solid surface or even a ripple on a liquid surface. Therefore, the spinning solution must be capable of forming solid jets that can be drawn to a fine diameter and then transformed smoothly into a solid gel fibre. It must do this at a rate sufficiently slow to allow the draw of the fibre but quick enough to suppress the growth of varicose or elastic disturbances. The transformation from the liquid to solid must be continuous, with the liquid viscosity increasing smoothly until a glassy gel is formed without a phase change. This kind of transformation occurs in weakly branched or linear structures, enabling hydrolysed polymers to become highly concentrated with out premature gelation. Such a state is limited by the ratio of hydrolysing water molecules to the number of alkoxy groups, and it should be noted that a linear molecular structure is not always necessary to produce linear fibres.

1.3 Inorganic alumina sols

Fibres spun from aluminium chlorohydrate, a sol of polyions with the nominal formula $Al_2(OH)_5Cl$, undergo the transformation from the liquid state to the glassy gel which is observed in many basic salt solutions of group III and IV metals, credited to their small ionic radii. Gel permeation chromatography has shown aluminium chlorohydrate to comprise a wide size range of species up to 100 nm in diameter [193], but 96 -98% of the solution is below 20 nm. The polymeric $Al_{13}(OH)_{24}(H_2O)^{7+}$ species is reported to be predominant in many commercially available solutions [194], although investigations done at ICI suggest that it may contain up to 40 aluminium atoms. In sols containing a range of spherical species a polydispersity of at least 6% is required to prevent the crystallisation of a separate phase [177]. It has been speculated that polydispersity in the main species is sufficient to form glassy gels, and it is suggested that polyions absorb onto the coarser colloidal particles in aluminium chlorohydrate and prevent flocculation between them by setting up hydration barriers [195].

To render an alumina sol spinnable it must have a viscosity between 10 and 1000 poise (1 poise = 100 mPa). Only 10 poise is needed for blow or centrifugal spinning, whereas a viscosity of several hundred poise is required for the extrusion and wind-up of a continuous fibre [109]. A non-colloidal salt solution will show a much slower increase in viscosity, and the salt will usually precipitate out at concentrations far too low to be spinnable. For example aluminium chloride precipitates out of solution at only 12 wt% alumina, whereas aluminium chlorohydrate is still in solution at over 40 wt% alumina, although by this stage the viscosity of 1 x 10^{13} poise has become so high that the sol has set as a glassy gel. *Saffil* fibres are spun from solutions concentrated from 23.5 wt% alumina, and the original solution viscosity can vary from 0.1 - 0.6 poise between manufacturers, and even batches. A 0.1 poise solution would consist of a solution of equiaxed polyions, and a solution with a viscosity of 0.6 poise would have some limited aggregation and open structuring of the coarser fractions. However, both solutions would lead to perfectly spinnable solutions.

1.4 Alkoxide derived aqueous sols

In a study of silica sols made from the hydrolysis and condensation of an alkoxide precursor, the amount of water used in the hydrolysis step and the condensation catalyst were found to be crucial. It was already known that the composition of the alkoxide solution, the catalyst used, amount of water added, conditions and the rates of hydrolysis and condensation greatly affected the sol thus produced. If the hydrolysis is catalysed with an acid and the water ratio is lower than 4:1 water:alkoxide then the sol will always exhibit spinnability at viscosities over 10 poise and will draw into fibres. However, if the sol had a larger amount of water or was catalysed with a base there was no spinnability, despite the alkoxide having digested to form a sol. [196]. It was found that there were several differences between the two sols. The spinnable sols have rod-like siloxane polymers and they show Newtonian flow behaviour up to high viscosities, where the fibre can be drawn. On the other hand , the non-spinnable sols consisted of spherical sol particles, while the sol exhibited structural viscosity and thixotropy.

The viscosity increases with time as the hydrolysis reaction progresses and the reaction needs less time with an increase in temperature. Initially the viscosity increases slowly at the start of the reaction, but then the rate of increase of viscosity rapidly rises. With a water:alkoxide ratio of 2:1 the reaction took over 80 hours to gel at over 100 poise at 30°C, but at 80 °C the solution took only 5 hours and was spinnable after 2 hours. It was also found that once the reaction solution reached a viscosity of 10 poise it slowed down drastically. If the ratio was less than 1.7 then the reaction rate decreased, and if it equalled 1 then the reaction stopped at almost exactly 10 poise, and the viscosity only increased slightly due to absorption of water from the air, which could be prevented by cooling and sealing the sol [196]. An addition of more alcohol to the solution could extend the gelling time needed to reach 100 poise, and still resulted in a spinnable sol.

The spinnability and viscosity of silica-zirconia sol systems produced from alkoxides has also been investigated. The base catalysed condensation of a hydrolysed silica-zirconia sol never resulted in a spinnable sol. However, acid catalysed sols with a viscosity of 1- 100 poise were made, and fibres were pulled from these when the water:alkoxide ratio was 2. The non-spinnable sols all had a 3D network of fractal polymers or consisted of spherical particles, whereas the spinnable sols consisted of linear polymeric species [197]. The nature of the polymeric particles in the silica-zirconia system is still not fully understood, as a water:alkoxide ratio of 4 gives the 3D branched structure whereas a ratio of 8 gives spherical particles.

The Sumitomo process involves the hydrolysis of triethylaluminium or trialkoxyaluminium to give the respective polymers, which are then dissolved into a solvent with a silane, and the resulting viscous mixture is spun into gel precursor fibres [198]. These can then be calcined to yield the aluminosilicate product, but the viscous spinning mixture decomposes easily to a gel, and with the relatively bulky triethyl groups this results in a low conversion [199]. Polymethylaluminium can be used instead, as it has less weight to lose in the formation of alumina fibre, but the hydrolysis is complicated, and alcohol and a carboxylic acid

must be added to slow down the hydrolysis, and prevent the chains from cross linking and the sol becoming unspinnable [200]. A more successful technique is to modify an aluminium alkoxide with a carboxylic acid to a soluble aluminiumcarboxylate. This can then be hydrolysed with equimolar amounts of water to aluminium to give a polymeric sol which exhibits Newtonian behaviour and is easily spinnable. Continuous gel fibres several kilometres long can be drawn at a spinning rate of 200 m min^{-1}, without any further organic additives, and the sol is stable for at least a year [201].

However, linear species always appear to be required in alkoxide derived sols to produce a spinnable product [202], and a slow hydrolysis rate of the alkoxide and a ratio of metal:HCl of less than 0.03 is recommended to form a linear polymer [129].

1.5 Spinning aids

It has been shown that linear species are not essential for gelling, and duPont and 3M claim that they are also not essential for spinning, apparently producing fibres without an added linear polymer spinning aid. However, the spinning process can be eased and improved if a linear species is present, especially in low viscosity spinning processes like blow spinning. ICI add small amounts of a linear long-chain polymer to their alumina spinning solutions, and Sumitomo utilise a linearly structured organic precursor. If the 3M *Nextel* procedure as detailed in their patent [123] is followed the solution is too fluid to pull fibres easily, and any which do form dry rapidly and break. However, if 1 wt%-to-alumina polyethylene oxide is added with a molecular weight of 1 x 10^6, long fibres can immediately be drawn easily which resist snapping when drying [109]. As Bayer held the dominant patents on spinning additives in the 1970's [203], commercial interests may have led to the omission of a spinning aid in the described procedure.

The addition of a spinning aid can also help stabilise a sol with a very fine solid fraction, but in large amounts the polymer can interact with the particulate causing flocculation. Too much organic in the gel fibre can also lead to a swollen fibre, crystallisation

of the polymer during storage and drying, runaway exotherms during heating and the induction of irremovable porosity, so it is important to keep the spinning aid at a minimum level. The amount of spinning aid required can be reduced as the molecular weight of the polymer is increased, but too much molecular weight increases the polymer relaxation time, slowing down spinning and causing elastic instabilities in the spinner. For this reason Bayer recommend using polyethylene oxide with MW of 2,200,000 with alumina sols. What is beyond doubt is that the addition of a small amount of a linear polymeric spinning aid helps spinning to such an extent that it outweighs any disadvantages.

1.6 Coalescence

The problem of coalescence between adjacent jets of fibre often occurs in fibre development work, usually caused by elastic recovery in the spinning solution when a high molecular weight spinning aid is used. When fibre is blown into a diverging duct or spun off a centrifugal atomiser into still air the draw force decays as the liquid fibre moves away form the spinning hole. The polymer spinning aid is stretched in draw and the recovery of this elasticity when those draw forces are removed causes neighbouring fibres to whip or twist back upon themselves.

1.7 The stable Newtonian jet length

When spinning from a spinneret hole, the stable Newtonian (i.e., ideal) jet length, L, is given by Weber's equation,

$$L = 12 d_o \left(\frac{W_e^{0.5} + 3W_e}{R_e} \right) \qquad \text{Eqn. 3.1}$$

where W_e = the Weber number for flow from the spinneret (= $U_o^2\ d_o\ \rho\ /\ \sigma$) and R_e = the Reynolds number (= $d_o\ U_o\ \rho\ /\ \eta$). The variables U_o, η and d_o are the solutions velocity in the hole, viscosity and the hole diameter respectively, and these can all be measured directly. The other variables ρ, the density of the spinning solution, and σ, the surface tension of the

solution, must be estimated for the sol-gel solution [109].

The Newtonian jet length is too short for blow spinning fine fibres, as a low feed rate per hole and low solution viscosity are required. In fact, the Newtonian drying time for blow spinning is too short, but the addition of a spinning aid increases the stable jet length enabling the fibre to have time to dry. Bayer showed that linear polymers in low viscosity systems have a large effect on the stable jet length [203]. Centrifugal spinners need long stable jet lengths to enable the fibre to dry, and after ICI added some spinning aid to a centrifugal spinning process the yield increased from 20% to 90%. [204]. A quicker drying time also allows the wind up rate to be increased during the collection of an aligned fibre.

1.8 Spinneret holes

At a fixed liquid rate the shear rate in a spinning hole, S, can be written as

$$S = \frac{Q}{32\pi d^3} \qquad \text{Eqn. 3.2}$$

where Q = liquid feed rate. Therefore, an increase in hole size greatly reduces the rate of shear agglomeration and helps prevent build-up of particulate on the wall of the hole [205]. The critical particle size to stop spinning is much smaller than the hole diameter, and both 3M and ICI patents include filtration down to 1 μm in an attempt to minimise hole blockage - a blockage of 20% of the hole is enough to prevent spinning from that site. Larger holes are also cheaper to make and easier to clean, and the size of the hole does little to determine the size of the fibre in blow spinning, unlike in extruded fibres.

2. Results and discussion

The solution used for spinning is referred to here as the spinning solution, to distinguish it from the sol before the addition of PEO, as this addition changed the physical character of the sol.

2.1 Polyethylene oxide (PEO) spinning aid

PEO is the non-ionic, water soluble linear polymer $(-O-CH_2CH_2-)_n$, with a molecular unit weight of 44, and the degree of polymerisation, n, varies from 2,000 to 100,000. Three different grades of PEO were used, depending on the concentration of the sol. The more dilute the sol, the thinner and weaker the fibres produced, and it was partly by increasing the molecular weight of the PEO used with dilute sols that it was ensured that virtually no fibres were produced with diameters below the dangerous threshold of 3 μm. Most spinning solutions had a concentration of 14 - 17% Fe, and in these cases the standard 1% 1,000,000 MW PEO solution was used to make fibres between 4 and 8 μm wide. For more dilute solutions of borderline spinnability a 1% 2,000,000 MW PEO solution was used, which had a viscosity approximately 5 times higher, and this tended to produce thicker fibres around 10 μm or more in diameter, but which were also often less flexible and too brittle to collect on the rotating drum. In sols with higher concentrations, which were only pure iron and M ferrite sols, a less viscous 400,000 MW 2% PEO solution was also used. PEO is known to degrade in UV light [206], so both the powders and solutions were stored in a dark cupboard. PEO also degrades with time, resulting in a loss of spinnability. It was found that solutions only had a lifetime of 1 month, and the stock of powders was replaced with a fresh supply yearly. Unless otherwise stated all spinning solutions were made with 1,000,000 MW PEO.

2.2 The spinning solution

Because of lone pairs on the oxygen atoms PEO behaves as an electron donor, and PEO can bond with other species through hydrogen bonding, sometimes resulting in an insoluble product. It is also known to form association compounds with mineral acids, bromine and metal halide salts. In the case of bromine a maximum weight of 17% Br_2 to PEO is possible before the compound becomes insoluble in water and alcohol [207]. It is therefore unsurprising that, as well as the desired linear fibre-pulling properties, PEO addition also decreased the stability of the sols in other ways, increasing the general structuring and

reducing the maximum stable concentration of the sols, a factor more apparent in the Co^{2+} containing sols.

Without 18-crown-6-ether slight mudding occurred with PEO addition in sols containing cobalt, which increased with time. With 18-crown-6-ether no mudding occurred for at least 24 hours after PEO addition, and the spinnable lifetime could be extended to several days if the sol was stored in a fridge. It also led to a smoother spinning operation, with less irregularities such as holes blocking, spluttering or pulsing. This was further evidence of an interaction between the barium and cobalt ions in the sol, which was harmful to stability. The viscosity of PEO solutions is also reduced over time by reaction with dissolved halides and transition metal ions, especially Fe^{3+} [206], reducing the spinnability of stored solutions. Although PEO is soluble in solution with a pH <2, the catalytic activity of halides and Fe^{3+} in the degradation of PEO becomes greater with an increase in acidity, and chlorine has been found to drastically reduce viscosity through the formation of hydroperoxides, although this can be stabilised by the addition of an alcohol encouraging the hydroperoxide to form on the alcohol and not on the polymer [208].

The spinning sols still had tendency to form a thixotropic gel on standing, a problem as the sol was stationary for the duration of the spinning process, and these structure effects became more apparent as cobalt levels rose. This could be avoided by adding 3 - 6% methanol to the concentrated sol immediately prior to spinning, which also reduced the viscoelasticity of the sol. An addition of methanol, in which PEO is not normally soluble, has the effect of increasing solubility and reducing viscosity of any PEO-metal halide association compounds [207], and it appears to eliminate gelling from the interaction of PEO and $CoBr_2$ in these sols. It has been speculated that the methanol-cation interaction resembles that of the crown ethers [209], and this could be a further reason why 18-crown-6-ether appeared to aid the spinning. Although chloride was also found to make sols thixotropic, a small amount of Cl^- helped spinning by adding a small amount of localised structure between sol particles. Before addition of methanol, the spinning solutions typically had a viscosity of 6 - 9 poise.

2.3 Blow spinning of hexagonal ferrite fibres

Photographs of the blow spinning and collection apparatus are shown in figure 71, and a schematic diagram is shown in figure 72. The solution was spun from 10 or 20 ml syringes, at ideal rate of 2 - 3 ml hr^{-1} $hole^{-1}$ and an air temperature of 70 °C at the spinneret. Two spinners were used, with 4 and 6 holes respectively, and the holes were each 280 μm in diameter. Gel fibres were observed under a microscope at up to 400X magnification, lit from underneath. Although all of the fibres varied between reddish and golden brown in colour, any internal structure could easily be seen as the gel fibres were still transparent. 20 ml of a 16% Fe spinning solution would give 10 g gel fibre after 60 - 90 min of spinning time, which would in turn yield around 5 g of ceramic fibre when fired. It was important that the precursor sol resulted in a spinnable sol which produced smooth, regular fibres, which could be collected as a well aligned product, as this is an important factor in their potential use in composite materials. Any effects from flocculation, structuring or lack of viscosity in the sol were clearly apparent during the spinning process.

The spun fibres, being under 10 μm in diameter, were much smaller than the holes and this differentiates spinning from simple extrusion. If 10% of diameter of hole was blocked by particulate this stopped spinning from that hole, resulting in blocking, candling (when dribbles of solution dangle from holes) and spluttering (intermittent wet spurts, not fibres). However, particles of 30 μm are not needed to cause this, as either structuring between particles during solution concentration in the spinning process, or shear agglomeration of particles within the spinnerets can lead to blockage. It has been found that any sizeable population with a diameter over 0.01% of the hole diameter (~30 nm) will be likely to flocculate in the holes during spinning.

Blocked holes often stopped and started again as one blockage left the hole and another arrived, caused by precipitation, flocculation, structuring or crystallisation in the solution, and if any fibres were produced they tended to be uneven and full of internal structure. Fibre which was not collecting on the drum but also was not floating around, or

which had a wiry look if random fibre, was too thick (>15 μm) and brittle, snapping into lengths of a few cm when bent around the rotor, and so was not continuous.

Twinning (coalescence) of fibres to give a figure of eight cross section was a typical symptom of viscoelastic & thixotropic behaviour, caused as the elastic fibres became stretched and whipped back upon themselves through recoverable elasticity, drying as twins. Such behaviour has been seen in solutions with either a large upper limit of particle size, or through interactions with PEO. The fibres so produced were usually smooth and optically clear, but viscoelasticity could cause an uneven pulsing in the flow of the solution from the spinnerets, and thixotropic behaviour led to stoppage of spinning. If the spun fibre was still too wet, thin fibres tended to develop as too much liquid was lost in drying during spinning, and if collected as an aligned blanket sections could fly off from drum as the fibre shrank too much. If random fibre was being produced dense mats of fibre would gather, instead of the usual candy-floss like loose clumps. If the solution was too dilute, with insufficient structuring or too much distance between particles, it would tend to produce wet splatters, and any splatters landing on a blanket dried and caused breaks in that blanket, resulting in fly-offs. Fibres catching in the spinning duct, or being very thin and floating around were also typical of dilute solutions or too little / too low MW PEO. This caused shot, balls of gel several times larger than the fibre diameter but still attached to it, like a necklace, that gave the fibre sideways momentum and caused it to stick to the sides of the duct. Once fibre had become stuck on the sides of the duct it acted as a site, catching more fibre and eventually blocking the entire duct. Shot also led to thin fibres, as much of the solution volume was lost to the bulky shot.

2.3.1 Iron oxide fibres

The Fe/Br iron solution was concentrated to 20% Fe after the addition of 3% 400,000 MW PEO by weight to iron oxide. The spinning solution viscosity was about 3 poise, as measured on a paint cone-and-plate viscometer at 1000 s^{-1}, and this was lower than the doped iron sols at corresponding concentrations. The particle size was increased by the addition of PEO (fig. 73),

and this could be seen as the volume average of 6.0 nm and upper limit of 20.0 nm in the sol increased to 7.6 and 29.9 nm in the solution, with a distribution of 99.6% within 3.8 - 18.9 nm. Similarly the number and volume averages were raised from 5.1 and 14.2 nm to 5.7 and 18.9 nm, with a distribution of 99.4% between 3.8 - 11.9 nm.

The gel fibres were smooth and even in appearance, with straight and parallel sides and a diameter of between 2-10 μm, with a mean of 6 μm. The coarser fibres occurred because of coalescence of the parallel fibre streams during spinning, and some twinned fibres were also present. These twinned fibres accounted for the wide variation in the diameter of the fibres, and the true average diameter of single fibres was estimated to be 3 μm. This was much smaller than the diameter of ferrite sols spun at equivalent concentrations, and was more evidence that the divalent metal species interacted with the iron sol, decreasing stability whilst increasing localised structuring and mimicking the behaviour of a more concentrated sol. The problem of fibre coalescence could be resolved with further development of the spinning process, resulting in fibres with a much smaller diameter deviation, and the average fibre diameter increased by using a higher MW PEO.

Following the problems encountered with the 400,000 MW PEO in the Fe/Br solution, it was decided to use 1,000,000 MW PEO with a nitrate based sol. The slightly less stable Fe/NO_3 sol was spun at a concentration of 19.25% Fe, and there were problems from the start with holes blocking. When spun at a rate of 2.3 ml $hr^{-1}hole^{-1}$ a temperature of 100 °C was needed to dry the fibres, which were mostly smooth, clear fibre 3 - 4 μm in diameter with no internal structure, but there was also some shot 12 - 120 μm in diameter. It was this small percentage of the product which was causing the problems of blocking and fibre catching in the duct, but nevertheless, all of the solution was spun.

2.3.2 BaM fibres

As with the undoped Fe/Br sol, the addition of PEO caused an increase in particle size in the sol, and the solutions and sols are compared in table 3.1. The volume distribution of the

solution was 99.5% between 3.6 - 22.6 nm, with an average of 7.9 nm and an upper limit of 35.8 nm, compared to an average and upper limit of 6.6 nm and 33.2 nm in the sol. The number distribution exhibited a proportionally greater increase in number average from 5.1 to 6.0 nm and upper limit from 16.7 - 22.6 nm, but with a much lower absolute value of 99.2% between 3.6 - 11.3 nm.

The solution was spun at 17.0 - 17.3% Fe through a four hole spinner, at 2.3 - 2.8 ml hr^{-1} $hole^{-1}$ and 70 - 80 °C, with all of the solution being used without any hole blockage to give fibres 3 - 5 μm wide. When the spinning solution was made with 400,000 MW PEO however, a rate of 3.5 ml hr^{-1} $hole^{-1}$ at 90 - 100 °C was needed, and the fibres contained some shot, a symptom of insufficient PEO. This produced 4 μm fibres with uneven, wobbly sides, but some of the fibres were as small as 2 μm in diameter, and this sample was not fired for safety reasons.

When an attempt was made to spin BaM fibres made from a sol doped with $Ba(ac)_2$, the solution flocculated and gelled at a point between 11.7% and 14.2% Fe. This reversible reaction was attributed to the acidification of acetate ions (CH_3COO^-) in the sol, leading to the formation of ethanoic acid (CH_3COOH), which is a known gelling agent and would interact with the PEO. This was another reason for the use of acetate salts to be abandoned.

Solution	Z Av.	Vol. Av.	Vol. upper	No. Av.	No. upper	Polyd.	Range
10.5% Fe sol	4.7 nm	6.0 nm	20.0 nm	5.1 nm	14.2 nm	0.760	1.2 - 18.7 nm
16.7% Fe spin. soln	6.7 nm	7.6 nm	29.9 nm	5.7 nm	18.9 nm	0.733	1.7 - 25.9 nm
10.5% M sol	7.4 nm	6.6 nm	33.2 nm	5.1 nm	16.7 nm	0.630	2.1 - 26.1 nm
15.7% M spin. soln	8.0 nm	7.9 nm	35.8 nm	6.0 nm	22.6 nm	0.676	2.2 - 29.4 nm
10.5% Z sol	6.8 nm	8.1 nm	36 nm	7.5 nm	22.7 nm	0.690	2.3 - 27.9 nm
14.6% Z spin. soln	11.2 nm	14.1 nm	47.1 nm	12.0 nm	29.7 nm	0.741	3.7 - 48.0 nm

Table 3.1 Comparison of precursor sols and spinning solutions for iron, M ferrite and Z ferrite fibres, with concentration of sol / soln given at % iron

2.3.3 SrM fibres

As with the undoped sols, the size distribution and average increased slightly for the SrM solution compared to the BaM solution, as shown in figure 74. The halide spinning solution was spun at a high concentration of 16.9% Fe, at a rate of 2.4 ml hr^{-1} hole $^{-1}$ and a temperature of 80 °C, to give clear even fibres with a low diameter of 3 - 4 μm. When the rate was increased to 3.5 ml hr^{-1} hole $^{-1}$ the diameter was increased to 6 μm, but the temperature had to be increased to 90 °C to dry the fibre sufficiently. All of the solution was spun through a six hole spinner without any holes stopping, and the resulting fibres had a more ginger hue than the BaM gel fibres.

2.3.4 CoTiM fibres

A series of fibres with the formula $BaCo_xTi_xFe_{12-2x}O_{19}$ were successfully spun to give the stoichiometric ferrite with x = 0.5, 0.75, 1.0 and 1.1, from a doped ion sol mixed with a titania sol. A higher loading than x = 1.1 rendered the solution unspinnable due to the detrimental effects of the barium / cobalt interactions with the iron / titania sol. As can be seen in figure 46, the spinning concentration remained nearly constant from undoped solutions up to levels of x = ~0.8, although it then dropped sharply the rate was still less than that of the sol. This indicated that interactions within the sol would become the limiting factor in the stability of spinning solutions with higher substitution levels, rather than the effect of any PEO interactions, and that the spinning solution was less sensitive to increasing substitution than the sol. All of these fibres were collected only as random staple, due to mechanical problems with the collection apparatus at the time.

The x = 0.5 solution was spun at a concentration of 16.04% Fe through a four hole spinner at a rate of 3.4 ml $hr^{-1}hole^{-1}$ and a temperature of 100 °C. Despite the high concentration of the sol it was not at all elastic and if anything was a bit too wet still even at 100 °C, but no shot was produced. One hole stopped spinning, but all of the solution was spun to give smooth and even fibres 5 μm thick, with no internal structure visible. The x = 0.75

solution was spun at 16.56% Fe and a rate of 3.4 ml hr^{-1} $hole^{-1}$, again at a high temperature of 95 - 100 °C. The entire solution was spun without any stoppages to give fibres 5 - 6 μm in diameter with no structure and smooth even sides.

The x = 1.0 solution was much more viscous at relatively low concentrations, and was spun at a very low level of 12.22% Fe. There was some evidence of viscoelasticity and many of the fibres were coalesced, and one hole of four was intermittently stopping through out the spinning, but nonetheless all of the solution was spun. A high rate of 4.8 ml hr^{-1} $hole^{-1}$ was needed to keep the spinning smooth, and consequently a high temperature of 110 °C was needed to dry the fibres. The fibres were 5 - 6 μm thick and full of submicron structure, but even and parallel sided. The x = 1.1 solution was also spun at a low concentration of 12.03% Fe, but this time at a low rate of 2.3 ml hr^{-1} $hole^{-1}$ and a temperature of 95 - 100 °C, to give good fibres 4 - 5 μm thick, and without any visible structure inside.

The addition of titanium actually seemed to ease many of the viscoelastic effects encountered in the undoped fibres during spinning, reducing structuring to such an extent that the less substituted sols behaved as if they were very dilute. This aided the collection of the more substituted sols which were unusually viscous at low concentrations.

Barium was substituted with strontium to compare a series of aligned halide stabilised and halide free $SrCo_xTi_xFe_{12-2x}O_{19}$ fibres to the BaCoTiM sol fibres. The halide stabilised solutions were spun at concentrations of 14.1% and 15.15% Fe for x = 0.5 and 1.0 respectively, but in both cases the spinnerets showed signs of blockage, spluttering and intermittently stopping. This was attributed to the small trace of high diameter material seen in the PCS of the ostensibly very spinnable sol, and the gel fibres were full of a visible internal structure and had a lumpy surface. The solutions were spun at a rate of 3 ml hr^{-1} $hole^{-1}$ using four hole spinners, and although in both cases one hole stopped soon into spinning all of the solution was spun and collected as an aligned blanket of fibres 4 - 6 μm in diameter. After drying for a week small clear crystals, probably of PEO, had appeared on the surface by syneresis, leaving the fibres smooth and without internal structure. The halide free sols proved

to be unspinnable due to the larger particle size.

2.3.5 Co_2Y fibres

The spinning solution was concentrated to 14.59% Fe and spun from a four hole spinner at a rate of 3.4 ml hr^{-1} $hole^{-1}$ and a temperature of 90 - 100 °C. Despite one hole blocking, fibre catching inside the duct and the fibres being too wet, the entire solution was spun to make both random and surprisingly well aligned fibres, considering the viscoelastic behaviour of the solution and shot content seen in the non-aligned fibres. The fibres were 4 - 8 μm in diameter, but with some internal structure clearly visible. When extra crown ether was added the solution became more viscoelastic, and coalesced fibres resulted.

The other Y ferrite sols proved more difficult to spin. Ni_2Y was spun on the limit of spinnability at 13.3%, even though the viscosity was low at 1.5 poise, as the solution precipitated at higher concentrations. Nevertheless the solution spun well at 2.3 ml hr^{-1} $hole^{-1}$ and 90 °C, to give smooth and clear random fibres 6 - 10 μm thick, many of which were coalesced, and were wiry and brittle due to their joint thickness'. Mn_2Y solution could not be concentrated over 12.4% Fe, and appeared to be barely spinnable. Despite this the entire solution was spun from a four hole spinner without any holes blocking or stopping, at 80 - 90 °C and at a rate of 2.3 ml hr^{-1} $hole^{-1}$. The resulting random fibres were poor, being rough, full of internal structure, coalesced and a bit too wet, but considering the dilution of the solution this was to be expected. The fibres were 5 - 15 μm in diameter, and rather than wiry and brittle they crumbled easily under pressure, but appeared quite resilient under tension. The Zn_2Y solution could not be concentrated over 12.9 % and appeared totally unable to pull fibres at that concentration. On further investigation this was found to be because the PEO had precipitated out of solution as a rubbery lump, and the Zn^{2+} ions proved to be totally incompatible with PEO in these sol systems.

2.3.6 Co_2Z fibres

The Z spinning solution was also studied by PCS, after the addition of the spinning aid and concentration to the required viscosity, and the results are shown in table 3.1, compared to the undoped and BaM spinning solutions and sols. This showed a near doubling in average particle size (fig. 75), but despite this the sol remained spinnable due to only a slight increase in the upper limit of particle size. The fibres were spun at a concentration of 16.23% through a six hole spinner at a rate of 2.3 ml hr^{-1} $hole^{-1}$ and a temperature of 82 °C, to give a well aligned blanket of smooth, structureless fibres 5 - 7 μm thick. The halide free solution was spun at a similar concentration and a rate of 3.3 ml hr^{-1} $hole^{-1}$, but proved much harder to spin, producing very thin fibres 2 - 3 μm thick which were too wet even at air temperatures over 100 °C, again indicating that some structuring from chloride acts as an aid to spinning.

2.3.7 Co_2Z fibres containing additives

Solutions with just silica up to 0.7% as an additive were spun without problem, but this was not the case with a 1% SiO_2-1% B_2O_3 doped solution. It could be reduced to a spinnable concentration with PEO, but had trouble spinning, with holes blocking, candling and spluttering, stopping and starting again. It was spun at 5 ml hr^{-1} $hole^{-1}$ and a temperature of 75 - 85 °C, to give 6 μm fibres, but they were rough and bumpy on the surface, with a clearly visible internal structure. Fibres made from a sol with silica, boria and 1% alumina were even worse, with a slight mudding in the solution which had to be spun at a low concentration, resulting in the same problems as before plus wet fibres that would not gel fully even when spun at a rate of 2.3 ml hr^{-1} $hole^{-1}$ and a temperature over 100 °C. The spinning eventually stopped as all the holes blocked and the solution within the spinner set and formed a crust, having produced uneven fibres alternatingly stringy and lumpy in appearance. It was shown that the boric acid was responsible for the flocculation and the alumina sol for thixotropy when a solution containing only 1% each of alumina and silica was spun. This produced smooth transparent fibres at first without any structure, but as the thixotropic solution became more

viscoelastic twinned fibres began to appear and eventually the spinning solution set within the spinner. This was attributed to the Cl^- ions present in the alumina sol. With the reduced level of Cl^- in the 1% $CaSiO_3$-0.3% Al_2O_3 doped solution, all of the material was spun over a 150 min period at a rate of 2.3 ml hr^{-1} $hole^{-1}$, despite the viscoelasticity of the solution resulting in many twinned fibres.

A small amount of the large trivalent ions La^{3+}, Gd^{3+} or Y^{3+} (0.1 mol Fe:0.00125 mol lanthanide) was found to increase the viscoelasticity of the Z spinning solution, giving 6 μm fibres which were often twinned, distorted and too wet despite being spun at concentrations in excess of 14.6% Fe. However, equal additions of the equally large Sr^{2+} or Ca^{2+} had no effect on the spinning of a doped Z solution. The Ca doped solution was spun at a concentration of 14.4% Fe at a rate of 2.3 ml hr^{-1} $hole^{-1}$ and 80 - 90 °C to produce 5 - 6 mm fibres, which spun all of the solution from a six hole spinner over 90 minutes.

2.3.8 Co_2W fibres

The spinning solution was concentrated to 15.13% Fe, and gave trouble-free spinning. The Co_2W gel fibres were spun through a six hole spinner at a low rate of 1.5 ml hr^{-1} $hole^{-1}$ and at 90 °C, to give clear fibres with an average diameter of 6 μm, and the entire solution was spun

2.3.9 Co_2X fibres

The solution was spun at a concentration of 15.33%, over which point it began to mud. The entire solution was collected using a four hole spinner as random fibre 4 - 6 mm in diameter, but full of internal structure and with uneven, twig-like sides. The fibres were too wet despite being spun at 100 °C, and became too brittle upon drying to collect as an aligned blanket, the fibre diameter being reduced by shot production. The solution had to be spun at a fast rate of 4.6 ml hr^{-1} $hole^{-1}$, accounting for its wetness, but despite these problems no blockages or stoppages occurred.

2.3.10 Co_2U fibres

The spinning solution was concentrated only to a normally unspinnable 11.90% Fe, but the increased viscosity of the U sol rendered the sol just spinnable. All of the solution was spun through a six hole spinner, with just one hole blocking, at a rate of 3 ml hr^{-1} $hole^{-1}$ and a temperature of 110 °C, to give smooth, clear and structureless fibres. Unfortunately a large proportion of the solution was lost as shot, and this reduced the diameter of the fibre to only 3 - 4 μm, a dangerously small diameter. Consequently only minimal amounts of this fibre for analysis were fired, and samples handled and prepared in a fume cupboard.

2.3.11 Alkoxide based BaM fibres

A fibre of M ferrite was successfully spun from a sol prepared by the organic-based alkoxide route, but the resulting gel fibres were twisted, full of internal structure and difficult to spin. The solution was spun at a concentration of 13.7% Fe, at rates between 2.8 - 3.3 ml hr^{-1} $hole^{-1}$ and temperatures as high as 116 °C in an attempt to dry the wet fibres. They had an average diameter of 6 μm, but a wide spread from 3 - 9 μm, and many were coalesced by viscoelastic effects.

2.3.12 Alkoxide based Co_2Z fibres

If any 2-methoxyethanol remained in the sol the PEO came out of solution as a rubbery lump below 10% Fe. Otherwise the sol was spun at 13%, right on the limit of spinnability, so 2,000,000 MW PEO solution was needed to spin the solution. 4% MeOH was added, and the fibres spun at a high temperature of 115 °C and a high feed rate of 10 ml $hole^{-1}$ hr^{-1}. A four hole spinner was used, but three of the holes blocked almost immediately, but nevertheless 3.3 g of random gel fibre was collected. Despite the high temperature the fibres were a bit wet and matted, and were less "fluffy" looking than fibres made from aqueous precursors. Due to the high feed rate and high MW PEO, the fibres were thick with an average diameter of 10 - 12 μm and they had a rough surface and internal structure, with an uneven, twig-like appearance,

probably due to a destructive interaction between the spinning aid and organic solvents remaining in the spinning solution.

2.4 Alignments of hexagonal ferrite fibres

The diameters and alignment of the gel fibres did not change to any detectable degree during subsequent processing, except when DGG occurred and massively elongated grains formed that maintained the cross-sectional width of the fibre in one dimension only. In Z ferrite fibres a waviness was observed to appear which sometimes resulted in "smearing" of alignment, and steaming was also found to destroy alignment. The proprietary *Safimax* fibre collection process [125], designed for the manufacture of aligned *Saffil*-like fibres, was modified to allow the collection of the aligned hexagonal ferrite gel fibres. *Safimax* alumina fibre was a commercial development product, in which all the fibres were within $^{+}/_{-}20°$ and 90% were within $^{+}/_{-}10°$ of the axis of alignment. In the modified process used for the ferrite fibres the collection rotor was operated well below, rather than slightly above the fibre generating velocity, and an open diverging rather than a converging air duct was used. A known result of this differential between the velocity of the fibre draw and the speed of the collection drum was the looping seen in the generally well aligned fibres, and as a result 5 - 20% of the ferrite fibres crossed the general alignment because of looping on to the rotor. These could not be removed by subsequent tensioning and could affect the packing into composites. However, the remaining 80 - 95% were well aligned, and this problem would be removed with further optimisation of the spinning process, improving the alignment of the fibres. The slight waviness seen in the ferrite fibres was also present in *Safimax*. The fibres seen crossing perpendicularly across the alignment on the surface of the fibres were disturbed during sample preparation, from a combination of loose fibres from the edge of the blanket and sticky gel fibres catching on the scalpel blade, and were not a true alignment feature.

2.4.1 Iron oxide fibres

When the undoped iron sols were spun and collected as aligned fibres, 5-10% of the fibre

length crossed the general alignment because of looping on to the rotor. The remaining 90-95% was well aligned as can be seen in figure 76, which shows the aligned haematite fibres. 88.8% of the fibres were within $^{+}/_{-}20^{\circ}$ and 69.2% were within $^{+}/_{-}10^{\circ}$ of the axis of alignment, and this compared reasonably well with *Safimax* alumina

2.4.2 M ferrite fibres

The BaM ferrite fibres were well aligned with 88% of the fibres being within $^{+}/_{-}20^{\circ}$ of the axis of alignment and 69% within $^{+}/_{-}10^{\circ}$ (fig. 77). However, the SrM ferrite fibres were not as well aligned. The fibres were undulating, with some individual fibres being looped almost perpendicularly to the axis of alignment. Although only some 80% of the SrM fibres were aligned within $^{+}/_{-}20^{\circ}$ of this axis and 62% within $^{+}/_{-}10^{\circ}$ (fig. 78), it is thought that the differences between the two fibres are due to minor variations during the actual spinning and collection, rather than any intrinsic variance in the properties of the two sols. The $SrCo_xTi_xFe_{12-2x}O_{19}$ fibres showed better alignment than the unsubstituted M ferrites, with an alignment of 94% within $^{+}/_{-}20\%$ and 78% within $^{+}/_{-}10\%$ for x = 0.5 (fig. 79), due to the improved spinnability of the substituted solutions.

2.4.3 Co_2Y fibres

The Co_2Y gel fibres possessed excellent alignment, superior to that of the M fibres, in which 96% were within $^{+}/_{-}20^{\circ}$ of the axis of alignment and 76% within $^{+}/_{-}10^{\circ}$, as can be seen in Figure 80.

2.4.4 Co_2Z ferrite fibres

The Co_2Z and Ca-doped Co_2Z fibres behaved identically during the spinning procedure, and the addition of calcium conferred no advantage to the alignment or quality of the gel fibres. The fibre diameter was between 5-10 μm in both cases, and the gel fibres were smooth and parallel sided. 98% of the fibres were found to be within $^{+}/_{-}20^{\circ}$ of the axis of alignment, and 76% were within $^{+}/_{-}10^{\circ}$ (fig. 81).

2.4.5 Co_2W fibres

The W fibres were extremely very well aligned, with 94% of the fibres being within $^{+}/_{-}10^{\circ}$ of the axis of alignment (fig. 82), and this is superior to some commercially manufactured fibres.

3. Conclusions

All of the fibres which appeared spinnable from their sol characteristics proved to be so, albeit after some optimisation of the blow spinning parameters such as feed rate, temperature and air velocity. The gel fibres were collected as both random fibre and aligned blankets, collected on a drum rotating at 1000 RPM. As the sols were insufficiently viscous to draw fibre, 2 - 5% PEO was added as a linear polymer spinning aid, and most spinning solutions had a concentration of 14 - 17% Fe. Usually a 1% 1,000,000 MW PEO solution was used to make fibres between 4 and 8 μm wide, but for more dilute solutions of borderline spinnability a higher MW PEO was used.

PEO is also known to form association compounds with mineral acids, bromine and metal halide salts, and even in the undoped Fe/Br sol the addition of PEO caused an increase in particle size in the sol because of interaction with the Fe^{3+} and halide ions. However, these effects were not enough to compromise the spinnability of the solutions. The addition of barium or strontium in BaM and SrM sols appeared to make little difference, indicating the PEO did not interact with Ba^{2+}, perhaps because it was partially protected by the crown ether. Crown ether also aided spinning, perhaps by forging a degree of localised structuring between barium ions by hydrogen bonding between the chelating rings, and a small amount of chloride also seemed to improve spinning compared to totally chloride free systems. This implied that a certain degree of localised induced structuring appeared to be a good feature for improving the spinnability of a sol, but too much and thixotropy occurred.

Addition of Co^{2+} led to an increased structure in the fibres, but it can be seen from figure 67 that most of the loss of stability was from interactions with the Fe/Br sol. It is clear

in figure 83 than the rate of loss of stability of the sol from Co^{2+} addition was greater than that from PEO addition in the spinning solution, and with further addition this effect alone would determine the spinnability of the sol, which normally required a concentration of 13% Fe. The spinning sols containing cobalt had an increased tendency to form a thixotropic gel on standing, and these structure effects became more apparent as cobalt levels rose. This could be avoided by adding 3 - 6% methanol to the concentrated sol immediately prior to spinning, which also reduced the viscoelasticity of the sol. Only the spinning solutions for Y, Z and W ferrites were compared, as the X and U solutions were only spun once as random fibre and never optimised.

A series of fibres with the formula $BaCo_xTi_xFe_{12-2x}O_{19}$ were successfully spun, but a higher loading than x = 1.1 rendered the solution unspinnable due to the detrimental effects of the barium / cobalt interactions with the iron / titania sol discussed in chapter two. The spinning concentration remained nearly constant from undoped solutions up to levels of x = ~0.8, and although it then dropped sharply the rate of decrease was still less than that observed in the maximum stable concentration of the sol (fig. 46). This suggested that interactions within the sol would become the limiting factor in the stability of spinning solutions with higher substitution levels, rather than any PEO interactions. However, the addition of titanium actually seemed to ease the viscoelastic effects encountered in the undoped fibres during spinning, reducing structuring to such an extent that the less substituted sols behave as if they were very dilute, but aiding the collection of the more substituted sols which were unusually viscous at low concentrations. $SrCo_xTi_xFe_{12-2x}O_{19}$ fibres were spun, but the spinnerets showed signs of blockage, spluttering and intermittently stopping. This was attributed to the small trace of high diameter material seen in the PCS of the ostensibly very spinnable sol, and the gel fibres were full of a visible internal structure and had a lumpy surface.

Other divalent ions such as Ni^{2+}, Mn^{2+}, and Ca^{2+} could be substituted and still result in a spinnable sol, but Zn^{2+} ions proved to be totally incompatible with PEO, making it

precipitate out of solution as a rubbery lump. A small amount of the large trivalent ions La^{3+}, Gd^{3+} or Y^{3+} was found to increase the viscoelasticity of the Z spinning solution, making spinning more difficult. Silica surfactant seemed to have little effect, but boric acid was responsible for flocculation, and 1% of added alumina sol caused thixotropy, giving viscoelastic twinned fibres, because of Cl^- ions present in the alumina sol.

Most of the fibres were aligned well, with 90 - 95% of the fibres within 20 ° of the axis of alignment. The alignment distributions of the Y and Z fibres are shown in figure 84, and it can be seen that around 35% of the fibres were precisely along the axis of alignment, with an very few fibres more than 20 ° out and none over 30 ° out of alignment. Many of the fibres seen crossing the alignment perpendicularly in micrographs were disturbed from the very top layer during sample preparation. The worst aligned fibre collected was SrM, although this was attributed to variations in the spinning process rather than an intrinsic problem in the spinnability of the solution. The distribution of SrM fibres is shown in figure 85, and it can be seen that the fibre had a much more uneven distribution, with half the fibres being at an angle of 10 ° to the axis but only 12% along the axis, and much larger populations at higher deviations up to 40 ° from the axis. This was caused by looping, as the rotor speed was only 80% of the fibre velocity at the base of the duct.

4. Experimental

4.1 Preparation of PEO solution

The PEO solutions made were 1% for 1,000,000 and 2,000,000 MW and 2% for 400,000 MW PEO. 1 g or 2 g of powdered PEO, as appropriate, was dispersed in 20 g of IPA. 80 ml of water was then added, and the solution mixed at 200 RPM for two hours resulting in an even solution without any lumps. While viscous and slightly sticky, this was too dilute to pull fibres readily until concentrated further.

4.2 Preparation of spinning solution

The sol, with a concentration of 10.5% Fe was filtered through a 0.7 μm pressure filter, the viscous sol driven through the filter by compressed air. The PEO solution was also filtered through the 0.7 μm pressure filter and acidified to pH 3 with HBr immediately before addition to the sol. The suitable grade of PEO was added, between 2% and 5% by weight to ceramic product, and the solution reduced to the highest concentration, i.e. lowest volume, possible on a rotary evaporator at 35 °C and under a vacuum of 95 kPa. This had to be done extremely carefully, with careful control of bumping at the beginning and rotation rate near the end. MeOH was then added (3 - 6 wt% to Fe), the solution mixed for two minutes, and a syringe loaded with the solution ready for spinning.

4.3 Blow spinning

The entire spinning and collection apparatus was contained within a closed Perspex cabinet during spinning, with a filtration / extraction system to prevent the release of potentially toxic gel fibres into the environment. The sol was loaded into a syringe, which was then placed in a variable rate syringe pump within the spinning rig, and the syringe connected to the spinner by a piece of tubing. The spinner consisted of a parallel line of four or six spinnerets, each 280 μm in diameter, with two parallel air slits either side. The spinner was then primed by hand so that the reservoir beneath the spinnerets was full, the cabinet closed and the syringe pump and two air streams started. The sol was drawn as a stream of liquid from the row of spinnerets by slits on either side, which directed the impinging high velocity primary air jets, carrying streams of air with a relative humidity of over 80% at 25 °C at a velocity of around 50 - 60 m s^{-1}. The fibre draw velocity was around 10 m s^{-1}. The fibre was then dried to a gel by mixing in a drying secondary air stream at 60 – 110 °C with a velocity of 4 - 9 m s^{-1}, this process taking place within 5 cm of travel from the spinning sites. The fibre-air mixture was passed down a short diverging section into a parallel duct of 70 cm in length, the two air streams providing a total air velocity of ~4 m s^{-1} at the bottom of the duct.

Random staple fibre was then collected in a stainless steel gauze basket at the bottom of the duct. Aligned fibres were collected at the bottom of the duct on a fast rotating drum with a diameter of 15 cm, which also had a transverse movement of 20 cm travel perpendicular to the duct to collect the fibres as an aligned blanket roughly 20 x 50 cm. Both movements of the drum were controlled by programmable stepper motors, and the velocities were typically a rotation of 1000 RPM and a transverse movement period of 5 min. After collection the fibres were removed from the drum and immediately stored in a circulating oven at 110 °C to await subsequent heat treatment.

4.4 Assessment of fibre alignment

The small proportion of fibres crossing the general alignment was estimated using an optical microscope at 40X magnification. The number of aligned fibres in a field was counted, together with the few crossing the alignment in the same field. Counts were made in up to 5 separate fields summing to several hundred generally aligned fibres and up to about 50 crossing the alignment. The direction of the generally aligned fibres was analysed by traversing the electron micrographs with a protractor normal to the axis of alignment and measuring the deviations of at least 100 individual fibres. Two sets of data were taken from opposite sides of each micrograph. Both the protractor measurements on micrographs and direct measurement at 40X magnification were viewing deviations set into the fibre on a 1-2 mm scale.

Chapter Four

The Solid State Reactions, Crystallisation, Sintering and Microstructure of Hexagonal Ferrite Fibres

1. The conversion of gel to ceramic

In the sol-gel technique a liquid colloidal solution, or sol, of dissolved metallic ions is prepared, usually from a organometallic solution which is then hydrolysed and condensed to form polymer-like chains of metallic ions and oxygen. On solvent evaporation amorphous oxy-hydroxide particles form a rigid gel, which can then be dried and fired to provide a sintered and dense ceramic. Due to their small size and extreme homogeneity the initial particles are more reactive and therefore they react at lower temperatures than standard ceramic powders, often leading to a ceramic product with smaller particle dimensions. It has been shown that the size and distribution of the sol particles will have a large effect on the resulting gel and ceramic microstructures. Small particles with a small size distribution will give a small and monodisperse gel structure, which will in turn produce a dense and well sintered ceramic with a relatively small grain size. Larger particles will result in larger grains, and a more polydisperse sol will lead to a less monodisperse gel, and give a ceramic with a wide range of grain sizes, maybe consisting of islands of large grains surrounded by smaller grains. A bimodal sol will retain two distinct species at all stages, with pores forming between the grains due to the size mismatch. [153].

1.1 Drying

As a gel dries, the actual particle size shrinks slightly as there is some water and hydroxide within the primary particles, and not just on the surface. However, the viscoelastic solid gel fibre produced from blow spinning also contains 10 - 25% free water or solvent, the ceramic precursor compounds and any additives, and this is removed by drying. At first the gel body will shrink by an amount equal to the volume of liquid lost, with the liquid / vapour interface for evaporation at the surface, and the liquid is lost at a constant and rapid rate. The solid gel

network is drawn together by capillary and osmotic pressure as the liquid between the particles is removed, and as the gel shrinks the surface tension within the pores increases and vapour pressure decreases.

The critical point is reached when the radius of the meniscus of the solvent becomes small enough to enter the pores, and this is the point when the particles are no longer separated by the liquid, except for a very thin film. Shrinkage virtually ceases as this point of the drying process, and cracking often occurs at this point as capillary pressure forces the particles to rearrange until they are packed as densely as possible. Thus the rate of liquid loss decreases greatly after the critical point, and it is no longer linear, as air enters the pores with further evaporation and a vapour diffusion process will occur. However, a continuous liquid film still covers the pore surfaces, allowing the liquid to flow to the surface and evaporate, and both flow and diffusion process happen simultaneously, emptying the larger pores of liquid first. Eventually, if the body is large enough, the liquid is isolated into pockets, and this leads to a second large drop in the rate of evaporation, as the remaining isolated liquid cannot flow directly to the surface and must evaporate inside and diffuse as a vapour to the outside for further drying to occur.

In a typical sol-gel material this results in a shrinkage to 10 - 20% of the original volume, but the gel fibres are both made from a concentrated sol and are dried in the spinning process, resulting in typically $^{1}/_{10}$ of this expected shrinkage. Shrinkage and cracking at the critical point can be controlled by the addition of a surfactant to reduce the interfacial energy and thus reduce capillary stress. Shrinkage can also been avoided by removing all of the liquid without encountering the vapour / liquid phase boundary, either by supercritical drying to give an aerogel, or by freezing and subliming the liquid under vacuum in freeze drying. Once all the liquid has been removed, the solid skeletal phase is left, which is determined by the structure at the gel point and the extent of collapse during drying. Dried gels have larger surface areas and smaller pores than standards porous ceramic green bodies because of these processes, with a surface area of typically 500 - 1000 $m^2 g^{-1}$ for xerogels, and over this for aerogels [153].

Gel fibre is plasticised by water / solvent in the structure and is vulnerable to internally generated vapour and decomposition products, and if left in the fibre the free moisture can evaporate generating macroporosity in the gel structure which will not sinter out on subsequent firing [124]. Therefore, the free water must be removed before storage, although this must be done carefully to prevent boiling in the fibres which results in blistering. In the Sumitomo process, the mainly organic precursor fibre is treated at 70-80% relative humidity to convert much of the organic content to hydroxides and evaporate the alcohol solvent [213]. The 3M process recommends drying at 15 - 30 °C at 20 - 60% relative humidity, followed by a more intense drying at 70 °C to allow the fibre to dry more uniformly in cross section. However, bundles or thick blankets of fibre need more care as the fibres in the centre do not lose their moisture if drying by conduction only, so the blankets must be penetrated by a convection current of warm air.

1.2 Decomposition

When a dried gel is heated, a weight loss accompanied by an endotherm occurs between room temperature and 150 °C as any physically absorbed water is lost, with no shrinkage. Between this point and 500 °C both weight loss and shrinkage occur as any volatile and organic compounds are burnt out, usually producing exotherms, except the loss of any remaining water or hydroxide which produces and endotherm. This shrinkage is caused by continued condensation or polymerisation and structural relaxation as any excess free volume is removed.

The soft plastic gel fibre is converted to a brittle, porous, and usually amorphous ceramic fibre in the decomposition stage. The gel fibre must be slowly heated to over 400 °C, guarding against any sudden exotherms, to remove all traces of solvent and any organic components from the fibre. ICI steam their *Saffil* and *Safimax* fibres between 200 and 500 °C, to give an amorphous alumina fibre which is 40% porous, with 5 nm pores and a surface area of 150 m^2 g^{-1} but still with good tensile strength and stiffness [125]. Virtually all of the

shrinkage occurs below 500 °C, and the resulting amorphous fibre has to fired to higher temperatures to be converted to a crystalline ceramic material.

1.3 Crystallisation

The crystal state is an ordered solid state with units repeating regularly with large distances on the nm scale, as opposed to the unordered amorphous state, which has regular units only up to the second coordination sphere. This defines the limit of resolution by which XRD can differentiate a recognisable crystalline pattern from a noisy amorphous background, the smallest detectable crystallite size being around 3 nm. The crystalline state is more stable than the amorphous and unstable glasses often formed by gel structure. However, to reach the stable crystalline state the energy barrier of nucleation must be overcome, and a crystal cannot form unless the energy involved in forming a liquid / solid or glass / solid interface is at least balanced by the free energy gain from crystallisation. This crystal formation will always decrease the free energy, but as long as the crystallite size is below the critical radius, r_c, they will melt or redissolve, while crystals larger will grow spontaneously. The critical radius increases with temperature, being infinite at the melting point, but at lower temperatures r_c is small enough to form crystals with ease, in a process known as homogeneous nucleation, which only involves liquid / glass and crystal phases of the same material. If another substance or impurity facilitates nucleation, for instance by lowering the energy barrier or by acting as a template for nucleation to occur on, heterogeneous nucleation occurs, and for this reason crystallisation often first occurs on the surface of a body, contaminant or vessel which acts as a nucleation site.

1.4 Sintering

Sintering is different from structural relaxation and crystallisation, in that it is a densification caused by the collapse of pores driven by surface energy, and is a diffusion-led irreversible process with no associated weight loss. In amorphous materials transport can occur by viscous flow but in crystals only by diffusion, so it is both easier and quicker to densify an amorphous

material, but unfortunately the high temperatures required often mean that crystallisation occurs before sintering. Sintering is a key process in the control of properties in hexaferrites, and factors such as precursor particle size, homogeneity, stoichiometry, impurities, degree of reaction and atmosphere all effect the density, microstructure and magnetic characteristics of the final product [214].

In sintering, ions diffuse along grain boundaries and surfaces to points of contact between particles, providing bridging and connections between individual grains. Grains fuse together along the boundary, shrinking the pores by diffusion of material from grain boundaries to fill the pores. This increases density, while the pores become more less curved and surface area is reduced. Positive convex curvature has a higher energy than negative concave curvature, so material tends to move from convex to concave sites, filling in the necks between grains. Finer initial particle sizes and higher temperatures accelerate the rate of pore shrinkage, by increasing the initial driving force and speeding up transport rates respectively. Even after long sintering times porosity may still remain, but sintering aids can help achieve maximum density by introducing a low melting glassy phase. Unfortunately this can also impair creep resistance and encourage grain growth, with surface diffusion often being the dominant coarsening mechanism [215]. Sintering with reduced grain growth can also be obtained through hot isostatic pressing (HIP), in which the ceramic powders are sealed in a container and then heated and compacted simultaneously under pressure, but this process obviously cannot be applied to fibres.

1.5 Grain growth

Grains are the discrete particles from which a polycrystalline material is made, and they are different from crystallites, which are the crystalline blocks composed of unit cells detected by x-ray powder diffraction. Many crystallites may co-exist in a single grain, and for this reason the average crystallite size derived from the width at half height of the 100% peak in x-ray diffraction patterns is often much smaller than the observed grain size, although both will

increase with grain growth. For example, in SrM samples with a crystallite size of 5 nm the average grain size was 42 nm, and with an increase in temperature of 200 °C the crystallite size had grown to 20 nm and the grain size to 116 nm, the grains consisting of agglomerations of crystallites [51]. In a single crystal material the crystallite size and grain size are equivalent. There are several different models of grain growth [216], which are not necessarily mutually exclusive.

In Ostwald ripening an increase in the average grain size of a dispersed phase in a matrix is driven by the reduction of the interfacial energy between the two phases, and this is achieved by many smaller dispersed phases becoming fewer larger phases. Material must be transferred from one grain to another, and the transport mechanism is preferential solution of smaller grains, which then diffuse and precipitate onto larger grains [217]. Ostwald ripening can be incorporated into the Potts model, in which a collection of microstructural building blocks have energies determined by their characteristics and neighbours [218], and in diffusion controlled models it has been proven that the grain growth exponent is 3, so that for a grain of radius R, R^3 is proportional to time [219]. Other proposed processes include the Voronoi method, dependent solely upon topology and growth [220], the curvature driven growth model [221] and thermodynamic models [222].

Grain growth inhibitors often work via a particle pinning process, in which an added secondary phase is immobile with respect to the moving grain boundaries, preventing coarsening by Ostwald ripening. The secondary phase is often insoluble in the bulk material, and therefore it gathers on the surface on the bulk phase, at the grain boundaries.

2. The solid state chemistry of the hexagonal ferrites

Many studies have been made of the solid state reactions of the $BaO.Fe_3O_3.MeO$ system using standard ceramic preparations from oxides and $BaCO_3$. Russian workers have constructed several phase diagrams (fig. 86) and obtained the x-ray spacings of BaM, Y, Z and W for samples containing more than 50% Fe_2O_3. In samples which were heated to 1200 °C / 2hr,

pressed and then annealed at 1250 °C / 4hr, no Co_2X or Co_2U could be detected even at their stoichiometric compositions in polycrystalline samples [223]. Also changes in the lattice parameters for compositions near the borders of the Z and W regions in the phase diagram suggested that M, Y and W can dissolve in Z, and M dissolves in W better than Y or Z, to form solid solutions at these border compositions. The magnetic hexagonal ferrites are often mixed with $BaFe_2O_4$ which is also hexagonal but nonmagnetic, but this can be removed by dissolving in HCl, as the other phases dissolved much more slowly [11]. It was also found to be extremely difficult to produce a single phase sample of polycrystalline Y, Z or W ferrite, and the first sample produced had to be reduced to a single phase by grinding the grains down [11]. Single crystals several mm long of Co_2Y and Fe_2W could easily be grown by the flux method, but the higher melting Co_2W, Z, X and U ferrites were more difficult to produce [224].

As can be seen in figure 87, many of the different phases involved coexist at the same temperatures, and all of the hexagonal ferrites overlap [24;225]. α-Fe_2O_3 has a peak wt% of 65% at 700 °C, the spinel phase peaks at 5% at 700 - 900 °C, $BaFe_2O_4$ has a peak of 25% at 800 °C, BaM = 75% at 800 °C, Y = 60% at 1100 °C, Z = 85% at 1300°C and W = 60% at 1400 °C. The X and U phases are often indistinguishable from this background of mixed phases, and as the hexagonal ferrites share the same basic building blocks in their structures, their x-ray diffraction patterns and magnetic characteristics are often very similar as well. It must also be remembered that this data is for a non stoichiometric mix of oxides, and that an accurate stoichiometry for the desired hexagonal composition in the starting materials improves the yield of that phase, often enabling a single phase product to result. At temperatures over 1350 °C Fe^{3+} is reduced to Fe^{2+}, and this forms the solid solution $Co^{2+}{}_{1-x}Fe^{2+}{}_xFe^{3+}{}_2O_4$ which leads to the decomposition of the Y, Z and W phases [223].

A detailed investigation into the formation of M, Y, Z and W ferrites was also undertaken using co precipitated precursors [14]. Nitrate salts were mixed with ammonium oxalate and stirred in solution under an IR lamp until a critical concentration was reached, at

which point the simultaneous precipitation occurred, resulting in an intimate mixture of already partially decomposed oxalates. These were then decomposed fully at 500°C, ground, calcined at 800°C, ground, pressed, and finally fired at 1100 - 1400 °C. The spinel phase was seen to form at 650 °C and the BaM phase at 800 °C, both remaining until over 1100 °C. Manganese spinel ferrites are atmosphere sensitive at high temperature, and MnO and Mn_2O_3 can precipitate out of the ferrite if the partial pressure of oxygen is lowered [226].

2.1 BaM ferrite

The $BaO.Fe_2O_3$ system was first investigated in depth in 1946 [227], and in this and other early studies found many contradictory results, with the hexagonal $BaFe_2O_4$ phase sometimes being reported as coexisting with α-Fe_2O_3 up to 1400 °C, and sometimes not forming at all. The confusion may have arisen from other metastable phases that have since been identified. BaM and $BaFe_2O_4$ are mutually insoluble in each other as solids [229], and both form from 650 - 1000 °C, after which point a third phase can also develop until the ternary mixture reaches its liquidus point at 1175 °C. This third phase was identified as the metastable hexagonal $Ba_2Fe_6O_{11}$, which is stable up to its melting point of 1350 °C, reverting to BaM and $BaFe_2O_4$ on cooling [230]. In standard ceramic preparations the hexagonal $BaFe_4O_7$ phase can coexist with the BaM and $BaFe_2O_4$ phases below 1000 °C [231], and there are also two different phases of $BaFe_2O_4$, β-$BaFe_2O_4$ existing up to 1000 °C and α-$BaFe_2O_4$ over 1000 °C [232]. BaM crystallisation was found to have an activation energy of 73.2 kcal mol^{-1} at temperatures above 735 °C [233].

The products of $BaCO_3$ and Fe_2O_3 heated at 750 - 1200 °C and in the ratios of Fe:Ba of 2 - 12 were thoroughly investigated in 1973, and it was found that this ratio greatly affected the products. In all ratios, BaM and $BaFe_2O_4$ coexisted below 1000 °C until they reacted to form $Ba_2Fe_6O_{11}$ over this temperature, but from 1000 °C to 1150 °C the products were $Ba_2Fe_6O_{11}$ and $BaFe_2O_4$ for the ratios 2 - 3, and BaM and $Ba_2Fe_6O_{11}$ up to a ratio of Fe:Ba = 12. The $BaFe_4O_7$ phase was never observed, and all mixtures decomposed back to BaM and

$BaFe_2O_4$ over 1150 °C [232]. There is much ambiguity over the precise compositional solid solution range in which pure BaM can exist, with claims varying from an Fe:Ba ratio of 10 - 12 [231] to 11.4 – 12 [229;234], 11.6 - 12 [235] or only at exactly 12 [236]. Another phase has been identified between 600 and 950 °C as $BaO.nFe_2O_3$ where n = 4 - 5.8, which has a very similar XRD pattern to the M ferrite, which may explain some of these apparent discrepancies [237]. Rapid grain growth occurs above 1200 °C leading to DGG [238], and BaM melts around 1500 °C, dissociating to the W and X phases [239].

As can be seen from the phase diagram of the ternary system (fig. 86), M ferrite forms in regions clustered around the stoichiometric point to make the intermixed phases M + α-Fe_2O_3, M + W, M + Z, M + W + Z, and the pure phase is formed around 14.3% BaO-85.7% Fe_2O_3 [223]. The rate of the solid state reactions can be enhanced by radiation effects, and the radio stimulated diffusion of Fe, Mn and Zn ions is more than an order of magnitude faster than thermal diffusion in ferrite synthesis [240].

M ferrites produced from standard ceramic methods typically shrink by 20% in linear dimensions during sintering and densification, and a further 1% upon cooling, and this is also true for magnetically isotropic bulk specimens with no magnetic alignment of the individual particles. In magnetically anisotropic samples however, in which the grains are all oriented with their c-axes parallel, the shrinkage is also anisotropic during sintering, typically 23% parallel to the c-axis and 11.5% perpendicular to it [91].

As BaM is the most commercially important hexagonal ferrite, its solid state chemistry has been studied in much greater detail than that of the other hexagonal ferrites. The differences in reaction and product are highly dependent upon the manufacturing process employed, and these differences are summarised below.

2.1.1 Coprecipitated BaM

In coprecipitated BaM ferrite an iron-deficient non-stoichiometric mixture is needed, usually with an Fe:Ba ratio between 10 and 11, to form the single phase product [25]. The dried

hydroxide coprecipitates FeOOH and $Ba(OH)_2$ go through an endotherm between 130 - 350 °C as water is lost and the hydroxides are decomposed to oxides, but the material remains amorphous until BaM starts to form at 700 °C, with no crystalline precursors. M_s begins to increase at this point as the M phase crystallises, and there is a sharp exotherm at 760 °C corresponding to this crystallisation. The heating rate of 10 °C / min used in differential thermal analysis (DTA) leads to an artificially high temperature value for rapid processes, such as crystallisations. The material is all converted to BaM at 900 °C and grain growth occurs over 1000 °C. No phases other than BaM are ever seen [27]. In a variation an iron(II) salt is used instead to produce the precipitate $Fe(OH)_2$ which has a sparse structure, and 70% of the Ba^{2+} ions are contained within this, not as separate $Ba(OH)_2$ molecules [241]. Normally the iron(II) precipitate will slowly oxidise to iron(III) by redissolving and precipitating as α-FeOOH, the form of iron(III) hydroxide that is usually formed from iron(III) salts. This is too dense to keep the Ba^{2+} ions within its structure, but if the intimate mixing could be maintained in an iron(III) hydroxide long range diffusion would not be needed to form BaM, and lower reaction temperatures would be needed. This can be achieved by vigorous oxidation of the $Fe(OH)_2$ precipitate with H_2O_2 which bypasses the dissolution / reprecipitation step entirely by simply extracting part of the hydrogen from $Fe(OH)_2$ to give δ-FeOOH. Ba^{2+} ions are retained within, but it also has a hexagonal structure and so it acts as a good template for BaM formation. At 300 °C δ-FeOOH dehydrates to form a poorly crystalline barium-doped α-Fe_2O_3 which still retains the barium ions even when it becomes fully crystalline at 550 °C, and as a result of this atomic scale mixing the activation energy of BaM crystallisation is lowered. The barium-doped α-Fe_2O_3 is also less thermodynamically stable and so single phase BaM is formed at a very low temperature of 600 °C with a grain size of 80 nm. The c parameter is 0.02% smaller than expected, and it is suggested that M structure is not fully developed at this point as the five-coordinate Fe^{3+} site does not exist in haematite, but the material has the exact BaM cell length at 700 °C [31].

2.1.2 *Salt-melt process*

In an investigation of the salt-melt process the coprecipitated precursor powder was shown to be a mixture of crystalline δ-FeOOH in the form of 50 - 100 nm hexagonal platelets and amorphous agglomerates of $Ba(OH)_2$ and $Fe(OH)_3$. This fine precursor then forms even finer α-Fe_2O_3 with a grain size of only 40 - 50 nm, and BaM begins to crystallise at 638 °C, possibly because the hexagonal template acts as a template for topotactic BaM formation [242]. After being heated to 1000 °C / 4hr in a NaCl / KCl flux and separated from the alkaline metals the product was pure BaM with a wide range of grain diameters between 0.2 - 1.5 μm. If a flux containing only NaCl was used the single phase ferrite could be made with 300 nm grains after only 850 °C / 1hr while retaining excellent magnetic properties, and Co-Ti or Zn-Ti doping further reduced both the grain size to 50 - 150 nm and the size distribution [35].

A variation of this process uses a higher melting mixture of NaCl and B_2O_3 in smaller quantities so an incomplete flux is achieved, and the rate of formation is closer to that of normal solid state diffusion. With this technique 250 nm particles of BaCoTiM were produced at 980 °C / 1hr, so it does not seem to have any advantage over the full melt flux process [37]. However, if the melt-flux is heated radiothermally with an electron beam the single phase ferrite is produced at a lower temperature of 900 °C as platelets below 100 nm in diameter and of reduced thickness [38]. In all of these techniques an iron deficient stoichiometry is needed to form the pure M phase, as in the purely coprecipitated materials.

2.1.3 *Sol-gel synthesis of BaM*

Even when BaM was made from a sol-gel route involving the evaporation of a sol containing coprecipitated salts and glycol to give a homogeneous gel, it was still found that a non-stoichiometric mixture was needed, and a ratio of Fe:Ba of 10.5 gave M ferrite at 900 °C / 1hr with a grain size of only 200 nm [43]. Only the barium rich precursor yielded pure M without any α-Fe_2O_3 as a second phase, but with a ratio of less than nine $BaFe_2O_4$ appeared as a secondary phase instead [44], indicating that there is only a narrow compositional window for

the formation of BaM by this method.

Investigations into an acidic sol made with a citrate coordinating agent revealed that the prefiring of the gel at 450 °C / 5hr to remove the organic component is a crucial step, reducing the formation temperature of pure BaM from 1050 °C to 750 °C, and consequently the grain size. Without the prefiring step, when heated directly at a rate of 4.5 °C hr^{-1} BaM began to form at 550 °C, but coexisted with α-Fe_2O_3 until the single phase product resulted at 750 °C. At 900 °C this had an average grain size of 129 nm, but it was found to consist of two distinct phases, 20 - 30 nm spherical α-Fe_2O_3 and 500 nm hexagonal BaM. With prefiring BaM started to form at the higher temperature of 650 °C, but α-Fe_2O_3 never formed, and the product's average size was 101 nm, consisting of homogeneously sized hexagonal platelets between 90 - 110 nm. $BaFe_2O_4$ was present as a minor phase in both specimens between 650 - 750 °C. The determining factor was found to be the γ-Fe_2O_3 phase, which was present in both specimens at 500 °C but decomposed to α-Fe_2O_3 without prefiring. In the prefired samples the γ-Fe_2O_3 was more crystalline before BaM formation, and the deficient cubic spinel structure ($FeFe_{1.67}\square_{0.33}O_4$) resembles the S block and therefore may easily react with $BaFe_2O_4$ to form BaM [45]. BaM made by the stearic acid gel method formed as a single phase at 650 °C [49].

The synthesis of BaM from an organic sol-gel precursor has been studied by neutron powder diffraction. All the organic compounds were removed at 420 °C to leave crystalline γ-Fe_2O_3 as the major phase up to 680 °C, the crystallites growing from 15 nm at 150 °C to 30 nm at 600 °C. At this temperature $BaCO_3$ appears out of the amorphous background, and α-Fe_2O_3 and $BaFe_2O_4$ form soon afterwards. BaM forms at 680 °C as the γ-Fe_2O_3 decomposes, along with the other iron phases, until single phase BaM is left at 1000 °C. It is suggested that the Ba^{2+} ion moves into the cation-deficient spinel structure of γ-Fe_2O_3 [46]. In an ethanol based sol made from iron(III) nitrate and barium metal it was found that to form pure BaM the barium had to be 0.72 - 0.95 wt% of the sol, and again γ-Fe_2O_3 and $BaFe_2O_4$ appeared to be essential for the formation of BaM at 800 °C with a grain size of 150 - 200 nm [47].

2.1.4 *Citrate synthesis of BaM*

BaM was synthesised by the citrate route, from a 10 nm stoichiometric amorphous precursor decomposed at 420 - 470 °C. This appeared to form BaM as the sole crystalline product after 550 °C, giving a single phase XRD pattern at 700 °C and with a grain size of only 60 nm [51]. Mossbauer studies suggested that the nonmagnetic $BaFe_2O_4$ may be present and that some cations had not diffused fully into the lattice at this temperature, but by 800 °C the Mossbauer data agreed with XRD that the pure M phase had formed, and the grain size was still below 100 nm [50]. When a sample of the amorphous precursor decomposed at 425 °C was left standing for one year at room temperature it had become a metastable γ-Fe_2O_3, which has been seen as an important species for the formation of BaM in other precipitation-based techniques. Upon standing for another six months the material had transformed to a near-hexagonal structure with physical and magnetic characteristics between those of BaM and γ-Fe_2O_3, but as the temperature was too low for a solid state reaction to occur it was assumed to have been an ionic rearrangement [243].

2.1.5 *Hydrothermal synthesis of BaM*

Pure phase BaM can be made from stoichiometric mixtures of iron and barium by hydrothermal synthesis, and at ratios below Fe:Ba = 10 the excess barium causes $BaCO_3$ to form as an impurity. However, the product is poorly crystalline, and must be annealed at 900 °C to allow the Ba^{2+} ions to diffuse fully from the surface into the M lattice [52].

2.1.6 *BaM hollow spheres*

Hollow spheres of BaM were made by spraying an aerosol of a solution of salts into a heated zone for only one second, to give 90 nm spheres with a wall thickness of only 30 nm and a hollow centre. When made at 527 °C the spheres were mainly amorphous with some iron oxide and barium nitride (an N_2 gas jet was used), and although this became fully crystalline after annealing at 727 °C, it was not BaM. When the spheres were produced at 1027 °C the

product was a fully crystalline mixture of oxides, nitrides and BaM, and this formed pure BaM upon annealing at 727 °C / 3hr [62].

2.1.7 Thin films

BaM Thin films are typically made by coating a substrate or rf sputtering a layer on to a substrate at 200 - 500 °C, to give an amorphous layer 100 - 300 nm thick. This then has to be annealed to around 800 °C to produce the M ferrite phase, with a grain size as low as 50 nm even in undoped BaM. The precursor sol or target must be very non stoichiometric, with a heavy bias towards barium to give an Fe:Ba ratio between 4 - 8 [70]. BaM films which formed the pure crystalline phase after firing at only 600 °C were made via a facing target sputtering process, using a mixture of xenon, argon and oxygen gases and an iron rich sintered BaM target, to give a product with a grain size of 400 nm and a very high M_s [244].

2.2 SrM ferrite

The SrO-Fe_2O_3 system resembles that of barium, with again a very narrow compositional range in which the M phase can exist [245], but the Fe^{4+} ion is found more frequently in the strontium systems [246]. $SrFe_2X$ has been seen as a minor product at 1420 °C after 2 hours, but both this and the remaining SrM decomposed to $SrFe_2W$ at 1435 °C which then melted at 1465 °C [247].

An investigation of the synthesis of SrM from coprecipitated salts fired at 800 - 1100 °C showed that the M phase only forms as a pure product in a non-stoichiometric mixture, with an Fe:Sr ratio no more than 9, the best product requiring a ratio of 8 [28], which is lower than required to form BaM. It has also been found that stoichiometric mixtures of standard ceramic powders never fully sinter, whereas with a ratio of 11 the material is fully sintered by 1150 °C, and this is attributed to increased diffusion rates in the non-stoichiometric mixes due to induced lattice defects [91]. However, when made from a sol-gel precursor with a stoichiometric composition, the M phase was obtained mixed with a small amount of α-Fe_2O_3 between 800 and 1000 °C, and the single phase material fired to 1200 °C had magnetic

properties comparable to those found in standard ceramic materials [48]. Another strontium-iron phase was found when, after SrM was treated with nitrogen and hydrogen atmospheres, it decomposed to form iron oxides and $Sr_7Fe_{10}O_{22}$ [248]. SrM was synthesised by the citrate route, and the amorphous precursor began to crystallise as SrM at the very low temperature of 550 °C with a grain size of only 42 nm, and had formed the pure M ferrite at 800 °C with grains of only 116 nm. The material had a relatively high surface area of 10.12 $m^2\ g^{-1}$ indicating it was poorly sintered, and this is a typical feature of this method of synthesis [51].

2.3 Other M ferrites

It has been shown that a solid solution exists between BaM and SrM, with a steady change in lattice constants, and magnetic properties with substitution [249]. PbM is less thermally stable than BaM or SrM, decomposing at 1250 °C to α-Fe_2O_3 and melting at 1315 °C [250], and no complex hexaferrites are seen due to the high vapour pressure of PbO [251]. Pure CaM has never been synthesised, but an addition of 2 mol% La_2O_3 or La_2O_3/Nb_2O_5 can stabilise the phase, and a substitution of up to 70% of Ba with Ca has been achieved whilst retaining the M structure [252].

2.4 Substituted M ferrite

$BaFe_{11.5}Co_{0.5}O_{19}$ has been made by ion exchange, forming the impure product at 750 °C. At 800 °C the grains were 90 nm wide and 49 nm thick, growing to 200 nm by 130 nm at 900 °C, but maintaining the ratio of length to thickness of 1.5 [39]. When thin films were made of $BaFe_{11.9}Me_{0.1}O_{19}$ (Me = Cr^{3+} or Y^{3+}) and annealed at 800 °C, both dopants had the effect of producing a material made of small equiaxed particles 50 nm wide, as opposed to the 500 nm wide and 50 nm thick platelets produced in the undoped BaM in the same process [253].

The Al^{3+} ion can also be substituted into BaM ferrite up to $BaFe_{4.2}Al_{7.8}O_{19}$ [254], and a complete solid solution exists between SrM and $SrAl_{12}O_{19}$ [255]. Of the trivalent lanthanides Ga^{3+} and La^{3+} have the highest solubility limit in BaM, and both lanthanide doped [256] and galium doped [257] hexaferrites have been made with total substitution of iron despite the

large size of the La^{3+} ion. In^{3+} and Sc^{3+} ions have only been substituted for iron up to $BaIn_{3.4}Fe_{8.6}O_{19}$ [258] and $BaSc_{1.8}Fe_{1.2}O_{19}$ [259].

When Pb_2Me_2Y was attempted using mixtures of two small divalent metals such as Ni^{2+}-Cu^{2+}, or a trivalent and a monovalent metal such as Li^{+}-Yb^{3+}, no Y phase was formed but two distinct M phases were formed with different cell dimensions [14]. This suggested that the M structure will tolerate a certain amount of solid solution of transition metals without collapsing, and this has been proven correct by the manufacture of a wide range of doped M ferrites, in which iron is substituted either by a Me^{3+} or a mixture of M^{2+} / M^{4+} ions, provided they have similar ionic radii to the substituted ions.

The most common substituted M ferrite is $BaCo_xTi_xFe_{12-2x}O_{19}$, which has improved properties for use in magnetic recording applications. A solid solution exists between iron(III) and titanium(IV) oxides, in which Fe^{3+} is replaced by a pair of Fe^{2+} and Ti^{4+} ions, with a resulting increase in unit cell size, to form titanospinels, magnetites and maghemites [21]. Therefore, if Ti^{4+} is added with a divalent metal which can also form a solid solution with iron, such as Co^{2+}, a simple substitution of Fe^{3+} can occur. The a lattice parameter, grain size, saturation magnetisation, coercivity and remanence are all decreased with increasing x, but it was found that the Ti^{4+} ion had more effect on the grain size while the Co^{2+} ion was mostly responsible for the change in magnetic properties [260]. It has been suggested that the grain size is reduced with Ti^{4+} ions by enhancement of nucleation sites [71]. The a lattice parameter is 5.89 angstrom, the same as for BaM, but the c-axis has been found to increase with substitution, being 23.20 angstrom at x = 0.8 [261], 23.21 angstrom at x = 1.1 and 23.23 angstrom at x = 1.5 [348], because the average radius of Co^{2+} / Ti^{4+} (0.627 angstrom) is larger than that of Fe^{3+} (0.550 angstrom).

For x = 1.1 when fired to 1150 °C the grains had grown to form 1 μm platelets, and these increased to 50 - 150 μm between 1230 - 1290 °C [348]. However, in a sample of BaCoZrM made by the citrate route the grains were only 5 μm even after heating to 1300 °C, and DGG was never observed [370]. Nickel-zinc-titanium substituted BaM was found to have

a smaller grain size than BaCoTiM, consisting of 100 by 10 nm platelets at 900 °C at x = 1 [371]. It is typical of these doped BaM systems that they form even more acicular grains that usual, with a large width-to-thickness ratio. This was found to be even more pronounced in BaCoSnM, forming very flat particles with a large surface area, but the fusion between particles was reduced inhibiting grain growth [347].

An investigation of the $BaO.TiO_2.Fe_2O_3$ system at 1240 °C revealed at least 12 different mixed compounds, ranging from $BaTi_2O_5$ with 0.2 mol% Fe_2O_3 to $Ba_{12}Ti_{16}Fe_{30}O_{89}$, a hexagonal ferrimagnetic compound [390]. In a study of BaCoTiM coprecipitated from chloride salts the mixture formed α-Fe_2O_3 at 500 °C, with $BaCO_3$ and $CoTiO_3$ also appearing at 600 °C. The M phase had formed as the major phase with α-Fe_2O_3 at 750 °C, becoming pure M at 900 °C as hexagonal platelets 50 - 80 nm in diameter [336]. $BaCo_{0.6}Ti_{0.6}Fe_{10.8}O_{19}$ made from the stearic acid gel method began to crystallise at 650 °C, becoming single phase at 750 °C with very small 10 - 20 nm grains, growing to 100 nm at 1000 °C and 500 nm at 1150 °C [49]. When $BaCo_xTi_xFe_{12-2x}O_{19}$ was produced from the glass crystallisation method it was found that TiO_2 in the glass matrix acted as a nucleation agent and accelerated the crystallisation of the M phase [260]. It has been claimed that $BaCo_{0.8}Ti_{0.8}Fe_{10.4}O_{19}$ was prepared by this method to give platelets only 7.6 nm long and 2.4 nm thick [261].

2.5 Y ferrite

Investigations of the $BaO.Fe_2O_3.CoO$ system showed that Y ferrite not only formed at the stoichiometric point 20% BaO-20% CoO-60% Fe_2O_3, but over a region of compositions 2.5 - 45% BaO-5 - 45% CoO-50 - 69% Fe_2O_3. Y coexists with the $BaFe_2O_4$, spinel, W and Z phases or a mixture of these phases over this range, but to form single phase Y the mixture must be near the stoichiometric point (fig. 86) [223].

For stoichiometric mixtures made by coprecipitation the Y phase was found to begin to form at 950 °C, as α-Fe_2O_3 vanishes and the BaM and spinel phases drop to half their maxima, giving equal proportions of M, Y and spinel phases at 970 °C. By 1000 °C the

material was virtually all Y, reaching a maximum at 1100 - 1300 °C. After this point Y rapidly decomposes to give mostly W and some spinel. At 1300 °C Co_2Y consisted of hexagonal grains 3-10 μm wide and 0.75 - 2 μm thick [14]. Zn_2Y was made from the coprecipitation of hydroxides and barium carbonate, forming α-Fe_2O_3 at 350 °C, $BaFe_2O_4$ at 780 °C and Zn_2Y at 1100 °C. This did not become the single phase material until 1200 °C with a grain size of 2 μm, and it decomposed at 1250 °C into the $ZnFe_2O_4$, α-Fe_2O_3 and BaO [262].

Using Ba^{2+} as the large cation, pure Co_2Y, Ni_2Y, Zn_2Y and Mg_2Y have all been made successfully [4], and Cu_2Y was also produced, although only as a mixed phase with BaM ferrite [14]. However, when the Pb^{2+} ion was used as the large cation, the Y structure was never formed for stoichiometric Y mixes, forming the W phase instead. This W phase was pure for Cobalt and Zinc, but it was also mixed with the PbM phase for Nickel, Copper and Manganese, and a similar lack of any Y phase was found with the smaller Sr^{2+} cation. However, the Co_2Y and Ni_2Y phases did form with up to 50% substitution of Barium by lead, and 80% by Strontium, with the X phase also present as a small impurity in the nickel series. Therefore, the Y phase can only tolerate up to 50 mol% lead and 80 mol% strontium substitution of barium. In the pure Pb_2Co_2Y mixtures DGG had already begun at only 1100 °C / 3hr, with grains over 100 μm in diameter, and grain growth inhibitors or variations in the heating cycle seemed to make little difference. This excessive growth of the PbM phase was attributed to its persistence, as the homogeneous mixture of oxides separates into fractions of differing compositions, eventually forming W and X. The T block in Y ferrites requires the diffusion of a second lead atom through the oxygen layers, but due to their low surface area diffusion of the large lead atoms will be very slow. The structure of W and X resemble M more than Y, Z or U which all contain the T block, so these phases are formed preferentially. The large M plates also had amorphous MeO and PbO at their grain boundaries resulting in a deficiency of these in the structure, and possibly a solid solution of M^{2+} in PbM ferrite, changing the lattice parameters [14].

2.6 Z ferrite

Z ferrites are difficult compounds to form. A temperature of at least 1200 °C is required, the Z phase usually coexisting with some or all of the phases M, Y, W and spinel. It has been reported that 1225°C appears to be the optimum temperature, but the Z phase was only obtained as a major component mixed with the W phase [263]. Single phase Z is notoriously hard to produce. However, in the phase diagram (fig. 86) Z extends over a wider range of compositions than Y ferrite, forming the regions Y + Z, Z + $BaFe_2O_4$, M + Z, M + Z + W, Z + W, Y + Z + W, and pure Z near the stoichiometric region 17.65% BaO-11.73% CoO-70.60% Fe_2O_3 [223]. This may be because, unlike Y ferrite, the structure of Z is related to both Y and M, and therefore all the hexagonal ferrites.

In experiments comparing the formation of Z from both salts and oxides, it was found that Z is never formed directly, and must result from the topotactic reaction of the two previously formed M and Y stages, irrespective of the starting materials [264]. With salt precursors the Z phase starts to form at 1100°C, and at 1200 °C the M and Y phases begin to decrease rapidly as the Z phase increases, to form a maximum of 90 mol% Z at 1260 °C / 2hr. Any longer at this temperature, or an increase in this temperature, and the Z phase decomposes to the W phase. With oxides, the Z phase formed at the same temperature, but the W phase forms simultaneously causing the Z phase to decompose as it is being made, and resulting in a maximum yield of only 62 mol% Z. Assuming that the rate limiting step is diffusion driven and the reaction occurs at the interface between the hexagonal faces, it was suggested that two simultaneous stages must coexist. one decisive at low temperatures, one at high temperatures. At 1100 - 1200 °C Z product accumulation between the M and Y reagent surfaces could restrict the surface diffusion, and at temperatures over this the rate limiting step could be a topotactic reaction at the M / Y interface [264]. The kinetics of this reaction have not so far been elucidated.

Above certain temperatures it is evident that some grains grow at an enormous rate relative to the others, giving a material containing a wide range of grain sizes, and this seems

concurrent with formation of the Z phase at 1250 °C, resulting in the large platey grain morphology. This growth is much greater in the direction of the hexagonal plane, perpendicular to the c-axis [265]. The grain size becomes even more exaggerated by DGG after 1260 °C / 10hr, 1290 °C / 10hr or 1300 °C / 10min, giving huge plates tens or even hundreds of μm in diameter but still only a few μm thick, and with a corresponding loss of density in the final product, probably as pores are enclosed within the grains. [266]. No DGG was seen after heating Co_2Z at 1220 °C for 24 hours.

The decrease observed in bulk density accompanying this grain growth could be explained by surface diffusion, but the rate of growth of individual grains was too great to be explained by solid state diffusion alone. Electron microscopy showed the plates contained elevated layers, a typical feature of growth from vapour or melting. No evidence was seen for melting, but there were signs of vaporisation / condensation and supersaturation mechanisms, as well as of solid state diffusion. Some regions of higher energy on the surface, the result of dislocations, inhomogeneity or defects, form points where material would be expected to escape as a vapour phase, which then condenses on regions of lower energy as stacks of a spiral or circular shape, and this was observed on the interior in Co_2Y grains. On the exterior of the grains there were clear stacks of hexagonal plates, and this is typical of slower growth from a lower degree of vapour supersaturation, as would be expected for the outside of the grain. All the laminas were roughly the same thickness, of 0.1 = 0.5 μm, and the same features were observed in Co_2Y particles heated to 1250 °C [267].

When prefired Co_2Z samples were sintered in a magnetic field to produce oriented samples, the oriented particles were observed to grow at the expense of the unaligned grains. This resulted in an oriented product, but the grains were no larger than in randomly aligned samples fired without an external field. Some large grains 10 - 20 μm in diameter appeared after 1260 °C / 24hr, and DGG occurred at temperatures over 1290 °C [266]. The transport mechanism was suggested as being a mixture of grain boundary and volume diffusion, but porosity data indicated that the densification mechanism was via pore removal through a

volume driven lattice diffusion process. The oriented samples were more sintered, with a density of 97% achieved [266].

The Z phase is sensitive to barium substitution with lead in a similar manner to Y, only able to withstand up to 17 mol% substitution [14]. The Z structure can also only withstand a substitution of Ba^{2+} by La^{3+} up to = 13 mol%, with a decreasing cell length with substitution [268], but it is much more tolerant of substitution with strontium up to 100% [269].

2.7 W ferrite

The W phase forms over a wide range of compositions to form the mixed phases W + $CoFe_2O_4$, W +$CoFe_2O_4$ + α-Fe_2O_3, W + M, W + Z, W + M +Z, W + Z + Y, W + $CoFe_2O_4$ + Y, and single phase Co_2W around 9.1% BaO-18.2% CoO-72.7% Fe_2O_3 [223]. It is the most iron rich of the hexagonal ferrites to contain a small divalent ion, requiring a higher temperature to form than the other common hexagonal phases, and it is often formed as a decomposition product of these. When made by standard ceramic techniques from stoichiometric mixtures of oxides and barium carbonate, Co_2W does not begin to form until 1200 °C, as a mixed phase with BaM and the spinel ferrite, and forms the pure compound over a narrow range from 1250 - 1300 °C, at which point DGG has begun and the grains grow to 60 μm. Over this temperature it begins to decompose to mixtures of W, BaM and spinel again, resulting in grains 90 μm in diameter containing traces of $BaFe_2O_4$ over 1350°C, and finally fusing at 1440 °C. The ferrite material contains 7% FeO at 1400 °C, and the lattice parameter of the decomposition spinel is between those of magnetite and cobalt spinel indicating that a solid solution of the two has formed, and this reduction may be a driving force for the decomposition [270].

Like BaM ferrite, the W phase can withstand total replacement of barium with strontium or lead, implying it is the T block which is sensitive to barium replacement, as shown in the Y and Z ferrites [14]. $SrZn_2W$ is the most important W ferrite for its magnetic and microwave properties, usually when doped with another divalent metal ion, and forms at a

low temperature of 1100 °C [271].

The addition of sodium to $SrZn_2W$ had the effect of lowering the grain size dramatically to only 0.5 - 1.5 μm at 1225 °C, increasing to 1.8 - 4.0 μm after 1300 °C for only 30 minutes, and after 2 hours at this temperature the grains had undergone DGG to become 3 - 60 μm in diameter [272].

2.8 X ferrite

The X ferrites are usually seen mixed with M and W phases, and are extremely hard to separate. Fe_2X was the first X ferrite to be produced as a pure single crystal sample only after 70 attempts, and even then a section of BaM phase had to be ground out of the crystal [7]. Pure Co_2X has also been grown from a flux [12], as has Zn_2X [13] and Cu_2X [273] . Polycrystalline Fe_2X has been made from the coprecipitation of oxalates, the X phase forming at 950 °C and becoming pure phase between 1000 - 1200 °C. Beyond this temperature it decomposed to BaM and α-Fe_2O_3, the Fe^{2+} making the compound unstable at elevated temperatures [274].

2.9 U ferrite

These are extremely hard to make as a pure polycrystalline material, and with the exception of Zn_2U have only been seen as mixed phases with Z and Y ferrites. Zn_2Y single crystals were grown from a flux, and although they were mostly intermixed with Z and Y phases, some pure single crystals were identified and separated by their Curie point [16].

2.10 Sintering aids

Most sintering aids seem to involve the formation of relatively low temperature glassy phases between the particles of the ceramic compound. For example, an undoped sample of BaM with a grain size of 1 - 2 μm had a density of 67% at 1100 °C, 72% at 1200 °C and was still only 82% dense at 1300 °C. However, with an addition of 0.55% silica this was drastically

increased to 72% at 1100 °C, 91% at 1200 °C and 96% at 1300 °C [275], as the silica forms a glassy intergranular phase above 1050 °C [276]. The addition of silica with CaO has also been claimed to increase densification while reducing grain growth in M ferrites [277. B_2O_3 has been found to help densification of BaM through liquid phase sintering below 1000 °C, but only leads to enhanced grain growth at levels exceeding 0.1 mol%. An addition of 0.1 mol% gave a 98% dense product at only 1000 °C, compared to 93% for undoped BaM with a grain size of 0.5 μm [278].

The densification of SrM is also enhanced by the addition of silica [279], and there are several proposed mechanisms for this effect. It is known that SrO preferentially reacts with silica forming a low viscosity liquid phase which aids sintering, but some strontium can be lost to the sample [215]. This is unlikely to be a factor as the material is usually pure M phase at the temperatures required to melt silica. Above 1075 °C Fe^{2+} ions appear in silica-doped SrM, and the conductivity increases sharply at levels over 0.4 wt% silica because of this. As the concentration of Fe^{2+} ions increases the number of oxygen vacancies increase, and this in turn increases the rate of sintering, lowering the maximum densification temperature [280].

2.11 Grain growth in ferrites

The grain growth in hexagonal ferrites is most likely a combination of grain boundary movement and Ostwald ripening, and the latter seems the most likely process for the extreme growth seen during DGG [216], which often results in extremely acicular platelets instead of regular hexagons. In microstructural studies of BaM films it was found that a higher Ba content led to higher nucleation rates and lower growth rates, giving a finer grained product with smaller diameter:thickness ratios [281].

When up to 1 mol% B_2O_3 was added to BaM it was found to diffuse into the lattice over 1000 °C to form $BaFe_{12-x}B_xO_{19}$, the material being a mixture of BaM, α-Fe_2O_3 and $BaFe_2O_4$ at temperatures below this. However, over 750 °C $BaFe_2O_4$ forms an intermediate with B_2O_3 which nucleates rapidly and causes growth with long or high temperature sintering.

This enhances crystallisation, promotes BaM formation and reduces porosity of the system, but also forms acicular platelets which become larger and more elongated with increasing boria addition. With additions from 0.1 - 0.3 mol% the grain size does not increase too much, being 2 - 10 μm at 1200 °C and still no larger than 10 μm at 1400 °C, but with higher levels plates up to 50 μm long are formed. The acicular platelets form over 1250 °C, but as the a parameter increases in one direction the c parameter decreases, reducing the length of the c-axis but maintaining the cell volume. As the basal plane is no longer a regular hexagon, a third lattice parameter, b, is required to describe the width of the cell in the non-elongated axis, perpendicular to a. Thus as this elongated growth occurs the ratio of c:a decreases, and this may resemble the undetermined processes involved in DGG. The largest c:a ratio is seen with an addition of 0.2 mol% B_2O_3 or less, and the mechanism of boria addition to BaM is suggested to be the following: with boria addition of only 0.1 mol% it is taken into the core of the lattice, promoting ferrite formation by homogeneous nucleation. With an increase of up to 0.3 mol% the extra boria behaves as a molten flux allowing the transport of reaction species, so most of the additive is promoting reactions between crystals, instead of their formation. With further addition the boria melt is thick enough to leave layers of B_2O_3 between reaction centres on the faces of the platey grains, but they will float on this layer and can grow out sideways, forming the elongated grains. [282]. Another investigation into the addition of smaller amounts of boria to BaM agreed with these findings, with both 0.1 mol% and 0.2 mol% producing 0.5 μm grains at 1000 °C, but the large growth up to 10 μm at 1200 °C only occurred with 0.2% addition [278].

A small amount of chloride is retained in M ferrite powders at high temperatures, and it has been shown to encourage grain growth, although levels up to 1 wt% have also been claimed to promote crystallisation and inhibit shrinkage [283]. In M ferrite powder which was heated at 1200 °C in an oxygen atmosphere 80% of the residual chloride was removed, and a product with a grain size of only 0.5 μm was made [284]. Sumitomo make commercial aluminosilicate fibre from chlorohydrate and siloxane which retains a large proportion of

chloride, which is removed by steaming the fibre [285], and ICI have used a similar process to improve the quality of their product [125].

2.12 Grain growth inhibitors

The doping of SrM with La^{3+} and Zn^{2+} to make $Sr_{1-x}La_xFe_{12-x}Zn_xO_{19}$ was found to reduce the grain size while still producing a sintered material. When x = 0.3 the product was 97% sintered at 1200 °C, but with a grain size of only 0.8 μm, increasing to several μm over 1250 °C [286]. Nb_2O_5 acts as a very good grain growth inhibitor in the sintering of $BaTiO_3$ when added in quantities over 0.5 wt% [215], and it has been used to produce nanocrystalline spinel ferrites [287].

Addition of Silica to BaM has been claimed to both promote and hinder grain growth in various amounts. It seems that grain growth occurs with an addition of below 0.55 wt% as this is below the solubility limit of silica in BaM. Above this loading grain growth is suppressed even at 1250°C, either because of the impurity drag of solid phases on grain boundaries slowing their movement, or because the silica reduces Ostwald ripening by suppressing surface diffusion [288].

An addition of 0.2% Al_2O_3 to SrM inhibits grain growth even at temperatures of 1250 °C, giving a material consisting of grains 2 - 5 μm in diameter, compared to the large grains present in the undoped material from DGG at this temperature. Unfortunately the alumina also massively hinders densification, giving a product full of pores of the same dimension as the grains which is only 66% dense [289]. It was found in the same investigation that B_2O_3 has the opposite effect, giving a duplex structure consisting of smaller grains and pores under 10 μm wide interspersed with huge plates measuring 25 μm and over. Although silica is normally considered to cause grain growth, it has been reported that silica can reduce grain size in SrM, either by forming as a solid at grain boundaries, or by the drag of the segregated silica between grains preventing them from joining [290]. In extruded alumina fibres, in which an unwanted rapid formation of large α-alumina grains often occurs, SiO_2, MgO, P_2O_3, B_2O_3 and ZrO_2 have

all been used as grain growth inhibitors [129].

3. Results and discussion

The bulk of the solid state characterisation and investigation of these fibres was focused on the hexagonal ferrites BaM, Co_2Y and Co_2Z. The M and Z ferrites were of particular interest due to their magnetic properties, both having large magnetic moments, but M being an anisotropic hard magnet and Co_2Z being a ferroxplana soft magnet. The Y phase was studied as it contained the highest level of divalent cation, as well as being one of the two precursor phases, coexisting with M, which have been always been seen to form together before the onset of the Z phase. Some bulk ceramic samples were supplied by DERA for comparison, which were apparently pure phase from their magnetic properties and XRD patterns. Unless stated otherwise, all fibres were produced from stoichiometric dopings of the standard Fe/Br sols. Most of the fibres were fired and characterised when freshly spun, but some M and Y fibres were also re-investigated after storage at 110 °C for three years.

3.1 Shrinkage and weight loss

The shrinkage and weight loss of SrM, BaM and Co_2Z aligned fibres are compared in table 4.1, and were typical of the hexagonal ferrite fibres, with those spun from more dilute sols experiencing only a few more %. The fibre shrank by 12% in drying after collection, and by a further 22 - 23% total shrinkage at 1200 °C, with no more shrinkage after this until fibres begin to fuse together. This is in line with the 20 - 40% linear shrinkage normally seen in the firing of gels, as opposed to the 10 - 15% seen in standard ceramic powders. This shrinkage in blankets was only in the axis of alignment and without loss of alignment; across this axis there was no observed decrease in width, although individual fibres shrank isotropically in all dimensions. All of the aligned fibre blankets behaved in this 1D fashion, except for the Co_2Z fibres in which DGG occurred at higher temperatures. This appeared to form connections between the otherwise always discrete fibres (or twinned / coalesced bunches of fibre), and while the general alignment was maintained, a waviness was clearly visible in the fibres. This is

discussed further in the relevant sections. The only other loss of alignment was seen when fibres began to fuse together at temperatures of 1300 °C and over.

It appeared from the shrinkage measurements and calculated porosities that, in the M ferrites at least, the final densification of the fibre occurred between 800 and 1000 °C, leading to a well sintered product at a low temperature of 1000 °C, and this was confirmed by the measured porosity and surface area results discussed individually for each fibre in the following sections. It should be noted, however, that the lack of a plateau in the isotherms indicated the presence of macro pores over 100 nm in diameter, probably occurring between the hexagonal plates of the ferrite crystals. The porosity values discussed below are only estimates, and the degree of sintering of the ferrite fibres cannot be confirmed without precise density measurements, which are extremely difficult to carry out on fibre samples.

Temp.	Linear Shrinkage			Weight Loss			Calculated Porosity		
	BaM	SrM	Co_2Z	BaM	SrM	Co_2Z	BaM	SrM	Co_2Z
200 °C	12%	12%	12%	n/a	n/a	11.0%	30.4%	33.0%	33.0%
400 °C	14%	15%	18%	37.8%	36.4%	33.3%	25.4%	25.7%	17.2%
600 °C	14%	16%	n/a	n/a	n/a	n/a	25.4%	23.0%	n/a
800 °C	19%	17%	n/a	42.0%	40.4%	n/a	10.7%	20.1%	n/a
1000 °C	22%	22%	22%	45.3%	41.6%	41.3%	0%	3.8%	3.8%
1200 °C	22%	23%	23%	45.4%	41.8%	42.0%	0%	0%	0%

Table 4.1 Total shrinkage and weight loss of dried BaM, SrM and Co_2Z aligned fibres with temperature. The shrinkage was linear, measured to +/- 0.5 mm from 10 cm long samples along the axis of alignment. The porosity estimate was calculated from shrinkage, assuming the ceramic to be fully sintered at 1200 °C.

The slight differences between the SrM and BaM fibres could be explained by differences in the rates of diffusion of Ba^{2+} and Sr^{2+} ions, or by the slightly larger initial particle size in the sol precursor, and the SrM also formed the ferrite phase at a lower temperature than BaM. While the Co_2Y fibres also appeared to be well sintered at 1000 °C, the Z, W and U phases only formed after the M and Y phases had fully crystallised and densified, accompanied by DGG. Their porosities could not be accurately estimated as there was no

further shrinkage, the surface areas were too small to be measured, and it was likely that pores could be trapped within the grains during the DGG process.

It can be seen that the bulk of the weight loss occurred below 400 °C, as any water and organic compounds are driven out and the iron(III)oxide is formed. The remaining weight loss is attributed to halides, which are retained to some in degree in the fibre up to 800 - 1000 °C. The thermal analysis of the Co_2Z fibres is shown in figure 88, and was virtually identical for all of the ferrite fibres. Initially a steady weight loss of 15% occurred between 25 - 280 °C with a mild endotherm, corresponding to loss of water and resulting in haematite formation. There were two sudden drops in weight, of 14% at 285 °C and 6% at 420 °C, accompanied by sharp exotherms. The first sudden weight loss observed was attributed to the expulsion of bromine as the iron(III)hydroxide decomposes to haematite, and the second due to organic components being combusted. For this reason all the ferrite fibres were prefired at a slow rate of 100 °C / hr up to 400 °C to avoid any uncontrolled runaway exotherms, and maintained at that temperature for 3 hr to ensure total combustion. The remaining weight loss occurred between 800 - 900 °C as the halides were removed, and no exothermic peaks were observed for sudden crystallisation of any of the crystalline phases.

XRF analysis of the halide content of Co_2Z fibres at various temperatures is shown in table 4.2. The bulk of the bromide was lost quickly below 400 °C, but the total halide content remains as ~10 wt% of the fibre by weight up to 600 °C, with chloride persisting until over 800 °C. The amount of bromide in the fibres at 200 °C was roughly equivalent to the amount in the original $BaBr_2$ and $CoBr_2$ used to make the sol, which was 2.4 Fe:Br. This indicated that this bromide could be associated with the metals in the fibre and therefore in the sol, and that the added HBr was lost during drying. Indeed a small peak for $BaBr_2$ was found in the XRD patterns for Z ferrite at 200 °C, although it was nearly masked by the amorphous background. This peak had disappeared by 400 °C, and the amount of bromide lost at this temperature (16.1 wt%) corresponds well with the weight loss seen in the DTA/TGA at 285 °C. No crystalline $CoBr_2$ was ever detected, and no crystalline $BaBr_2$ was ever seen in the BaM fibres,

although BaBrCl was occasionally observed in the BaM and Co_2Z precursor fibres at 600 °C, and a similar unidentified peak was observed in the SrM precursor fibres at around 29°, which is also attributed to an unidentified mixed strontium halide compound. All of these mixed halide phases were only seen at 600 °C prior to ferrite formation, and they had all gone at higher temperatures when the ferrites had begun to form.

Temp. / °C	wt% Fe_2O_3	wt% Cl	W% Br	Fe:Cl	Fe:Br
200	48.0	5.4	22.0	4.26	2.18
400	64.2	5.4	5.9	5.28	10.89
600	66.9	5.1	4.7	5.82	14.24
800	72.6	2.5	0.9	12.74	80.72
1000	75.0	0.1	0.03	333.71	2503.58

Table 4.2 Loss of halides with temperature in Co_2Z fibres, and ratios of Fe to Br and Cl.

3.2 Iron oxide fibres

All of the amorphous ferrite gel fibres formed α-Fe_2O_3 as the first major crystalline phase, which is unsurprising as in the dehydration of α-FeOOH at 135 °C water molecules are removed to leave the hexagonal anion array intact [21], forming haematite. Therefore, pure undoped iron(III)oxide fibres were also spun and characterised for comparison. The dried gel fibre was amorphous, showing just a broad hump between 20 and 50° on the XRD pattern before firing.

After heating in air for just 1 hour at 250 °C the gel fibres were found to have formed haematite, and the XRD pattern (Fig. 89) indicated that the α-Fe_2O_3 was present as a single phase product. Previous nanocrystalline haematite made from sol-gel precursors has not formed a crystalline product until 400 °C, with a crystallite size of 12 nm [291]. Using the XRD data the Scherrer equation yielded an average crystallite size of 17 nm. The surface and interior microstructure, as seen in figure 90, consisted of small spherical grains around 25 nm in diameter. The general fibre morphology of smooth, parallel sides was also retained, and the alignment of the fibres was unaffected. BET porosity and surface area measurements of the

haematite fibres gave an average pore diameter of 13 nm, a pore volume of 0.129 $cm^3 g^{-1}$ and a surface area of 30.9 $m^2 g^{-1}$.

Upon firing to 400 °C / 3hr, at which point the organic material had been removed, the surface area had reduced slightly to 24.8 $m^2 g^{-1}$, but the average pore diameter and volume had increased to 23 nm and 0.141 $cm^3 g^{-1}$ respectively, although the crystallite and grain sizes had remained virtually the same. It can be seen from figure 89 that at 1000 °C the XRD peaks had become much sharper, indicating a very crystalline product, and the crystallite size had increased to 64 nm, comparable to some of the hexagonal ferrite fibres discussed later.

The 250 °C sample was subjectively quite strong and handleable, but gave a low strain to break estimated to be 0.3 - 0.4% when tested. This combination of good cohesion in the bulk combined with a poor response to a crushing or indentation test has been previously observed with porous catalytic grade *Saffil* [292], and was indicative of a porous structure, confirmed by the porosity data above. These results are summarised and compared with the M ferrites in table 4.3.

Fibre	Fe_2O_3	SrM	BaM
Crystallite size / nm	17	59	57
Fibre diameter / μm	3 - 4	3 - 6	3 - 5
Surface area / $m^2 g^{-1}$	30.9	0.88	0.86
Average pore diameter / nm	13	48	53
Strain to Break	0.3 - 0.4%	0.67 %	0.6 - 0.75 %
Alignment within $^+/_-20^o$ of axis	89%	80%	88%

Table 4.3 Comparison of α-Fe_2O_3 fibres fired to 250 °C / 1hr SrM and BaM fibres fired to 1000 °C / 3hr.

3.3 BaM ferrite fibres

The dried fibre was strong and very handleable and the fibres remained very smooth and fibrous at 1000 °C, becoming slightly less so above 1000 °C but remaining tough enough to handle even up to 1200 °C. The XRD patterns of the BaM fibres taken immediately after

spinning, for samples fired between 400-1200 °C, are shown in figure 91. As oriented samples show different XRD patterns to anisotropic samples [4], it can be seen that the fibres consist of randomly oriented crystals. Haematite has formed by 400 °C, and by 800 °C M ferrite has started to form, with haematite still as the major phase (~67%). Although no $BaFe_2O_4$ was seen at any stage, BaBrCl peaks were detected in the pattern at 600 °C, at around 29°. By 1000 °C the sample was single phase M ferrite and no further change in phase occurred up to 1200 °C. This agreed with previous studies on the reaction kinetics of hexaferrite formation, with M ferrite starting to form above 735 °C [233], and becoming a major phase by 1000 °C [227;228], although it is normally commercially sintered at higher temperatures of 1200-1250 °C for several hours [81] to achieve sufficient densification. The XRF elemental analysis for the oxides BaO and Fe_2O_3 confirmed the composition to be $Ba_{0.96}Fe_{12}O_{18.96}$ at 1000 °C, and all the halides had been lost by this temperature.

At 800 °C The fibre was still fairly porous, with a surface area of 4.0 $m^2 g^{-1}$, and a pore volume and diameter of 0.028 $cm^3 g^{-1}$ and 34 nm respectively. This indicated a porosity of 13%, which compared reasonably well with the calculated porosity from shrinkage of 10.7% at this temperature (table 4.1). The fibres had a slightly rough looking surface, but no grains were apparent (fig. 92).

The average crystallite size was estimated to be 50 nm at 1000 °C, and there was a grain structure apparent which was unclear and poorly defined, but consisted of features up to the 1 μm level (fig. 93). It was believed that these needle-like grains were edge-on hexagonal grains, and there was further evidence for this in both M fibres at higher temperatures and other hexagonal ferrite fibres. No pores were seen, and surface area and porosity data on the fibre fired to 1000 °C agreed with this, giving a low surface area of 0.86 $m^2 g^{-1}$, and a much lower porosity of 0.004 $cm^3 g^{-1}$ = 2% porous, with an average pore diameter of 53 nm (below the resolution of the SEM). It must be noted that results measured by this technique become unreliable below a surface area of 1 – 2 $m^2 g^{-1}$ for small samples, and the actual porosities could be higher than these values, although the results are close to the estimated porosity from

shrinkage. Sintering usually occurs between 900 - 1300 °C in standard ceramic samples, with an increase in density from 3 to 5 g cm^{-3} along with a corresponding loss of porosity from 45% to 5% [283] over 1200 °C, and therefore the BaM sol-gel derived fibres were clearly sintering at a much lower temperature than usual.

At 1100 °C individual grains could be seen between 0.5-2 μm, but the fibres had maintained their shape (fig. 94). However, by 1200 °C large plates up to 1-4 μm in diameter had formed, and the material had started to lose its fibrous nature (fig. 95). Commercial M ferrite specimens exhibit a grain size of 1-5 μm at 1000 °C and an exaggerated growth of 5-15 μm at 1225 °C [283]. Therefore, the fibrous M ferrite appeared to have a much reduced grain size than standard powder mixes at equivalent temperatures.

Despite producing a well sintered, small grained single phase M ferrite at relatively low temperatures, the formation temperature of the hexagonal ferrite phases was surprisingly high compared to other reported sol-gel products. However, α-$BaFe_2O_4$ was always present in these sol-gel derived ferrites, and the low formation temperatures were attributed to the reaction between the γ-Fe_2O_3 and α-$BaFe_2O_4$ phases which had been formed first (see section 2.1). The presence of either α-$BaFe_2O_4$ and/or γ-Fe_2O_3 precursor appears to be an essential step in the usual formation of BaM, and some factor must be preventing the crystallisation of this phase in the ferrite fibres, which could in turn prevent the early formation of the M ferrite phase.

The fibres retained ~10 wt% halides at 600 °C, and halides remained to some degree in the fibre up to 1000 °C. The formation of the hexagonal ferrite phases seemed to be delayed until most of the halides were lost, indicating that the barium remained separate from the iron until ferrite formation occurred. Further evidence that the fibres were not a totally homogeneous mix on the atomic scale was the detection of the barium halide phases prior to ferrite formation, and the lack of exotherms indicated that ferrites crystallised gradually as halide was lost. The heats of formation, in kcal mol^{-1}, of $BaBr_2$, $BaCl_2$ and BaO are -181, -205

and –133 respectively [212], so the formation of M ferrite from a barium halide precursor will be more difficult than from the oxide. Also $BaBr_2$ is an extremely stable compound, more so than the oxide [212], and will not decompose readily to give the ferrite. However, the appearance of BaBrCl at 600 °C indicates that Cl^- has displaced Br^- above 200 °C to give a mixed halide compound, and it is suggested that this occurs as chlorine contained within the iron(III)hydroxide matrix is released during haematite formation. The bromine level was below 1 wt% at 800 °C, while BaM still did not become single phase until 1000 °C was reached, indicating that the greater amount of chloride retained at 800 °C must also have had a retarding effect upon ferrite formation, maybe through the formation of $BaCl_2$, which is even more stable than $BaBr_2$. These barium halide phases prevented the formation of $BaFe_2O_4$, and delayed the formation of the ferrite until higher temperatures than would be expected for sol-gel precursors, these higher temperatures being needed to climb over the higher thermodynamic barrier to ferrite formation presented by the barium halides compared to oxides.

When the fibres were stored for three years at 110 °C and subsequently fired they behaved differently, giving a mixture of haematite and α-$BaFe_2O_4$ at 700 °C even after firing for 100hr, but at 800 °C they were nearly pure BaM, with only a trace of α-Fe_2O_3 (fig. 96). At 800 °C the crystallite size was 35 nm, and this had increased only to 41 nm at 1000 °C, at which point the fibres were pure BaM. There were no grains seen in the fibre, but the surface was markedly different at 800 and 1000 °C, being covered with either parallel ridges along the fibre axis or a "honeycomb" structure, and the ridges or "honeycomb" walls were 0.2 μm wide (fig. 97). Unlike the freshly fired samples, the stored fibres formed the pure M phase after only 10 min at 1000 °C with a crystallite size of 41 nm. After 1000 °C / 24hr the ridges / walls had grown to 0.3 μm thick, and after 100 hr the "pores" in the "Honeycomb" structure were up to 0.5 μm wide, but still no grain structure was observed. These differences were attributed to the loss of halide during storage, which was known to contribute to delay of ferrite formation, and the possible crystallisation of haematite in the gel fibres which could promote the

formation of the M phase at a lower temperature. An XRD of the stored but unfired material showed it was purely amorphous, and that no iron compounds had crystallised to act as nucleation sites, promoting earlier crystallisation. $BaFe_2O_4$ was also seen for the first time, indicating the barium could be still associated with the halide prior to M formation, when halide is present. These conclusions were confirmed by the steaming experiments discussed in section 3.13.

The halide free fibres produced from the nitrate-based sol also confirmed the effects of halides in hindering BaM formation. At 600 °C the fibres were also only haematite, but by 650 °C BaM was the major phase at ~75% with a crystallite size of 43 nm, and it had formed the pure ferrite at 750 °C, with a crystallite size of 51 nm (fig. 98). However, due to the problems encountered in spinning this sol detailed in chapter three, the fibres were poor with uneven sides, a wide range of diameters, and many cracks and splits in the surface of the fibres. Once the M phase had formed, grains 0.5 μm in diameter also appeared, and although it had formed at a lower temperature the product was otherwise inferior to the halide-containing fibres.

When the strain-to-break test was carried out on BaM fibres fired to 1000 °C, damage started to occur with a 1 mm wire with general breakage at 0.8 mm, indicating a strain to break given by the ratio of fibre to wire diameters, of the order of 0.6 to 0.75%. This strain to break of at least 0.6% is a promising result for a 6 μm fibre at the earliest stage of development and compares well with commercial *Saffil* alumina which shows a strain to break of 0.7% at 3 μm.

3.3.1 Doping of BaM fibres

Various elements were added to the stoichiometric BaM sol to study their effects, if any, on the microstructure of the fibres, as discussed in section 2.12. An addition of 0.28 mol% of the rare earth metals Gd^{3+} and La^{3+} both caused BaM to form as the major phase at a lower temperature of 800 °C, forming the pure ferrite at 1000 °C, as shown in figure 99. The fibres exhibited no discernible grain structure at 800 °C, and at 1000 °C they seemed to be more

porous than the undoped fibre, with small equiaxed grains 0.1- 0.2 μm instead of the thin plates seen in the pure BaM fibres (fig. 100). At 1200 °C the average grain size had increased greatly to 1 – 4 x 0.5 μm, and DGG had occurred, resulting in some massively elongated grains up to 15 μm long (fig. 101). 0.25 wt% V_2O_5 and 0.06 wt% Nb_2O_5 had similar effects, with BaM appearing as a minor phase at 700 °C and as the pure phase at 800 °C with a crystallite size of 48 nm (fig. 102). At 1000 °C the crystallite size had increased to 63 nm, and the morphology resembled the rare earth doped fibres in both cases, but with less equiaxed looking grains (fig. 103). At 1200 °C larger grains had appeared, but there was no sign of DGG, unlike in the rare earth metal doped fibres. Other additives investigated, such as 1.0 wt% ZrO_2, Y_2O_3, Cr_2O_3 only appeared to hinder the formation of the BaM phase even at 1000 °C, giving a mixture of α-Fe_2O_3, α-$BaFe_2O_4$ and BaM, and with no appreciable benefits in microstructure (fig. 104).

3.4 SrM ferrite fibres

The XRD patterns for the SrM fibres at various temperatures are shown in figure 105, and it can be seen that the formation of the M phase occurred at a slightly lower temperature than in the BaM fibres. Again α-Fe_2O_3 was the only crystalline phase up to 700°C, but SrM was ~40% of the material at 750 °C, and by 800 °C the fibre was 90% SrM with a crystallite size of 53 nm. At 900 °C the pure M phase had formed with a crystallite size of 55 nm, increasing to 59 nm at 1000 °C, and the XRF elemental analysis for the oxides SrO and Fe_2O_3 confirmed the composition to be $Sr_{0.98}Fe_{12}O_{18.98}$. Again the SrM crystallisation temperature was higher than expected for a sol-gel product, suggesting that the presence of haildes was delaying ferrite formation. However, although $SrFe_2O_4$ was never detected, SrM both crystallised and became the single phase at slightly lower temperatures than BaM, indicating that the halides had a lesser retarding effect on the reaction of strontium and iron. The heats of formation, in kcal mol^{-1}, of $SrBr_2$, $SrCl_2$ and SrO are -172, -198 and –142 respectively [212], the lower strontium halide values making the formation of SrM from halide precursors comparatively

easier than BaM.

At 800 °C there was no grain structure apparent, but by 1000 °C the grain size was found to be at the submicron level, mostly between a range of 0.1-0.5 μm, the grains being more equiaxed and less plate-like than in the BaM fibres, and there were no pores visible on the surface of the fibres (fig. 106). Surface area data on the SrM ferrite fibre gave a low surface area of 0.88 $m^2 g^{-1}$ and an average pore diameter of 48 nm, and when estimated from the shrinkage results, the porosity of the fibres was 4%. Various characteristics of the two aligned M ferrite fibres are compared in table 4.3, and the similarities between the two different fibres can clearly be seen. The strain to break of SrM fibres fired to 1000 °C / 3hr was 0.67%, similar to the BaM fibres.

The SrM fibres which were stored at 110 °C for 3 yr prior to firing proved to contain poorly crystalline α-Fe_2O_3 in the usually amorphous gel fibre, and the M phase had begun to form, as a very minor component, at only 700 °C / 3hr (fig. 107). However, in contrast to the stored BaM fibres, when fired at 700 °C / 100hr the material had become virtually pure SrM with a crystallite size of 50 nm, but although the material had no observable grains, it was also poorly sintered. When fired to 1000 °C / 10min the stored fibre had a markedly different microstructure to the fresh fibre, and also consisted of two apparently different morphologies. Some fibres seemed very porous with relatively equiaxed grains <1 μm and pores <0.5 μm wide, while others contained little porosity, but clearly consisted of larger platelets 0.5 – 2 μm x 0.1 μm, with "islands" of platelets on the surface of the fibre. After 3hr at 1000 °C the fibres all resembled this second type, and in the bottom right corner of figure 108, a fibre which seems to be an intermediate between these two stages can be seen. After 24hr at 1000 °C all of these surface "islands" had disappeared, and the grains had become both more equiaxed and larger at 0.8 – 1.5 x 0.2 – 0.4 μm (fig. 109). The fibres also had a "scaly" look, as the platelets seemed to overlap along the fibre axis, perhaps as a result of growth from the "island" platelets, and this feature became more pronounced after 1000 °C / 100hr.

The potential advantage of SrM was that it could be more easily produced from a halide-free, nitrate stabilised sol, and then compared to the halide containing fibres. Similar to the halide free BaM fibre, the phase changed suddenly from only α-Fe_2O_3 at 650 °C to pure SrM at 700 °C with a crystallite size of 53 nm (fig. 110), and no microstructure was seen at all in these fibres (fig. 111), until 900 °C at which point grains on the edge of the resolution of the SEM (0.1 μm) had appeared. However, again the fibres were not well sintered at this temperature, and would require further densification to optimise their magnetic properties.

3.5 Co^{2+} / Ti^{4+} substituted M ferrite fibres

The series of fibres with the formula $BaCo_xTi_xFe_{12-2x}O_{19}$ were fired to give the ferrite with x = 0.5 - 1.1, and they demonstrated a markedly different microstructure to the standard BaM ferrites. For x = 0.5 and 1.0 XRF analysis showed the compositions to be $Ba_{1.00}Co_{0.52}Ti_{0.51}Fe_{10.97}O_{18.99}$ and $Ba_{0.98}Co_{1.02}Ti_{0.99}Fe_{9.99}O_{18.78}$, almost exactly the correct stoichiometric values. The microstructural features of these fibres are compared to each other and BaM in table 4.4. All formed the pure M phase by 900 °C, and their XRD patterns at 1000 °C are compared in figure 112. The incorporation of the substituents into the M structure as a solid solution was indicated by an increase in intensity of the two peaks at 2θ = 55° and 57° in the XRD patterns, which became more pronounced with increasing x.

x	Surface area / $m^2 g^{-1}$	Porosity / %	Crystallite size / nm	Grain size / μm	Microstructure
0	0.86	2.2%	57	<1	Unclear / Thin platelets?
0.5	3.4	21.3%	46	0.3 – 0.5	Separate grains, very porous
0.75	n/a	n/a	56	0.5 – 1	"Bark"-like, less porous
1.0	5.1	39.5%	57	1 - 2	Linear ridges, "mossy" plates
1.1	n/a	n/a	63	0.5	0.5 μm grains, 0.2 μm pores

Table 4.4 Comparison of microstructural characteristics of $BaCo_xTi_xFe_{12-2x}O_{19}$ fibres fired to 1000 °C / 3hr.

Porosity seemed to decrease with x from SEM evidence, but this could be caused by the size of pores decreasing to below the resolution available on the SEM. The lower

substitution level ferrites of $x < 1$ showed individual, regularly sized grains, but they also appeared to be quite porous. The $x = 0.5$ fibres, fired to 1000 °C / 3hr, demonstrated a surface area of 3.38 m^2g^{-1}, much greater than that of the BaM fibres, and a porosity of 0.043 cm^3g^{-1} = 21.3% porous, and a larger pore diameter of 88 nm. At 800 °C the $x = 0.5$ fibres were mostly α-Fe_2O_3 with ~25% M, but by 850 °C they had become almost pure M phase, and they were pure M at 900 °C with a crystallite size of 29 nm (fig. 113). At 800 °C the fibres already had small grains ~0.1 μm in diameter (fig. 114), and by 900 °C this had developed into a rough pitted surface which did not contain any clear individual grains (fig. 115). However, by 1000 °C the microstructure had changed again to yield a fibre composed of regularly sized, plainly separate grains 0.3 – 0.5 μm in diameter, with many pores 0.1 – 0.2 μm wide (fig. 116), and the crystallite size had increased to 46 nm. As shown in figure 113, after only 10 min at 1000 °C the pure M phase had formed, but the crystallite size was smaller at 35 nm, and the microstructure resembled that of the 800°C sample. Upon firing to 1200 °C / 3hr the regular grains had become random platelets 1 – 2 x 0.2 – 0.4 μm in diameter, and the pores had grown to 0.5 μm. The $x = 0.75$ fibres were similar to the $x = 0.5$ fibres at 1000 °C, except that the grains were less well separated and larger in size, up to 1 μm. The surface of the fibre had a texture resembling tree bark, as can be seen in figure 117, and when fired to 1200 °C platelets as large as 3 x 1 μm had appeared.

The $x = 1.0$ fibres had also begun to form M at 800 °C, but by 850 °C the sample was pure M phase, with a crystallite size of 29 nm (fig. 118). At 800 °C the surface of the fibres had a rough, bark-like appearance, but by 900 °C this had developed into linear ridges along the fibre axis, although these were wider (0.3 – 0.5 μm) and not as straight as those seen in the stored BaM fibres (fig. 119). When fired to 1000 °C / 10min they resembled the 900 °C fibres, but after 3hr at 1000 °C they consisted of what seemed to be larger plates, up to 2 μm in diameter, which were themselves made up of smaller grains, but with no discernible hexagonal symmetry, giving a "moss"-like appearance (fig. 120). However, at 1100 °C this

had been replaced by a more familiar random assortment of hexagonal platelets, and at 1200 °C these resembled the x = 0.75 fibres at the same temperature (fig. 121). Despite seeming to have less porosity from SEM evidence, the x = 1.0 fibres were even more porous at 1000 °C than the x = 0.5 fibres, with 0.079 $cm^3 g^{-1}$ (39.5%), and had a surface area 50% higher at 5.0 $m^2 g^{-1}$, but with a smaller average pore size of 72 nm. Therefore, the "mossy" surface grains probably hid the pores from view, as at 1100 °C, when these features had gone, the fibres where clearly porous. These changes in surface features unique to the x = 1.0 fibres could be related to the structure seen in the gel fibre, which was not apparent in any others in the series, even the more substituted x = 1.1 fibres. At 1000 °C these resembled the x = 1.0 fibres at 1100 °C, consisting of grains no larger than 0.5 μm, and they were riddled with pores 0.2 μm wide (fig. 122). However, by 1200 °C they had undergone large growth giving grains up to 10 μm long, although they were not like the thin plates seen in DGG in the other ferroxplana ferrites.

3.5.1 $SrCo_xTi_xM$ ferrite fibres

The substituted SrM fibres showed quite different morphologies from the substituted BaM fibres, as did their unsubstituted counterparts. At 800 °C the x = 0.5 fibres were already 75% M ferrite with a crystallite size of 45 nm, and they had formed the pure ferrite at 1000 °C with a crystallite size of 64 nm (fig. 123). However, at 800 °C the fibres had no grain structure, contained surface cracks and had patches of small crystals on their surface (fig. 124), which were not seen in other fibres, and suggested that the components were not homogeneous at this stage, and that the M phase was not fully substituted. At 1000 °C / 3hr the fibres were smooth and featureless, still with no apparent grains, although after 100hr at this temperature they had developed a rougher surface and pores up to 0.5 μm wide (figs. 125 and 126). At 1200 °C they had developed the scaly-looking grains 0.5 – 1 x 0.2 μm in diameter, similar to those seen in the stored SrM fibres. The x = 1.0 fibres had a similar phase development (fig. 123), having a crystallite size of 41 nm at 800 °C and 64 nm at 1000 °C. At 800 °C they were covered with many more clumps of surface crystals, confirming that these were a separate

phase consisting of the substituted components (fig. 127), probably caused by the mixture of the two Fe/Br and ultrasonic titania sols discussed in chapter two. Again they had disappeared at 1000 °C to give smooth, even fibres, but this time with cracks / ridges generally along the fibre axis, although these were less clearly defined than in the BaCoTiM fibres (fig. 128). By 1200 °C scaly grains had formed, larger than for x = 0.5 at 2.5 – 5 x 0.3 μm.

3.6 Y ferrite fibres

The XRD patterns of the Co_2Y fibre taken between 400-1200 °C are shown in figure 129. Haematite had formed by 400 °C, and at 600 °C it was still the major phase, the background remaining amorphous. At 800 °C the haematite peaks have disappeared and M ferrite has stared to form, along with the spinel $CoFe_2O_4$ and α-$BaFe_2O_4$. This was supported by the findings of Vinnik [223] and Castelliz [14], who reported that the M phase can persist to 1100 °C and that α-$BaFe_2O_4$ may co-exist with Co_2Y once it has formed as the major phase above 1100 °C. Indeed, by 1000 °C Co_2Y had crystallised as the major phase with α-$BaFe_2O_4$ persisting as a minor phase and no further change occurred up to 1200 °C. The average crystallite size was estimated to be 70 nm at 1000 °C. The presence of α-$BaFe_2O_4$ in the Co_2Y fibres could be due to the higher levels of barium in the Co_2Y fibres (Fe:Ba = 6) than any other compositions, leaving some free Ba^{2+} ions to form the oxide compound.

The dried fibre was strong and very handleable, becoming slightly less so when heated above 1000 °C and becoming brittle at 1200 °C. At 800 °C the freshly spun fibres were very smooth and still fibrous, and some microstructure was apparent as edge-on platelets with a grain size in the order of 1 x 0.1 μm (fig. 130). After firing to 1000 °C the fibres appeared to consist of a densely packed mass of randomly oriented thin hexagonal plates (fig. 131), which were 1 – 3 x 0.1 – 0.2 μm, and which did not compromise the fibrous nature of the material. Upon heating further to 1100 °C individual grains could be seen to be increasing in size at the expense of their neighbours, and by 1200 °C many larger and more equiaxed hexagonal crystals had formed, still no more than 3 μm in diameter, but now up to 1 μm thick (fig. 132).

The fibres had become mechanically very weak and virtually unhandleable by this stage. Bulk powdered Co_2Y specimens are usually prepared at temperatures over 1100 °C to obtain Co_2Y as the major phase, and show a uniform distribution of close packed grains between 3 and 10 μm in size across the hexagonal plane, and between 0.75 and 2 μm in thickness between 1200 and 1300 °C [14]. Therefore, the fibrous Co_2Y ferrite also appeared to have a much reduced grain size than standard powder mixes at equivalent temperatures. Surface area and porosity data on the fibre fired to 1000 °C supported the results above, giving a low surface area of 0.93 $m^2\ g^{-1}$ and a similar porosity to the BaM fibres (0.004 cm^3/g), with an average pore diameter of 44 nm.

The Co_2Y fibres stored for 3 yr had formed the Y phase at only 900 °C, albeit still with α-$BaFe_2O_4$ as a secondary phase, and after only 10 min at 1000 °C single phase Co_2Y had formed (fig. 133). The 900 °C fibres consisted of small grains well below 1 μm, and seemed to be quite porous (fig. 134), whereas the fibre fired to 1000 °C / 10min resembled the freshly spun fibre after 3 hr at this temperature, and after 3 hr the grains had become thicker, up to 3 x 0.5 μm and with pores around 1 μm wide (fig. 135).

Because the ferroxplana compounds have such complex chemical compositions, a deviation in either the stoichiometries or oxidation states of the components can have an adverse affect on their magnetic properties [7], so this had to be confirmed. The quantitative XRF elemental analysis confirmed the composition to be $Ba_{1.94}Co_{1.91}Fe_{12}O_{21.85}$ at 1000 °C, and all the halides had been lost at this temperature. The DERA Co_2Y ceramic powder sample proved to have a composition of $Ba_{2.12}Co_{0.92}Fe_{12}O_{21.04}$ with a cobalt deficiency of over 50%, demonstrating the difficulties encountered in forming pure forms of these phases.

3.6.1 Other Y ferrites

Stoichiometric sols of Ni_2Y, Mn_2Y and Zn_2Y were spun and fired to 1000 °C. The Ni_2Y and Zn_2Y fibres both formed a mixture of Y ferrite and $BaFe_2O_4$, whereas the Mn_2Y fibres only formed an M ferrite, as can be seen in figure 136. The Ni_2Y fibres resembled Co_2Y, but were

more porous looking and had larger, thin platelets 2 – 7 x 0.2 – 0.5 μm, whereas the Zn_2Y fibres more resembled Co_2Y at 1200 °C, consisting of thicker random platelets 3 – 5 x 0.5 – 1.0 μm.

3.7 Z ferrite fibres

The quantitative XRF elemental analysis confirmed the composition to vary between $Ba_{2.93}Co_{1.85}Fe_{24}O_{40.78}$ and $Ba_{2.79}Co_{2.07}Fe_{24}O_{41.86}$, which was very close to the ideal pure phase stoichiometry. To give an idea of the difficulty in forming pure phase stoichiometric Z ferrite, the ceramic powder sample supplied by DERA which was said to be pure Co_2Z from magnetic and XRD characterisation had a composition of $Ba_{2.38}Co_{1.83}Fe_{24}O_{40.21}$. The surface homogeneity of the Z fibres fired to 1250 °C was examined using SEM with an elemental mass analyser, using back-scattered electrons and with a resolution down to an area of 1 μm^2, well below the grain size. This gave an average surface composition of $Ba_{2.88}Co_{1.80}Fe_{24}O_{40.48}$, indicating that overall the surface was near the stoichiometric Z composition. However, on the micron scale there were variations in composition even in individual grains, between a minimum of $Ba_{2.37}Co_{1.45}Fe_{24}O_{39.82}$ and a maximum of $Ba_{3.38}Co_{2.32}Fe_{24}O_{41.70}$ (relative to iron), such localised differences being caused by the existence of minor quantities of other phases, such as the barium and cobalt deficient BaM and overly abundant Co_2Y, both of which are the precursors of Co_2Z.

The XRD patterns for the Co_2Z fibres taken between 400 °C and 1250 °C are shown in figures 137 and 138. At 400 °C haematite had formed as the only identified crystalline phase from the amorphous background and this remained at 600 °C, along with BaBrCl. However, at 800 °C these peaks had either been replaced by the appearance of BaM and $CoFe_2O_4$ as the major phases. The formation of these two phases between 600 °C and 1000 °C, coincidental with the loss of haematite, paralleled the formation processes observed for the Co_2Y fibres, but without the presence of α-$BaFe_2O_4$. In the Co_2Z fibre, $CoFe_2O_4$ also formed at a higher than expected temperature [24], whilst BaM appeared at similar temperatures to the M ferrite

fibres, suggesting that it is not only the group II metal ions which are affected by the presence of halides, but also Co^{2+}. Nitrogen adsorption measurements taken at 800 °C gave the surface area of the fibres as 7.9 $m^2 g^{-1}$ and a porosity of 0.071 $cm^3 g^{-1}$, with an average pore size of at least 40 nm. This suggested a porosity of 27% remaining at this temperature, which was much higher than in BaM at equivalent temperatures, and the surface area was also double. By 1000 °C the spinel had been lost due to the formation of Co_2Y, and the two ferrites BaM and Co_2Y appeared to co-exist in equal proportions. This seems to be an unavoidable step in the production of Co_2Z [24;225], which is stoichiometrically made up from one unit of each of BaM and Co_2Y; the crystallisation of Co_2Z has never been reported without undergoing either the formation or mixing of these two phases first, and then only when there is a further increase in temperature to at least 1200 °C.

The relationships between the components of this system are notoriously complex [223] and the precise mechanism is unknown for the formation of Co_2Z, although it has been suggested that it proceeds via a topotactic reaction between the interfaces of the phases involved [264]. The fibres still had smooth parallel sides at 1000 °C, although a rapid increase in grain size had already been observed above 800 °C, the microstructure consisting of what appeared to be random hexagonal platelets 1 - 3 μm long, as in Co_2Y ferrite at this temperature (fig. 139). By this temperature the surface area had decreased to 1.0 $m^2 g^{-1}$ with a further loss of porosity to levels resembling the other ferrite fibres at this temperature, indicating a high degree of sintering concomitant with the formation of the Co_2Y phase. Firing for extended periods at this temperature only resulted in grain growth, with no change of phase.

These two phases persisted to over 1100 °C with a further increase in both the size of the hexagonal plates up to 6 μm long, but the material retained a fibrous nature despite this (fig. 140). The formation of Co_2Z at 1200 °C seemed to coincide with the loss of BaM, but not Co_2Y, which co-existed with Co_2Z in approximately equal amounts. Furthermore it remained a major phase above 1200 °C until the formation of single-phase Co_2Z, and although

this is concordent with the published data it remains unclear why the two precursor ferrites should not decompose together equally to form Co_2Z. There are some unidentified peaks among the XRD patterns at this point, and it is suggested that these may be due to the formation of Co_2U ferrite (Z + M) as an intermediate stage, although the XRD patterns are too unclear to confirm this theory. Accompanying the creation of Co_2Z was the rapid and exaggerated DGG, which compromised the integrity of the fibres due to the formation of large hexagonal plates 1 - 2 μm thick and up to 25 μm long, several times the actual diameter of the fibres (fig. 141). Amazingly, although the material had been mechanically weakened, the elongated growth occurred along the fibre axis and they remained as discrete, separate fibres of between 4-7 μm in diameter despite resembling a stack of building bricks about to topple over. This DGG was correspondingly accompanied by a drastic lowering in surface area and surface porosity to negligible values It is another common feature of the crystallisation of Co_2Z, sometimes resulting in a grain size as large as hundreds of microns [293] along with a corresponding loss of porosity, but it has not been noted to occur at temperatures as low as these. It has been reported to happen after 10 hours at 1260 °C and only 10 minutes at 1310 °C, but no growth at all has been previously observed even after heating for 24 hours at 1220 °C with conventionally prepared ceramic specimens [266]. In the Co_2Z fibres DGG occurred after only 5 min at 1200 °C, whereas the Z phase did not begin to form until after 15 min at this temperature, suggesting that the occurrence of DGG is indeed unavoidable in the formation of undoped Co_2Z under normal firing conditions. In fibre containing high levels of Cl^-, DGG never occurred even at 1250 °C / 3hr, but the Z phase also failed to form.

From the XRD data at 1250 °C the fibres appeared to consist of only Co_2Z, a relatively low temperature for single phase Co_2Z to occur, but it was thought unlikely that 100% pure Co_2Z had been formed, as the system is so complex and there are usually either traces of Co_2Y from the formation process, or Co_2Z begins to decompose to Co_2W [264]. Due to the sharing of many peak positions the signals of small amounts of these compounds are extremely difficult to distinguish from the major phases in the very convoluted and similar XRD spectra

of the hexagonal ferrites, and the magnetic results discussed in chapter five proved to be a more reliable method of determining the quality of the Z product. The average crystallite size of the Co_2Z ferrite fibre was calculated to be 0.2 μm using the Scherrer equation on the 100% peak at $2\theta = 32.72°$, but it can be seen in figure 142 that the grains have formed huge, thin plates. There was no evidence of the Co_2Z fibres decomposing to give Co_2W either at temperatures up to 1300 °C or through a prolonged heat treatment of 24 hours, as has been previously reported to happen with firing times of as little as four hours at 1200 °C [264]. There was also no worsening in the morphology of the fibres during the transition from a mixed to a single phase material, although on firing to 1300 °C some individual fibres fused together into a larger crystalline mass, ruining the fibrous nature of the product (figs. 143 and 144). When the 1200 °C mixed phase Z sample was fired at 700 and 1100 °C / 100 hr, there was no evidence of loss of Z and increase in Y and M phases, and no change in morphology, indicating that the formation of Z ferrite is a kinetic reaction. An attempt was also made to seed a Z sol with 10% by weight of crystals of prefired Z ferrite, ground to 10 μm before hand. This failed to encourage the formation of Z ferrite at a lower temperature, although further seeding experiments with either smaller grains or other materials will be investigated in the future.

The hexagonal nature of the DGG grains can clearly be seen in figure 145, and the elongation occurs along the fibre axis as this is the only direction in which growth can progress, once the grain is the full width of the fibre. These grains are relatively thin hexagonal plates, and although to the naked eye the fibres appear to have remained well aligned, it can be seen from figure 146 why the fibres become extremely weak following DGG. Figure 147 shows random Co_2Z fibre, in which the fibres touch and cross each other more often, enabling DGG to occur not only along the fibre axis and resulting in more hexagonal-looking grains, and a total loss of their fibrous nature. Stacks of layers of hexagonal plates can be seen to form the grains in figure 148, suggesting that the growth process is indeed by a diffusion and condensation process, as discussed earlier in this chapter.

Although low porosity is a desirable property for microwave applications, so is a small grain size. The porosity of the Co_2Z phase could not be accurately estimated as there was no further shrinkage above 1000 °C and the surface areas were too small to be measured. Furthermore, the rapid growth process may also enclose pores within the structure of the material between old grain boundaries, possibly explaining why densities less than the theoretical maximum are obtained even with fully sintered Co_2Z [266]. Therefore, a method of preventing or limiting the exaggerated platey growth process would be extremely advantageous in the manufacture of these materials.

3.7.1 Doping of Co_2Z fibres

In an attempt to either lessen the exaggerated grain growth or produce Z ferrite at a lower temperature, the sol was doped with various known sintering aids used in other ceramic materials. It was supposed that ions of a similar size to Fe^{3+} (0.064 nm), Co^{2+} (0.072 nm) and Ba^{2+} (0.134 nm) would substitute directly into the structure. Therefore, ions smaller than Fe^{3+} (Si^{4+}, B^{3+} and Al^{3+}) were added in the hope that they would be more likely to segregate at grain boundaries and hinder grain growth. A series of refractory oxides, some of which were known to form solid solutions with the hexagonal ferrites, and with ionic radii between Co^{2+} and Ba^{2+} (Y^{3+}, Gd^{3+}, La^{3+}, Ca^{2+} and Sr^{2+}) were also added as 1 mol% to barium. A summary of the results are shown in table 4.5.

Most of the flux-type sintering aids just caused a fusing of the fibres or worsening of the microstructure, with no advantage in either formation temperature or grain size, and in some cases actually hindered the formation of the Z phase. However, amongst the metal additives gadolinium, calcium and strontium all showed much better Z ferrite characteristics than usual at 1200 °C, with calcium seeming to form pure phase Z ferrite at this temperature, where normally only a mixed phased is observed. Of the three samples only calcium showed no corresponding worsening in microstructure, and so this was examined more closely. With calcium the Z phase begins to form at 1150 °C, and is the major phase at 1175 °C, still without

DGG occurring, and the grains looking much more equiaxed. This step has always been observed at the onset of Z formation before, but did not happen in this case until the sample appeared to become single phase Z from the XRD pattern at 1200 °C, and these fibres are discussed in detail in the section below. Although showing a deterioration in microstructure (fig. 149), the strontium and gadolinium doped fibres did show an increased Z phase content over the undoped Z fibres at equivalent temperatures, and considering the possible advantages of using strontium in the sol, $Sr_3Co_2Fe_{24}O_{41}$ fibres were investigated. At 1100 °C the XRD pattern indicated only SrM, α-Fe_2O_3 and $CoFe_2O_4$ with no trace of Y or Z phases, but at 1200 °C a pure Z phase had formed (fig. 150), with the values all shifted upfield slightly, and a crystallite size of 91 nm.

Dopant	% Wt.	Result at 1200 °C / 3 hr
SiO_2	0.3	No effect
SiO_2	0.7	Increase in grain size, fusing of fibres
SiO_2 - B_2O_3	2.0	Fused mass, but no better formation of Z
SiO_2 - B_2O_3 - Al_2O_3	3.0	No Z formed, oct. & hex. crystals mixed
$CaSiO_3$ - Al_2O_3	1.3	Unusually good Z sample, same grain size
SiO_2 - Al_2O_3	2.0	More grain growth,
La_2O_3	1.9	No effect
Gd_2O_3	2.1	More grain growth, better Z
Y_2O_3	1.3	No effect
CaO	0.67	Excellent pure Z, but same morphology
SrO	1.2	More grain growth, better Z

Table 4.5 Effects of various additives on formation and morphology of Co_2Z ferrite fibres.

3.7.2 CaO-doped Co_2Z fibres

The 0.67% CaO-doped Co_2Z fibres behaved exactly as the undoped Co_2Z fibres up to 1100 °C, consisting of equal amounts of BaM and Co_2Y ferrite and having a similar morphology to the Co_2Z at this temperature. At 1150 °C the Co_2Z phase had already begun to form with the corresponding loss of the BaM phase, with the XRD data indicating roughly equal amounts of

Co_2Z and Co_2Y (fig. 151), just as with the Co_2Z fibres at 1200 °C. However, the microstructure of the Ca-doped fibres was drastically different, with the runaway platey growth process seemingly controlled and resulting in more equiaxed looking grains, and maintaining the fibrous characteristics of the fibres to a higher degree (fig. 152). The hexagonal grains were 1 - 3 μm across the hexagonal plane and around 1 μm thick, and the fibres were decidedly more robust and handleable as a result, even as a thin web, although they were still not as mechanically strong as fibres fired to lower temperatures.

By 1175 °C, Co_2Z seemed to be the major of the two components, and although grain growth had occurred the grains were still relatively small and equiaxed, all being below 5 μm wide and some appearing to be rounded at the edges, a feature not seen before, suggesting that a different process was occurring (fig. 153). The presence of Co_2Y was not indicated at all by the XRD pattern at 1200 °C, indicating that Co_2Z was the sole phase at this temperature, although again caution must be used as it is unlikely that pure single phase Co_2Z ferrite was actually obtained. Unfortunately at this stage the exaggerated grain growth had accompanied the full transformation to Co_2Z, resulting in the now familiar large, plate-like grains seen also at this temperature in the undoped Co_2Z fibres (fig. 154). Nevertheless, this was a very low temperature for Co_2Z to form as the major component, and the average crystallite size derived from the 100% peak at $2\theta = 32.69°$ was 97 nm, less than half the size of the undoped Co_2Z fibres at 1250 °C.

An addition of calcium oxide and silica to spinel ferrites can cause an increase in the resistivity and a corresponding decrease of eddy current loss due to the additives segregating at grain boundaries [294] and forming an insulating layer upon cooling. An addition of CaO to manganese-zinc spinel ferrites has also been reported to decrease grain growth rate and sintering rate by the same segregation process [295]. It is suggested that the rate of growth in the plane perpendicular to the c-axis of the Co_2Z is being slowed by the segregation of calcium at the grain boundaries, allowing the growth along the c-axis to "catch-up", thus preventing the exaggerated grain growth stage and resulting in the more equiaxed grains observed. The

increase in temperature to 1200 °C causes the dissolution of the additive in to the crystal lattice resulting in the onslaught of the exaggerated growth seen at this point.

3.8 Co_2W ferrite fibres

The XRD patterns of Co_2W fibres taken between 600 - 1200 °C are shown in figure 155. Haematite had formed by 400 °C, and at 600 °C it was still the only phase, the background remaining amorphous. At 800 °C the haematite peaks had disappeared and M ferrite had formed along with the spinel ferrite $CoFe_2O_4$. These two phases then persisted as the only ones present even over 1150 °C. The dried fibre had a diameter of 3-5 μm and was strong and very handleable, and remained so through changes to the haematite and mixed phase fibres up to 1100 °C, when the fibres started to become slightly brittle. Up to 800 °C the fibres were very even sided and fibrous in nature, and although some surface roughness was apparent any microstructure present was below the level of resolution of the SEM. After firing to 1000 °C the fibres appeared to consist of a densely packed mass of randomly oriented thin hexagonal plates, similar to the Co_2Y fibres. These plates did not compromise the fibrous nature of the material, but on reaching 1100 °C they had begun to do so. Individual grains could be seen to be increasing in size at the expense of their neighbours, and although they had an average size of 2 μm, some crystals had started to grow into large planar crystals up to 8 μm in diameter and 1 μm thick (fig. 156).

Surface area and porosity data on the fibre fired to 1000 °C indicated a low surface area (2 $m^2\ g^{-1}$) and some porosity (0.02 $cm^3\ g^{-1}$ = 10%), with an average pore diameter of 51 nm. This was compared with the data for pure M ferrite and Co_2Y fibres, and the mixed M / Y phase Co_2Z precursor fibres fired to 1000 °C, which had lower surface areas (0.9 $m^{2\ -1}$) and very little porosity (0.004 $cm^3\ g^{-1}$), but similar average pore diameters of around 50 nm. The nitrogen adsorption technique used can only detect pores up to about 200 nm, so the greater porosity could be due to much larger spaces forming between the grains, indicating that the crystallites were undergoing greater growth than in either the other formulations at equivalent

temperatures. This was borne out by visual evidence from the SEM, which showed a large increase in both grain size and visible pore size on the micrographs, the 0.1-0.3 μm sized pores at 1000 °C becoming as large as 1 μm at 1100 °C.

Suddenly, at 1200 °C, the XRD revealed that the fibres had transformed in to single phase Co_2W, and there was no further change in phase up to 1300 °. This formation of the Co_2W phase was coincident with a drastic increase in the brittleness of the fibres, and under the SEM it could be seen that DGG had occurred, producing some grains over 10 μm long (fig. 157). Despite this the calculated crystallite size was found to be 60 nm, much smaller than that for the Z ferrite fibres, using the 100% peak at 2θ = 34.54°. As with the Z fibres, this exaggerated grain growth had mechanically weakened the fibres and reduced their handleability, although they were still discrete, separate fibres. As the temperature increased so did the crystal growth until the separate fibres began to fuse together into a single mass at 1300 °C (fig. 158).

Previous investigations have also reported that the Co_2W phase does not begin to form until between 1150-1200 °C, but they maintain that the Co_2W does not become the major phase until at least 1250 °C [264], and that Co_2Y, Co_2Z and other compounds may co-exist with Co_2W once it has started to form [14]. This very rapid transformation from M ferrite/spinel to single phase Co_2W appears unusual, and may have helped cause the extreme growth associated with Co_2W formation in this material. $SrZn_2W$ ferrite has been produced at temperatures as low as 1100 °C using a co-precipitation method [296], but most W ferrites are usually sintered commercially between 1250-1400 °C to obtain a homogeneous product [296;297]. The quantitative XRF elemental analysis confirmed the composition to be $Ba_{1.03}Co_{1.91}Fe_{16}O_{26.94}$ at 1000 °C, and all the halides had been lost at this temperature.

3.9 Co_2X ferrite fibres

The XRD patterns for the Co_2X composition fibres are shown in figure 159, although there are no published patterns of Co_2X for comparison. At 1000 °C the fibres consisted of BaM

and $CoFe_2O_4$, and the microstructure resembled the freshly spun BaM fibres at this temperature. At 1200 °C an unidentified phase had formed, which could be Co_2X, and the fibres had experienced grain growth with most grains being 1 – 2 x 0.2 – 0.4 μm (fig. 160), and even though some were as large as 15 μm, DGG had not occurred. XRF analysis showed the composition to be close to that of the X ferrite at $Ba_{1.98}Co_{1.85}Fe_{28}O_{45.83}$.

3.10 Co_2U ferrite fibres

As with Co_2X, there are no published XRD patterns for Co_2U ferrite, and the XRD patterns shown in figure 161 could be either a mixture of BaM and Co_2Z or the U ferrite, which is a combination of these two phases. At 1000 °C the fibres resembled the Z precursor fibres at the same temperature, but at 1200 °C DGG had not occurred despite the large grain size of up to 10 μm (fig. 162), perhaps indicating that the material was indeed the U phase and not a mixture of M and Z, the latter always forming after the onset of DGG. At 1250 °C DGG had occurred, and the grains had begun to fuse together. The composition was confirmed by XRF to be $Ba_{4.30}Co_{2.13}Fe_{36}O_{60.43}$, close to that of Co_2U.

3.11 Confirmation of oxidation states

As even small deviations in oxidation state, especially of Fe^{3+} to Fe^{2+}, can have a large effect on magnetic properties [298], the species and oxidation states present were confirmed by non-quantitative XPS, and the binding energies were all referenced from "The Handbook of X-ray Photoelectron Spectroscopy" [299]. This technique looks at the binding energies of electrons of the elements and oxides, into which the photons can penetrate between 1 - 10 μm into the surface of a material, but only electrons ejected from the top few nm of the surface can be analysed.

All of the fibres showed a large peak at 530 eV corresponding to the O1s peak of oxygen in Fe_2O_3 and any other oxides would be covered by this peak as it is quite wide, from 528 - 533 eV. Also the unfired fibres showed small peaks at 285, 199 and 69 eV,

corresponding to carbon (C1s), chlorine ($Cl2P_{3/2}$) and bromine ($Br3d_{5/2}$) peaks respectively, and these vanished as these components were removed with further firing. The XPS analysis of BaM fibres fired to 1000 °C showed the oxidation state of the iron on the surface to be Fe(III) with a binding energy of 710.8 eV for the main $Fe2p_{3/2}$ peak, compared to the literature values of 710.9 eV for Fe_2O_3 and 709.3 eV for FeO, and the secondary $Fe2p_{1/2}$ peak was present 14 eV higher. The $Ba3d_{5/2}$ peak was also clearly apparent at 780 eV, with the secondary $Ba3d_{3/2}$ peak at 795 eV. The XPS analysis of both Co_2Y and Co_2Z fibres fired to 1000 °C also showed the oxidation state of the surface iron to be Fe(III) with a binding energy of 711 eV for the main $Fe2p_{3/2}$ peak. Unfortunately the $Co2p_{3/2}$ peak = 780.4 eV for CoO and the secondary $Co2p_{1/2}$ peak is 15 eV higher, in virtually the same positions as BaO. Therefore, although two peaks could be clearly seen around 780 - 782 and 795 - 797 eV, it was impossible to distinguish between the CoO and BaO peaks.

3.12 Alternative preparative methods

3.12.1 Coprecipitation

The DTA/ TGA plots for stoichiometric Co_2Z samples between 25 - 1000 °C, from iron nitrate and barium and cobalt acetate salts coprecipitated with NH_3, NH_4HCO_3, $NaHCO_3$ and Na_2CO_3, are shown in figure 163. These samples were not made into a sol or spun as fibre, and contained no halides.

The NH_3 precipitate sample had a large endotherm at 90 °C and a smaller one at 200 °C, representing the loss of water and hydroxides, and an exotherm at 700 °C, probably coincident with BaM formation. The weight loss was steady up to 12% at 400 °C, then a steady but slower loss of 4% up to 1000 °C. The XRD pattern at 1000 °C showed mostly haematite, with a small amount of BaM and cobalt spinel, corresponding to loss of 44% Ba from the precipitate, and the Z phase never formed at higher temperatures.

The sample coprecipitated with NH_4HCO_3 was similar, but there was another large endotherm at 600 °C too, which was also present in the samples precipitated with sodium

bases, and which seemed to be coincident with α-$BaFe_2O_4$ formation, and could be caused by the decomposition of $BaCO_3$ to form this. There were no other large exotherms and weight loss was a steady 20% up to 600 °C, and virtually none after this, with a sudden drop of 2% at the 600 °C peak. The XRD patterns, shown in figure 164, gave BaM and 20% α-Fe_2O_3, plus α-$BaFe_2O_4$ and a trace of Co_2Y at 1000 °C, and some other unidentified phase. At 1100 °C this was reduced to a mixture of Y, M and $BaFe_2O_4$, and by 1250 °C some Z had also formed and the α-$BaFe_2O_4$ was nearly all gone.

In the $NaHCO_3$ precipitated sample the two endothermic peaks at 100 and 200 °C were of equal magnitude. As well as both the endotherm at 600 and exotherm at 700 °C, there was also a small endotherm at 800 °C, which could be from $NaFeO_2$ formation. The weight loss was a steady 12% to 700 °C, with almost none after, and again a definite drop of 1.5% at the 600 °C peak. The XRD was the same as the other coprecipitates at 950 °C, but contaminated with $NaFeO_2$ to give M, Y, α-$BaFe_2O_4$ and $NaFeO_2$. The powder melted and fused over 1100 °C as the sodium acted as a flux, giving and XRD of only M, Y and $NaFeO_2$ at this temperature.

The Na_2CO_3 precipitated sample was the same, but with no peak at 100 °C, probably as there was no H to lose as water. There was not much weight loss until 200 °C, then a steep drop of 5% with the curve flattening out again and losing 4% up to 600 °C, at which point there was a sudden drop of 3% around the peak, and the sample was still steadily losing $% weight between 600 - 1000 °C. The XRD was also identical to the $NaHCO_3$ samples.

The 100 °C peak seemed to be due to loss of water from the base, 200 °C due to acetate loss, and as the samples were not spun there were no other organics to combust at 300 – 400 °C. The 600 °C peak was only in CO_3 containing samples suggesting it corresponded to the loss of carbonate, and the exotherm at 700 °C occurred with BaM formation. The peak at 800 °C was only in Na containing samples, possibly related to $NaFeO_2$ formation. Unlike in most of the sol-derived ferrites, there was α-$BaFe_2O_4$ formation, as reported previously for

coprecipitated powders. The loss of barium at pH below 9 caused loss of stoichiometry, resulting in failure to obtain the Z phase, and this was confirmed by XRF analysis. To obtain the Z phase a sodium base was required, but sodium caused the material to flux and fuse over 1100 °C, and resulted in contamination of the product with 2 wt% sodium. Therefore, the coprecipitation route was abandoned.

3.12.2 Alkoxide derived fibres

Stoichiometric gel fibres of BaM and Co_2Z ferrite were spun from alkoxide derived precursor sols, but the resulting gel fibres were twisted, full of internal structure and difficult to spin, probably due to a destructive interaction between the spinning aid and organic solvents remaining in the spinning solution. Upon firing the BaM fibres formed M ferrite but showed no advantage in either formation temperature or microstructure over the standard preparation. At 400 °C the only crystalline phase was haematite, and although by 800 °C the M phase had appeared, it coexisted with a spinel phase which persisted as ~25% even at 1000 °C (fig. 165). It was known that the alkoxide precursors were unavoidably contaminated with up to 5% Li^+ from their production process, and therefore this spinel phase was the highly magnetic but soft ferrite $LiFe_5O_8$, which would disrupt the magnetic properties of the magnetically hard BaM. Stoichiometric Co_2Z fibres were also made from an alkoxide precursor, and their XRD patterns are shown in figure 166. A spinel was formed at 500 °C, and unusually there was no sign of α-Fe_2O_3 even at 700°C, but as the spinels $CoFe_2O_4$ and $LiFe_5O_8$ have overlapping peaks, the fibre could have contained a mixture of both compounds. At 1000 °C the M and Y phases had formed as minor products, but the spinel phase was still the major component, even up to 1200 °C, and although the Z phase never formed more Y ferrite developed at higher temperatures.

3.12.3 Ultrasonic preparation

The fibres made from the ultrasonically peptised BaM sol had formed the pure BaM phase by 1000 °C with a crystallite size of 41 nm, but they were very porous looking, with

comparatively equiaxed grains up to 1 μm wide (fig. 167), and hence offered no microstructural advantage over the standard preparations.

3.13 Steam firings

It was clear that the fibres retained a large portion of the halides even after drying, and that this was not lost until ~1000 °C. It appeared also that this halide retention inhibited the formation of the ferrite phases, and fibres stored for several years behaved differently due to gradual loss of halide, and so the removal of halide from the fibres at a lower temperature could be beneficial. Chloride is removed by the steaming of aluminosilicate fibres made from chlorohydrate and siloxane precursors [125;285], and so the steaming of ferrite fibres between 500 – 900 °C was investigated. The fibres were prefired to 400 °C to remove all organic components, and in all cases the steaming process resulted in loss of alignment of the fibres. The fibres were either steamed at a fixed temperature for 3hr, having been brought up to that temperature in air, or were fired over a temperature range, for example from 400 – 800 °C, over a period of 3hr in total.

3.13.1 BaM ferrite

The XRD patterns of the BaM fibres steamed at fixed temperatures in the range 500 - 900 °C / 3 hr are shown in figure 168. At 500 °C the fibres had no visible grains, like the unsteamed fibres at this temperature, and from the XRD were mostly α-Fe_2O_3 with a crystallite size of 25 nm, and some α-$BaFe_2O_4$ was also present. This indicated that some halide had already been lost at this low temperature, and confirmed that normally in the halide containing fibre the barium remains associated with the halides. Indeed, by 600 °C there was a greater amount of α-$BaFe_2O_4$ and BaM had begun to form as a minor phase, such a low temperature only having been reported previously in citrate derived M ferrites [300;301]. The linear ridges observed in the stored BaM ferrites had also begun to form, indicating that they were a feature of the M phase (fig. 169), and by 700 °C these had become clearly defined continuous ridges 0.2 – 0.3

μm wide, with no individual grains. The fibres were virtually pure BaM at 700 °C with just a trace of haematite, and a crystallite size of 41 nm, which had grown to 47.4 nm with steaming at 800 °C, although there was no change in phases or morphology (fig. 170). At 900 °C the fibre was pure BaM from the XRD with a crystallite size of 51 nm, but platelets 1 – 2 x 0.5 μm had grown, some of which seemed aligned flat on the surface, and the resulting fibre appeared very porous (fig. 171). When the fibres were steamed over a temperature range from 400 – 800 °C / 3hr, they resembled the fibres fired at 800 °C and demonstrated no improvement in morphology, although a similar tactic has proven beneficial for some commercial fibres [302] and YAG fibres produced by the author [303].

3.13.2 SrM ferrite

As with the BaM fibres, the SrM fibres contained both α-Fe_2O_3 and $SrFe_2O_4$ when steamed at 500 °C, and the M phase began to appear at only 600 °C (~15%), as shown in figure 172. At 700 °C the fibre was nearly single phase SrM with a crystallite size of 59.4, and there was no microstructure apparent, only a slight patchiness on the fibre which could have been the onset of the "island" formations seen on the surface of the stored SrM fibres (fig. 173). When steamed at 800 °C there was no change in the XRD pattern, but linear ridges had begun to appear on the surface on the fibres, again along the fibre axis. However, these lines were less well defined and less continuous than those seen on the BaM fibres, as can be seen in figure 174. After steaming at 900 °C the pure M phase was achieved, accompanied by the obvious growth of grains as the crystallite size also increased to 69 nm, and the surface of the grains had the scaly look seen in the stored SrM fibres fired to 1000 °C for long periods (fig. 175). Unlike the BaM fibres, when steamed from 400 – 800 °C / 3hr there was no microstructure visible, including the absence of the linear ridges, so an apparent improvement in morphology was observed.

3.13.3 Co_2Y ferrite

When steamed at 600 and 700 °C the Co_2Y fibres consisted of a mixture of α-Fe_2O_3, α-$BaFe_2O_4$ and $CoFe_2O_4$, but at 800 °C the product was mostly Y phase, with a trace of α-$BaFe_2O_4$, and a crystallite size of 92 nm (fig. 176). Perhaps unsurprisingly, at 700 °C the fibres resembled the steamed BaM fibres, having linear ridges along the fibre axis, although less well defined than in the BaM fibres. At 800 °C they matched the freshly spun Co_2Y fibres after 1000 °C / 3hr, but at 900 °C the platelets had grown thicker to 1 – 4 x 0.2 – 0.4 μm, more like Co_2Y at 1200 °C (fig. 177). As with BaM, the fibres steamed over 400 – 800 °C / 3hr were inferior, containing less of the Y phase with a crystallite size of 65 nm, and had a much finer grain structure of 1 – 2 x 0.1 – 0.2 μm, which was riddled with small pores.

3.13.4 Co_2Z ferrite

Fibres of Z ferrite steamed at 500 °C showed no change over conventional firing, but at 600 °C contained only 0.06% bromine and 0.15% chlorine (compared to 4.7% and 5.1% respectively in unsteamed fibres), and they had lost all of the halide at 700 °C. Steaming at these temperatures did not show any improvement in the microstructure of the Z fibres fired to 1250 °C. However, they did form M ferrite as a mixed phase with cobalt ferrite and haematite at an unusually low temperature of 600 °C. Co_2Z fibres steamed at 900 °C / 3hr exhibited a larger grain size than the normal Z precursor fibres, up to 4 μm (fig. 178), with the scaly appearance seen in some of the stored M fibres, which were also thought to have lost some halide over time. The XRD pattern of the fibres steamed at 900 °C contained only the M phase, with no Y or spinel components, but at 1250 °C the Z phase had formed as a minor product, coexisting with what appeared to be M ferrite (fig. 179), and DGG had occurred. It was found that if Z fibres were prefired to 1000 °C / 3hr in air and than steamed at 900 °C / 3hr, even at 1250 °C DGG had not occurred and the grains were below 6 μm, but seemed to be an unclear mixture of phases from XRD evidence. When the Co_2Z fibres were a steamed

over 400 - 900 °C / 3hr they formed poorly crystalline M as the major phase with some α-Fe_2O_3, and they demonstrated no advantage.

3.14 Vacuum firings

BaM fibres were fired for 600, 700 and 800 °C / 3hr under an unknown vacuum, pulled by a high performance rotary pump. At 600 °C the XRD patterns showed only α-Fe_2O_3 with a crystallite size of 23 nm, with no trace of BaBrCl, and by only 700 °C the material consisted of about 33% BaM (fig. 180). At 800 °C the pure M phase had formed with a relatively small grain structure and a reduced average crystallite size of 47 nm. The fibres had been stored for one year prior to firing. The formation temperatures of the ferroxplana ferrites were beyond the range of the vacuum furnace.

4. Conclusions

No cobalt halides or oxides were ever seen in the XRD patterns, but the crystalline $BaBr_2$ was observed at 200 °C, the rest of the fibre being amorphous below 250 °C, and mixed barium halides were seen at 600 °C in freshly made fibres. All fibres formed crystalline α-Fe_2O_3 by 300 °C with a crystallite size of 17 nm, but the haematite fibres were porous with a high surface area and lower strain to break than most ferrite fibres. Crystalline γ-Fe_2O_3, α-FeOOH or γ-FeOOH were never observed, the undoped iron oxide fibres remaining as haematite to at least 1000 °C. No $BaFe_2O_4$ was seen in undoped M fibres fired soon after spinning, but α-$BaFe_2O_4$ and $CoFe_2O_4$ were seen in ferrites containing cobalt when they were fired to 800 °C immediately after spinning. The Z, W, X and U phases formed only after the full crystallisation of M or M / Y at 1000 °C, accompanied by DGG in the case of Z and W fibres. Pure phase fibres of all ferrites were produced from stoichiometric mixes, unlike the standard ceramic preparations, coprecipitated ferrites or inorganic sol precursors reported previously, which required an excess of barium.

In shrinkage, aligned fibre blankets behaved as 1D materials, with shrinkage only in the axis of alignment and not across the width of the blanket. The fibre shrank by ~12% in drying after collection, and by a further 22 - 23% total shrinkage at 1200 °C, with no more shrinkage after this until fibres begin to fuse together. Alignment was not affected by shrinkage or sintering, except when DGG occurred at higher temperatures giving large hexagonal plates up to 25 μm long, or when fibres began to fuse together at temperatures of 1300 °C and over. The freshly spun M and Y fibres appeared fully sintered by the low temperature of 1000 °C, the slight differences between the SrM and BaM fibres being due to differences in the rates of diffusion of Ba^{2+} and Sr^{2+} ions or initial particle size in the sol precursor. The decrease in porosity and increase in pore size with temperature are shown in figure 181.

XPS analysis confirmed the metal ions to be Fe^{3+} and Co^{2+} at 1000 °C, and the stoichiometric compositions of the ferrite fibres were confirmed by XRF analysis. They proved to be much more accurate than bulk ceramic samples supplied by DERA, which were claimed to be pure phase from XRD and magnetic analysis but had barium and cobalt deficiencies up to 50%, emphasising the difficulties in obtaining pure phases of the hexagonal ferrites.

The bulk of the weight loss (20%) occurred below 400 °C as water, some bromine and organic compounds were driven out, and all of the fibres were heated slowly at 100 °C / hr to 400 °C to control the exotherms produced by these processes. The fibres retained ~10 wt% halides after this which were retained to some degree in the fibre up to 1000 °C. The formation of the ferrite phases seemed to be delayed until the halides were lost, indicating that barium, and maybe cobalt, remain separate from iron until ferrite formation, and that the fibres were not a totally homogeneous mix on the atomic scale. This was confirmed by the existence of crystalline barium and strontium halide compounds prior to ferrite formation, which are more thermodynamically stable than the oxides, resulting in formation of the ferrites at a higher temperature. The lack of exotherms indicated that ferrites crystallised slowly as halide is lost, and in the halide free coprecipitated Z ferrite powders a sharp BaM formation exotherm was observed.

BaM had begun to form by 800 °C, and SrM fibres formed the M phase at a slightly lower temperature of 750 °C. At 900 °C the pure SrM phase had formed and fully crystalline single phase BaM ferrite was produced at 1000 °C. Although the ferrite did not appear to form at a significantly lower temperature, it did appear to be more fully sintered and with a much improved submicron microstructure than at equivalent temperatures in conventionally manufactured specimens, and SrM had grains more equiaxed and less plate-like than in the BaM fibres. The crystallite and pore sizes in both BaM and SrM fibres were around 50 nm at 1000 °C, the fibres were ~98% sintered at this low temperature, and the strain-to-break was 0.6 to 0.75%. The formation process for freshly spun BaM can be summed up as follows:

$$\text{Gel fibre} \xrightarrow[400\ ^\circ\text{C}]{} \alpha\text{-}Fe_2O_3 + \text{Ba Halides} \xrightarrow[-\ \text{Hal}]{} \text{BaM}$$

In halide free fibres made from a nitrate based sol the pure M phase formed at a temperature ~200 °C lower confirming the effects of halides in hindering ferrite formation. However, due to the problems encountered in spinning and a coarser microstructure, the product was otherwise inferior to the halide-containing fibres. An addition of 0.28 mol% Gd^{3+} or La^{3+} caused BaM to form as the major phase at a lower temperature of 800 °C, forming the pure ferrite at 1000 °C but more porous than the undoped fibre, with small equiaxed grains 0.1- 0.2 μm instead of the thin plates seen in the pure BaM fibres. 0.25 wt% V_2O_5 and 0.06 wt% Nb_2O_5 had similar effects, with BaM appearing as a minor phase at 700 °C and as the pure phase at 800 °C, but 1.0 wt% ZrO_2, Y_2O_3, Cr_2O_3 only appeared to hinder the formation of M, giving a mixture of α-Fe_2O_3, α-$BaFe_2O_4$ and BaM at 1000 °C. DGG was never seen in the M ferrites at 1200 °C, except for the rare earth metal doped fibres. Fibres made from the ultrasonically peptised BaM sol formed the pure BaM phase at 1000 °C, but they were very porous looking and offered no microstructural advantage over the standard preparations.

$BaCo_xTi_xFe_{12-2x}O_{19}$ fibres with x = 0.5 - 1.1 all formed the M phase by 900 °C. Porosity was greater than in unsubstituted M, and increased with x, and the grains were 0.5 -

1 μm in diameter but less platey than the BaM fibres. The morphology of the x = 1.0 fibres was different from the rest, and could be related to the structure seen in the gel fibre during spinning. Therefore, the substitution had little effect on actual grain size, unlike reported substituted ferrites with more than ten fold reductions in grain size at these levels, although the morphology of the grains were changed. $SrCo_xTi_xM$ fibres showed quite different morphologies to the substituted BaM fibres. After 1000 °C / 3hr the x = 0.5 fibres were smooth and featureless with no apparent grains, developing a rougher surface and pores up to 0.5 μm wide after 100hr at this temperature, and the x = 1.1 fibres had cracks / ridges along the fibre axis.

At 800 °C the Co_2Y fibres had formed M, $CoFe_2O_4$ and α-$BaFe_2O_4$, producing fully crystalline Co_2Y at 1000 °C. It had a crystallite size of 70 nm, but the fibres consisted of randomly ordered hexagonal platelets 1 – 3 x 0.1 – 0.2 μm. This is a low temperature for pure Y ferrite to form, and it did appear to be more fully sintered and with a much smaller grain size at equivalent temperatures than in conventionally manufactured specimens. No DGG had occurred even at 1200 °C / 3hr, but the fibres had become weakened by grain growth at this temperature. Ni_2Y and Zn_2Y fibres both formed a mixture of Y ferrite and $BaFe_2O_4$ at 1000 °C, whereas the Mn_2Y fibres only formed an M ferrite with no Y phase.

The Co_2Z fibres resembled the Y fibres at 800 °C, and at 1000 °C they were a 50/50 mixture of Co_2Y and BaM, with a microstructure like the Y ferrite. They appeared to form pure Co_2Z ferrite at a temperature of 1250 °C from XRD evidence, but considering the complex range of similar phases which can co-exist at these temperatures it was thought unlikely to be a truly pure phase. The seemingly unavoidable DGG process was always observed with Z formation, compromising the structural integrity of individual fibres, and had occurred after only 5 min at 1200 °C, before the formation of the Z phase. This suggests that under normal conditions DGG is an unavoidable part of the ordering process required to arrange the M and Y units sequentially to form Z. Although the grains had rapidly grown to form elongated hexagonal plates up to 25 μm long at 1200 °C / 5min, this was much less then

reported grain sizes as large as hundreds of microns, and DGG has not previously been noted to occur at temperatures / times as low as this. In fibre containing high levels of Cl^-, DGG never occurred but the Z phase also failed to form, confirming both the necessity of DGG for Z formation and the harmful effect that chloride has on ferrite formation. Stacks of layers of hexagonal plates could be seen in the grains, suggesting that DGG is a diffusion and condensation process. The average surface composition was near the stoichiometric Z composition, but on the micron scale there were variations in composition even in individual grains caused by the existence of minor quantities of other phases, such as BaM and Co_2Y. The formation of Co_2Z coincided with the loss of BaM but not Co_2Y, which co-existed with Co_2Z in equal amounts and remained a major phase above 1200 °C until the formation of single-phase Co_2Z. Unidentified XRD peaks suggest that M and Y do not decompose together equally to form Co_2Z, and that this could be due to the formation of Co_2U ferrite as an intermediate stage, which is a combination of the Z and M phases. The formation of Z was shown to be a kinetic process, as firing for extended periods at 1000 °C only resulted in grain growth, with no change of phase, while firing the 1200 °C mixed phase Z sample at 1100 °C / 100 hr gave no loss of Z and no increase in Y and M phases. The formation process for Co_2Z can be summed thus:

$$\text{Gel fibre} \xrightarrow{400\,^\circ C} \begin{matrix}\alpha\text{-}Fe_2O_3 \\ + \\ \text{Ba Halides}\end{matrix} \xrightarrow{\text{-Hal}} \begin{matrix}CoFe_2O_4 \\ + \\ \text{BaM} \\ + \\ Co_2Y\end{matrix} \xrightarrow{1250\,^\circ C} Co_2Z$$

In an attempt to either lessen the exaggerated grain growth or produce Z ferrite at a lower temperature, the Z fibres were doped with various known sintering aids. The flux-type sintering aids (boria, silica) caused a fusing of fibres or worsening of the microstructure with no advantages, but gadolinium, calcium and strontium all showed much better Z ferrite characteristics than usual at 1200 °C. The addition of 0.67% CaO improved both the morphology and formation temperature of the Co_2Z fibres significantly. The Z phase was a major component of the material at only 1150 °C, and a much improved microstructure was

observed with no DGG, resulting in smaller, more equiaxed grains even up to 1175 °C, by which point Co_2Z was the dominant phase. It is suggested that was is due to the calcium segregating at the boundary edges and slowing the rate of grain growth in the plane perpendicular to the c-axis. This allowed the growth to proceed in a slower and less two dimensional manner, until the dissolution of calcium into the lattice occurred and the runaway grain growth proceeded as usual. At 1200 °C DGG had occurred and Co_2Z appeared to be the only phase present by the XRD pattern at this temperature. $Sr_3Co_2Fe_{24}O_{41}$ fibres were also made, and produced the pure Z phase after 1200 °C / 3hr.

Upon heating to 800 °C the Co_2W fibres formed BaM and $CoFe_2O_4$, and these two phases then persisted as the only ones present even until pure Co_2W formed at 1200 °C. Although this is the temperature at which Co_2W would be expected to form, this is a lower temperature than expected for the ferrite to exist as the sole phase. As with the Z ferrite fibres, DGG accompanied this formation, and the separate fibres began to fuse together into a single mass at 1300 °C.

There were no published XRD patterns for Co_2X and Co_2U to confirm the phases of these fibres. At 1000 °C the X fibres resembled Co_2W (BaM and $CoFe_2O_4$) and the U fibres resembled Co_2Z (BaM and Co_2Y) fibres at the equivalent temperature, as would be expected from their structures. At 1200 °C unidentified phases had formed, and although grains as large as 10 μm had developed there was no DGG, indicating that whatever phases had developed were not W or Z respectively, and that the X and U phases may have been formed.

After storage at 110 °C for 3yr α-$BaFe_2O_4$ was seen for the first time in the M fibres at 600 °C. They were virtually pure phase M at only 800 °C, and formed single phase M after only 10 min at 1000 °C. Although there was no microstructure visible at 800 °C, at 1000 °C their surfaces were markedly different, being covered with either parallel ridges along the fibre axis 0.2 μm wide or a "honeycomb" structure in BaM, or grains up to 2 μm with "islands" of platelets on the surface of the fibre giving it a scaly look in SrM. The Co_2Y fibres stored for 3yr formed the Y phase at only 900 °C with α-$BaFe_2O_4$ as a secondary phase, and seemed to

be quite porous with small grains well below 1 μm. After only 10 min at 1000 °C single phase Co_2Y had formed. These differences were attributed to the loss of halide during storage, promoting the formation of the M phase at a lower temperature, and the unfired fibre was still amorphous, with no crystallisation of haematite in the gel fibres. $BaFe_2O_4$ was also seen for the first time in halide containing M ferrites, suggesting barium was normally associated with the halide prior to M formation.

These conclusions were confirmed by the steaming of fibres to remove halides at a lower temperature. At 500 °C BaM fibres were mostly α-Fe_2O_3 with some α-$BaFe_2O_4$, indicating that some halide had already been lost at this low temperature, and confirming that the barium normally remains associated with the halides at this temperature. By 600 °C there was more α-$BaFe_2O_4$ and BaM had begun to form as a minor phase, and the linear ridges seen in the stored BaM ferrites had also begun to form. The fibres were virtually pure BaM at 700 °C, with no grains visible, and the SrM fibres followed the same pattern. To get a totally pure M phase steaming at 900 °C / 3hr was required, although this led to the development of grains up to 2 μm. When steamed at 600 and 700 °C Co_2Y fibres consisted of a mixture of α-Fe_2O_3, α-$BaFe_2O_4$ and $CoFe_2O_4$, and they resembled the steamed BaM fibres. At 800 °C the product was mostly Y phase, with a trace of α-$BaFe_2O_4$, and their microstructure resembled the freshly spun Co_2Y fibres after 1000 °C / 3hr. Steaming Co_2Z at 700 °C showed no improvement in microstructure when fired to 1250 °C, but they formed M ferrite as a mixed phase with $CoFe_2O_4$ and haematite at only 600 °C. When steamed at 900 °C / 3hr they had a larger grain size up to 4 μm with the scaly appearance seen in some of the stored M fibres. They contained only the M phase with no Y or spinel components, but at 1250 °C Z coexisted with M. If Z fibres were prefired to 1000 °C in air and than steamed at 900 °C / 3hr, even at 1250 °C DGG had not occurred with grains were below 6 μm, but the phases present were unclear from XRD. When steamed over temperature range from 400 – 800 °C / 3hr, BaM fibres were ~40% α-Fe_2O_3, Co_2Z fibres formed poorly crystalline M as the major phase with

some α-Fe_2O_3, and Co_2Y fibres contained less of the Y phase and were full of small pores. However, there was no deterioration in SrM content compared to the 800 °C sample, and an apparent improvement in morphology was observed. BaM fibres fired under a vacuum at 800 °C also formed the pure M phase, with smaller grain and crystallite sizes than fibres fired in air.

Powders from coprecipitated salts with Co_2Z stoichiometry were made using the bases NH_3, NH_4OH, NH_4HCO_3 and Na_2CO_3. An endotherm at 600 °C was seen only in CO_3^{2-} containing corresponding to the decomposition of $BaCo_3$, and an exotherm at 700 °C occurred with BaM formation. There was a peak at 800 °C in Na containing samples related to $NaFeO_2$ formation. Unlike in most of the sol-derived ferrites, there was α-$BaFe_2O_4$ formation, as reported previously for coprecipitated powders. The loss of barium at pH <9 caused loss of stoichiometry, and to obtain the Z phase a sodium base was required, but sodium caused the fibres to flux and fuse over 1100 °C, and resulted in contamination of the product with 2 wt% sodium.

Stoichiometric BaM fibres from an alkoxide sol formed M ferrite at 800 °C, but showed no advantage in either formation temperature or microstructure over the standard preparation, and it coexisted with $LiFe_5O_8$ spinel which persisted as ~25% even at 1000 °C. Co_2Z fibres were also made, and a spinel was formed at 500 °C with no sign of α-Fe_2O_3 even at 700°C. The spinels $CoFe_2O_4$ and $LiFe_5O_8$ have overlapping peaks, and the fibre could have contained a mixture of both compounds. At 1000 °C M and Y had formed, but the spinel phase was the major component up to 1200 °C, and the Z phase never formed. The alkoxide precursors were unavoidably contaminated with up to 5% Li^+ from their production process, forming the highly magnetic but soft ferrite $LiFe_5O_8$, which would disrupt the magnetic properties of the magnetically hard BaM.

5. Experimental

5.1 Analytical techniques

5.1.1 X-ray powder diffraction (XRD)

XRD patterns of the samples treated at various temperatures were recorded in the region of $2\theta = 10 - 80^{\circ}$ with a scanning speed of 0.25° min^{-1} on a Philips PW1710 diffractometer using CuK_{α} radiation with a nickel filter. Philips APD 1700 software was used to calculate the average size of the crystallites in a sample using the Scherrer equation:

$$D = K \lambda / h_{1/2} \cos \theta \qquad \text{Eqn. 4.1}$$

where D = average size of the crystallites, K = Scherrer constant (0.9 x 57.3), λ = wavelength of radiation (1.5405 Å), $h_{1/2}$ = peak width at half height and 0 corresponds to the peak position. BaM and Co_2Z powder samples made from standard ceramic methods and supplied by DERA were used as reference standards, and the Philips JPDS files were used for the reference patterns.

Due to the presence of halides which remained in the sample below 1000 °C, these XRD patterns were taken using a glass sample holder, and this is responsible for the large background hump between $2\theta = 15\text{-}40^{\circ}$. The XRD patterns of samples taken at 1000 °C or above, made from a halide free precursor, or treated to remove any halide used a polished silicon wafer to mount the sample, and therefore contained no such background hump.

5.1.2 X-ray fluorescence spectrometry (XRF)

The elemental composition of the samples was measured on a Philips PW2400 sequential x-ray spectrometer fitted with a rhodium target end window x-ray tube, and Philips X-40 analytical software. The samples were analysed in the form of a fused bead, where 0.25 – 1 g of sample was fused with 10 g of lithium tetraborate flux at 1250 °C for 12 minutes and then cast to form a glass bead. Stoichiometric standards for calibration of XRF analysis were made

from stoichiometric amounts of α-Fe_2O_3, $BaCO_3$, Co_3O_4, and TiO_2 fired to 1000 °C / 3hr. When looking for relative amounts of these four specific elements using these standards the statistical and sampling errors were about 1% for Fe, Ba and Ti and 2% for Co. This quantitative method was used to determine to the stoichiometries of the ferrite fibres The broad band analysis of virtually all elemental ratios used to look for impurities gave results that were only semi-quantitative, with an error between 5 - 10%, although they generally gave a good correlation with the quantitative results. These samples were prepared as a resin composite at temperatures below 100 °C.

5.1.3 X-ray photoelectron spectroscopy (XPS)

The XPS analysis was performed using a Kratos XSAM 800 spectrometer fitted with a dual anode (Mg/Al) x-ray source and a multichannel detector. The spectrometer was calibrated using the $Ag3d_{5/2}$ line at 397.9 eV and the AgMVV line at 901.5 eV. Al Kα radiation (1486.6 eV) was the exciting source (120W) and spectra were collected in the high resolution mode (1.2 eV) and Fixed Analyser Transmission (FAT). The Kratos DS800 software was used for data acquisition and analysis.

5.1.4 Differential thermal analysis (DTA) and thermogravimetric analysis (TGA)

Simultaneous differential thermal analysis and thermogravimetric analysis (DTA-TGA) was performed on gel fibres in flowing air up to a temperature of 1200 °C at a rate of 10 °C min^{-1}, using a Rheometric Scientific STA 1500. Due to the rapidity of this heating rate, features may occur at a temperature slightly higher than normal for the same event under a slower heating regime.

5.1.5 Scanning electron microscopy (SEM)

Scanning electron micrographs and analysis of the morphology of the samples was carried out on a Cambridge Instruments Stereoscan 90 SEM operating at 5 - 10 kV, except for figure (fig. 89), which was taken using an ICI Hitachi 4000 SEM at 3kV. Conducting samples were

prepared by gold sputtering fibre specimens, but due to the intrinsic low conductivity of the samples well resolved micrographs were not possible at magnifications above 5K - 10K on the apparatus used. Mass analysis was carried out by the Department of Physics.

5.1.6 Porosity and sintering measurements and calculations

Surface areas and pore size distributions of the fibres were directly measured on a Micrometrics ASAP 2000 using N_2 as the adsorption / desorption gas, with a maximum uptake of N_2 at $p/p_o = 0.98 - 0.99$. Samples were degassed at 300 °C for 6 hours prior to analysis, and surface area was calculated by the BET technique, and pore characteristics derived from the BJH adsorption / desorption plots. This was only a minimum estimate as pores over 200 nm were not measured by this technique, and the absence of any plateau in the isotherm indicated the probable existence of many pores over 100 nm. The surface area results also become unreliable at values below 1 – 2 $cm^2\ g^{-1}$, and due to their fibrous nature the samples measured were small, all being < 0.5 g. The percentage porosity (% volume of free space) was estimated by dividing the pore volume g^{-1} by (volume g^{-1} of ferrite (0.189 cm^3) plus the pore volume g^{-1}).

The weight loss and shrinkage in length of the fibres was measured over a range of temperatures from 100 - 1200 °C. The ultimate shrinkage from sol to gel, and then to fully dense refractory can be calculated from the concentration of ceramic at different stages of the process and reasonably accurate estimates of sol and gel densities. The porosity of fibres during a firing sequence can then be inferred from the linear shrinkage of an aligned sample of fibre, assuming that the fibre is fully sintered when no more shrinkage occurs. To calculate the estimated porosity it was assumed that the shrinkage occurred uniformly in all three dimensions of the individual fibres. The estimated porosity was then calculated from the equation:

$$P = 1-\left(\frac{1-S}{1-S_T}\right)^3$$

Where S_T = % linear shrinkage measured at a given temperature, S = total % linear shrinkage for fully sintered material and P = % calculated porosity. This method provides only an estimate, with the error becoming greater as porosity increases, and fibre is unreliable for values of $S < 0.5S_T$. At lower temperatures below 800 °C the density of the solid phase in the fibres is less than that of the pure ferrite. Therefore the volume of solid in the ferrite precursor fibre is actually more than can be accounted for in this estimate, resulting in porosity estimates higher than the true values, and so the ASAP porosity values will be the more accurate for samples fired at lower temperatures.

5.1.7 Estimation of strain-to-break

Strain-to-break was measured using the wire indentation stress test [304], which was done by gluing a thin strip of fibres on to the surface of transparent double sided adhesive tape which in turn was glued to a soft rubber pad. The blanket was indented with stainless steel wires of reducing diameter from 1.2 down to 0.3 mm. The wires were held in toolmakers clamps and pressed into the sample. The tape was then carefully removed with the adhering fibre strip from the rubber pad, and the lines of indentation examined for lines of breakage under an optical microscope at 100X magnification. The technique is useful for a rough estimate but is not preferred in routine work because the wires stretch and break too easily.

5.2 Heat treatments

5.2.1 Drying of gel fibres

All gel fibres were dried immediately after spinning at 110 °C, and stored at this temperature until subsequent firing. When left to dry at room temperature syneresis was observed, with small transparent crystals of PEO forming on the surface of the fibre.

5.2.2 *Firing of fibres*

Unless otherwise stated, all fibres were fired to 400 °C at a rate of 100 °C / hr, and kept at that temperature for 3 hr to allow all the organic material to be removed. All samples were then fired to the desired temperature at 200 °C / hr, unless otherwise stated in the text. All samples heated up to 1100 °C were fired on recrystallised alumina, and a platinum mat was used at higher temperatures. The fibres were heated in a Carbolite muffle furnace controlled by an Isotherm programmable temperature controller, and allowed to cool naturally before removal from the furnace. Unless otherwise stated all were fired in air at atmospheric pressure.

5.2.3 *Special firing atmospheres*

All fibres were prefired to 400 °C. The fibres were vacuum fired in a recrystallised alumina tube furnace up to 1200 °C at a rate of 200 °C / hr. The steam firings were carried out in a fused silica tube furnace with a volume of 1020 cm^3, at either a fixed temperature or over a temperature range for 3 hr. The fixed temperature samples were brought up to temperature in air at a rate of 200 °C hr^{-1}, and then steamed at that temperature for 3hr, whereas the samples steamed over a range were steamed for 3hr while the temperature was increased from 400 – 800 °C over this period. Water was injected into the tube through a *Saffil* wick at a rate of 18 ml hr^{-1}, providing a gas flow of up to 87 l hr^{-1} at 800 °C and ensuring that the tube was flushed every 45 - 90 s.

Chapter Five

The Magnetic Properties of Hexagonal Ferrite Fibres

1. Magnetism in hexagonal ferrites

Most hexagonal ferrites have a preferred axis of magnetisation along the c-axis, so loose crystals in an applied field will align themselves with the c-axis parallel to the field, showing a different XRD pattern to randomly oriented samples. The magnetic properties are different if measured in the direction of alignment, with higher values for the saturation magnetisation and remanent values and lower coercivities. The ratio of M_r / M_s for isotropic unaligned samples is around half that for well oriented samples [7], and T_c is also higher in the direction of the c-axis in oriented samples [305]. The degree of this magnetocrystalline anisotropy (MCA) is given by the crystalline anisotropy, H_A, in kOe, and the anisotropy constant K_1 is a measure of the difficulty to move the magnetisation out of that direction in the crystal lattice. It is the contribution of the spin from the iron atom in the five-coordinate trigonal bipyramidal site which causes the large anisotropy in the uniaxial ferrites [306].

However, most Y ferrites and all the Co_2 ferrites are ferroxplana [4], with a preferred direction of magnetisation either in the hexagonal basal plane, or in a cone at an angle to the c-axis. As in the uniaxial ferrites the magnetisation is locked rigidly in this orientation, but in the ferroxplana ferrites it can rotate within the plane or cone of magnetisation. The first order anisotropy constant, K_1, is positive for the uniaxial ferrites, but negative for the ferroxplana ferrites, indicating that the magnetisation is out of the c-axis. However, the second and third order constants K_2 and K_3 become more important, and often must be considered with the ferroxplana ferrites. The K_2 constant, which is positive and relatively large and therefore reduces the total anisotropy effect, is attributed to the presence of Co^{2+} in octahedral positions, as it is negligible in hexaferrites containing another divalent ion, except for the Y ferrites where the absence of the five coordinate Fe^{3+} site accounts for the ferroxplanar anisotropy [250]. The anisotropy energy is required only to move magnetisation out of the

plane or cone, and although shape anisotropy will oppose rotation within the plane this is a weak energy compared to the crystalline anisotropy, H_A, which is high in all the hexagonal ferrites. Therefore, the magnetisation is able to rotate freely within this plane, and as a result the ferroxplana ferrites are not good permanent magnets, but the combination of high permeability and low coercivity makes then excellent soft magnets for use in electrical devices, and they suffer low magnetic losses at high frequencies. The K_1 constant dominates at lower temperatures and K_2 becomes more important at higher temperatures, resulting in the observed changes in anisotropy with temperature of the ferroxplanar ferrites [250].

It is possible to produced a magnetically oriented sample of the ferroxplana ferrites, as the MCA perpendicular to the c-axis is much greater than the shape anisotropy parallel to the c axis [11]. In the ferroxplana Co_2 ferrites the suggested mechanism is due to the anisotropic partition of cations and vacant cation sites, resulting in a textured product in which the basal planes of the particles are all aligned [307].

1.1 Magnetic moments of the hexagonal ferrites

Each S block consists of two layers of four oxygen atoms with three cations between each layer, in octahedral and tetrahedral sites having opposing magnetic spins. There are four octahedral magnetic moments and two opposing tetrahedral moments, giving a net total of two moments. The R block has five octahedral moments, but due to the effects of the large barium atom two of then are really distorted tetrahedral sites and so they oppose the other three octahedral sites. The moment of the five-coordinate trigonal bipyramidal site is aligned with three of the octahedral moments as it is a distorted octahedral site, and so the total also results in a net of two moments. The T section has six octahedral and two tetrahedral moments, but again two of the octahedral moments are aligned with the tetrahedral, giving a net of zero magnetic moments. The tetrahedral sites are formed by the two barium atoms distorting two trigonal bipyramidal sites [7].

S block = 2↓ tetrahedral and 4↑ octahedral = 2↑

R block = 1↑ trigonal bipyramidal and 3↑ 2↓ octahedral = 2↑

T block = 2↓ tetrahedral and 4↑ 2↓ octahedral = 0

These net values are only true if all the cations are Fe^{3+}, which has a magnetic moment of 5 μ_B. For example in BaM, which consists of S + R, and therefore has a net magnetic moment of 4↑ = 20 μ_B [7]. In ferrites other than M, and in doped M ferrites, some of the cations are other metals with different magnetic moments, which may occupy different sites depending upon composition and temperature, and may occupy on a fraction of the total number of a certain site. The opposing spins of the T block, which is antiferromagnetic if all the ions are identical, lead to the lower magnetic saturation values for the Y ferrites compared to the other hexagonal ferrites. This explains the many variations seen in the magnetic properties of the hexagonal ferrites with temperature and composition, but it also means that to calculate the magnetic moment of a compound the exact positions of all the cations must first be known. However, the contribution towards the moment of each site in a compound can still be summed up as:

M = 1↑ trigonal bipyramidal + 7↑ 2↓ octahedral + 2↓ tetragonal

W = 1↑ trigonal bipyramidal + 11↑ 2↓ octahedral + 4↓ tetragonal

X = 2↑ trigonal bipyramidal + 10↑ 4↓ octahedral + 2↓ tetragonal

Y = 8↑ 2↓ octahedral + 4↓ tetrahedral

Z = 1↑ trigonal bipyramidal + 15↑ 4↓ octahedral + 6↓ tetragonal

U = 2↑ trigonal bipyramidal + 22↑ 6↓ octahedral + 8↓ tetragonal

These orientations are depicted in figures 7 - 15. It should be noted that these are the moments for the molecular units of the ferrites, and not their unit cells. As all the Y ferrites and all Co_2 ferrites are ferroxplana, their spins are opposed in the orientation of the plane or cone, and not parallel to the c-axis, as shown for Y ferrite in figure 13.

1.2 Magnetic superexchange

In metals the spins are linked by exchange interactions between the magnetic moments of directly neighbouring atoms, and this short range interaction is negligible over longer distances. However, in ferrimagnetic ferrites the magnetic ions are separated from one another by oxygen atoms making them too far apart for direct exchange, and there are also shielding effects from the oxygen lattice. In 1948 the idea of superexchange was suggested, which involves the non-magnetic oxygen atoms in the interactions [308].

The spins of opposing neighbouring ions are linked by interactions which take place via the intermediate oxygen atom (Me_1-O-Me_2), and this process is called superexchange. The superexchange interactions of the R and Y blocks are depicted in figure 182. The magnitude of the exchange can be estimated from the Me_1-O-Me_2 distance and the angle formed by this, with a shorter distance and a larger angle strengthening the interaction [7]. An angle of 180° gives the largest interaction and an angle of 90° the smallest, and the effect decreases rapidly with distance, becoming negligible over an Me-O distance of 3 Å [309]. It is these interactions which determine the spins of the ions detailed above.

2. Survey of magnetic properties of hexagonal ferrites

A better sintered, and therefore denser, ferrite has more magnetic moments per unit volume and hence a higher M_s, but the heat treatment needed to maximise densification also usually results in grain growth giving a multidomain particle with a lowered coercivity as some of the domains will oppose one another. Therefore, the optimisation of magnetic properties in hexagonal ferrites is dependant upon the particle size of the starting material and the sintering conditions employed [310]. A material with high M_r and H_c can be made by mixing nano-sized powders of a high M_r magnet such as a-iron and a high coercivity magnet such as $Nd_2Fe_{14}B$ together, to form a composite magnet [311], and this would also work with ferrites. Clearly reducing the grain size to, or below, the domain size will raise the coercivity, but a material with magnetically aligned domains will also have a higher coercivity, and oriented single

crystal materials will approach the theoretical maximum values permitted. The magnetisation process under an applied field depends upon the size and shape of the ferrite particles. If it consists of plates under 5 μm the material is magnetically conditioned by rotational processes, with grain over 10 μm wall movement dominates, with the critical grain size falling at temperatures below room temperature [312]. The magnetic properties of some hexagonal ferrites are shown in table 5.1.

Ferrite	Formula	M_s / emu g^{-1}	H_c / T	Isotropic M_r / M_s	H_A / kOe	K_1 / 10^6 erg cm^{-3}	T_c / °C
BaM	$BaFe_{12}O_{19}$	72	high	0.50	17	3.3	450
SrM	$SrFe_{12}O_{19}$	92.5	high	0.50	20	3.5	460
Co_2Y	$Ba_2Co_2Fe_{12}O_{22}$	34	low	0.38	28	-2.6*	340
Co_2Z	$Ba_3Co_2Fe_{24}O_{41}$	50	v. low	?	13	-1.8*	410
Co_2W	$BaCo_2Fe_{16}O_{27}$	?	low	?	?	-3.5 to -5	490
Co_2X	$Ba_2Co_2Fe_{28}O_{46}$	57.1	v.low	?	9.5	?	467

Table 5.1 Some magnetic characteristics of hexagonal ferrites at room temperature. ? indicates the value has not been reported, and no precise value is given for H_c as it varies too much with processing methods and grain size. Anisotropy constants marked * are in fact $K_1 + K_2$ values.

2.1 BaM ferrite

BaM has 20 μ_B and this gives it a high saturation magnetisation of 72 emu g^{-1} and a high Curie temperature of 450 °C. It also has a high anisotropy constant, $K_1 = 3.3 \times 10^6$ erg cm^{-3}, which give BaM a large crystalline anisotropy of 17 kOe along the c-axis [7]. This uniaxial character gives BaM a large theoretical maximum coercivity of 0.746 T, although the reported H_c values for BaM prepared from standard ceramic methods are low, at around 0.200 - 0.320 T, because of the large grain sizes in such materials, but $M_s = 70$ emu g^{-1} which is close to the maximum value [3]. The critical domain diameter in BaM is also large, being 1.3 μm compared to 0.24 μm for cobalt metal and 28 nm for iron, and unusually this domain size increases with temperature so that a multidomain grain will have fewer Bloch walls as

temperature increases. This also means that the coercivity will increase with temperature in a polycrystalline material, for example from 0.170 T at -200 °C to 0.320 T at 25 °C and peaking at 0.477 T at 250 °C, after which point H_c then decreases [3]. This was for 3 μm grains, but the coercivity can be up to 40 times smaller in grains as large as 1 mm. Although coercivity will increase with a decrease in grain size, especially below the single domain size [313], there is also a minimum grain diameter for maximum coercivity. This is 0.1 μm for BaM, as at smaller diameters the grains start to become superparamagnetic and this magnetic state has a coercivity of zero [314]. Coercivity is not purely determined by domain structure, but is also affected by shape and magnetic anisotropy effects, and for this reason oriented samples can have increased coercivities. The effects of processing upon magnetic characteristics has been studied in much greater detail for BaM than that of the other ferrites, and the findings are summarised below.

2.1.1 Standard ceramic preparation

In the standard ceramic preparation of BaM, iron oxide and barium carbonate are calcined at 1000 °C, ground, pressed and sintered at 1200 - 1400 °C in air. For the magnetic properties, the oxygen content of the atmosphere is most critical during the cooling down process after sintering. This gives a permanent magnet material with a high resistance for low losses, good chemical and thermal stability, and a high coercivity.

BaM has been made by standard ceramic methods from magnetite, recovered from recycled pickling liquors, to give a high coercivity product of 0.660 T after 1100 °C / 3hr [315], and a sample made from haematite by the same process had a similar coercivity but an extremely high M_s of 75 emu g^{-1} [80]. A high coercivity of 0.650 T was also obtained in 1 μm BaM, which was made from a precursor powder of BaM ground to under 10 nm and then resintered at 1000 °C. The grains were still covered with a paramagnetic surface layer of amorphous grains 5 - 10 nm in diameter, and while this raised the coercivity it also resulted in a low M_s of 55 emu g^{-1} [316].

2.1.2 *Coprecipitation*

Chemical coprecipitation usually gives a product at a lower temperature and with a smaller grain size than standard ceramic methods, and BaM made by this process tends to have a higher M_s [25], up to 0.64 emu g^{-1} for 0.1 μm grains [317]. In a stoichiometric mixture fired at 925 °C / 5hr H_c = 0.503 T, but this can be increased by using iron deficient mixes, and with an Fe:Ba ratio of 10.6 a maximum coercivity of 0.597 T was achieved [27]. When coprecipitated iron(II) salts were rapidly oxidised, extremely fine BaM was formed as 80 nm hexagonal plates with a reasonable M_s of 59 emu g^{-1}, but the coercivity was only 0.470 T, probably as a result of superparamagnetic effects [318].

2.1.3 *Salt-melt process*

Nanocrystalline BaM has been made from an alkaline metal chloride salt-melt at low temperatures. The material was amorphous at 600 °C, with M_s = 5.3 emu g^{-1} and H_c = 0.340T, but by 650 °C some BaM had crystallised and M_s had risen to 26.8 emu g^{-1}, and it was pure BaM at 700 °C with small grains 100 nm wide and 40 nm thick, M_s = 61.5 emu g^{-1}, H_c = 0.470 T [319]. BaM made at the higher temperature of 900 - 1050 °C in flux of only NaCl had vastly superior magnetic characteristics, with coercivities up to 0.475 T, a high M_s of 71.6 emu g^{-1} and a very high remanence for an isotropic material giving an M_r / M_s ratio of 0.77 [35]. BaM single crystals made from the ion exchange of b''-ferrite by a salt-melt process also had a high M_s of 72 emu g^{-1} [41].

2.1.4 *Sol-gel*

BaM made from a non-stoichiometric aqueous sol-gel route at 900 °C / 1hr with a grain size of only 200 nm had a high H_c of 0.590 T but a low M_s of only 55.7 emu g^{-1} [43]. Similarly sized BaM particles produced from an organic sol precursor at the same temperature had a much higher M_s of 70 emu g^{-1} and a large M_r / M_s ratio of 0.57, but a low coercivity of only 0.302 T [47]. It was shown to be important to prefire sol-gel derived BaM powders

containing organic compounds if a high coercivity material is desired. In unprefired samples BaM was single phase at 1050 °C with a coercivity of 0.360 T and M_s of 70 emu g^{-1}, but prefired samples gave BaM at a temperature 300 °C lower and with a much reduced grain size, and their properties were optimised at 900 °C when H_c = 0.595 T and M_s = 70 emu g^{-1} [45].

2.1.5 Citrate synthesis

An extremely fine grained BaM was made from citrate synthesis, having a grain size of only 50 nm at 600 °C, but the magnetic properties were unexpectedly low for an apparently single phase material, with a coercivity of only 0.058 T and M_s = 32.8 emu g^{-1}. This was proved to be caused by the extremely small size of the particles, as with an increase to 60 nm at 650 °C the coercivity rose to 0.400 T, although M_s was still very low and did not increase much with further heating [51]. The grain size was still below 100 nm at 800 °C, and the magnetisation values suggested that the ferrite, although no longer superparamagnetic, was still suffering from size effects such as demagnetisation, inhomogeneity effects and a non-magnetic surface layer [320].

2.1.6 Glass crystallisation method

BaM particles made from the glass crystallisation method using fine filaments of B_2O_3 glass produced hexagonal platelets less than 0.1 μm at 800 °C which grew to over 1 μm at 1000 °C. M_s and H_c reached maximum values of 75 emu g^{-1} and 0.573 T at 900 °C [54].

2.1.7 Hollow spheres

Hollow spheres of pure BaM with diameters of only 90 nm were made from an aerosol spray, but they had poor magnetic properties of M_s = 38 emu g^{-1} and H_c = 0.062 T even after annealing for 48 hrs. This was because the walls of the spheres were only 30 nm thick, and a high proportion of the material existed as nonmagnetic surface layers several nm thick on both the inside and outside surfaces [62].

2.1.8 *Magnetically oriented BaM*

If the BaM is heated in a magnetic field before sintering, anisotropic materials can be produced which are tailored to be either remanence biased (high M_r, low H_c) or coercivity-biased (high H_c, low M_r), the remanence biased product having a very square loop with a sudden, almost vertical drop. [321]. Magnetically anisotropic, oriented BaM was first made in 1954, and the remanence was found to be nearly doubled by this and the energy product quadrupled, but the coercivity was decreased [322].To become oriented a polycrystalline ferrite must consist of grains over 0.1 μm, but ideally below the domain size [277]. The shape anisotropy is very low because of the large crystalline anisotropy, and in oriented polycrystalline samples M_s parallel to the c-axis was 70 emu g^{-1}, but only 40 emu g^{-1} perpendicular to it. The remanence also varies greatly with orientation, with the ratio M_r / M_s being close to 1 along the c-axis in oriented BaM, but reduced to 0.5 in randomly oriented samples [3].

2.1.9 *Thin films*

Thin films typically have M_s values lower than those of the bulk ceramics annealed at the same temperature, as much as 50% less, but similar coercivities, and M_s has also been observed to increase with film thickness [68]. They can be produced with the anisotropy aligned either parallel or perpendicular to the surface of the film, which being essentially a two dimensional object has differing magnetic properties in and out of this plane, the properties being enhanced along the axis of anisotropy [70]. BaM films with extremely high M_s values were made using a mixture of xenon, argon and oxygen gases and an iron rich sintered BaM target. M_s = 70.6 emu g^{-1} and H_c = 0.24 after sputtering at 475 °C, and after the pure crystalline phase was formed at only 600 °C M_s reached 76.6 emu g^{-1}, exceeding that of bulk materials, with the anisotropy oriented perpendicular to the surface [244]. $SrGa_{12}O_{19}$ has been shown to be a good substrate material for BaM thin films, providing a structural match for the hexagonal basal plane and encouraging axial alignment perpendicular to the plane of the film [323].

2.1.10 Composite multiphase ferrites

To lower the coercivity of BaM while maintaining the high saturation magnetisation for use in magnetic recording applications, composite ferrites have been made, in which BaM is coated with 36 wt% nanocrystalline superparamagnetic particles of iron oxide, which have zero coercivity. The original M ferrite had a coercivity of 0.340 T and M_s = 70.3 emu g^{-1}, and after particles of δ-FeOOH (M_s = 19.7 emu g^{-1}) were added to the surface the composite had an H_c of 0.229 T but a much lower M_s of 45.5 emu g^{-1} [324]. More successful was a coating of superparamagnetic magnetite particles (M_s = 62.2 emu g^{-1}) which gave a composite with H_c = 0.147 T and M_s = 58.9 emu g^{-1} [325]. In both cases there must be magnetic coupling interactions between the two components, as the composite values are less than the simple sum of the component values. It was also found that in BaM with 36% magnetite the anisotropy had been moved to a preferred magnetisation in a cone at an angle of 22° to the c-axis. This could be restored by using a mixed spinel $Co_xFe_{3-x}O_4$ to make the composite with x > 0.25, and if x = 1 then M_s was increased to 65 emu g^{-1} [326].

A composite BaM / α-Fe material was made by reducing 100 nm sized BaM, with H_c = 0.420 T and M_s = 50.2 emu g^{-1}. After reduction at 380 °C / 4hr the coercivity had dropped to 0.049 T but the M_s increased greatly to 97.2 emu g^{-1}, due to the formation by reduction of α-iron. The paramagnetic effects of the α-iron also interfered with the superexchange interactions of the ferrite, changing the magnetic anisotropy from uniaxial to planar, moving through a cone at an angle to the c-axis at lower reduction temperatures [327].

Mixed BaM / spinel ferrite compounds were also made from the glass crystallisation method at 800 °C, using the spinels $CoFe_2O_4$, $NiFe_2O_4$, $ZnFe_2O_4$, $Co_{1-x}Zn_xFe_2O_4$ and $Ni_{1-x}Zn_xFe_2O_4$. All of these were found to increase M_s except $NiFe_2O_4$, and usually the higher the M_s of the spinel the higher the M_s of the composite. $NiFe_2O_4$ has a lower M_s than BaM, and the sum of the compounds gave a lower net M_s for this material. The non-magnetic $ZnFe_2O_4$ was the exception, as the zinc ion prefers the tetrahedral sites in the M structure to such an extent that they displaced Fe^{3+}, raising M_s as a result. The coercivity was also raised with

increasing spinel addition, especially in the case of the very hard $CoFe_2O_4$ [328].

2.2 SrM ferrite

The magnetic properties of SrM have slightly higher values than those of BaM, and SrM has 20.6 μ_B. The Curie point is around 470 °C [230] and the anisotropy constant is 3.5 x 10^6 erg cm^{-3} giving a very high H_A of 20 kOe in the c-axis [329]. The saturation magnetisation of single crystal SrM has been variously reported at values between 92.6 emu g^{-1} [230] and 74.3 emu g^{-1} [250] and the maximum coercivity is around 0.670 T [330], but polycrystalline samples rarely approach these high values. As with BaM, the values first reported for the coercivity of polycrystalline SrM were very low due to the large grain size of the early samples, and H_c was typically reported as 0.302T [331]. SrM made with standard ceramic methods with a wide diameter range of 0.5 - 50 μm has a reported coercivity of 0.360 T [332], and 0.1 μm specimens have been reported with H_c = 0.65 T [333]. SrM made from the standard ceramic route but then treated in nitrogen and hydrogen atmospheres before being recalcined in air gave a material with a much higher coercivity of 0.503 T, and no loss of M_s, in a material with a grain size under 0.5 μm. [248]. Recently a fine grained (0.2 μm) sample has been made from coprecipitated salts, which when fired to 900 - 950 °C gave M_s and H_c which were both 94% of the single crystal values, at M_s = 87 emu g^{-1} and H_c = 0.630 T [28]. SrM has also been successfully made from a sol gel precursor, which consisted of mixed phases with α-Fe_2O_3 as a minor product in the 800 °C and 1000 °C samples, but single phase SrM at 1200 °C. At 800 °C the ferrite had a low M_s of 18 emu g^{-1} due to it being an impure phase, and a very high H_c of 0.700 T because of the small grain size. At 1000 °C M_s had increased to 56 emu g^{-1} and H_c decreased to 0.520 T, and in the pure M phase at 1200 °C M_s = 70 emu g^{-1} and H_c = 0.330 T [48].

As with BaM, the low coercivities of standard ceramic specimens can be increased greatly by reducing the grain size of the ferrite. Size can be reduced by milling, but the harmful

effect of milling on coercivity is well established, and in SrM samples 2 - 3 μm in diameter H_c was reduced to only 0.200 T after milling for 24 hours [334]. After 80 hours of ball milling such structural disorder had been imposed on the SrM that it had partially decomposed to a-Fe_2O_3, and superparamagnetic relaxation effects had reduced H_c and M_s significantly [335]. SrM made from the coprecipitation of chloride salts had a small grain size of 70 nm at 900 °C, and this resulted in very high coercivity in isotropic samples, with M_s = 71.8 emu g^{-1}. If a non-stoichiometric SrM was made with a small iron deficiency it was found that the coercivity was raised even higher, peaking at H_c = 0.680 T with a Fe:Ba ratio of 11.6, compared to a theoretical maximum H_c of 0.750 T [336]. Nanocrystalline SrM made from citrate precursors at 800 °C had a high coercivity and saturation magnetisation of 0.650 T and 67.7 emu g^{-1} respectively, in a material with a grain size of 116 nm [51]. A material was made with the extremely high coercivity of 0.720 T but a lower M_s of 57 emu g^{-1} from a glass crystallisation method, which involved rapid quenching from 1400°C. After annealing at 700 °C and leaching of the glass phase extremely small grains measuring 54 nm in the hexagonal plane and 41 nm in the c-axis were obtained, but they were also highly non-stoichiometric with a Fe:Sr ratio of only 8.8 [337]. SrM powder sized 0.5 - 50 μm was ball milled for 800 hours to produce superparamagnetic sized powders of around 13 nm, which produced ferrite with a coercivity of 0.500 T after being fired at 1000 °C / 4hr, despite the strain induced by the extended milling. After milling in a vacuum the ferrite powder was even smaller, around 8 nm, and mixed with 3 nm magnetite crystals [332].

Oriented SrM was produced using a standard ceramic sample milled to 0.8 μm, giving an oriented product in which M_s = 70.7 emu g^{-1} and H_c = 0.554 T [277]. Over 75% oriented SrM was made by pressing the submicron ferrite powder with 2 - 6% stearic acid in toluene, so that the hydrophobic end of the stearate bonded with the solvent and the hydrophilic end with the ferrite. The finely dispersed ferrite was then aligned and pressed in an external field before sintering. To achieve this degree of orientation the coercivity of the product first had to be reduced by milling the precursor to confer lattice strain, reducing H_c from 0.550 T to below

0.400 T in samples fired to 1180 °C [338]. Sputtered films of SrM can be made in which the easy axis of magnetisation is oriented either parallel or perpendicular to the film by varying the rf power of the deposition process, giving an anisotropy perpendicular to the plane of the film at a low rf power of 60 W, but giving parallel orientation with a high power of 330 W. Although the as-sputtered films were amorphous, when annealed at 80 °C the two orientations exhibited different textures as well as magnetic anisotropies [339].

2.3 PbM ferrite

Although PbM was the first M ferrite to be characterised, its magnetic properties are inferior to those of SrM and BaM. The K_1 anisotropy constant is only 2.2 x 10^6 erg cm^{-3} giving an anisotropy of 13.7 kOe, which while high is considerably lower than the other M ferrites. PbM has a lower net moment of 18.6 μ_B and M_s is also low at 56 emu g^{-1}, but the Curie point is similar to that of the other M ferrites at 452 °C [8]. Pure PbM has been made from the decomposition of a sol-gel precursor at 900 °C to give a material with high M_s and H_c values of 54 emu g^{-1} and 0.500 T [340].

2.4 Cobalt-titanium doped ferrites

Although these are a substituted M ferrite, the cobalt-titanium doped ferrites, BaCoTiM ($BaCo_xTi_xFe_{12-2x}O_{19}$), are of major commercial interest in the magnetic recording industry, and so they are considered here along with the other major ferrites. They were first synthesised in the 1960's as a way of lowering grain size and coercivity considerably without much loss of M_s [341], and were commercially developed by Toshiba in the 1980's to give particles 50 nm wide and 15 nm thick with a coercivity of 0.2 T [95]. Since then coercivity has been lowered considerably with further substitution to give a series of ferrites with the formula $BaCo_xTi_xFe_{12-2x}O_{19}$, which can be tuned with a variation in x to give the desired properties, reducing H_c to a minimum value at x = 1.2 [250]. It was also found that in films of BaCoTiM the coercivity varies differently with orientation relative to the film, exhibiting a very thin, almost paramagnetic hysteresis loop parallel to the plane of the film, but a 0.200 T wide

square loop perpendicular to the film [94]. This is because in thin layers the domains and Bloch walls are of comparable width. For example, a $BaCo_{1.1}Ti_{1.1}M$ thin film had a grain size of only 16 nm and coercivity of 0.100 T compared to 380 nm and 0.400 T for the unsubstituted ferrite [342].

The axial anisotropy also reduces with substitution, until it becomes in-plane at x = 1.3 [343]. This is because although the Ti^{4+} ion only substitutes in octahedral sites, the Co^{2+} ion substitutes in tetrahedral sites and the trigonal bipyramidal site, which is the major contributor to the uniaxial anisotropy [344]. The Co^{2+} ions were shown to be in tetrahedral positions with a value of $x < 0.8$ [72], and after this substitution level they begin to occupy the five-coordinate sites as well, and a cone of magnetisation begins to develop as a result of this non-colinearity, and this also has an effect of reducing H_c [345]. The angle of the cone was calculated to be 61° from the c-axis at room temperature for a substitution level of x = 1 [346].

The values for the magnetic properties vary with morphology, purity and processing method used, but some values are mentioned for here for comparison. In standard ceramic specimens all heated at 1000 °C / 5hr, for x = 0.5, M_s = 58.4, H_c = 0.221 T and M_r / M_s = 0.49; for x = 0.7, M_s = 56.6, H_c = 0.056 T and M_r / M_s = 0.38; for x = 0.8 M_s = 54.0, H_c = 0.041 T and M_r / M_s = 0.35 [347]; and for x = 1.1, M_s = 56 and x = 1.5, M_s = 48 emu g^{-1} [348].

$BaCo_xTi_xFe_{12-2x}O_{19}$ made from precipitated chloride salts and fired to 900 °C had comparable values with standard samples, with M_s = 55 emu g^{-1} and H_c = 0.094 T at x = 0.6 and M_s = 56 emu g^{-1} and H_c = 0.031 T at x = 0.85. Even after firing the material at 900 °C for 24 hours M_s only reached a maximum of 58 emu g^{-1} [336]. BaCoTiM has been made by melt-flux precipitation at 980 °C with a high M_s of 58 emu g^{-1} and a coercivity of 0.080 T [37].

When made from a mixture of FeOOH, $Ba(OH)_2$ and cobalt and titanium alkoxides, the M phase always existed with some minor haematite impurity. None the less a good quality magnetic product was produced, with M_s = 49 emu g^{-1} and H_c = 0.170 T at x = 0.5, M_s = 48

emu g^{-1} and H_c = 0.110 T at x = 0.7 and M_s = 45 emu g^{-1} and H_c = 0.020 T at x = 1 [96]. A nanosized BaCoTiM ferrite was made from the stearic acid gel method, with a grain size of only 30 nm but a coercivity of 0.110 T for a substitution level of x = 0.8 [349]. The glass crystallisation method resulted in more loss of H_c than in coprecipitated samples, probably through increased lattice diffusion, so that at x = 0.65, M_s = 60 emu g^{-1} and H_c = 0.157 T, at x = 0.85, M_s = 54 emu g^{-1} and H_c = 0.063 T [336], and at x = 0.9 H_c = 0.052 T [328].

2.5 Y ferrites

The Y ferrites all have lower magnetic permeabilities than the M ferrites, the highest being for Zn_2Y (18.4 μ_B,M_s = 72 emu g^{-1} at 0 K [7]), and getting lower in the sequence Zn>Mn>Co>Ni [350]. At room temperature M_s = 42 emu g^{-1}, but the Curie point of Zn_2Y is only 130 °C, and it has a low crystalline anisotropy of only 9.0 kOe [7].

Co_2Y has the highest MCA of any hexagonal ferrite, uniaxial or ferroxplana, with a K_1 + K_2 value of -2.6 x 10^6 erg cm^{-3}, K_3 = 800 erg cm^{-3} and the crystalline anisotropy H_A = 28 kOe in the preferred plane and only 1.5 kOe in the c-axis. Co_2Y has a moment of 9.8 μ_B, the room temperature saturation magnetisation is 34 emu g^{-1} and the coercivity is small, with a relatively high Curie point of 340 °C [7]. The Y ferrites may have larger negative K values because there is no five-coordinate site in the T block, and therefore there is a lower spin-orbit coupling contribution to K [341]. The Co^{2+} ions are all in octahedral positions, with the spin orientations 1.1↑ and 0.9↓ [351]

180° domain walls were first demonstrated in Zn_2Y [352], and since then Co_2Y has also been shown to contain stacked layers of domains of equal width separated by 180° walls (Fig. 183), giving the domains a rectangular and not a hexagonal shape [353]. A single domain crystal has also been seen to become split by a 180° domain wall as the magnetisation drops below M_s [12].

2.6 Z ferrites

All the Z ferrites have a uniaxial anisotropy with spontaneous magnetisation in the c-axis, except Co_2Z which has a preferred plane at room temperature perpendicular to the c-axis [4]. Co_2Z has a net magnetic moment of 31.2 μ_B, giving it an M_s of 69 emu g^{-1} at 0 K and 51 emu g^{-1} at room temperature, with an extremely small coercivity and a high Curie point of 410 °C [7]. It is also strongly anisotropic, with $K_1 + K_2 = -1.8 \times 10^6$ erg cm^{-3} and $K_3 = -120$ erg cm^{-3}, and this gives a high crystalline anisotropy of 13 kOe in the plane [7], but an extremely low anisotropy of only 120 Oe to in the c-axis [348]. Despite going through at least four changes in anisotropy between 0 K and the Curie point, M_s decreases steadily and evenly, without any jumps, to zero at T_c. These changes in anisotropy are attributed to variations in the anisotropy constants K_1 and K_2, caused by a strong temperature dependence of the choice of site of the cobalt ions. In the planar state the spin alignments of the Co^{2+} ions are 1.08↑ and 0.92↓, and they are all in octahedral sites, the same as in Co_2Y [15].

In polycrystalline Co_2Z at room temperature domains as large as 2 μm have been found in 50 μm grains, and the domains are aligned in the plane perpendicular the c-axis, similar to Co_2Y [12]. Unlike in the Y ferrite however, the domains are not of even thickness, the structure consisting of alternating thick and thin domains oriented opposite to each other, separated by 180° domain walls (Fig. 183) [12].

Single crystals 3 mm x 500 μm with the domains oriented exhibited a definite anisotropy of the magnetisation, with a high M_s of 57 emu g^{-1} in the hexagonal plane, but a low M_s of 36 emu g^{-1} in the c-axis. There was almost no hysteresis loop in the plane, whereas in the c-axis coercivity was higher but with a very low remanence, caused by the much higher number of domain walls to be crossed in this direction [12]. Oriented polycrystalline samples have been produced from sintering prefired Co_2Z in a magnetic field at 1260 °C, which show a fan like texture as the hexagonal crystals align their basal planes. This became more pronounced as the crystals grew with more sintering, with the best orientation achieved after

DGG occurred at 1320 °C giving grains up to 250 μm wide, and after being fired at 1300 °C / 24hr the oriented samples were denser than random samples [293]. A fibre-like texture was also achieved by sintering the grains in a rotating magnetic field, and these produced a denser product (97%) than the fan textured samples made in a static field, although density was not improved by DGG [266].

2.7 W ferrites

The first W ferrite to be discovered, Fe_2W, has a large saturation magnetisation (M_s = 60 emu g^{-1}) and coercivity, and the Curie point is also high at 455 °C. The crystalline anisotropy constant, $K_1 = 3.0 \times 10^6$ erg cm^{-3}, is of a similar magnitude to that of BaM, but with contributions from the higher constants H_A = 19.0 kOe, greater than that of the M ferrites [7]. The uniaxial W ferrites not only have large crystalline anisotropies, but also high saturation magnetisations, which are caused by not just superexchange mechanisms across one oxygen atom (Fe-O-Fe), but also super-superexchange processes across two oxygen atoms (Fe-O-O-Fe) [354].

Very few values seem to have been reported for the saturation magnetisation of Co_2W, perhaps because of difficulties in preparing the pure material, although it has an established high Curie point of 490 °C and is known to be a soft ferrite [10]. With doped $BaZn_{2-x}Co_xW$ prepared from the glass crystallisation method, M_s, H_c and M_r/M_s are reported to decrease with increasing cobalt substitution, to reported minimum values of M_s = 74 emu g^{-1}, H_c = 0.010 T and M_r/M_s = 0.1 for small grained samples around 1 μm in diameter fired to 1150 °C [355]. However, in samples of $BaZn_{2-x}Co_xW$ prepared by standard ceramic methods and fired to 1270 °C / 8hr, M_s was reported to reach a maximum of 77.1 emu g^{-1} at x = 1.0. This sample was also reported to be an n-type superconductor at x = 1.0, due to hopping of electrons between Fe^{2+} and Fe^{3+} ions in the S block, suggesting that it was not totally stoichiometric [297].

Co_2W has a magnetic anisotropy in a cone at an angle of 70° from the c-axis at room

temperature, but the large K_1 constant variously reported as -5.0 x 10^6 erg cm^{-3} [7] or -3.5 x 10^6 erg cm^{-3} [10] would suggest the ferrite to have a planar anisotropy. This deviation from the planar orientation is caused by the contribution of the two large and positive second and third order anisotropy constants, K_2 = 0.8.0 x 10^6 erg cm^{-3} and K_3 = 0.9 x 10^6 erg cm^{-3}, and this is a particularly large value for the K_3 constant [10]. The Co^{2+} ions are mostly divided between the S block octahedral and tetrahedral sites, with 1.4 Co^{2+} in the octahedral S block sites, and a few in the R block octahedral sites [10;356].

2.8 X ferrites

The first X ferrite discovered was the uniaxial Fe_2X, and this was found to have a high anisotropy of 15.5 kOe, a high M_s of 74.5 emu g^{-1} and a high Curie point at 522 ^{0}C in polycrystalline samples. When this was substituted with 0.3% Gd_2O_3 to BaO, M_s and T_c dropped slightly to 72.4 emu g^{-1} and 512 °C respectively, but H_A increased to 17.8 kOe. It was found that instead of substituting for barium as intended, the smaller Gd^{3+} preferred the octahedral sites to the Ba^{2+} positions in the oxygen lattice [274].

Co_2X has a preferred cone of magnetisation at an angle of 74° to the c-axis, with a weaker anisotropy of 9.5 kOe, a high M_s of 57.1 emu g^{-1}, and a very low H_c of only 0.005 T in single crystal samples. It also exhibits a six-fold magnetic symmetry with 60°, 120° and 180° domain walls [12]. The Curie point has been measured as 467 °C [13].

2.9 U ferrites

There are no magnetic characteristics reported for Co_2U, except that it has a planar anisotropy. All the other U ferrites are axially orientated, and Zn_2U has a K_1 constant of 1.4 x 10^6 erg cm^{-3} giving a moderately strong H_A of 9.6 kOe [7]. Due to the large molecular size it has 60.5 μ_B [7], a saturation magnetisation of 54.9 emu g^{-1} [16] and the Curie point is at 400 °C [7].

3. Effect of additives on the magnetic properties of ferrites

For high quality commercial ferrites total impurities should not exceed 0.02% by weight, as quantities this small can change the magnetic properties of the material.

3.1 Spinel ferrites

Permeability is lowered by strain induced in the lattice, and so a larger ion substituted for a smaller one will decrease μ and increase the losses, the drop increasing with the size of the ion [357]. The exception to this is the addition of 0.2% Ca^{2+} to Mn-Zn spinel ferrite, which reduces eddy current losses by a factor of 10 because the Ca^{2+} gathers at the grain boundaries, insulating the grains from one another [358]. An addition of 0.3% Li^{+} to Ni-Zn spinel ferrite doubles the magnetic permeability, and small amounts of molybdenum, copper, cadmium, aluminium and lanthanum oxides and carbon have been reported to raise μ of some ferrites by up to 50%, typically with an addition of less than 1% of the dopant [359].

3.2 M ferrites

The magnetic saturation of M ferrites can be increased with substitution by some non-magnetic ions, such as Zn^{2+}. This is because the zinc ions greatly prefer tetrahedral positions, and in M ferrites the tetrahedral sites oppose the spin of most of the octahedral sites, which produce the net moment. Therefore, substitution with Zn^{2+} reduces this negative contribution, increasing the net magnetic moment [360]. Zn substituted BaM has a very square shaped loop with a sudden drop in remanence, a high M_s of 65 emu g^{-1} and a coercivity of 0.250 T, making it a suitable candidate for some magnetic recording applications [361]. $BaFe_{11.5}Co_{0.5}O_{19}$ was made by ion exchange, and although the material was only 75% pure with a non-magnetic impurity the saturation magnetisation was high, and H_c rose with annealing temperature as more five-coordinate sites were occupied, although the Curie point was unaffected by the substitution. After heating to 800 °C M_s was 51 emu g^{-1} and the coercivity was 0.190 T, at 900 °C M_s was 62 emu g^{-1} H_c was 0.210 T and at 1000 °C M_s = 65 emu g^{-1} and H_c = 0.220 T,

as grain size increased from 90 nm to 200 nm [39].

Lanthanide doped BaM has been made with up to the total substitution of iron to give $BaLa_{12}O_{19}$ [256]. Lanthanum has also been added with an equal amount of a divalent ion to give the compounds $Ba_{1-x}La_xFe_{12-x}Me_xO_{19}$ (Me = Zn or Mg) [362] and $LaMFe_{11}O_{19}$ [363], and this increases both M_s and H_c compared to the undoped ferrite. SrM has been doped with up to 1% La_2O_3, and a level of 0.7% was reported to be the optimum for raising M_s and T_c and gave a square loop, but also raised the crystallisation temperature to 1200 °C [364]. The substitution of SrM with La^{3+} and Zn^{2+} was found to enhance the magnetic properties, giving the compound $Sr_{1-x}La_xFe_{12-x}Zn_xO_{19}$. The lattice constant decreased with x as the substituted ions were smaller than Ba^{2+} and Fe^{3+}, and for x = 0.3, K_1 was lowered by 10%. However, after firing to 1200 °C the grains were still only 0.8 μm resulting in a large H_c of 0.470 T, and M_s was increased by 4% [286]. When PbM was doped with Ga^{3+} the compound $PbGa_xFe_{12-x}O_{19}$ was made up to full substitution at x = 12. However, with increasing gallium substitution the magnetisation decreased until the compound became totally non-collinear at x - 6 with an M_s of zero [365].

Antimony doped BaM up to x = 1 made by a hydrothermal process had nanosized acicular grains and a small coercivity (H_c = 0.045 T), and maintained the uniaxial anisotropy of the M ferrite, but the M_s was lowered by the formation of Sb_2O_3 as a minor product [366], and BaM doped with arsenic and antimony made by a sol gel route also had drastically reduced magnetic properties and a grain size up to 6 μm [367]. BaM single crystals and thin films were made doped with Ti^{3+}, which exhibited perminvar behaviour with a loop closed in the centre at an applied field of zero T but open between 0.5 and 0.8 T, caused by a relaxation of Fe^{2+} / Ti^{4+} pairs [368].

Polycrystalline BaM was made by normal ceramic techniques with the addition of up to 1 mol% B_2O_3 and the boria was found to exist in a molten state over 1000 °C, diffusing into the M structure to form $BaFe_{12-x}B_xO_{19}$, and at temperatures over 1300 °C it caused large distortions in the lattice in amounts over 0.3 mol%. With 0.2 mol% addition M_s was raised by

13% to 79 emu g^{-1}, because the non-magnetic B^{3+} ion substitutes for Fe^{3+} in tetrahedral sites, increasing the net spin. The boria also had a huge effect on coercivity and remanence, both decreasing with 0.2 mol% to minimum values of H_c = 0.0005 T and M_r / M_s = 0.2 after 1400 °C, the thousand-fold decrease in coercivity transforming BaM into a soft ferrite! [282]. At 1000 °C H_c = 0.280 T, the extremely low coercivity being associated with an increase in grain size up to 10 μm after 1400 °C / 10hr, although these grains were still relatively small compared to the Y, Z and W ferrites at equivalent temperatures. The addition of 0.2 - 0.6% sodium to standard ceramic preparations increased density and coercivity slightly when added before calcination, but lowered them both when added after calcination but before sintering [29].

Silica dopant has been used to raise the energy product of BaM, and the magnetic properties of SrM have also been improved by the addition of CaO and SiO_2, dopants also used in doped W ferrites [369], and an addition of 0.2% Al_2O_3 limits the grain size in SrM at high temperatures to under 5 μm, thus increasing coercivity [289]. The addition of silica with CaO has been claimed to reduce grain size and aid sintering in M ferrites, and a similar effect can be seen if BaO or SrO is used instead of CaO, but in this case the c and a lattice parameters shrink equally, maintaining the anisotropy of the crystal [277].

Many doped ferrites analogous to the CoTiM ferrites have been investigated, and CoZrM has been reported as having the largest drop in coercivity whilst maintaining M_s [35]. CoZrM made from the citrate process had a very small coercivity of 0.015 T for an M_s of 48 emu g^{-1} when fired to 1300 °C [370]. The $BaZn_xTi_xFe_{12-2x}O_{19}$ series has been investigated for x = 0.1 - 0.8, and while H_c and grain size decrease with x, M_s peaked at x = 0.3 with a value of 59 emu g^{-1}. The formation temperature also increased with x, and the grains were extremely acicular, having dimensions of 150 nm long and 10 nm thick for x = 0.5 at 800 °C [319]. These specimens were made from the salt-melt method, but ZnTiM has also been made from a sol gel route at 850 °C, and at x = 0.75, M_s = 49.8 emu g^{-1} and H_c = 0.019 T [44]. Ni-Zn-TiM had a constant M_s of 52.5 emu g^{-1} with increasing substitution, but H_c decreased from 0.145 T

at x = 0.5 to 0.050 T at x = 1, and the anisotropy changed from uniaxial to planar [371]. There is also little loss of M_s with increasing substitution in BaCoSnM, which had a coercivity of 0.053 T in coprecipitated samples at x = 1.4, which were still uniaxial with M_s = 56.2 emu g^{-1} and a high M_r / M_s ratio of 0.39 [372]. BaCoSnM was found to have a finer grain size but inferior magnetic characteristics than BaM. However, this can be optimised in mixed BaCoTi-SnM ferrites, with superior magnetic properties than pure BaCoSnM but a finer product than BaCoTiM [347].

$BaCo_{0.45}Sn_{0.17}Ti_{0.23}Fe_{10.55}O_{19}$ with a grain size of 50 nm by 20 nm had a low coercivity of 0.053 T and M_s of 55 emu g^{-1}. However, after heating in a reduction atmosphere the magnetic properties were greatly changed. After 280 °C / 4hr the coercivity had increased greatly to 0.135 T and M_s slightly to 62 emu g^{-1}, whereas after reduction at 380 °C / 4hr the coercivity had dropped back down to previous levels at 0.060 T but the M_s has now increased to a massive 114 emu g^{-1}. These changes were due to the formation by reduction of cobalt metal at the lower temperature and α-iron at the higher temperature, and the paramagnetic effects of the α-iron also interfered with the superexchange interactions of the ferrite, changing the magnetic anisotropy from uniaxial to a cone at an angle to the c-axis [327]. Titanium was found to inhibit the transformation through reduction.

In the compounds $BaA_xMe_xFe_{12-x}O_{19}$ where A = Ru^{4+} or Ir^{4+} and me = Co^{2+} or Zn^{2+}, it was found that the substitution level at which the anisotropy transforms from axial to planar could be reduced from the value of x = 1.3 required for BaCoTiM. The A^{4+} ions substitute in the octahedral and tetragonal bipyramidal sites and the Me^{2+} ions in the tetrahedral and tetragonal bipyramidal sites, rotating the magnetisation from the c-axis to the hexagonal plane. Ti^{4+} ions only ever occupy the tetrahedral sites, and this explains the quicker transformation to planar anisotropy in these materials [73]. The crystalline anisotropy reaches a minimum value at this transition point. For example, in BaZnRuM at x = 0.25 K_1 has a value of 1.4 x 10^6 erg cm^{-3} and H_A = 3.5 kOe, whereas at x = 0.35 the anisotropy constant K_1 has now changed sign to -0.9 x 10^6 erg cm^{-3} indicating a planar anisotropy and H_A = 1.75 kOe. At the transition level

of x = 0.30 the anisotropy is very weak and $K_1 = 0.3 \times 10^6$ erg cm^{-3}, but there is little change in M_s and T_c over this transition . The transition level is also x = 0.3 for BaZnRuM, at x = 0.5 for BaZnIrM and at x = 0.6 for BaCoIrM [373]. Thin films containing praseodymium and lanthanum with nickel to make BaPrNiM and BaLaNiM have also been produced [74].

The coercivity and grain size of BaM films have also been lowered by doping with small quantities of Cr_2O_3, ZrO_2 and $Zr_{0.84}Y_{0.16}O_{1.92}$ (yttria-stabilised zirconia) [70]. When larger amounts of Cr_2O_3 were added to BaM, M_s and T_c both dropped with substitution until a paramagnetic material resulted [26]. A similar effect was seen with PbM, but with a massive peak in coercivity of 0.850 T when three Cr^{3+} ions had been substituted for iron [374].

3.3 Y ferrites

Sr_2Zn_2Y showed a strange, non-collinear magnetic structuring due to the Sr^{2+} ion distorting the lattice [269], and therefore the replacement of barium with strontium in Y ferrites steadily reduced the permeability, but a 50% substitution of lead increased it dramatically [14]. In substitutions of Co with Zn to give the compound $Co_{1-x}Zn_xY$ fired at 1000 °C / 10hr, T_c falls linearly from 340 °C (x = 0) to100 °C (x= 1). The M_s values increased with addition, but they were lower than expected with M_s = 26.6 (instead of 34) and 32.9 (instead of 42) emu $g^{-1}$for x = 0 and 1 respectively [375]. Zinc weakens the super interactions and lowers T_c, but there is no change in the spin directions so the net magnetic moment increases with addition. M_s showed a peak of 34.9 emu g^{-1} at x = 0.75, but this was attributed to thermal agitation of the x = 1 compound at room temperature as M_s showed a steady increase at when measured at 77 K. The low M_s and T_c values also suggest that perhaps the material was not single phase Y. When made from the coprecipitation of superparamagnetic δ-FeOOH and heated to 1200 °C, Zn_2Y was produced in which the grain size = 2 μm, M_s = 32.7 emu g^{-1} and M_r / M_s = 0.06 [262].

3.4 Z ferrites

The substituted Sr_3Zn_2Z shows a lattice distorted by the Sr^{2+} ion, reducing drastically the magnetic properties of the compound compared to Ba_3Zn_2Z [269], and the Z structure collapses with substitution of the barium by lead [14]. Substitution with La^{3+} to give $Ba_{3-x}La_xCo_2Z$ can be made up to x = 0.4, with a peak M_s of 58 emu g^{-1} for x = 0.1 [268].

3.5 W ferrites

The most important W ferrites are the Zn_2W series, which have a high M_s but a low H_c, despite being strongly uniaxial. Pure $SrZn_2W$ has a saturation magnetisation of up to 77 emu g^{-1} and a coercivity of around 0.050 T, and $M_r / M_s = 0.01$ [376], while for $BaZn_2W$ $M_s = 79$ emu g^{-1},$H_A = 12.5$ kOe [377], $H_c \equiv 0.010$ T and $M_r / M_s = 0.01$ [355]. $PbZn_2W$ is a borderline hard magnetic material, with a high M_s of 53.99 emu g^{-1} but a high H_c of 0.111 T; the Curie point is at 326 °C and $H_A = 11.8$ kOe [378]. However both M_s and H_c of the Zn_2W ferrites can be raised by the substitution of Zn^{2+}, which prefers tetrahedral sites, with divalent metal ions which either adopt octahedral positions or inhibit grain growth, and the magnetic properties tailored with careful addition [376].

Sodium doped $SrZn_2W$ had a grain size of only 0.5 - 1.5 μm at 1225 °C, with a coercivity of 0.173 T and $M_s = 60.5$ emu g^{-1}. After 1300°C for only 30 minutes the grains had grown to 1.8 - 4.0 μm and H_c dropped to 0.045 T with an increase in M_s to 67.8 emu g^{-1}, and after 2 hours at this temperature the grains had undergone DGG to become 3 - 60 μm in diameter, with a corresponding drop in H_c to 0.018 T but no further increase in M_s [272]. Zn^{2+} was substituted with (Fe^{3+} / Li^+) to produce the ferrite $SrZn_{2-x}(FeLi)_xW$, made from finely ground oxide precursors < 0.1 μm in diameter. When x = 0.5 W ferrite was produced after 1100 °C / 15hr, and all of the properties were increased to $M_s = 91$ emu g^{-1}, $H_c = 0.126$ and $M_r / M_s = 0.036$. With further heating at 1320 °C / 5 hr there was no change in M_s and the other values had fallen to un-doped levels, and with a substitution of over x = 0.5 the Li^+ ion distorts the lattice, drastically lowering M_s [376]. $Sr_{0.9}Ca_{0.1}Zn_2W$ which was made from a fine grained

precursor had a domain-sized particle diameter of only 1 μm, and subsequently a high coercivity of over 0.365 T and a saturation magnetisation of 65 emu g^{-1} at 1100 °C. On heating to 1300 °C the grains had grown, and although M_s had increased to 85 emu g^{-1} the coercivity had dropped to only 0.010 T [379].

4. Results and discussion

As the magnetic properties were not investigated until near the end of this project, most of the VSM measurements were taken on freshly fired samples that had been stored as dry gel fibres for several years at 110 °C. Where possible, measurements of old samples fired when the gel fibre was freshly spun were also taken for comparison. Unless otherwise stated all fibres were made from standard Fe/Br sols.

4.1 Development of sample preparation and mounting

Standard ceramic VSM samples are in the form of either a sintered ceramic monolith, a sintered pressed pellet, or a powder set in a resin or wax. This is then either placed securely in a capsule or mounted on a stick with a glue or varnish. The problem of mounting a fibre sample so that it retains alignment whilst remaining fixed in place as is it vibrated in a large magnetic field does not appear to have been addressed prior to this work. Various methods of preparing and measuring an aligned sample were investigated, many of which proved to be excellent ways of reducing nicely aligned fibres to powdery specimens of random fibre.

Initially samples were placed in a gelatine pill capsule, wedged in place with a tight wad of cotton wool and mounted in the VSM. This method proved utterly useless for both random and aligned fibres, as the aligned fibres were instantly broken up by vibration in the magnetic field, and both types of fibre were mobile within the capsule. This resulted in a jumpy and unsymmetrical loop, with unreliable and unreproducible values. Attempts were then made to sandwich the fibres between layers of paper, plastic and *Sellotape*, but while this reduced slightly the movement of the fibres when being measured, it resulted in damage to the

alignment of the fibres due to the pressure applied.

It was then attempted to prepare samples by impregnation with a resin, in effect to make a composite material containing a known weight of fibre in a non-magnetic matrix. The first matrix material tried was a *Superglue* but the glue set before it could fully impregnate the fibre blankets. Next was *Araldite Rapid*, an epoxy resin which sets in 1 hour, but this proved too viscous to penetrate the fibre blanket even when heated to 60 °C. The use of a simple wax was investigated, but while this proved sufficient to make a random fibre sample, it again did not fully penetrate the fibre blankets, resulting in movement and fragmentation of some of the sample, and it was impossible to see the direction of alignment in the final sample. Methyl methacrylate (CH_2=C(CH_3)C(O)CH_3), a clear liquid between -48 - 100 °C, was found to be sufficiently thin to penetrate the fibre, and with the addition of 0.1 wt% azo-iso-butyronitrile ((CH_2)$_2$C(CN)N:NC(CN)(CH_2)$_2$) this polymerised to form a sturdy, solid, transparent resin composite when heated over night at 75 °C. This held the fibre firmly during measurement and retained the alignment, but some bubbles were generated within the resin during the setting process, which could lead to the movement of some material if one formed around a fibre. To avoid these problems a much faster setting form of methacrylate was investigated, a mixture of methyl methacrylate and styrene with 5 wt% dibenzoyl peroxide as a hardener. Although more viscous than pure methacrylate, this proved able to permeate the blankets and after ten minutes set rapidly, with no shrinkage or bubble formation. This exothermic reaction was observed to generate high localised heat, but this appeared to have no adverse effects on the fibres.

It was found that when the aligned samples were prepared in the capsule it was sometimes difficult to determine the direction of alignment of the fibres, sometimes the resin would move the blanket out of its desired orientation within the capsule and sometimes an airlock would form under the resin and prevent all of the fibres from being impregnated. The preparation of samples lying flat on a piece of tissue paper was then investigated, with an excess of resin soaking into both the fibres and the paper, the paper then being trimmed down

to a suitable size for sample mounting. The resulting flat, square specimen was attached to a flat sided sample holder with one of the sides of the square in the vertical axis parallel to the applied field. The sample could then easily be rotated and reattached to measure the alignment effects of the fibre relative to the applied field, and if the sample was square and evenly thick, it could be rotated through 90° and suffer no change in shape demagnetising effects. For direct comparison the random fibre samples were made in the same way and with similar dimensions, although this produced composites with a much higher volume fractions than the aligned specimens. As methyl methacrylate has a melting point of 100 °C, no measurements were taken above room temperature (300 K).

4.1.1 Volume fraction of samples

The aligned samples were square with sides of roughly equal length between 3 - 4 mm, but their thicknesses varied according to the depth of the blanket, which in turn depended upon the amount of sol spun to produce that blanket. The heights of the sample composites could be measured on a microscope, and even though the surface was slightly irregular an estimate could be made from the average of measurements on each side. From this the volume of each composite could be calculated, and knowing the weight of fibre a volume fraction could also be calculated. The thickness of the composites varied between 160 - 560 μm, but most were close to 400 μm, and the volume fractions were between 3 - 4%. An exception to this was the Co_2W ferrite, which had a much higher volume fraction of 7%. The reason for this higher volume density within this aligned fibre is not fully under stood, but it was the best aligned of all samples. The random fibre samples had similar square dimensions, but due to their nature they did not have a level surface and their volume fractions could not be accurately estimated. However, the random samples did contain at least a ten-fold increase in weight for a similarly sized composite, and therefore their volume fractions could be expected to be accordingly larger.

4.1.2 Error in M_s values

As all M_s values were calculated as emu g^{-1}, there was an intrinsic error from the weighing of samples, which were accurate to $^{+}/_{-}$ 0.05 mg. However, many of the aligned samples had unavoidably low masses, and had errors as high as $^{+}/_{-}$ 10%. This error was only relevant when comparing one sample to another or previously published values; when showing the alignment effects within a sample relative to that sample's alignment in the field, the same specimen was merely rotated for each measurement, so the error was constant within that specimen, and any alignment effect seen was independent of this error. In investigations of measurement temperature effects, the same sample was also kept within the VSM while the temperature was lowered, so there was no error within the trends shown. For this reason the percentage weight errors of the samples are also included in the following results. However, these errors only affected the M_s and M_r values, with the ratio M_r/M_s and H_c being unaffected by calculation from sample weight.

4.2 BaM fibres

BaM has a maximum M_s of 72 emu g^{-1} and although it is a hard ferrite many polycrystalline samples have low coercivities of around 0.3 T, approximately half the theoretical maximum, because of micron-sized grains, and M_s values of up to 67 emu g^{-1} [7].

There was an old sample of BaM fibre available for measurement, fired to 1000 °C / 3hr immediately after spinning, and it had a fairly high M_s value for a polycrystalline ferrite of 63.8 emu g^{-1} (0.6% error) and a high coercivity of 0.538 T, as would be expected for a material with a grain size < 0.1 μm. However, when the aligned fibres were measured, a clear alignment effect could be observed, as can be seen in figure 184. Parallel alignment to H had an M_s value 48.9% larger than perpendicular to H, and at 45° to H it was 51.3% larger than perpendicular. The apparent slight superiority of 45° alignment is discussed in section 4.10, and as the two values were almost always equal the discussion will focus on parallel and perpendicular alignment to H. It could be seen that the random sample had an M_s value almost

exactly midway between the two extremes of the aligned fibre, as would be expected if the feature were purely due to alignment of the fibres. That the average of the two (64.4 emu g^{-1}) matched the value for the random fibres indicated that the M_s values of the aligned blanket were reliable, despite the greater error of 3.6%, and this proved to be true for most of the aligned samples. There was virtually no change in H_c or M_r with alignment.

Two samples were measured after being stored, one for 2 yr (fig. 185) and one for 3 yr (fig. 186), and then fired to 1000° / 3hr. These gave very similar values for random fibre and the average of the parallel and perpendicular M_s to the older sample, and all three are compared in table 5.2. The larger difference of 4.9% between the average aligned M_s and random M_s of the fibres stored for 3 yr indicated that the weight error (6.3%) was greater in these fibres, and an M_s value of around 63 emu g^{-1} was thought to be accurate for the random fibre, with no real change over the storage period in M_s, H_c or M_r. However, there was a definite increase in alignment effect in both stored fibres, which is independent of any weight errors, with the change greatest in the fibres stored for two years. This could be due to the loss of halide during storage discussed in Chapter 4, which resulted in a lower crystallisation temperature, smaller crystallite size and the strange linear ridges 0.2 μm wide seen parallel to the fibre's long axis. The lack of change in H_c indicates no great difference in grain size between the old and recent samples, but the increase in ||:_|_ M_s would appear to be influenced by this morphology, as it is less in the more recent sample which exhibited a mixture of the linear and "honeycomb" type surface features.

	Aligned || to H			Aligned _|_ to H			|| vs. _|_		Random fibre		
Age	M_s	H_c	M_r/M_s	M_s	H_c	M_r/M_s	||:_|_	|| + _|_ / 2	M_s	H_c	M_r/M_s
0 yr	77.0	0.534	0.46	51.7	0.527	0.51	1.49	64.4	63.8	0.538	0.52
2 yr	80.0	0.525	0.46	45.0	0.525	0.51	1.78	62.5	n/a	n/a	n/a
3 yr	81.0	0.525	0.48	50.3	0.530	0.52	1.61	65.7	62.5	0.523	0.50

Table 5.2 Comparison of aligned and random BaM fibres, fired to 1000 °C / 3hr after being stored for 0, 2 and 3 yr after spinning. The M_s values of || and _|_ alignments are compared in the || vs. _|_ columns.

All of the loops were of a good hard magnet as expected for BaM, and they were not at all square with remanence at half the value of saturation. M_r = 50% in isotropic M samples, but in magnetically oriented samples it approaches M_s when the field is parallel to c-axis, and decreases down to 20% of M_s perpendicular to the c-axis, with the effect becoming greater as the firing temp rises (i.e. higher and lower values) [7]. Therefore, it could be seen that all of the BaM ferrite fibres were isotropic, with no alignment of the crystals within the fibres.

The sample fired to 1000 °C / 3hr after being stored for 3 yr was cooled below room temperature and measured parallel to H (table 5.3). The loops are compared in figure 187, and it can be seen that M_s increases with a drop in temperature. This agrees with previous reports of values for M_s of 72 emu g^{-1} at 300 K, 76 at 250 K, 84 at 200 K, 89 at 150 K, 98 at 100 K [306] and 100 at 0 K [7]. In a more detailed view of the actual loop itself (fig. 188) it can be seen that M_r gradually increases while H_c decreases with a decrease in temperature. However, the ferrite remained clearly hard even at 50 K, where H_c had been lowered by only 17.7% compared to reported drops from H_C = 0.320 at 298 K to 0.227 T at 173 K and 0.170 T at 73 K [3].

Temp. / K	M_s / emu g^{-1}	H_c / T	M_r / M_s
300	83.2	0.532	0.48
250	91.6	0.502	0.48
200	99.3	0.472	0.49
150	106.4	0.453	0.49
100	112.4	0.442	0.49
50	115.4	0.438	0.49

Table 5.3 Variations in magnetic properties with measuring temperature for BaM fibres (stored 3yr) fired to 1000 °C / 3hr and aligned ll to H. Error in M_s = 6.3%.

The changes in properties with firing temperature and time are detailed in table 5.4, and it can be seen from figure 189 that at 400 °C the material was barely magnetic, due to small amounts of highly magnetic γ-Fe_2O_3 in the paramagnetic haematite. By 700 °C / 3hr a hard ferrite loop had developed, although the low M_s value indicated that BaM is still a minor

phase, as shown in the XRD data, and the low H_c suggested a very small grain size well below the domain size. The irregular sides of the loop were typical of immature ferrites and maybe evidence of a mixed phase, as opposed to the smooth mature ferrite loops. After 700 °C / 100 hr there was little change, but at 1000 °C / 3hr M_s and H_c had reached their optimum values, and the perfect BaM loop developed. The BaM had obtained these values after only 10 min at 1000 °C, and no real change was observed after 100 hr at this temperature. Further heating to 1200 °C / 3hr reduced H_c by 42.9% to 0.3 T as the grain size increased to 1 - 4 μm, similar to standard ceramic BaM. Although M_s appears unchanged in figure 190, this is M_s aligned parallel to H, and M_s perpendicular to H had increased to 58.4 emu g^{-1} to give an average M_s of 71.0 emu g^{-1} (4.5% error), nearly at the maximum for BaM. The reduction in alignment effect could be due to the large grains interfering with alignment, as can be seen in Co_2Z fibres with DGG.

Temp / time	M_s	H_c	M_r / M_s	Grain Structure	Error in M_s
400 °C / 3hr	3.11	0.124	0.37	None apparent > 0.1 μm	10.0%
700 °C / 3hr	23.8	0.424	0.44	None apparent > 0.1 μm	10.0%
700 °C / 100 hr	24.3	0.489	0.50	None apparent > 0.1 μm	10.0%
1000 °C / 10 min	82.0	0.527	0.48	Linear ridges and "honeycombs"	10.0 %
1000 °C / 3hr	81.0	0.525	0.48	Linear ridges and "honeycombs"	6.3%
1000 °C / 24 hr	79.5	0.523	0.47	Linear ridges and "honeycombs"	7.1%
1000 °C / 100 hr	79.9	0.512	0.48	Linear ridges and "honeycombs"	7.1%
1200 °C / 3hr	83.5	0.300	0.47	larger grains all > 1 μm	4.5%

Table 5.4 Variations in magnetic properties with firing temperature and time for BaM fibres (stored 3yr) aligned ‖ to H.

The results for BaM fibres steamed between 500 and 900 °C are shown in table 5.5, measured parallel to H. There was a virtual negation of any alignment effect, and these values can be taken as approximating random fibre results, because the steaming process used severely disrupted the alignment of the fibres as can be seen in figure 191. The fibre steamed at 500 °C resembled the fibre at 400 °C before steaming, but with a harder coercivity, and at

600 °C a BaM-type loop had formed, although with the low M_s and H_c and uneven sides typical of the immature ferrite. The linear ridges seen in all stored BaM fibres had formed by this point, and remained until 900 °C when randomly oriented platelets up to 2 x 0.3 μm had formed. As can be seen in figure 192, by 700 °C the smooth BaM loop had formed and H_c peaked at a low value of 0.489 T, decreasing as M_s increased with temperature to values equal to the unsteamed BaM at 1000 °C. 700 °C was a low temperature for a good quality BaM to form, but it could be improved markedly by steaming from 400 - 800 °C / 3hr to give a product with both high M_s and H_c 193, perhaps due to a slightly smaller ridge width than the fibres steamed directly at 800 °C.

Steamed at	M_s	H_c	M_r / M_s	Grain Structure
500 °C / 3hr	7.5	0.289	0.46	None apparent > 0.1 μm
600 °C / 3hr	23.1	0.365	0.45	Aligned linear ridges 0.2 μm wide
700 °C / 3hr	56.8	0.489	0.47	Aligned linear ridges 0.2 μm wide
800 °C / 3hr	64.8	0.440	0.47	Aligned linear ridges 0.25 - 0.3 μm wide
400 - 800 °C / 3hr	65.4	0.530	0.48	Aligned linear ridges 0.2 μm wide
900 °C / 3hr	67.6	0.400	0.46	Random platelets 1 - 2 x 0.2 - 0.3 μm

Table 5.5 Effects of steaming on magnetic properties for BaM fibres (stored 3 yr) aligned ll to H.

Random BaM fibres made from Fe/NO_3 sols and ultrasonically peptised sols, and fired to 1000 °C / 3hr, are shown in figure 194. The Fe/NO_3 route demonstrated no advantage over the halide route, with M_s = 58.4 emu g^{-1} (1.0% error) and H_c = 0.504 T, while the ultrasonic sol had a high M_s of 66.2 emu g^{-1} (0.2% error) despite the obvious porosity, but a low H_c of 0.377 T, caused by the platelikel x 0.2 - 0.4 μm grains.

4.2.1 Doped BaM fibres

Several dopants were added to BaM for microstructural reasons, but only the rare earth metals were found to have any effect on the magnetic properties. M ferrites have been doped with up to 1% La_2O_3, and a level of 0.7% was reported to be the optimum for raising M_s and T_c and

gave a square loop [364], and Gd^{3+} has also been claimed to have beneficial effects. Random BaM fibres doped with 1% La_2O_3 and Gd_2O_3 fired to 1000 °C / 3hr are compared to normal BaM in figure 195, and it can be seen that the dopings had little effect on H_c, which is only slightly lower due to a grain size of 0.2 μm. However, while La^{3+} lowered M_s slightly to 56.0 emu g^{-1}, Gd^{3+} had raised M_s to 82.1 emu g^{-1}, much higher than the maximum possible for undoped BaM. Upon firing at 1200 °C / 3hr M_s had increased even more to 96.0 emu g^{-1} , and extremely high saturation magnetisation for an M ferrite, although most grains had grown to 1 - 4 μm x 0.5 μm at this point, and DGG had commenced giving some elongated plates up to 15 μm long and reducing H_c accordingly to 0.296 T.

4.3 SrM fibres

The saturation magnetisation of single crystal SrM has been variously reported at values between 92.6 emu g^{-1} [230] and 74.3 emu g^{-1} [250] and the maximum coercivity is around 0.670 T [330], but polycrystalline samples would be expected to have lower values. An old sample of SrM was measured and found to be similar to BaM but with lower H_c, with M_s = 63.3 emu g^{-1} (0.7% error) and H_c = 0.430 T at 1000 °C. This was precisely between the parallel and perpendicular M_s values for aligned SrM fibres, the M_s of the sample at 45° to H was slightly higher than for parallel, and unlike BaM there was a small increase in H_c for all the aligned samples (fig. 196). SrM is reported as having a larger coercivity than BaM, and in the old fibres the smaller H_c was explained by the microstructure which was larger at up to 1 μm. However, fibres which were stored for 3 yr before firing to 1000 °C / 3hr had a much greater coercivity of 0.570 T, as can be seen in figure 197, although coercivity was also much reduced to 0.485 T in the random sample. Again in these fibres the random sample came midway between the parallel and perpendicular aligned samples (fig. 198), with M_s = 58.3 emu g^{-1} (0.8% error) for random SrM and the average M_s of the aligned fibres = 59.0 emu g^{-1}, indicating as before that any error was well within the 7.1% weight error. As shown in table 5.6 both SrM fibres exhibited greater magnetic alignment effects than the BaM fibres despite a

worse degree of visible alignment than BaM, and this was improved to an enhancement in M_s of 39.2% from random values with alignment parallel to H.

	Aligned || to H			Aligned _|_ to H			|| vs. _|_		Random fibre		
Age	M_s	H_c	M_r/M_s	M_s	H_c	M_r/M_s	||:_|_	|| + _|_ / 2	M_s	H_c	M_r/M_s
0 yr	80.5	0.464	0.46	46.1	0.470	0.51	1.75	63.3	63.3	0.430	0.50
2 yr	82.1	0.568	0.49	35.8	0.568	0.51	2.29	59.0	58.3	0.485	0.51

Table 5.6 Comparison of aligned and random SrM fibres, fired to 1000 °C / 3hr after being stored for 0 and 2 yr after spinning. The M_s values of || and _|_ alignments are compared in the || vs. _|_ columns.

1000 °C for	M_s / emu g^{-1}	H_c / T	M_r / M_s
10 min	78.2	0.268	0.49
3hr	82.1	0.568	0.49
24 hr	85.1	0.470	0.48
100 hr	88.9	0.499	0.48

Table 5.7 Variations in magnetic properties with firing time at 1000 °C for SrM fibres (stored 2yr) aligned || to H. Error in M_s = 7.1%

The increased coercivity would suggest a reduced grain size in the stored fibres, but the opposite was found to be the case, with the fibre consisting entirely of platelets 0.5 - 2 μm x 0.1 μm, which appear to be randomly arranged except for some larger plates forming with the plane on the surface of the fibre, and pores up to 0.5 μm clearly visible in SEM micrographs (fig. 199). The fact that coercivity dropped by up to 15% when these aligned fibres were broken up to make a random sample, combined with the greater alignment effects in the apparently less well aligned SrM fibres, suggested that the alignment of the plane of the surface platelets with H was responsible for these improvements in a fibre which was otherwise microstructurally inferior to the BaM stored fibre, and which had a lower average and random M_s value than the old SrM fibre. M_s of the stored fibres fired at 1000 °C was found to increase with firing time (fig. 200), unlike the BaM fibres, while H_c decreased sharply (17.3% fall) between 3 and 24 hr, as the microstructure became less porous looking and the

grains grew up to 1.5 μm x 0.4 μm (table 5.7). In all SrM samples M_r/M_s indicated that the grains were magnetically isotropic.

The evolution of magnetic properties with temperature are detailed in table 5.8, and figure 201 for the stored SrM fibres, and it appeared that they developed more slowly than for BaM which had a well developed minor M phase at 700 °C. However, by 800 °C a good quality M phase had formed with a peak H_c of 0.592 T, indicating a smaller grain size than at 1000 °C. The fibres contained none of the grains seen at 1000 °C, just the linear ridges seen in the stored BaM fibres, and they exhibited less of an alignment effect, as can be seen in figure 202. The parallel and perpendicular M_s values were 69.3 and 43.2 emu g^{-1}, giving an average of 56.3 emu g^{-1} (7.1% error) and a ratio of ||:_|_ = 1.6, resembling the BaM fibres, supplying more evidence that it was the "surface island" grains that gave the increased alignment effects in the 1000 °C samples. Unlike the BaM fibres, when fired at 700 °C / 100 hr a well developed SrM loop had formed with smooth sides and M_s of 54.1 emu g^{-1}, although H_c had not increased indicating that no further grain growth had occurred (fig. 203). At 1200 °C / 3hr grain growth had caused H_c to drop by 34.9%, and the parallel and perpendicular M_s values of 95.0 and 79.9 emu g^{-1} gave an average M_s of 87.5 emu g^{-1}, with a drop in alignment effects to ||:_|_ = 1.19. Due to its better resemblance to the BaM fibres, the SrM fibre fired to 800 °C / 3hr was cooled and the results are in table 5.9. They show the same trends at BaM with Ms increasing and H_c decreasing with temperature while M_r/M_s remains constant (figs. 204 and 205).

Temp. / 3hr	M_s	H_c	M_r / M_s	Grain Structure	Error in M_s
400 °C	3.0	0.143	0.39	None apparent > 0.1 μm	10.0%
700 °C	10.0	0.387	0.43	None apparent > 0.1 μm	10.0%
800 °C	69.3	0.592	0.50	Aligned linear Ridges	7.1%
1000 °C	82.1	0.568	0.49	Random platelets 0.5 - 2 x 0.1 μm	7.1%
1200 °C	95.0	0.370	0.49	Hexagonal plates up to 5 μm	7.1%

Table 5.8 Variations in magnetic properties with firing temperature for SrM fibres (stored 2yr) aligned || to H.

The steamed SrM fibres showed much improvement in microstructure and lower coercivities (table 5.10), much like the BaM fibres, and their alignment effects were accordingly more normal as well. An uneven M-type loop appeared at 600 °C and was well formed by 700 °C, the linear ridges were present at 800 °C / 3hr, and there was little increase in M_s and only a small drop in H_c when scaly platelets appeared at 900 °C /3hr (fig.206). However, steaming from 400 - 800 °C / 3hr not only increased H_c by 18.6% compared to the 800 °C / 3hr sample, but there was no microstructure over 0.1 μm, M_s was increased greatly, and the sides of the loop were smoothed (fig. 207), probably because the SrM fibres form a magnetically mature product at lower temperatures than BaM.

Temp. / K	M_s / emu g^{-1}	H_c / T	M_r / M_s
300	72.4	0.608	0.50
250	78.1	0.572	0.50
200	83.9	0.541	0.51
150	88.9	0.518	0.51
100	92.8	0.503	0.51

Table 5.9 Variations in magnetic properties with measuring temperature for SrM fibres (stored 2yr) fired to 800 °C / 3hr and aligned ‖ to H. Error in M_s = 7.1%.

Steamed at	M_s	H_c	M_r / M_s	Grain Structure
500 °C / 3hr	6.5	0.294	0.48	None apparent > 0.1 μm
600 °C / 3hr	18.2	0.441	0.50	None apparent > 0.1 μm
700 °C / 3hr	55.1	0.464	0.48	None apparent > 0.1 μm
800 °C / 3hr	69.2	0.485	0.49	Aligned linear ridges 0.2 μm wide
400 - 800 °C / 3hr	81.4	0.575	0.49	None apparent > 0.1 μm
900 °C / 3hr	71.2	0.432	0.48	Random platelets 0.5 - 1.5 x 0.2 μm

Table 5.10 Effects of steaming on magnetic properties for SrM fibres (stored 2 yr) aligned ‖ to H.

SrM random fibres made from an Fe/NO_3 sol proved better than BaM, with M_s = 65.0 emu g^{-1} (0.7%) and H_c = 0.553 T at 1000 °C / 3hr (fig. 194), and they had no grain structure over 0.1 μm. A mixed $Ba_{0.5}Sr_{0.5}M$ random fibre was made and compared to BaM and SrM, but its properties did not fall between those of the pure M ferrites (Fig. 208). The fibres at

800 °C / 3hr had a structure of pores and grains up to 0.4 μm wide, and a low M_s of 50.8 emu g^{-1} and H_c = 0.379 T. While at 1000 °C the microstructure and M_s had become BaM-like, H_c had fallen even more to only 0.321 T.

4.4 Substituted CoTiM fibres

The substitution of Fe^{3+} in M ferrites with Co^{2+}/Ti^{4+} is known to greatly reduce coercivity and remanence without much loss of magnetic moment. The hard ferrite becomes increasingly soft and less anisotropic with increasing substitution until it becomes a ferroxplana ferrite. Such substitution has also been proved to change their magnetic properties over the microwave region, and a wide band of FMR frequencies are attainable with variations in doping levels. However, only the effects on H_c, M_s and the hysteresis loop are discussed in this thesis.

4.4.1 $BaCo_xTi_xFe_{12-x}O_{19}$ fibres

The characteristics of the random $BaCo_xTi_xFe_{12-x}O_{19}$ fibres for x = 0.5, 0.75, 1.0 and 1.1 are shown in table 5.11, and it can be seen that the ferrites became increasingly magnetically soft with substitution. There was a steady but small decrease in M_s with increasing x, and the values were very high for these ferrites, especially for the lower substitutions (fig. 209). Usually samples reported with high M_s have less of a drop in H_c, such as M_s of 58 emu g^{-1} and a coercivity of 0.080 T [37] or M_s = 45 emu g^{-1} and H_c = 0.020 T at x = 1 [96]. However, in the fibres, despite the decrease in M_s being steady there was a very noticeable jump from hard to soft ferrite between x = 0.75 and 1.0 to give products with almost no loop width for x > 1.0 (fig. 210), and at x = 1.1 the loop developed the lobes seen in the ferroxplana fibres discussed in later sections. In the fibres fired to 1200 °C / 3hr all of the fibres had become soft and M_r had decreased drastically as grain growth occurred, with little change in M_s (fig. 211). The x = 1.1 fibre had a coercivity as small as the best Co_2Z ferrites (fig. 212) as grains as large as 8 μm appeared, but without DGG. The x = 0.5 and 1.0 fibres resembled the stored SrM fibres at 1000 °C and "surface islands" were seen in the x = 0.5 fibres, suggesting that an aligned form

could have the same enhanced alignments effects. The properties are shown in table 5.12. When the x = 0.5 ferrite was made with a range of grain sizes from various synthetic routes it was found that H_c was directly related to grain size, with H_c = 0.360 T at 100 nm, 0.250 T at 200 nm and below 0.100 T with grains over 1 μm [380], and H_c also decreases from paramagnetic effects below 100 nm [381]. This indicated that the x = 0.5 fibres, with H_c = 0.221 T at 1000 °C / 3hr, had a grain size of around 300 nm.

x	M_s / emu g^{-1}	H_c / T	M_r / M_s	Error in M_s
0.5	63.9	0.221	0.48	0.6%
0.75	58.6	0.121	0.47	0.3%
1.0	53.6	0.024	0.33	0.5%
1.1	48.6	0.008	0.24	0.4%

Table 5.11 Variations in magnetic properties with x for random $BaCo_xTi_xFe_{12-2x}O_{19}$ fibres fired to 1000 °C.

x	M_s / emu g^{-1}	H_c / T	M_r / M_s	Error in M_s
0.5	57.9	0.085	0.36	0.9%
1.0	54.2	0.011	0.16	2.3%
1.1	53.8	0.007	0.13	0.4%

Table 5.12 Variations in magnetic properties with x for random $BaCo_xTi_xFe_{12-2x}O_{19}$ fibres fired to 1200 °C.

The behaviour of the CoTiM ferrites when cooled is unusual, in that M_s reaches a maximum and then begins to drop, and H_c and M_r reach a trough and then increase again. The M_s peak temperature and the degree of the rise of H_c and M_r once past their trough increase with x. The cooled x = 0.5 fibres are shown in figure 213, and it can be seen from table 5.13 that the M_s minimum had not been reached by 50 K, although the rate of decrease was slowing. The trend seen in M_s of an increase of 23.3% between 300 - 200 K and 12.3% between 200 - 100 K was greater than that reported for x = 0.5, where M_s = 49 emu g^{-1} at 300 K, 57 at 200 K (16.3% rise) and 61 at 100 K (7.0% rise) [96]. H_c and M_r both reached their minimum at 200 K, and it can be seen in figure 214 that H_c is larger at 50K than 300 K.

The loops of the cooled x = 1.0 fibres are shown in figure 215, and the soft ferrite became hard at low temperatures. Figure 216 shows that M_s reached a maximum between 50 - 100 K, dropping at 10 K to approximately the 150 K value. H_c and M_r quickly reached their minimum values between 250 - 200 K, reaching room temperature values at 150 K and the ferrite became hard between 10 - 50 K (fig. 217), with $M_r/M_s = 0.51$. The properties are shown in table 5.14.

Temp. / K	M_s / emu g^{-1}	H_c / T	M_r / M_s
300	63.9	0.221	0.48
250	70.0	0.208	0.48
200	78.8	0.203	0.47
150	83.0	0.208	0.48
100	88.5	0.222	0.48
50	91.9	0.241	0.49

Table 5.13 Variations in magnetic properties with measuring temperature for random $BaCo_{0.5}Ti_{0.5}Fe_{11}O_{19}$ fibres fired to 1000 °C / 3hr. Error in $M_s = 0.6\%$.

Temp. / K	M_s / emu g^{-1}	H_c / T	M_r / M_s
300	53.6	0.024	0.33
250	60.2	0.014	0.22
200	65.3	0.015	0.16
150	68.2	0.026	0.22
100	69.4	0.057	0.36
50	69.2	0.098	0.44
10	68.5	0.136	0.51

Table 5.14 Variations in magnetic properties with measuring temperature for random $BaCoTiFe_{10}O_{19}$ fibres fired to 1000 °C / 3hr. Error in $M_s = 0.5\%$.

4.4.2 $SrCo_xTi_xFe_{12-x}O_{19}$ fibres

There are no reports of this material, but would be expected to show similar pattern of behaviour to the barium analogues, and therefore the aligned fibres of x = 0.5 and 1.0 were investigated. The characteristics of the aligned and random fibres fired to 1000 °C are compared in table 5.15, and both exhibited alignment effects similar to the undoped ferrites.

The fibres were stored for 1 yr prior to firing.

Random x = 0.5 fibres at 1000 °C / 3hr had a slightly lower M_s of 59.9 emu g^{-1} (0.8%) and a much higher H_c at undoped levels of 0.525 T, indicating that the substitution has less effect on SrM. The parallel and perpendicular aligned samples were 17.7% above and below the average of 61.0 emu g^{-1}, well within the 8.3% weight error, but with a low alignment effect, probably caused by the high number of fibres crossing the alignment axis at 90° (fig. 218). Unusually the 45° aligned fibre sample had an M_s slightly lower than the parallel sample. After 1000 °C / 10 min the pure ferrite had formed, and the smooth and even fibres had no structure over 0.1 μm, with was no change after 3hr. The changes in magnetism with temperature are detailed in table 5.16. When fired to 800 °C / 3hr random fibres had already formed an M type loop, with a fairly high M_s at this temperature of 43.0 emu g^{-1} (0.6% error) but a lower H_c of 0.360 T, and this behaviour is different from SrM at this temperature. The fibres have no grains, but cracks in the surface and patches of white crystals give the fibres a rough surface. At 1200 °C the fibre consisted of regularly shaped random plates 0.5 - 1 x 0.2 μm, and while M_s was approximately the same as at 1000 °C, H_c had dropped to below the 800 °C value (fig. 219).

	Aligned || to H			Aligned _|_ to H			|| vs. _|_		Random fibre		
X	M_s	H_c	M_r/M_s	M_s	H_c	M_r/M_s	||:_|_	|| + _|_ / 2	M_s	H_c	M_r/M_s
0.5	71.8	0.551	0.48	50.2	0.564	0.51	1.43	61.0	59.9	0.525	0.49
1.0	57.4	0.343	0.50	38.9	0.317	0.48	1.47	48.0	47.3	0.306	0.48

Table 5.15 Comparison of aligned and random $SrCo_xTi_xFe_{12-2x}O_{19}$ fibres for x = 0.5 and 1.0. The M_s values of || and _|_ alignments are compared in the || vs. _|_ columns.

Temp. / 3hr	M_s	H_c	M_r / M_s	Grain Structure	Error in M_s
800 °C	43.0	0.360	0.49	No structure > 0.1 μm, white crystals	0.6%
1000 °C	59.9	0.525	0.49	No structure > 0.1 μm	0.8%
1200 °C	58.9	0.323	0.47	Random platelets 0.5 - 1.0 x 0.3 μm	3.1%

Table 5.16 Variations in magnetic properties with firing temperature for $SrCo_{0.5}Ti_{0.5}Fe_{11}O_{19}$ random fibres.

The surface of the x = 1.0 fibres at 1000 °C / 3hr consisted of series of discontinuous linear ridges, slightly wavy but aligned parallel to the long axis of the fibre, and they resembled the stored BaM fibres. Despite this they showed almost identical alignment effects to the x = 0.5 fibres, with a variation of 19.0% in parallel or perpendicular aligned fibres from the average of 48.0 emu g^{-1} (fig. 220). The random fibres had an M_s of 47.3 emu g^{-1} and H_c = 0.306 T, still a hard ferrite despite the high level of substitution. However, they showed a totally different change with temperature, as can be seen in figure 221. At 800 °C the fibres were covered in white crystals, and showed a weakly hard magnetic loop with M_s = 7.7. emu g^{-1} and H_c = 0.164 T, but the white crystals had gone and the true x = 1.0 ferrite phase formed after only 10 min at 1000 °C. By 1200 °C / 3hr not only had M_s reduced to 41.1 emu g^{-1} but the material had become a soft ferrite with H_c = 0.060 T and M_r/M_s = 0.25, as large grains up to 5 μm wide formed (table 5.17).

Temp. / 3hr	M_s	H_c	M_r / M_s	Grain Structure	Error in M_s
800 °C	7.7	0.164	0.46	Rough fibres covered in white crystals	2.6%
1000 °C	47.3	0.306	0.48	Discontinuous linear ridges 2.5 x 0.2 - 0.3 μm	10.0%
1200 °C	41.1	0.060	0.25	Random platelets 2.5 - 5.0 x 0.3 μm	2.8%

Table 5.17 Variations in properties with firing temperature for $SrCoTiFe_{10}O_{19}$ random fibres.

4.5 Co_2Y fibres

An old sample of Co_2Y ferrite fired to 1000 °C / 3hr was available, and also demonstrated alignment effects, although to a lesser extent than the M ferrite fibres with a variation of M_s of only 13.4% from the average value (6.3% error), as shown in figure 222. However, the average M_s of 34.4 emu g^{-1} was very close to the reported room temperature saturation magnetisation of 34 emu g^{-1} and small coercivity [7]. Apart from being soft ferrites, the Co_2Y fibres differed from the M ferrites in several ways. The 45° aligned sample exactly matched the parallel sample, implying that the true value for 45° was in fact lower than for parallel, probably due to the better alignment of the Y fibres compared to the M fibres. There was also

an alignment effect on the other properties with a small but significant reduction in H_c and increase M_r/M_s in the parallel and 45° samples. The coercivity of hexagonal ferrites is reduced by elongation effects in aligned crystals, as it resembles an increase in grain size, and M_r/M_s = 0.36 in isotropic samples, rising in oriented samples [7]. This implied that there was a higher degree of alignment of grains in the parallel sample, and it could be seen in SEM micrographs of Co_2Y microstructure that although the grains appeared to be randomly arranged hexagonal plates 1 - 3 μm wide, many were seen as flat plates on the surface of the fibre, parallel to the fibre axis (fig. 223). This small degree of anisotropy could result in the mean grain width being slightly larger along the fibre (parallel to alignment) than across the width of the fibre, accounting for the variations observed in H_c and M_r, and it was only because of the small coercivity that any effect could be seen. Another difference from the hard ferrites was the presence of "lobes" resulting in a slight thickening of the loop at low field just above and below the remanence values, giving almost a slightly perminvar-shaped loop. Conar anisotropy has been seen to induce a perminvar type loop in single domain particles of $Co_{1.75}Zn_{0.25}Y$ and $Co_{1.75}Zn_{0.25}Z$, and lobes have been seen in sub-domain-sized polycrystalline oriented Y, Z and W ferrites when at an angle of 45° to an applied field, which gave a perminvar loop at 90° and a paramagnetic loop when aligned with the field [382]. In the planar Y samples the lobes were larger (more perminvar-like) in perpendicular samples than the parallel and 45° samples, again giving evidence for very slight anisotropy effects.

In fibres stored for 3 yr prior to firing to 1000 °C / 3hr similar alignment effects were seen, with a variation of 22.9% from the average M_s of 35.4 emu g^{-1} (5% error), and again fibres aligned at 45° and parallel to H were identical (fig. 224). Random fibres had an M_s of 35.8 emu g^{-1} (0.3%) confirming the accuracy of the aligned sample, and the other properties resembled the 45° and parallel samples rather than the perpendicular sample (table 5.18). This implied that the small differences in lobes, H_c and M_r values were only apparent when aligned precisely perpendicular to H, as random, 45° and parallel samples were all equivalent in this respect, and that the definite alignment effects in M_s were separate from any possible

crystalline anisotropy. The improved alignment effect was typical for stored samples.

The loops for stored aligned fibres fired to 1000 °C for varying times are shown in figure 225, along with fibre fired to 1200 °C / 3hr. Any variation in M_s was within the errors of the small aligned samples at 1000 °C, but at 1200 °C M_s had clearly increased by around 10% as larger and more equiaxed grains up to 2 μm thick and 10 μm wide developed, and H_c was correspondingly reduced to only 0.014T. The evolution of the loop shape at 1000 °C over time is shown in more detail in figure 226, H_c increasing from 0.040 T after 10 min to a maximum of 0.050 T after 3hr, and the lobes had developed by this point. A change in morphology was observed in the 24 hr sample giving thicker, platy and more randomly distributed grains, and H_c decreased to 0.019 T with loss of lobes and a decrease in M_r/M_s to 0.35.

Age	Stored 3 yr before firing			Stored 0 yr before firing	
Alignment	|| to H	_|_ to H	Random	|| to H	_|_ to H
M_s / emu g^{-1}	43.5	27.3	35.8	39.0	29.8
||:_|_	1.59		n/a	1.31	
|| + _|_ / 2	35.4 emu g^{-1}		n/a	34.4 emu g^{-1}	
H_c / T	0.046	0.051	0.045	0.038	0.043
M_r / M_s	0.46	0.39	0.46	0.54	0.41
Lobe width / T	0.15	0.18	0.14	0.16	0.19
Error in M_s	5.0%	5.0%	0.56%	6.3%	6.3%

Table 5.18 Comparison of aligned and random Co_2Y fibres, fired to 1000 °C / 3hr after being stored for 0 and 3 yr after spinning. The M_s values of || and _|_ alignments are compared.

Co_2Y shows only a small increase in M_s with cooling, reported as being 35 emu g^{-1} at 300 K, 36 at 250 K, 37.5 at 200 K, 38 at 150 K and 38.5 at 100 K [306], and the aligned fibres fired to 1000 °C / 3hr exhibited a similar change as shown in figure 227. The changes in loop shape were more marked (fig. 228), with increases in lobe width, M_r and H_c as the ferrite becomes hard below 200 K, and the results are summarised in table 5.19.

When steamed the Co_2Y fibres had low M_s values similar to the M fibres at 500 and

600 °C / 3hr and with no apparent grain structure in SEM micrographs, but the fibres were magnetically soft with coercivities at Co_2Y values (table 5.20). Again the alignment was also lost, and these figures for fibre aligned parallel to H can be approximated to random fibre. As in the M fibres at 700 °C a smooth-sided hard ferrite loop had formed, with an M_s much higher than Co_2Y and a microstructure consisting of aligned linear ridges, confirming the XRD data that the BaM phase had formed as the major phase as a precursor to Co_2Y (fig. 229). This had been totally replaced in turn by a typical Y ferrite loop at 800 °C / 3hr with properties as good as the air fired 1000 °C / 3hr fibre, and the surface plates had begun to form as well suggesting there would be anisotropy effects even at this lower temperature. At 900 °C / 3hr the grain structure had deteriorated with little change in magnetic properties, and unlike the M fibres, steaming over 400 - 800 °C / 3hr gave an inferior product to 800 °C / 3hr, with lower M_s and H_c values and much wider lobes, resembling the magnetically immature sample fired in air at 1000 °C / 10min (fig. 230).

Temp. / K	M_s / emu g^{-1}	H_c / T	M_r / M_s	Lobe Width / T
300	43.25	0.050	0.49	0.18
250	46.0	0.075	0.52	0.21
200	48.3	0.095	0.54	0.26
150	49.7	0.121	0.56	0.35
100	50.6	0.153	0.59	0.41

Table 5.19 Variations in magnetic properties with measuring temperature for Co_2Y fibres (stored 3yr) aligned ∥ to H and fired to 1000 °C / 3hr. Error in M_s = 5.0%.

Steamed at	M_s	H_c	M_r / M_s	Grain Structure
500 °C / 3hr	13.4	0.044	0.14	None apparent > 0.1 μm
600 °C / 3hr	17.4	0.049	0.13	None apparent > 0.1 μm
700 °C / 3hr	49.0	0.123	0.42	Aligned linear ridges 0.2 μm wide
800 °C / 3hr	37.6	0.047	0.55	Random platelets 1 - 3 x 0.1 - 0.2 μm
400 - 800 °C / 3hr	36.0	0.039	0.39	Random platelets 1 - 2 x 0.1 - 0.2 μm
900 °C / 3hr	36.3	0.050	0.42	Random platelets 1 - 4 x 0.2 - 0.4 μm

Table 5.20 Effects of steaming on magnetic properties for Co_2Y fibres (stored 3 yr) aligned ∥ to H.

4.5.1 Other Y ferrites

Random fibres of stoichiometric Ni_2Y, Mn_2Y and Zn_2Y were fired to 1000 °C / 3hr and their magnetic properties measured, and their loops are compared in figure 231. The Ni_2Y fibres formed a good Y-type loop, with M_s = 25.7 emu g^{-1} (0.14% error), H_c = 0.043 T, M_r/M_s = 0.46 and lobes 0.18 T wide, which compared well with literature values of M_s = 24 emu g^{-1} [7]. The microstructure also resembled that of the Co_2Y fibres, but with larger grains and almost no plates flat on the surface. The Mn_2Y fibres had clearly not formed the Y phase, giving a very good hard ferrite loop with an M_s of 41.7 emu g^{-1}, H_c of 0.535 T and M_r/M_s of 0.50. The Zn_2Y fibres did form a soft ferrite, but it more resembled a magnetically good Z phase than Y, with small lobes 0.12 T wide, and a very low H_c of 0.009 T and M_r/M_s = 0.30. The M_s was 23.6 emu g^{-1} (0.6% error), well below the reported values for Zn_2Y of 42 emu g^{-1} and Zn_2Z of 58 emu g^{-1} [7]. The non-magnetic Zn^{2+} ion increases magnetic moment as it reduces the number of opposing spins to Fe^{3+} by prefiring tetrahedral sites, but the effect can be less pronounced in Y ferrites as substitution in the non-magnetic T block has no effect. Although as in the XRD patterns the phase cannot be identified, the microstructure does consist of large grain 3 - 5 μm x 0.5 μm which more resemble Z ferrite, although no DGG has occurred.

4.6 Co_2Z fibres

The pure Co_2Z phase is difficult to form and hard to identify from XRD due to the similarity of the other ferroxplana patterns, but it is easily distinguishable from the other phases by the magnetic hysteresis loop, which has an M_s of 51 emu g^{-1} at room temperature and an extremely small coercivity with almost no loop width [7]. DGG appears to be unavoidable in the Co_2Z phase, and while it can indicate the formation of Co_2Z from the precursor other phases such as Co_2W and Co_2X also occur only with the event of DGG.

All of the Co_2Z fibres first formed equal mixes of Co_2Y and BaM at 1000 °C / 3hr, with a morphology of 1 - 2 mm x 0.2 mm platelets, resembling the Co_2Y fibres. As could be

seen from figure 232 this was a hard ferrite with a smooth and even loop, but with H_c reduced to 0.145 T and $M_r/M_s = 0.46$, and an average M_s value similar to that of Co_2Y. The alignment effects were clear with a variation of 37.9% from the average of 31.7 emu g^{-1} (7.1% error), as good as in the best M ferrite aligned fibres. Upon firing for longer periods at 1000 °C no change is phase occurred and M_s remained constant, but unusually H_c increased by 82.8% to 0.265 T and $M_r/M_s = 0.49$ as the grains grew thicker and up to 5 μm wide (fig. 233).

The hysteresis loop of old aligned Co_2Z fibres fired to 1250 °C / 3hr after drying is shown in figure 234, and it could be seen that any alignment effect present in the precursor fibre was lost. This was found to occur in all of the Co_2Z fibres, and although they appeared well aligned on a large scale, it could be seen in SEM micrographs that the fibres had become wavy and twig-like, with many more fibres crossing the alignment than was seen in the precursor fibre (fig. 235). This seemed an inevitable result of DGG, and it can be seen in the SEMs of Co_2Z in chapter 4 that there is no apparent alignment on the small scale. M_s agreed precisely with reported values at 51.5 emu g^{-1}, and H_c was extremely low at 0.010 T with $M_r/M_s = 0.28$ and the presence of lobes 0.15 T wide, which were very large compared to the loop width. No gel fibre sample of this remained for retrospective firings after storage, so new fibres were spun.

Due to the difficulties discussed in chapter four with Z phase identification, it was not until VSM studies were under taken that a truly accurate assessment of the Z content in the fibre was possible. It was found that retention of chlorine in the original sol, from insufficient washing of the precipitate, greatly affected the end product with some fibres never forming the Z phase, only Y and W ferrite. The quality of the Z product could be assessed by the size of lobes, with larger lobes giving a product with higher H_c, presumably as the lobes were caused by the presence of either Co_2Y or Co_2W as a minor phase. It was also found that the original Co_2Z fibre was a relatively good sample. A typically poor Z ferrite, produced from a sol that was made from a precipitate washed with only 2 x 50 ml water instead of the usual 4 washes, is shown in figure 236 fired to 1250 °C. Although M_s was still near the expected value at 50.8

emu g^{-1}, H_c and M_r/M_s were increased to 0.049 T and 0.33 respectively, nearer to Co_2Y values, and the lobe width was 0.30 T. When a sol was made from a precipitate washed 10 times using a centrifuge until a conductivity of < 1 μS was obtained, the best Co_2Z fibre was produced at 1250 °C, and the loops of the fibre fired to 1000 °C and 1250 °C / 3hr are shown in figure 237. It can be seen that again the precursor fibres at 1000 ^{0}C exhibited good alignment effects which were lost in the final product, and that there is almost no loop or lobes, with H_c being 0.007 T and M_r/M_s = 0.18. The very high M_s of 61.8 emu g^{-1} was more than any previously reported value for even single crystals of this material, was unaffected by alignment, and even with the maximum weight error of 6.3% it was at least 57.9 emu g^{-1}.

The M_s of Co_2Z is reported to increase with cooling from 50 emu g^{-1} at 300 K to 56 at 200 K, 56 at 200 K, 64 at 100 K and 69 at 0 K [7]. When the pure Co_2Z fibres were cooled, M_s passed the highest value at only 150 K, reaching 77.7 emu g^{-1} at 50 K, and H_c and M_r/M_s only increased very slightly until below 50 K, as shown in figure 238. It could be seen in the expanded view in figure 239 that there was lobing even in this very narrow Z loop above 50 K, with the loop becoming even sided at this temperature. However, even though the initial M_s was lower, at low temperatures the poor Co_2Z fibres reached equally high values for M_s (fig. 240), indicating that they were essentially the same material as the superior fibres, and that the DGG morphology of the Co_2Z fibres resulted in an intrinsically superior material in which the various anisotropy constants behaved differently with temperature for differing preparations. These results are detailed in tables 5.21 and 5.22.

Temp. / K	M_s / emu g^{-1}	H_c / T	M_r / M_s
300	61.8	0.007	0.18
250	63.7	0.007	0.20
200	68.5	0.010	0.22
150	72.5	0.010	0.29
100	76.0	0.012	0.32
50	77.7	0.028	0.41

Table 5.21 Variations in magnetic properties with measuring temperature for pure Co_2Z fibres aligned 45° to H and fired to 1250 °C / 3hr. Error in M_s = 6.3%

Temp. / K	M_s / emu g^{-1}	H_c / T	M_r / M_s
300	50.8	0.049	0.33
250	56.7	0.049	0.33
200	63.0	0.050	0.34
150	68.8	0.056	0.37
100	73.6	0.056	0.38
50	76.7	0.066	0.39
5	77.6	0.080	0.41

Table 5.22 Variations in magnetic properties with measuring temperature for mixed phase Co_2Z fibres aligned 45° to H and fired to 1250 °C / 3hr. Error in M_s = 5.0%

Co_2Z fibres steamed at 900 °C / 3hr exhibited a larger grain size (up to 4 μm) than the normal Z precursor fibres, and as can be seen from figure 241 they bore no resemblance to the usual mixed M/Y fibres, having a soft loop with H_c of only 0.052 T parallel and 0.070 T perpendicular. This alignment effect in coercivity was seen in all the steamed Z fibres with soft loops, and again it was due to the growth of plates on the surface of the fibre, which developed into grains with the hexagonal plane elongated along the fibre axis, resulting in an increased mean grain size in that axis and therefore lower H_c. Unless stated other wise, all the values quoted for the steamed fibres were for those aligned parallel to H, and they are summarised in table 5.23. The fibres also showed a very slight alignment effect in M_s of 2.2% from an average of 49.5 emu g^{-1}, and the fibres had lobes 0.23 T wide and M_r/M_s = 0.36, implying that they were closer to poor Co_2Z than Co_2Y. It can be seen in figure 242 that the steamed fibres had lost their alignment, similar to the other steamed fibres. At 1150 °C there was little change in M_s and a loss of any alignment effect in this, although H_c was 76% bigger perpendicular to H. H_c had decreased further to 0.025 T and the lobe width to 0.13 T, indicating that the Z phase had definitely formed, and although the grains had grown to 1 - 6 μm, DGG had not occurred (fig. 243). This was the first unambiguous evidence of Co_2Z forming without DGG occurring first. At 1200 °C H_c had dropped to 0.015 T with a lobe width of only 0.07 T, but M_s had also decreased to 43.1 emu g^{-1} and DGG had commenced,

albeit still to a lesser extent than usual. By 1250 °C Z had begun to decompose, probably to W, with a lower M_s of 33.9 emu g^{-1} and increase of loop and lobe width (fig. 241).

Regime	Temp.	M_s	H_c	M_r / M_s	Lobes	Grain Size
A	Steam	48.4	0.052	0.36	0.23	1 - 4 x 0.3 - 0.4 μm
A	1150 °C	49.3	0.025	0.18	0.13	1 - 6 x 0.5 - 1.5 μm
A	1200 °C	43.1	0.015	0.17	0.07	5 - 20 x 0.5 - 2 μm, most < 10 μm
A	1250 °C	33.9	0.026	0.29	0.25	DGG, 5 - 20 x 0.5 - 2 μm
B	Steam	60.5	0.113	0.45	none	1 - 4 x 0.2 - 0.3 μm
B	1150 °C	59.8	0.084	0.36	0.25	1 - 4 x 0.2 - 0.3 μm
B	1200 °C	52.9	0.084	0.38	0.25	1 - 4 x 0.2 - 0.3 μm
B	1250 °C	29.1	0.121	0.35	0.50	DGG, > 20 μm long
C	Steam	63.9	0.082	0.38	Slight	2 - 4 x 0.3 - 0.4 μm
C	1250 °C	42.5	0.023	0.27	0.20	1 - 6 x 0.5 - 1.5 μm

Table 5.23 Effects of steaming on magnetic properties for Co_2Z fibres aligned ‖ to H. Steaming regime A = prefired to 400 °C / 3hr and steamed at 900 °C / 3hr, B = prefired to 400 °C / 3hr and steamed at 400 - 900 °C / 3hr, C = prefired to 1000 °C / 3hr and steamed at 900 °C / 3hr. Temp. is the firing temperature after steaming, where steam = values for steamed fibre.

Unlike the M and Y fibres, the Co_2Z fibres were actually made worse by steaming from 400 - 900 °C / 3hr, and it can be seen in figure 244 that the Z phase was never formed. The steamed fibre resembled unsteamed Co_2Z precursor fibres at 1000 °C, and although H_c was reduced with further firing, it never reached even Co_2Y levels, and DGG occurred as usual at 1250 °C as the product decomposed into an unidentified hard ferrite phase. It was found that if Z fibres were prefired to 1000 °C in air and then steamed at 900 °C / 3hr no alignment was lost (fig. 245), and an alignment variation of 18.1% from the average M_s of 54.1 emu g^{-1} was found. They had a grain structure resembling that of the fibres directly steamed at 900 °C, but had a soft loop with H_c of 0.82 T and $M_r/M_s = 0.38$ with slight lobing even at this temperature, implying that the fibres consisted largely of Y, Z or possibly U phases (fig. 246). Even at 1250 °C DGG had not occurred and the grains were all < 6 μm, with a decrease of both M_s and H_c

to 42.5 emu g^{-1} and 0.023 T with 0.20 T lobes. Unfortunately the familiar waviness had appeared in the fibres with grain growth (fig. 247), with corresponding loss of any alignment effects in M_s.

4.6.1 Doped Z fibres

The 0.67% CaO doped Co_2Z fibres appeared to form the pure Z phase at only 1200 °C / 3hr, and were mostly Z without DGG at 1175 °C / 3hr, with grains only 1 - 4 μm wide and 1 μm thick. At 1175 °C / 3hr the fibres were clearly still fibrous looking, and they exhibited an alignment effect of 32.2% as can be seen in figure 248. The average M_s was 35.4 emu g^{-1}, similar to both Co_2Y and the mixed M / Y precursor fibres for undoped Co_2Z at 1000 °C / 3hr. However, H_c and M_r/M_s were much lower at 0.019 T and 0.27, closer to the values seen in the old Co_2Z fibres but with a larger lobe width of 0.23 T, and superior to the poor Co_2Z fibres. At 1200 °C / 3hr DGG had occurred, although the fibres appeared slightly better aligned than the usually chaotic looking Co_2Z fibres, as shown in figure 249. Agreeing with the XRD patterns, these were good quality Z fibres, with a only slight decrease in loop width but a large drop in lobe width to 0.008T compared to the 1175 °C fibres (fig. 250). They had an average M_s of 58.8 emu g^{-1} (4.5% error), virtually equivalent to the undoped fibres at 1250°C, and also more than the previously quoted maximum values. They appeared to display a very small alignment effect (only 1.7%), unusually giving a larger M_s perpendicular to H than parallel to it, and while this could be because of the better alignment of the fibres after DGG it is a very small effect if real. A more apparent effect was the difference in H_c and M_r with alignment. In the parallel fibres H_c was smaller at 0.017 T compared to 0.026 T perpendicular to H, which could be because of the elongation of the grains along the fibre axis creating a larger mean grain width in that direction.

Considering the possible advantages of using strontium in the sol, $Sr_3Co_2Fe_{24}O_{41}$ fibres were investigated, even though substituted Sr_3Zn_2Z shows a lattice distorted by the Sr^{2+} ion, reducing drastically the magnetic properties of the compound compared to Ba_3Zn_2Z [269].

The random fibre, fired to 1250 °C / 3hr, gave a good M_s of 48.5 emu g^{-1} and a very narrow loop with H_c = 0.007 T and M_r/M_s = 0.16 with almost no lobes (fig. 251). Although this would normally constitute a perfect Z sample, it can be seen in figure 252 that the loop had a very strange shape, with unexplained sudden changes in magnetisation at fields of ~ 1.5 T, instead of the usual smooth curves.

4.7 Co_2W fibres

The only known feature of the magnetic properties of Co_2W is that it is a soft ferrite, although NiFeW has an M_s of 52 emu g^{-1}, and Co_2W would be expected to be a bit lower than this [7]. The measured loop for aligned Co_2W fibres fired to 1250 °C after drying is shown in figure 253, and it could be seen that there were no alignment effects in M_s, which was 44.3 emu g^{-1}. However, there were alignment effects in loop width, for the same reasons as explained in for the Ca doped Co_2Z in section 4.6.1 above. Parallel to H, H_c = 0.025 T, M_r/M_s = 0.56 and the lobes were 0.19 T wide, while perpendicular H_c = 0.038, M_r/M_s = 0.26 and lobe width = 0.13 T. These large differences in M_r and lobe width were very apparent, and much larger compared to H_c than those seen in Y and Z ferrites, giving the W loop a distinctive shape.

Temp. / K	M_s / emu g^{-1}	H_c / T	M_r / M_s	Lobe Width / T
300	44.3	0.025	0.56	0.19
250	49.0	0.022	0.44	0.16
200	52.9	0.033	0.64	0.19
150	56.0	0.037	0.62	0.22
100	58.9	0.043	0.70	0.28
50	60.7	0.056	0.73	0.34

Table 5.24 Variations in magnetic properties with measuring temperature for Co_2W fibres aligned ‖ to H and fired to 1250 °C / 3hr. Error in M_s = 2.8%

This shape can be seen clearly in figures 254 and 255 as it becomes more emphasised at lower temperatures, as the lobe width increases to a greater extent than H_c, and M_r grows to give ever steeper sides tot he loop as the measuring temperature is lowered. These results

are detailed in table 5.24, where it can be seen that a minimum coercivity is reached around 250 K, and the anomalous M_r result at 200 K is a measurement feature, shown by the stepped 200 K curve in figure 255.

4.8 Co_2X fibres

Single crystal Co_2X has a preferred cone of magnetisation at an angle of 74° to the c-axis, a high M_s of 57.1 emu g^{-1}, and a very low H_c of only 0.005 T in single crystal samples [12]. It can be seen in figure 256 that the fibres had not reached these values, and they may still have been a mixed phase at this temperature. At 1000 °C / 3hr the fibre was a hard ferrite with M_s = 54.4 emu g^{-1}, H_c = 0.282 T and M_r/M_s = 0.48 It resembled the mixed M/Y precursor fibres seen before the formation of Co_2Z, but the microstructure was similar to the M ferrites. By 1200 °C / 3hr the material had become a soft ferrite, with a decrease in all properties, although there were no lobes seen. Most grains had grown to 1 - 2 μm x 0.2 - 0.4 μm, and although DGG had not occurred there were some large hexagonal plates up to 20 μm wide, with a reduction of M_s to 45.0 emu g^{-1} (0.8% error), H_c = 0.085 T and M_r/M_s = 0.38. The loop was more smooth and even sided than Co_2Y, Co_2Z and Co_2W, but it had very slight lobes.

4.9 Co_2U fibres

The only known property of Co_2U is that is ferroxplana [7], and will therefore be a soft ferrite, but it could reasonably be expected to resemble Co_2Z. The hysteresis loops of Co_2U random fibres fired to 1000 and 1200 °C are shown in figure 257. At 1000 °C / 3hr the fibre was already a soft ferrite, and resembled the Co_2X fibres at 1200 °C, the loop having straight and smooth sides and a similar M_s, although the microstructure was much smaller consisting mostly of grains < 0.5 μm, with a few as large as 2 μm x .02 μm. By 1200 °C / 3hr the material resembled Co_2Z with an even sided and wider loop with no lobes. M_s was similar to Co_2Z at 51.5 emu g^{-1} (0.3% error), and although the grains had grown to hexagonal plates 5 μm x 0.5 μm, with some up to 10 μm, DGG had not occurred and H_c was still 0.059 T and

M_r/M_s = 0.26. The loop was smooth and even sided, unlike Co_2Y, Co_2Z and Co_2W, and had no lobes. At 1250 °C further growth had occurred and DGG begun, but M_s was still only 52.0 emu g^{-1} and H_c = 0.050 T and M_r/M_s = 0.32, and there were still no lobes.

4.10 Sample alignment and geometry effects

As it was noted in Chapter 1, the change in alignment effect with angle from that alignment is not a linear one, and the effect reduces at an increasing rate with a greater angle from the axis of alignment. Never-the-less, the similarity between 45° and parallel to the axis was greater than would normally be expected.

The aligned fibres had mostly had a good alignment of ~90 - 95% within $^{+}/_{-}$20° of the axis of alignment, but even in the best samples only 35% were exactly aligned along the axis. Therefore, the effect could be expected to be approximately the same within an angle of 20° from this axis, so there would be little difference between parallel and 45° to H in fibres which show such alignment effects, and a great difference when perpendicular. Indeed, in the relatively poorly aligned SrM fibres 50% of the sample was at an angle of 10° to the axis, and only 12% along it. However, these two effects alone can not explain why the M_s value should be equal, or even greater, at 45° than parallel to H, but it can be explained by the geometry of the sample itself.

All of the aligned samples measured were 3 or 4 mm squares, with the fibres aligned parallel to two sides of the square. This meant that while the parallel and perpendicular alignments were measuring across equal lengths of fibre, the 45° sample was measured diagonally across the square sample, and therefore had an uneven distribution of fibre across the sample from low at the edges to 41% longer in the centre. To compare the geometry effects two other samples were made, one a 4 mm square but with the alignment diagonally across the square, and one a circle of 4 mm diameter. Differences in volume fraction between the samples were unimportant as only the ratios of M_s in fibre aligned parallel, perpendicular and 45° to H, as well as random fibre, were compared for each shape, and the results are

shown in table 5.25. Well aligned BaM fibres fired to 1000 °C were used, as they were both magnetically and crystalinely isotropic.

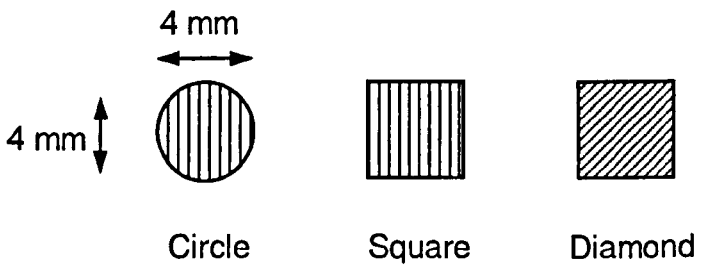

Shape	∥:⊥	∥:45°	∥:random	Random:⊥
Square	1.61	0.99	1.30	1.24
Diamond	1.57	1.07	1.23	1.27
Circle	1.43	1.03	1.20	1.19

Table 5.25 Summary of effect of sample geometry on alignment effects observed in M_s for BaM samples fired to 1000 °C / 3hr.

Several conclusions could be drawn from these results. Firstly the parallel aligned fibre always had a greater value than the perpendicular by a large factor between 40% and 60%. The 45° aligned sample was slightly higher (+1%) than parallel in the square sample, slightly lower (-3%) in the circular sample and significantly lower (-7%) in the diamond sample. As the ratios were diminished and inflated to equal degrees in the square and diamond samples, the true value was probably between these two values, which coincided with the value for the unbiased circular sample. This suggested that in reality the alignment effect at 45° alignment was 3% less than in parallel alignment, and although this is high it can be explained by the other phenomena mentioned above. This also confirmed that the fibres had a 90° cone of alignment in which M_s was enhanced, centred around the axis of fibre alignment.

The circular and diamond samples did not have an equal volume fraction in parallel and perpendicular alignments throughout the width of the sample, and this appeared to affect the ∥:⊥ and random ratios, which were smaller for both compared to the square sample. As fibres can be thought of as essentially 1D objects, any loss of area in the 2D shapes would have a disproportionately larger effect parallel to alignment than perpendicular to it, as the aligned

fibres have in effect different volume fractions in these two directions. The diamond sample had higher values than the circular sample because they were enhanced by the greater length of the sample near the centre, but this indicated that the square sample best represented parallel versus perpendicular effects as the sample had an equal width throughout. For all samples, parallel and perpendicular alignments were displaced by equal amounts from the random value, although again this effect was less in the circular and diamond samples for the reason explained above. However, this does indicate that in all cases the random fibre M_s value could be approximated as half the sum of parallel and perpendicular values.

5. Conclusions

Ferrite	Temp. / °C	M_s / emu g^{-1}	H_c / T	M_r/M_s
BaM	1000	62.5 - 63.8	0.523 - 0.538	0.50 - 0.52
SrM	1000	58.3 - 63.3	0.430 - 0.485	0.50 - 0.51
$BaCo_{0.5}Ti_{0.5}Fe_{11}O_{19}$	1000	63.9	0.221	0.48
$BaCo_{0.75}Ti_{0.75}Fe_{10.5}O_{19}$	1000	58.6	0.121	0.47
$BaCoTiFe_{10}O_{19}$	1000	53.6	0.024	0.33
$BaCo_{1.1}Ti_{1.1}Fe_{9.8}O_{19}$	1000	48.6	0.008	0.24
$SrCo_{0.5}Ti_{0.5}Fe_{11}O_{19}$	1000	59.9	0.525	0.49
$SrCoTiFe_{10}O_{19}$	1000	47.3	0.306	0.48
Co_2Y	1000	35.8	0.045	0.46
Co_2Z	1250	50.8 - 61.8	0.007 - 0.049	0.18 - 0.33
Ca doped Co_2Z	1200	57.3 - 59.2	0.017 - 0.026	0.20 - 0.34
Co_2W	1250	44.3	0.025	0.56
Co_2X	1200	45.0	0.085	0.38
Co_2U	1200	51.5	0.059	0.26

Table 5.26 Summary of magnetic properties of random hexagonal ferrite fibres.

The properties of random hexagonal ferrite fibres are shown in table 5.25, and it can be seen that the M ferrites had M_s values slightly below single crystal values, as seen in most polycrystalline samples, while the ferroxplana ferrites equalled the highest M_s values reported previously. The BaM and SrM fibres had high coercivities, implying a small grain size, and all

the M ferrites were isotropic, shown by their M_r/M_s values, any changes with fibre orientation must be due to fibre effects, and not from alignment of domains within the fibres.

All M and Y fibres showed alignment effects, enhancing M_s by 20 - 40% when the fibre was aligned to H, compared to the random fibre values, and the soft ferrites also exhibited alignment effects in loop width, due to crystalline anisotropy. It was found that fibres which had been stored as a dry gel for 2 - 3 yr showed an increase in alignment effects, and sometimes H_c, but no increase in M_s. While the differences could be due to decomposition of the fired samples stored for 3 yr, it is more likely that they were due to partial decomposition and halide loss in the gel fibres during storage for 3 yr. The fact that M and Y fibres exhibited this alignment enhancement with their alignment not only parallel to, but also at 45° to, H means in effect it covers a cone of 90° in which this phenomenon can be applied. If this broad enhancement was due to most of the fibres being within $^{+}/.20°$ of the axis alignment, as opposed to exactly along it, then it would be reasonable to expect the effect to be focussed and increased by an improvement in alignment. Improved alignment would also increase the volume fraction of the fibres, also increasing the effect. Sample geometry could also be used to slightly enhance or diminish the effect, but 45° and parallel to H were always roughly equal in well aligned fibres, and perpendicular to H was always lower than the random fibre value to an equal degree. This was true for all of the well aligned fibres except Co_2Z and Co_2W.

Both BaM and SrM fibres had similar M_s values of around 63 emu g^{-1} after 1000 °C / 3hr, with high coercivities for polycrystalline samples of 0.525T and 0.568 T, and an enhancement in M_s of 25 - 40% was observed in fibres aligned parallel to H. The variations in M_s and H_c with firing time at 1000 °C are shown in figures 258 and 259, and it can be seen that M_s of SrM fibres was increased greatly with longer firing times as H_c decreased. After only 10 min at 1000 °C the optimum BaM fibre had formed with M_s = 63 emu g^{-1} and H_c = 0.527 T, and these values were only slightly affected by longer firing periods. The evolutions of M_s, H_c and M_r/M_s with firing temperature are shown in figures 260 to 262, and both fibres had developed the M phase by 700 °C. The BaM fibres reached their peak in H_c and M_r at

1000 °C, and by 1200 °C the H_c of the BaM fibres had reduced to values seen in standard ceramic BaM, but M_s was near the maximum at 71 emu g^{-1}. SrM, although initially developing more slowly than BaM, showed peak H_c and M_r at the lower temperature of 800 °C, and a higher M_s at 1200 °C. The doping of BaM with Gd^{3+} raised M_s to 82.1 emu g^{-1}. The greater alignment effect, which also increased H_c, seen in the stored SrM fibres fired to 1000 °C despite a deterioration in microstructure, was attributed to the formation of islands of plates on the surface on the fibre with a long axis along the axis of alignment. At 800 °C and 1200 °C they resembled the BaM fibres. The trends in M_s and H_c with lowering temperature for BaM and SrM fibres aligned parallel to H are shown in figures 263 and 264, and it can be seen that the rates of change were very similar for both fibres, with the initial values determining the bulk of the difference between the fibres at all temperatures.

As expected the $BaCo_xTi_xFe_{12-2x}O_{19}$ fibres fired to 1000 °C showed a decrease of M_s, H_c and M_r with increasing x, but the decrease in M_s was much less than the other properties, giving a soft ferrite with high M_s at x = 1. The drop was not steady, with a sudden change in H_c and M_r between x = 0.75 and x = 1.0 but a fairly steady decrease in M_s, as can be seen from figures 265 to 267. These figures also show the fibres fired to 1200 °C, and although there was almost no change in M_s there was still a reduction in H_c and M_r, although to a lesser extent due to the larger grain size at this temperature. The plots of change in M_s, H_c and M_r with cooling are shown for x = 0.5 and 1.0 in figures 268 to 270. The x = 0.5 fibre showed a proportionally larger increase of M_s with cooling, and the x = 1.0 fibre appeared to reach a peak value between 50 - 100 K. Both fibres showed a trough in H_c and M_r around 200 K, but while there was very little variation in the x = 0.5 fibre, the x = 1.0 fibre had become a hard ferrite below 50 K. $SrCo_xTi_xFe_{12-2x}O_{19}$ fibres demonstrated the same general patterns, but they had lower M_s values and higher H_c, to such an extent that at 1000 °C even the x = 1.0 fibre was still hard, indicating that substitution had a lesser effect on SrM. Figure 271 shows that while the x = 0.5 the M phase had already formed at 800 °C, and lost H_c at 1200 °C from grain growth, the x = 1.0 fibre had barely begun to form M at 800 °C and had become soft at 1200

°C.

In Co_2Y ferrites the random M_s matched reported values of 34 emu g^{-1} and the fibres were soft ferrites with narrow loops of 0.049 T, but they exhibited possible small anisotropy effects on H_c and M_r caused by platy grains forming on the surface of the fibres. This effect was seen in all ferroxplana ferrite fibres, and was greater in those with elongated grains from DGG, and small perminvar-like deformations of the loop resulting in lobes were observed in Y, W and poor Z samples. The changes in properties with firing time are shown in figures 272 and 273, and there was little change in M_s until the fibres were fired for long periods > 24 hr. H_c and M_r width both showed large decreases between firing for 3hr and 24 hr, with little change after this, and the lobe width also decreased greatly in the first 3hr of firing, to give a loop with relatively small lobes relative to H_c compared to the W and Z fibres.

Co_2Z was found to be very dependent upon the amount of halide in the precursor sol, giving fibres with M_s ranging from 50 - 61 emu g^{-1} and H_c from 0.007 - 0.050 T, the higher M_s and lower H_c being found in those fibres with less halide to give a superior product to any reported previously. The Z phase formed from a mixed M/Y phase with a hard loop, but M_s and H_c values between those of M and Y ferrite, forming the Z loop at 1250 °C, and always accompanied by DGG in normal Z fibres. However, 0.67% CaO doped Co_2Z fibres formed the Z phase at only 1200 °C, with DGG and equivalent to all but the best non-doped samples, and an impure Z phase with low M_s had formed at 1175 °C without DGG having occurred.

Co_2W, Co_2X and Co_2U fibres were also characterised, although little is known about the magnetic properties of the materials for comparison. W had an M_s of 44.3 emu g^{-1} with no alignments effects, and despite the low H_c they had very wide lobes, giving the W loop a distinctive shape. The X fibres had M_s = 45.0 emu g^{-1} and a larger, almost hard H_c of 0.085 T with slight lobes, while U had M_s and H_c equivalent to the old Y samples but the loop was even sided with no lobes.

The behaviour of Co_2Y, Co_2W and both poor and the best Co_2Z fibres as temperature was lowered are shown in figures 274 to 277. It could clearly be seen that the Z fibre had the

highest M_s, and that although they had different values at 300 K they were approaching the same minimum at low temperatures. This indicated that they were essentially the same material and that differences in properties were due to processing differences, and that the very high M_s value for the best (low chloride) Z sample was a genuine result. There was very little change in M_s with temperature for Co_2Y, but it exhibited the largest change in H_c, becoming a hard ferrite between 200 K and 150 K, although the loop was still lobed and not M-like. The other ferrites showed lesser change in H_c, and the good Z sample remained very soft until < 100 K, and H_c was always much lower than the poor Z sample, which had higher values than the W fibre. Again the good Z fibre had a much lower M_r than the poor sample until it caught it up at 50 K, and the W fibre had a high M_r despite the low H_c because of the unique, extremely lobed loop shape, which became more exaggerated at lower temperatures

Firing BaM in steam was found to produce a product with good properties at only 700 °C / 3hr, and the optimum material was obtained by steaming from 400 - 800 °C / 3hr, and SrM was similarly improved by this later steaming regime. It can be seen in figures 278 and 279 that while any increase in M_s was small when steamed over 800 °C, H_c was lowered considerably above this temperature. At 700 °C the steamed Co_2Y fibres also formed BaM, but a magnetically excellent Co_2Y sample had formed at the low temperature of 800 °C / 3hr, and steaming at higher temperatures or at 400 - 800 °C / 3hr actually resulted in an inferior product. Co_2Z was made at very low temperatures of 1150 °C, giving a magnetically good sample without the usually omnipresent DGG, when first steamed at 900 °C. This is the first reported case of pure Co_2Z formation without DGG, giving a product with a relatively small equiaxed hexagonal grains between 1 - 6 μm wide. If the fibre was prefired to 1000 °C and then steamed, alignment could be maintained whilst still producing a Z phase without DGG at 1250 °C, but steaming over 400 - 900 °C was harmful to the Z ferrites, and they never formed the Z phase.

6. Experimental

6.1 The vibrating sample magnetometer (VSM)

In the VSM technique, which was developed in the 1950's, a sample is attached to the lower end of a rigid rod and oscillated rapidly over small vertical distance. This vibration in the z-axis is typically 1 - 2 mm at a frequency of 40 - 80 Hz. If the sample is surrounded by a set of detection coils and has a magnetisation, an AC current will be induced in these coils of an amplitude proportional to the magnetic moment of the sample [383]. The magnetic moment can then be measured as a function of applied field (M-H), temperature (M-K) or time (M-t). In the standard set up, or Foner coil, the field and vibration directions are parallel, although apparatus has been designed in which the applied field is perpendicular to the vibration [384].

A diagram of the apparatus used for this work is shown in figure 280, and it was a Maglab VSM with a helium cooled 12 T superconducting magnet, supplied by Oxford Research Instruments. Superconducting magnets have been used for around 25 years to provide a large applied field with a relatively small magnet [385]. To minimise the effects of external vibration the entire apparatus was supported on a 400 kg concrete plinth which was mounted on pads filled with compressed air. To prevent the vibrator transmitting vibrations to the body of the VSM cryostat and the sense coils within, it was mounted on a 100 kg steel table connected to the plinth by lead shot supports, and had two adjustable brass counterweights which oscillated anti-phase to the vibrator. The apparatus was controlled by six independent units, which were connected to both the VSM and a PC as shown in figure 281, and these were managed and the data collected using Oxford Object Bench software.

6.1.1 The superconducting magnet

The magnet used to produced the applied field was a 12 T Oxford Research Instruments Magnabond superconducting magnet. This was a concentric solenoid wound from multifilamentary NbTi wire in a stabilising matrix of copper, with inner coil sections of Nb_3Sn wire to give fields higher than 11 T. Such superconducting magnets have high inductances and

operate at high currents, storing large amounts of energy at high fields, of up to 2 megajoules. If the magnet suddenly changes from the superconducting state to a resistive state, for example by a rise in temperature, the current is lost almost instantly in a process known as quenching. This can be dangerous as the current can drop at a rate of 100 A s^{-1}, generating a voltage of many kV, and the VSM contained protection circuits for this eventuality. The magnet was powered by an Oxford IPS 120-10 independent power supply.

The magnet, sample, detection coils and sample heater were all situated within a two layer cryostat, consisting of an outer reservoir of liquid nitrogen and an inner 40 litre chamber of liquid helium. The cryogenic fluid levels were controlled by an Oxford ILM 211 independent level meter probe, and the helium level was never allowed to drop below 30% to reduce the risk of quenching the magnet.

6.1.2 The vibrator

The sample was vibrated through a distance of +/- 1.5 mm from zero in the z axis (parallel to the applied field), at a frequency of 55 Hz, +/- 0.05 Hz. The vibrator was a loudspeaker-type velocity transducer, consisting of two mechanically coupled loudspeakers. One of these drove the movement of the sample, and the other was a pick-up coil which fed the velocity back to the driver. The entire unit was sealed and could operate under a vacuum. The vibrator was driven by an AC power source controlled by an Oxford VCU 2 vibrational control unit.

6.1.3 Phase sensitive detector (PSD)

The current generated in the detector coils by the oscillation of the sample through them was detected by a Stanford Research Systems SR830 DSP lockin amplifier. This PSD looked for a signal oscillating in time with the vibration of the sample, but as a sine wave out of phase with the vibration by 3 - 5°, this lag caused by a time delay of around 300 ms as the signal filtered through the equipment. The detector had a range of 10 μV - 1 V, and an additional amplifier with a gain of 100 was employed for particularly weak samples. The PSD had differing levels

of sensitivity at 1 V, 500 mV, 200 mV, 100 mV, 50 mV, 10 mV, 5 mV, 2 mV, 1 mV, 500 μV, 200 μV, 100 μV, 50 μV, 20 μV and 10μV. The lockin amplifier was tuned to follow the vibrational frequency accurately (+/- 0.0001 Hz) using a reference signal from the VCU.

The lowest possible degree of sensitivity was required for each measurement, without overloading the PSD, to optimise the accuracy of the results, and for this reason a lockin amplifier was employed. In automatic mode this device tracked the level of the signal detected, and adjusted the sensitivity up or down accordingly to the lowest sensitivity range possible. However, this caused small deviations in the signal as the PSD overloaded and the signal increased to a value above the current sensitivity, and a small delay froze the signal while the lockin searched for the new sensitivity range. This was usually negligible, but in samples with a very sudden drop or increase in magnetisation, for example very soft or very square ferrites, the effect was noticeable in the hysteresis loop as a series of jagged steps as opposed to a straight line. In such samples the automatic lockin was switched off and the samples measured at a constant, high sensitivity range, with a corresponding but unavoidable small loss of accuracy. However, this only affected the regions in which the sudden decrease or increase of signal occurred at low applied fields, and the bulk of the loop and M_s were unaffected by this as the automatic lockin was reactivated at higher fields.

6.1.4 Translational movement and centring

Although the sample was oscillated up and down when the vibrator was activated, it had to be positioned precisely in the centre of the applied field before the measurement could begin. This translational movement in the z-axis was set using an Oxford SMC 4 stepper motor controller, which had a range of 0 - 30 mm between the two detector coils, although most samples were centred at 16-18 mm. To centre a sample, it was measured at a very low applied field to maintain as much of the initial magnetisation curve as possible, and with the automatic lockin deactivated. The sample was then moved between the 10 and 25 mm positions by the SMC, and a plot of M against z taken, the central position being where the highest value of M was

obtained in a smooth, symmetrical curve. The central position was determined to an accuracy of 0.1 mm, and then left unchanged until the sample was changed. As each sample was positioned slightly differently on the sample holder, each sample had to be re-centred before being measured. The field used for centring was 0.01 T for hard ferrites and 0.001 for soft ferrites, and for this reason the virgin magnetisations obtained were inevitably higher than the actual values.

6.1.5 Sample temperature

As the sample was contained within the helium chamber, it eventually cooled down to a temperature of 4.2 K unless heated. Most of the measurements were taken at a sample temperature of 300 K, and this was achieved by heating the sample chamber to the desired temperature. Obviously the low temperature of the magnet had to be retained despite this heating nearby, and the magnet temperature was maintained by the injection of liquid helium through a needle valve, which also kept the magnet sufficiently cool at high fields. Both the sample heater and the needle valve were controlled through an Oxford ITC SO3 independent temperature controller.

The samples were inserted once the sample chamber had reached 300 K, and left for 15 minutes to stabilise at that temperature, and in series where magnetisation was measured against sample temperature the sample was again left to stabilise for 15 minutes after each desired temperature had been reached. As can be seen in figure 282, this was sufficient for the sample temperature to have stabilised at all temperatures, with a variation of no more than +/- 0.1 K over a 20 minute hysteresis cycle up to 5 T.

6.1.6 Calibration

The equipment was calibrated regularly using a nickel sphere of known mass and magnetic moment, to give a voltage and phase difference when measured in a fixed field of 0.6 T at 300 K. A high purity (>99.99%) 2 mm nickel sphere annealed at 700 °C was supplied by Oxford for use in calibration, with a stated moment of 0.350 emu at 0.6 T. Such a sample is

recognised as becoming fully saturated in fields over 0.5 T with $M_s \cong 55$ emu g^{-1} at 300 K. However, there is some disagreement over the precise figure; for example, the reported M_s value ranges from 54.39 emu g^{-1} at 293 K [386] to 53.37 emu g^{-1} at 286.7 K [387], so there may be an error of up to 1% within the calibration technique.

6.1.7 Sample mounting

The sample was mounted on a sample holder made of PEEK, and secured with PTFE tape. This was than screwed into the end of a rigid carbon fibre rod, which was in turn secured in place with a head screw in the vibrator, so that the sample was situated inside the coils of the magnet in the helium chamber. These materials were all sufficiently nonmagnetic to have no discernible influence on the results. The sample was placed in the same position each time on the sample holder, so it would be situated roughly centrally between the two sets of detection coils.

6.1.8 Intrinsic field

The coils were found to retain an intrinsic field of 0.0006 T (6 G) at a sample chamber temperature of 300 K, even without an applied field. After using high fields over 5 T or when measuring extremely softly or poorly magnetic or small samples, it was necessary to degauss the coils. In this process the coils were cycled through a slowly decreasing range of fields from 1 - 0 T over a period of 5 minutes using a feedback loop, to randomise any alignment and remove any field generated in the coils. This process can also be used to demagnetise a sample and restore it to its virgin state. However, even after degaussing the intrinsic magnetisation was found to remain, and this could only be removed by heating up and quenching the magnet before cooling again - a costly, time consuming and therefore unviable process. Therefore, the loops are offset from the x axis by + 0.0006T, although this was found to be an insignificant amount even for the smallest and poorest hexagonal ferrite fibre samples.

6.2 VSM Sample preparation

Squares of aligned fibre 3 - 4 mm wide were cut from the centre of the fired blanket, with the direction of alignment parallel to two sides of the square. This was then weighed to $^{+}/_{-}$ 0.05 mg and placed on a piece of three ply tissue paper, and soaked liberally with a mixture of methyl methacrylate/styrene MCP casting resin and 5 wt% dibenzoyl peroxide, the surplus being absorbed by the tissue paper. After the clear resin had set it was left for at least 20 hours to harden fully, and then the sample was trimmed to give a rigid square 1 mm wider than the fibre sample. The direction of alignment could be observed by eye for sample mounting, and the sample was examined under low magnification (up to 50X) before and after measurement to ascertain that the alignment had been retained. The sample was then mounted at the correct position and with the desired orientation on a PEEK sample holder and secured with PTFE tape, so that when inserted into the VSM the plane of the square would be parallel with the applied field (fig. 283).

Random samples were prepared from either random or aligned fibre which was ground lightly in a pestle and mortar. This was sufficient to produce a sample of discontinuous random fibres with an average length of approximately 100 - 200 μm and an aspect ratio of at least 10. A portion of this was weighed and shaped into a square 3 - 4 mm wide and of approximately the same thickness as the aligned sample on tissue paper, and carefully soaked with the resin as with the aligned samples. By their nature the random samples tended to have a slight bulge in the centre, unlike the flat aligned samples, and contained much more material, but otherwise they were prepared, mounted and measured in the same manner.

6.3 Accuracy

As stated earlier, there is a slight disagreement in the literature regarding the exact M_s value of the nickel standard, but the calibration sample used here was certified by Oxford instruments to be 0.350 emu at 300 K. Any small error resulting from this would only be relevant when comparing these results to those reported by other authors, as all results here were calibrated

using the same sample. Oxford Research Instruments stated that the VSM was capable of producing reproducible results with an accuracy of 0.5% with a physically matched sample being measured at a fixed field over 1 hour. However, the flat aligned blankets of fibre 3 - 4 mm wide obviously did not resemble the 2 mm sphere of the calibration standard. This unavoidable difference in morphology would have resulted in a small, unknown error in the measurements due to the differing shape demagnetisation effects of the samples. The random fibre samples were more three dimensional in nature, resembling a low square-based pyramid. Samples demonstrated an excellent reproducibility even when removed from the sample holder and remounted, with a variation in M_s of less than 1% and a variation in H_c of zero.

Errors in the weighing of the samples were crucial, since the equipment only measured the sample moment in emu, and M_s and M_r must be expressed in units such as emu g^{-1} to have any relevancy. Due to their nature the aligned fibre samples tended to be very small, the smallest being only 0.5 mg, although most samples were between 1 -2 mg. These variations were due to differences in fibre density and blanket thickness, originating from the spinning process. Attempts to stack layers of blanket proved unviable on such a small scale, as they just separated and floated on the resin matrix. loosing alignment. The random fibre samples were lightly ground prior to VSM sample preparation, and so they formed a much denser composite with typically ten times as much fibre in the sample. All samples were weighed to an accuracy of 0.05 mg, so while the percentage error in the weight was a few percent for most aligned samples and below 1 % for random fibres, it was as high as 10% for some aligned samples.

Summary and Future Work

Hexagonal ferrites, especially M ferrite, are the most common magnetic materials in use today, and they also have uses in niche applications due to properties such as microwave adsorption and catalysis. A fibrous ferrite could be used in a composite material, and it has been predicted, although never demonstrated, that properties such as magnetisation should be enhanced in a well aligned fibre. Therefore the aim of this project was to develop a spinnable sol-gel precursor system capable of producing a range of hexagonal ferrite fibres when subsequently fired. The sol would be inorganic and aqueous, and the fibres would be collected in an aligned form to investigate effect upon their magnetic properties. It was also hoped that the sol-gel process involved would result in lower crystallisation temperatures and smaller grains sizes.

A stable iron(III) sol was successfully made from the peptisation of precipitated iron(III)chloride with HBr in a ratio of Fe:acid of 5:1. The sol was found to be sensitive to temperature, and with too much Cl^- the sol became thixotropic at low concentrations due to structuring and destabilisation effects from the Cl^-. An optimum precipitation time of 15 - 30 min and peptisation temperature of 35 °C under a vacuum of 95 kPa on a rotary evaporator were established, forming a sol in 30 - 60 min which required at least 24 hr to stabilise and give a constant particle size. This sol had a volume average particle size of 4 – 6 nm, with an upper limit of 20 nm at a concentration of 10.5% Fe. The absence of any large species (>50 nm), even in small numbers, and the degree to which the sol could be concentrated without flocculating or gelling (>13% Fe) were found to be vital for successful blow spinning. A halide free sol based on nitrate salts and HNO_3 was also investigated, but it gave an inferior product to the halide stabilised sol.

The presence of any NO_3^- ions tended to precipitate Ba^{2+} as $Ba(NO_3)_2$, so nitrate sols or salts were not used for the barium containing ferrite precursors, but the more soluble $Sr(NO_3)_2$ was investigated to make SrM fibres. When barium nitrite was added to the sol, an extremely exothermic reaction occurred upon concentration and partial dehydration when

containing Co^{2+}. Therefore to make the stoichiometric ferrite sols bromide salts were used as extra bromide had no effect on stability, and all the metal bromides were very soluble. With the higher barium levels needed for the ferroxplana ferrites, it was found that a chelating agent, 18-crown-6-ether, was needed to keep the barium in solution even with bromides. With the addition of cobalt there was also a harmful interaction between the two metals which reduced the stability of the sols slightly. Nevertheless stable and spinnable sols were made of all the hexagonal ferrites, and although there was a general increase in particle size with higher doping levels, all remained within spinnable limits. $BaCo_xTi_xFe_{12-x}O_{19}$ sols ($x = 0.5 - 1.1$) were made by adding a dilute titanium alkoxide solution to the Fe/Br sol, and it was probable that the hydrolysed titania was adsorbed onto the surface of the iron particles, leading to a further increase in size dependent upon x. Therefore the addition of Ti^{4+}/Co^{2+} had a disproportionately large effect on stability. Alternative methods of sol preparation were also investigated, but they all proved less successful than the doped aqueous FeOOH sol.

The sols were blow spun to give gel fibres between 4 and 8 μm wide. Which were collected as both random fibre and aligned blankets. As the sols were insufficiently viscous to draw fibre, 2 - 5% PEO was added as a linear polymer spinning aid. PEO caused an increase in particle size in the sol because of interaction with the Fe^{3+} and halide ions, but most sols were spun at concentrations of 14 - 17% Fe. A small amount of Cl^- and crown ether aided spinning, by forging a degree of localised structuring, especially useful in the more dilute three and four component sols. The spinning sols containing cobalt tended to form a thixotropic gel on standing, but this could be avoided by adding 3 - 6% methanol prior to spinning, also reducing the viscoelasticity of the sol, and the presence of titanium also eased the viscoelastic effects. Other divalent ions such as Ni^{2+}, Mn^{2+}, and Ca^{2+} could be substituted and still result in a spinnable sol, but Zn^{2+} ions proved to be incompatible with PEO, making it precipitate out of solution as a rubbery lump. Most of the fibres were aligned well, with 90 - 95% of the fibres within 20 ° of the axis of alignment, and this could be improved with further optimisation.

When the fibres were fired no cobalt halides or oxides formed, and the only crystalline

barium compound seen was $BaBr_2$ up to 200 °C. All fibres formed crystalline α-Fe_2O_3 at 250 °C, but γ-Fe_2O_3, α-FeOOH or γ-FeOOH were never observed, and no $BaFe_2O_4$ was seen in M fibres fired soon after spinning. Pure phase fibres of all ferrites were produced from stoichiometric mixes, and no excess of barium was required. The fibre shrank by ~12% in drying after collection, and by a further 22 - 23% total shrinkage at 1200 °C, and alignment was not affected by shrinkage or sintering. XPS analysis confirmed the metal ions to be Fe^{3+} and Co^{2+} at 1000 °C, and the stoichiometric compositions of the ferrite fibres were confirmed by XRF analysis. 20% weight loss occurred below 400 °C as water, bromine and organic compounds were driven out, and the fibres retained ~10 wt% halides after this which were retained to some in degree in the fibre up to 1000 °C. The formation of the ferrite phases were delayed until these halides were lost, indicating that barium, and maybe cobalt, remained separate from iron until ferrite formation.

BaM and SrM had begun to form by 800 °C and 750 °C, and at 1000 °C and 900 °C the pure BaM and SrM phases had formed respectively. Although the ferrite did not form at a significantly lower temperature, it did appear to be more fully sintered and with a much improved microstructure (<1 μm) than at equivalent temperatures in conventionally manufactured specimens. At 1000 °C the fibres were ~98% sintered. In halide free fibres the pure M phase formed at a temperature ~200 °C lower, confirming the effects of halides in hindering ferrite formation, but the product was otherwise inferior to the halide-containing fibres. Small additions of Gd^{3+}, La^{3+}, V_2O_5 and Nb_2O_5 caused BaM to form at lower temperatures, and DGG was never seen in the M ferrites even at 1200 °C, except for the rare earth metal doped fibres. $BaCo_xTi_xFe_{12-2x}O_{19}$ fibres all formed the M phase by 900 °C, and although the fibres were more porous than unsubstituted M, increasing with x, the substitution had little effect on grain size, unlike reported substituted ferrites. $SrCo_xTi_xM$ fibres exhibited no apparent grain structure at 1000 °C.

At 800 °C the Co_2Y fibres had formed M, $CoFe_2O_4$ and α-$BaFe_2O_4$, producing fully crystalline Co_2Y at a low 1000 °C, consisting of randomly ordered hexagonal platelets 1 – 3 x

0.1 – 0.2 μm. and again it was more fully sintered than conventionally manufactured specimens. No DGG had occurred even at 1200 °C / 3hr. All fibres containing cobalt formed α-$BaFe_2O_4$ and $CoFe_2O_4$ at 800 °C, and they resembled the Y fibres at 1000 °C, the Z, W, X and U phases forming only after the full crystallisation of M or M / Y, accompanied by DGG in the case of Z and W fibres.

Co_2Z ferrite formed at 1250 °C from XRD evidence, but due to its complexity it was thought unlikely to be a truly pure phase. The seemingly unavoidable DGG process was always observed with Z formation, after only 5 min at 1200 °C before the formation of the Z phase, suggesting normally DGG is an unavoidable part of the ordering process required to arrange the M and Y units sequentially to form Z. Although the grains had rapidly grown to form elongated hexagonal plates up to 25 μm long at 1200 °C / 5min, this was much less then reported grain sizes as large as hundreds of microns, and DGG has not previously been noted to occur at temperatures / times as low as this. In fibre containing high levels of Cl^-, DGG never occurred but the Z phase also failed to form, confirming both the necessity of DGG for Z formation and the harmful effect of chloride. Stacks of layers of hexagonal plates could be seen in the grains, suggesting that DGG is a diffusion and condensation process, and the formation of Z was shown to be kinetic. The formation of Co_2Z coincided with a disproportional loss of BaM but not Co_2Y, and it is suggested that Co_2U forms as an intermediate stage. The addition of 0.67% CaO improved both the morphology and formation temperature of the Co_2Z fibres significantly. Z was a major component material at 1150 °C, with an improved microstructure and no DGG, giving smaller, more equiaxed grains even up to 1175 °C, by which point Co_2Z was the main phase. It is suggested that the calcium segregated at the boundary edges, slowing the rate of grain growth in the hexagonal plane until the dissolution of calcium let DGG proceeded at 1200 °C DGG. $Sr_3Co_2Fe_{24}O_{41}$ fibres were also made, and produced the pure Z phase after 1200 °C / 3hr.

Co_2W formed at 1200 °C, a lower temperature than expected for the ferrite to exist as the sole phase, and DGG also accompanied this formation. There were no published XRD

patterns for Co_2X and Co_2U to confirm the phases of these fibres. At 1000 °C the X fibres resembled Co_2W and the U fibres resembled Co_2Z, and at 1200 °C unidentified phases had formed. Although grains as large as 10 μm had developed there was no DGG, indicating that whatever phases had developed were not W or Z respectively, and that the X and U phases may have been formed.

After storage at 110 °C for 3yr the M fibres were virtually pure phase M at only 800 °C, and although there was no microstructure visible at 800 °C, at 1000 °C their surfaces were markedly different. The stored Co_2Y fibres formed the Y phase at only 900 °C. These differences were attributed to the loss of halide during storage and the crystallisation of haematite in the gel fibres, promoting the formation of the M phase at a lower temperature. $BaFe_2O_4$ was also seen for the first time in halide containing M ferrites, suggesting barium was normally associated with the halide prior to M formation. These conclusions were confirmed by the steaming of fibres to remove halides at a lower temperature. By 600 °C M had begun to form as a minor phase, and the fibres were virtually pure BaM at 700 °C, with no grains visible. When steamed at 800 °C Co_2Y fibres were mostly Y phase, and their microstructure resembled the normal 1000 °C fibres. Steaming Co_2Z at 600 °C formed M, $CoFe_2O_4$ and haematite, and if Z fibres were prefired to 1000 °C in air and then steamed at 900 °C / 3hr, even at 1250 °C DGG had not occurred with grains were below 6 μm, the phases present being unclear from XRD.

The M ferrites had M_s values slightly below single crystal values, typical for polycrystalline samples, whereas the ferroxplana ferrites equaled the highest M_s values reported previously. The M fibres had high coercivities, implying a small grain size, and all were isotropic, so any changes with fibre orientation must be due to fibre effects, and not from alignment of domains within the fibres. All M and Y fibres showed alignment effects, enhancing M_s by 20 - 40% when the fibre was aligned to H, compared to the random fibre values, and the soft ferrites also exhibited alignment effects in loop width, due to crystalline anisotropy. This is the first time that an enhancement of magnetic properties in an aligned fibre

has actually been demonstrated. M and Y fibres had enhancement not only parallel to, but also at 45° to, H, in effect covering a cone of 90°. 45° and parallel to H were always roughly equal in well aligned fibres, and perpendicular to H was always lower than the random fibre value to an equal degree. This was true for all of the well aligned fibres except Co_2Z and Co_2W.

After only 10 min at 1000 °C the optimum BaM fibre had formed, and SrM peaked at the lower temperature of 800 °C, and a higher M_s at 1200 °C. The $BaCo_xTi_xFe_{12-2x}O_{19}$ fibres fired to 1000 °C showed a decrease of M_s, H_c and M_r with increasing x, but the decrease in M_s was much less than the other properties, giving a soft ferrite with high M_s at x = 1. $SrCo_xTi_xFe_{12-2x}O_{19}$ fibres demonstrated the same general patterns, but they had lower M_s values and higher H_c, to such an extent that at 1000 °C even the x = 1.0 fibre was still hard, indicating that substitution had a lesser effect on SrM.

In unaligned Co_2Y ferrites M_s matched reported values of 34 emu g^{-1} and the fibres were soft ferrites with narrow loops of 0.049 T, but they exhibited possible small anisotropy effects on H_c and M_r caused by platy grains forming on the surface of the fibres. This effect was seen in all ferroxplana ferrite fibres, and was greater in those with elongated grains from DGG, and small perminvar-like deformations of the loop resulting in lobes were observed in Y, W and poor Z samples.

Co_2Z was found to be very dependent upon the amount of halide, giving fibres with M_s ranging from 50 - 61 emu g^{-1} and H_c from 0.007 - 0.050 T, the higher M_s and lower H_c being found in those fibres with less halide to give a superior product to any reported previously. CaO doped Co_2Z fibres formed the Z phase at only 1200 °C, with DGG and equivalent to all but the best non-doped samples, and an impure Z phase with low M_s had formed at 1175 °C without DGG having occurred. Co_2W, Co_2X and Co_2U fibres were also characterised, although little is known about the magnetic properties of the materials for comparison.

Firing M in steam was found to produce a product with good properties at only 700 °C / 3hr, and the optimum material was obtained by steaming from 400 - 800 °C / 3hr. When steamed at 800 °C Co_2Y fibres formed a magnetically excellent sample, and Co_2Z was made at

very low temperatures of 1150 °C, giving a magnetically good sample without the usually omnipresent DGG, when first steamed at 900 °C. This is the first reported case of Co_2Z formation without DGG, giving a product with a relatively small equiaxed hexagonal grains between 1 - 6 μm wide.

In the future the processing of the ferrites should be examined in more detail, particularly the removal of residual chloride, which while beneficial in small amounts in the sol clearly hinders ferrite formation. Another possibility is the reduction of the fibres, in a process similar to that used by the author to make Fe_3O_4 fibres, to form γ-Fe_2O_3 which is claimed to encourage ferrite formation by some workers. The seeding of sols with hexagonal crystals should be investigated more thoroughly, and the use of nitrite salts could lead to a possible combustion-method of synthesis, although it would be too damaging to any fibre. The formation of M ferrites at lower temperatures with dopants deserves further study, with a view to optimising the magnetic properties of such material The probable creation of Z ferrite without undergoing DGG would be a major breakthrough regarding the manufacture of handleable fibres of this material. The possibility of U ferrite forming as an intermediate phase in Z formation also requires clarification.

Work needs to be carried out to understand the nature of the sol, and a finer control of halide levels would be beneficial. Ultrasonic peptisation is another method deserving of more investigation, as it results in a sol with very uniform size distributions. The spinning process itself can be endlessly improved and optimised, but as each ferrite sol has slightly different qualities this tends to be a never-ending process, and unless industrial scale up is considered, the current technique is adequate for R&D projects. However any improvements in alignment would be most welcome, and a better match must be found between the rotor speed and spinning rate. This is not as simple as speeding up the rotor, as 1000 RPM was found to be close to the maximum speed before fibre is lost as it flies off the drum.

Improved alignment should also improve alignment effects on magnetic properties, as would a higher loading of fibre in the composites. Heating the fibres to over their Curie point

and then letting them cool in a magnetic field aligned along the fibre axis may cause orientation along that direction, further enhancing any effects. As the M and Z ferrites are also good microwave absorbers, the use of microwave heating and processing techniques might also prove interesting.

In general the whole process could be applied to similar materials such as microwave garnet ferrites (YIG and GIG), and some spinel fibres maybe possible following more study. This work should also be used as a basis for developing other blow spun fibres, made from a parallel sol-gel precursor. However, the fibre process must be made cheaper if it is to be commercially viable, as it is too expensive for a cheap product like BaM, unless specialist applications can be found. It should be noted that this process can repeatedly produce fibres between 3 – 8 μm in diameter, averaging around 5 μm, and with none smaller than this. Incoming EU regulation will soon ban the use of fibres below the 3μm threshold as a health risk, and therefore this technology has potential value as a replacement for many current fibre production methods, which produce a far greater spread of diameters.

The Synthesis and Characterisation of Hexagonal Ferrite Fibres

Volume Two of Two

Robert Carlyle Pullar

University of Warwick
School of Engineering

December 1999

A thesis submitted in canditure for the degree of Doctor of Philosophy

Contents

Volume two

Figures

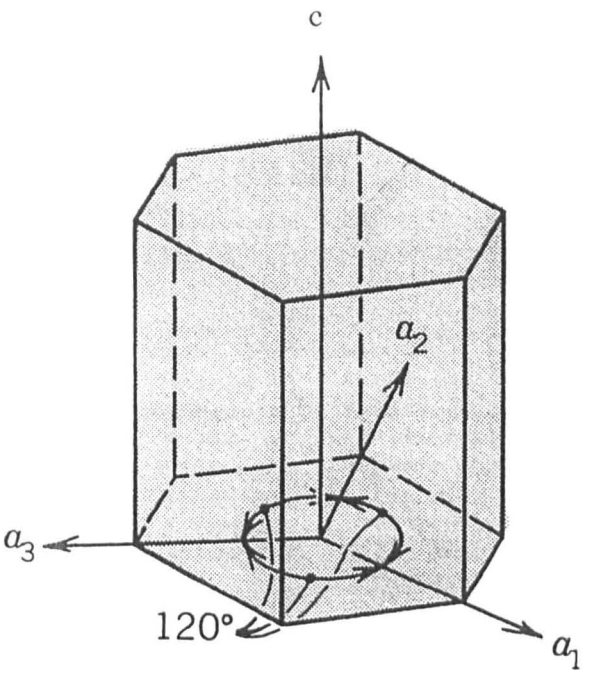

Fig. 1 A hexagonal Crystal, showing the two lattice parameters a and c.

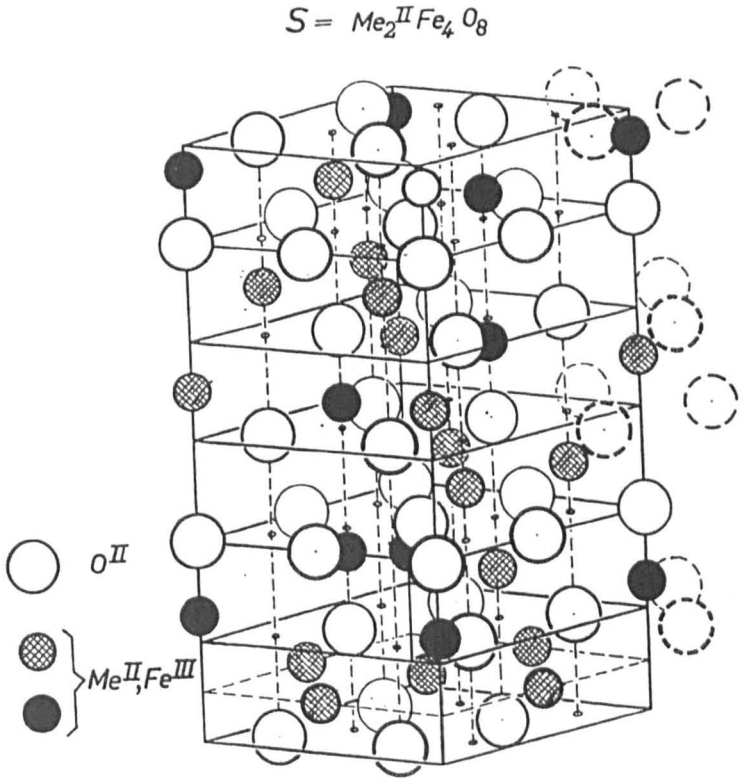

Fig. 2 Perspective view of the spinel structure. The hatched circles represent octahedral sites and the black circles represent tetrahedral sites for the metal atoms [7].

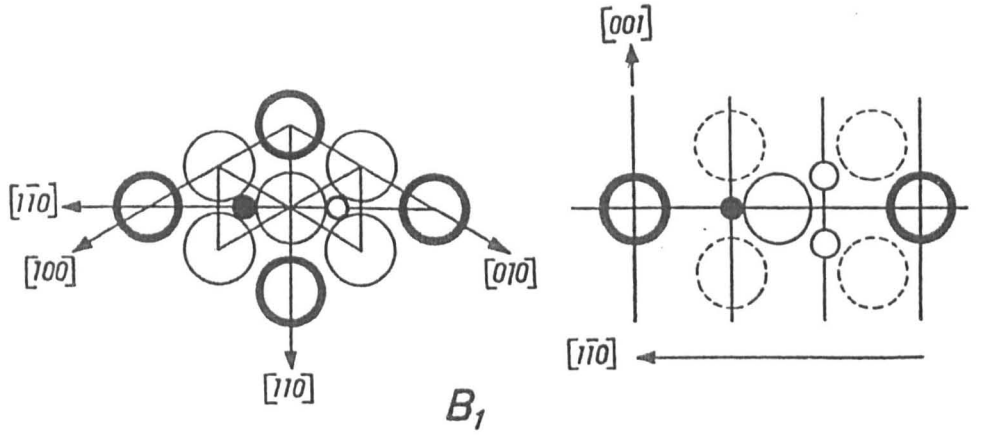

Fig. 3 Cross sectional view of the B_1 layer [11].

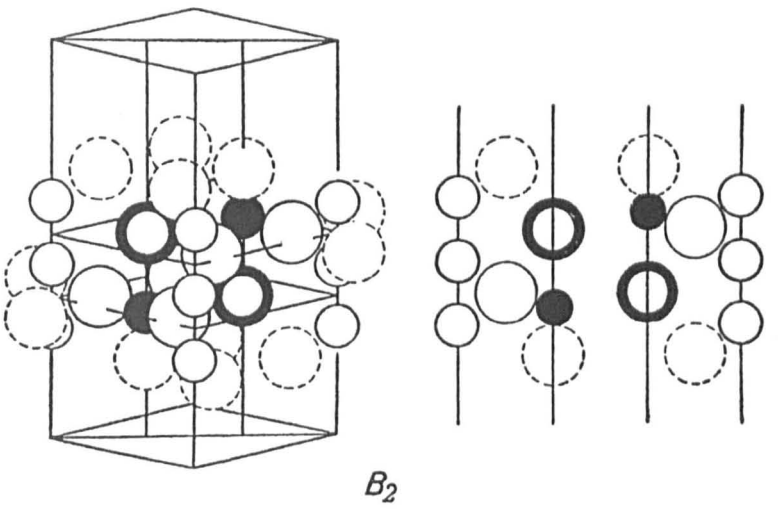

Fig. 4 Perspective and cross sectional views of the B_2 layer [11].

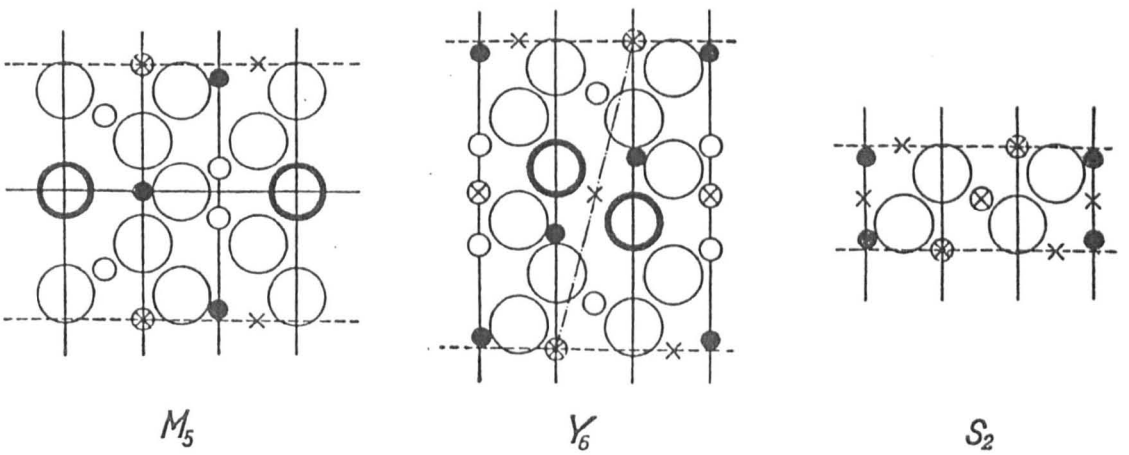

Fig. 5 Cross sectional view of the M_5, Y_6, and S_2 units [11].

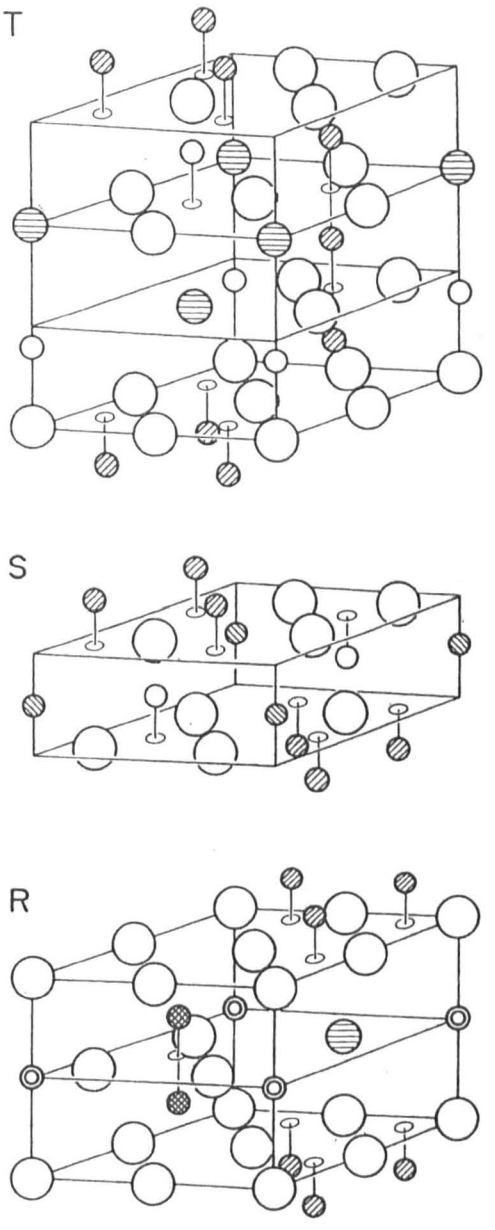

Fig. 6 Perspective view of the S, R and T blocks [389].

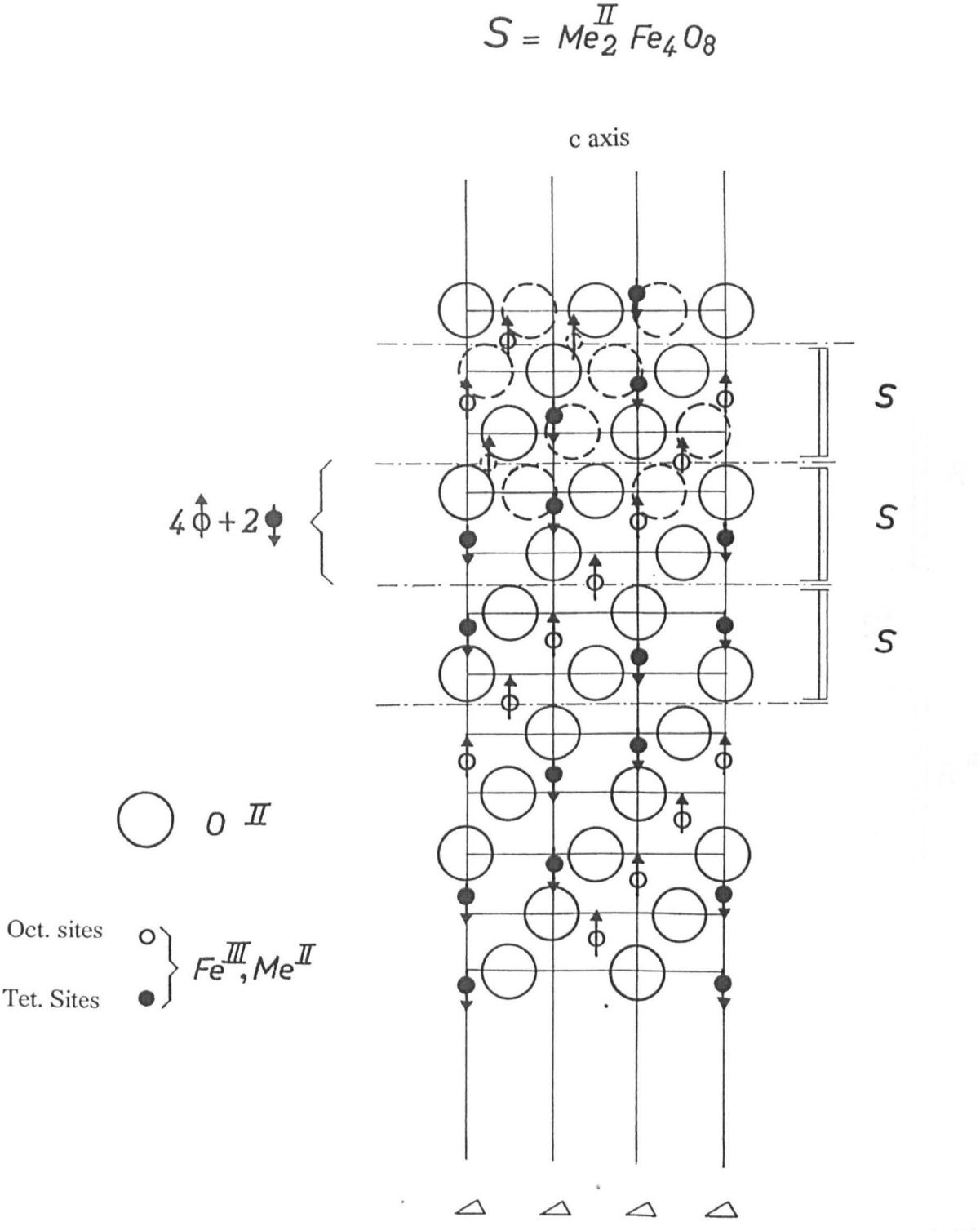

Fig. 7 Cross sectional view of the spinel structure, showing the S block, $Me_2Fe_4O_8$. The arrows represent the orientation of the magnetic moments of the cations [7].

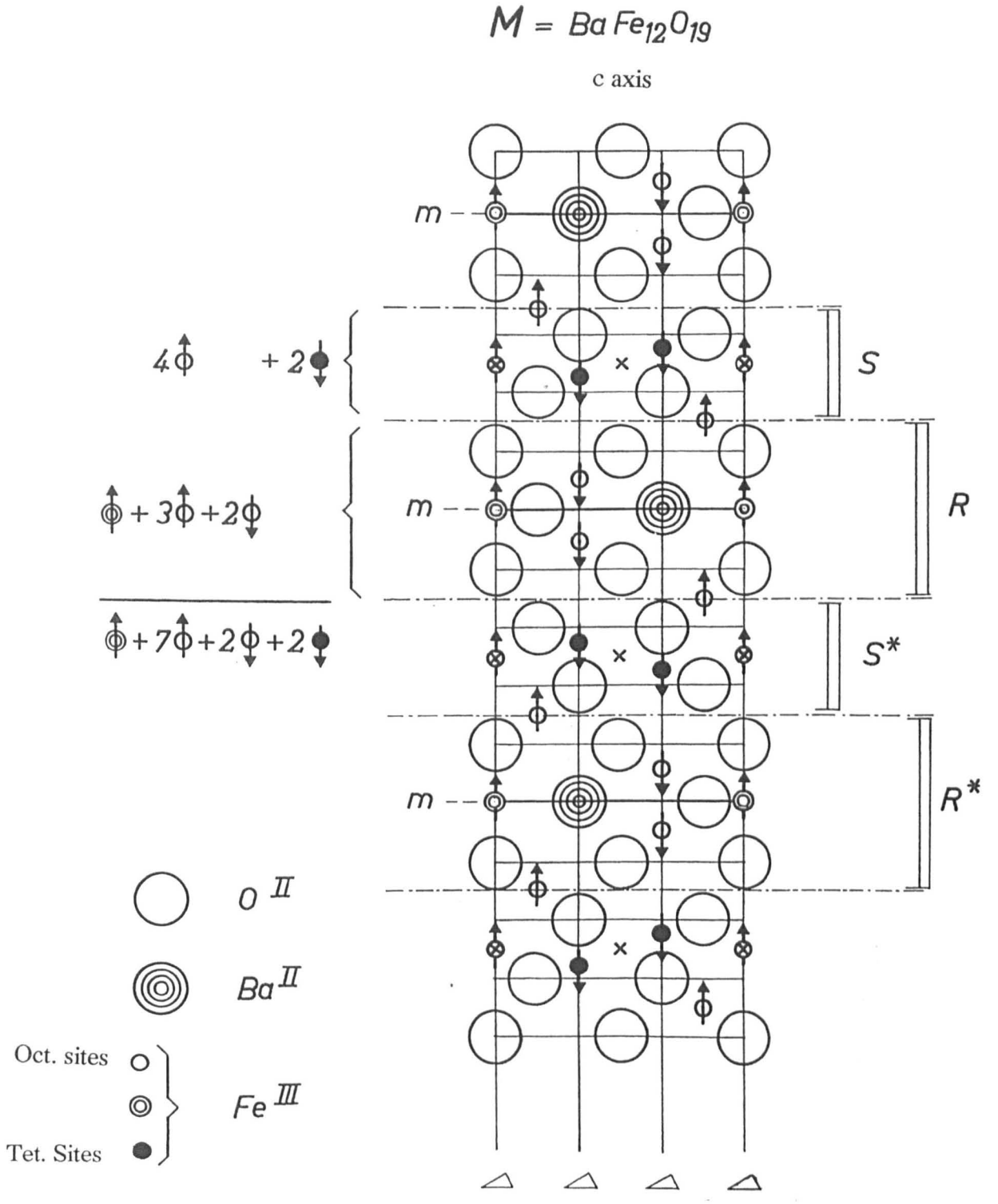

Fig. 8 Cross section view of the M ferrite ($BaFe_{12}O_{19}$) structure in which the vertical lines are axes of threefold symmetry. The arrows indicate the orientations of the magnetic moments of the cations relative to the c-axis, * = 180° rotation of the block around the c-axis, m = mirror plane [7].

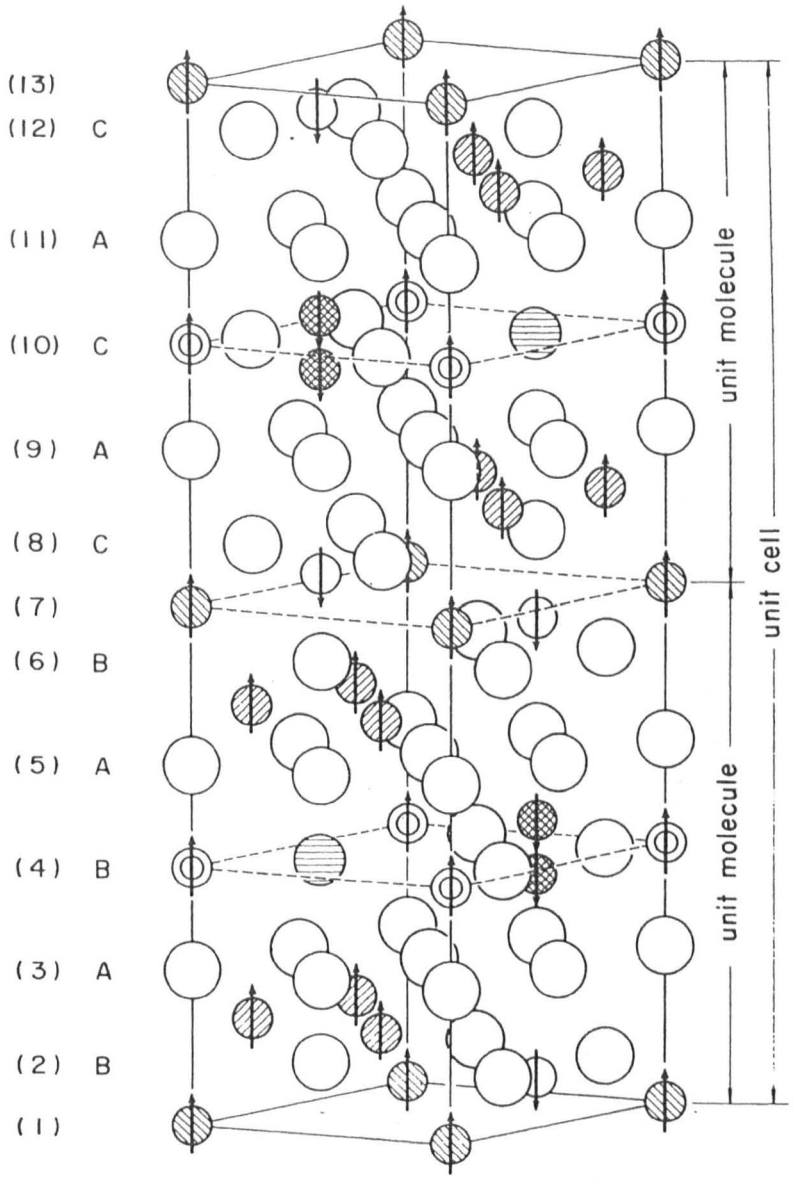

Fig. 11. Perspective illustration of $BaO{\cdot}6Fe_2O_3$.

Fig. 9 Perspective view of the M structure [389].

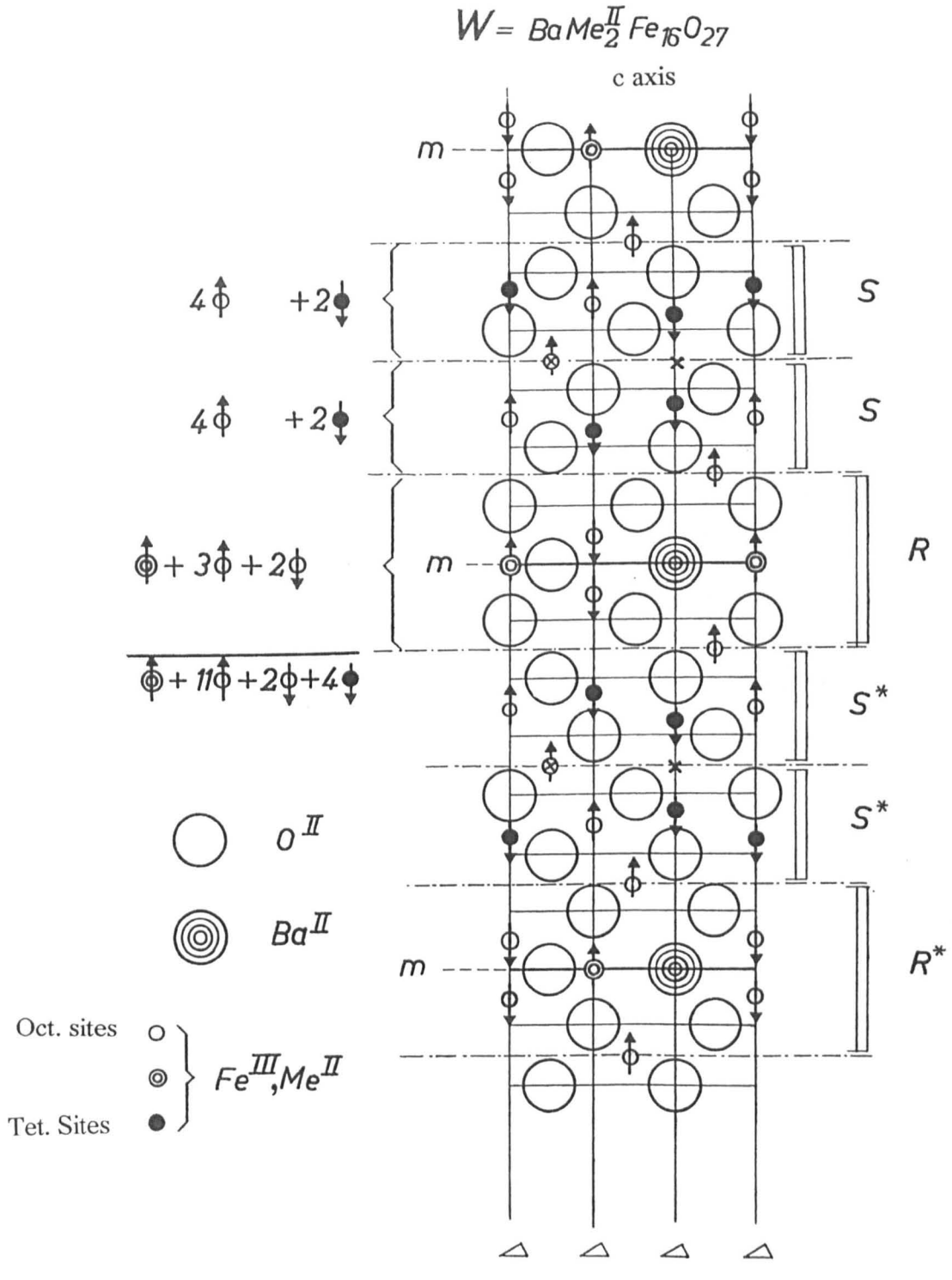

Fig. 10 Cross section view of the W ferrite structure ($BaMe_2Fe_{16}O_{27}$) in which the vertical lines are axes of threefold symmetry. The arrows indicate the orientations of the magnetic moments of the cations relative to the c-axis, * = 180° rotation of the block around the c-axis, m = mirror plane. In Co_2W the moments will be in the preferred cone of magnetisation, at an angle to the c-axis at room temperature [7].

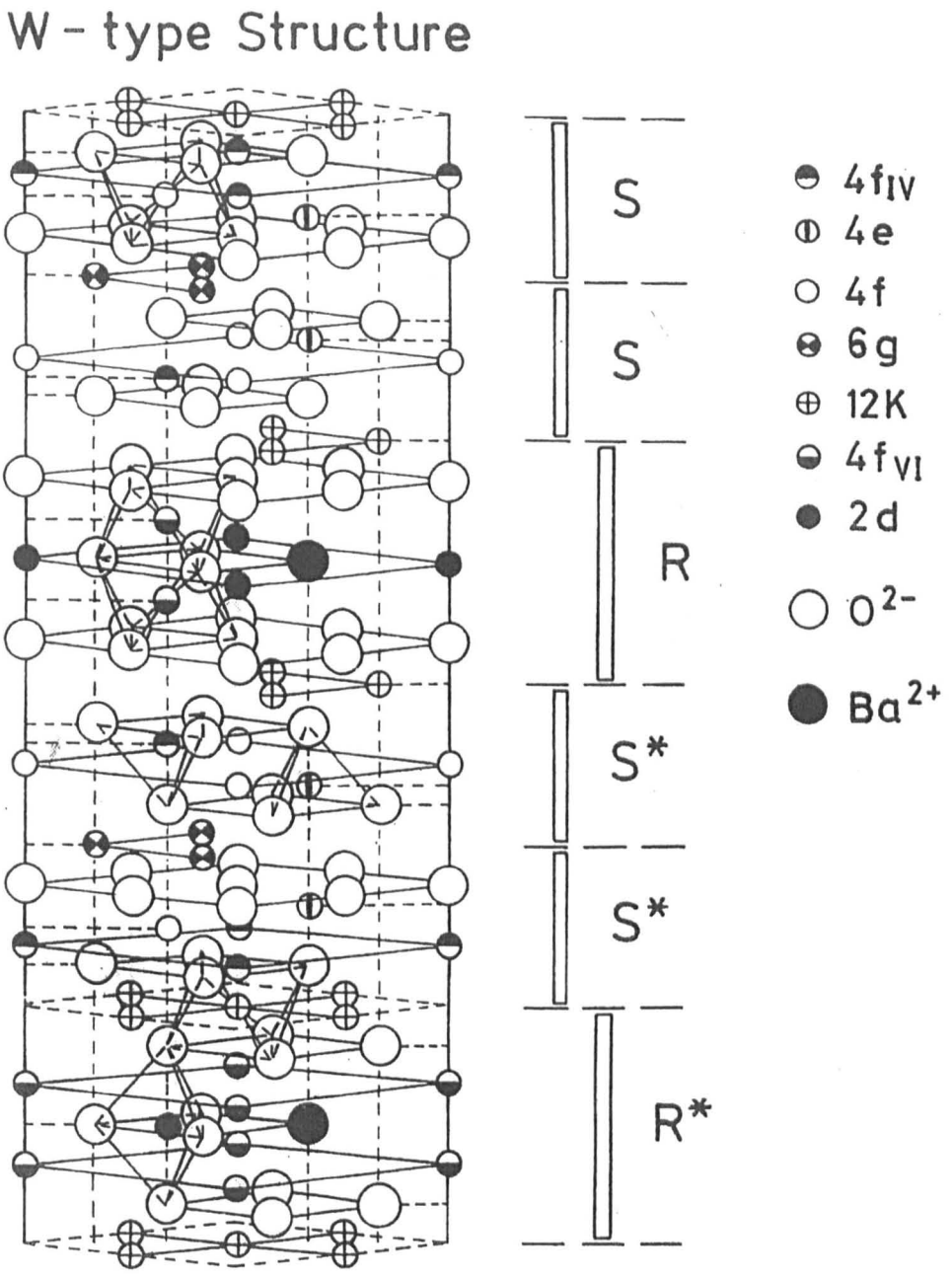

Fig. 11 Perspective view of the W structure [389].

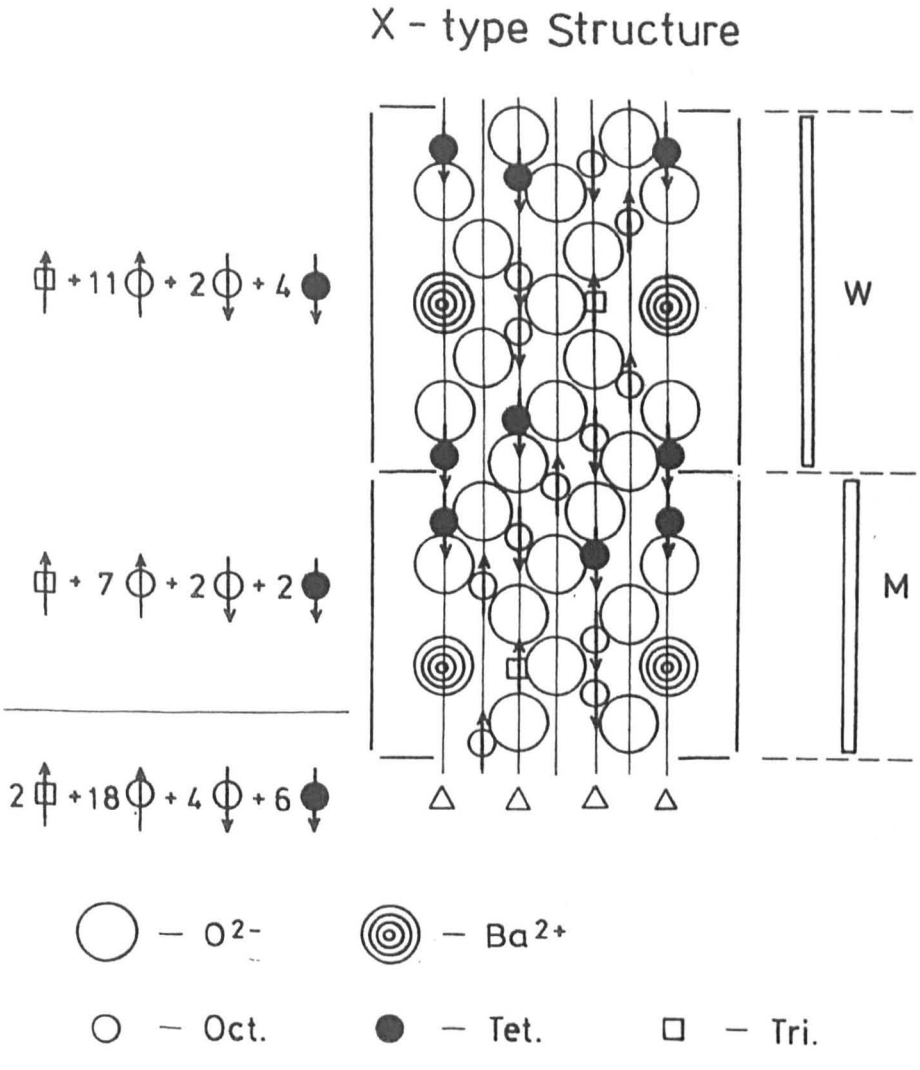

Fig. 12 Cross section view of the X ferrite ($Ba_2Me_2Fe_{28}O_{46}$) structure in which the vertical lines are axes of threefold symmetry [389].

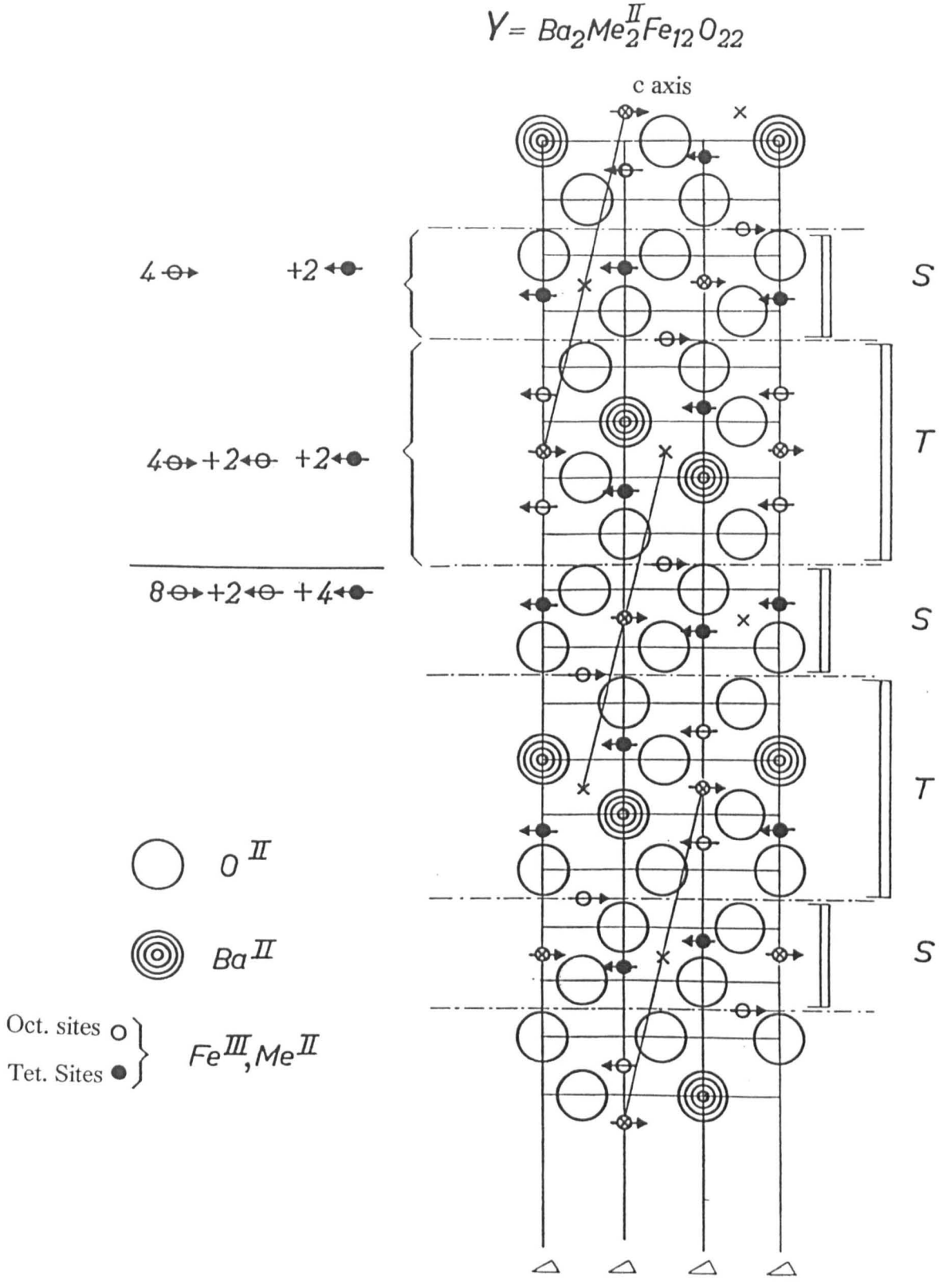

Fig. 13 Cross section view of the Y ferrite ($Ba_2Me_2Fe_{12}O_{22}$) structure in which the vertical lines are axes of threefold symmetry. The arrows indicate the orientations of the magnetic moments of the cations relative to the c-axis [7].

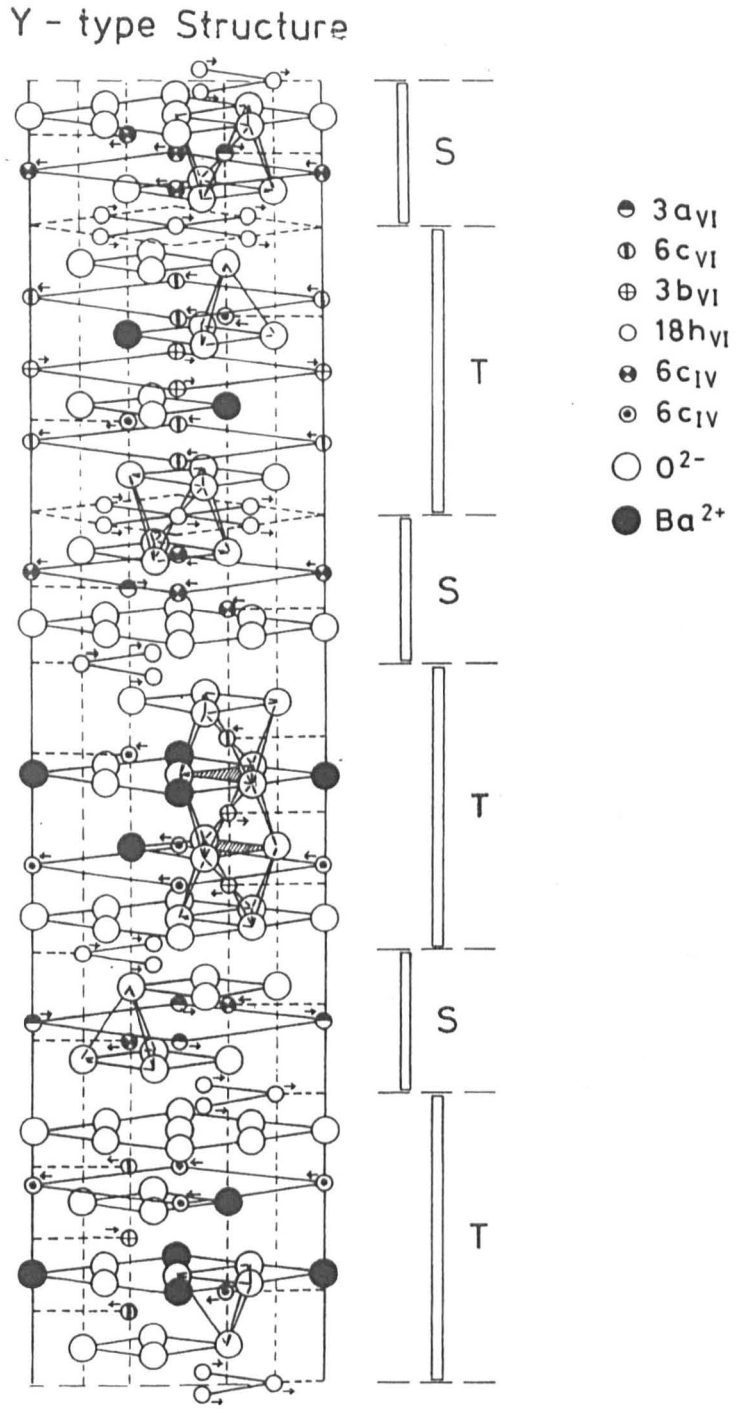

Fig. 14 Perspective view of the Y structure [389].

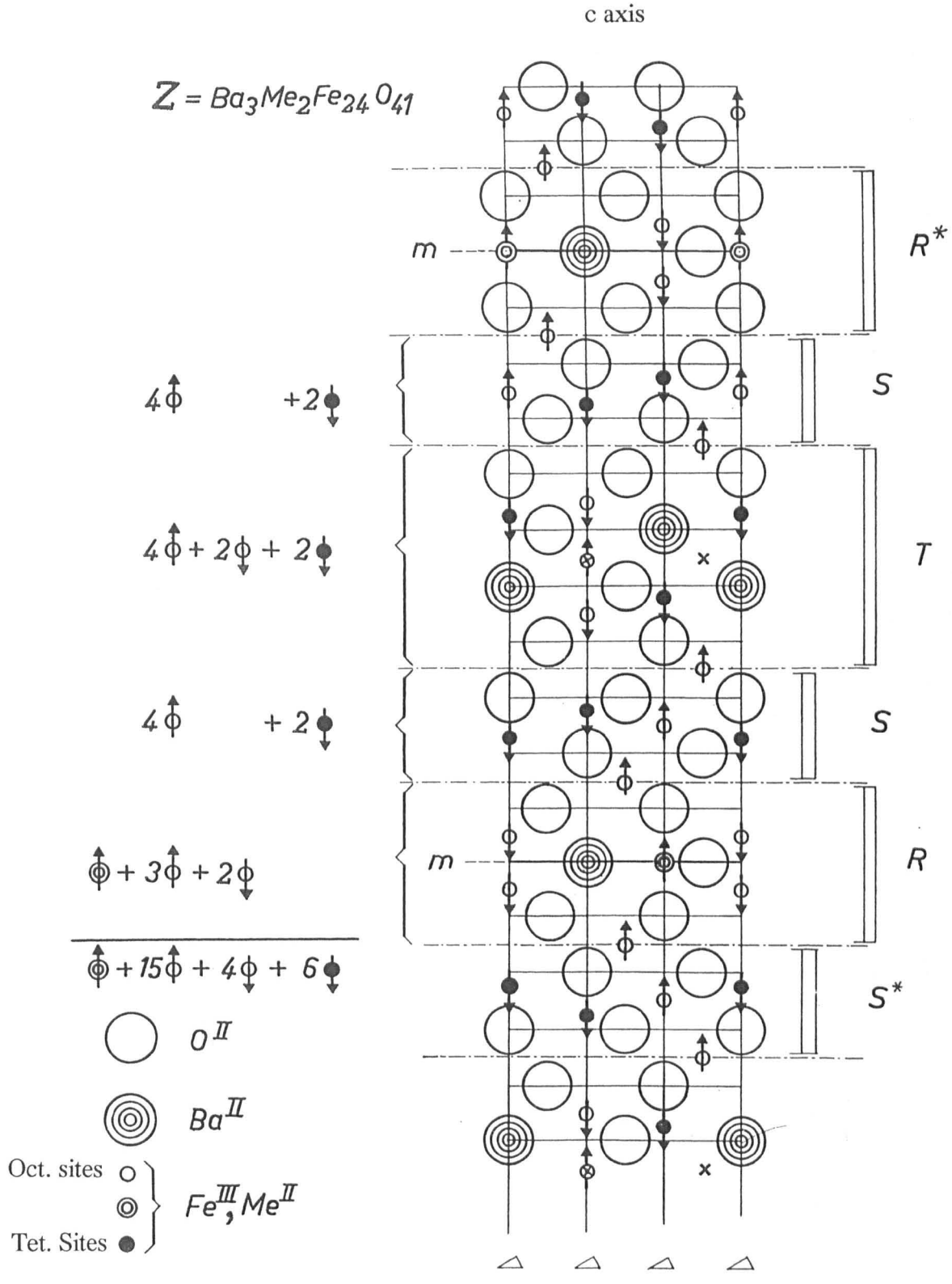

Fig. 15 Cross section view of the Z ferrite ($Ba_3Me_2Fe_{24}O_{41}$) structure in which the vertical lines are axes of threefold symmetry. The arrows indicate the orientations of the magnetic moments of the cations relative to the c-axis, * = 180° rotation of the block around the c-axis, m = mirror plane. In Co_2Z the moments will be in the preferred plane of magnetisation, perpendicular to the c-axis at room temperature [7].

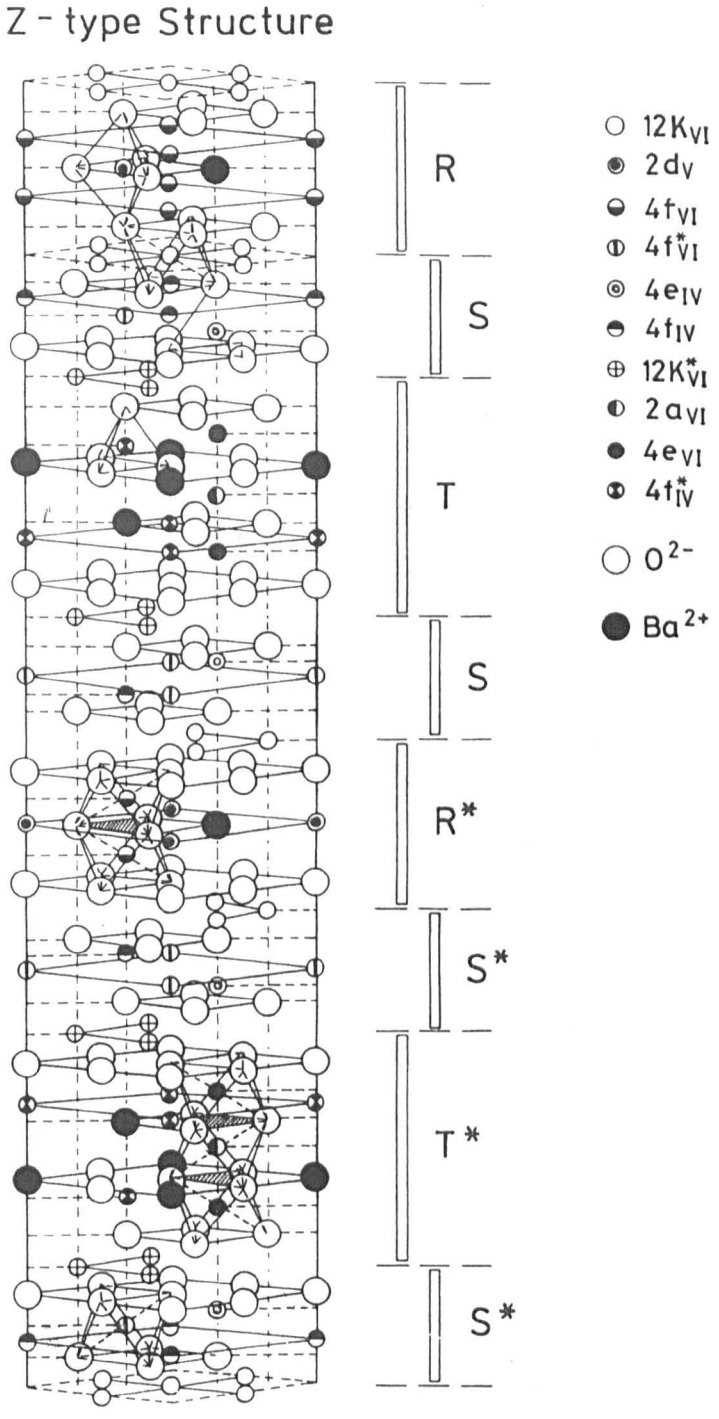

Fig. 16 Perspective view of the Z structure [389].

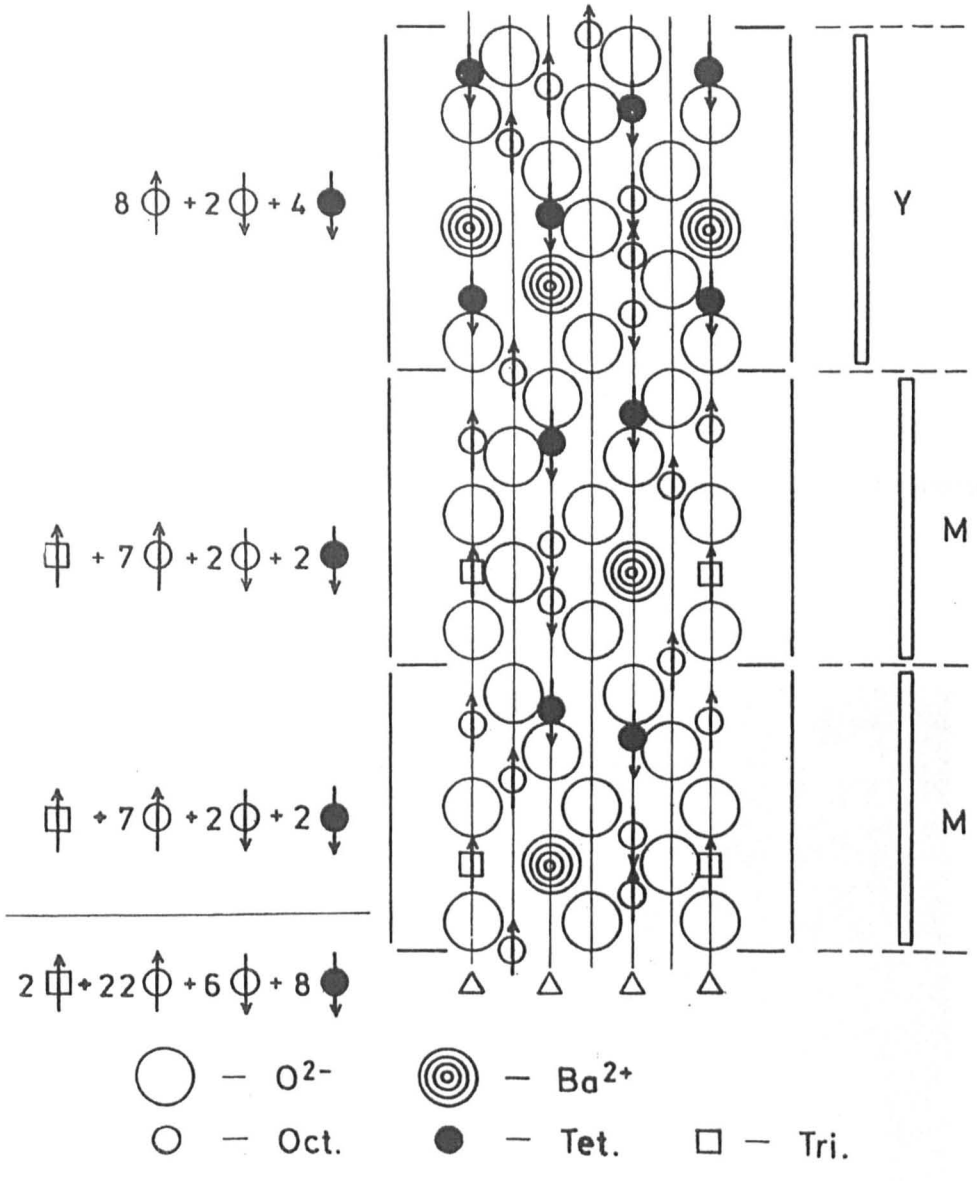

Fig. 17 Cross section view of the U ferrite ($Ba_4Me_2Fe_{36}O_{60}$) structure in which the vertical lines are axes of threefold symmetry [389].

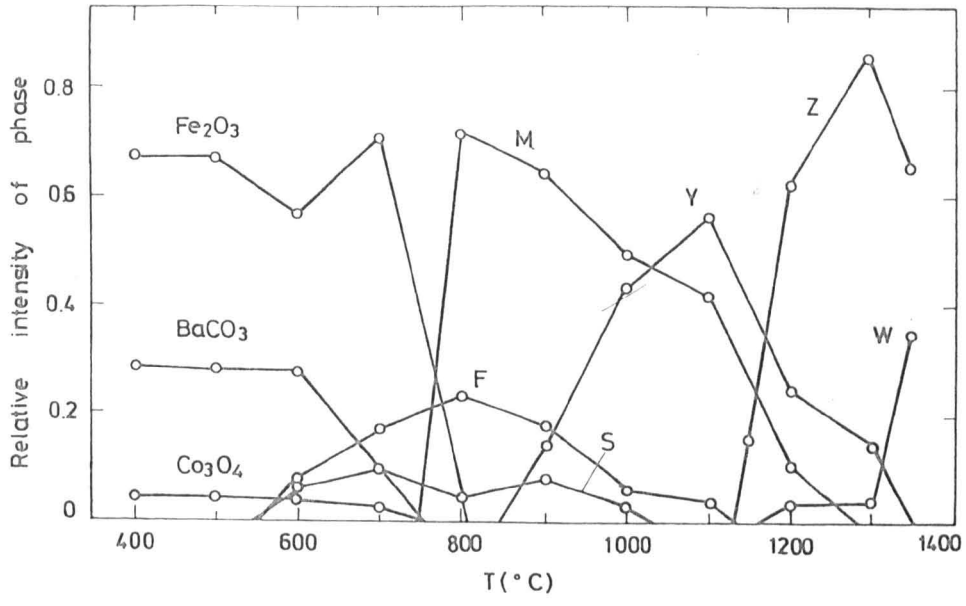

Fig. 18 The formation and stability temperature ranges for the hexagonal ferrites [24].

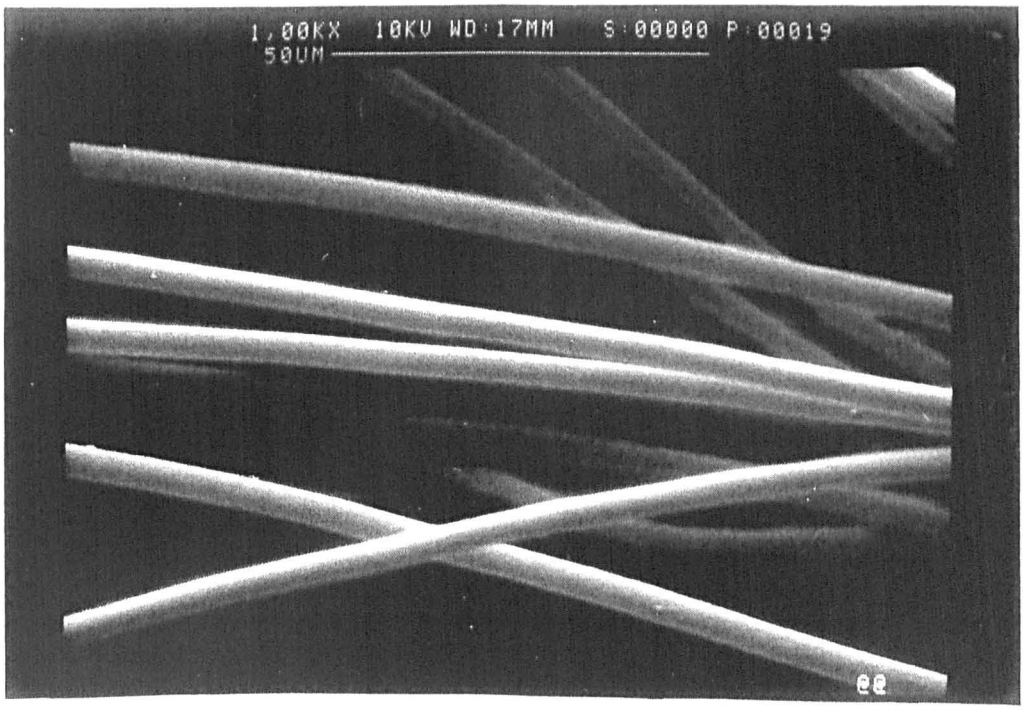

Fig. 19 An example of fine continuous aligned ceramic fibres blow spun from an aqueous sol-gel precursor. These fibres are yttrium aluminium garnet (YAG) fired to 800 °C, with an average diameter of 5.5 μm.

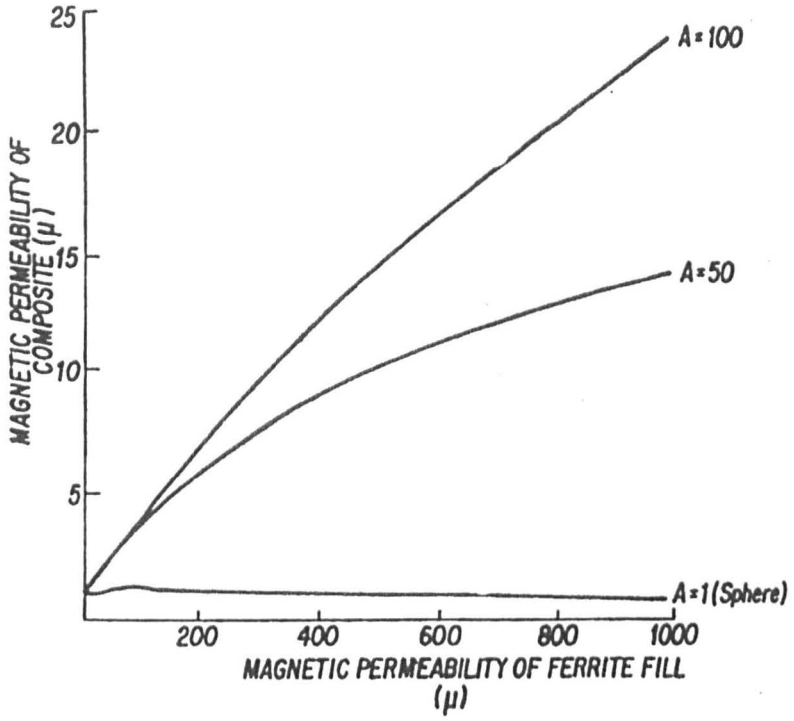

Fig. 20 The effect of increasing aspect ratio, A, of a fibre on the magnetic permeability of a ferrimagnetic fibre composite material [101].

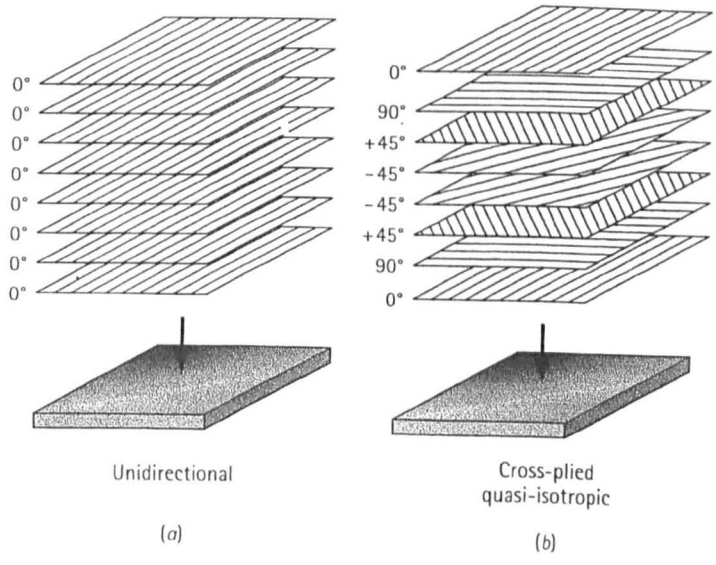

Fig. 21 Examples of alignment within a) unidirectional and b) 0°/45°/90° cross-ply fibre composites [105].

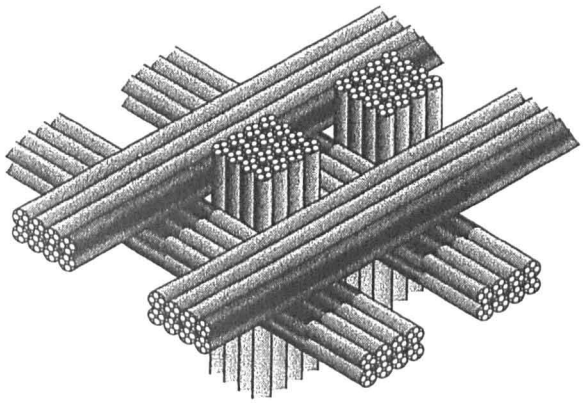

Fig. 22 A example of a three-dimensional weave in a multidirectional fibre composite material [105].

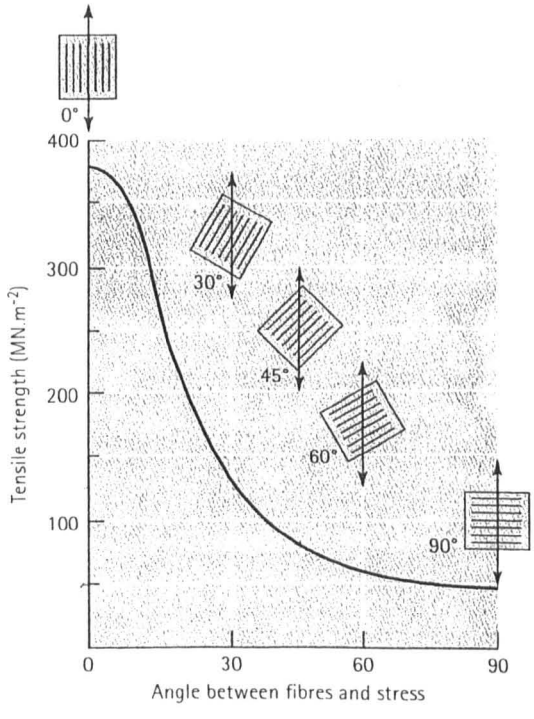

Fig. 23 The effect of fibre orientation on the tensile strength of E-glass fibre reinforced resin matrix composites [105].

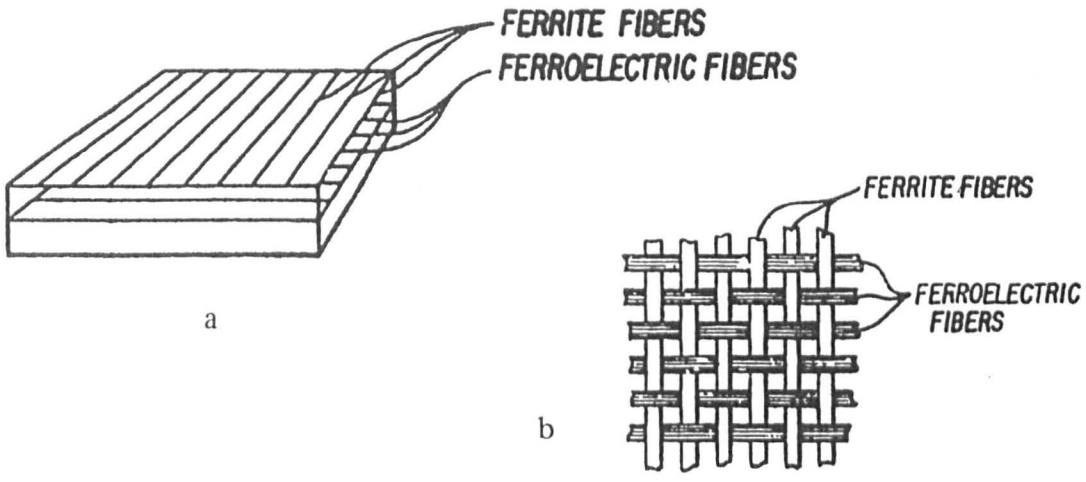

Fig. 24 Proposed fibre composites containing two complimentary aligned effect fibres, one dielectric and one magnetic, in a) layer formation and b) weave formation [101].

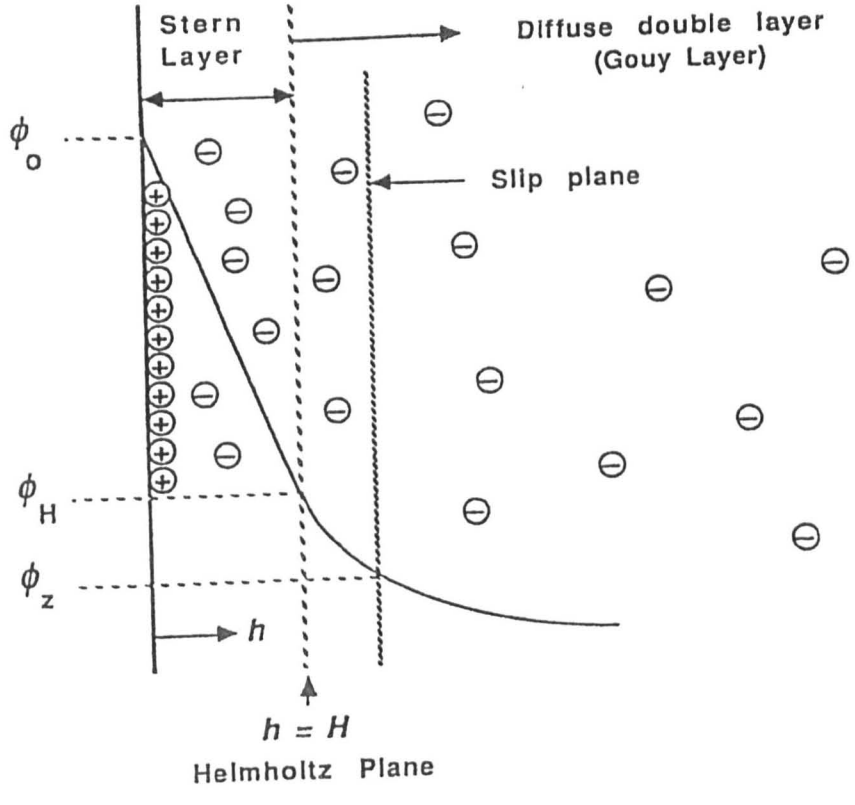

Fig. 25 The stabilising double layer of a sol particle [153].

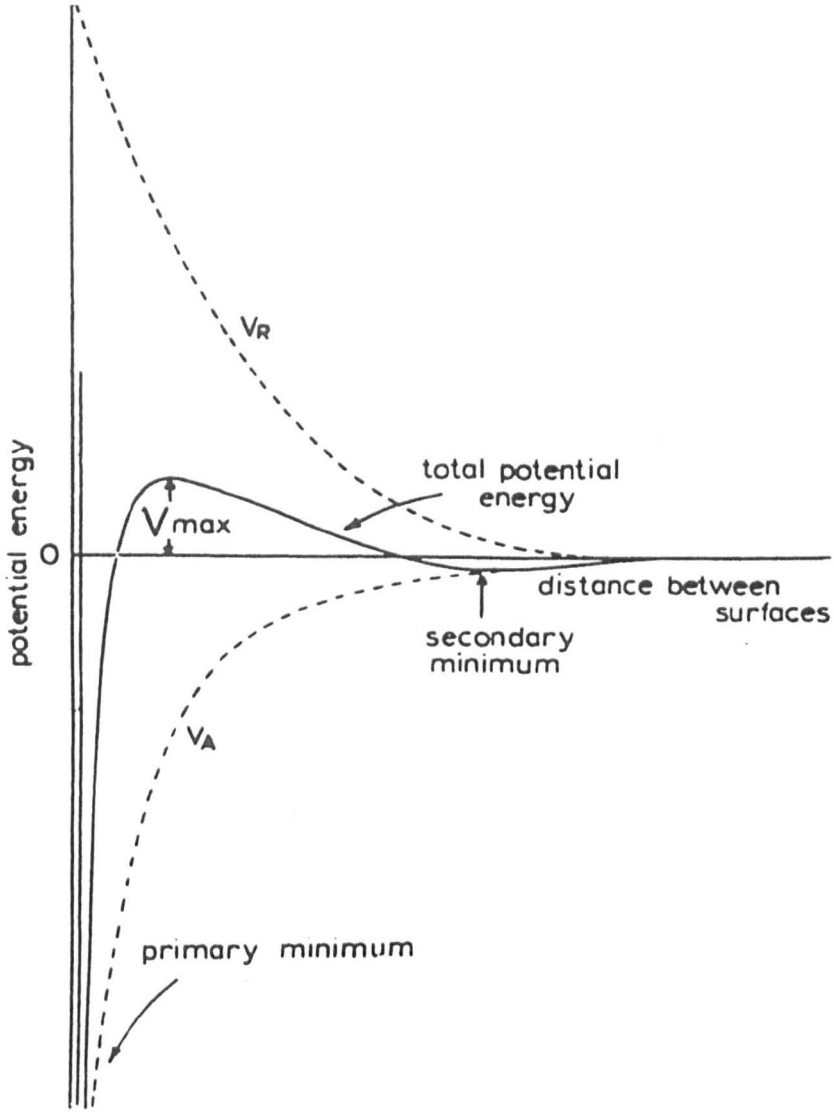

Fig. 26 The variation in net potential energy, summed from attractive (V_A) and repulsive (V_R) forces, with distance from the surface of a sol particle [153].

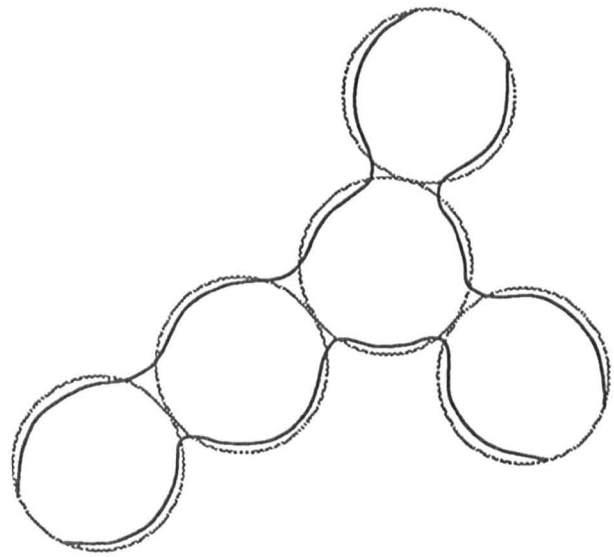

Fig. 27 The ripening and coarsening process in the ageing of sol particles [153].

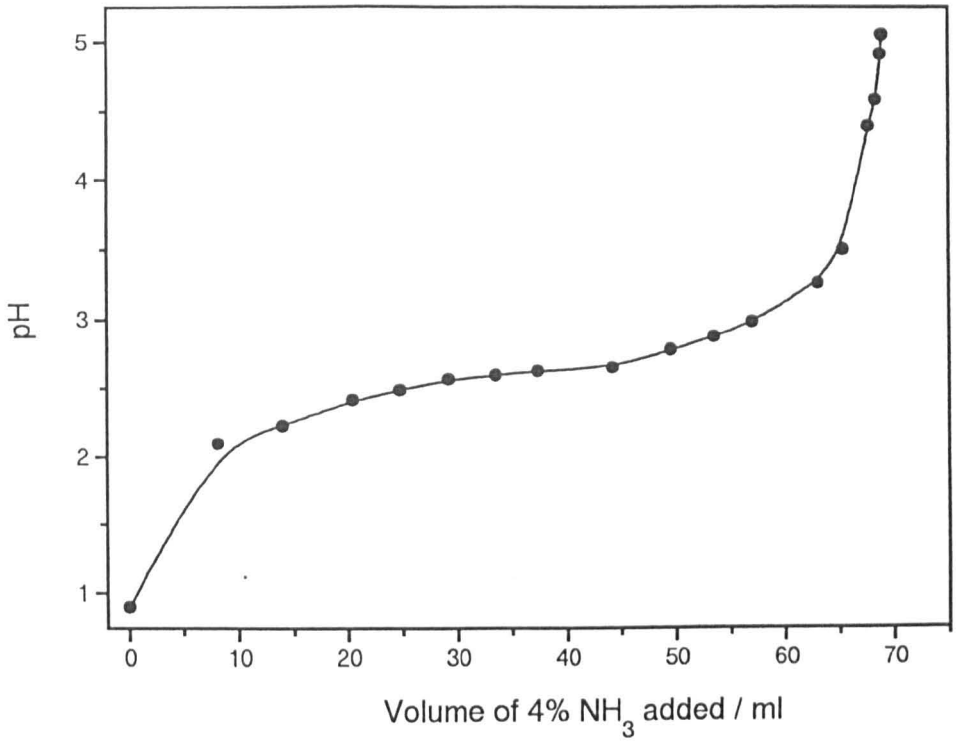

Fig. 28 Plot of solution pH versus volume of ammonia solution added for a typical 15 minute precipitation of $FeCl_3$, where precipitation commences at ~ pH 3.

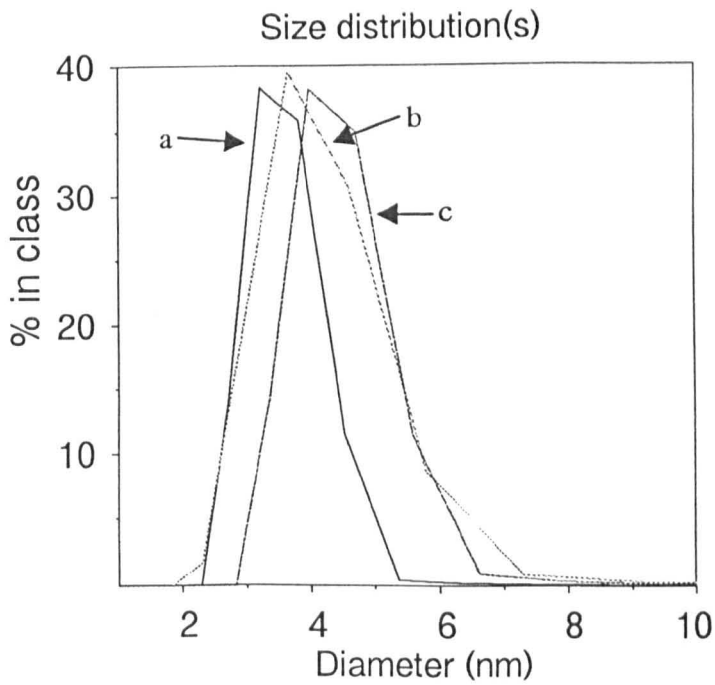

Fig. 29 Number average distributions for Fe/Br sols, made by precipitation to a) pH 4, b) pH 5 and c) pH 6.

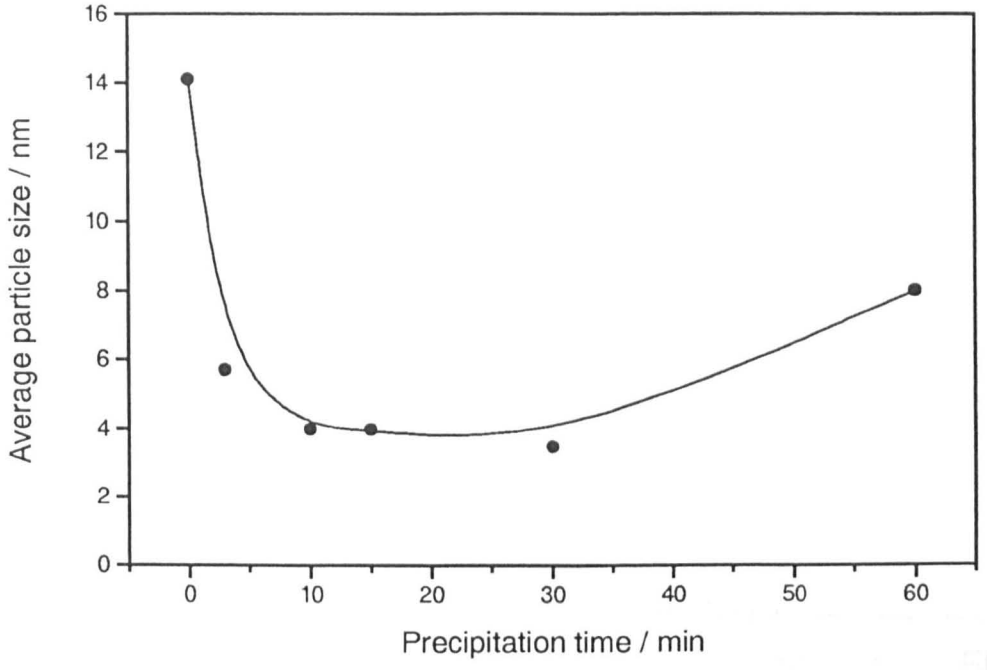

Fig. 30 Plot of precipitation time versus volume average for halide-$Fe(OH)_3$ sols.

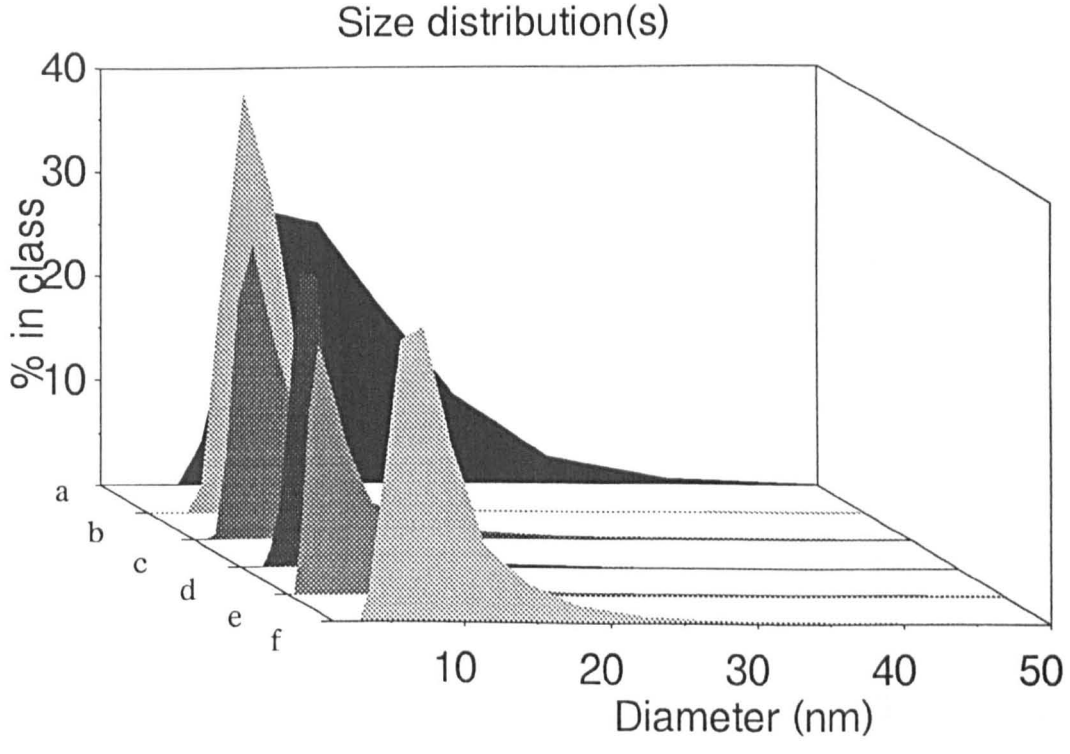

Fig. 31 *I* Variation in volume distribution with precipitation times of a) instant, b) mixer, c) 3 min, d), 15 min, e) 30 min and f) 60 min.

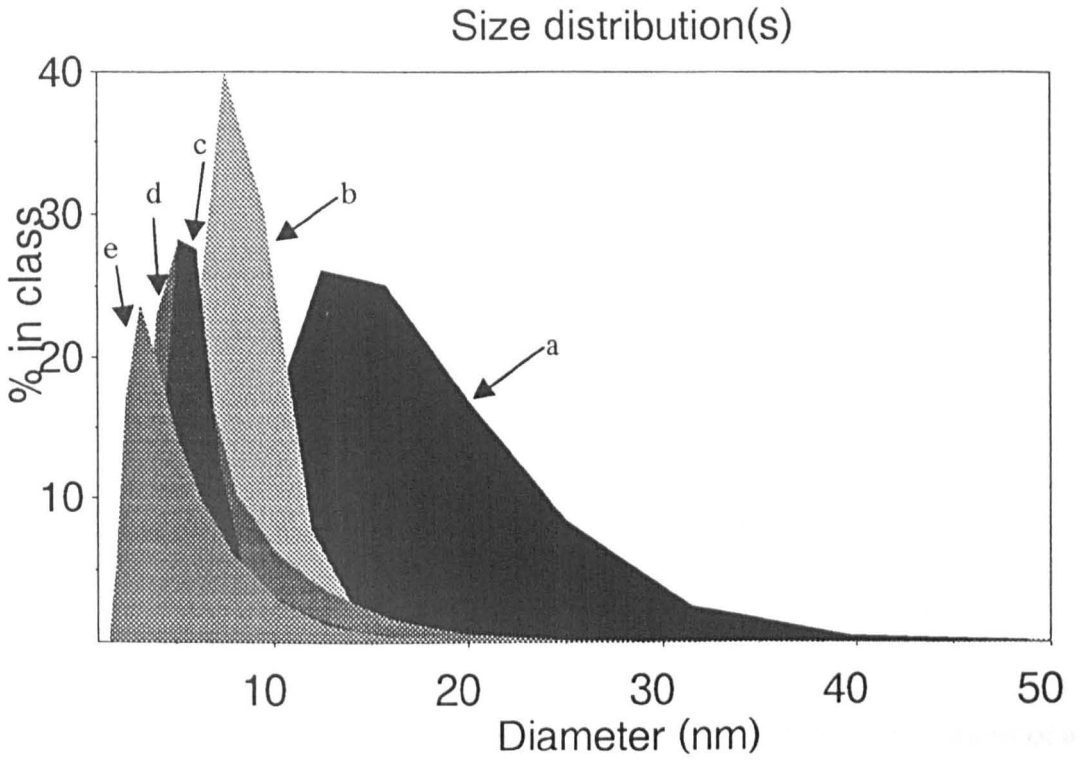

Fig. 31 *II* Variation in volume distribution with precipitation times of a) instant, b) mixer, c) 3 min, d), 15 min and e) 30 min.

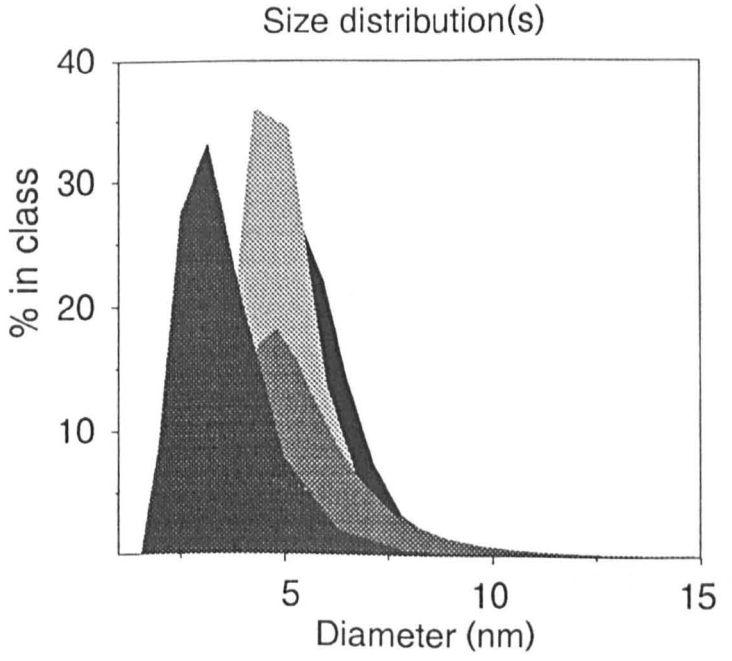

Fig. 32 Comparison of number average distributions of 15 min precipitation Fe/Br sols. From rear to front; lower HBr:Fe ratio, higher Cl^- content, standard sol, and sol made from fresh supply of $FeCl_3.6(H_2O)$.

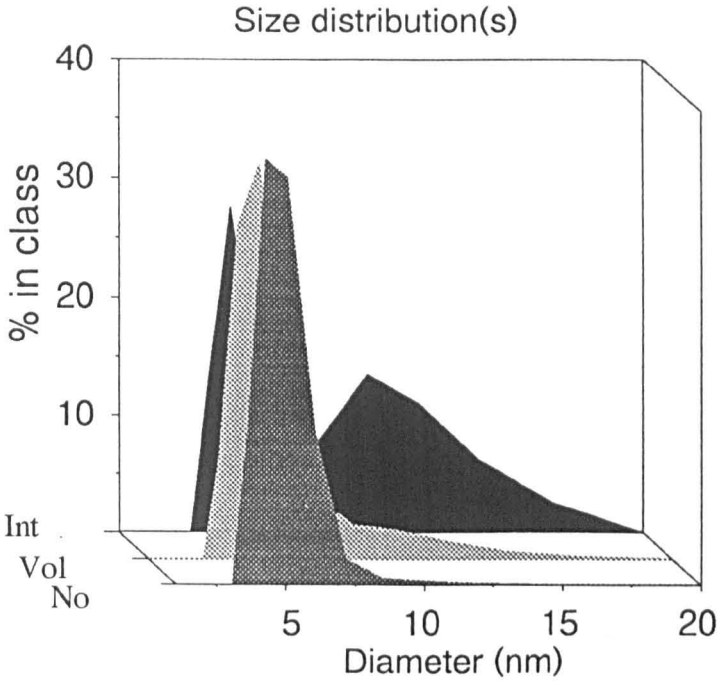

Fig. 33 From rear to front, the intensity, volume and number distributions of a standard Fe/Br sol.

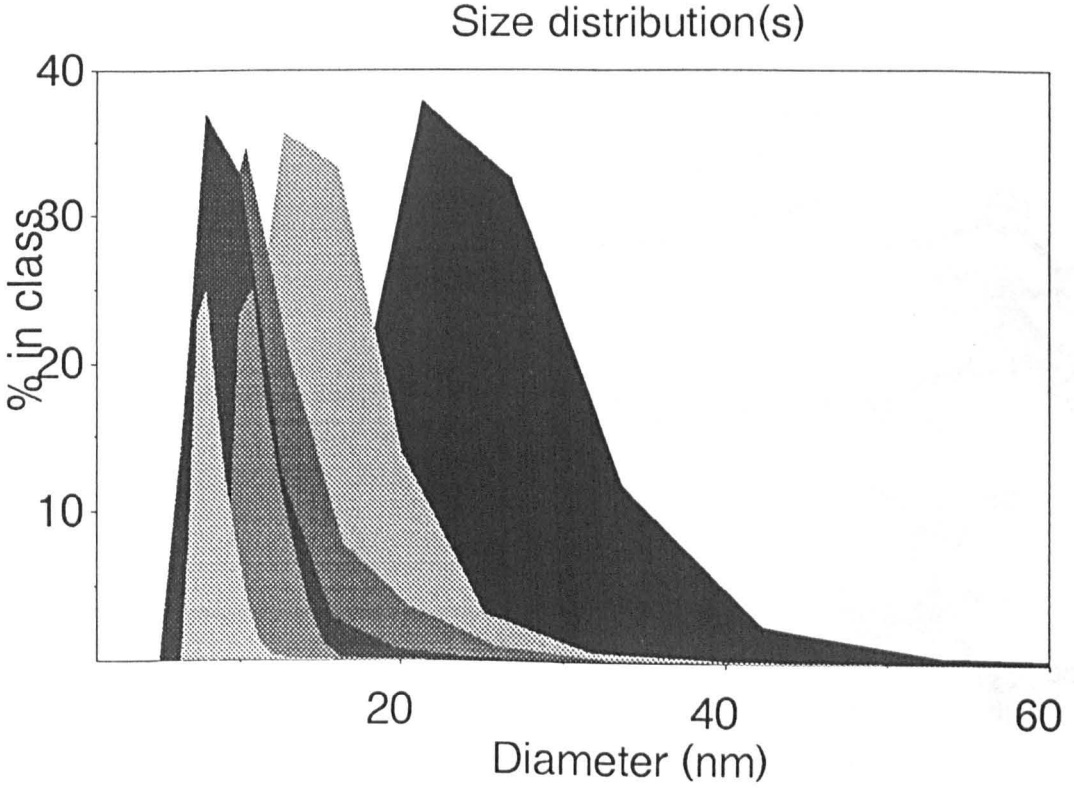

Fig. 34 The variation in volume distribution over time for Fe/NO_3 sol. From rear to front; 1, 2, 5, 10, 20 and 30 hr after sol formation.

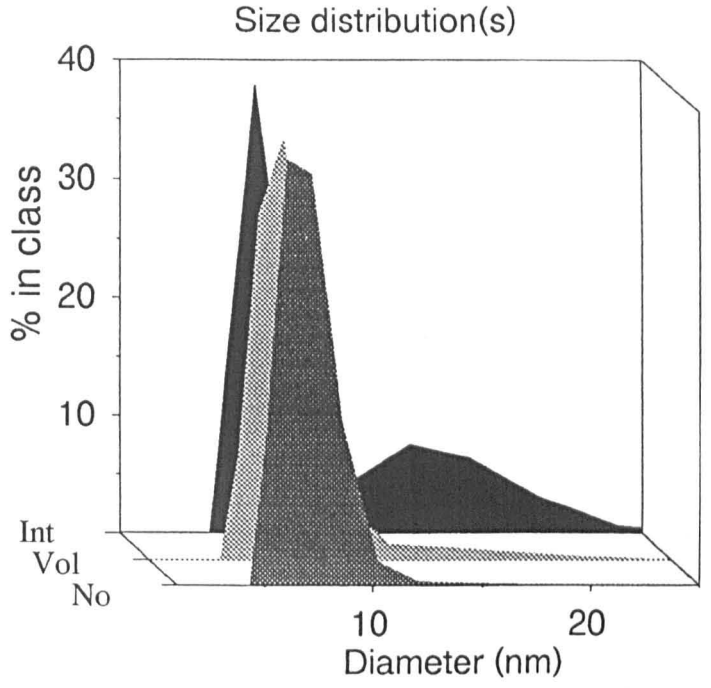

Fig. 35 From rear to front, the intensity, volume and number distributions of a standard Fe/NO_3 sol.

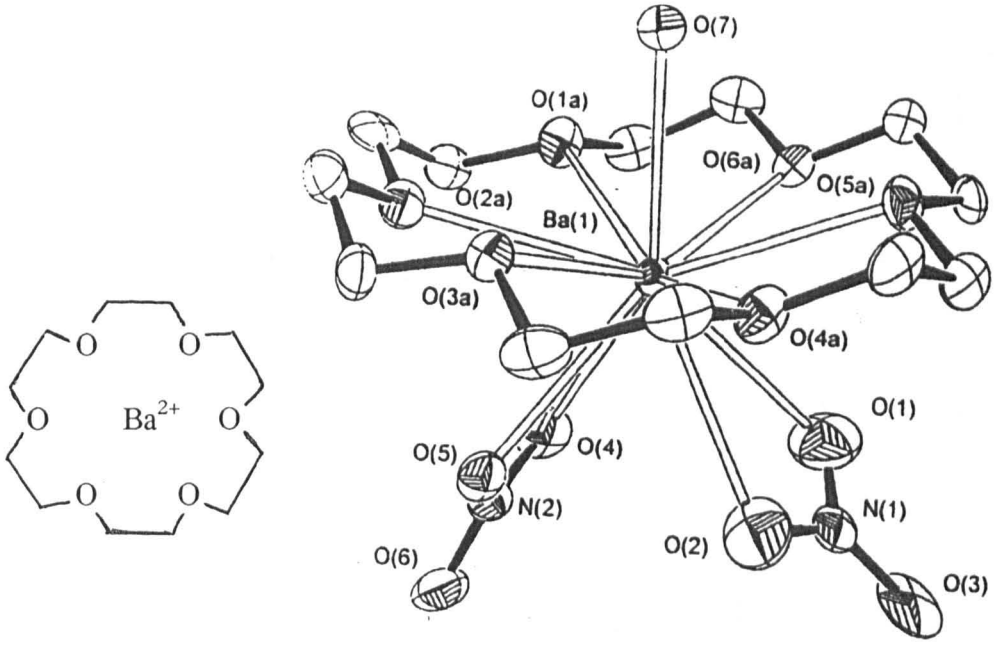

Fig. 36 The structure of 18-crown-6-ether and the $[Ba(NO_3)_2(H_2O)(18\text{-crown-6})]$ complex.

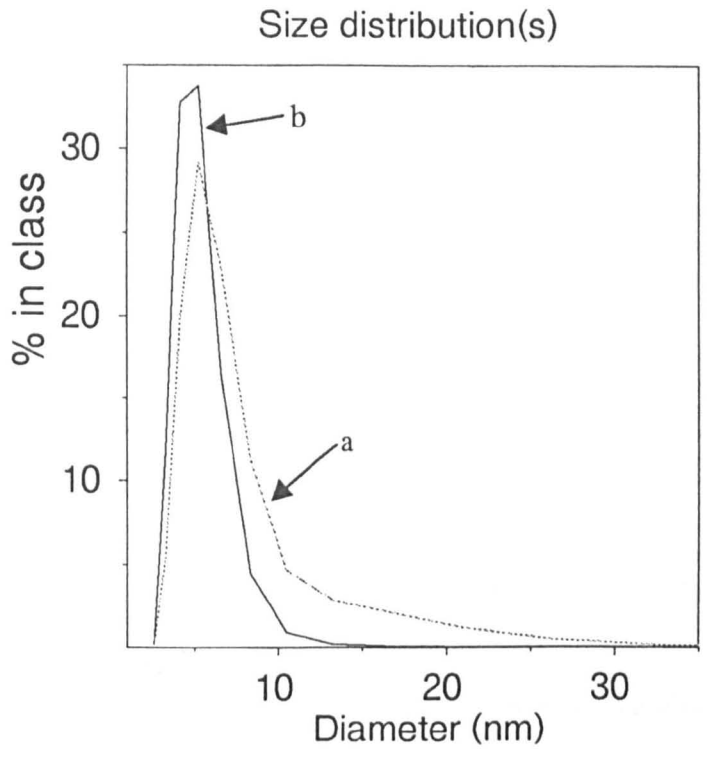

Fig. 37 The volume (a) and number (b) distributions of the standard BaM sol.

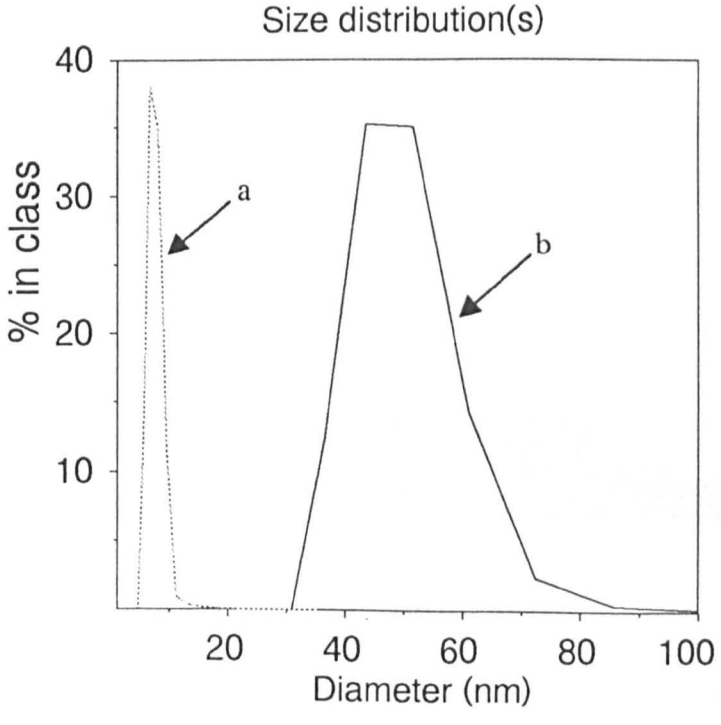

Fig. 38 Comparison of the number distributions of the halide free sols, for a) SrM and b) BaM.

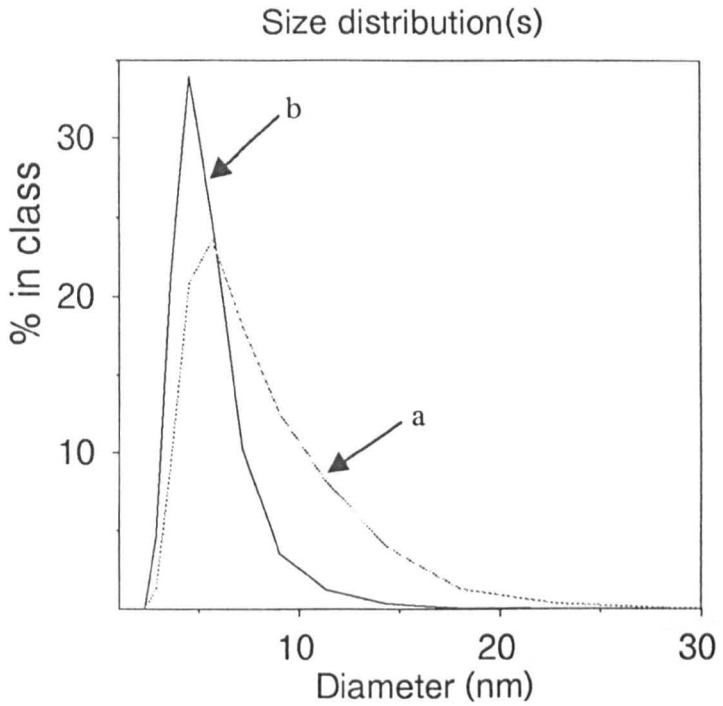

Fig. 39 The volume (a) and number (b) distributions of the standard SrM sol

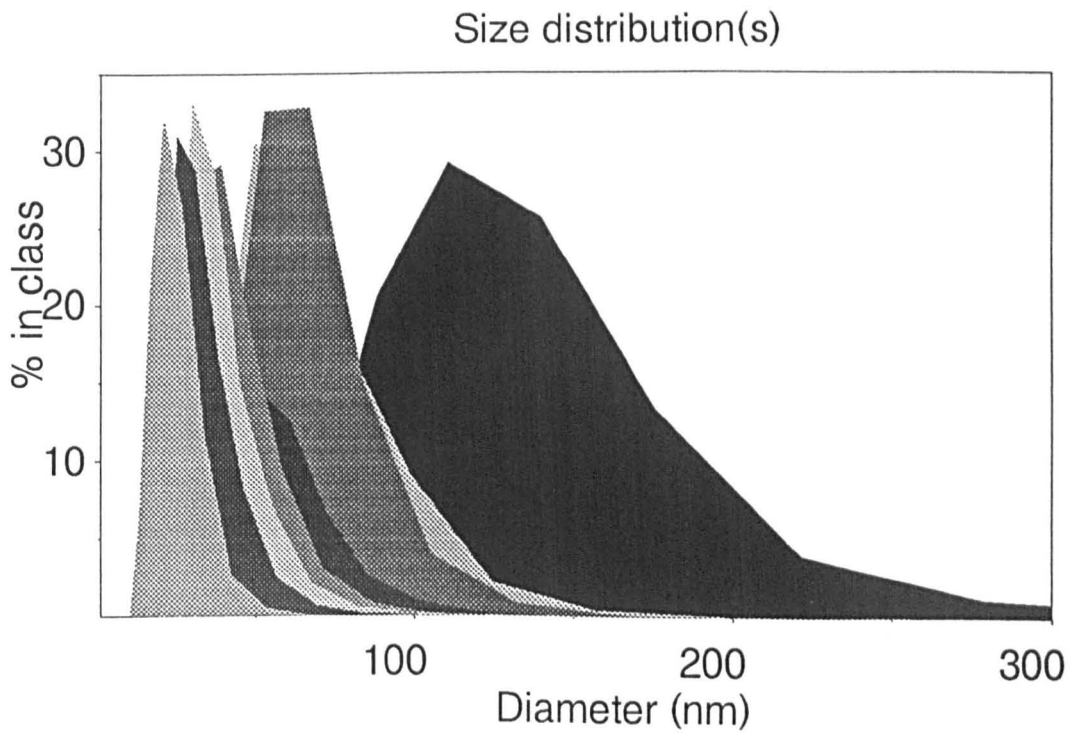

Fig. 40 Decrease in volume distributions of the totally aqueous titania sol over one week of peptisation, 0 to 7 days after initial digestion from rear to front.

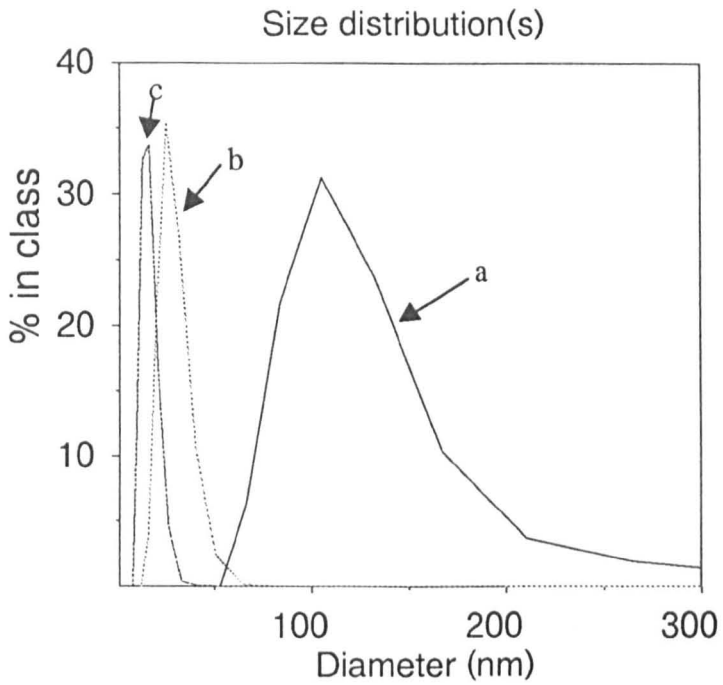

Fig. 41 Volume distributions of the totally aqueous titania sol a) 1 day, b) 7 days and c) 45 days after initial digestion.

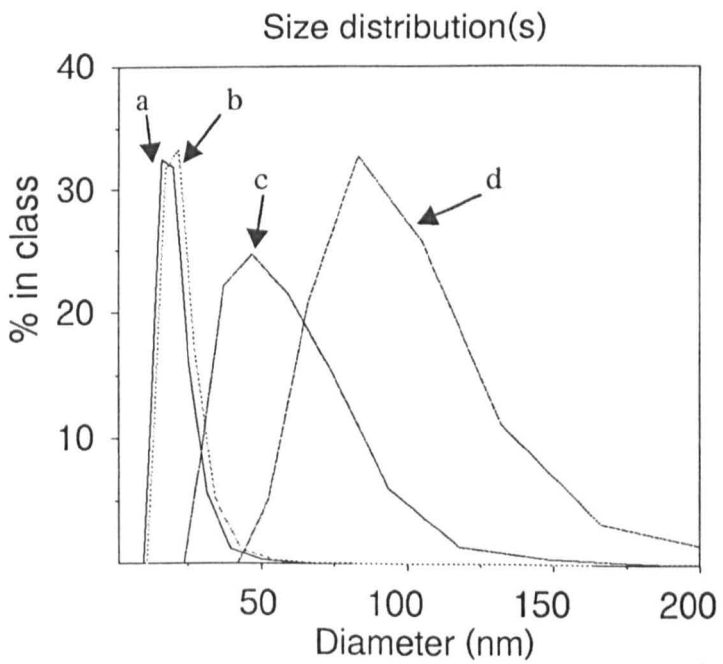

Fig. 42 Volume distributions of a) the original totally aqueous titania sol, and the redispersed sol after evaporation at b) ambient temperature, c) 35 °C and d) 95 °C.

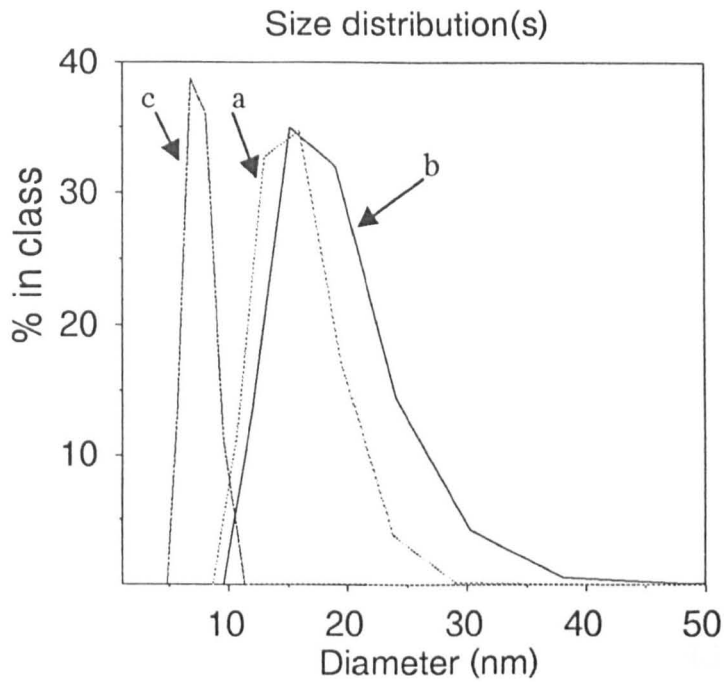

Fig. 43 The volume distributions of a) mixture of aqueous titania sol and Fe/Br sol (x = 0.5), b) alkoxide titania sol and c) mixed iron / titania sol (x = 0.5).

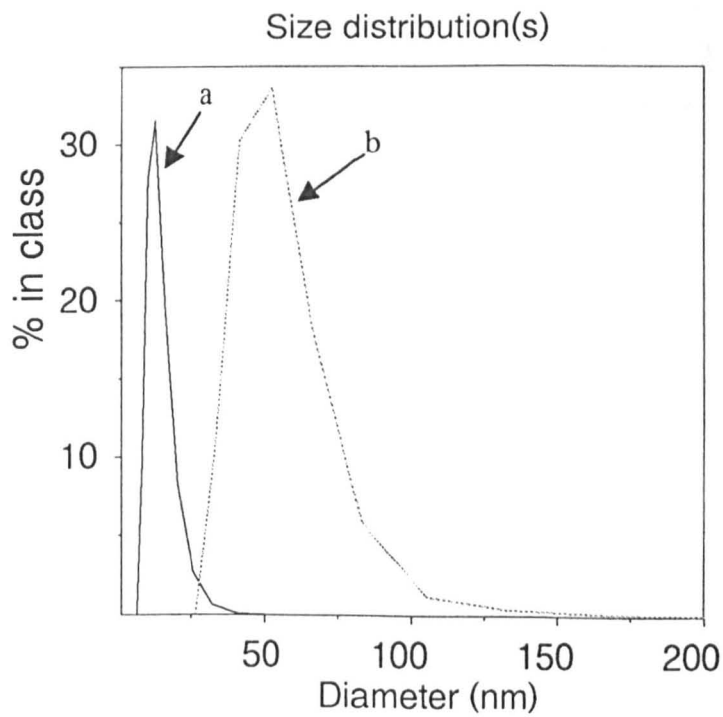

Fig. 44 Volume distributions for a) $Ti(n\text{-}OPr)_4$-$FeCl_3$ solution and b) precipitated and peptised sol.

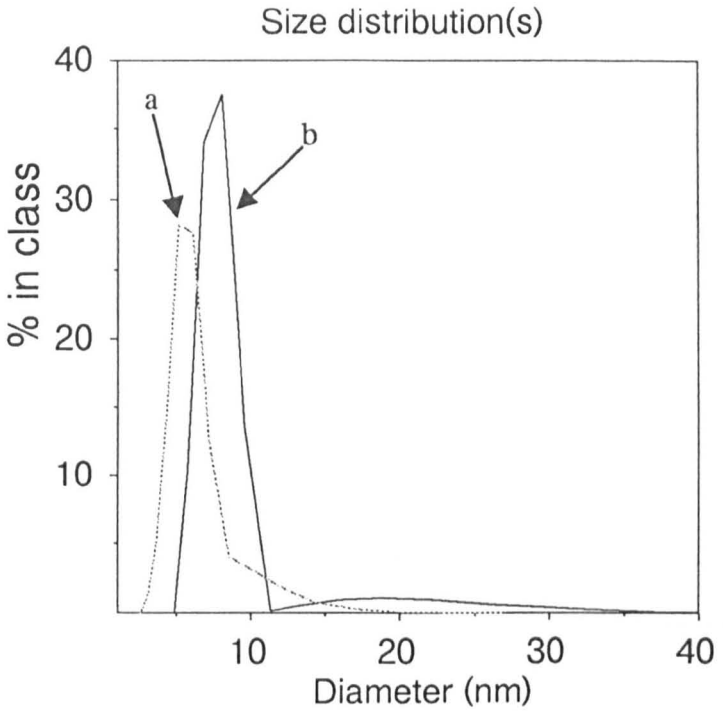

Fig. 45 Volume distributions for a) Fe/Br sol and b) Fe/Br-titania mixed sol.

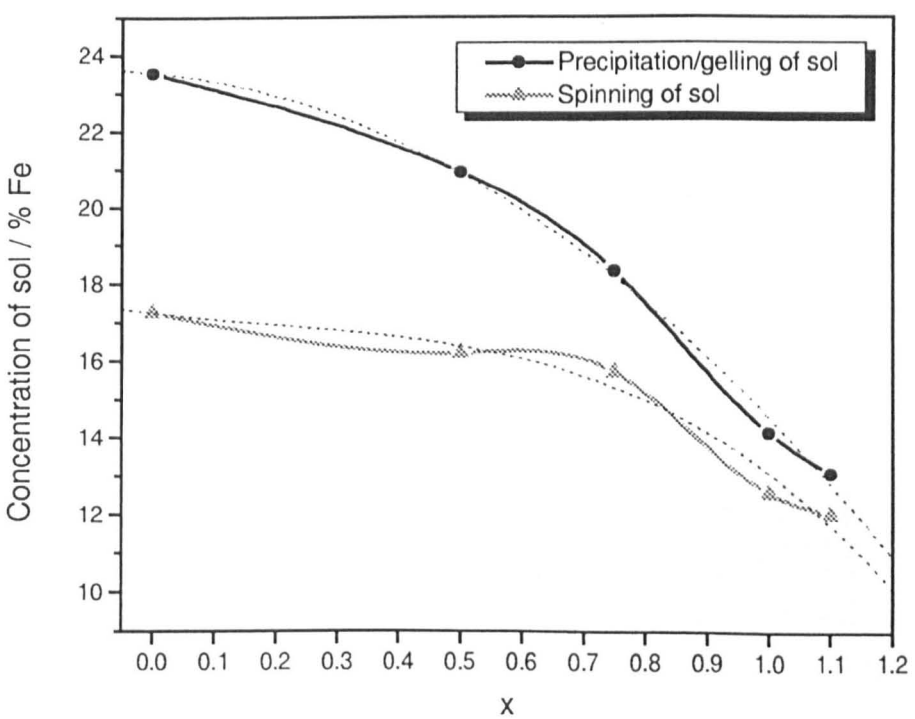

Fig. 46 Plots of maximum stable sol concentration and spinning concentration for $BaCo_xTi_xFe_{12-2x}O_{19}$ sols against x.

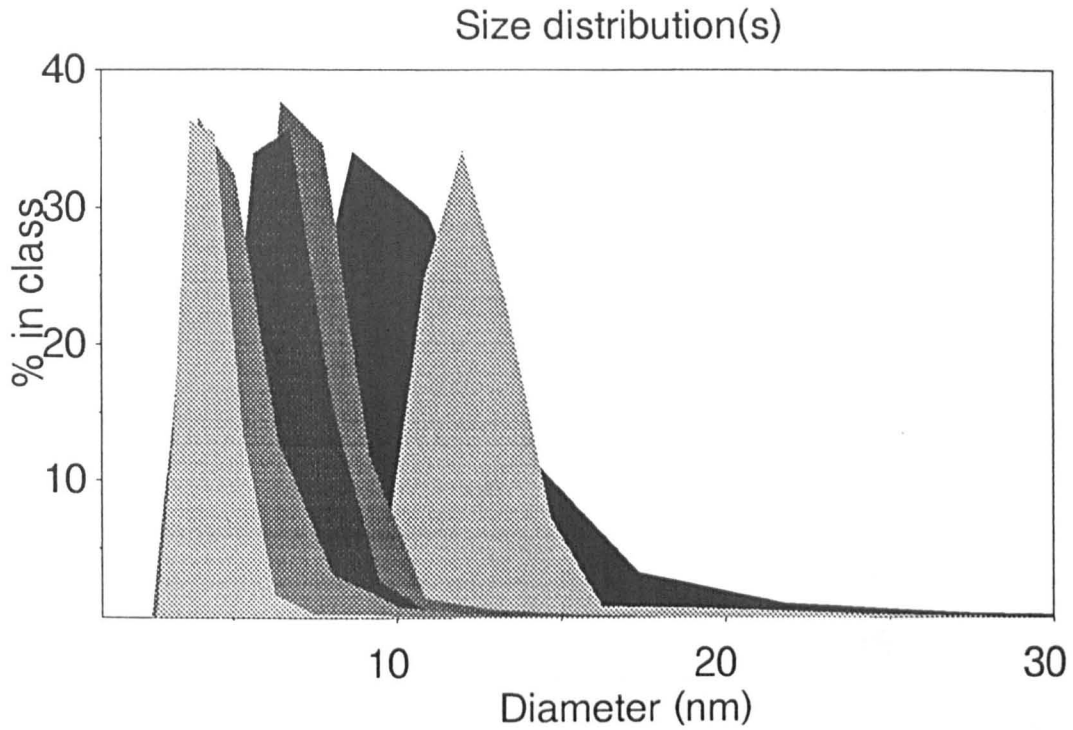

Fig. 47 Volume distributions of $BaCo_xTi_xFe_{12-2x}O_{19}$ sols. From rear to front, x = 1.1, 1.0, 0.75, 0.5, 0 and the undoped Fe/Br sol.

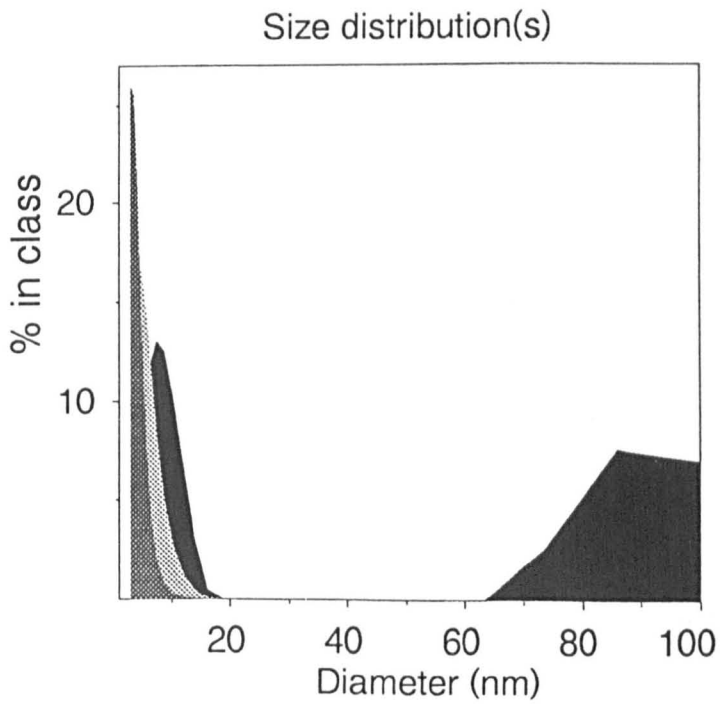

Fig. 48 The intensity (black), volume (pale grey) and number distributions (dark grey) of the ultrasonically peptised titania sol.

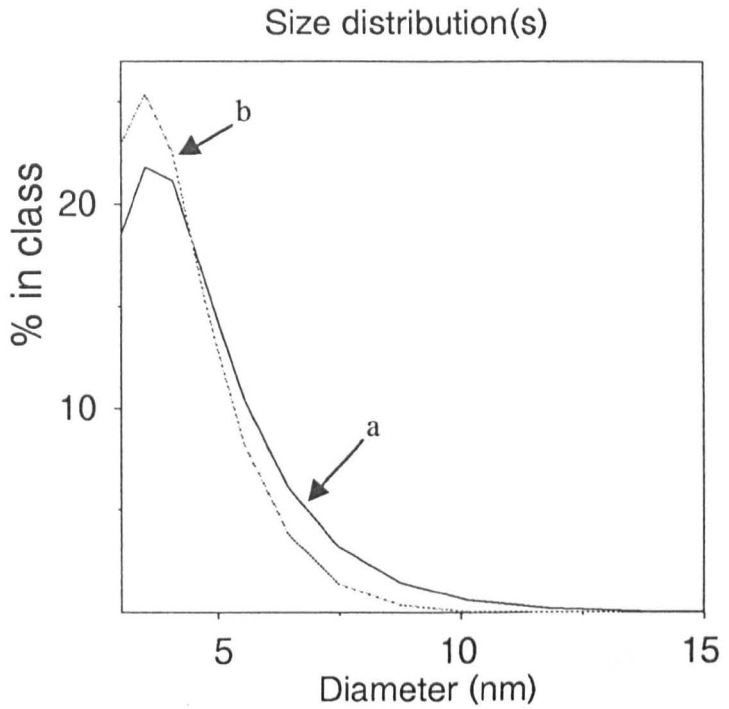

Fig. 49 Volume distributions of $SrCo_xTi_xFe_{12-2x}O_{19}$ sols with x = a) 0.5 and b) 1.0.

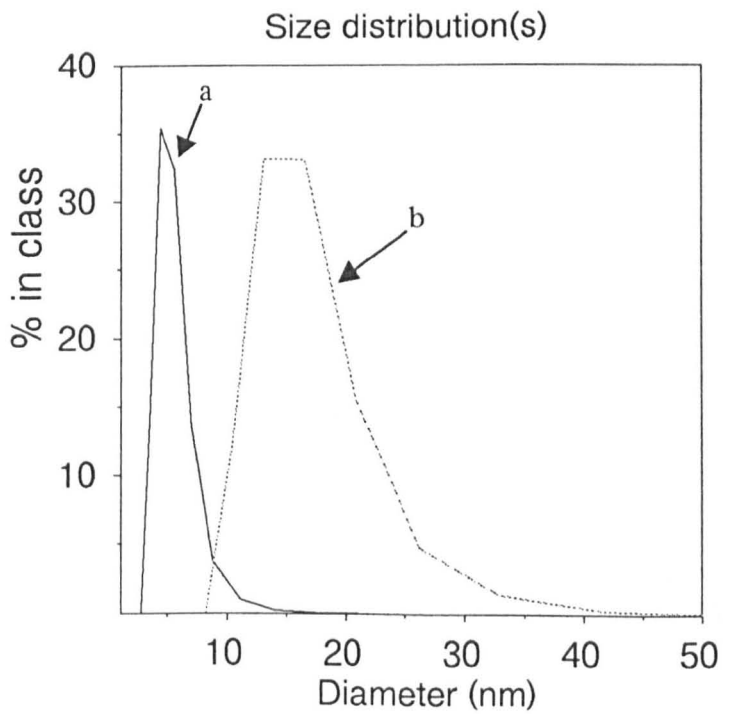

Fig. 50 Comparison of volume distributions of halide free sols for a) undoped SrM and b) $SrCo_{0.5}Ti_{0.5}Fe_{11}O_{19}$.

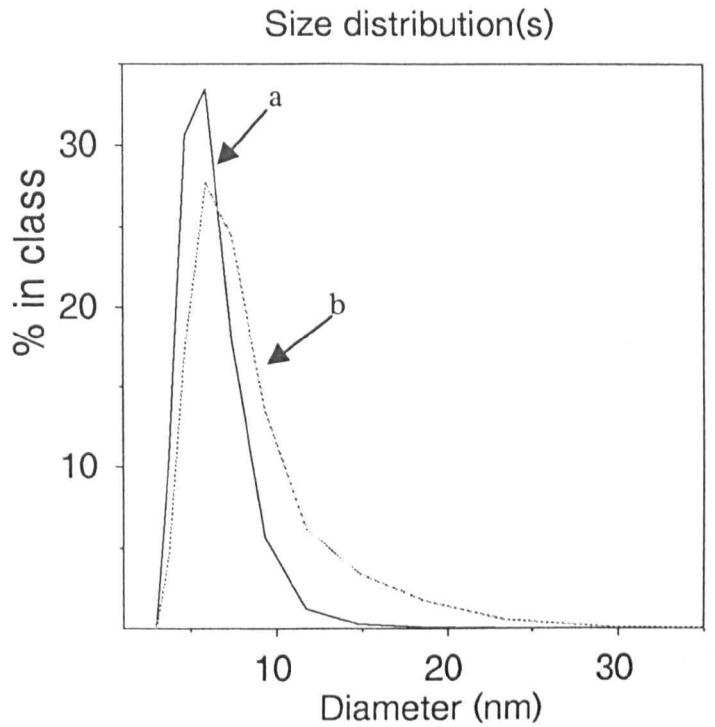

Fig. 51 Volume (a) and number (b) distributions of the Co_2Y sol.

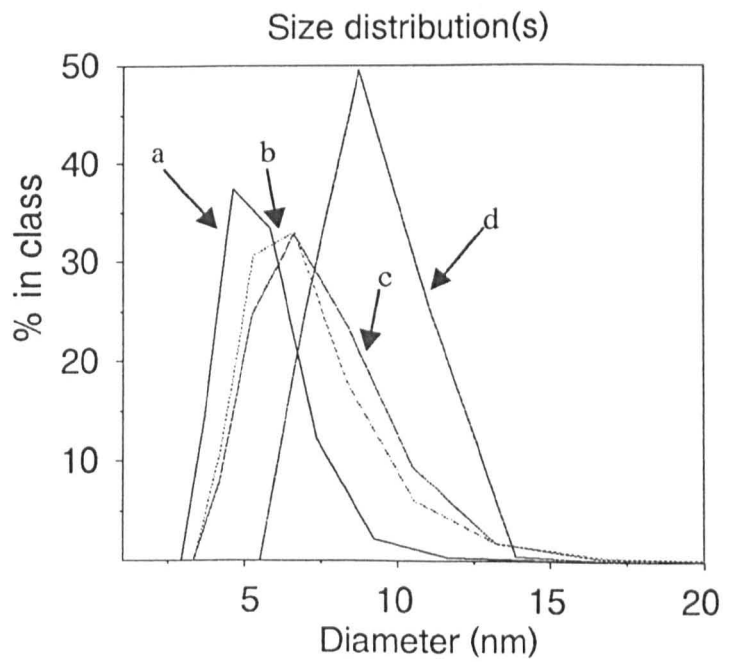

Fig. 52 Comparisons of the number distributions for a) Co_2Y, b) Ni_2Y, c) Mn_2Y and d) Zn_2Y sols.

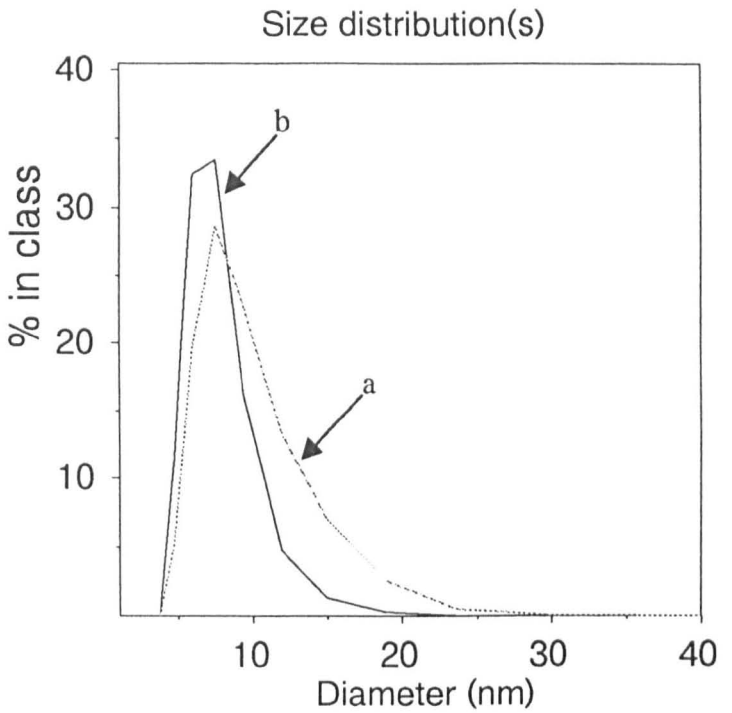

Fig. 53 Volume (a) and number (b) distrbutions of the Co_2Z sol.

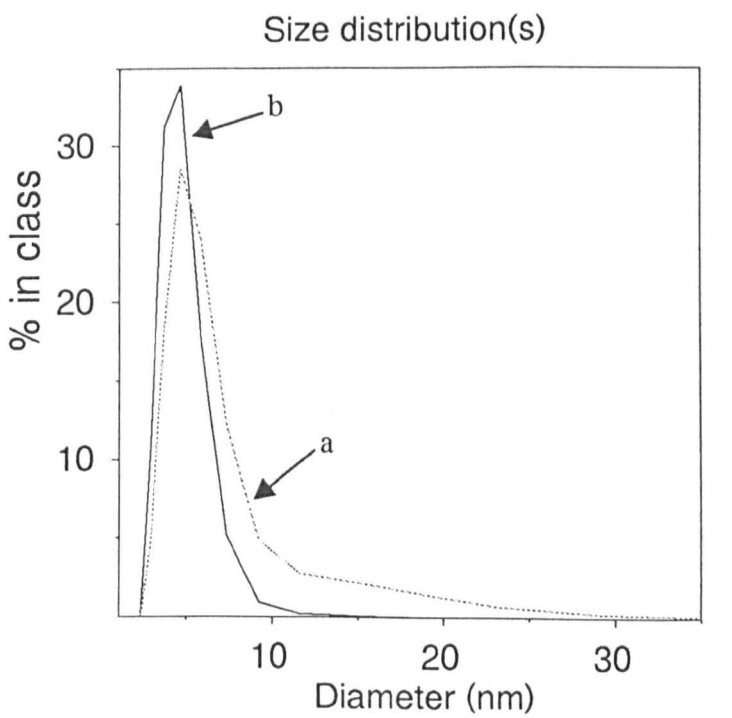

Fig. 54 Volume (a) and number (b) distributions of the Co_2W sol.

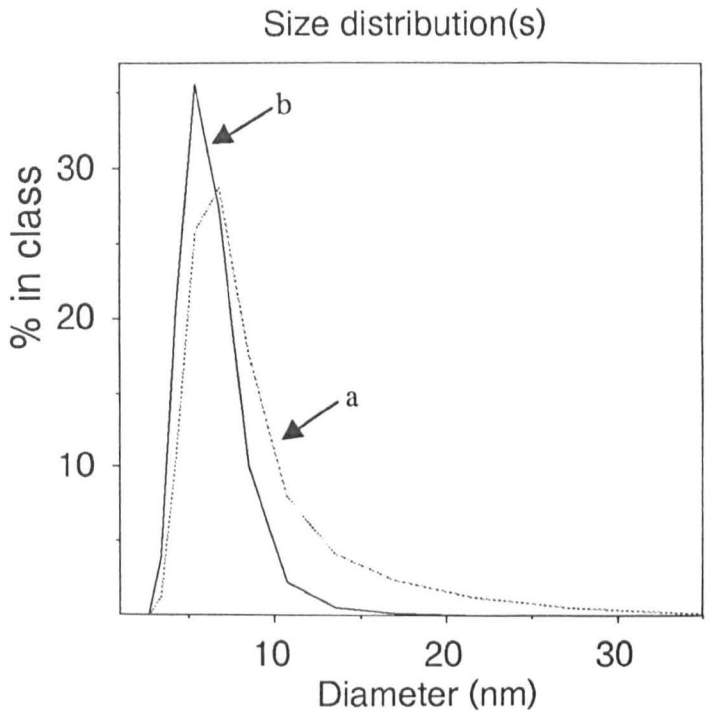

Fig. 55 Volume (a) and number (b) distributions of the Co_2X sol.

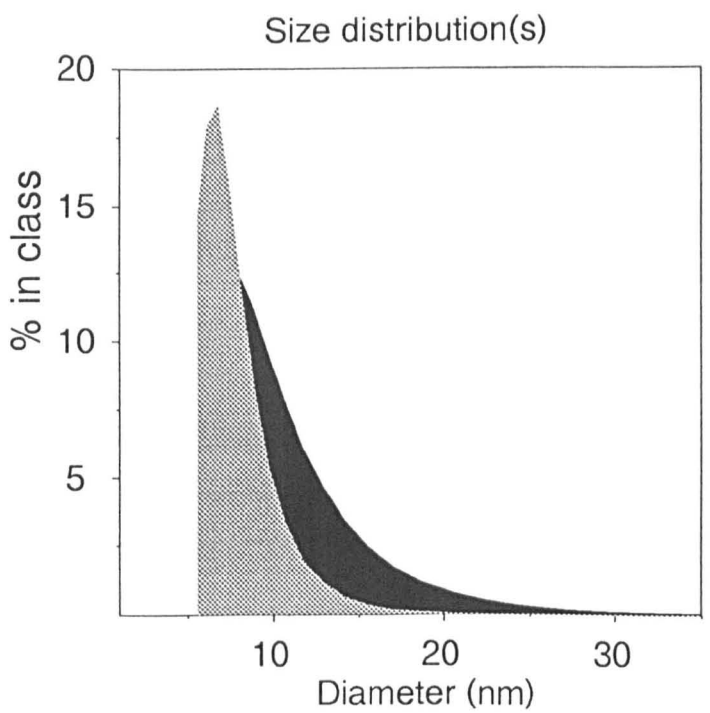

Fig. 56 Volume (black) and number (grey) distributions of the Co_2U sol.

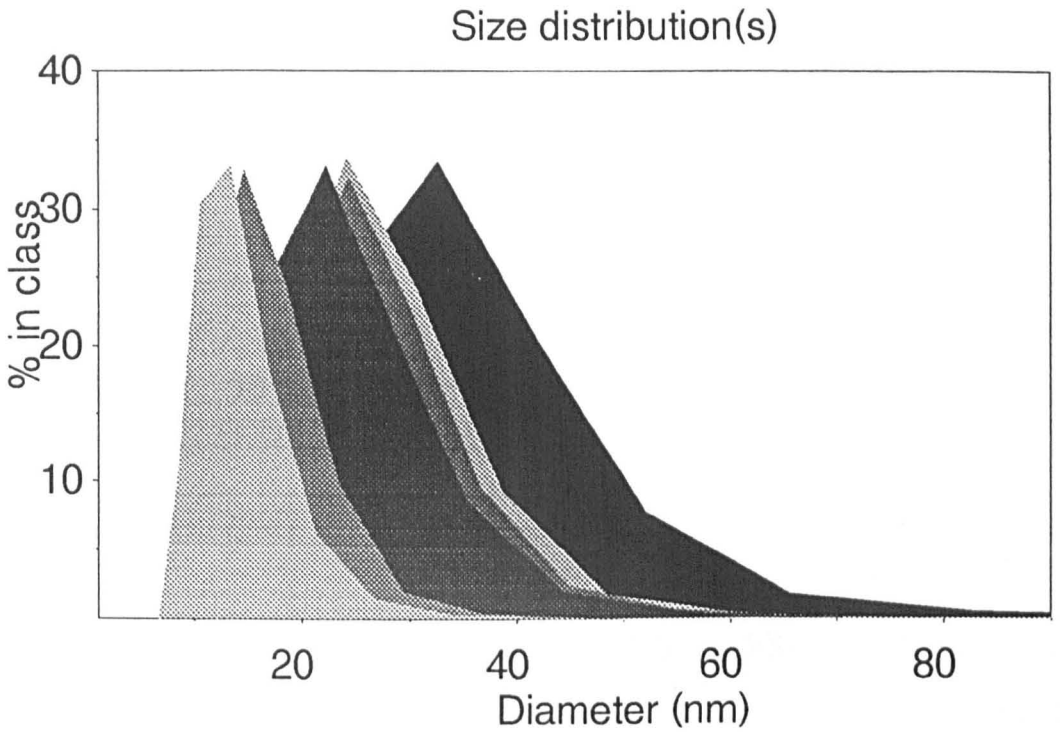

Fig. 57 Comparisons of the volume distributions of BaM sols doped with, from rear to front, 1% Y_2O_3, 1% ZrO_2, 1% Cr_2O_3, 1% stabilised ZrO_2, 0.25% V_2O_5 and 0.06% Nb_2O_5.

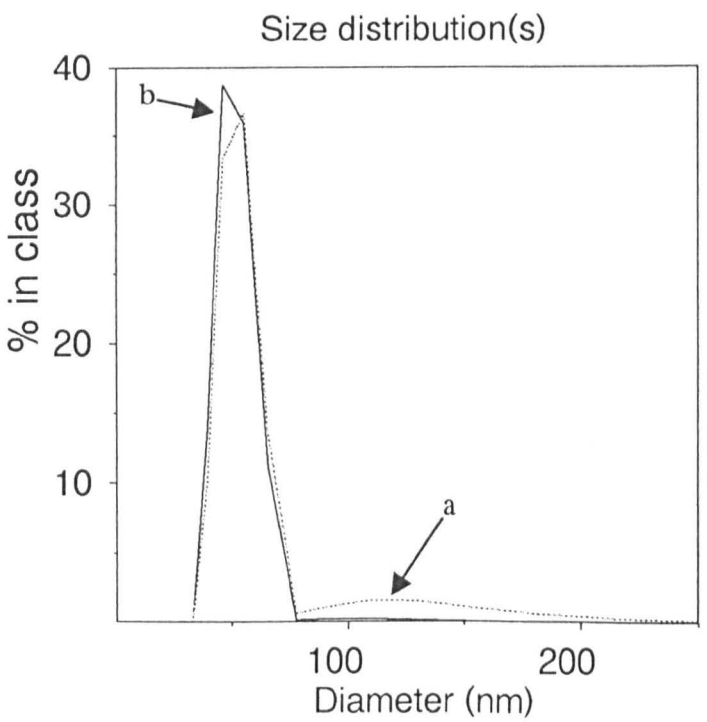

Fig. 58 Volume (a) and number (b) distributions of the alkoxide-derived Co_2Z sol.

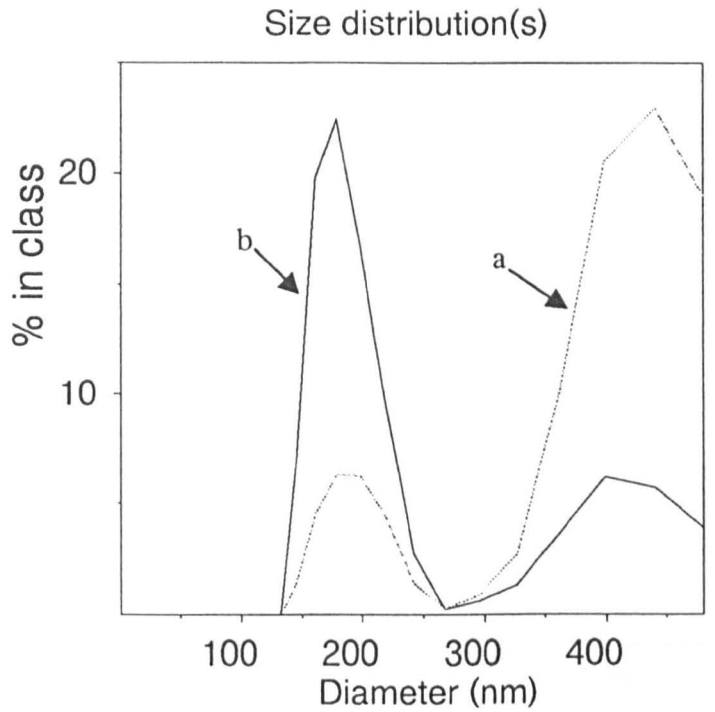

Fig. 59 Volume (a) and number (b) distributions of the alkoxide-derived BaM sol.

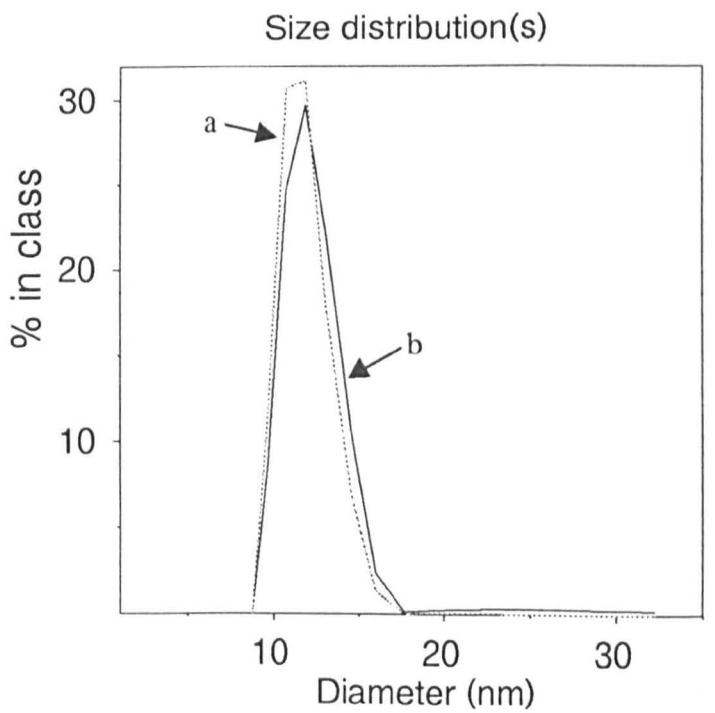

Fig. 60 Volume (a) and number (b) distributions of the ultrasonically peptised Fe/NO_3 sol.

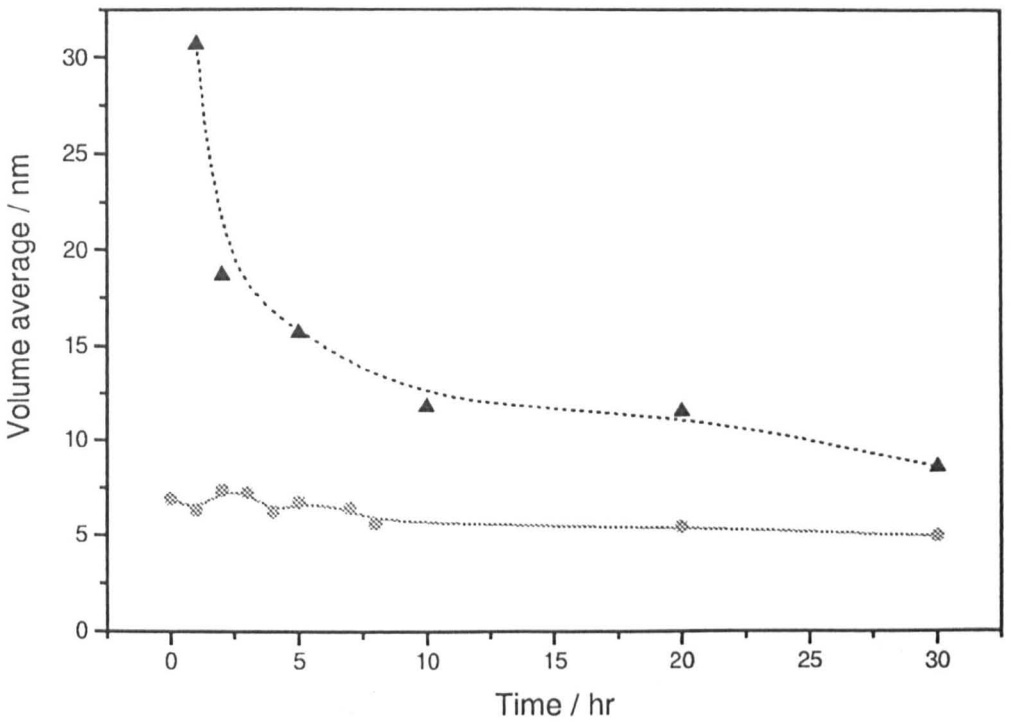

Fig. 61 Plots of change in volume average with time, from start of peptisation, for Fe/Br (solid line, ●) and Fe/NO_3 (dotted line, ▲) sols.

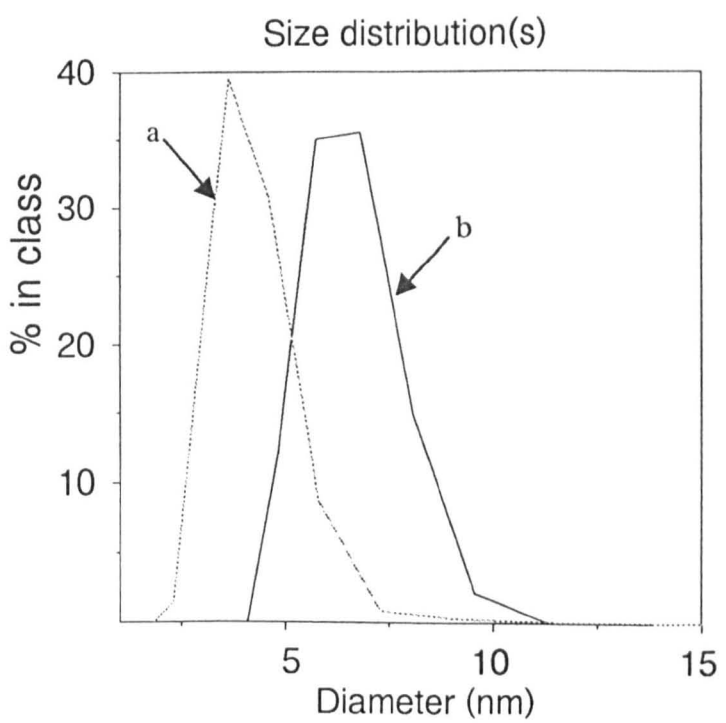

Fig. 62 Comparison of the number distributions of a) Fe/Br and b) Fe/NO_3 sols.

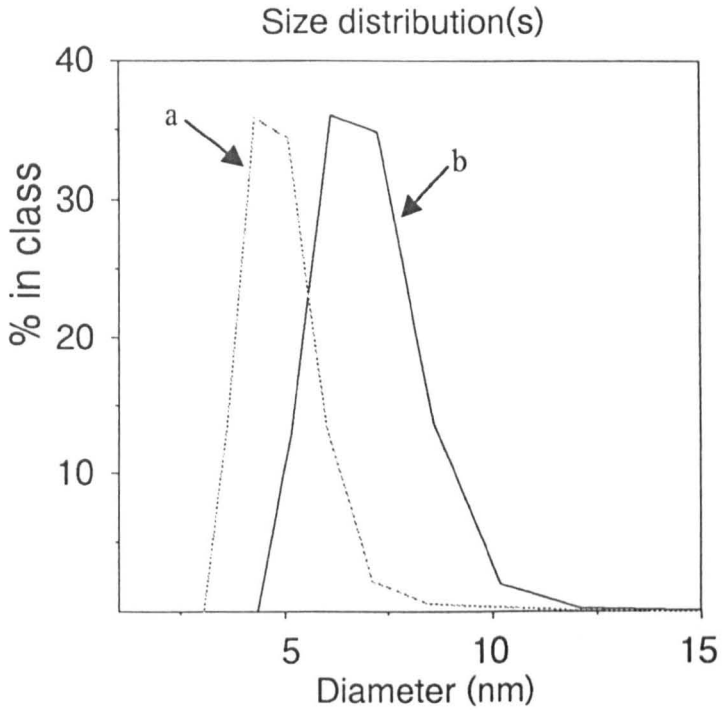

Fig. 63 Comparison of the volume distributions of a) Fe/Br and b) Fe/NO_3 sols.

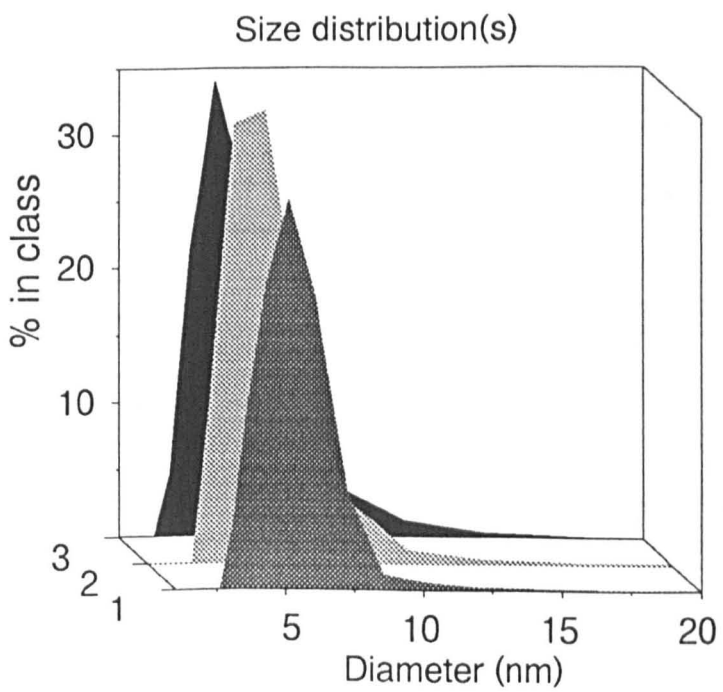

Fig. 64 Comparison of the number distributions of, from rear to front, the SrM, BaM and Fe/Br sols.

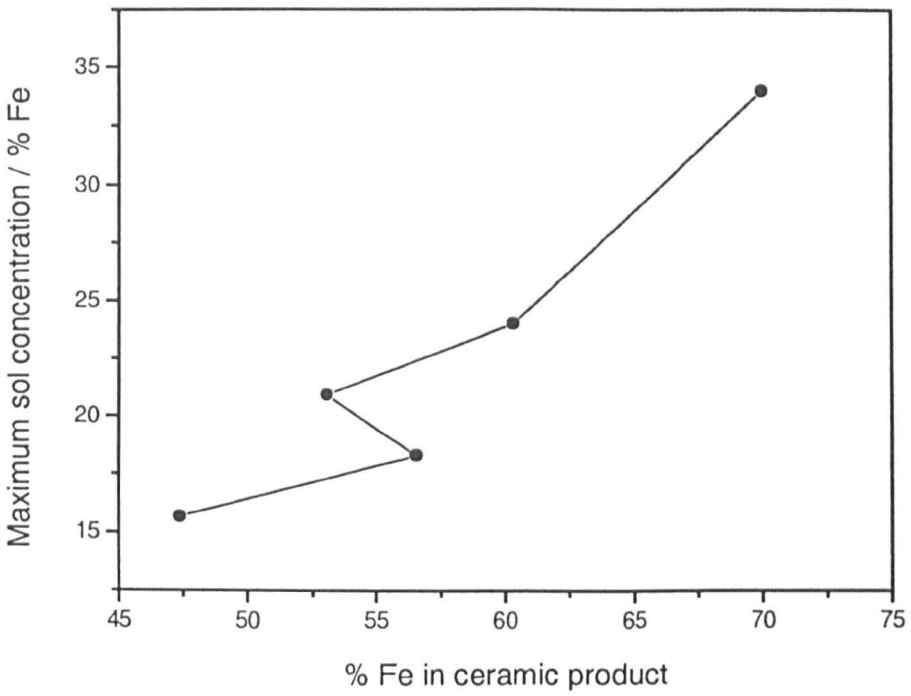

Fig. 65 Plot of maximum sol concentration against % Fe in the ceramic product for ferrite precursor Fe/Br sols.

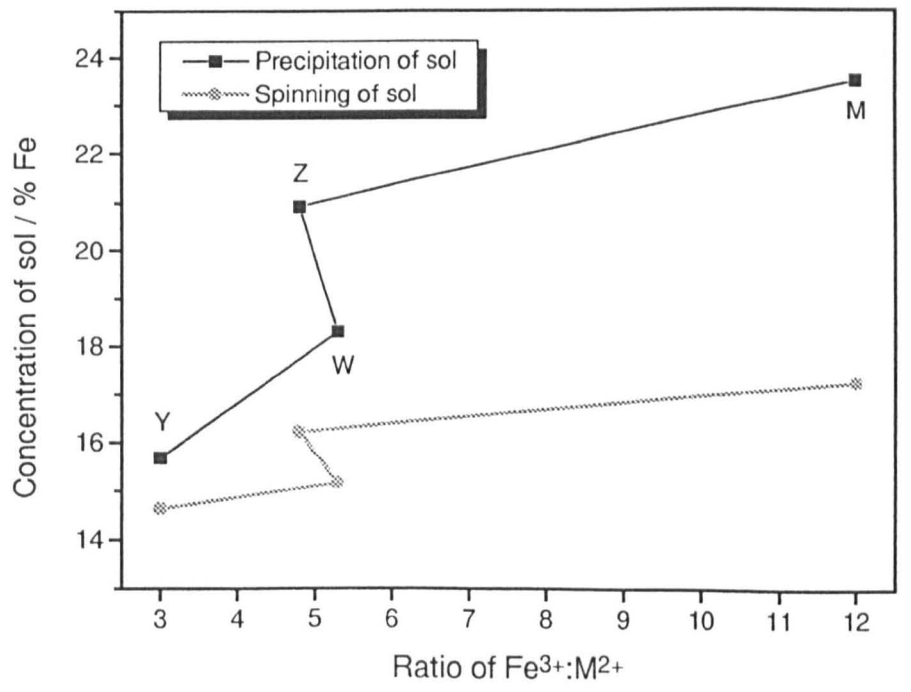

Fig. 66 Plots of maximum sol concentration and spinning concentration against the ratio of Fe^{3+}:M^{2+} in ferrite precursor Fe/Br sols.

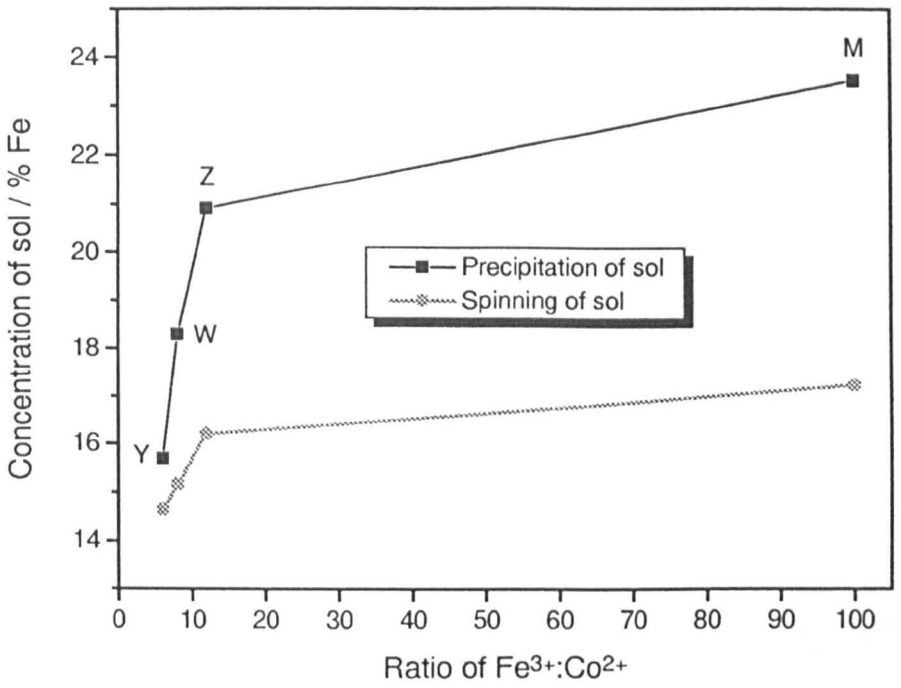

Fig. 67 Plots of maximum sol concentration and spinning concentration against the ratio of Fe^{3+}:Co^{2+} in ferrite precursor Fe/Br sols.

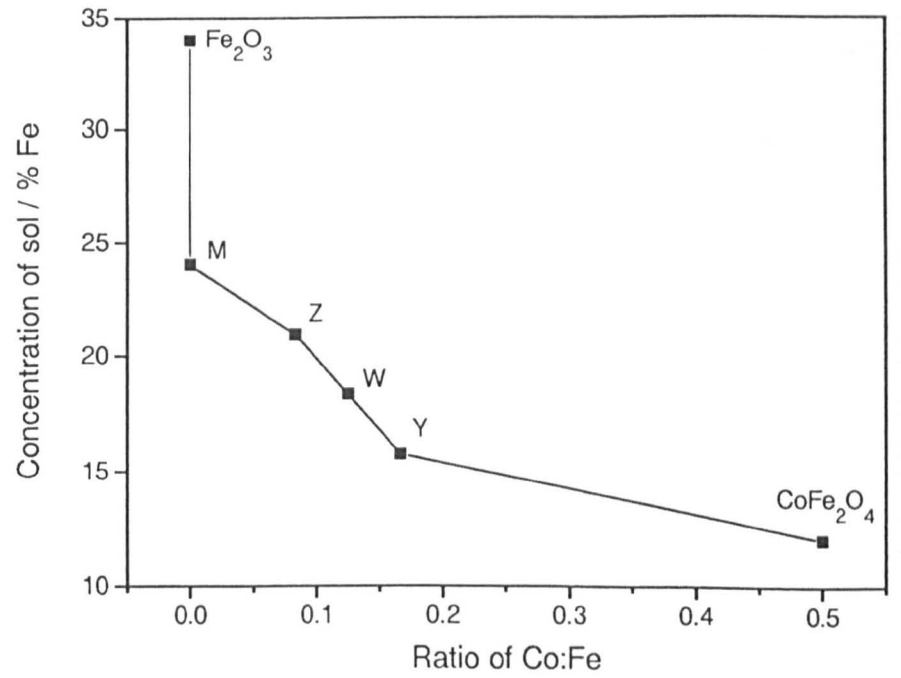

Fig. 68 Relationship between sol stability, barium addition and ratio of Co^{2+}:Fe^{3+} in ferrite precursor Fe/Br sols.

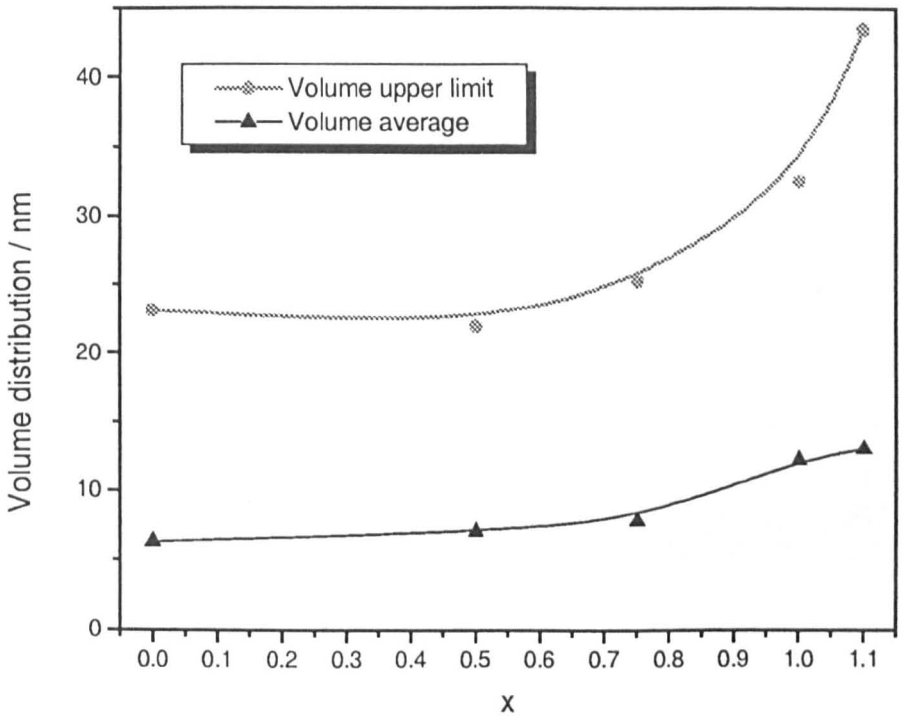

Fig. 69 Effect of Ti^{4+}/Co^{2+} addition on the volume distribution of the Fe/Br BaM sol.

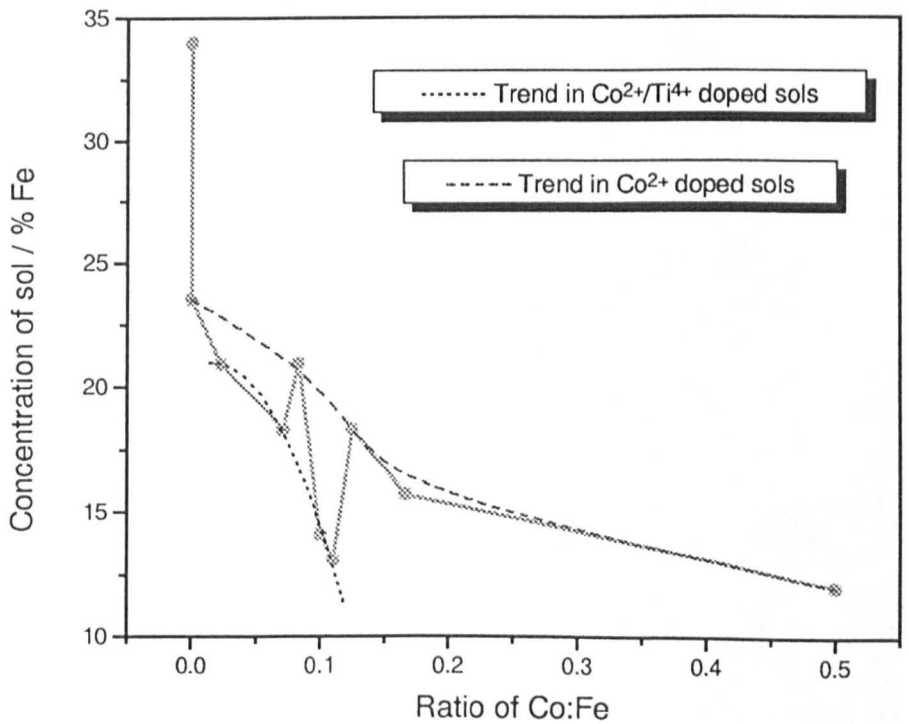

Fig. 70 Comparison of Co^{2+} addition and Ti^{4+}/Co^{2+} addition on Fe/Br sol stability.

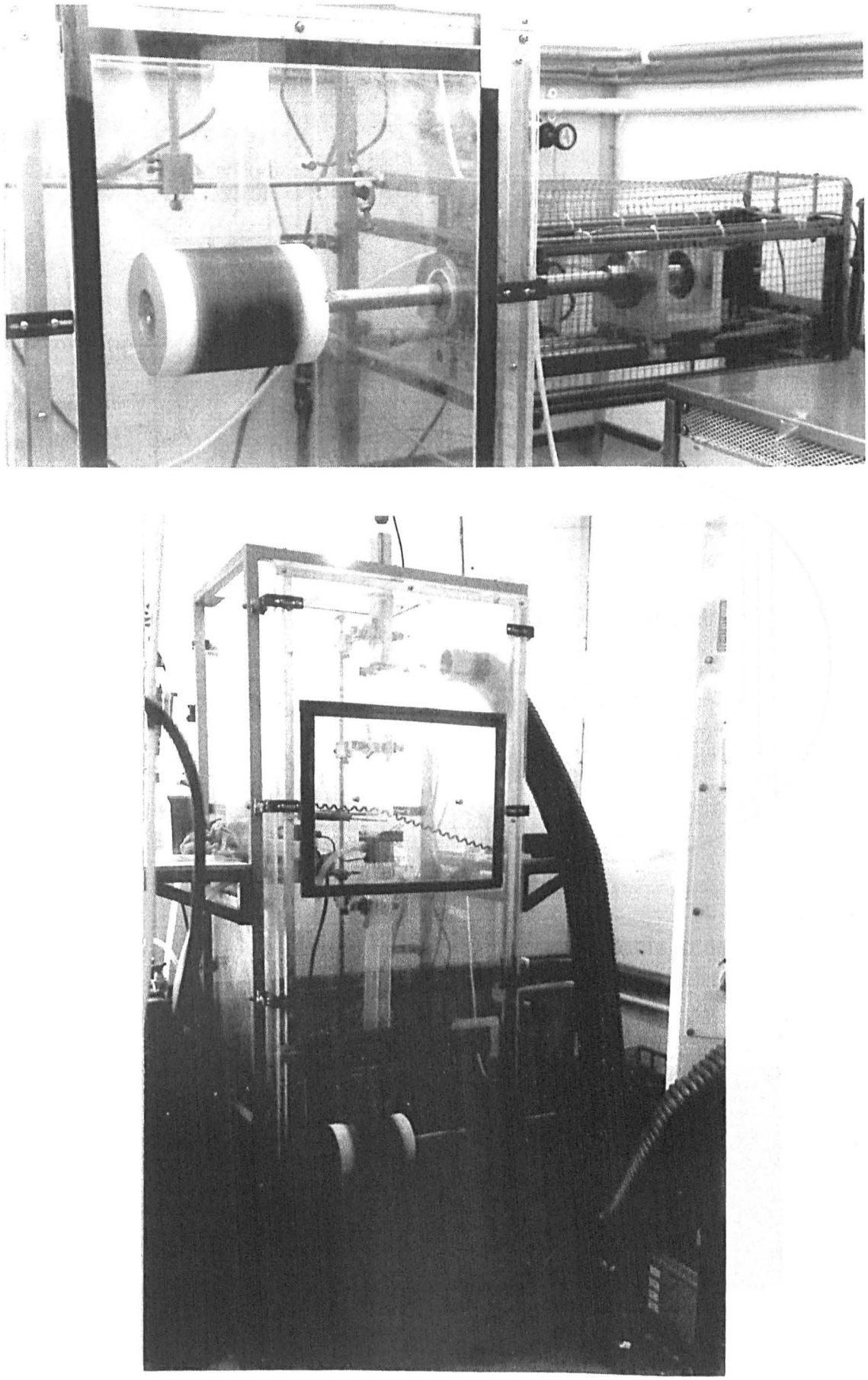

Fig. 71 Photograph of the blow spinning and collection drum used to producing aligned blankets of fibre.

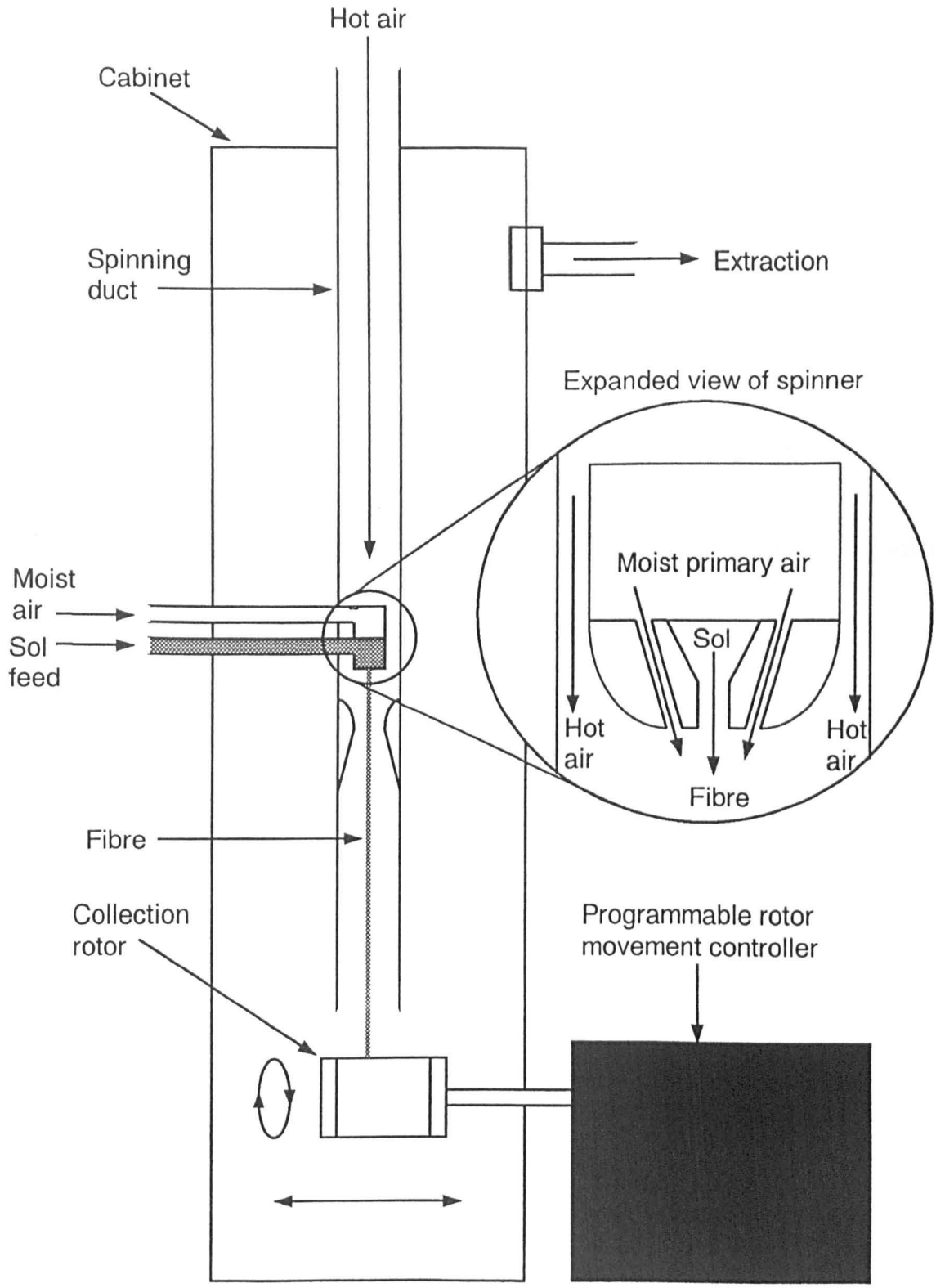

Fig. 72 A schematic diagram of the spinning apparatus.

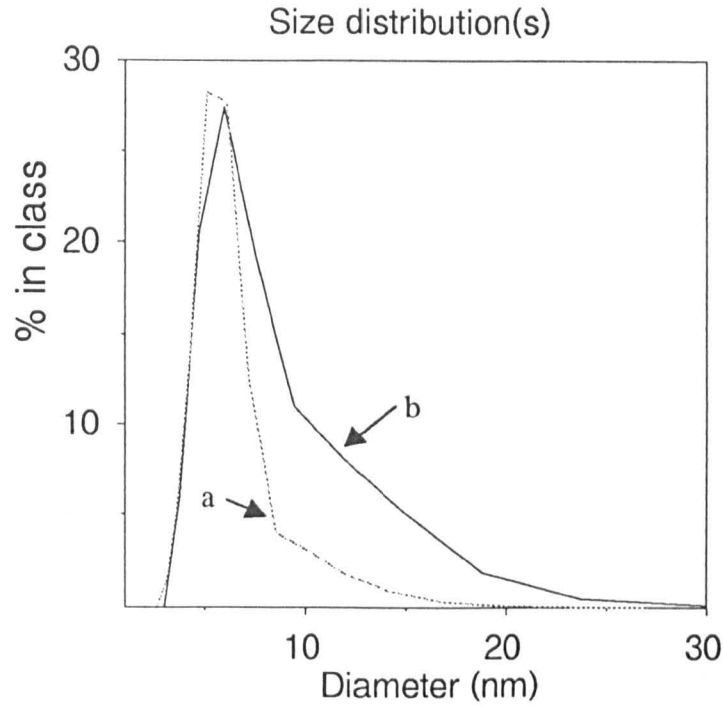

Fig. 73 Comparison of the volume distribution of a) Fe/Br and b) spinning solution.

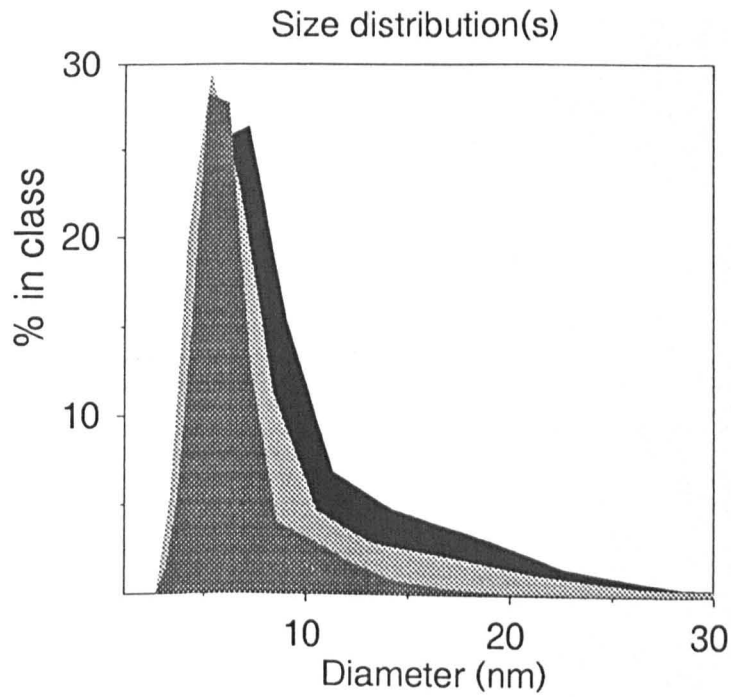

Fig. 74 The volume distributions of the spinning solutions of, from rear to front, SrM, BaM and undoped Fe/Br.

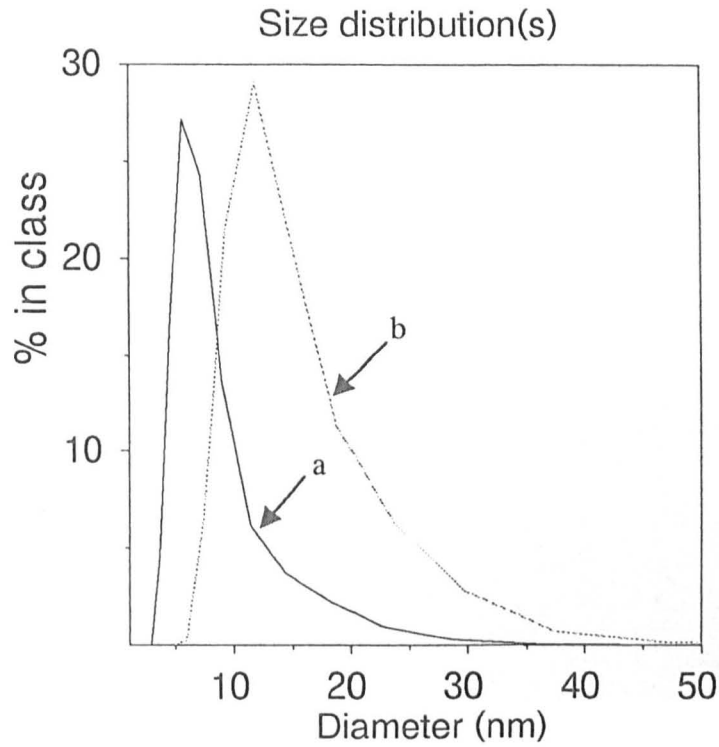

Fig. 75 Comparison of the volume distribution of a) Co_2Z sol and b) Co_2Z spinning solution.

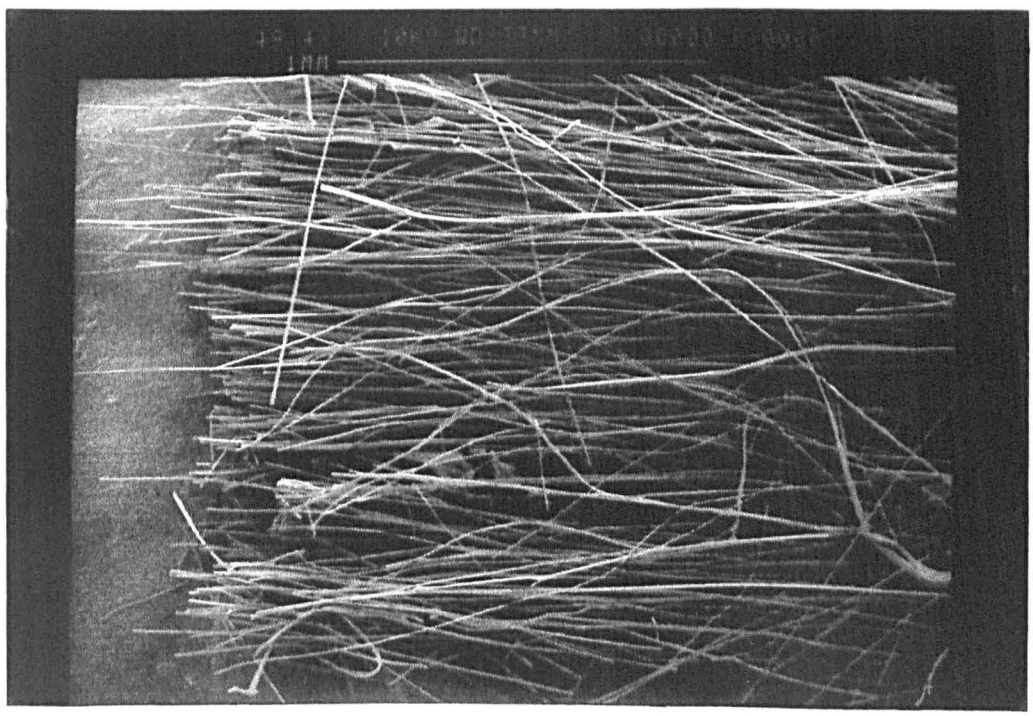

Fig. 76 iron aligned Photograph demonstrating the alignment of haematite fibres fired to 400 °C / 3 hr.

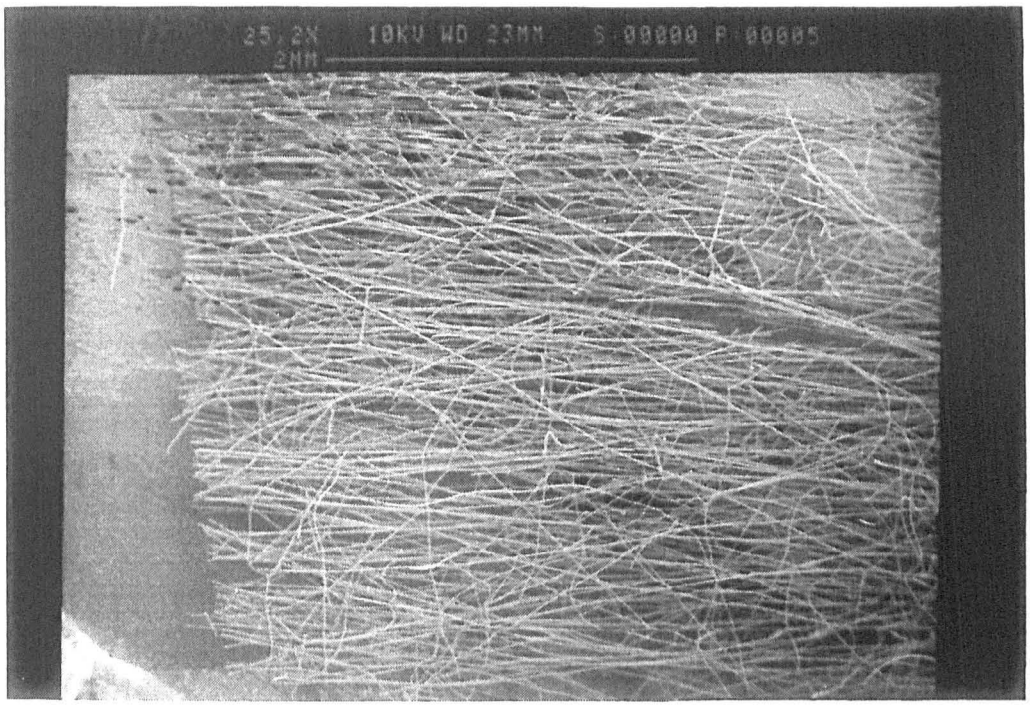

Fig. 77 SEM micrograph of an aligned BaM fibre blanket fired to 1000 °C / 3hr.

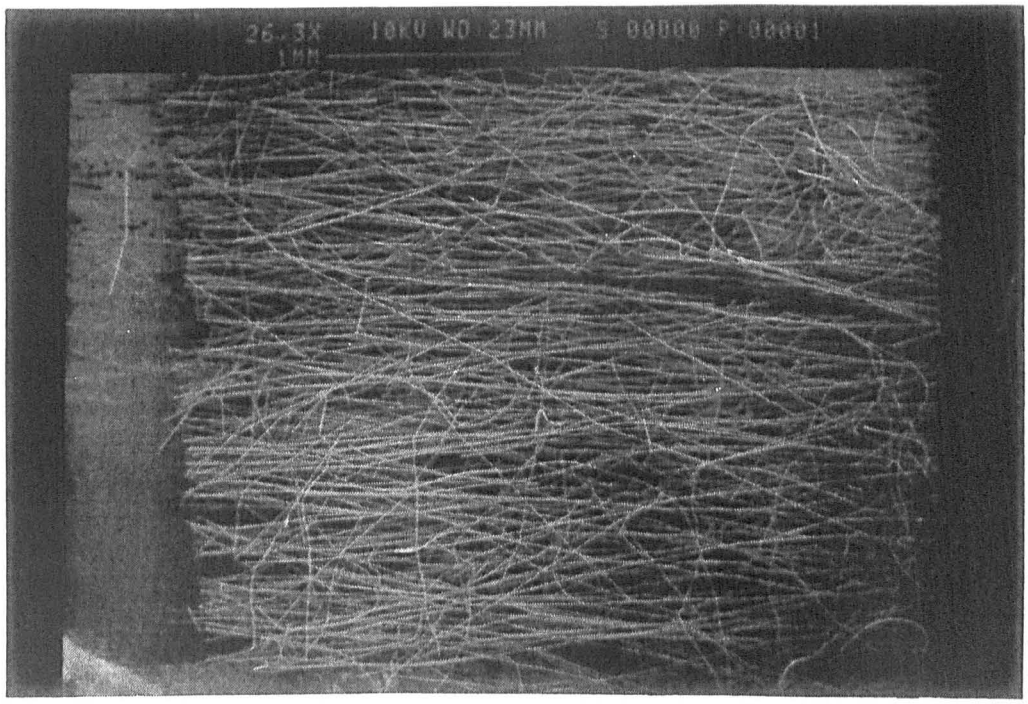

Fig. 78 SEM micrograph of an aligned SrM fibre blanket fired to 1000 °C / 3hr.

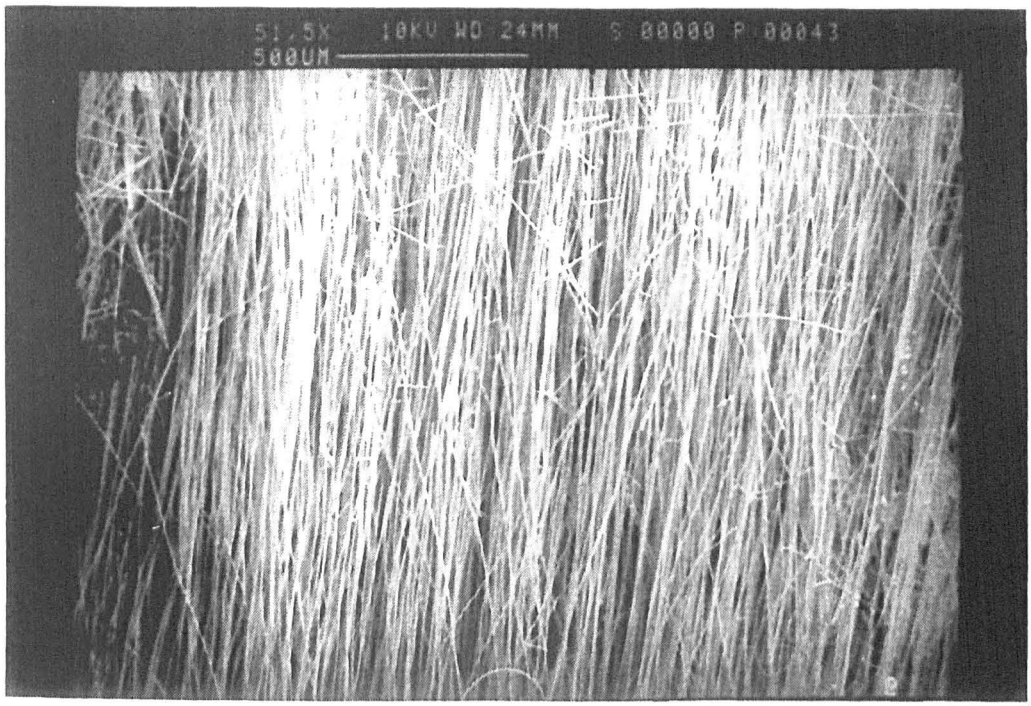

Fig. 79 SEM micrograph of an aligned $SrCo_{0.5}Ti_{0.5}Fe_{11}O_{19}$ fibre blanket fired to 1000 °C / 3hr.

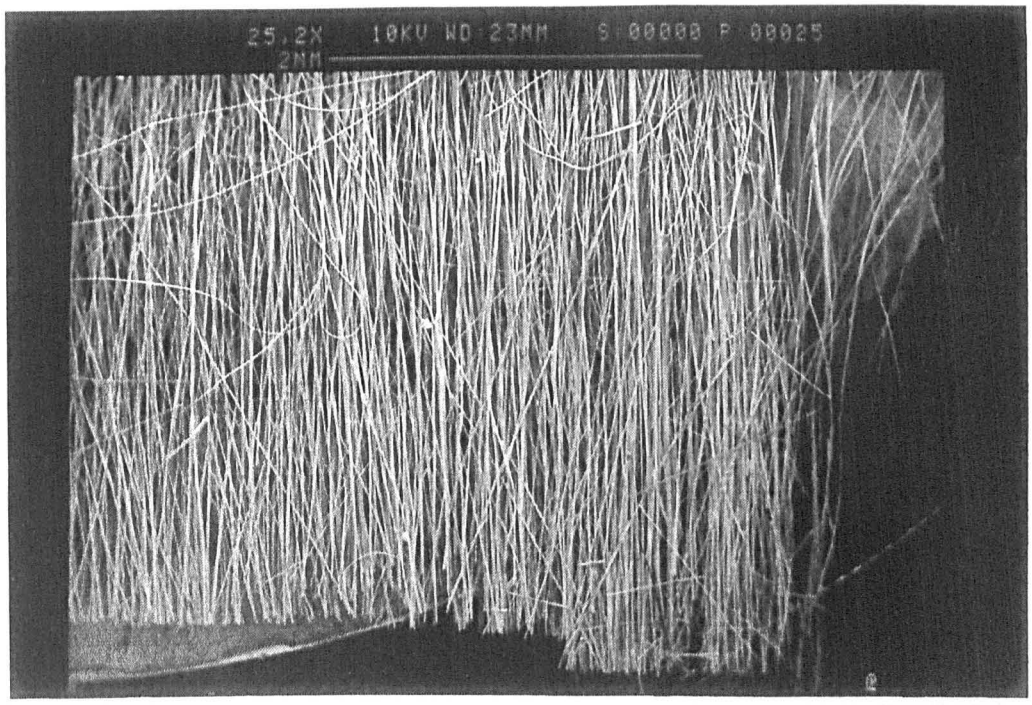

Fig. 80 SEM micrograph demonstrating the alignment of Co_2Y fibres fired to 1000 °C / 3hr.

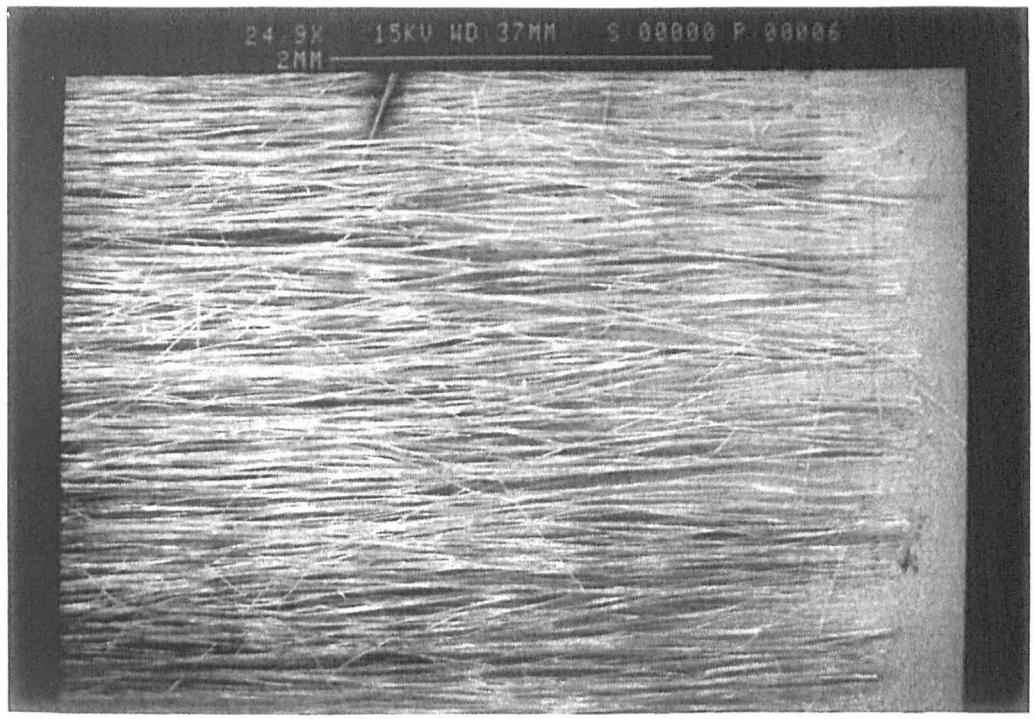

Fig. 81 SEM micrograph demonstrating the alignment of 0.67% CaO-doped Co_2Z fibres fired to 1200 °C / 3hr.

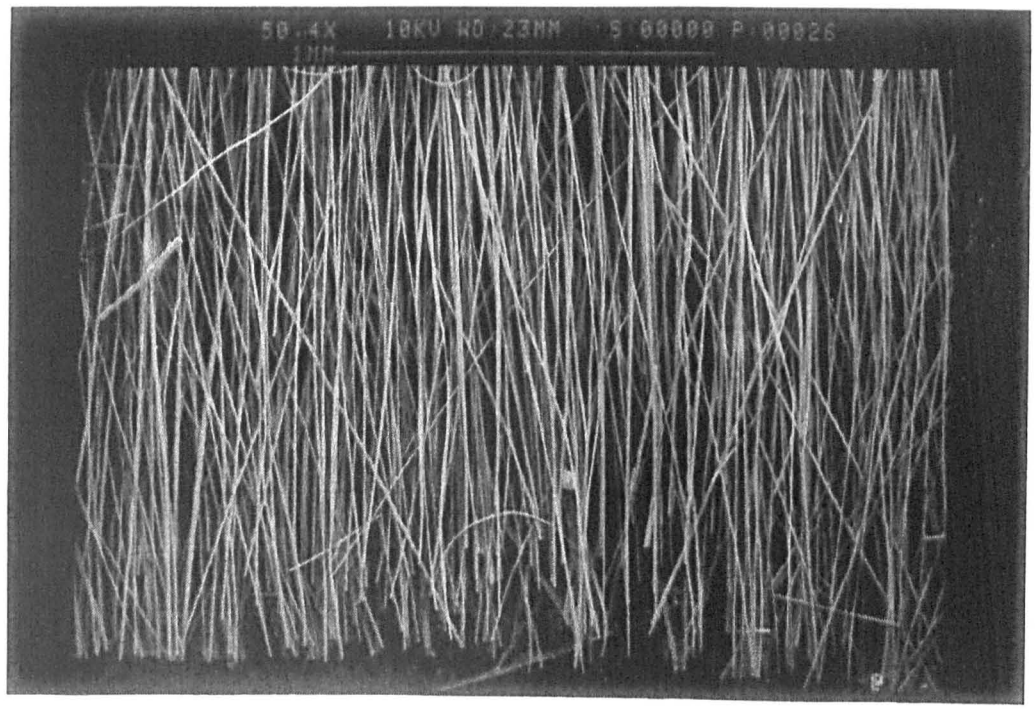

Fig. 82 SEM micrograph demonstrating the alignment of Co_2W fibres fired to 1250 °C / 3hr.

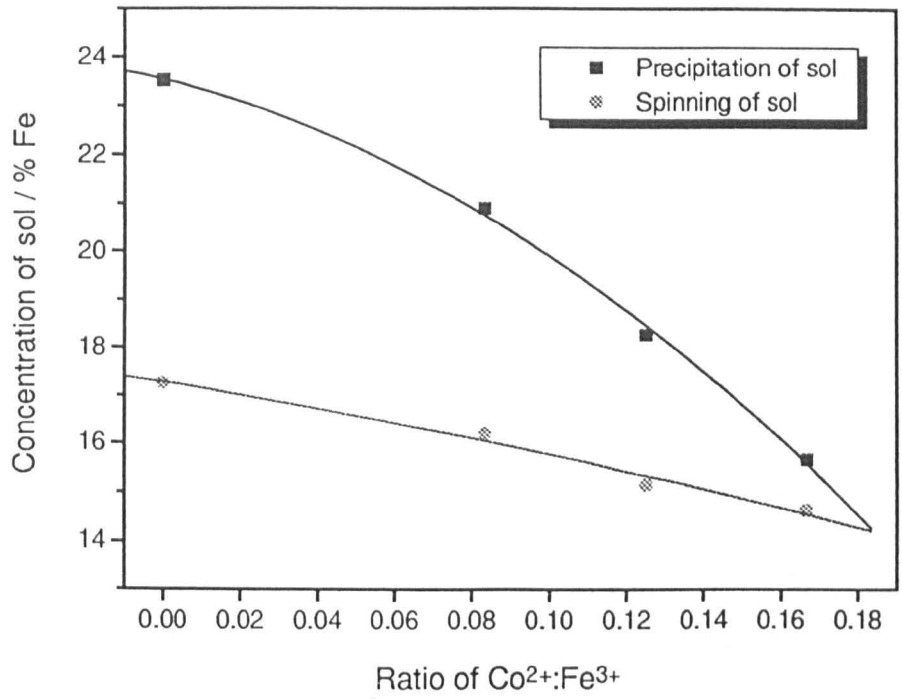

Fig. 83 The relationship between the ratio of Co^{2+}:Fe^{3+} and stability of hexagonal ferrite sols and spinning solutions.

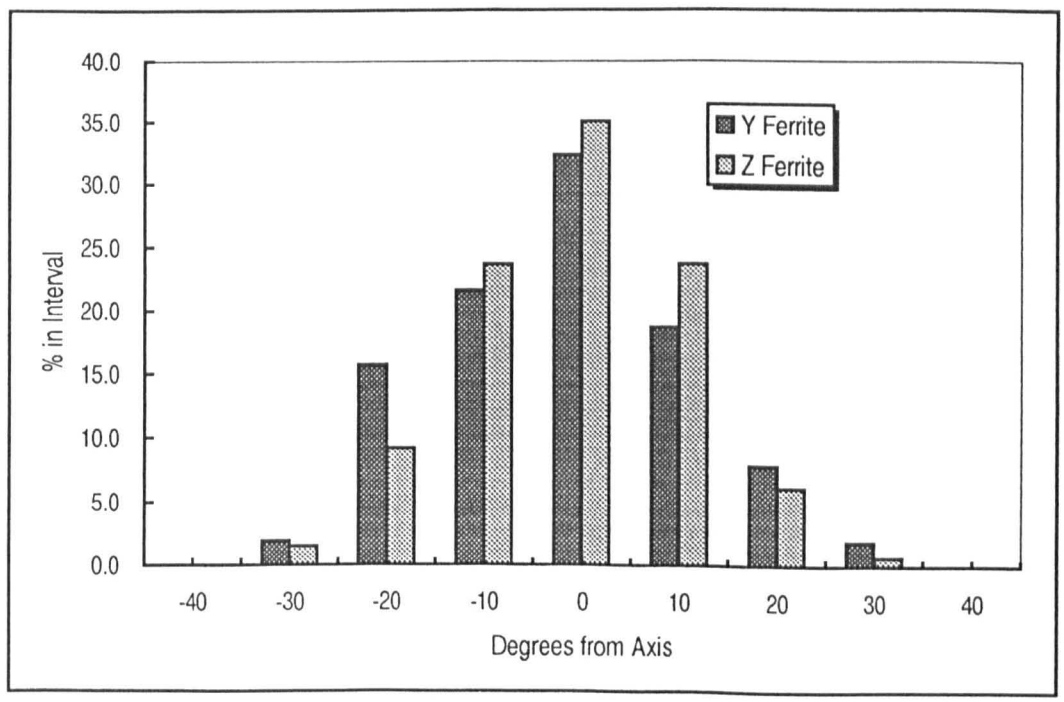

Fig. 84 The alignment distributions of Co_2Y and Co_2Z fibres.

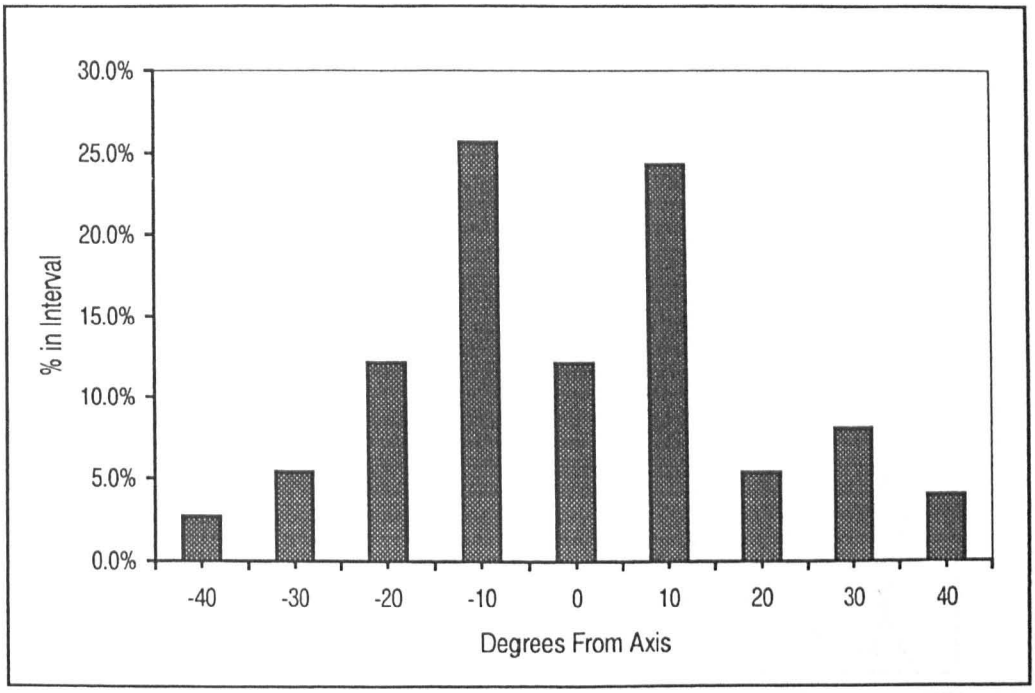

Fig. 85 The alignment distribution of SrM fibre.

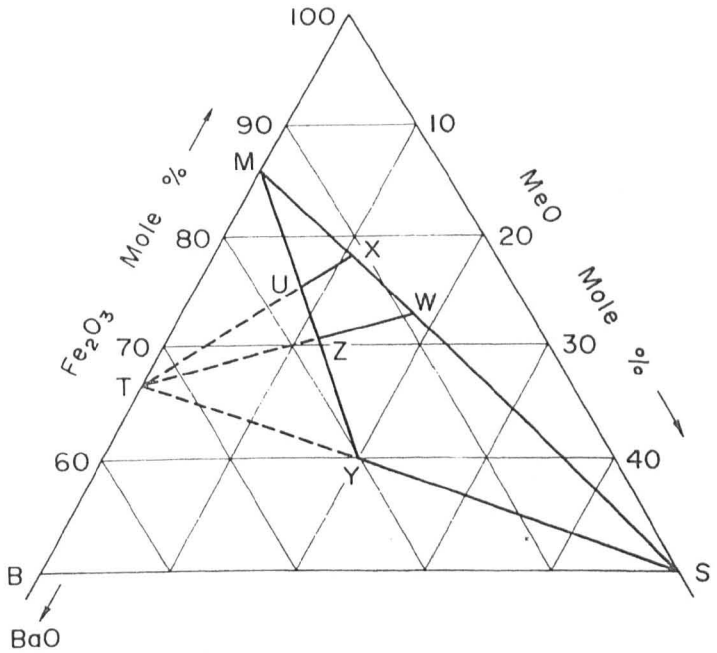

Fig. 86 Phase diagram of the $BaO.Fe_2O_3.CoO$ system [223].

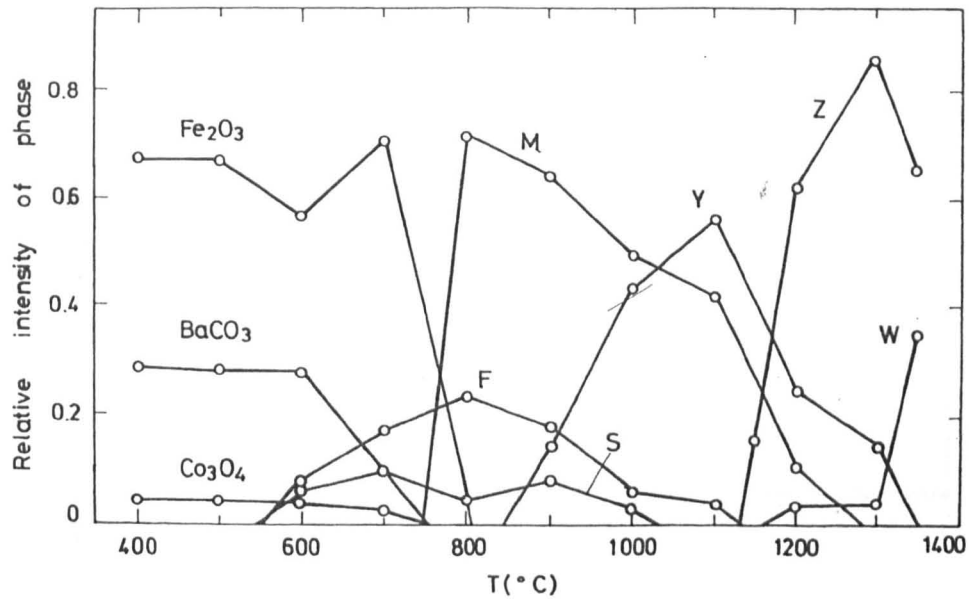

Fig. 87 Formation temperature and stability ranges of the major hexagonal ferrites in the BaO-FeO-CoO system [24].

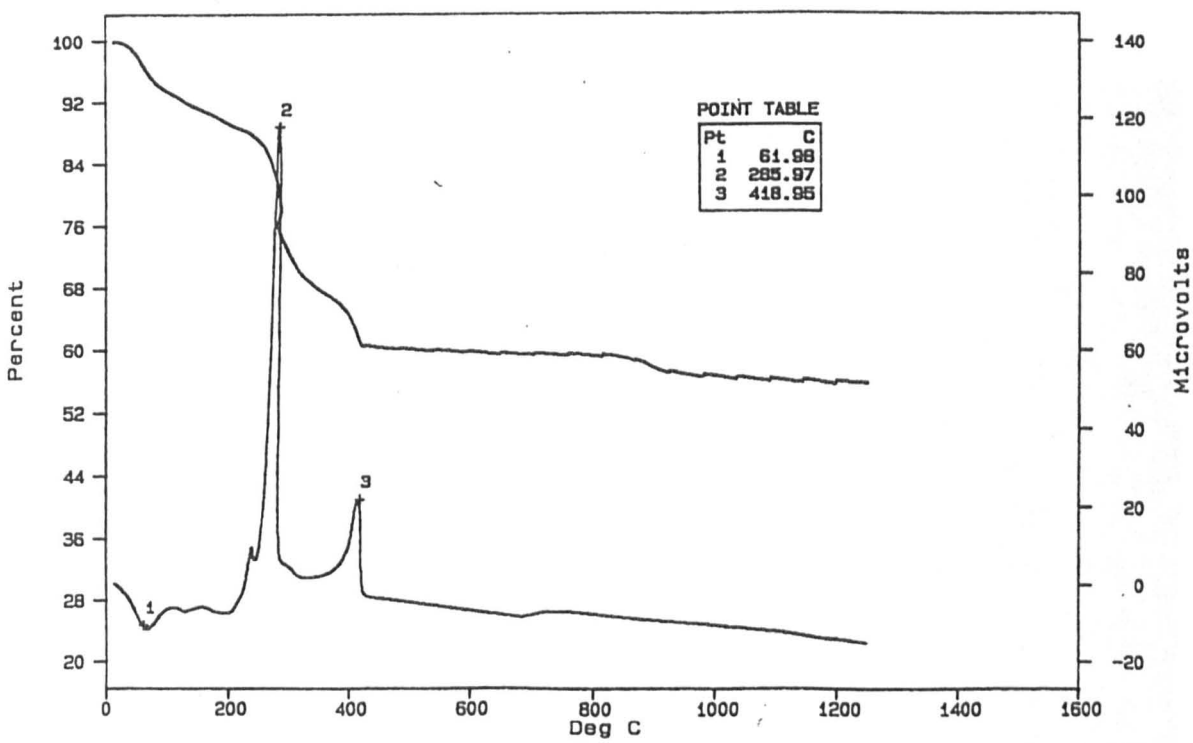

Fig. 88 The DTA / TGA plots of Co_2Z fibres heated at 10 °C min^{-1}.

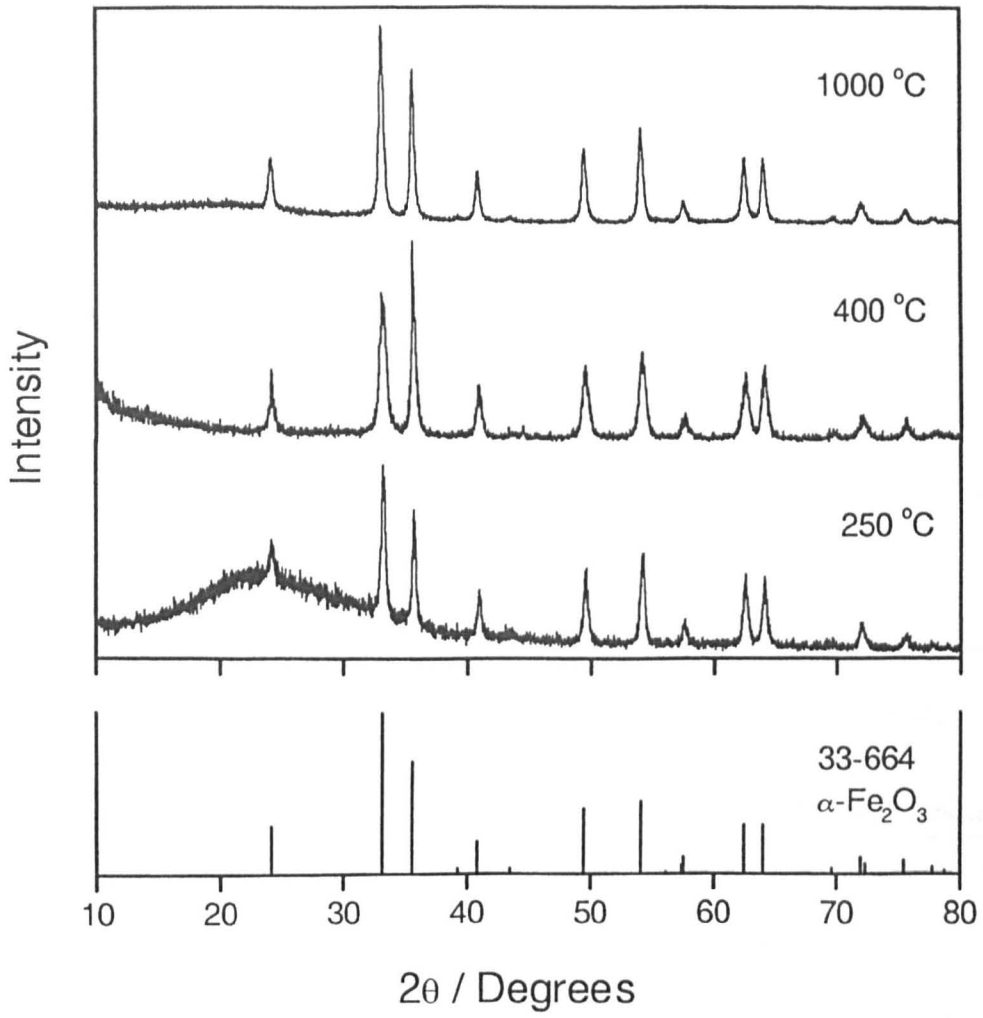

Fig. 89 XRD pattern of undoped Fe/Br gel fibres heated in air at 250, 400 and 1000 °C / 3hr.

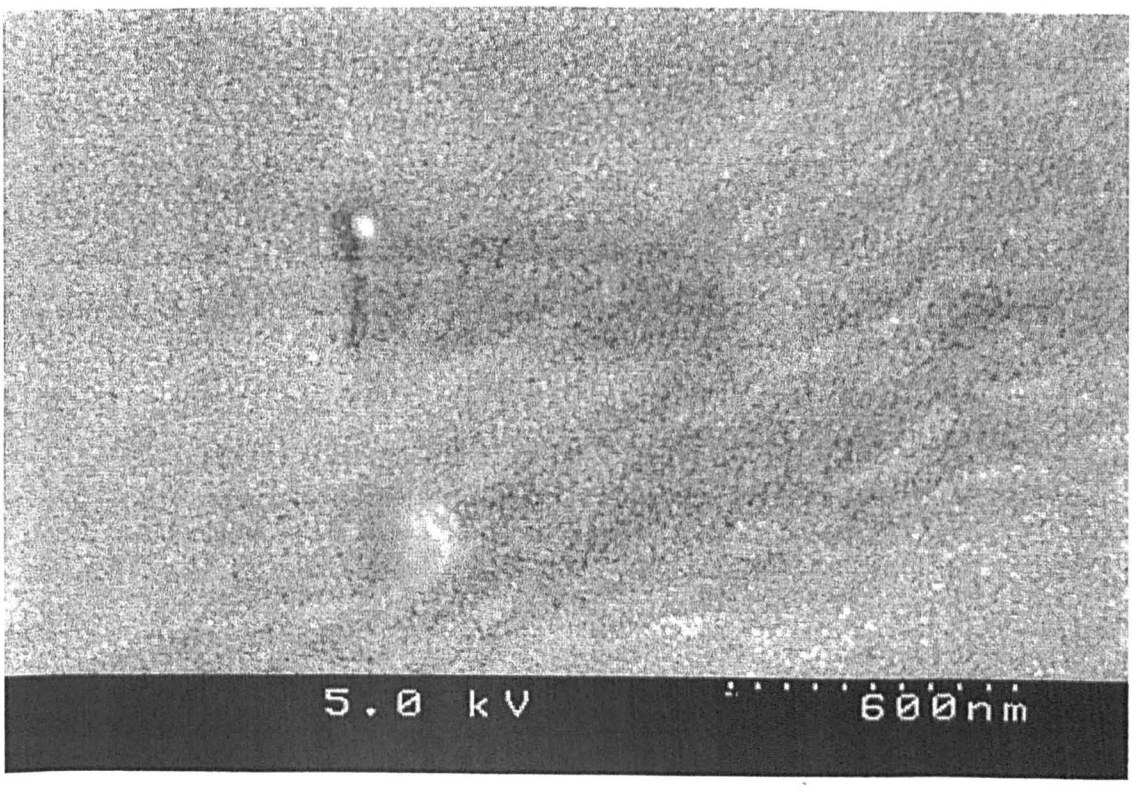

Fig. 90 SEM micrograph of haematite fibres after being fired in air at 250 °C / 3hr.

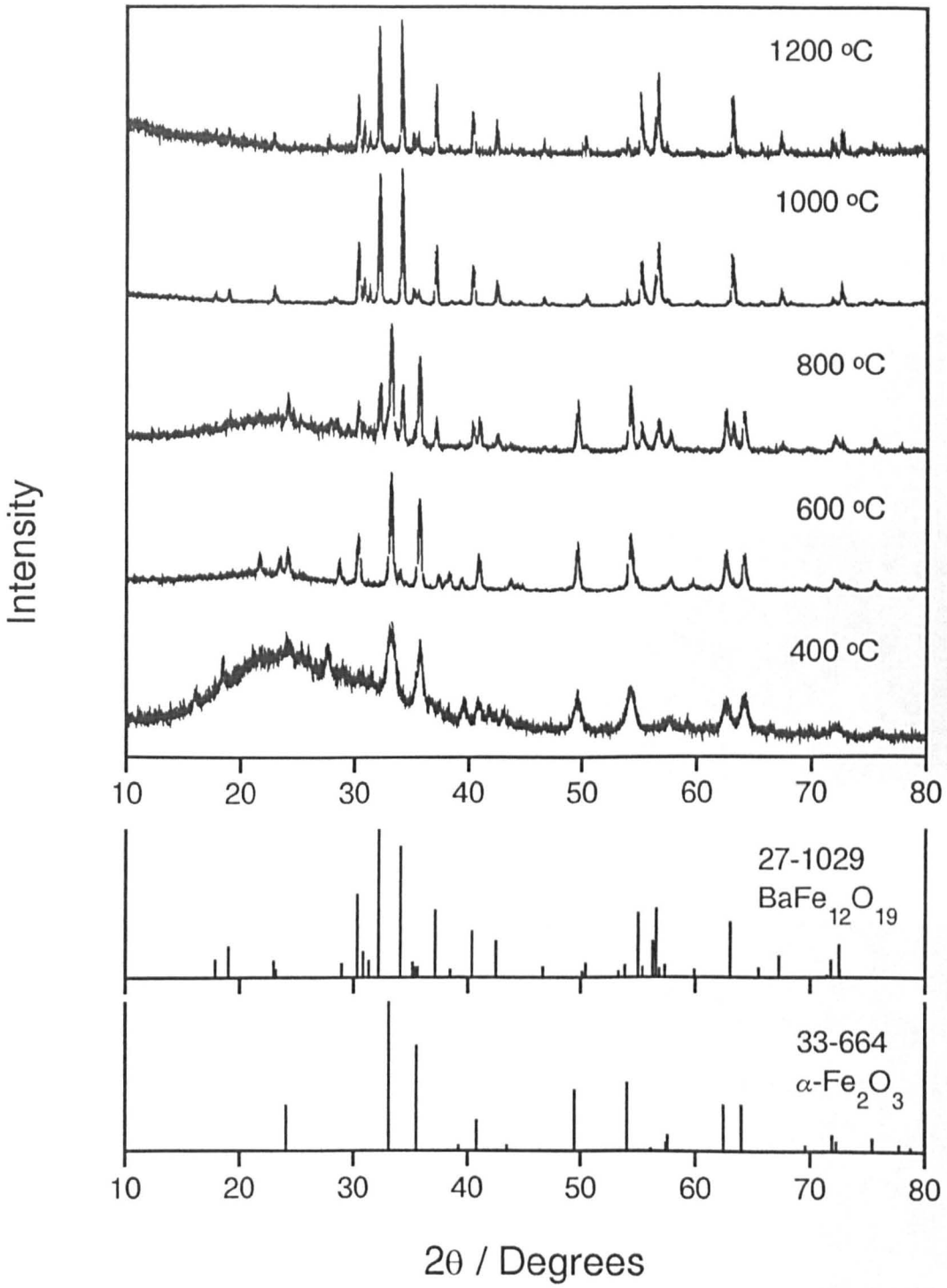

Fig. 91 XRD patterns of freshly spun BaM fibres fired to 400, 600, 800, 1000 and 1200 °C / 3hr.

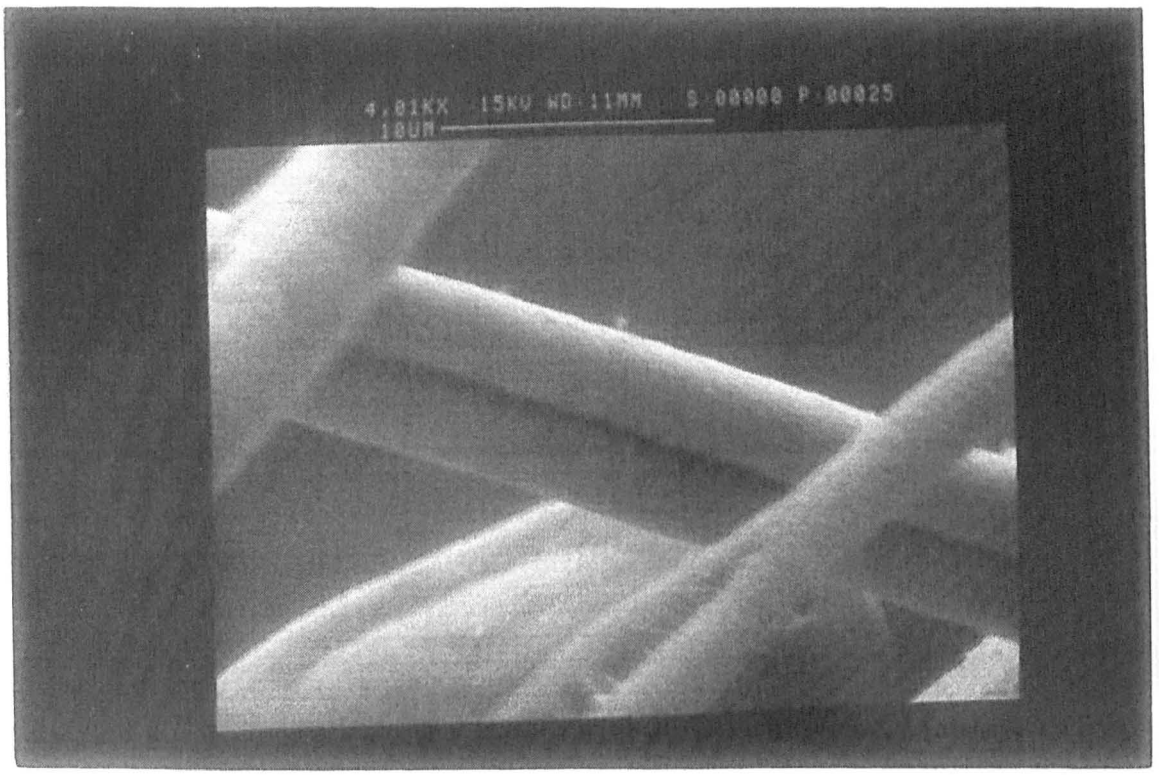

Fig. 92 SEM micrograph of freshly spun BaM fibres fired to 800 °C / 3hr.

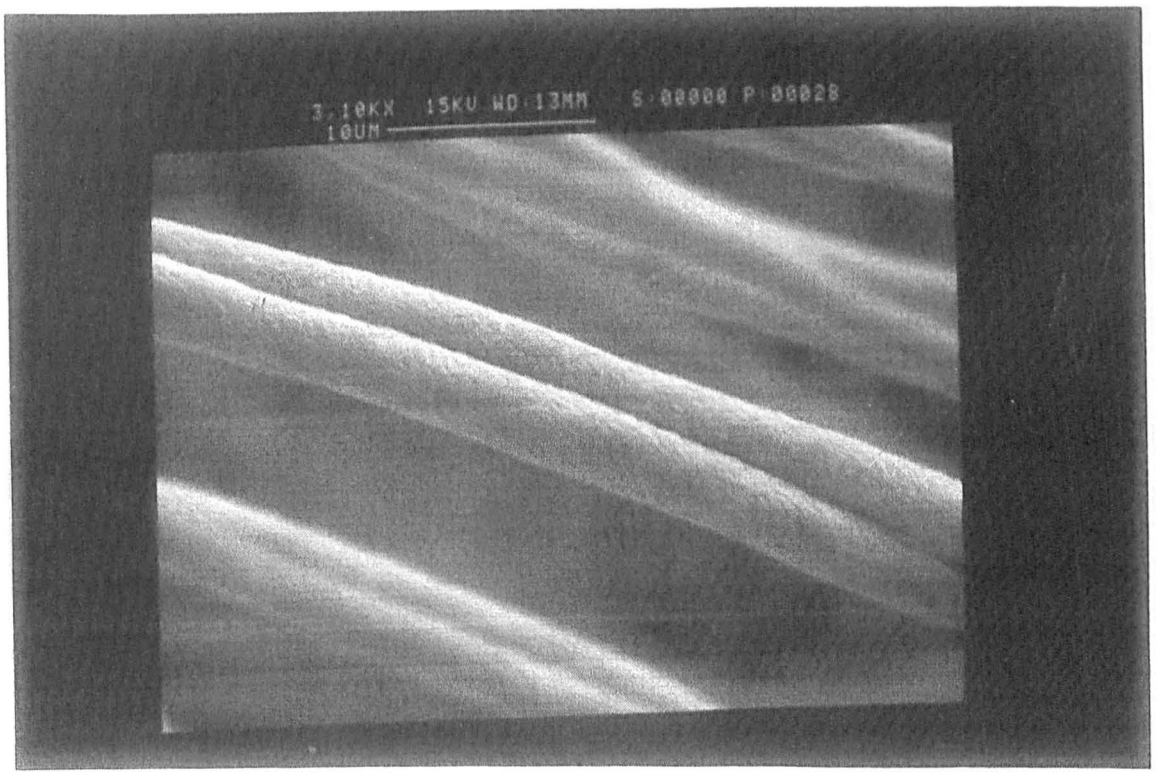

Fig. 93 SEM micrograph of freshly spun BaM fibres fired to 1000 °C / 3hr.

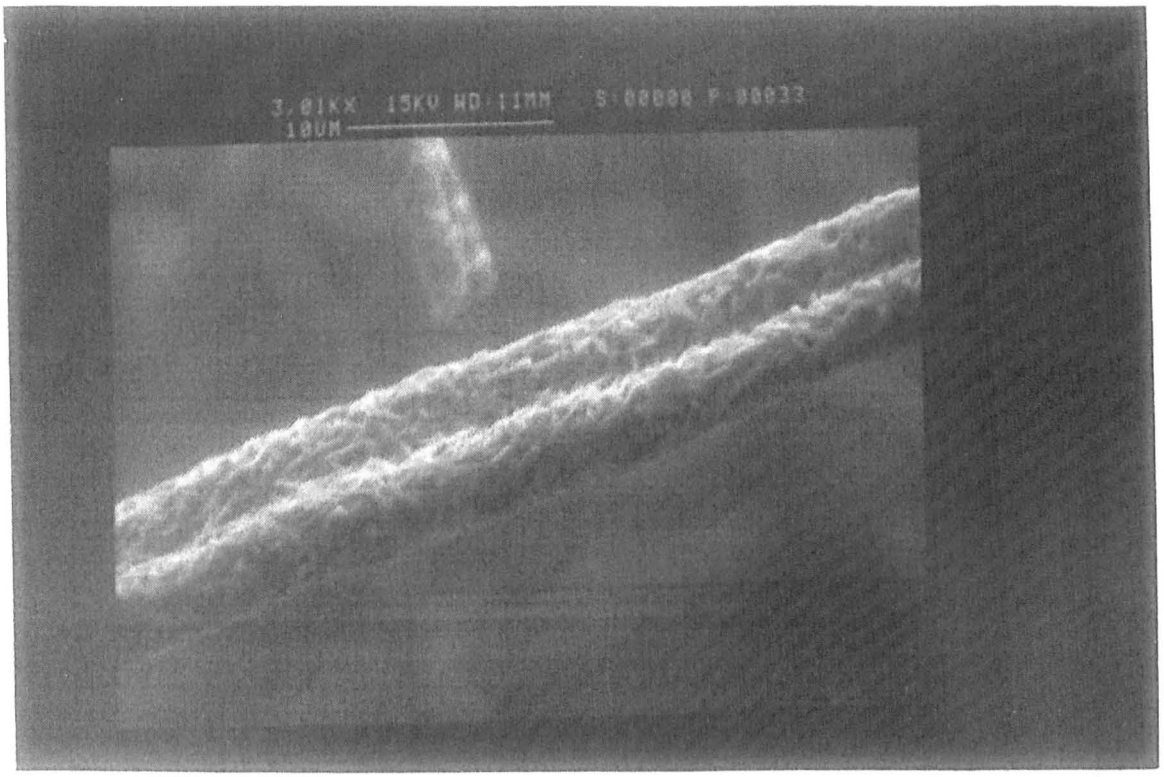

Fig. 94 SEM micrograph of freshly spun BaM fibres fired to 1100 °C / 3hr.

Fig. 95 SEM micrograph of freshly spun BaM fibres fired to 1200 °C / 3hr.

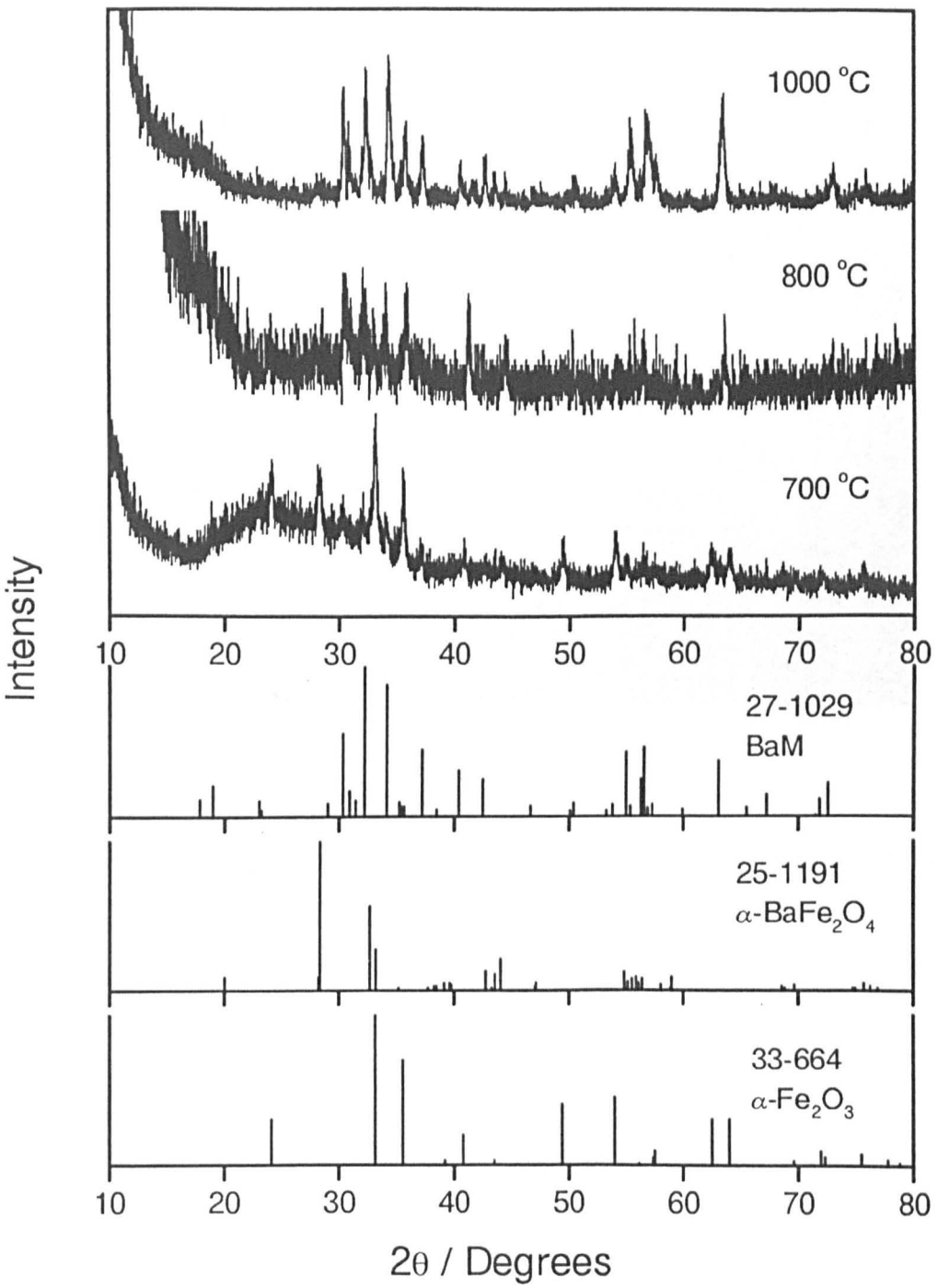

Fig. 96 XRD patterns of BaM fibres stored for three years, fired to 700, 800 and 1000 °C / 3hr.

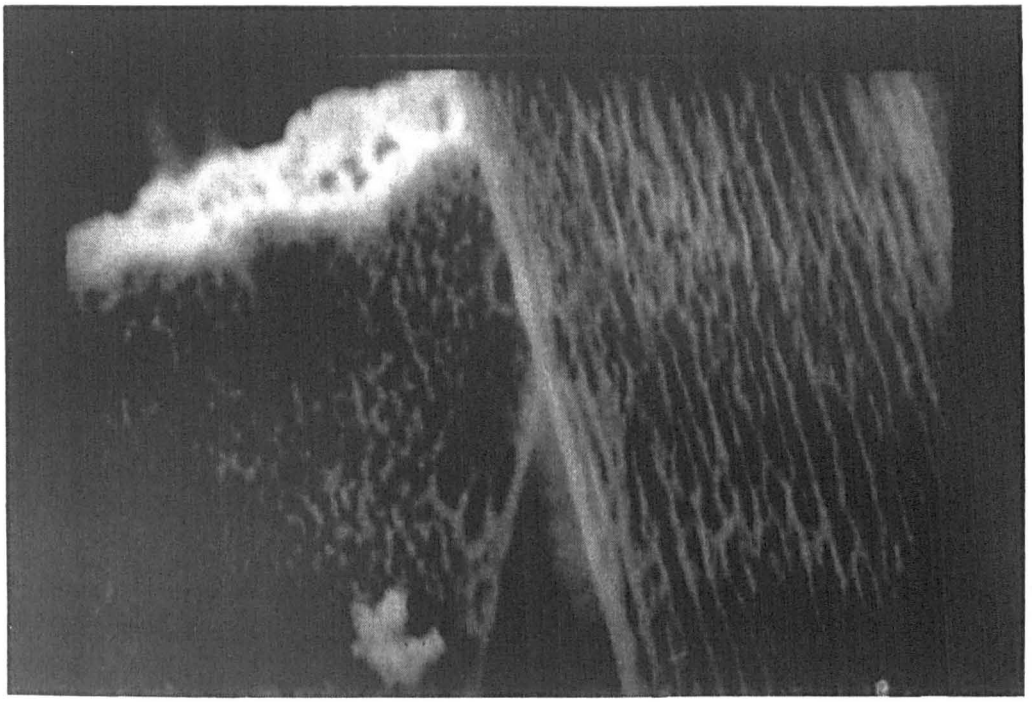

Fig. 97 SEM micrograph of BaM fibres stored for three years, fired to 1000 °C / 3hr.

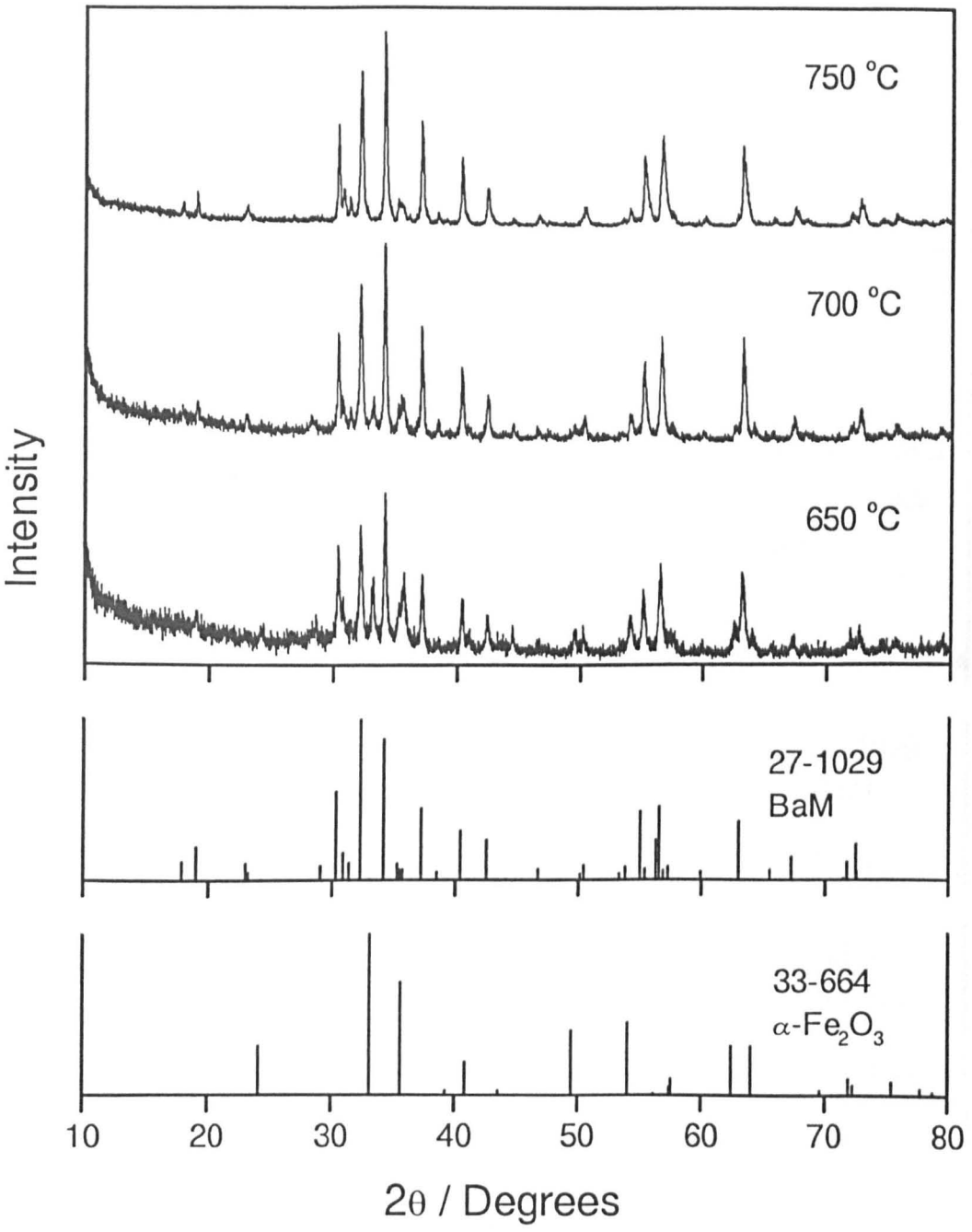

Fig. 98 XRD patterns of BaM fibres produced from a halide-free precursor, fired to 650,700 and 750 °C / 3hr.

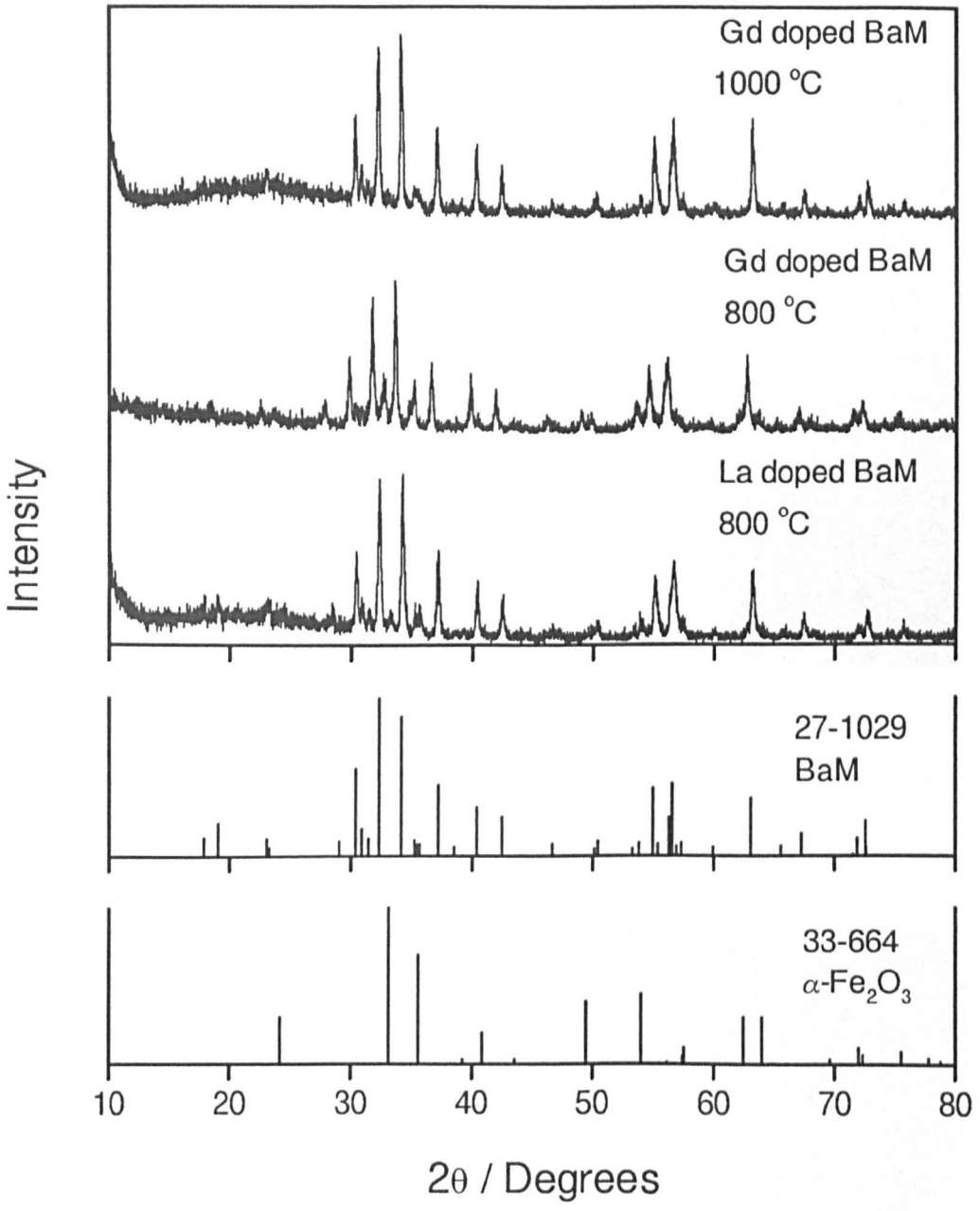

Fig. 99 XRD patterns of BaM fibres doped with 0.28 mol% La^{3+} and Gd^{3+} fired to 800 and 1000 °C / 3hr.

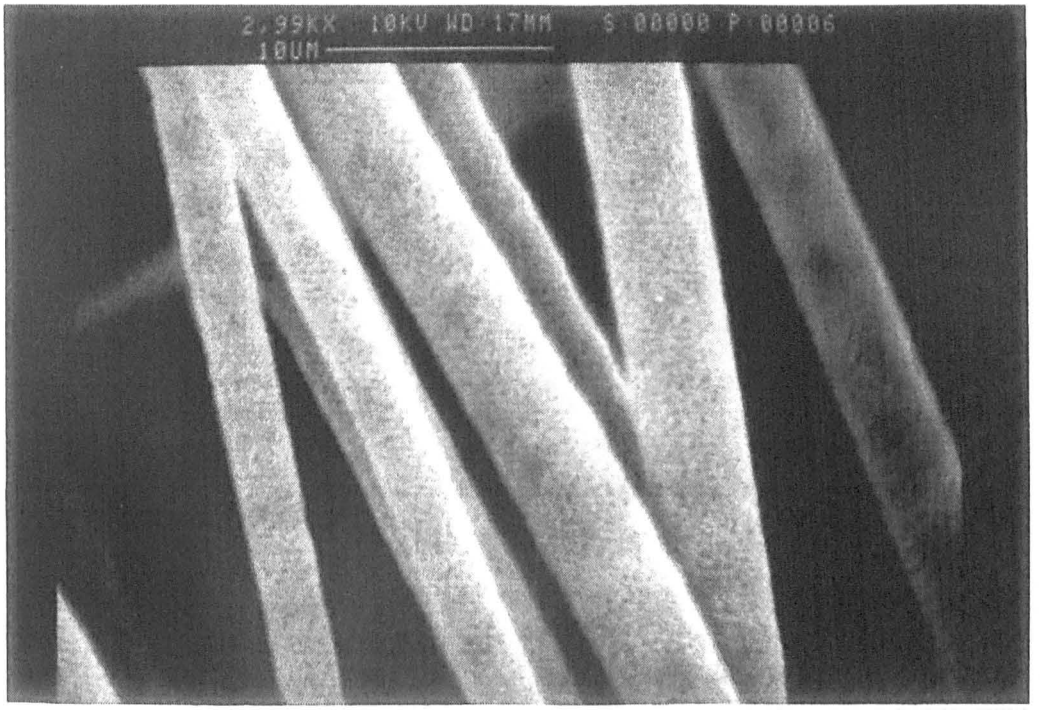

Fig. 100 SEM micrograph of 0.28 mol% La^{3+} doped BaM fibres fired to 1000 °C / 3hr.

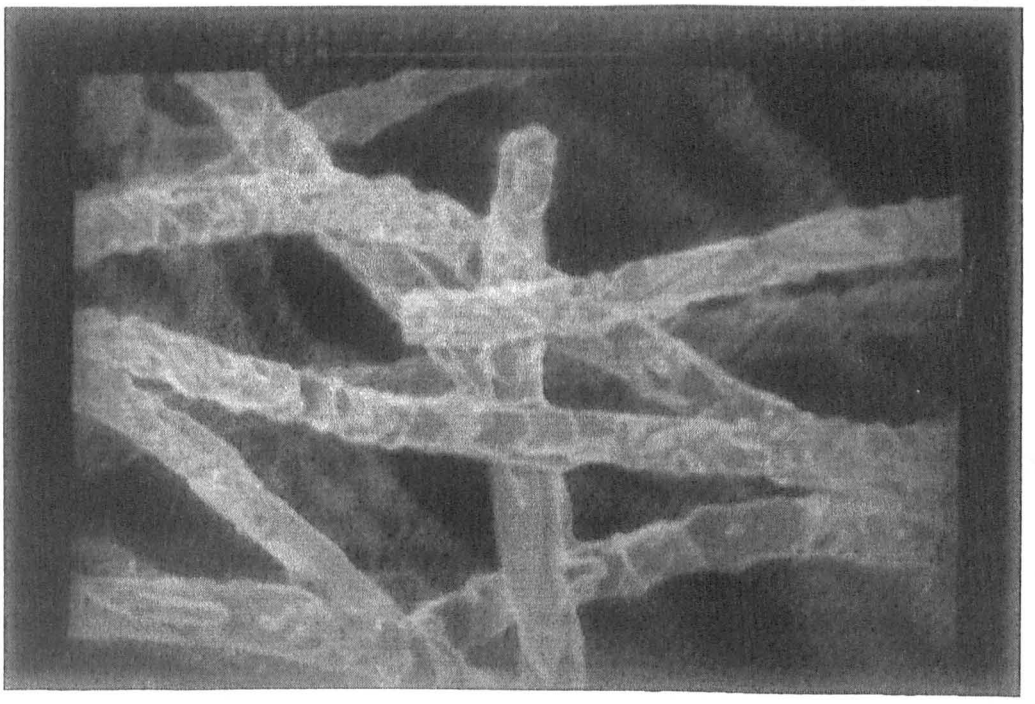

Fig. 101 SEM micrograph of 0.28 mol% Gd^{3+} doped BaM fibres fired to 1200 °C / 3hr.

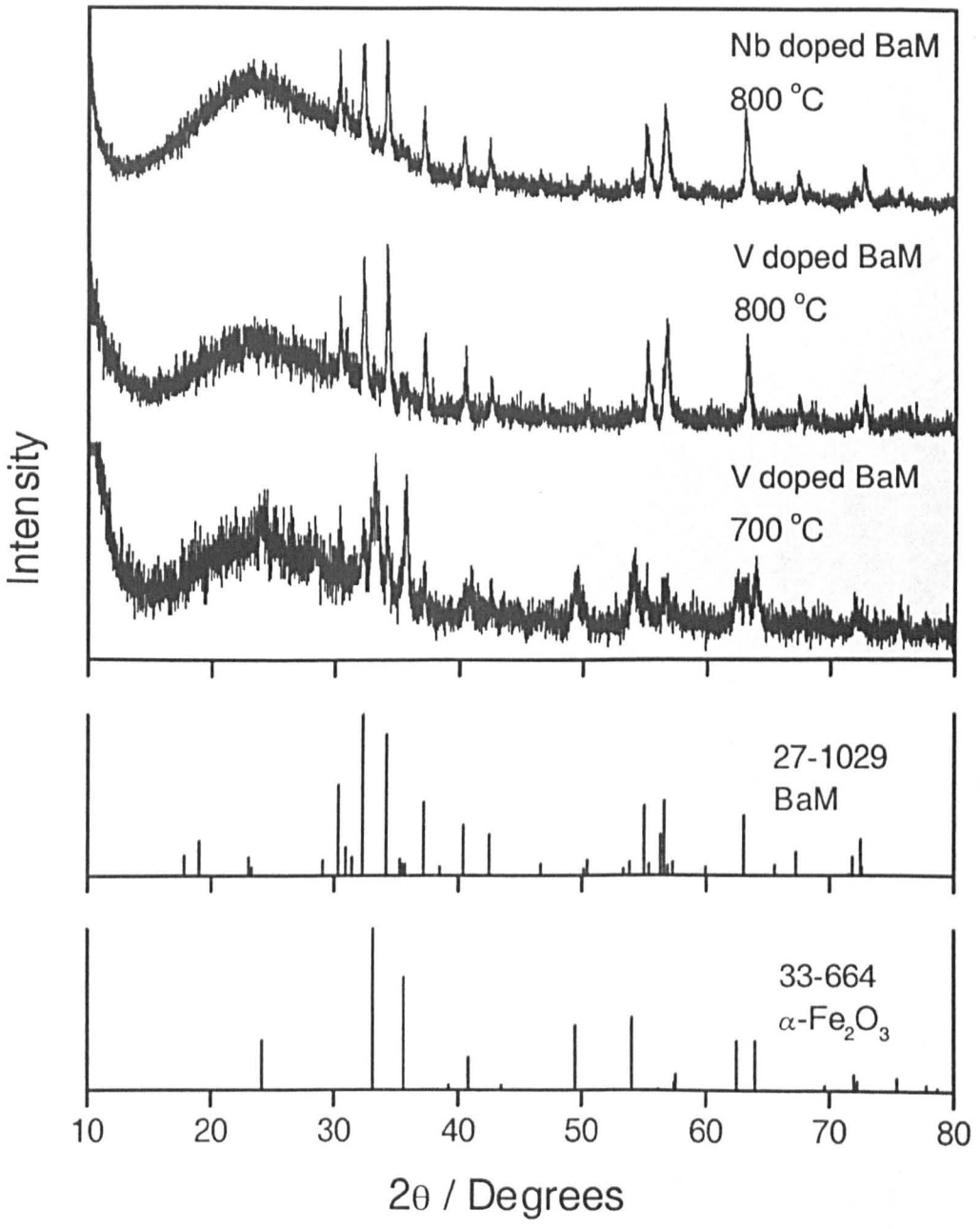

Fig. 102 XRD patterns of BaM fibres doped with 0.25 wt% V_2O_5 and 0.06 wt% Nb_2O_5 fired to 700 and 800 °C / 3hr.

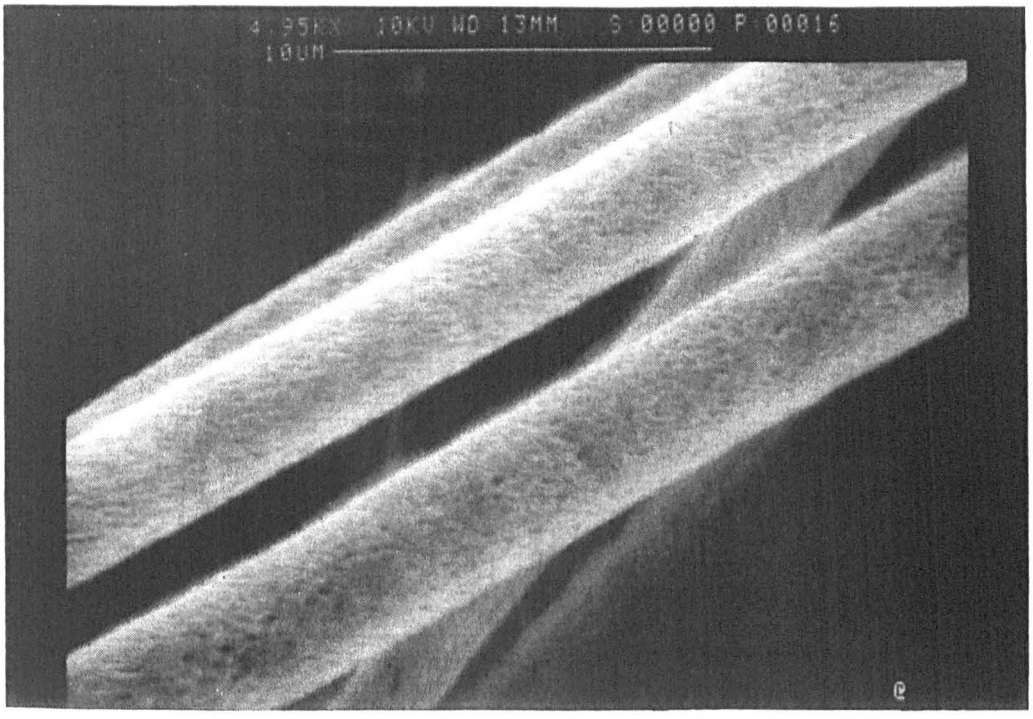

Fig. 103 SEM micrograph of 0.06 wt% Nb_2O_5 doped BaM fibres fired to 1000 °C / 3hr.

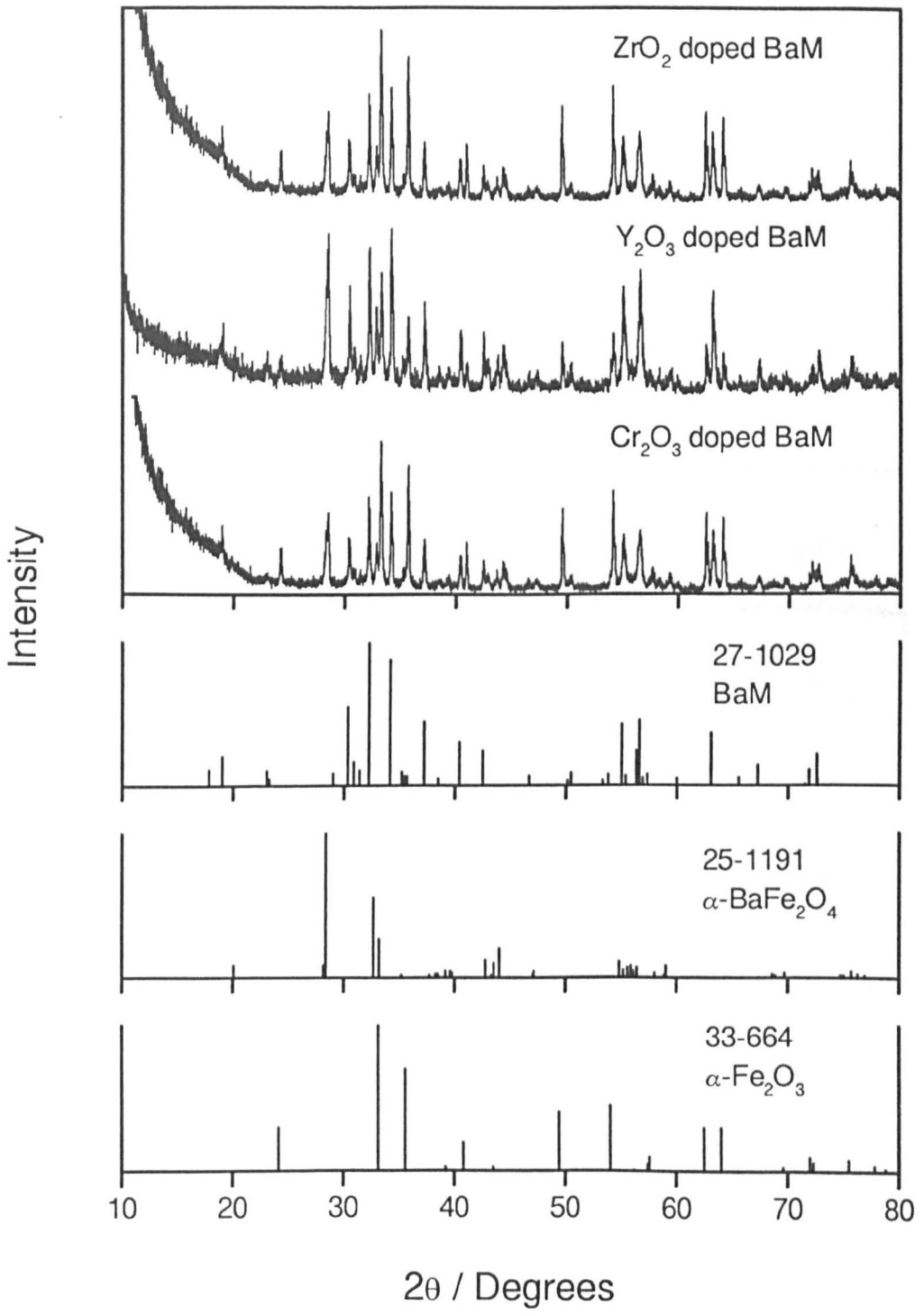

Fig. 104 XRD patterns of BaM fibres doped with 1.0 wt% ZrO_2, Y_2O_3 and Cr_2O_3 fired to 1000 °C / 3hr.

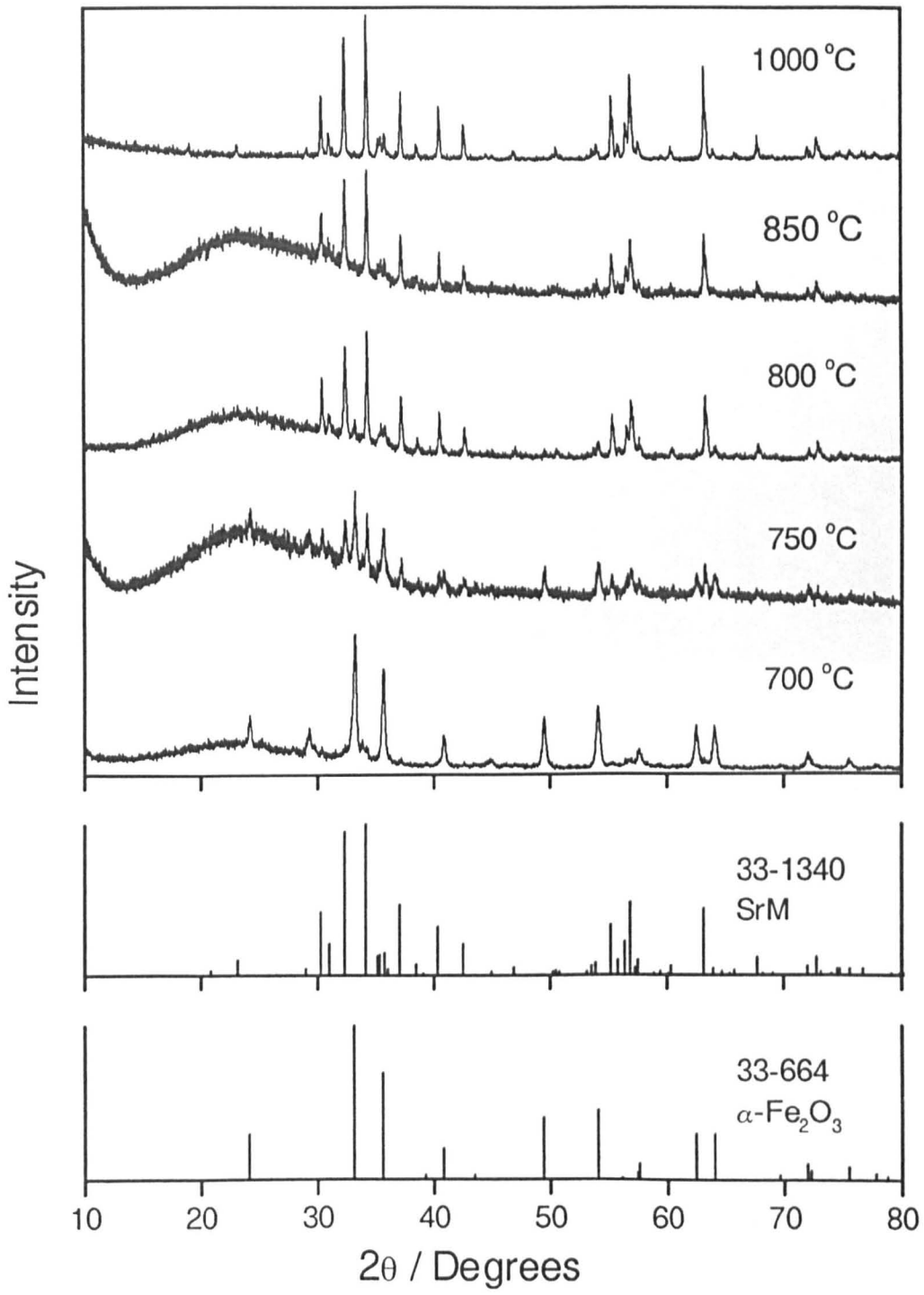

Fig. 105 XRD patterns of freshly spun SrM fibres fired to 700, 750, 800, 850 and 1000 °C / 3hr.

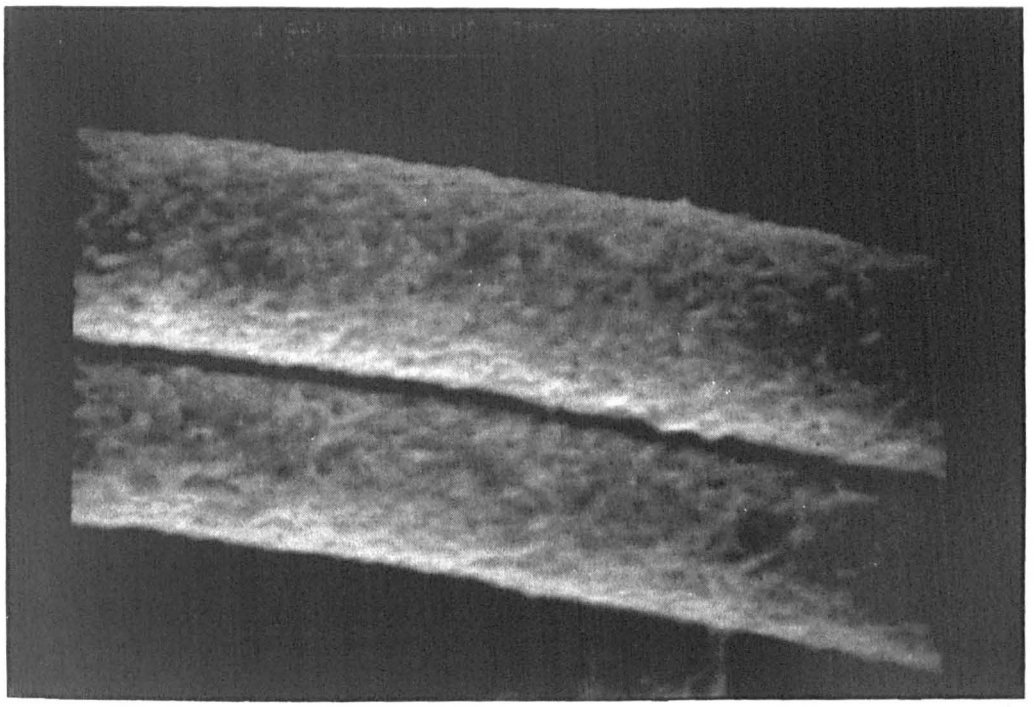

Fig. 106 SEM micrograph of freshly spun SrM fibres fired to 1000 °C / 3hr.

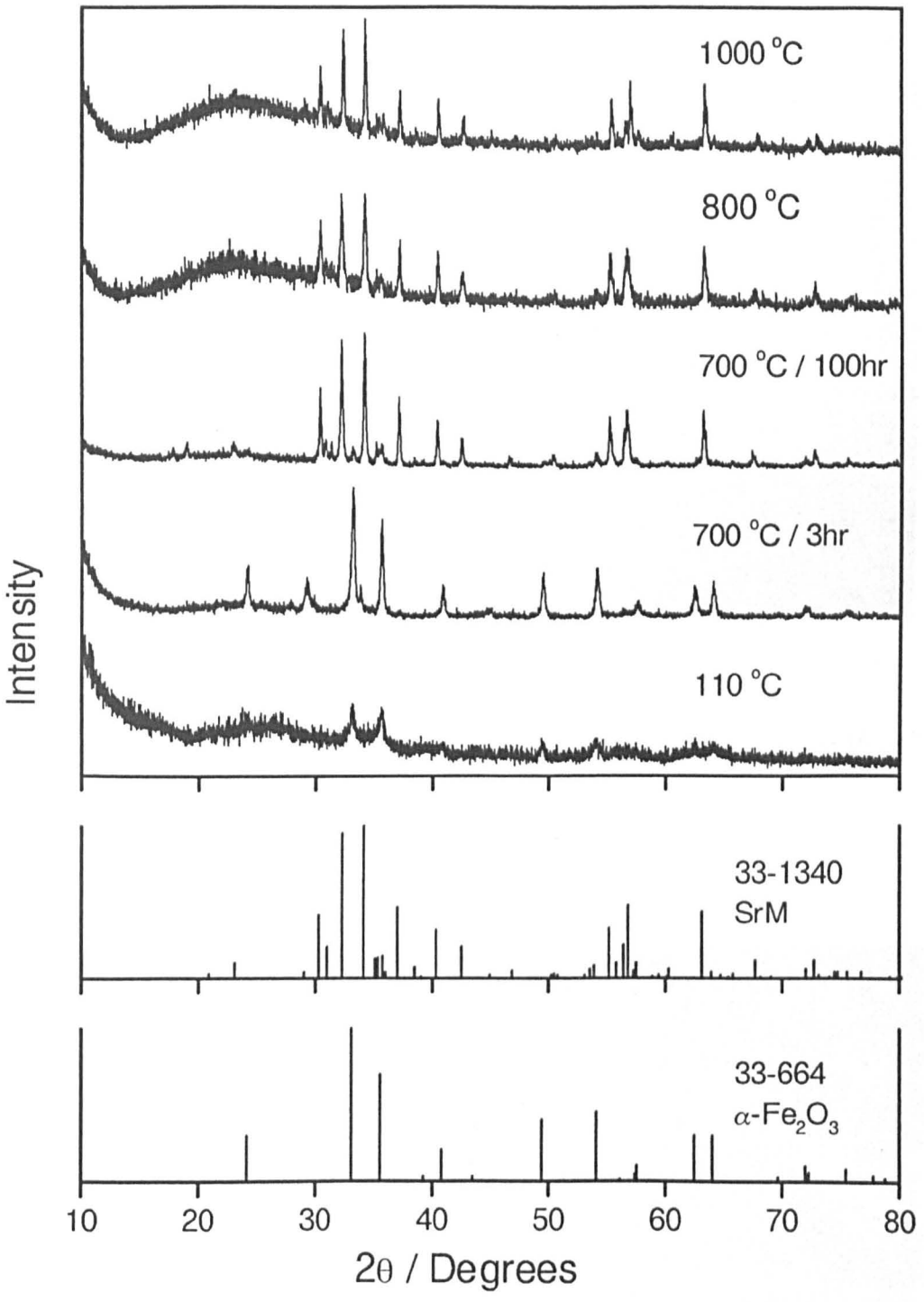

Fig. 107 XRD patterns of SrM fibres stored for three years, dried at 110 °C, and fired to 700 / 3hr, 700 °C / 100hr, 800 °C / 3hr and 1000 °C / 3hr.

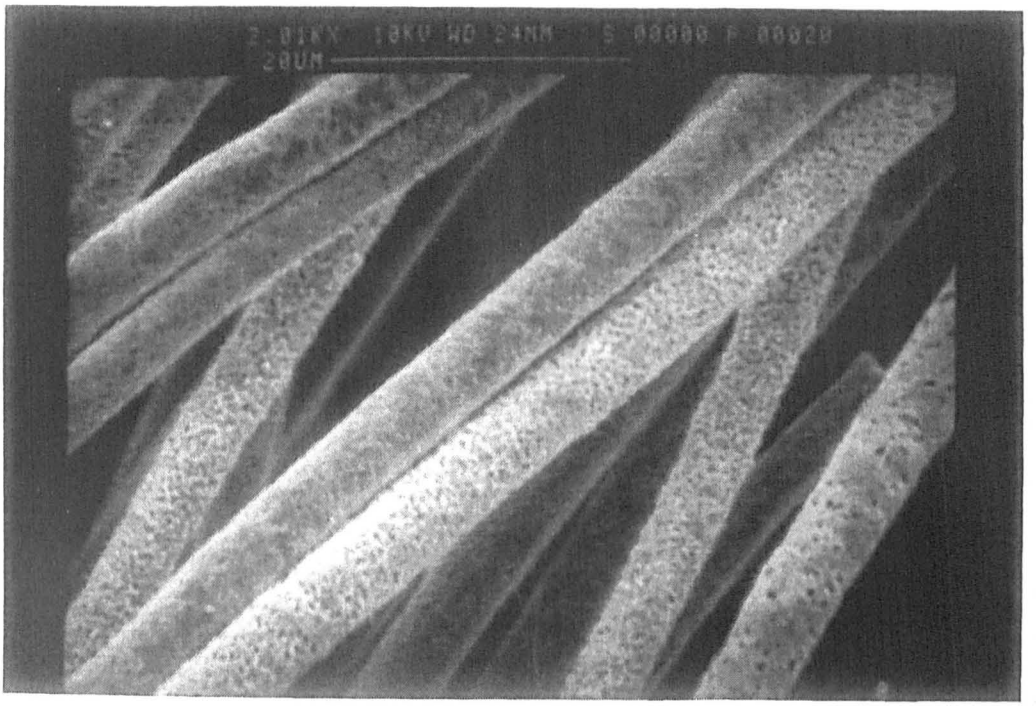

Fig. 108 SEM micrograph of SrM fibres stored for three years, fired to 1000 °C / 10min.

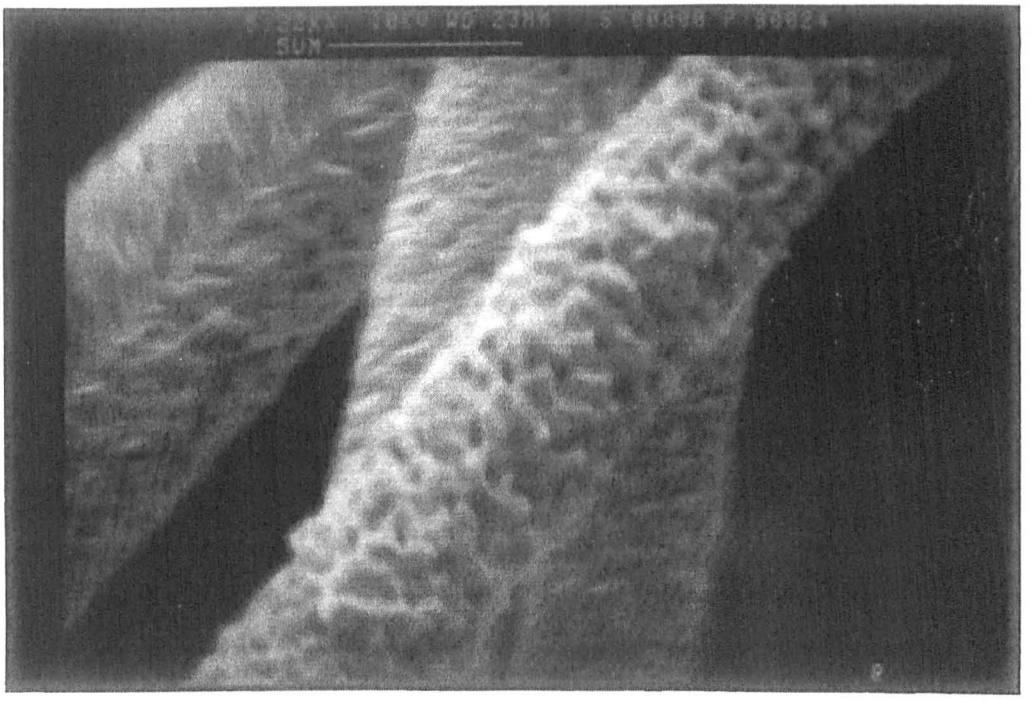

Fig. 109 SEM micrograph of SrM fibres stored for three years, fired to 1000 °C / 24hr.

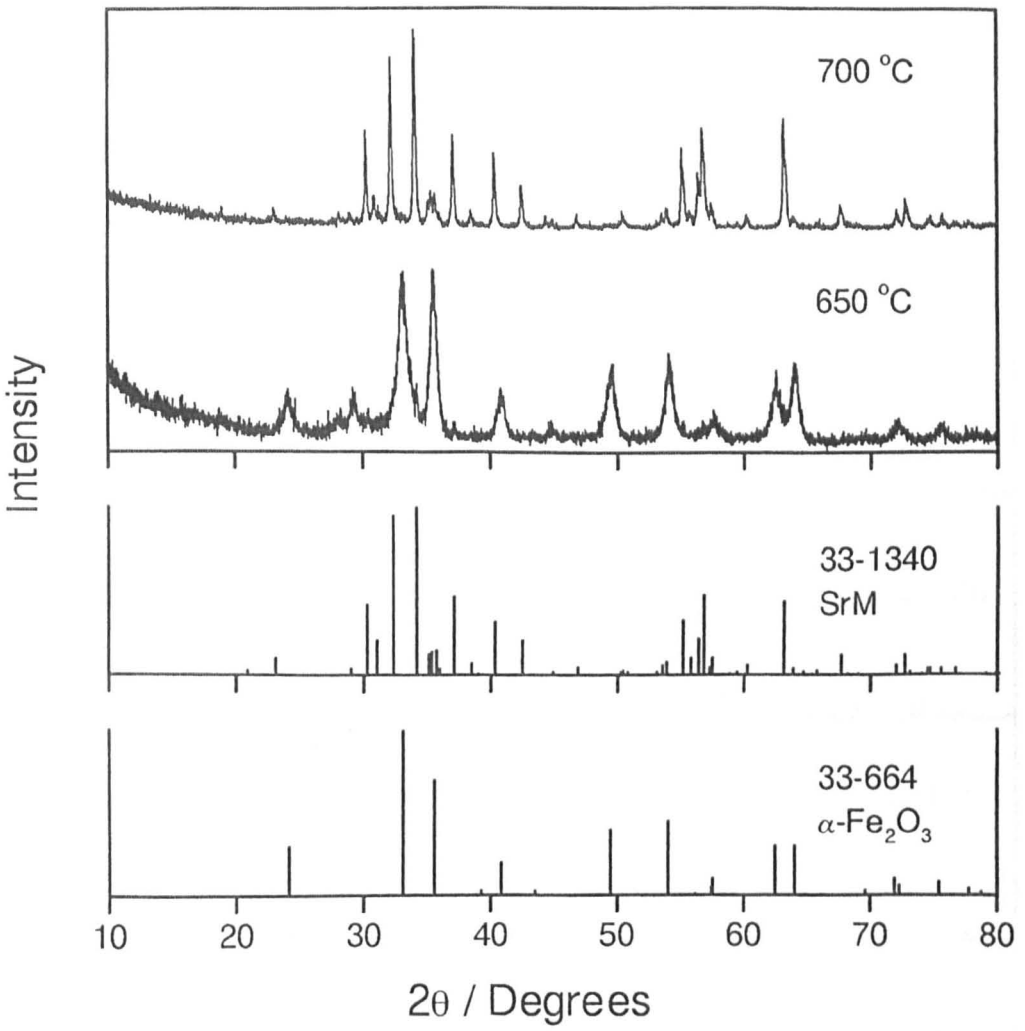

Fig. 110 XRD patterns of SrM fibres produced from a halide-free precursor, and fired to 650 and 700 °C / 3hr.

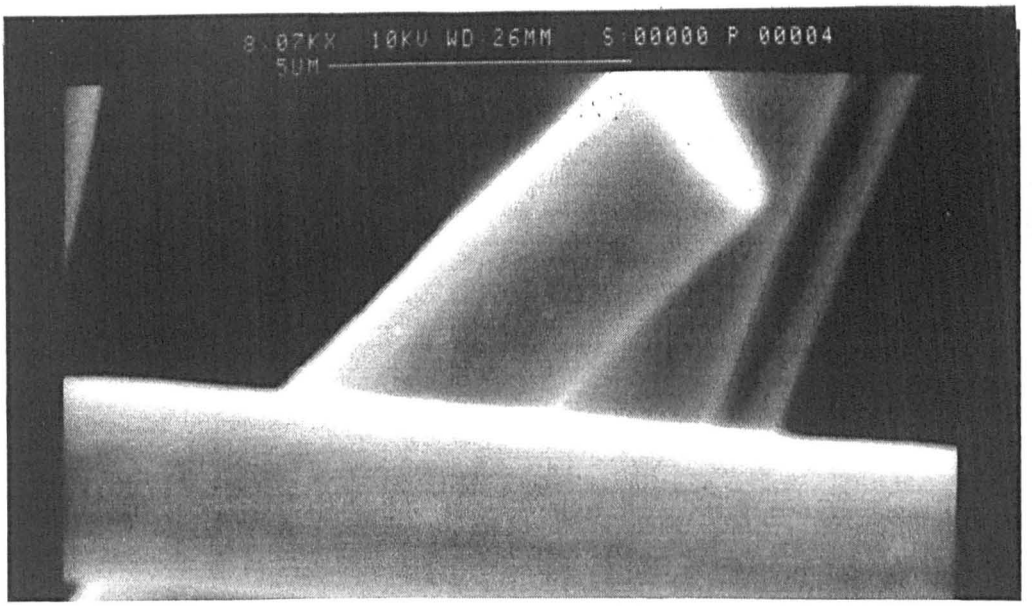

Fig. 111 SEM micrograph of SrM fibres produced from a halide-free precursor, and fired to 700 °C / 3hr.

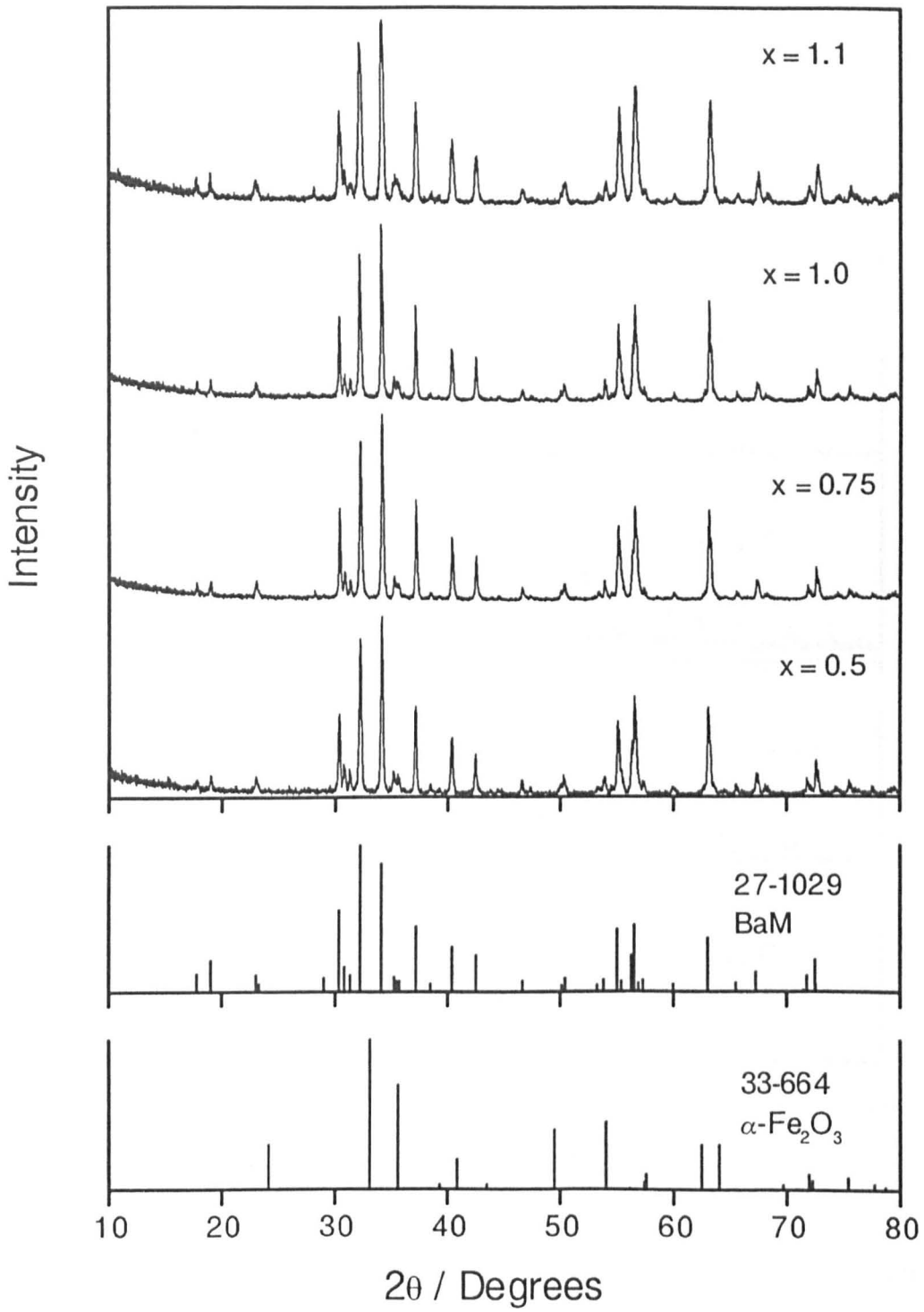

Fig. 112 XRD patterns of $BaCo_xTi_xFe_{12-2x}O_{19}$ fibres fired to 1000 °C / 3hr, for x = 0.5, 0.75, 1.0 and 1.1.

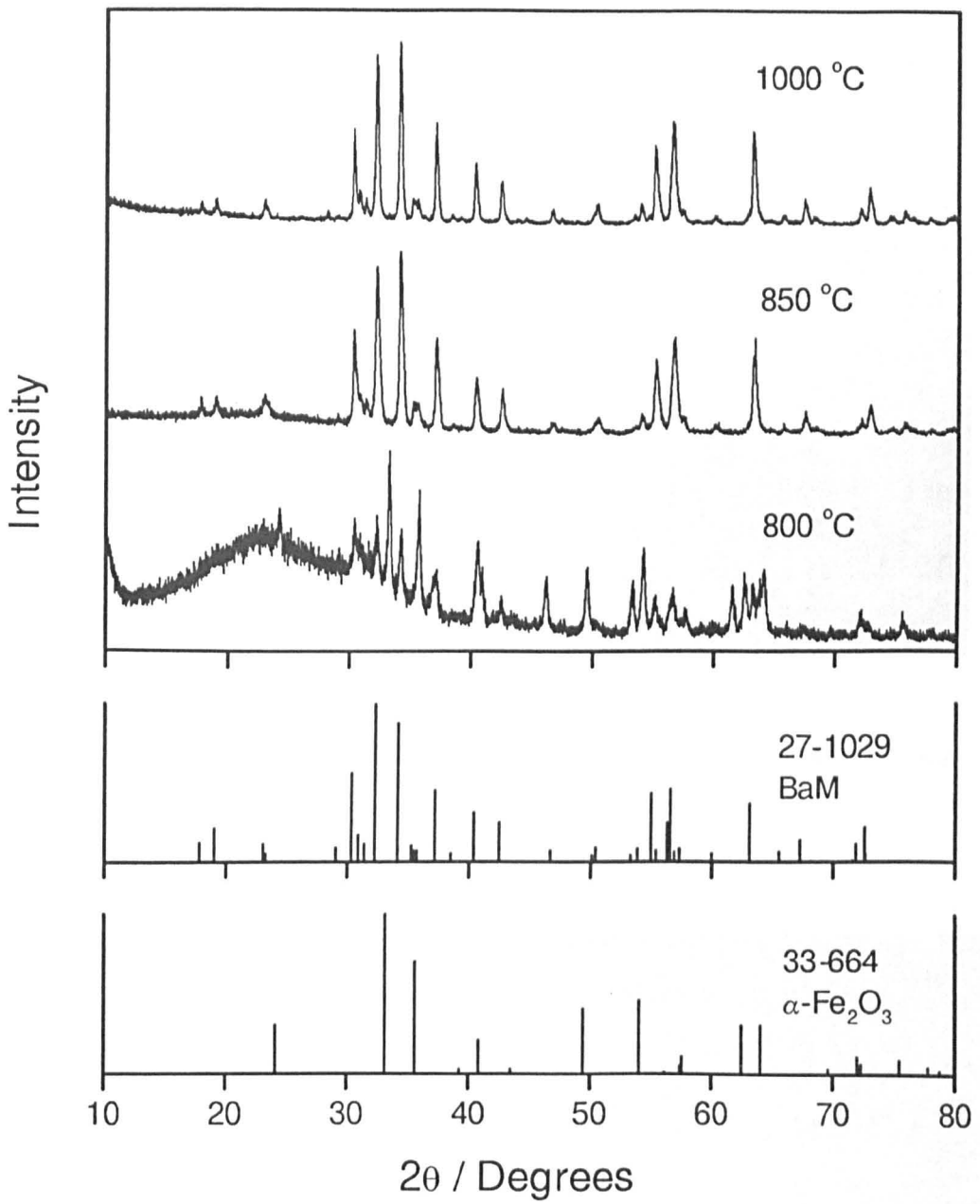

Fig. 113 XRD patterns of $BaCo_{0.5}Ti_{0.5}Fe_{11}O_{19}$ fibres fired to 800 and 850 °C / 3hr and 1000 °C / 10min.

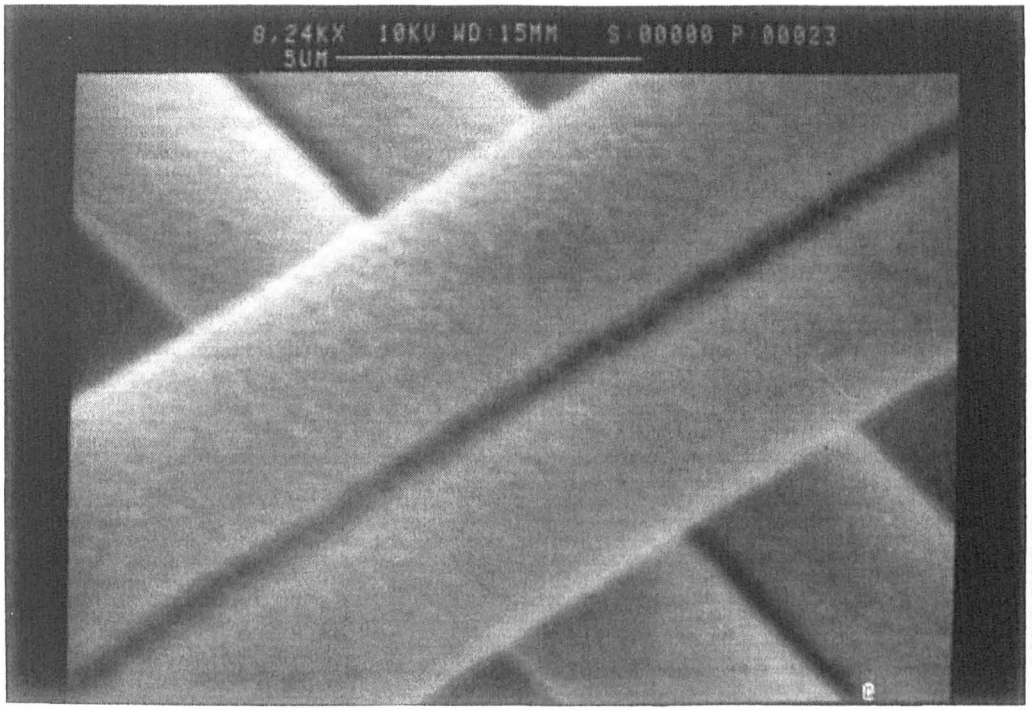

Fig. 114 SEM micrograph of $BaCo_{0.5}Ti_{0.5}Fe_{11}O_{19}$ fibres fired to 800 °C / 3hr.

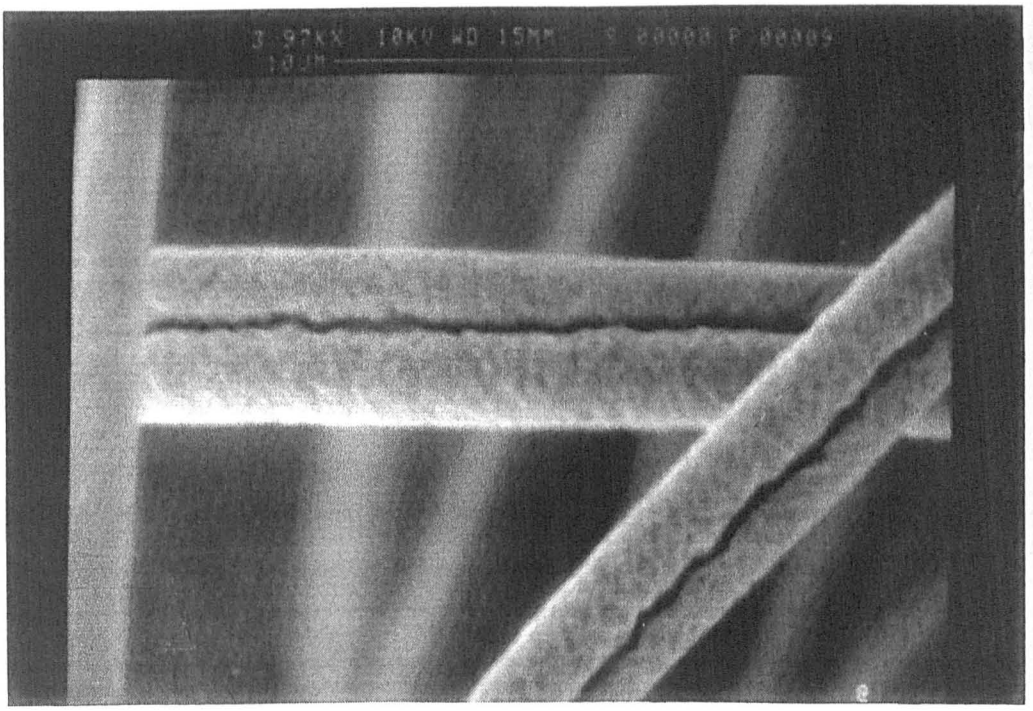

Fig. 115 SEM micrograph of $BaCo_{0.5}Ti_{0.5}Fe_{11}O_{19}$ fibres fired to 900 °C / 3hr.

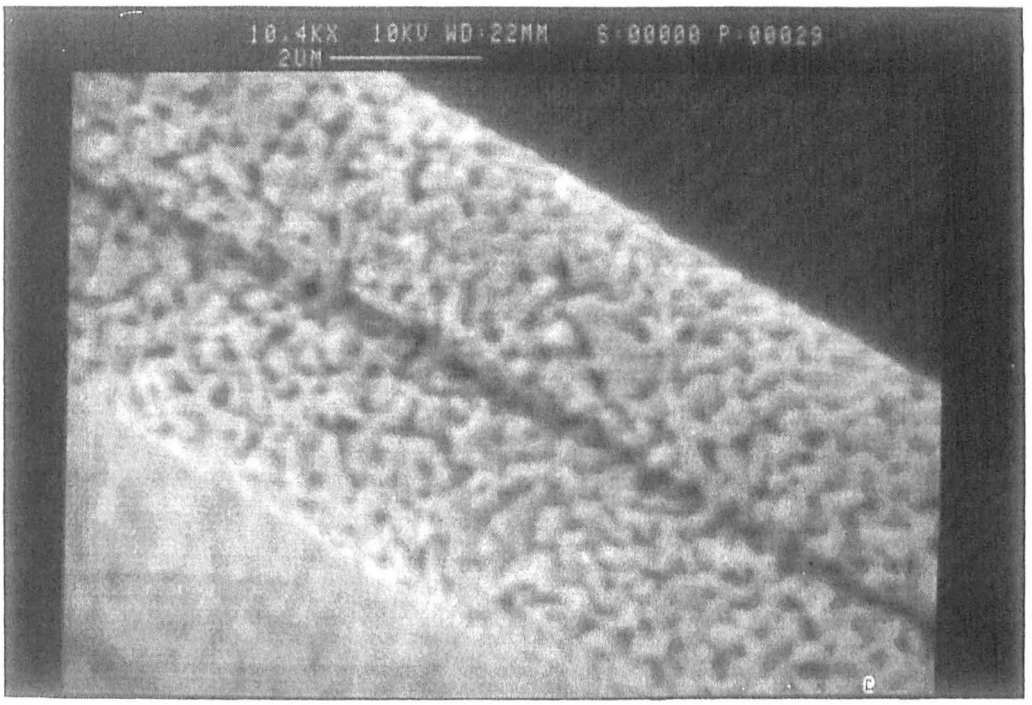

Fig. 116 SEM micrograph of $BaCo_{0.5}Ti_{0.5}Fe_{11}O_{19}$ fibres fired to 1000 °C / 3hr.

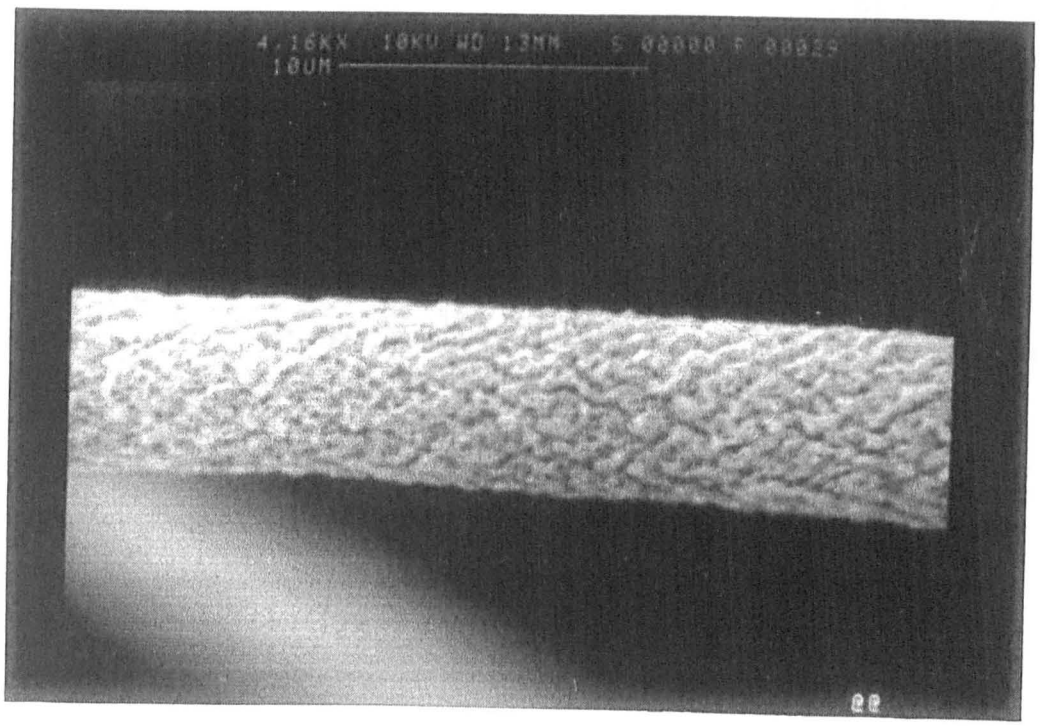

Fig. 117 SEM micrograph of $BaCo_{0.75}Ti_{0.75}Fe_{10.5}O_{19}$ fibres fired to 1000 °C / 3hr.

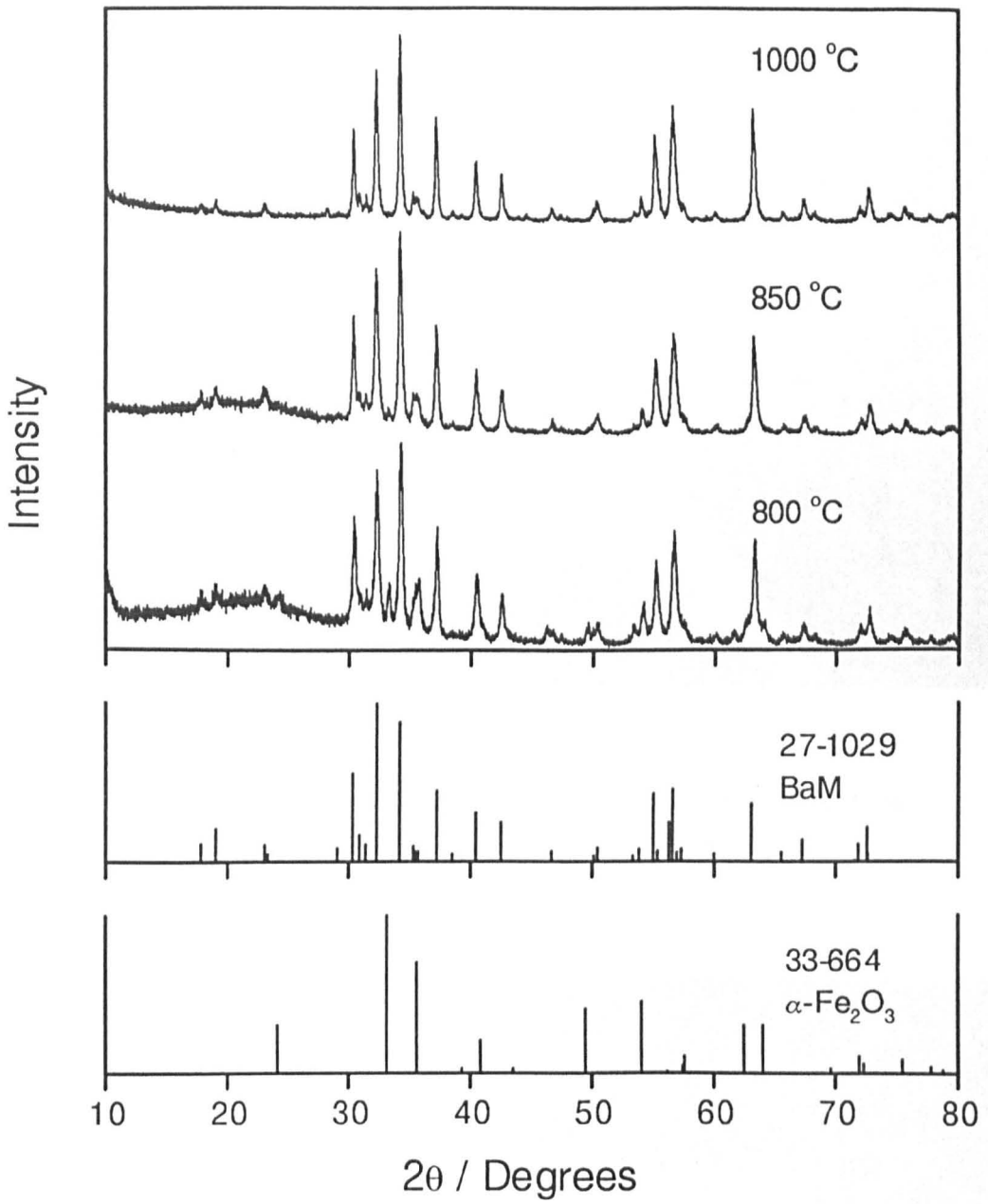

Fig. 118 XRD patterns of $BaCoTiFe_{10}O_{19}$ fibres fired to 800 and 850 °C / 3hr and 1000 °C / 10min.

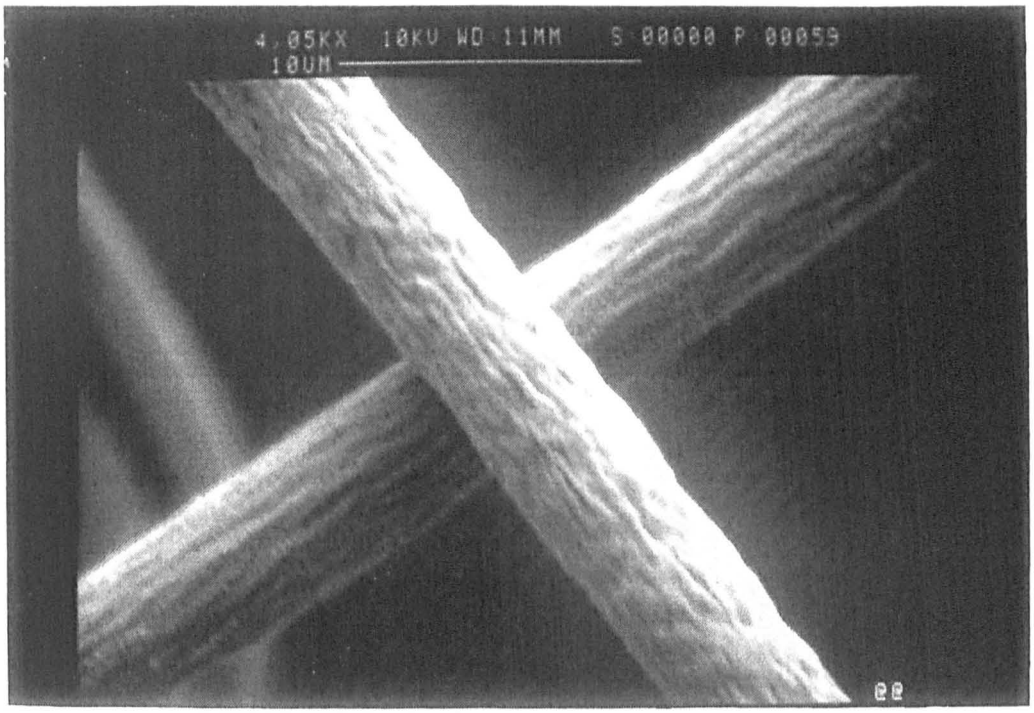

Fig. 119 SEM micrograph of $BaCoTiFe_{10}O_{19}$ fibres fired to 900 °C / 3hr.

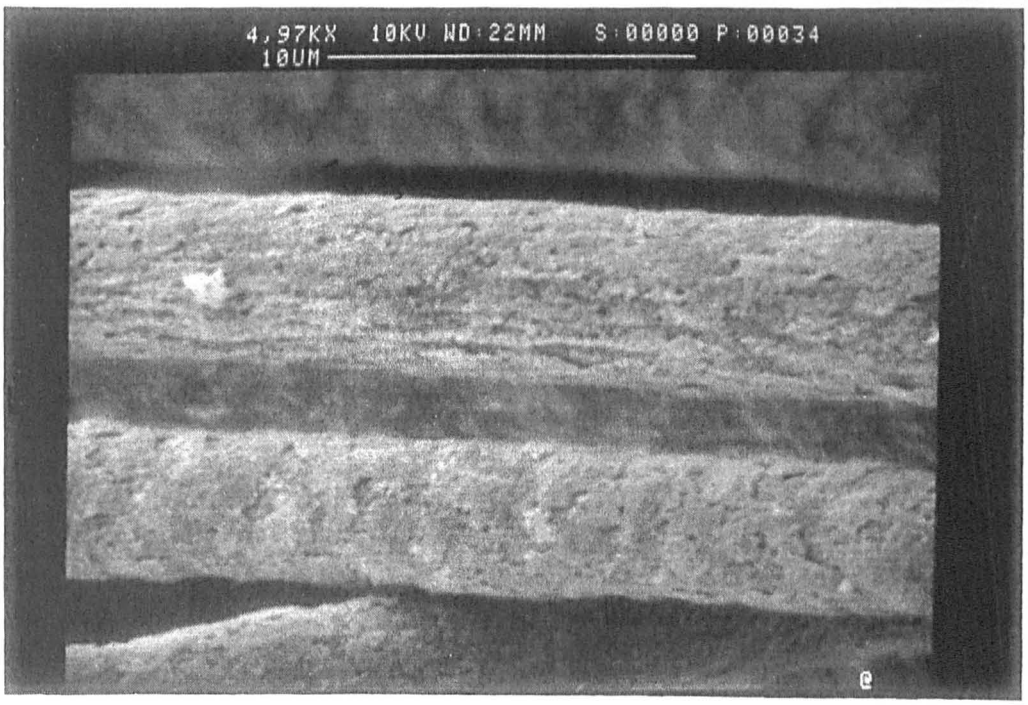

Fig. 120 SEM micrograph of $BaCoTiFe_{10}O_{19}$ fibres fired to 1000 °C / 3hr.

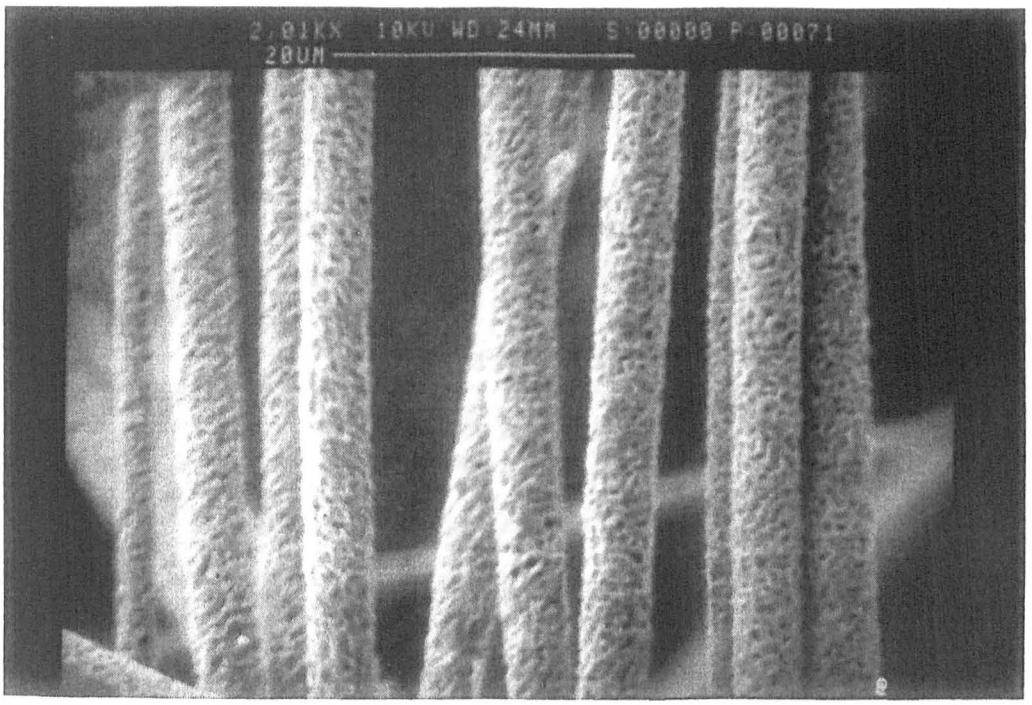

Fig. 121 SEM micrograph of $BaCoTiFe_{10}O_{19}$ fibres fired to 1100 °C / 3hr.

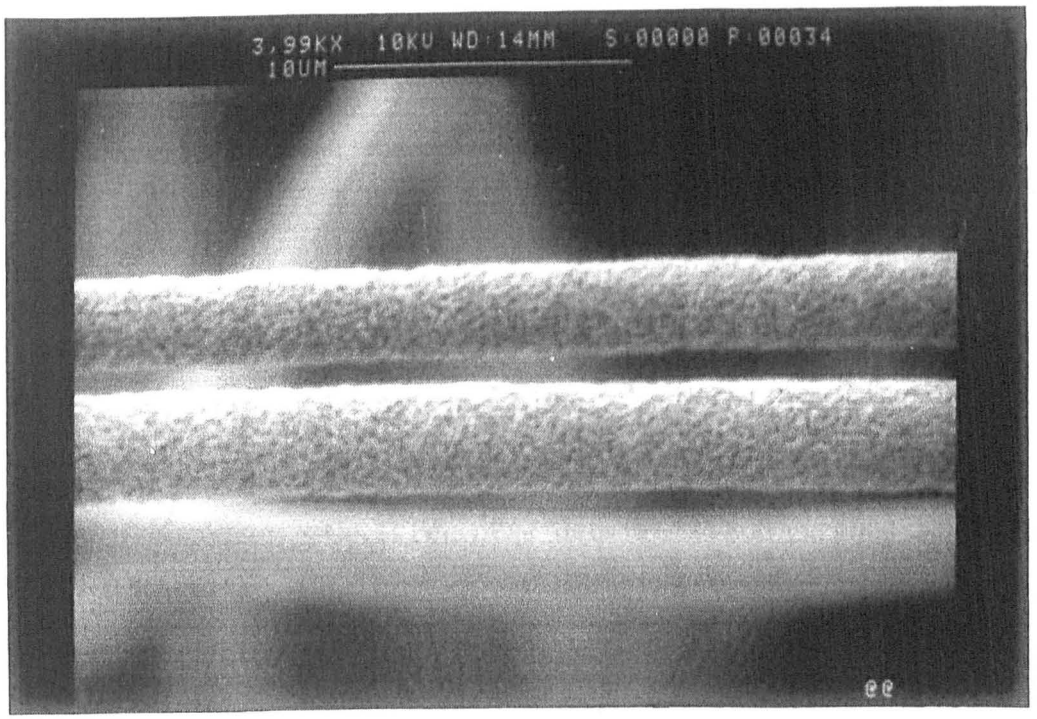

Fig. 122 SEM micrograph of $BaCo_{1.1}Ti_{1.1}Fe_{9.8}O_{19}$ fibres fired to 1000 °C / 3hr.

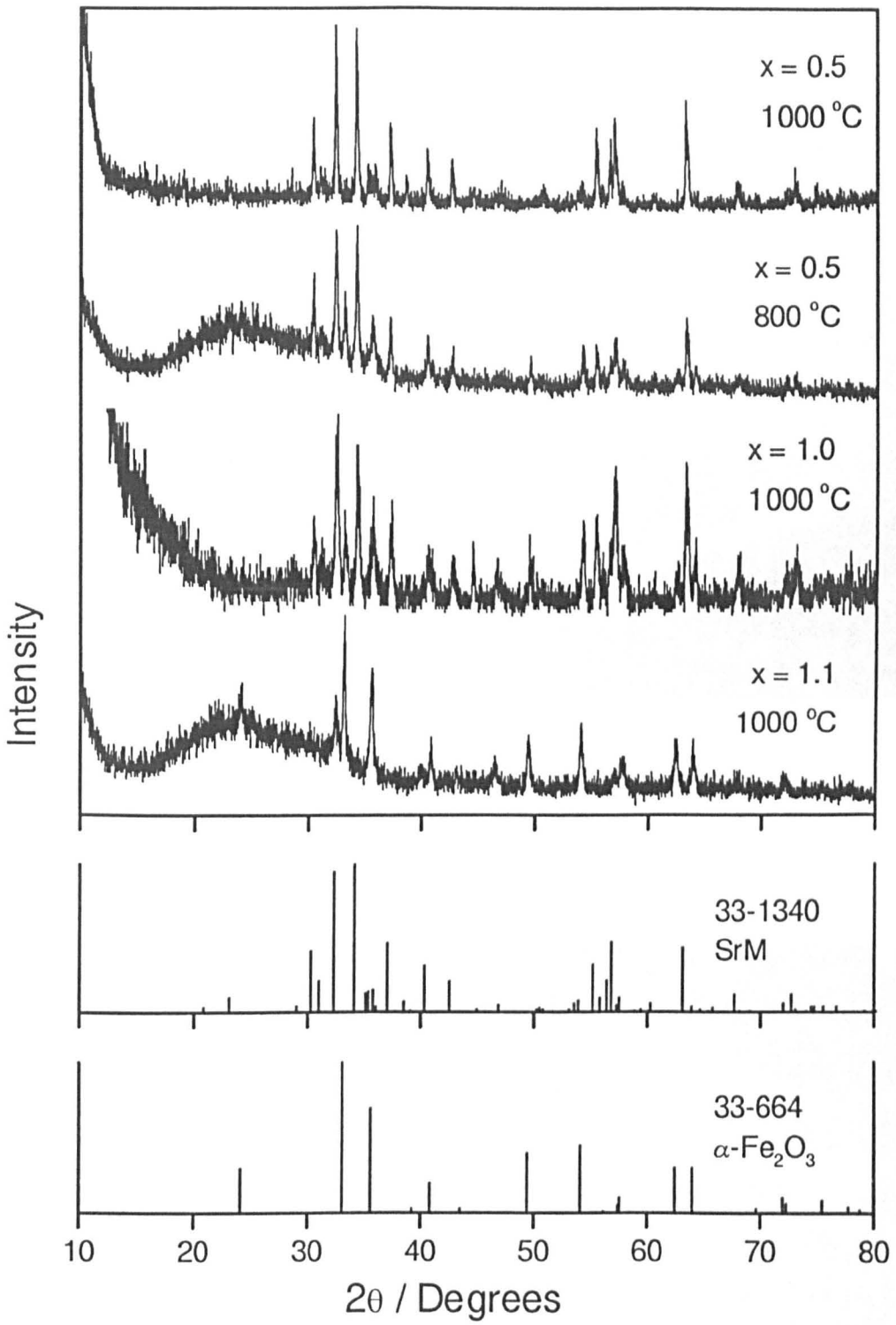

Fig. 123 XRD patterns of $SrCo_xTi_xFe_{12-2x}O_{19}$ fibres fired to 800 and 1000 °C / 3hr for x = 0.5 and 1.0.

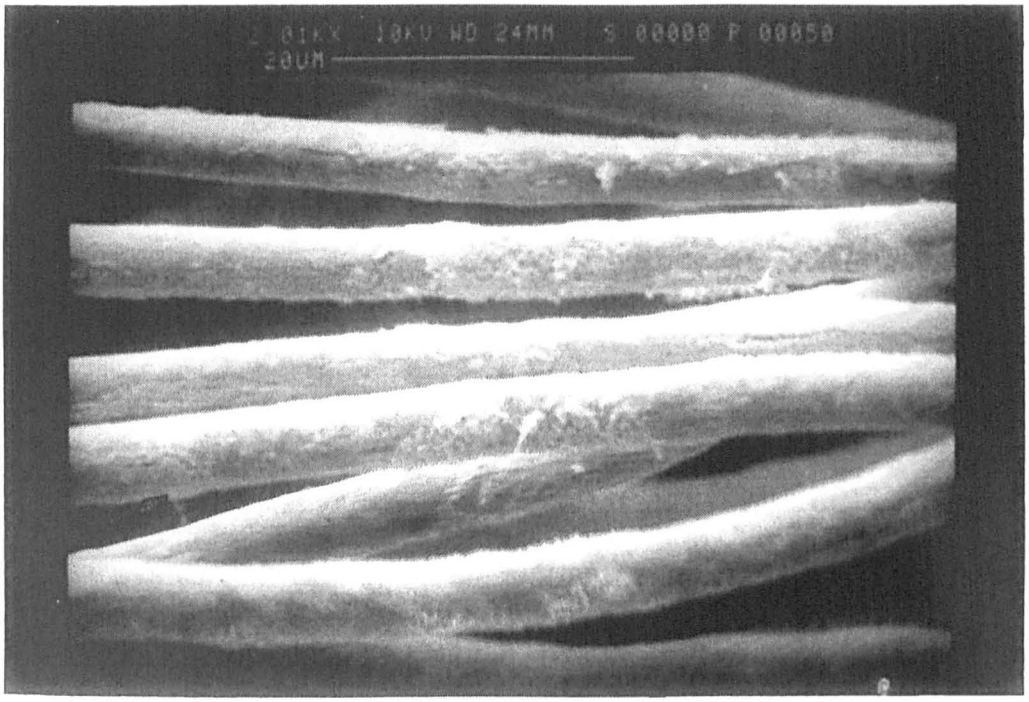

Fig. 124 SEM micrograph of $SrCo_{0.5}Ti_{0.5}Fe_{11}O_{19}$ fibres fired to 800 °C / 3hr.

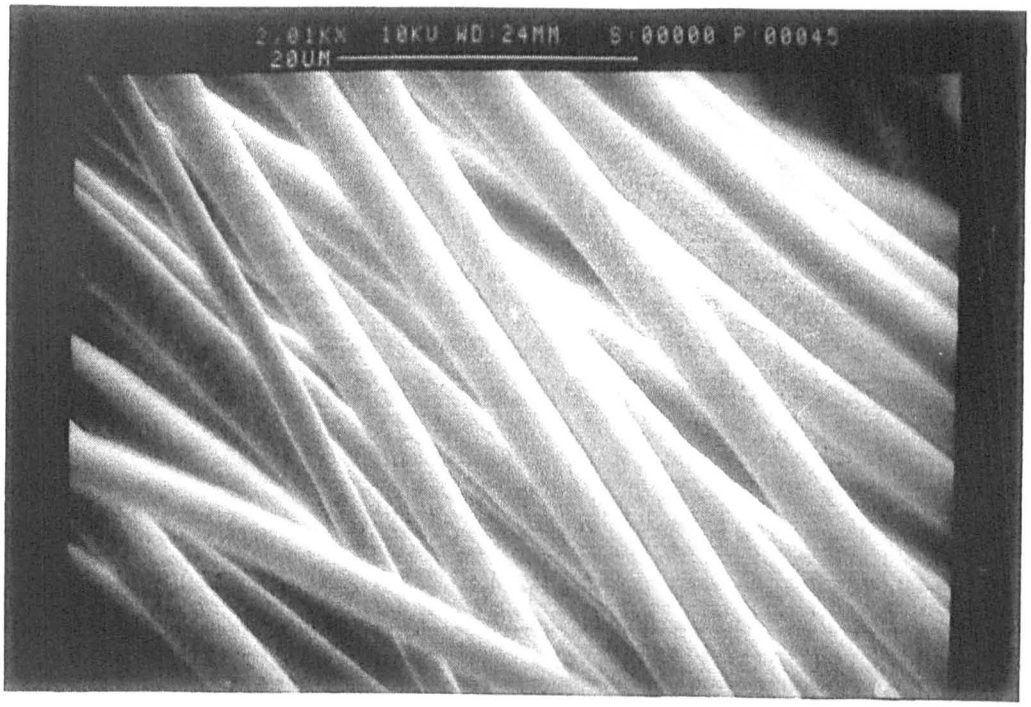

Fig. 125 SEM micrograph of $SrCo_{0.5}Ti_{0.5}Fe_{11}O_{19}$ fibres fired to 1000 °C / 3hr.

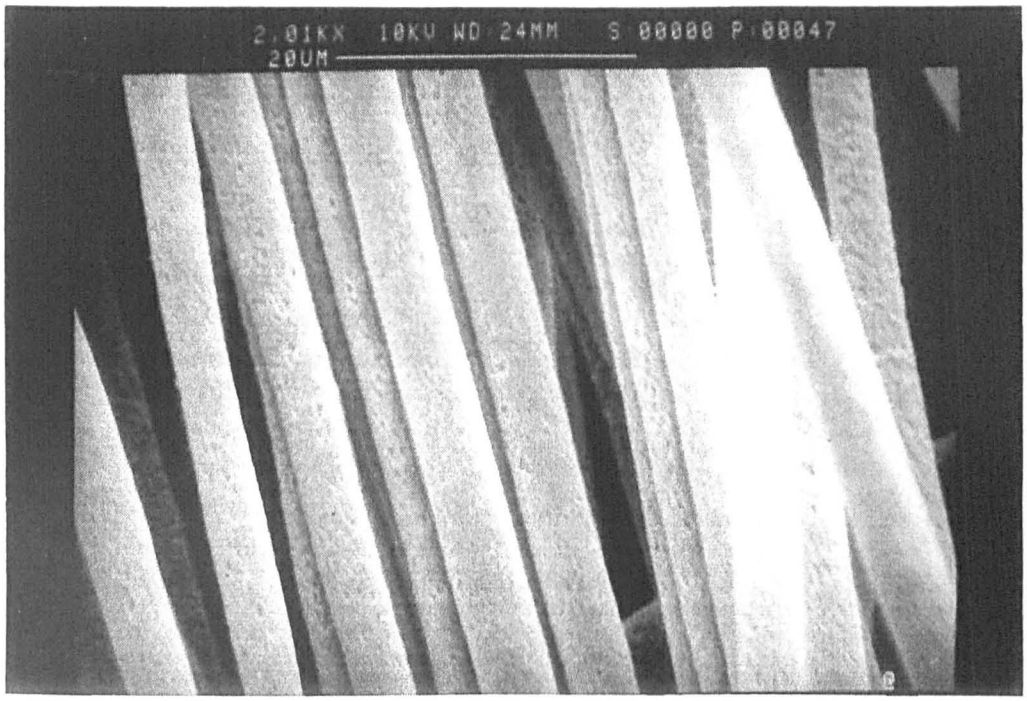

Fig. 126 SEM micrograph of $SrCo_{0.5}Ti_{0.5}Fe_{11}O_{19}$ fibres fired to 1000 °C / 100hr.

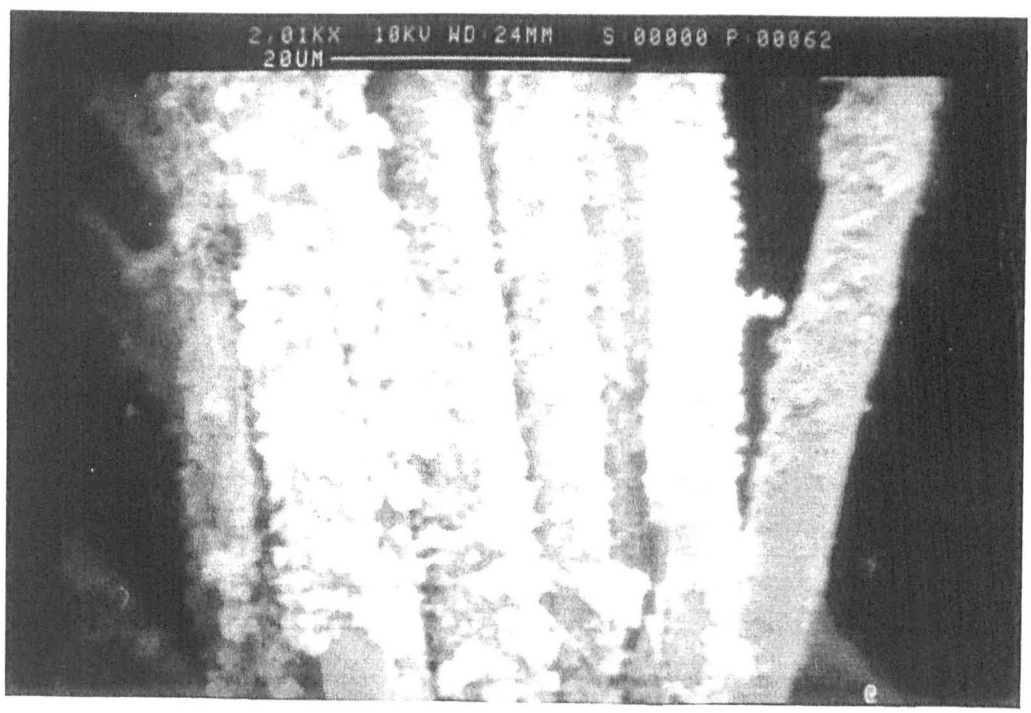

Fig. 127 SEM micrograph of $SrCoTiFe_{10}O_{19}$ fibres fired to 800 °C / 3hr.

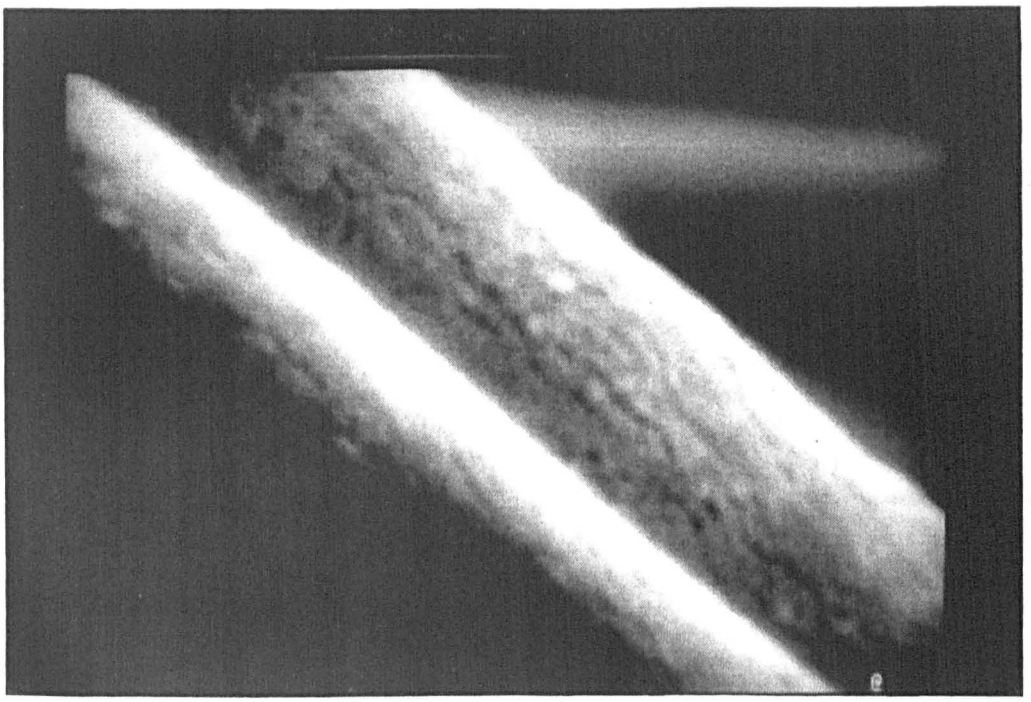

Fig. 128 SEM micrograph of $SrCoTiFe_{10}O_{19}$ fibres fired to 1000 °C / 3hr.

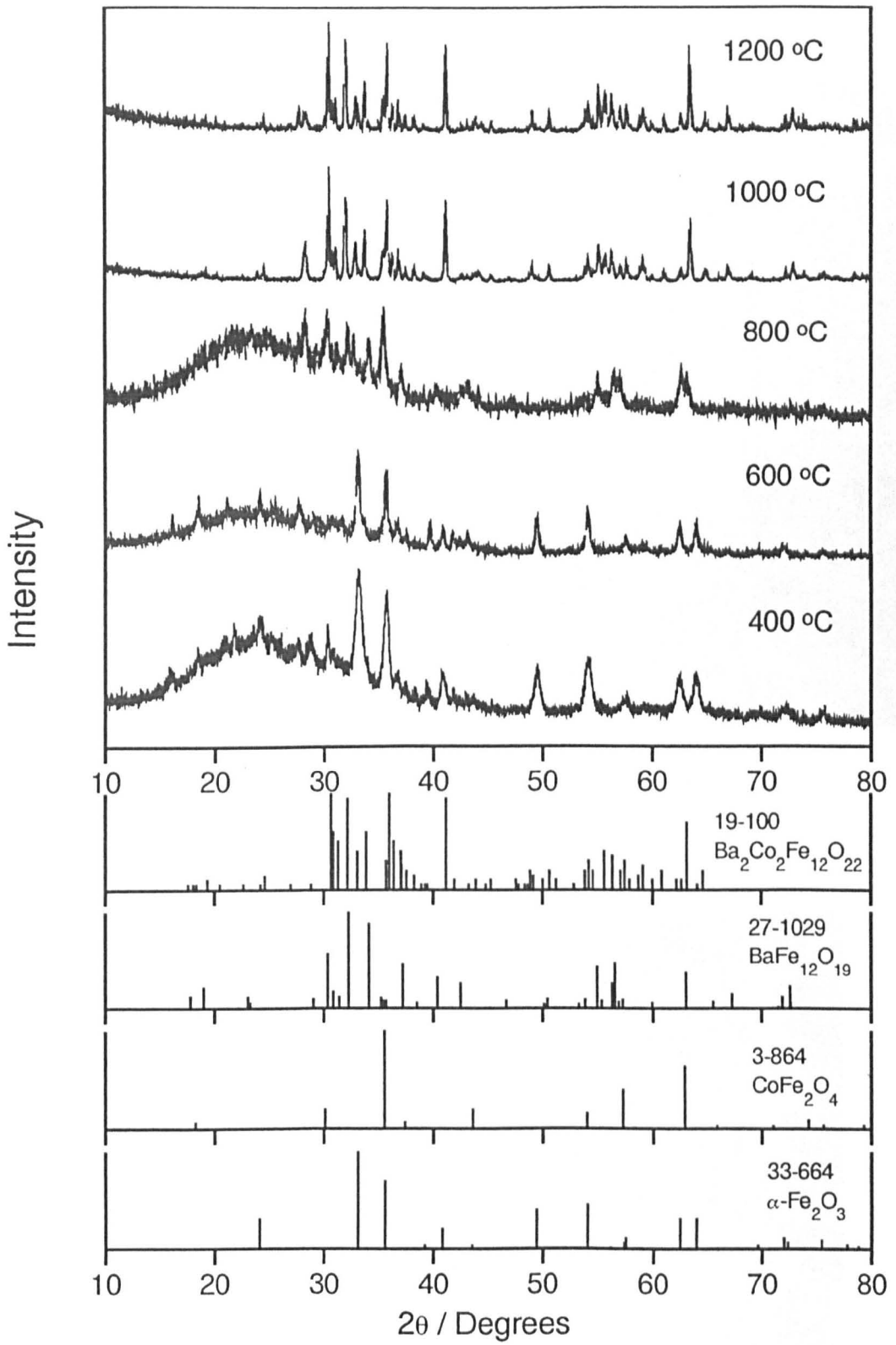

Fig. 129 XRD patterns of the freshly spun Co_2Y fibres fired to 400, 600, 800, 1000 and 1200 °C / 3hr.

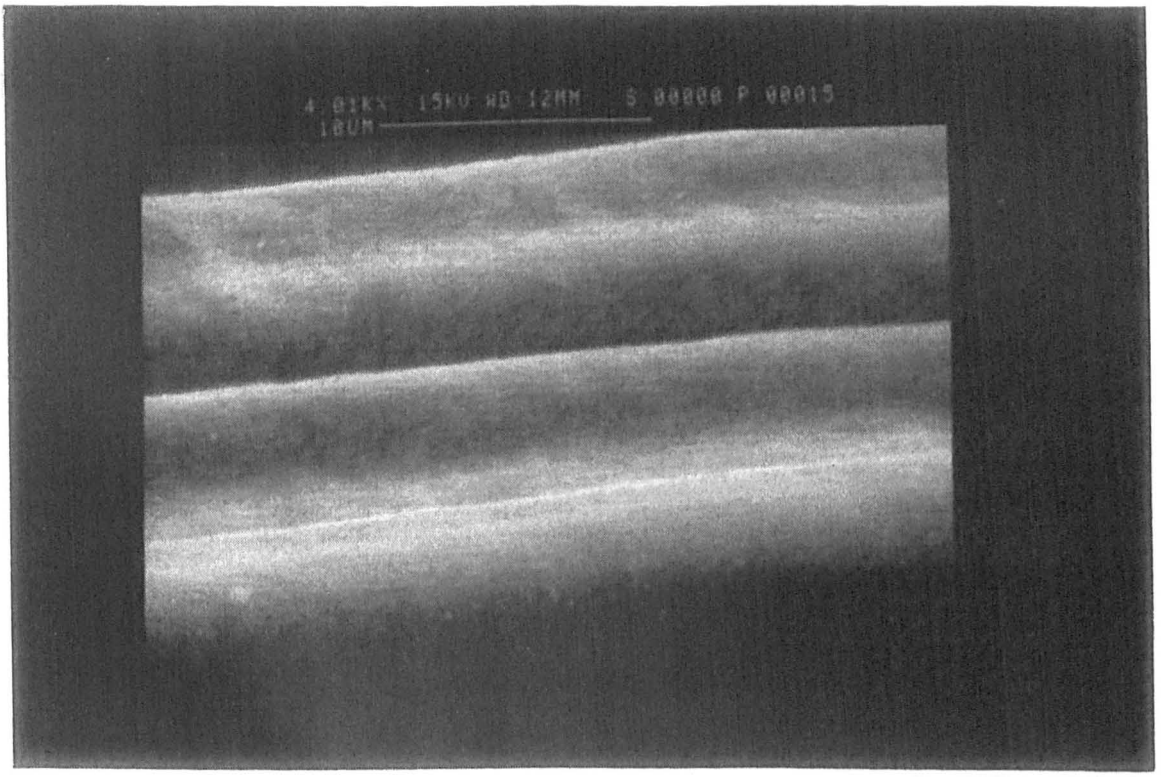

Fig. 130 SEM micrographs of freshly spun Co_2Y fibres fired to 800 °C.

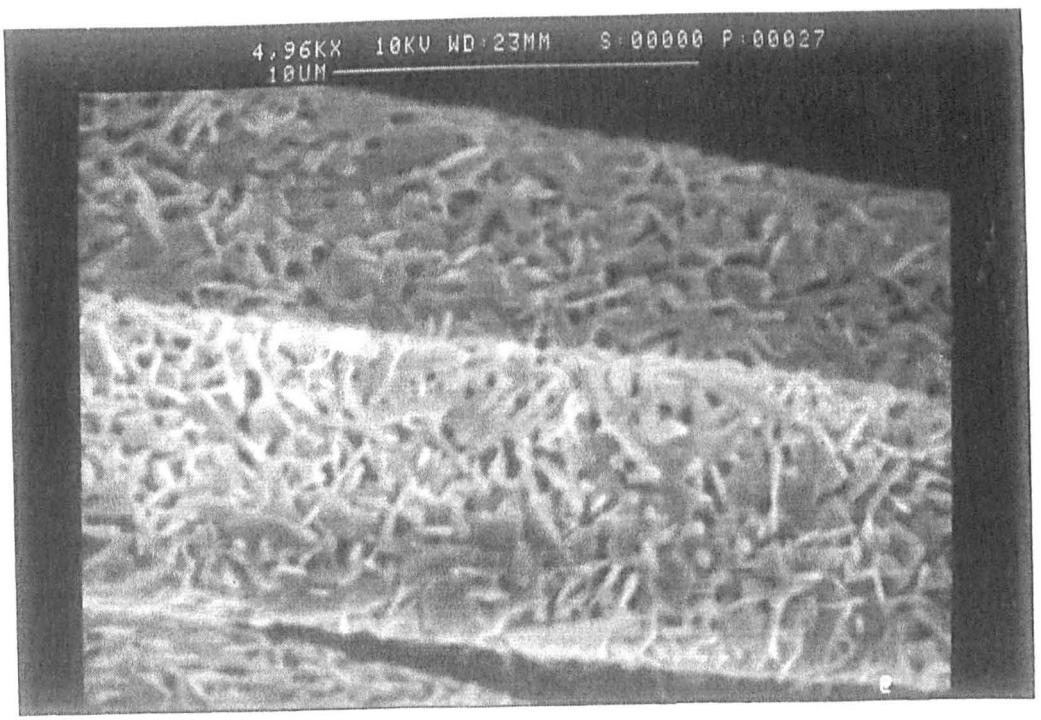

Fig. 131 SEM micrographs of freshly spun Co_2Y fibres fired to 1000 °C.

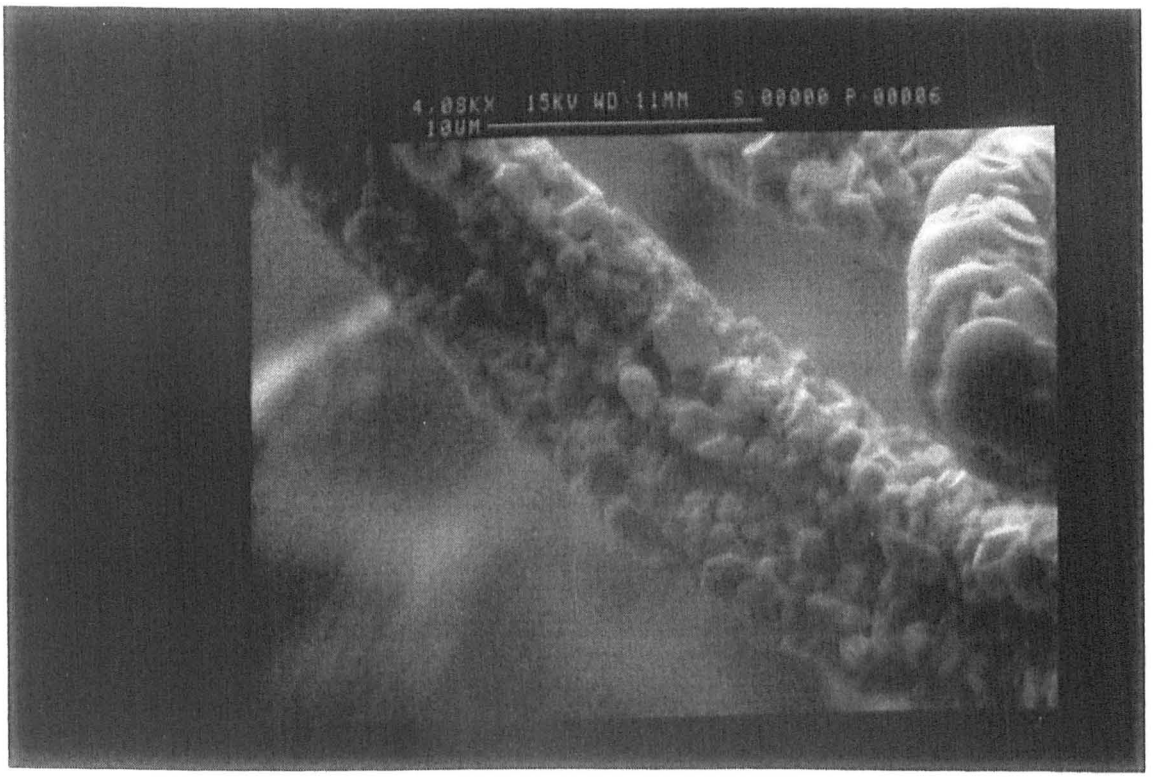

Fig. 132 SEM micrographs of freshly spun Co_2Y fibres fired to 1200 °C.

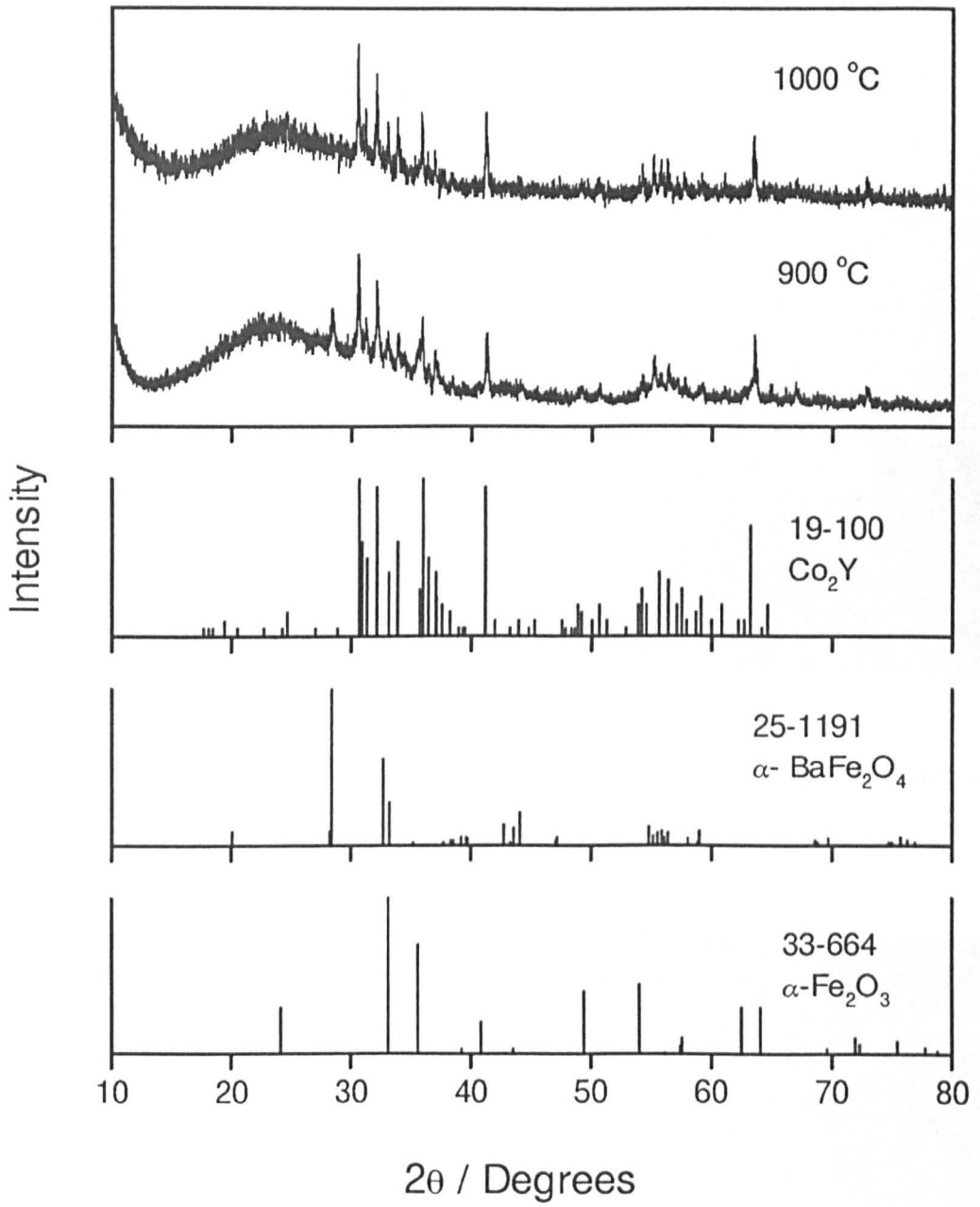

Fig. 133 XRD patterns of the Co_2Y fibres, stored for 3 yr, fired to 900 °C / 3hr and 1000 °C / 10min.

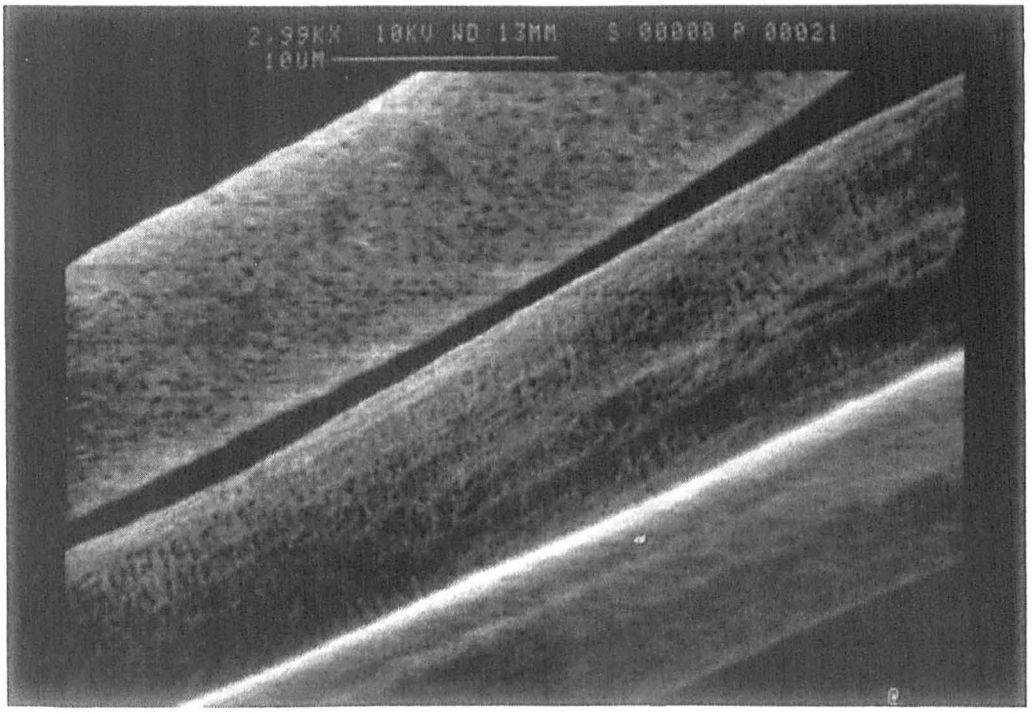

Fig. 134 SEM micrographs of the Co_2Y fibres, stored for 3 yr, fired to 900 °C / 3hr.

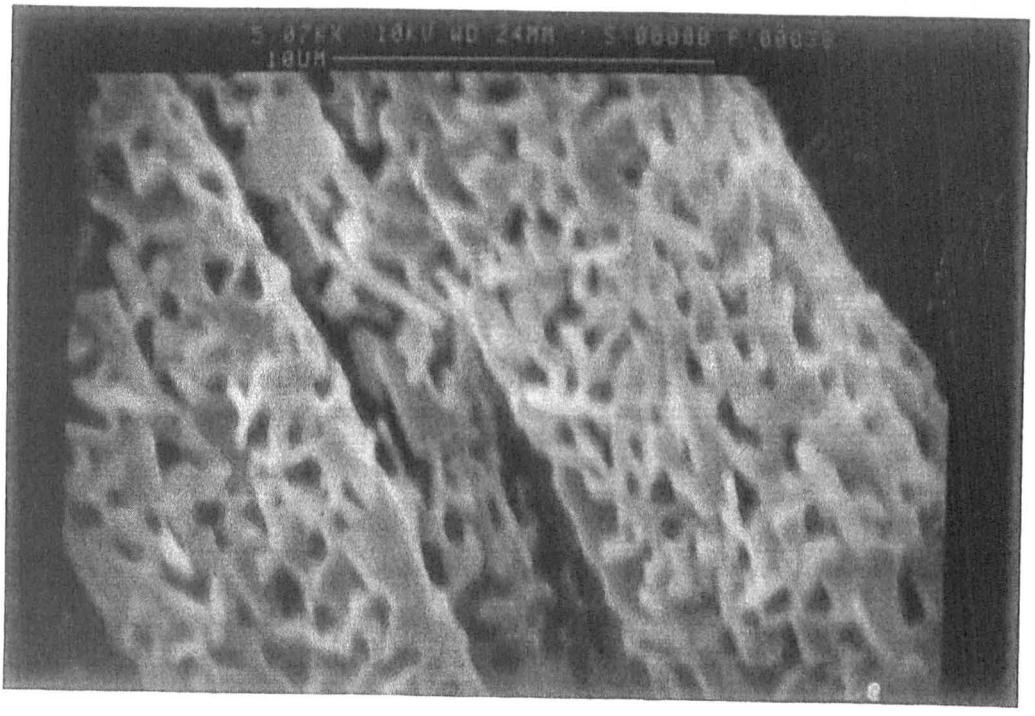

Fig. 135 SEM micrographs of the Co_2Y fibres, stored for 3 yr, fired to 1000 °C / 3hr.

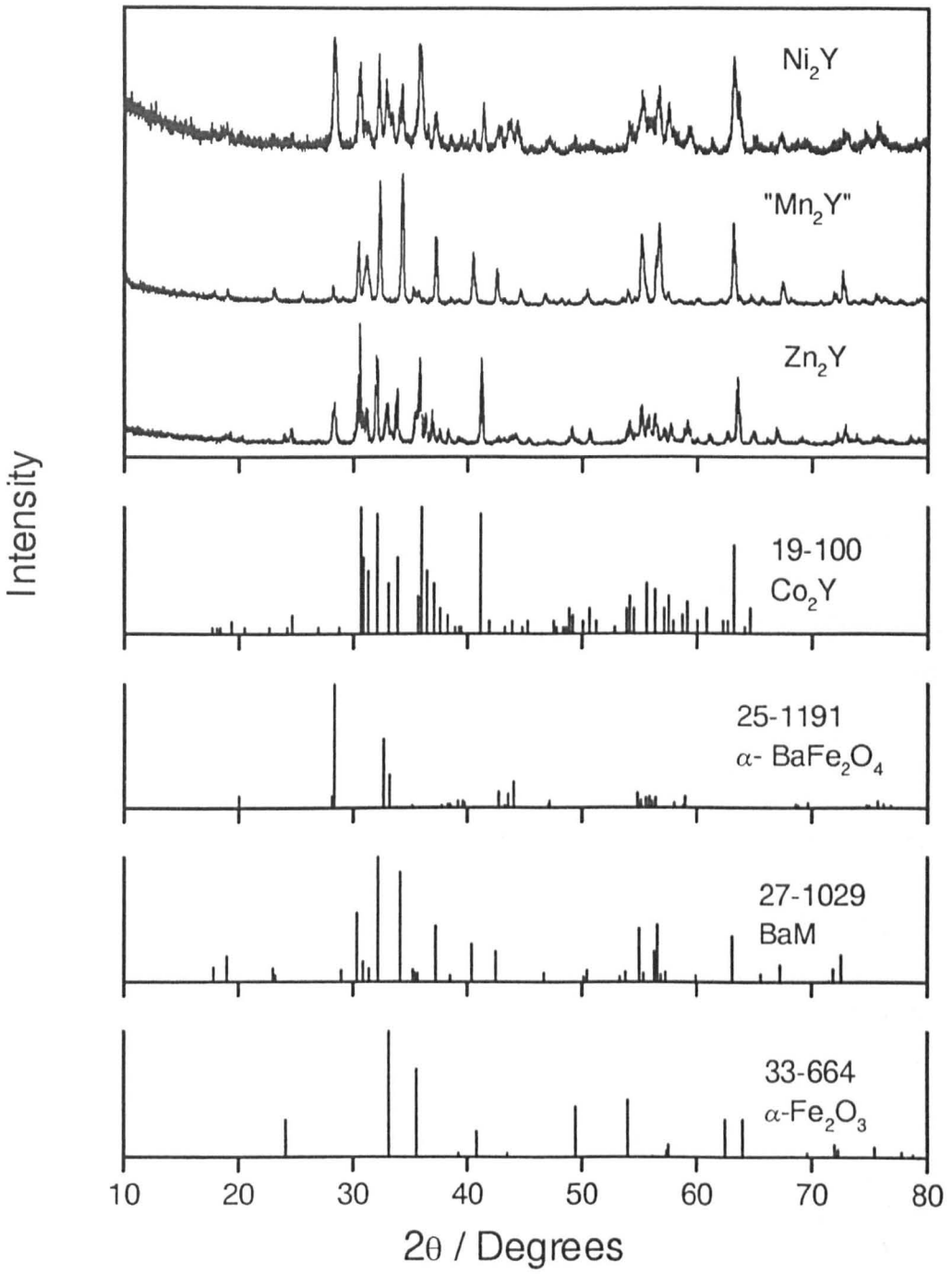

Fig. 136 XRD patterns of fibres with Ni_2Y, Zn_2Y and Mn_2Y compositions fired to 1000 ^0C / 3hr.

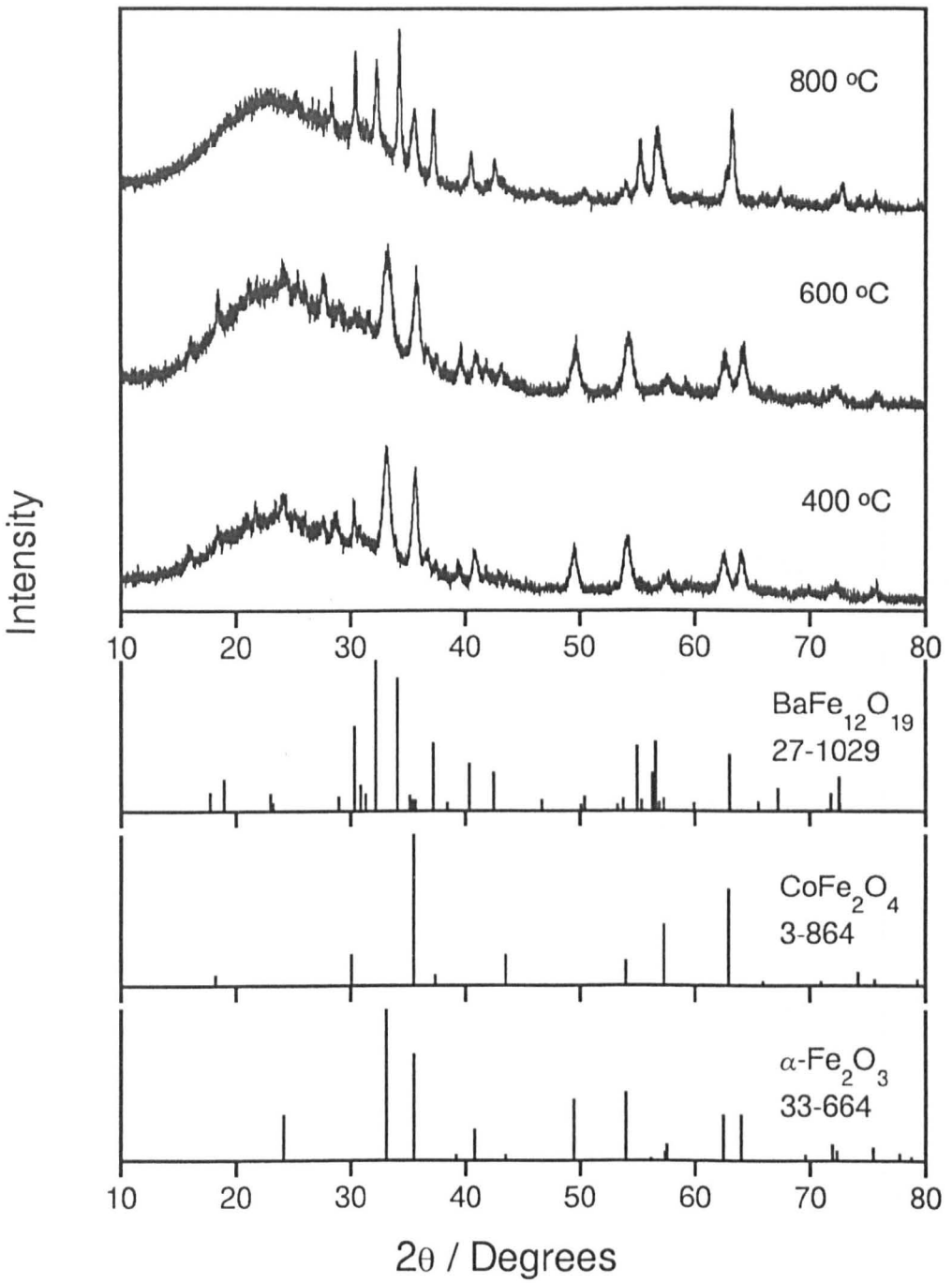

Fig. 137 XRD patterns of Co_2Z fibres fired to 400, 600 and 800 °C / 3hr.

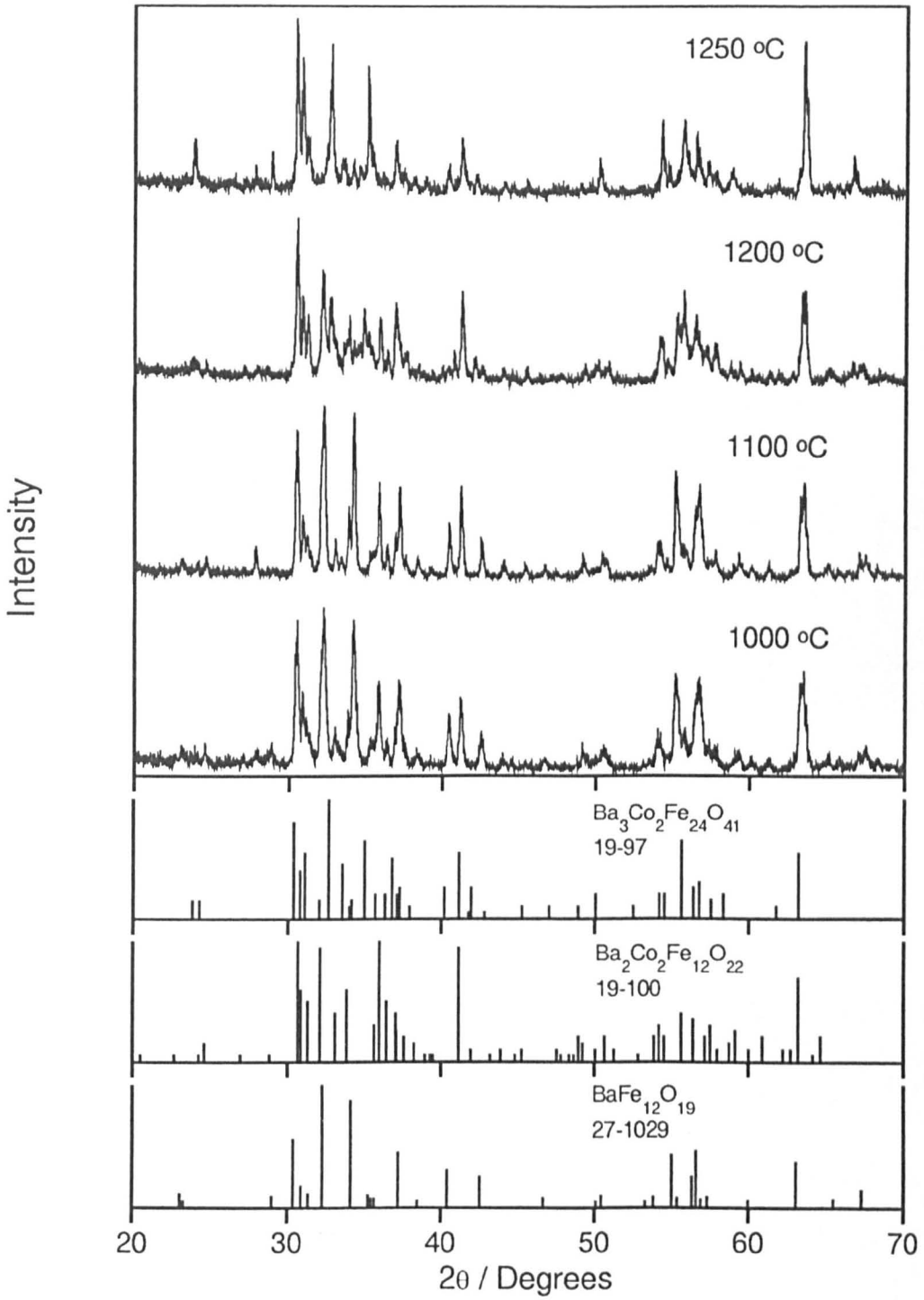

Fig. 138 XRD patterns of Co_2Z fibres fired to 1000, 1100, 1200 and 1250 °C for 3hr.

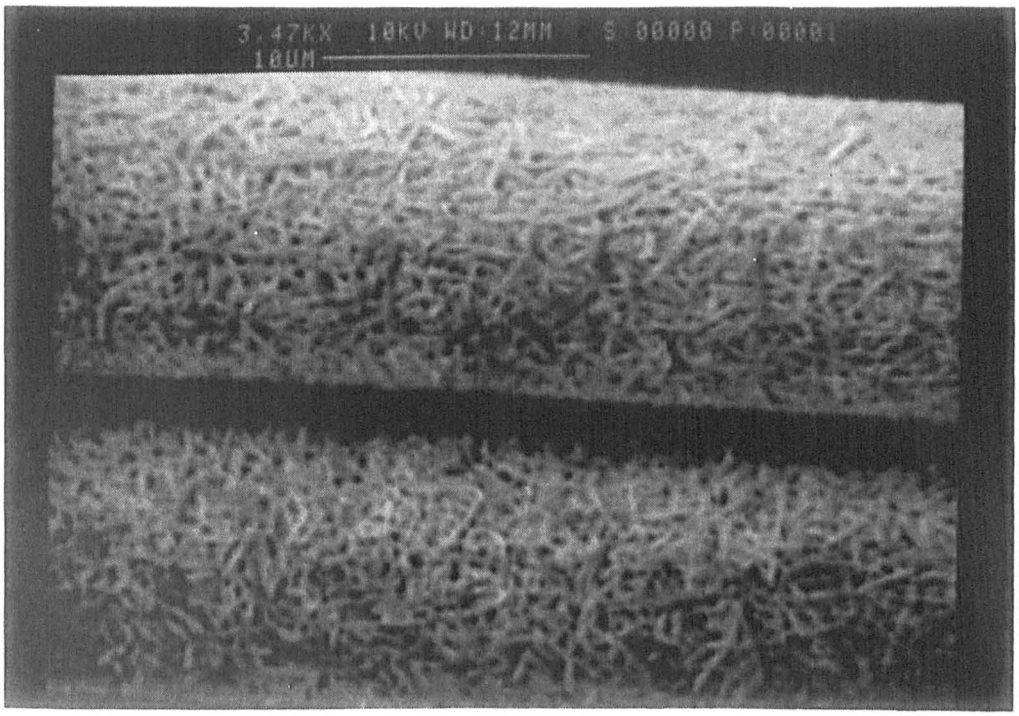

Fig. 139 SEM micrograph of Co_2Z fibres fired to 1000 °C / 3hr.

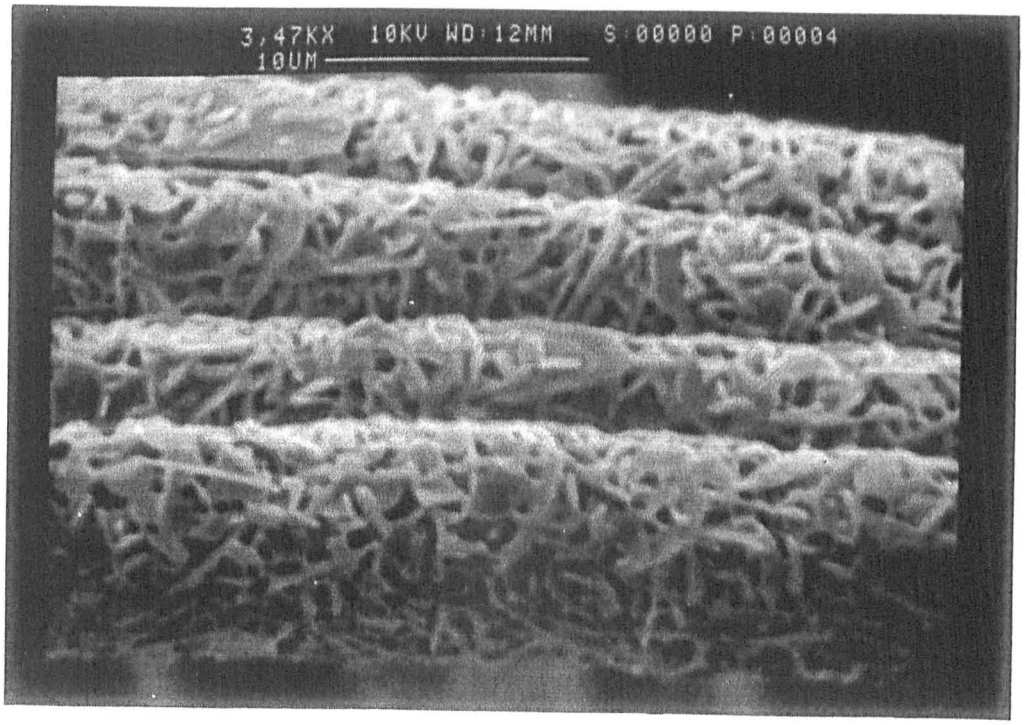

Fig. 140 SEM micrograph of Co_2Z fibres fired to 1100 °C / 3hr.

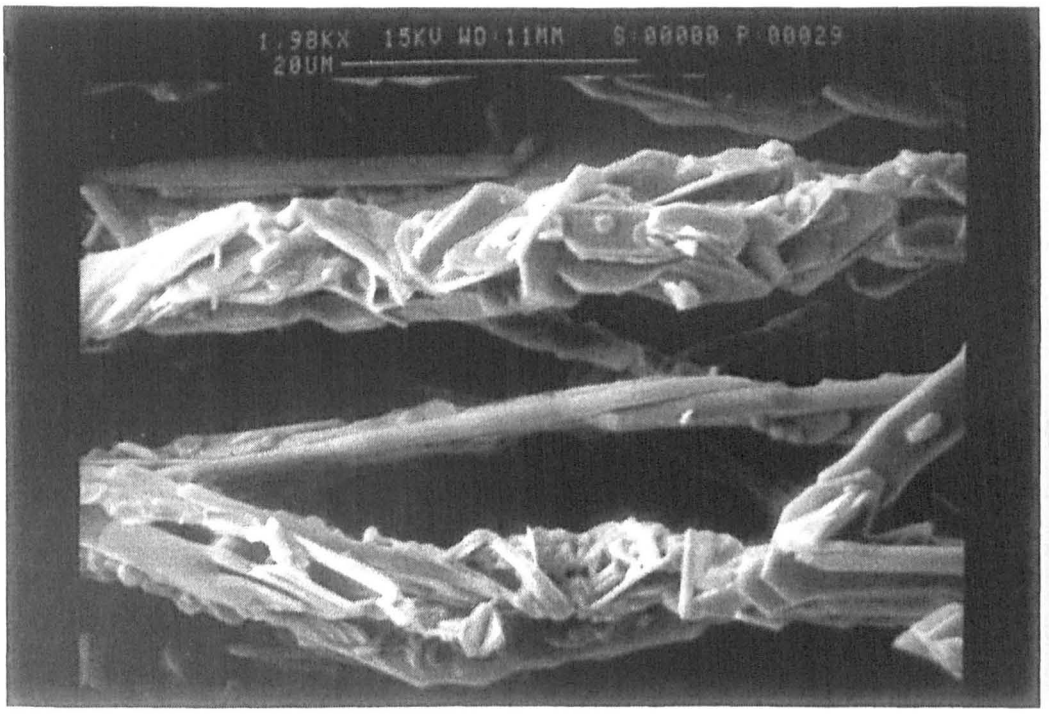

Fig. 141 SEM micrograph of Co_2Z fibres fired to 1200 °C / 3hr.

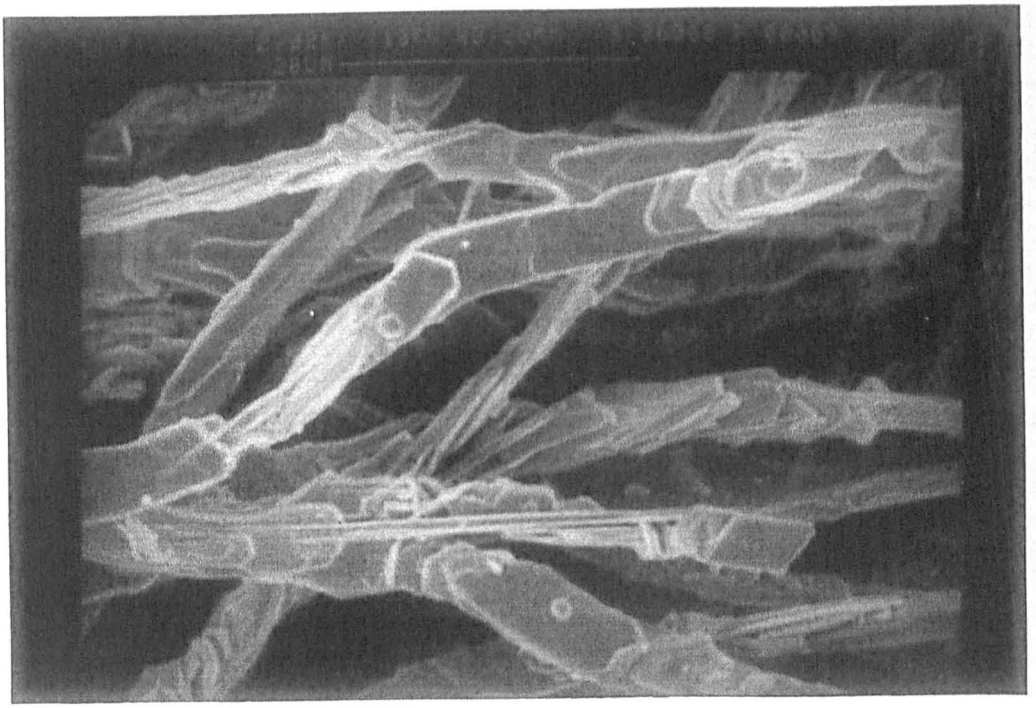

Fig. 142 SEM micrograph of Co_2Z fibres fired to 1250 °C / 3hr.

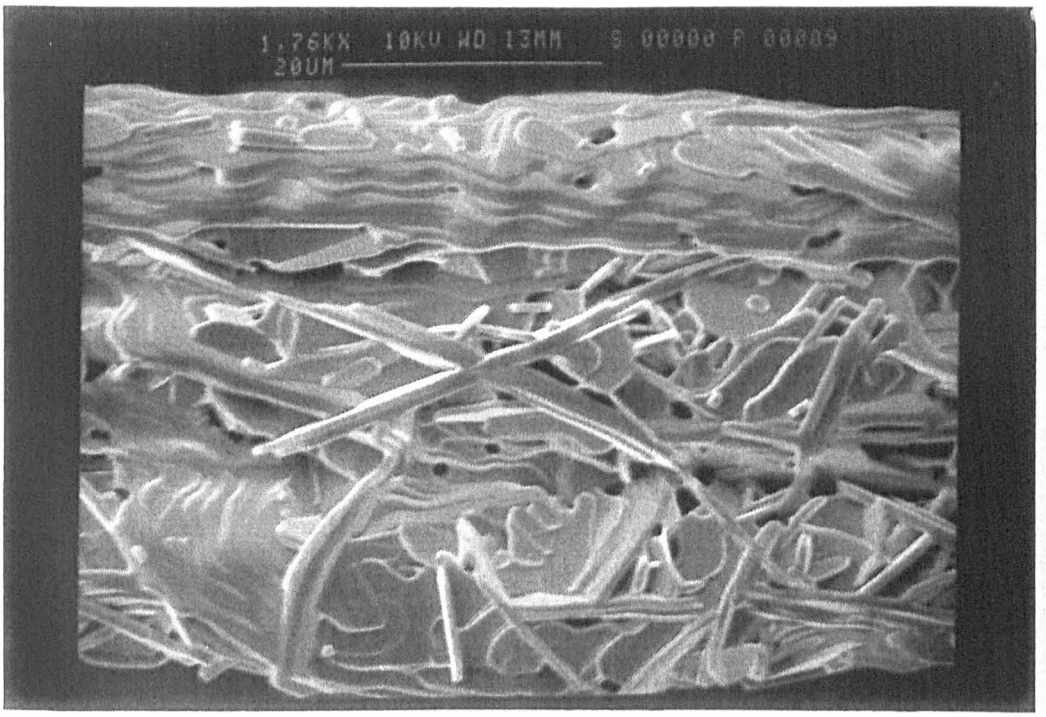

Fig. 143 SEM micrograph of Co_2Z fibres fired to 1350 °C / 3hr.

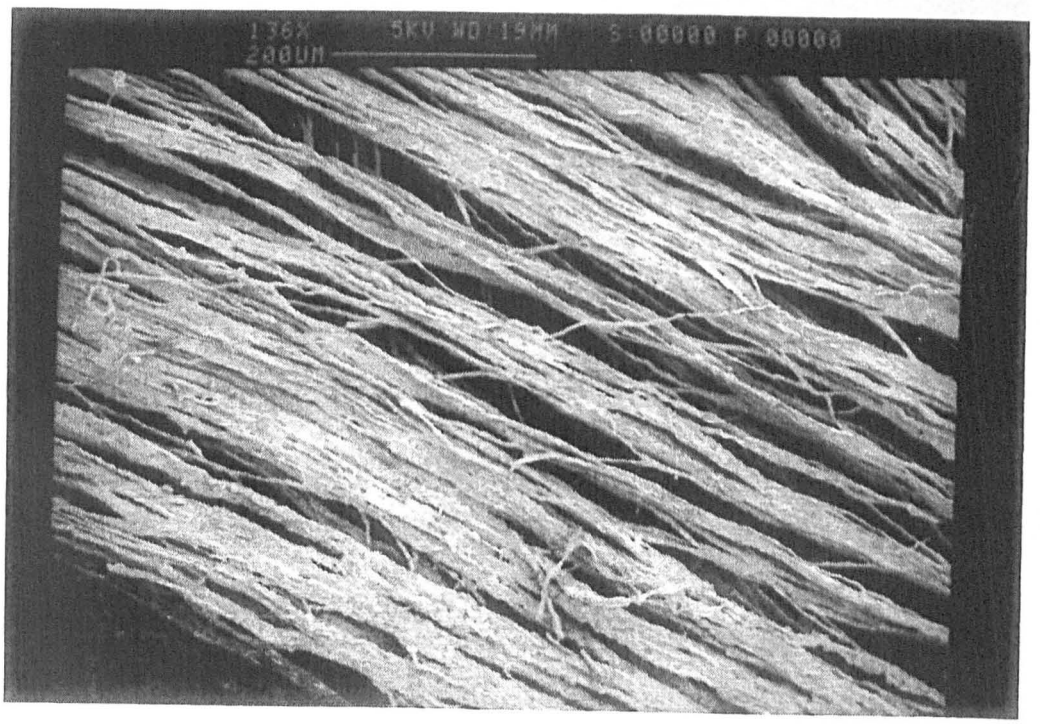

Fig. 144 SEM micrograph of fused Co_2Z fibres, fired to 1350 °C / 3hr.

Fig. 145 SEM micrograph of Co_2Z fibres, demonstrating the hexagonal nature of the DGG form.

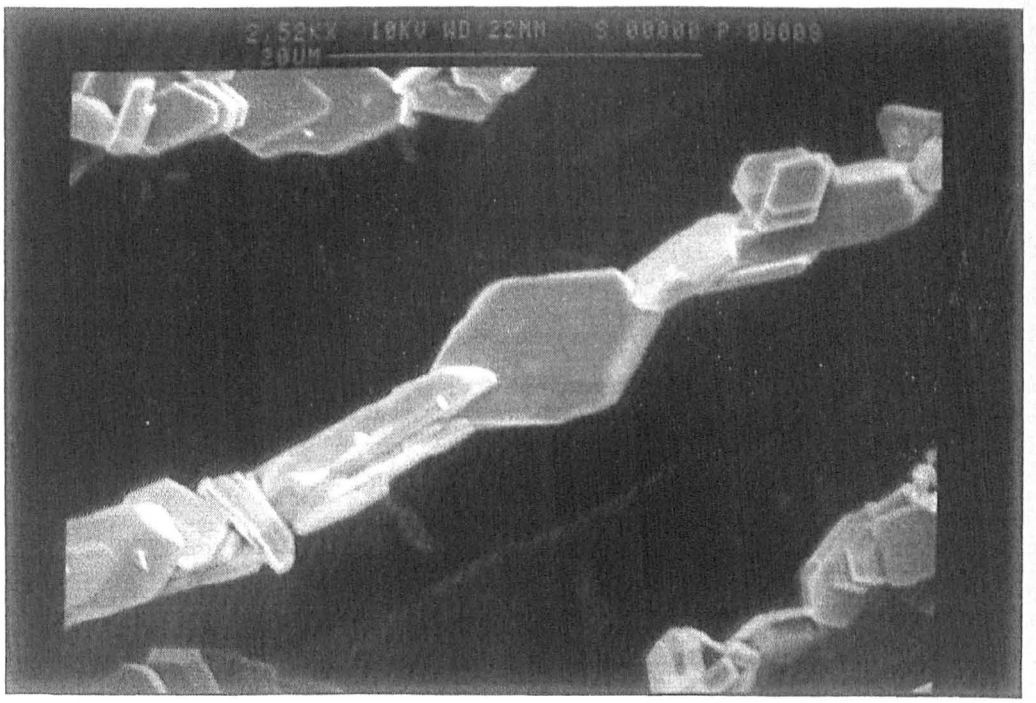

Fig. 146 SEM micrograph of aligned Co_2Z fibres, demonstrating the reason for the weakness inherent in the apparently still fibrous product following DGG.

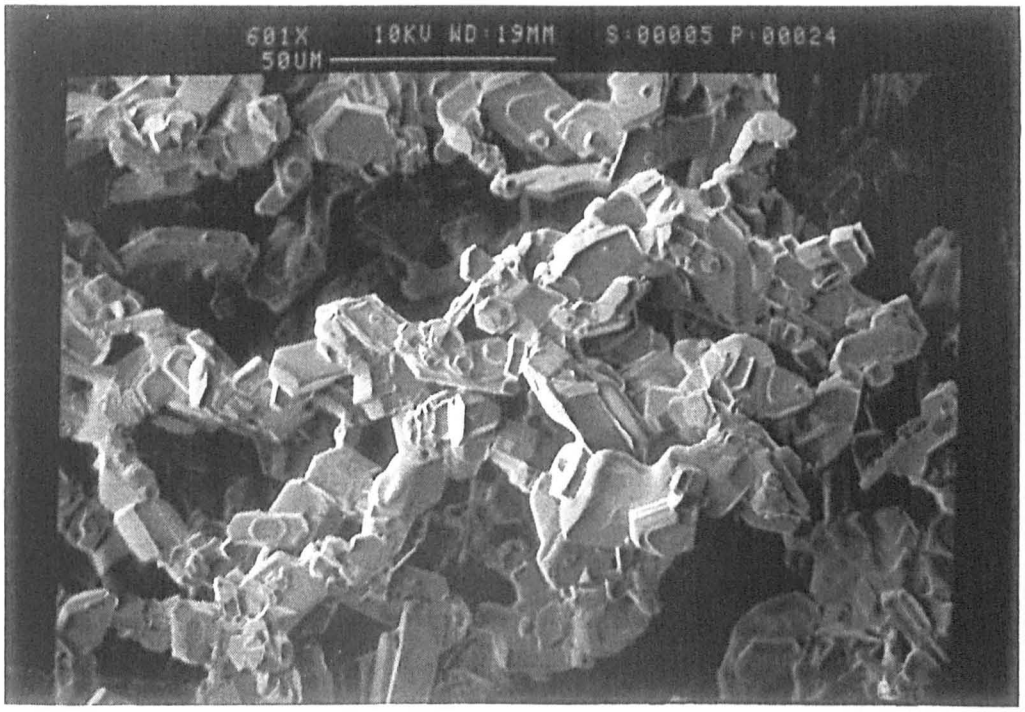

Fig. 147 SEM micrograph of random Co_2Z fibres, demonstrating the loss of fibrous nature following DGG.

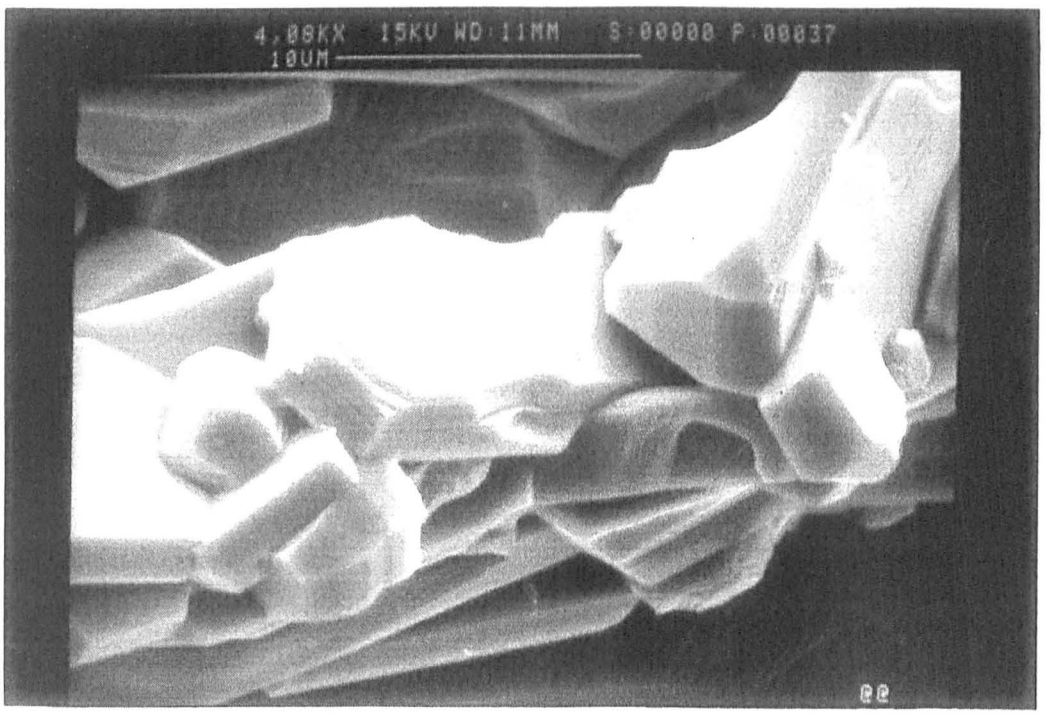

Fig. 148 SEM micrograph of Co_2Z fibres, demonstrating the stacking of hexagonal layers within the grains.

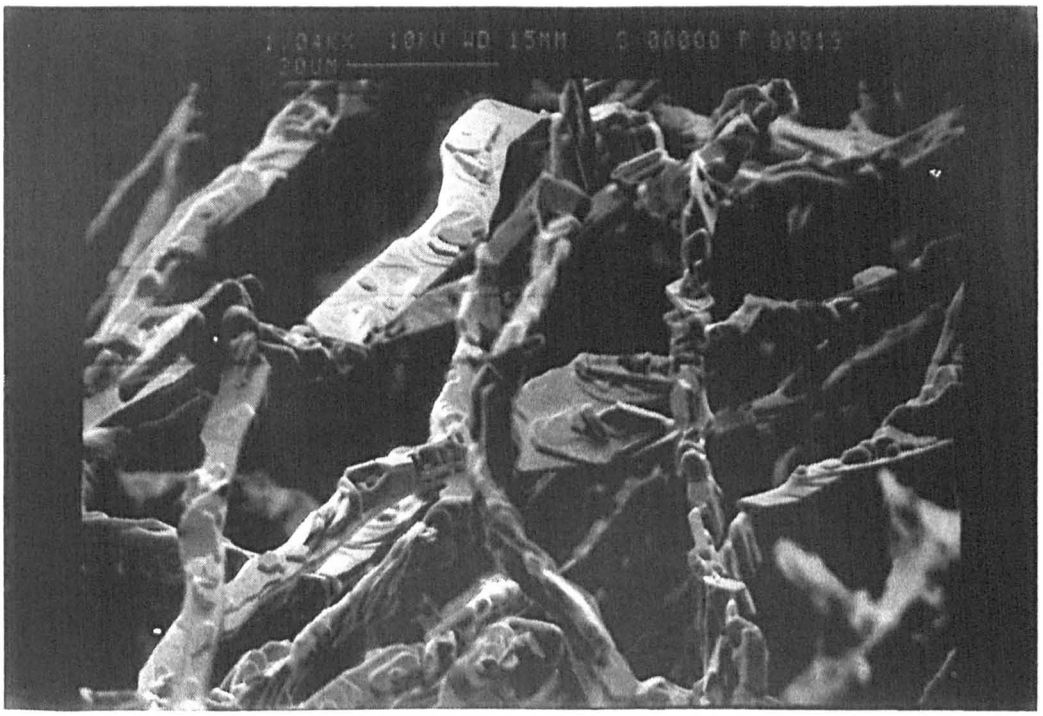

Fig. 149 SEM micrograph of 1 wt% Sr-doped Co_2Z fibres, fired to 1250 °C.

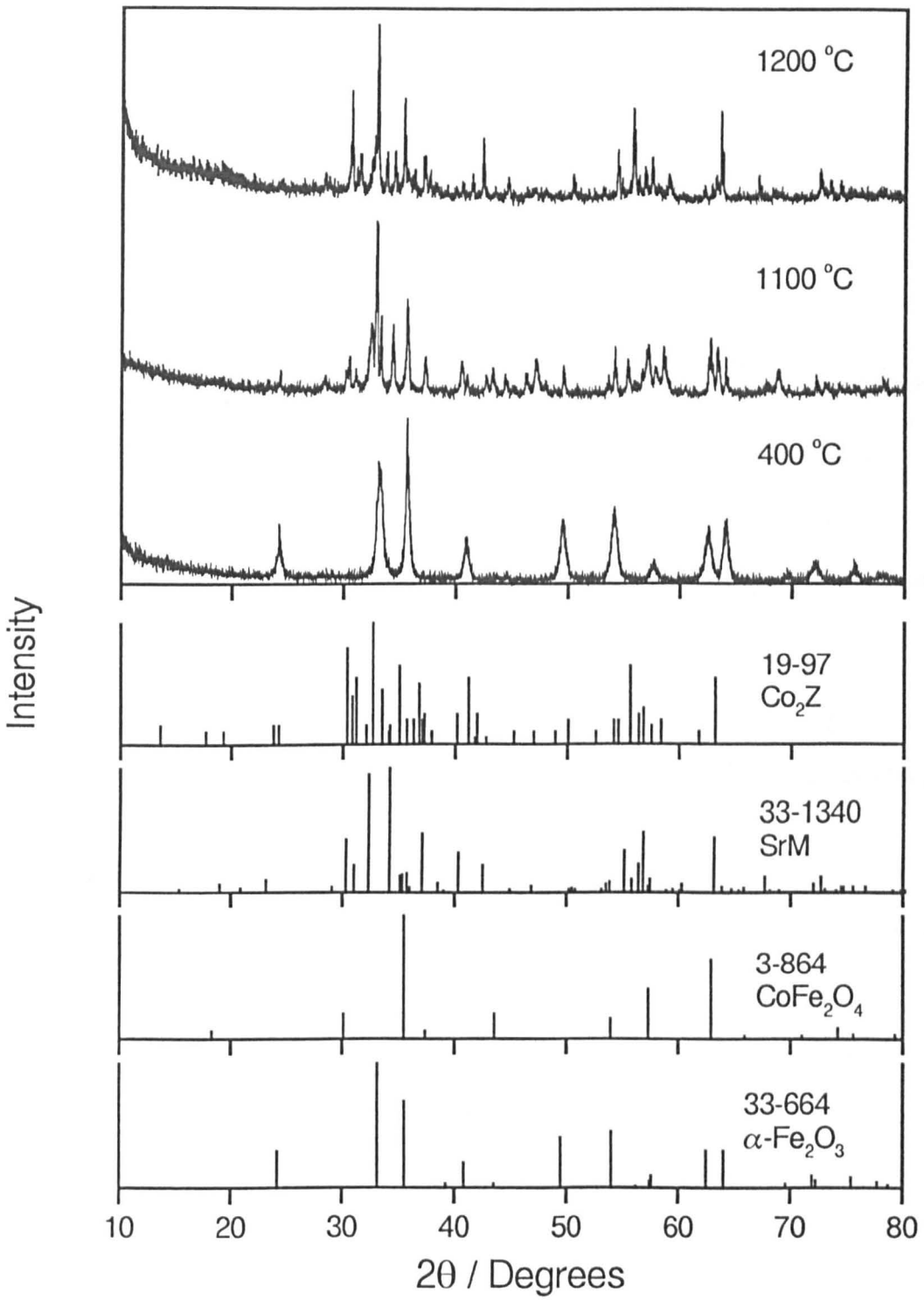

Fig. 150 XRD patterns of Sr_3Co_2Z fibres fired to 400, 1100 and 1200 °C / 3hr.

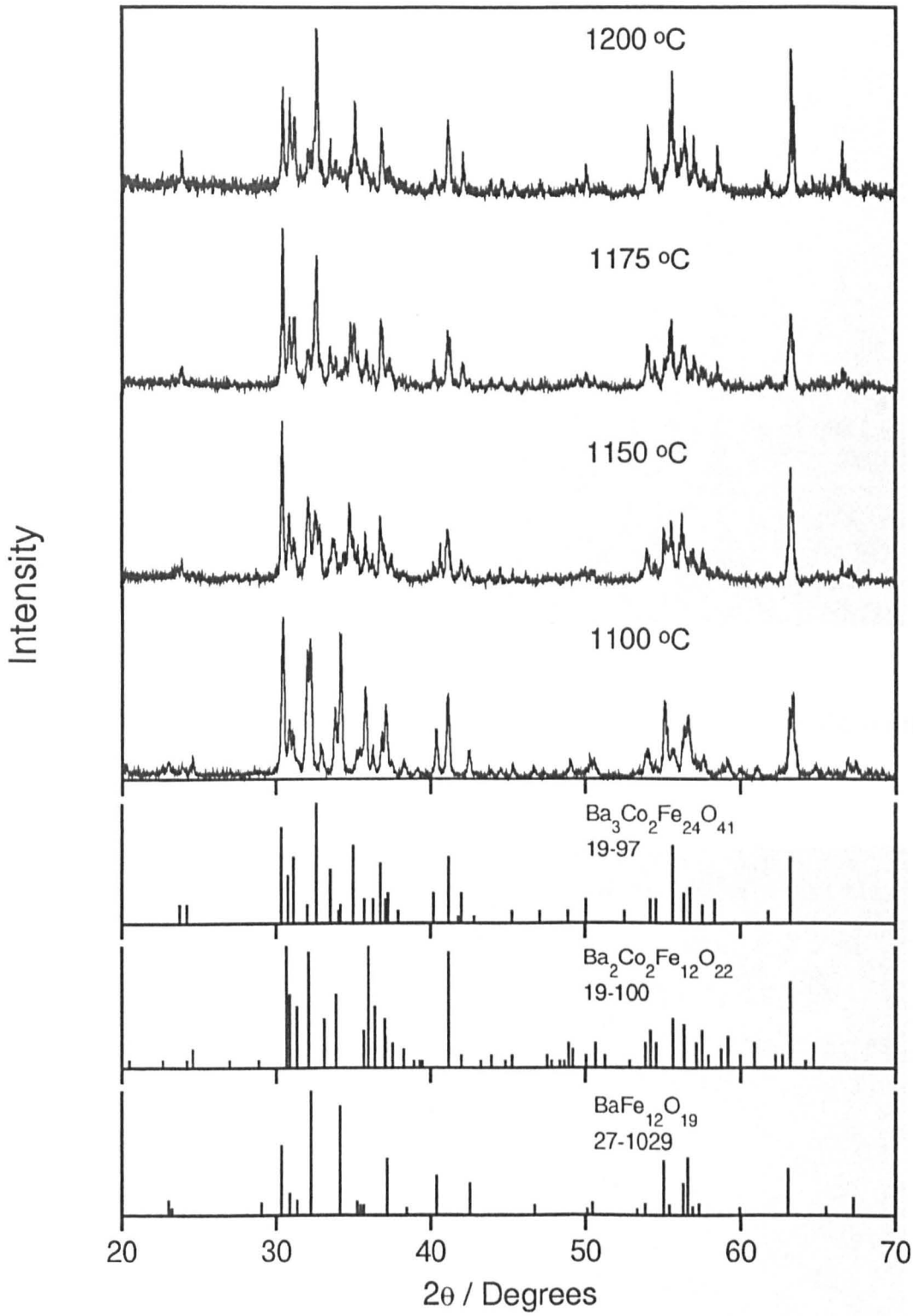

Fig. 151 XRD patterns of 0.67% CaO-doped Co_2Z fibres fired to (a) 1100 °C, (b) 1150 °C, (c) 1175 °C and (d) 1200 °C for 3 hours.

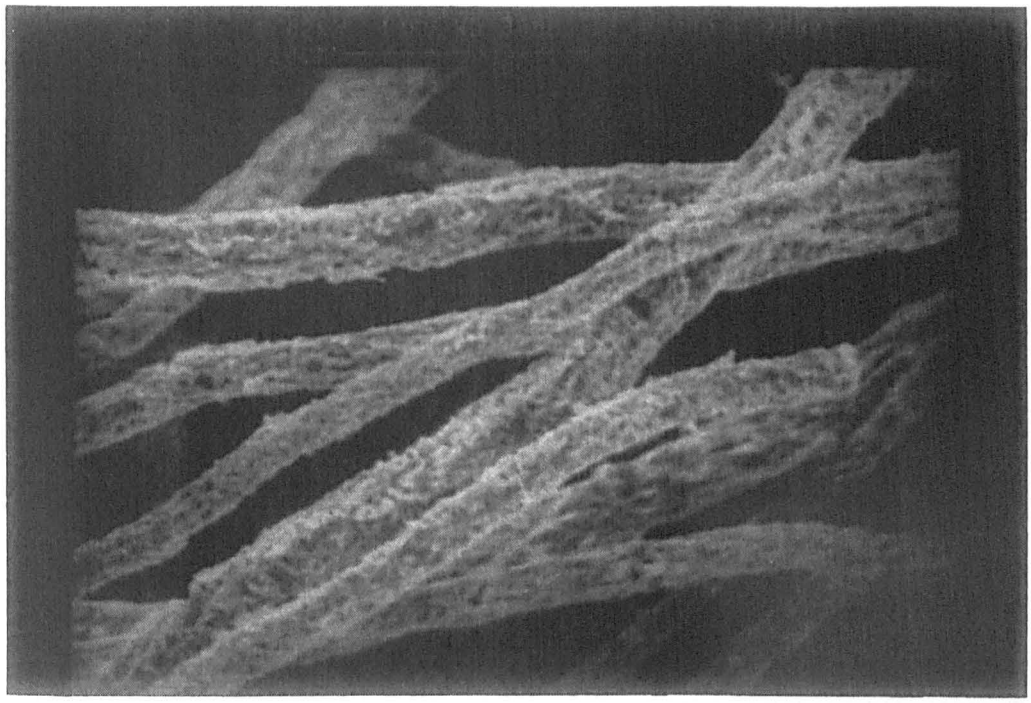

Fig. 152 SEM micrograph of 0.67% CaO-doped Co_2Z fibres fired to 1150 °C for three hours.

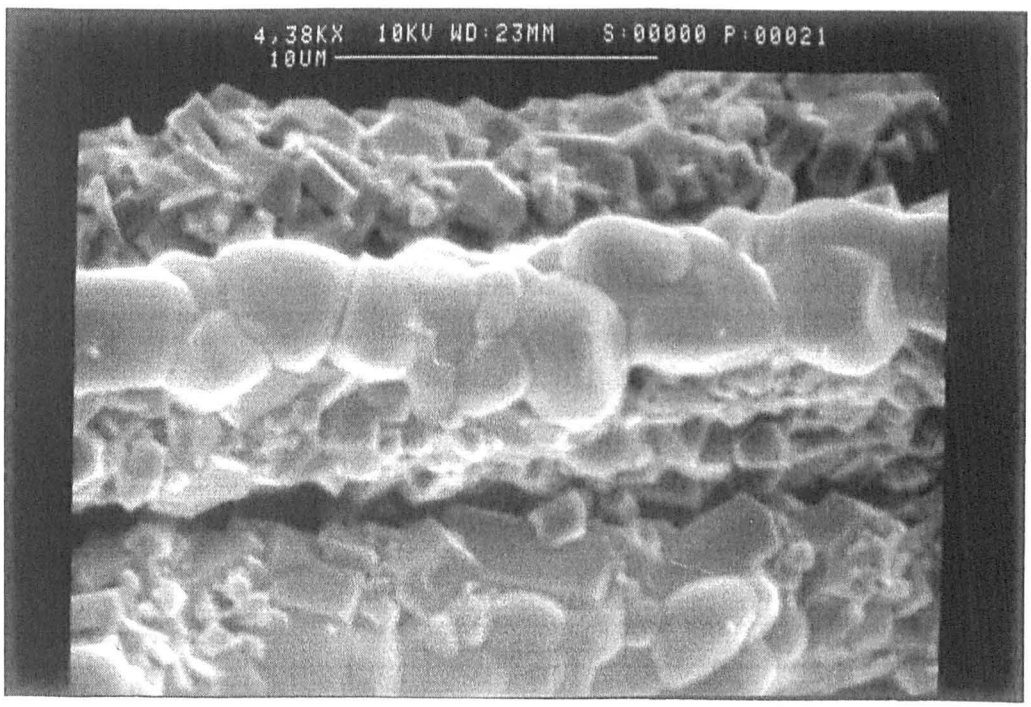

Fig. 153 SEM micrograph of 0.67% CaO-doped Co_2Z fibres fired to 1175 °C for three hours.

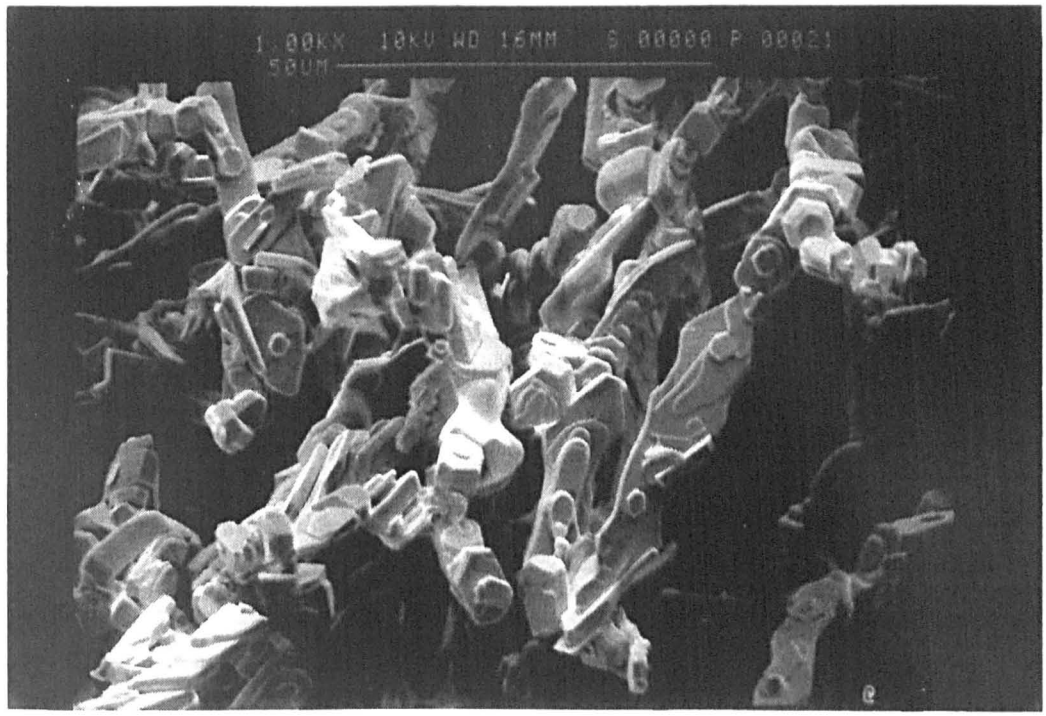

Fig. 154 SEM micrograph of 0.67% CaO-doped Co_2Z fibres fired to 1200 °C for three hours.

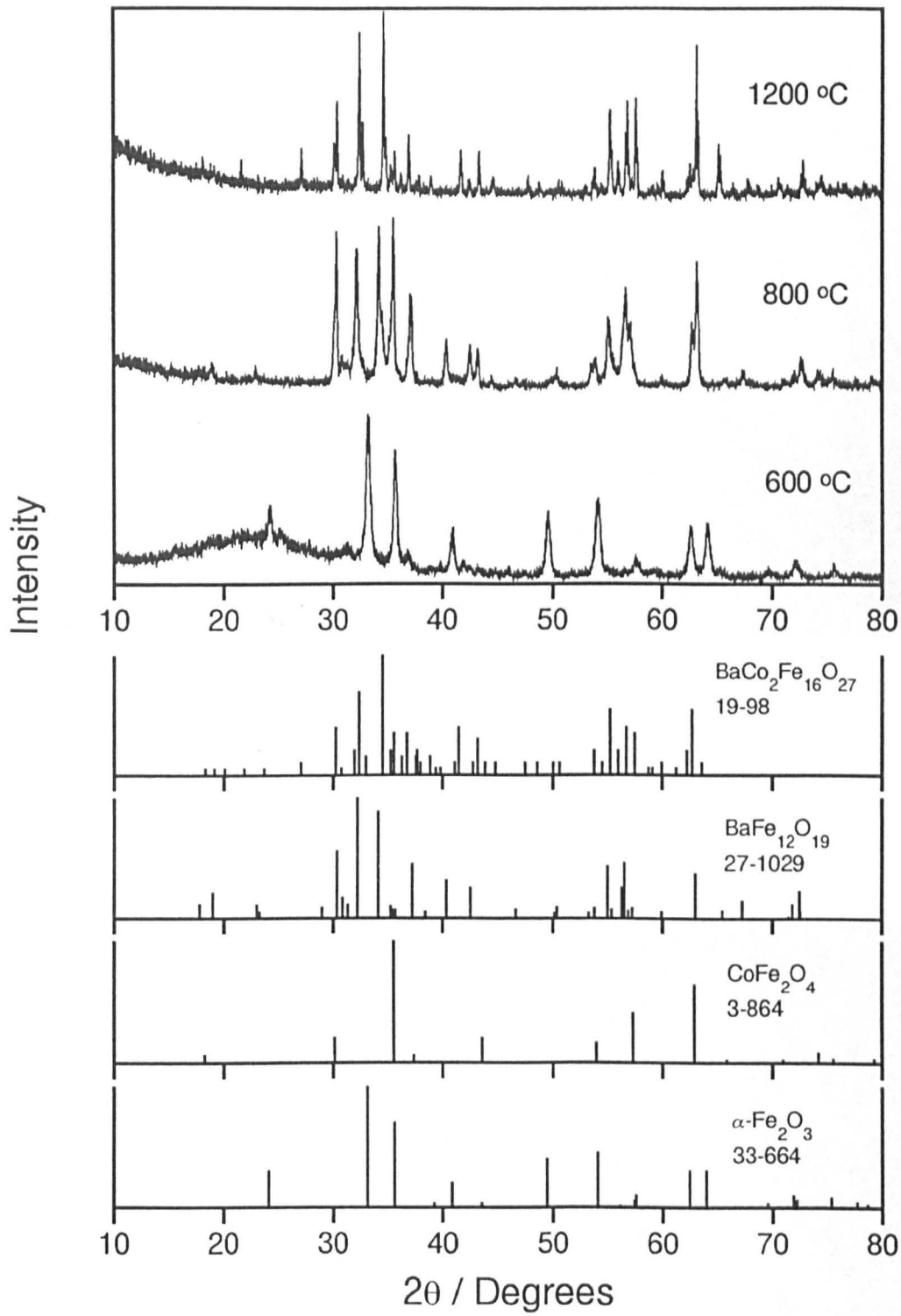

Fig. 155 XRD pattern of the Co_2W fibres fired to 600, 800 and 1200 °C / 3hr.

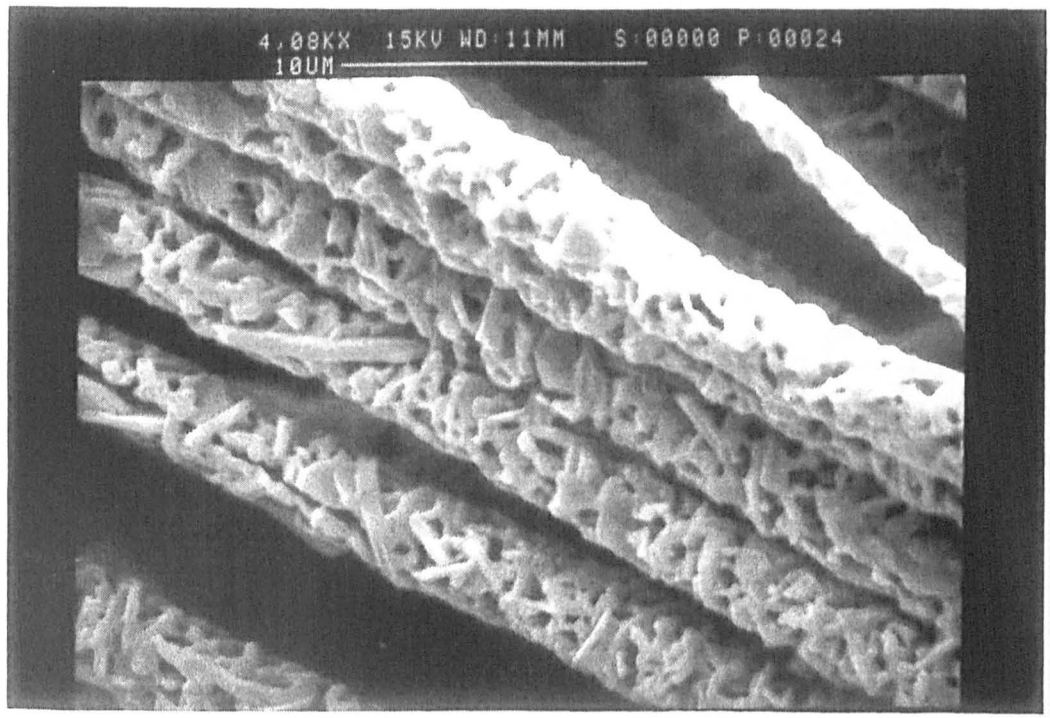

Fig. 156 SEM micrograph of Co_2W fibres fired to 1100 °C / 3hr.

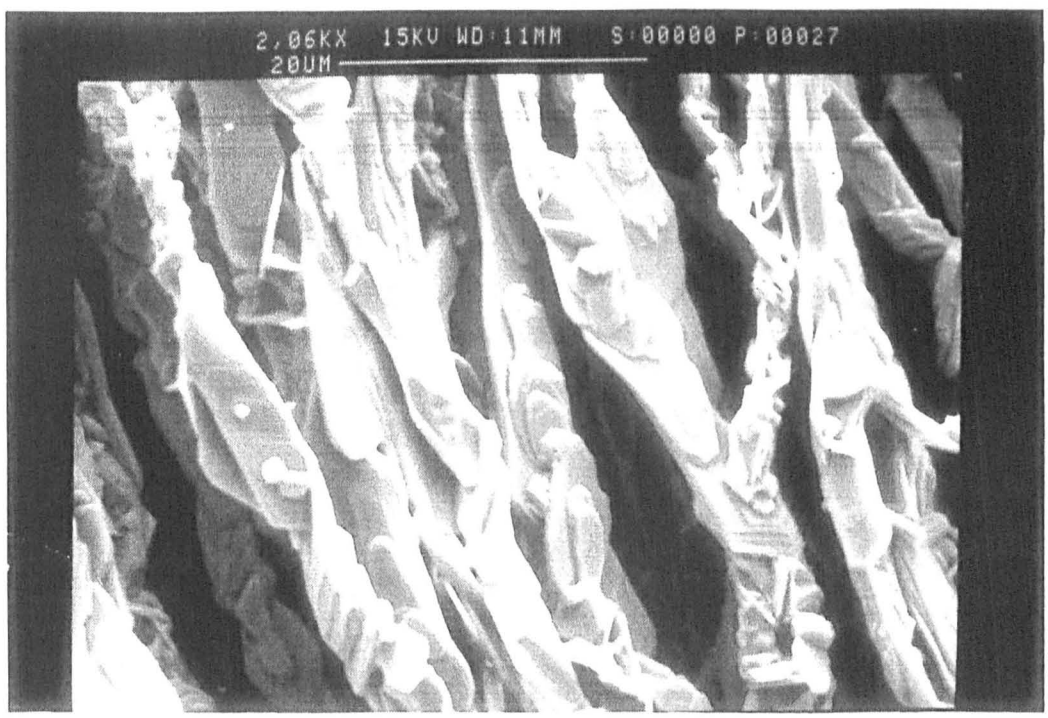

Fig. 157 SEM micrograph of Co_2W fibres fired to 1200 °C / 3hr

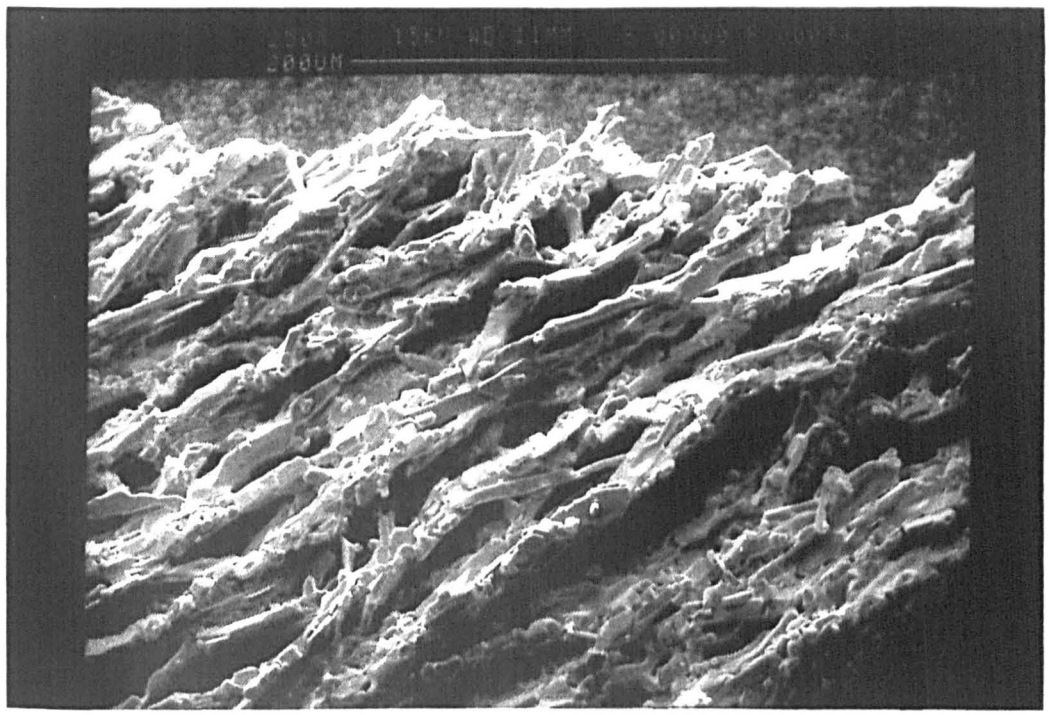

Fig. 158 SEM micrograph of fused Co_2W fibres, fired to 1300 °C / 3hr.

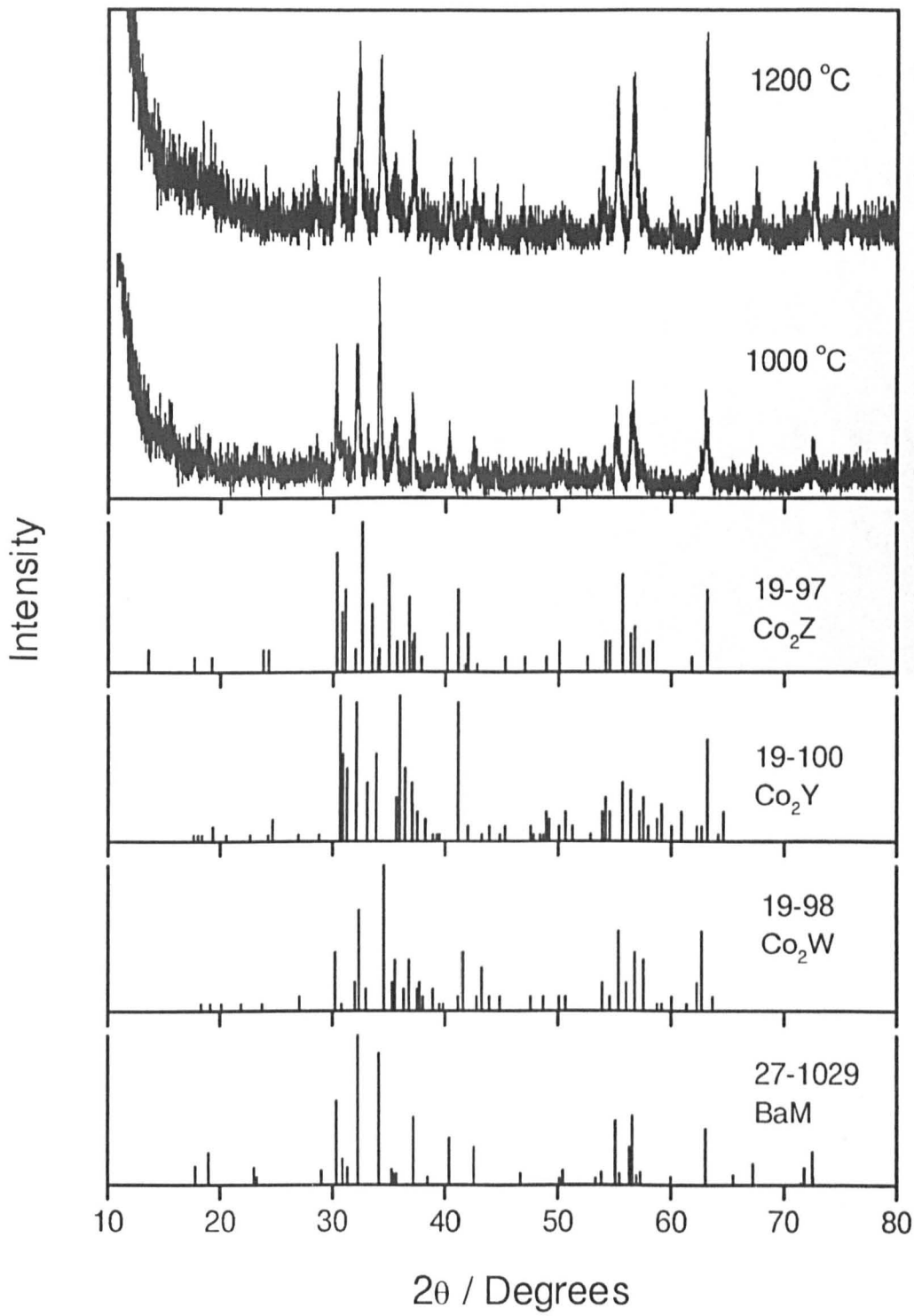

Fig. 159 XRD pattern of the Co_2X fibres fired to 1000 and 1200 °C / 3hr.

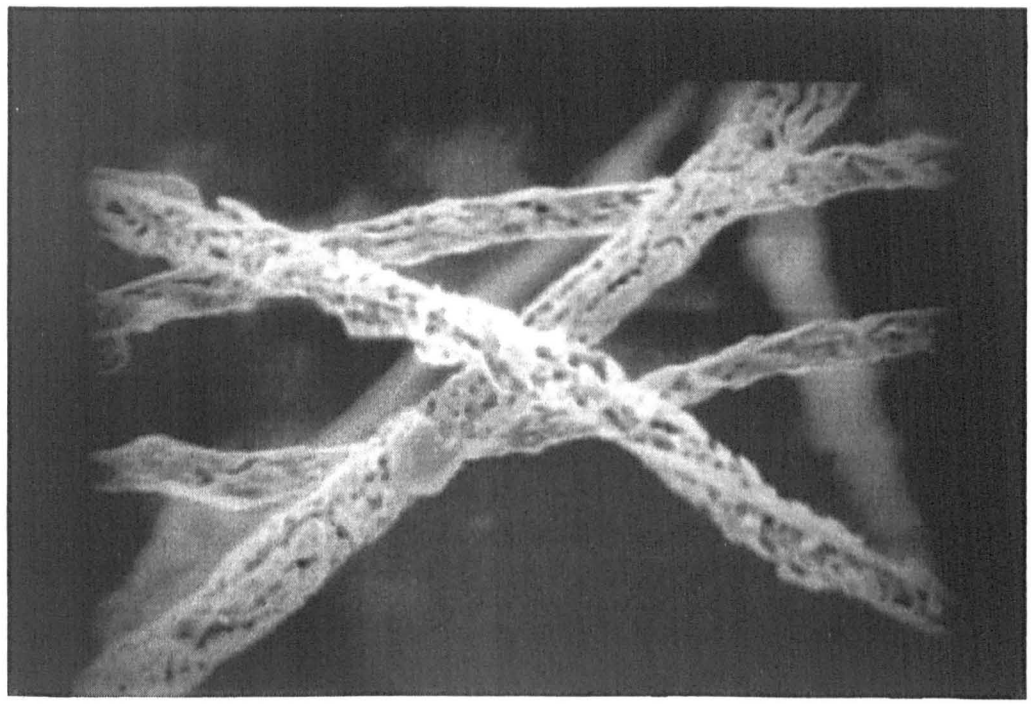

Fig. 160 SEM micrograph of Co_2X fibres, fired to 1200 °C / 3hr.

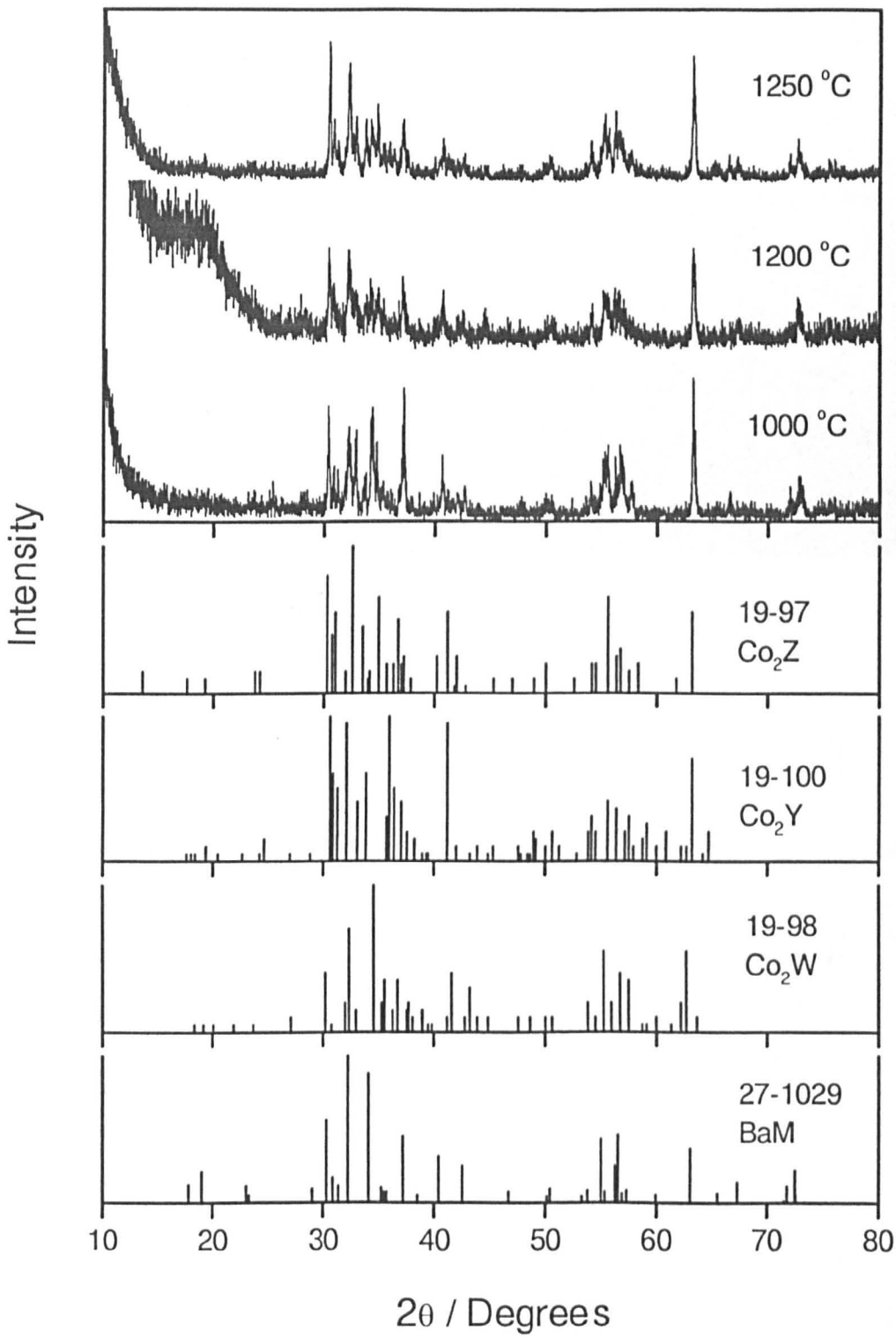

Fig. 161 XRD pattern of the Co_2U fibres fired to 1200 and 1250 °C / 3hr.

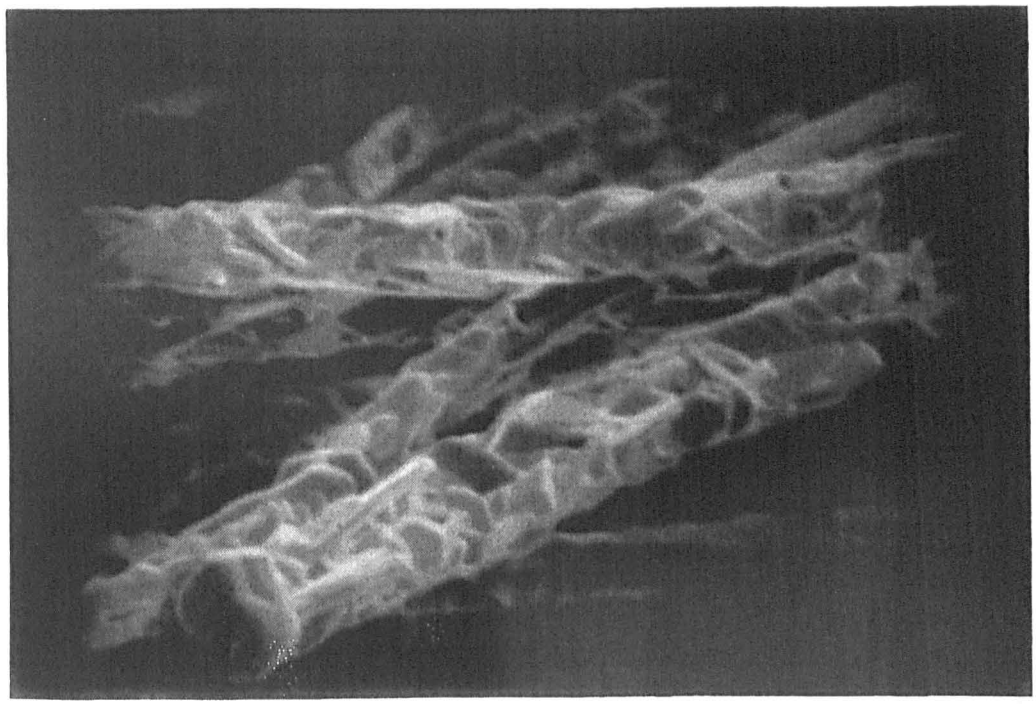

Fig. 162 SEM micrograph of Co_2U fibres, fired to 1200 °C / 3hr.

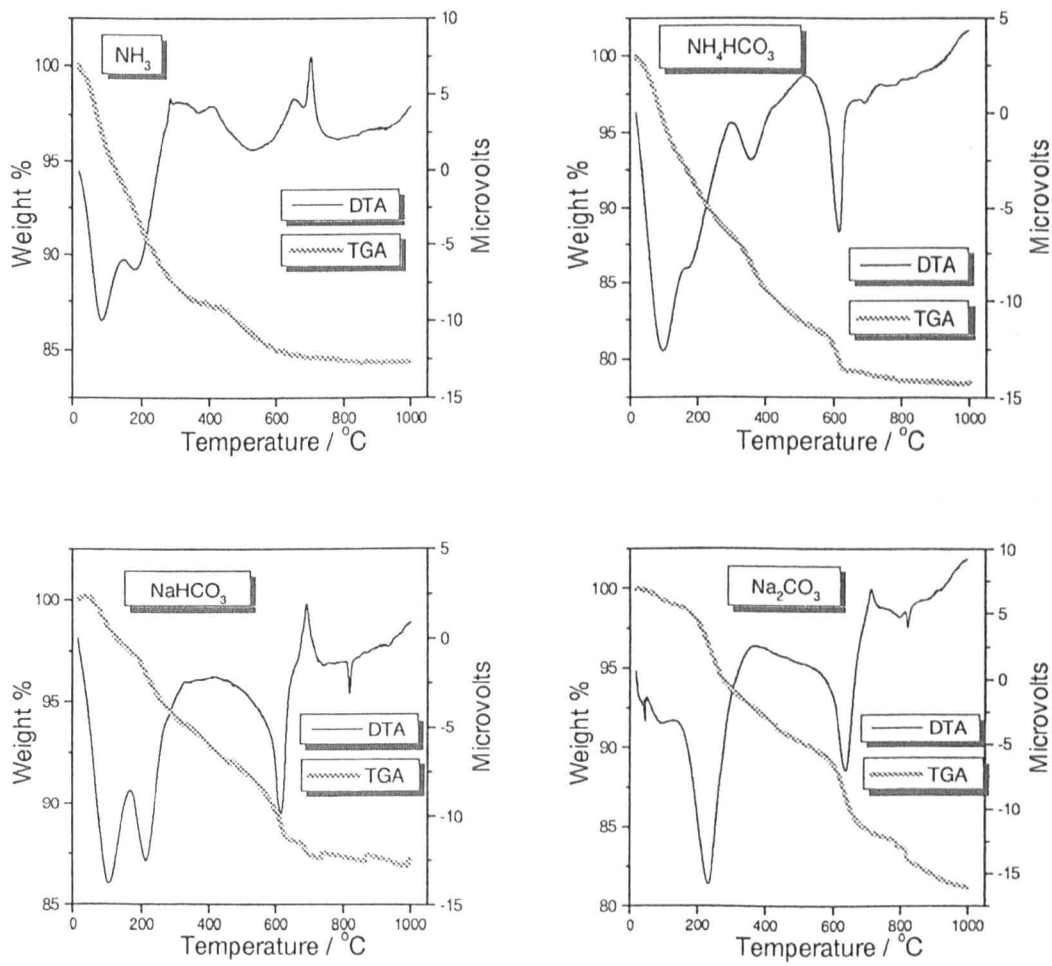

Fig. 163 DTA / TGA plots of iron, cobalt and barium nitrates coprecipitated at pH 7 by NH_3, NH_4HCO_3, $NaHCO_3$ and Na_2CO_3 from 25 - 1000 °C.

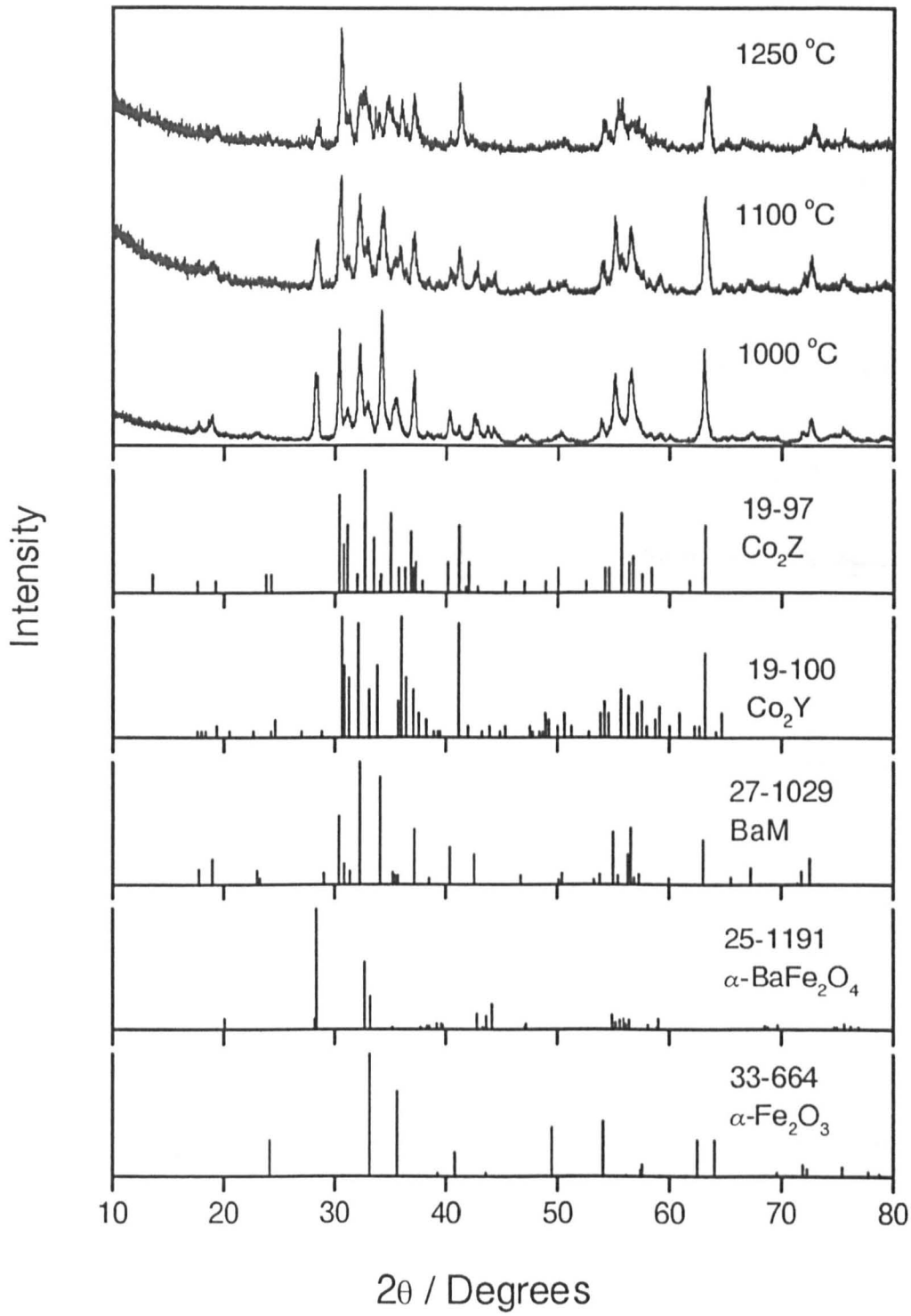

Fig. 164 XRD pattern of iron, cobalt and barium nitrates coprecipitated with NH_4HCO_3 at pH 7, fired to a) 1000, b) 1100 and c) 1250 °C.

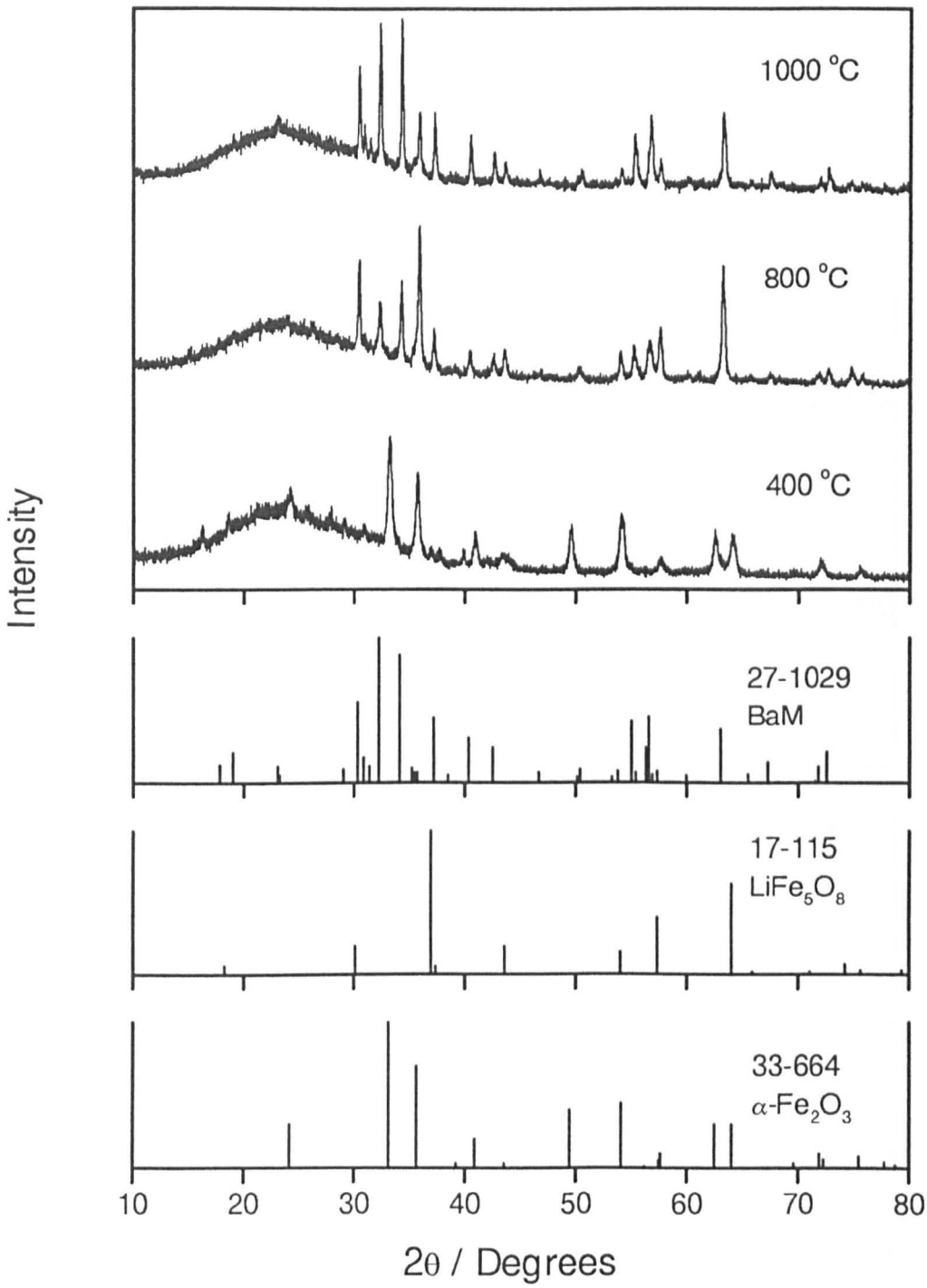

Fig. 165 XRD patterns of BaM fibres produced from an alkoxide precursor, fired to 400, 800 and 1000 °C / 3hr.

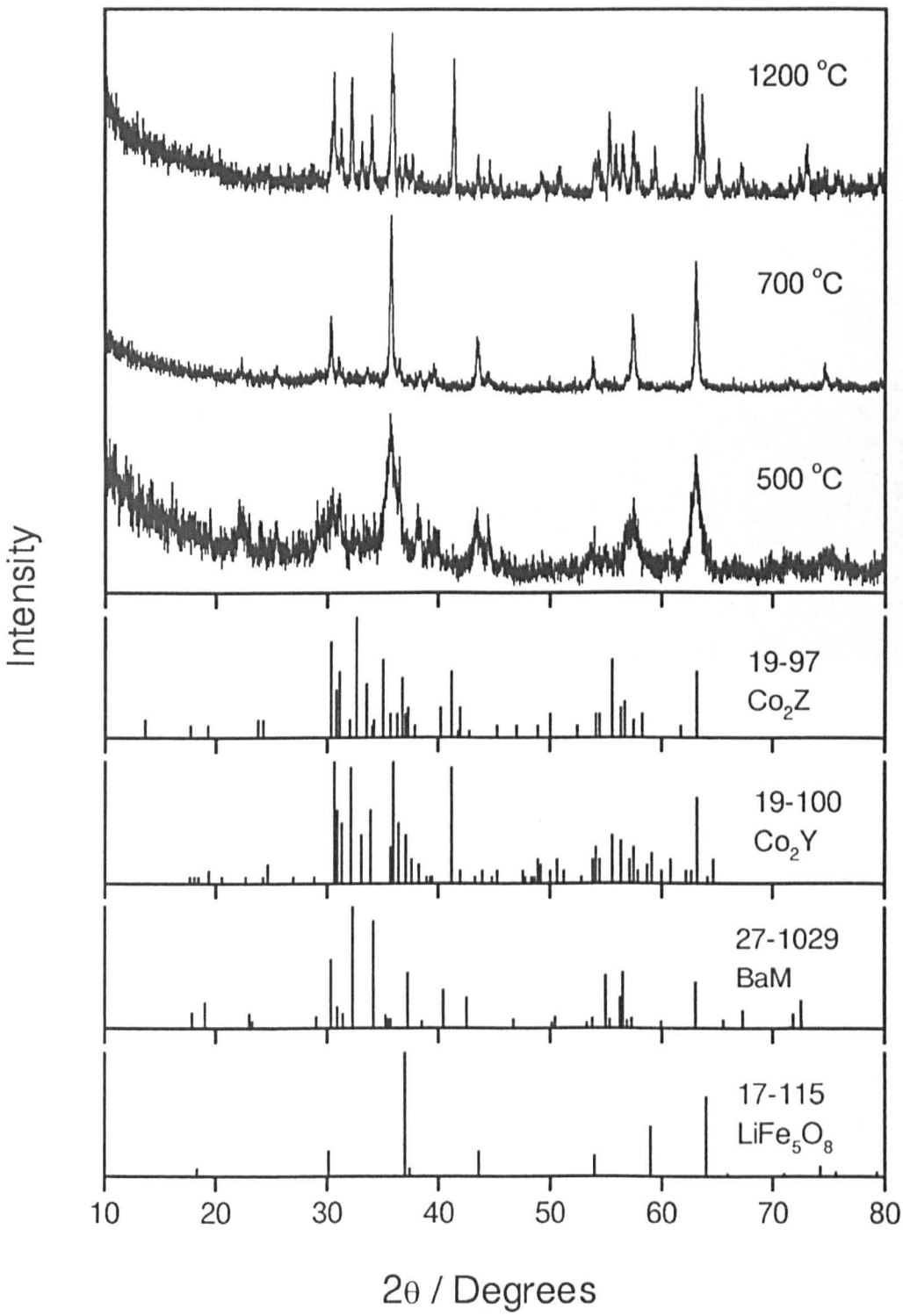

Fig. 166 XRD patterns of stoichiometric Co_2Z fibres produced from an alkoxide precursor, fired to 500, 700 and 1000 °C / 3hr.

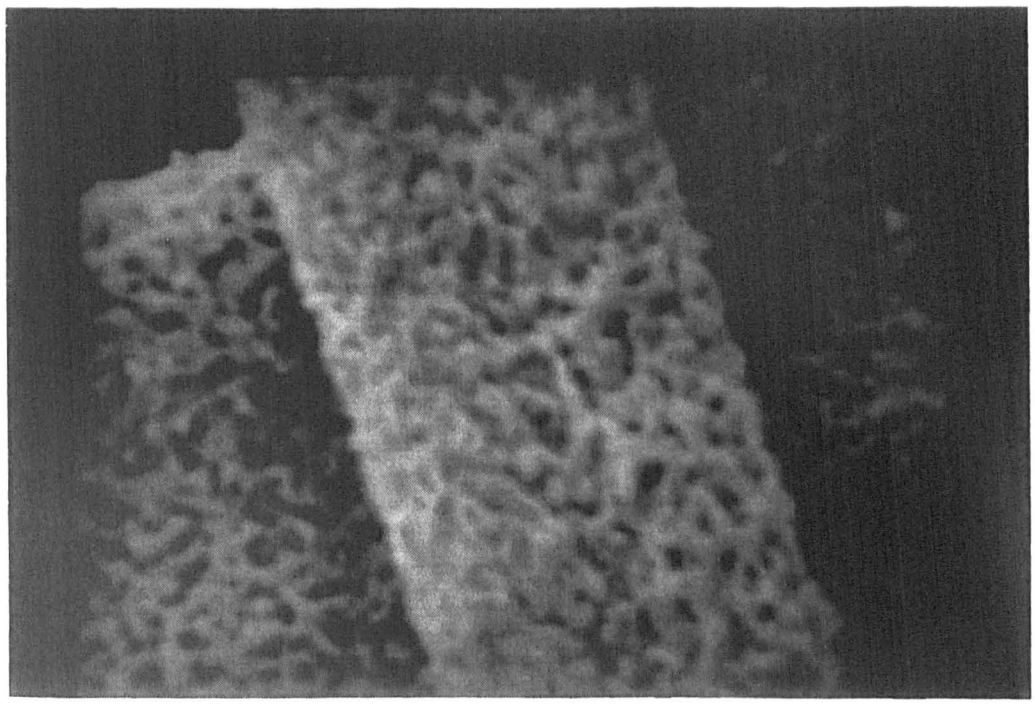

Fig. 167 SEM micrograph of BaM fibres made from an ultrasonically peptised sol, fired to 1000 °C / 3hr.

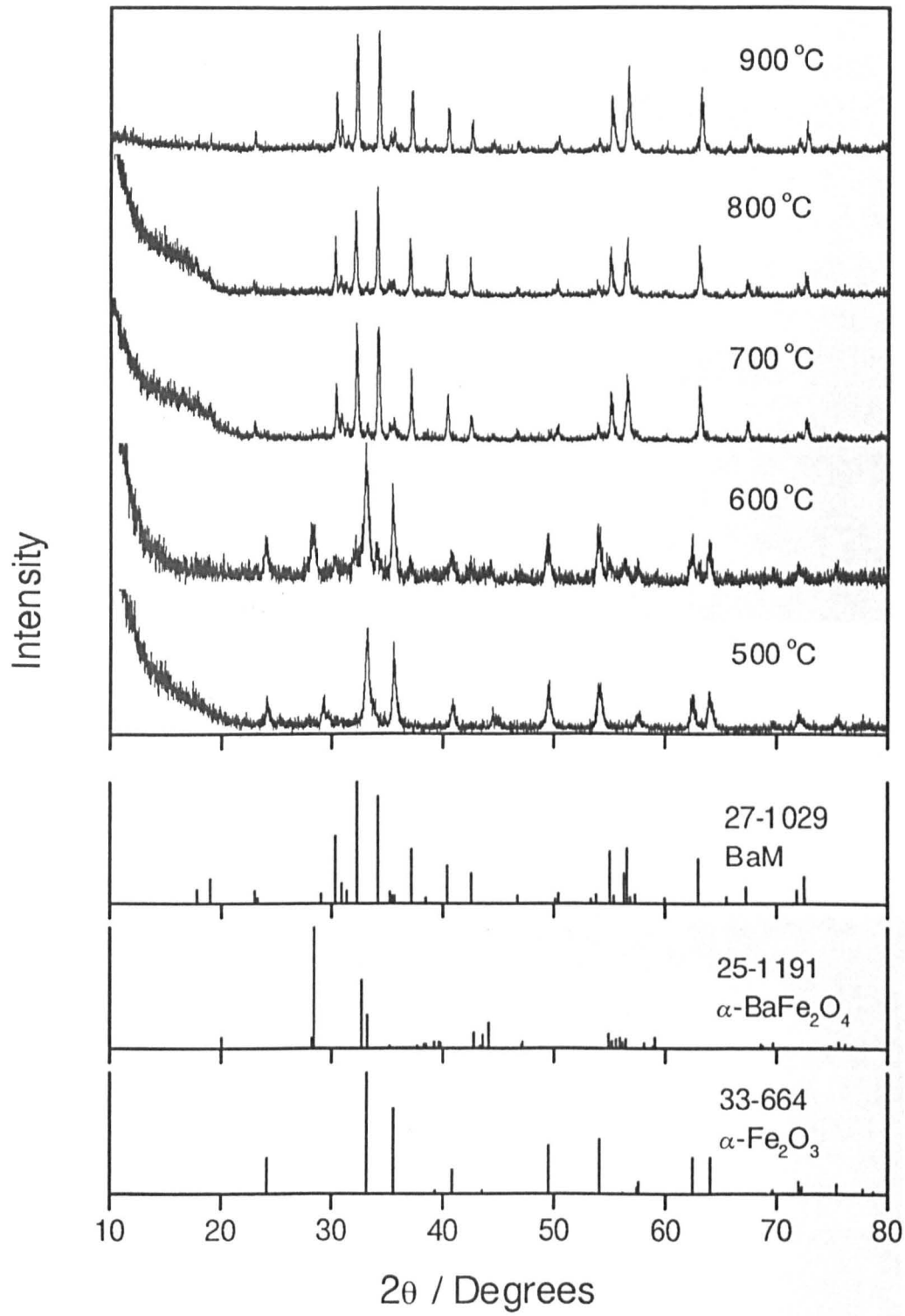

Fig. 168 XRD patterns of BaM fibres steamed at 500, 600, 700, 800 and 900 °C / 3hr.

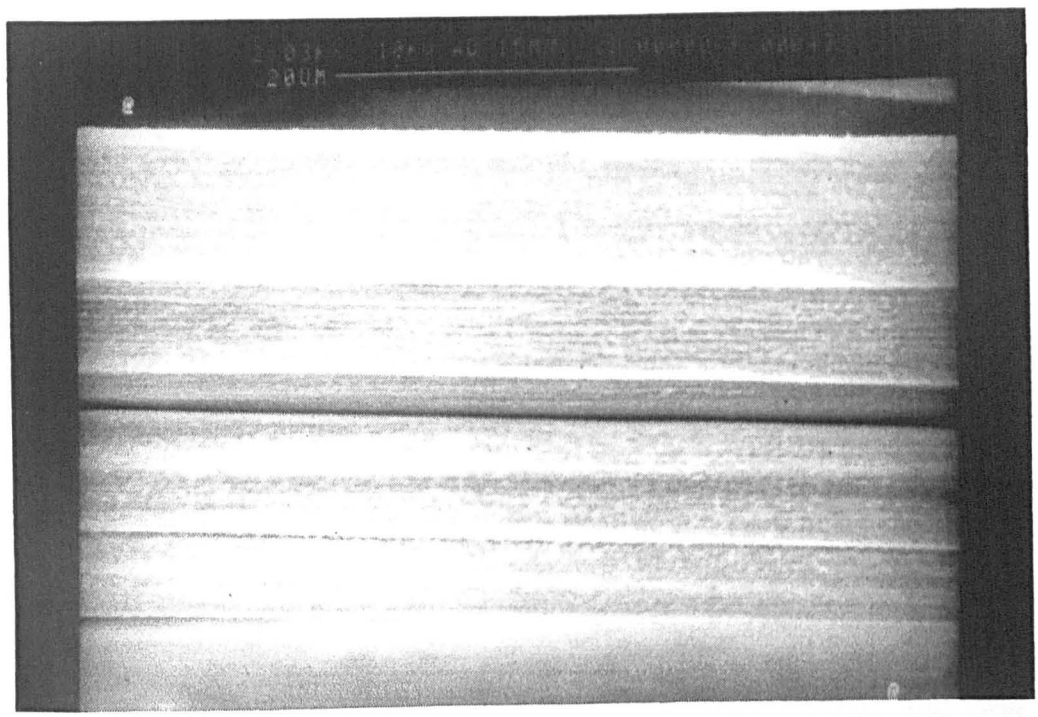

Fig. 169 SEM micrograph of BaM fibres steamed at 600 °C.

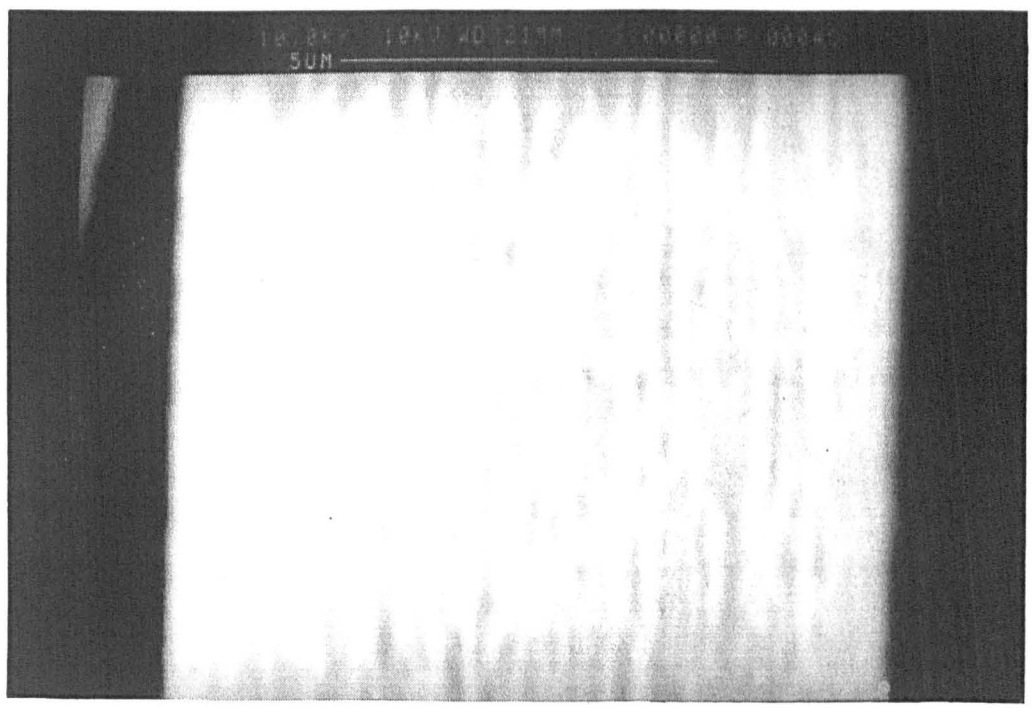

Fig. 170 SEM micrograph of BaM fibres steamed at 800 °C.

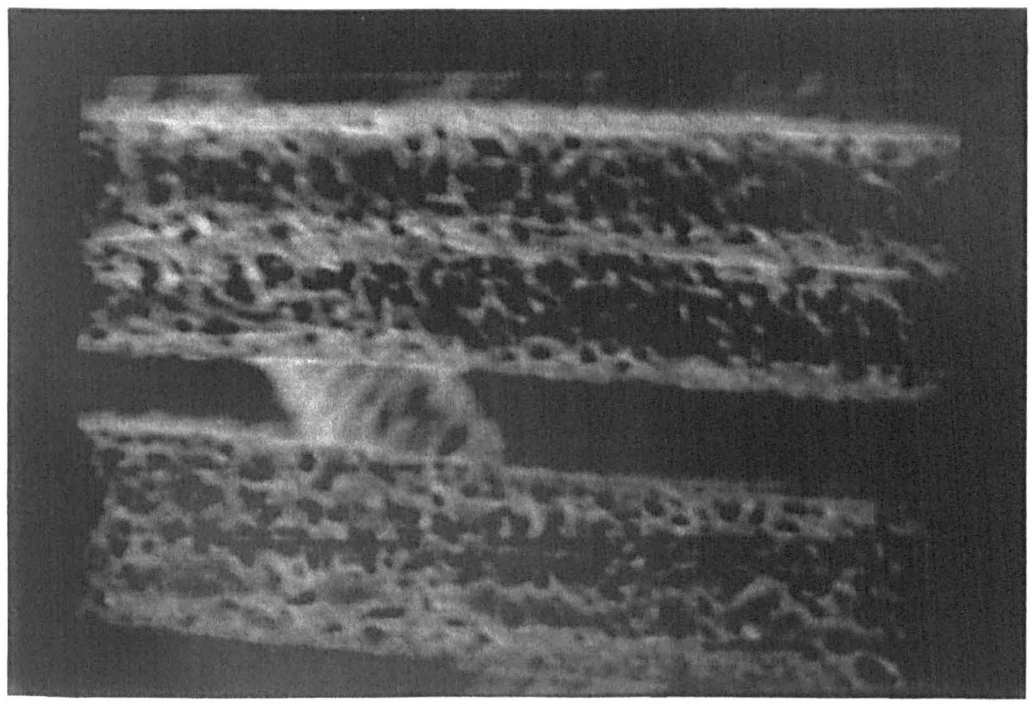

Fig. 171 SEM micrograph of BaM fibres steamed at 900 °C.

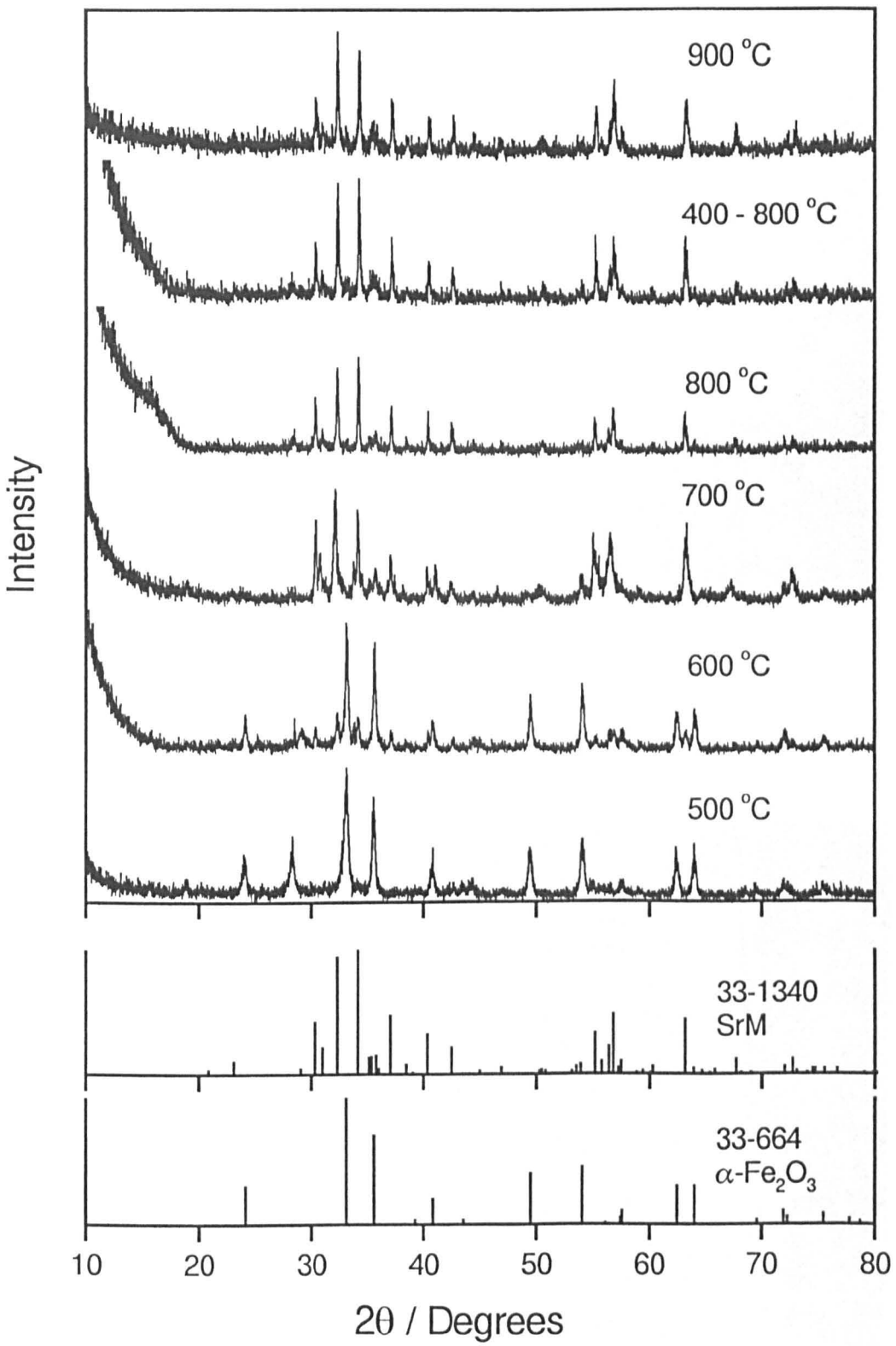

Fig. 172 XRD patterns of SrM fibres steamed at 500, 600, 700, 800, 400 - 800 and 900 °C / 3hr.

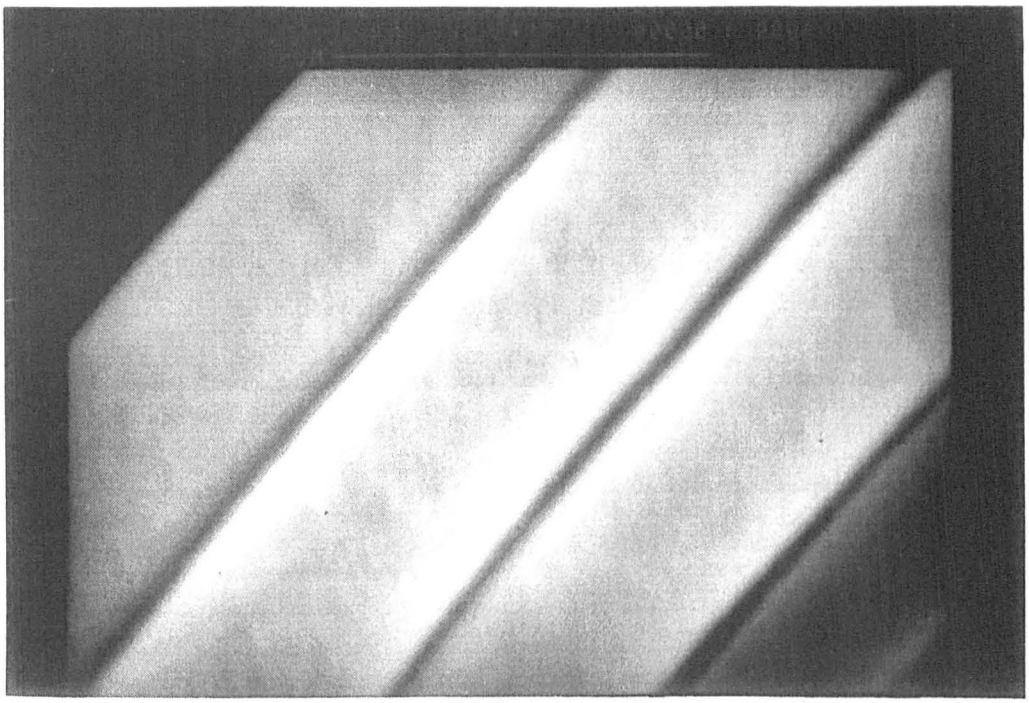

Fig. 173 SEM micrograph of SrM fibres steamed at 700 °C.

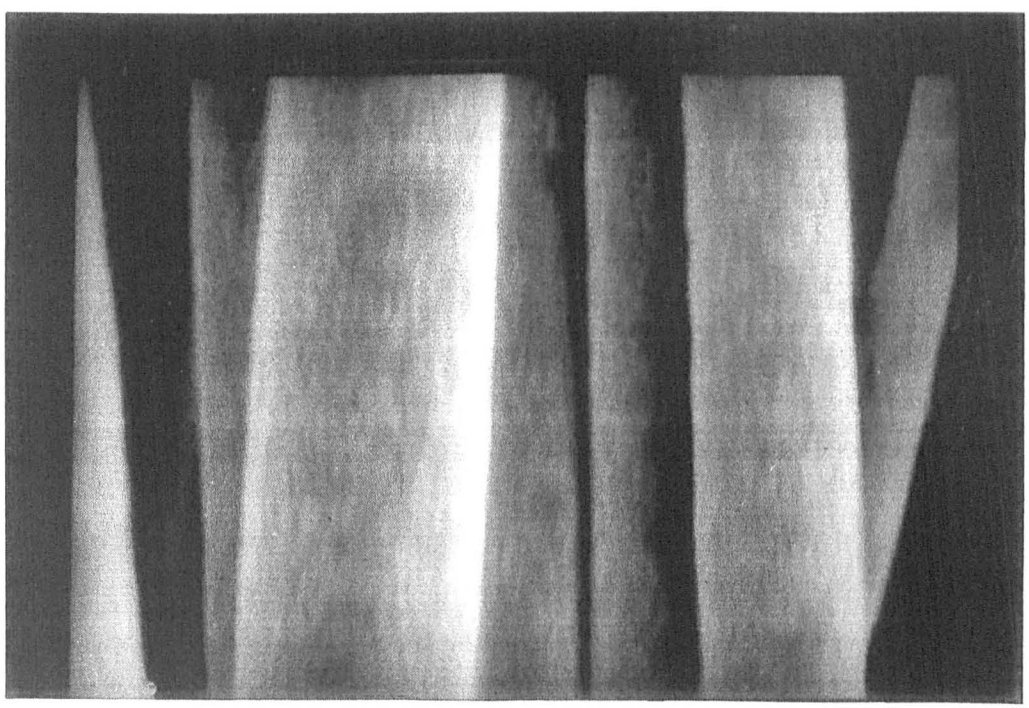

Fig. 174 SEM micrograph of SrM fibres steamed at 800 °C.

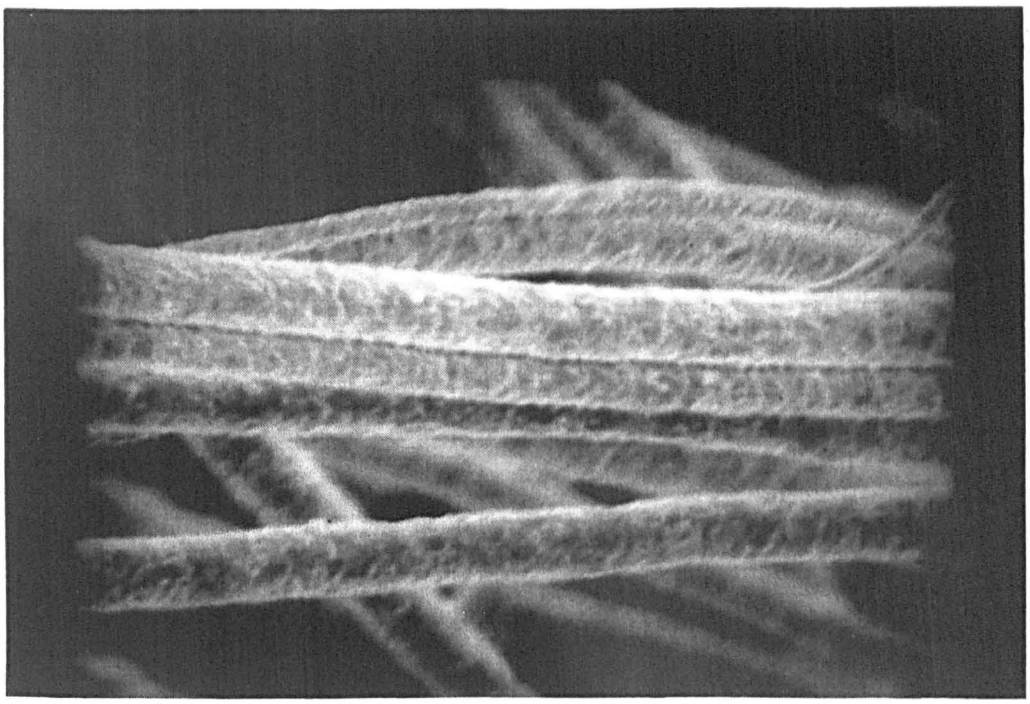

Fig. 175 SEM micrograph of SrM fibres steamed at 900 °C.

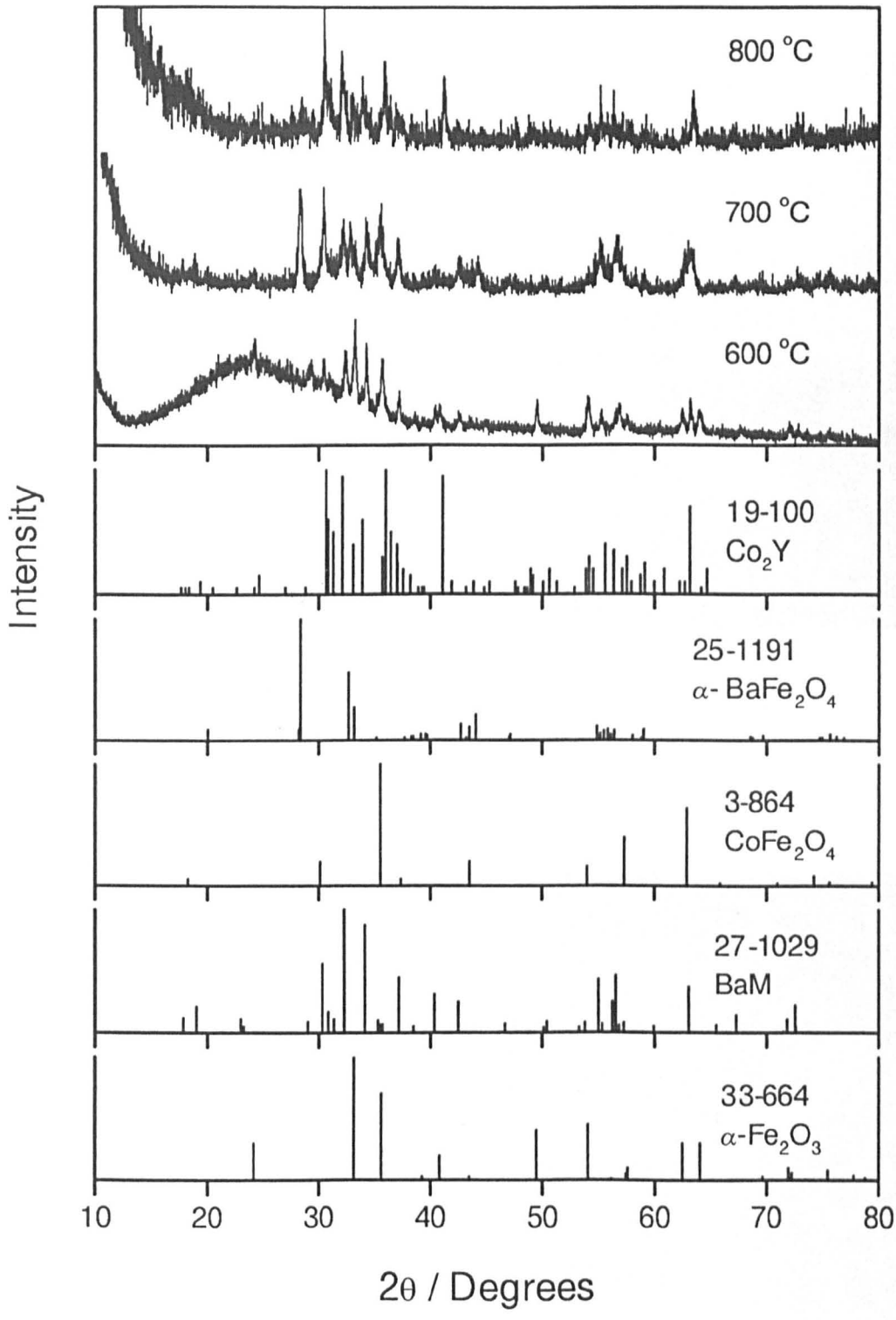

Fig. 176 XRD patterns of Co_2Y fibres steamed at 600, 700 and 800 °C / 3hr.

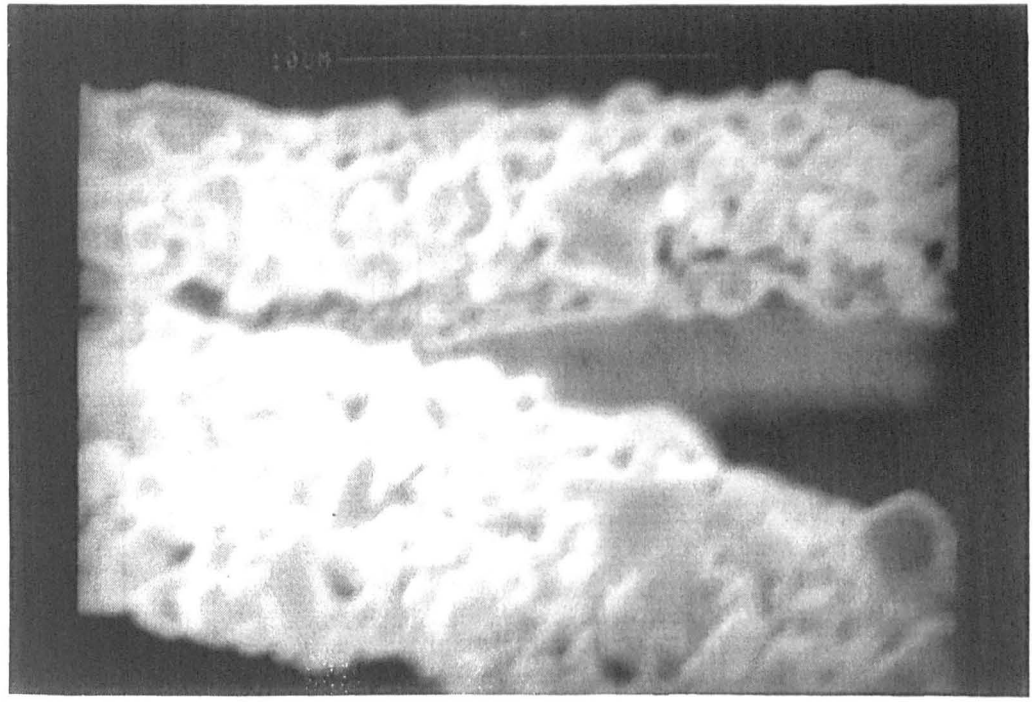

Fig. 177 SEM micrograph of Co_2Y fibres steamed at 900 °C.

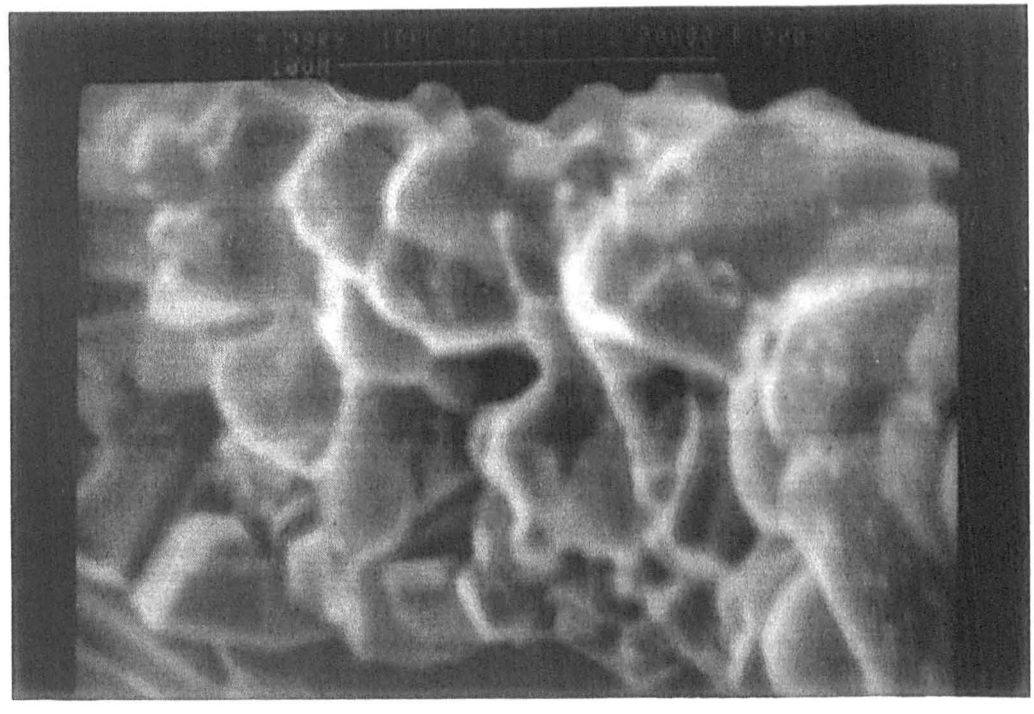

Fig. 178 SEM micrograph of Co_2Z fibres steamed at 900 °C / 3hr.

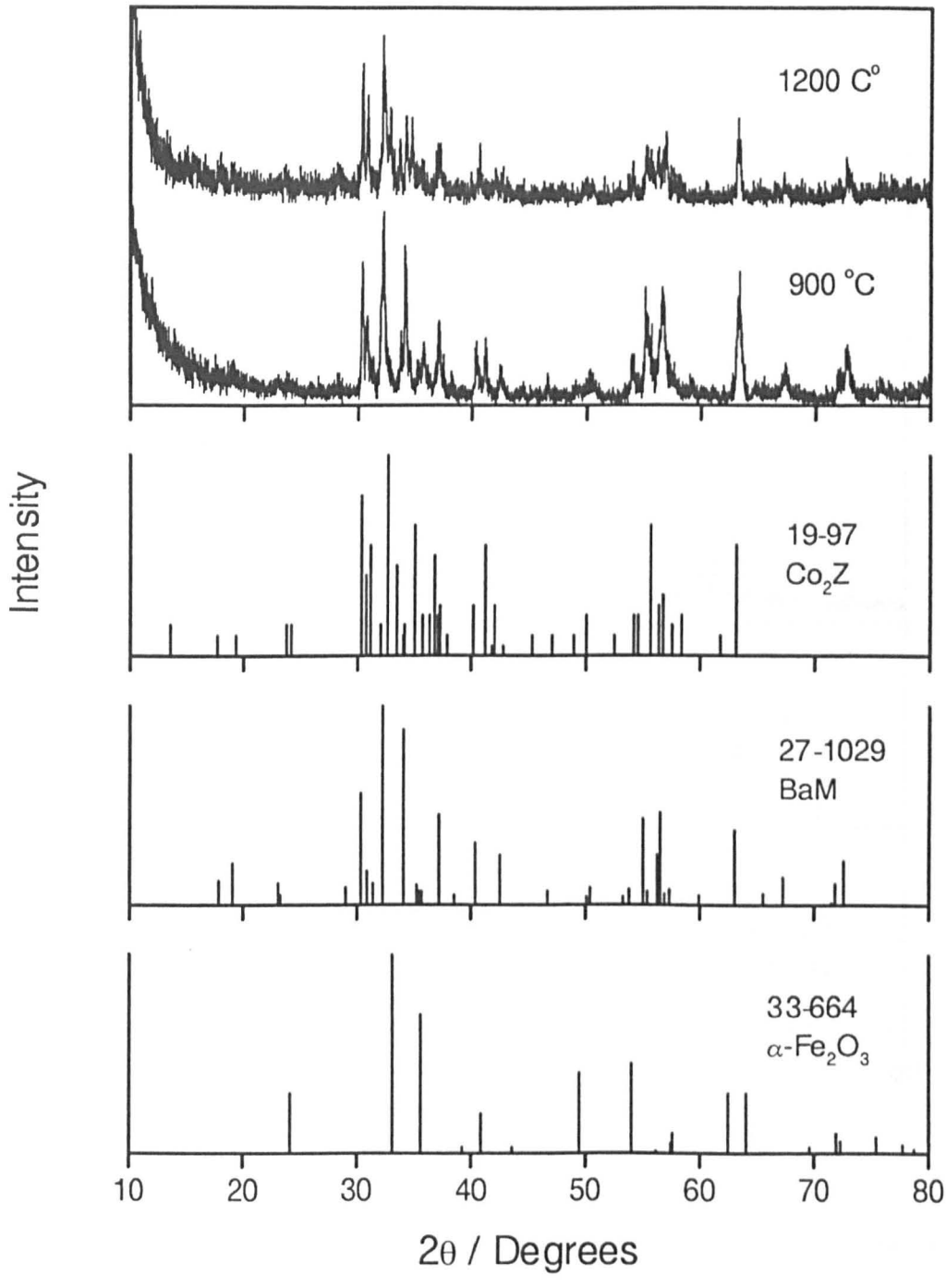

Fig. 179 XRD patterns of Co_2Z fibres steamed at 900 °C / 3hr and then fired to 1250 °C / 3hr.

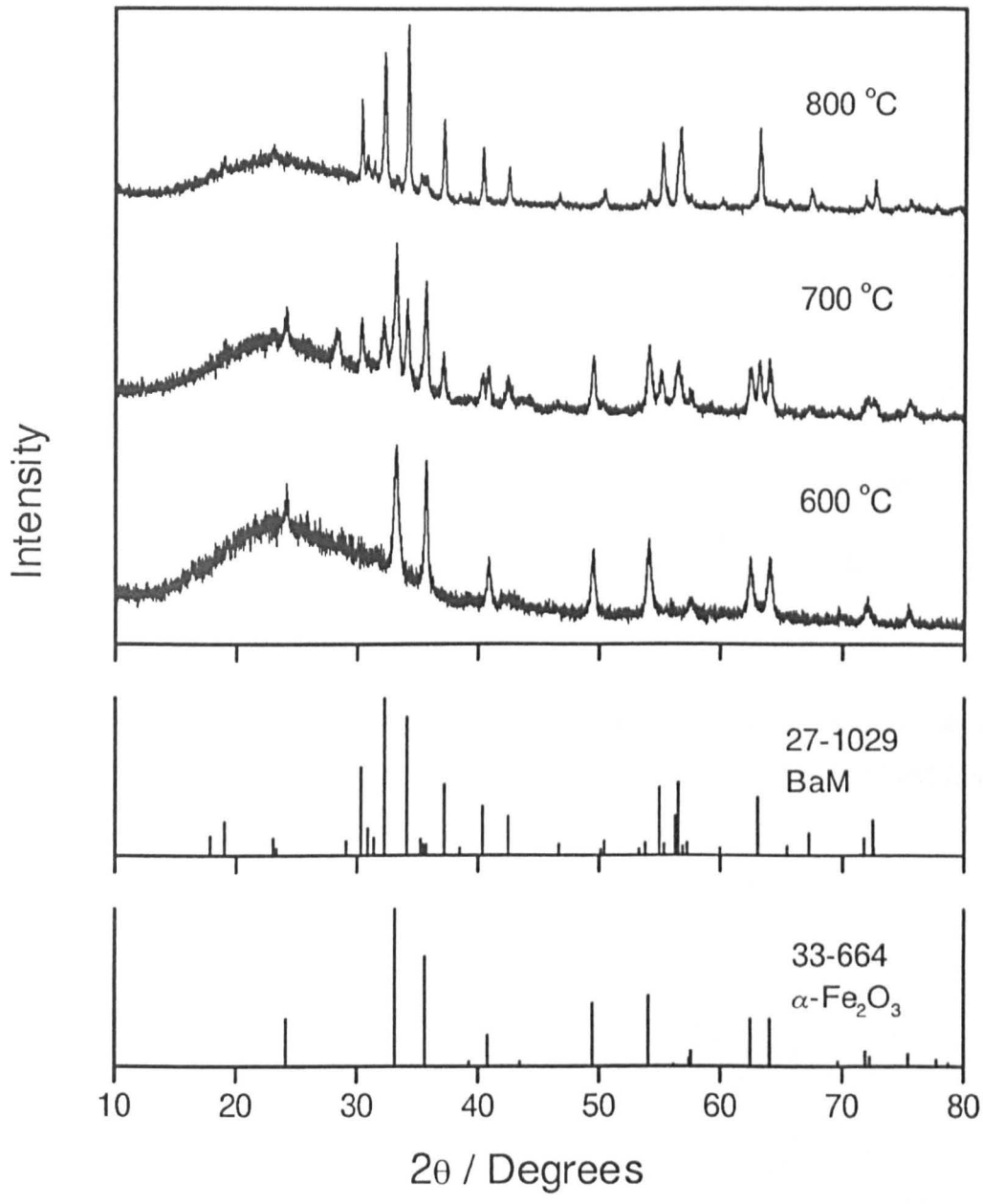

Fig. 180 XRD patterns of BaM fibres fired under a vacuum at 600, 700 and 800 °C / 3hr.

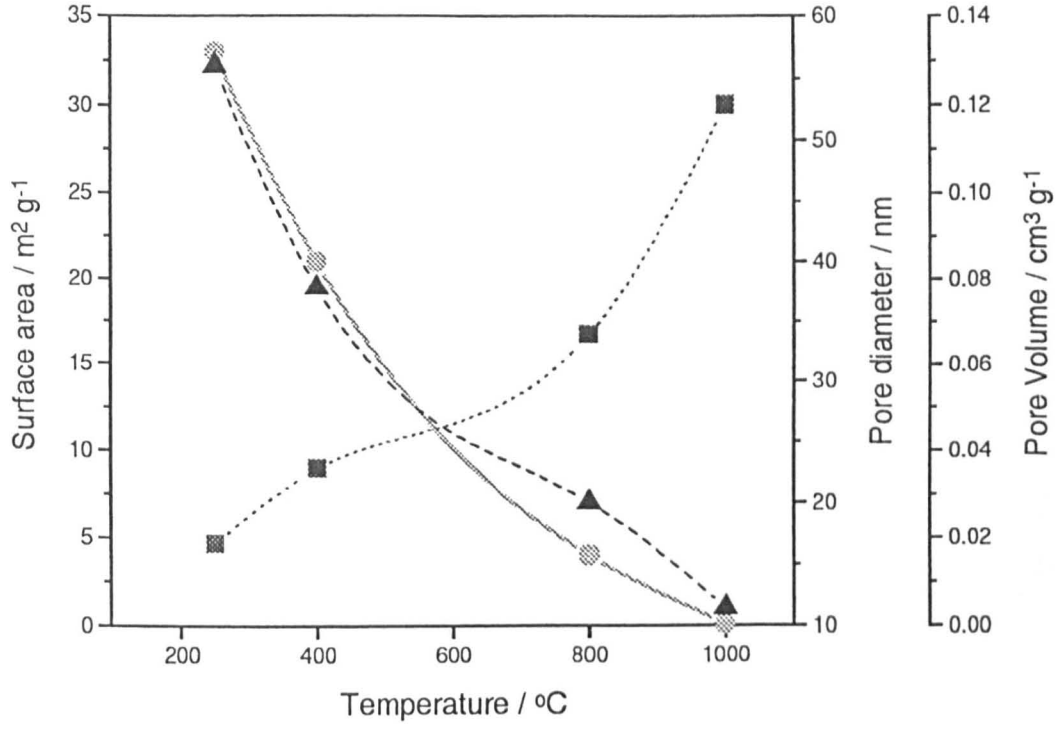

Fig. 181 Plots of variation in surface area (full line, ●), pore size (dotted line, ■) and pore volume (dashed line, ▲) against temperature for α-Fe_2O_3 / BaM fibres.

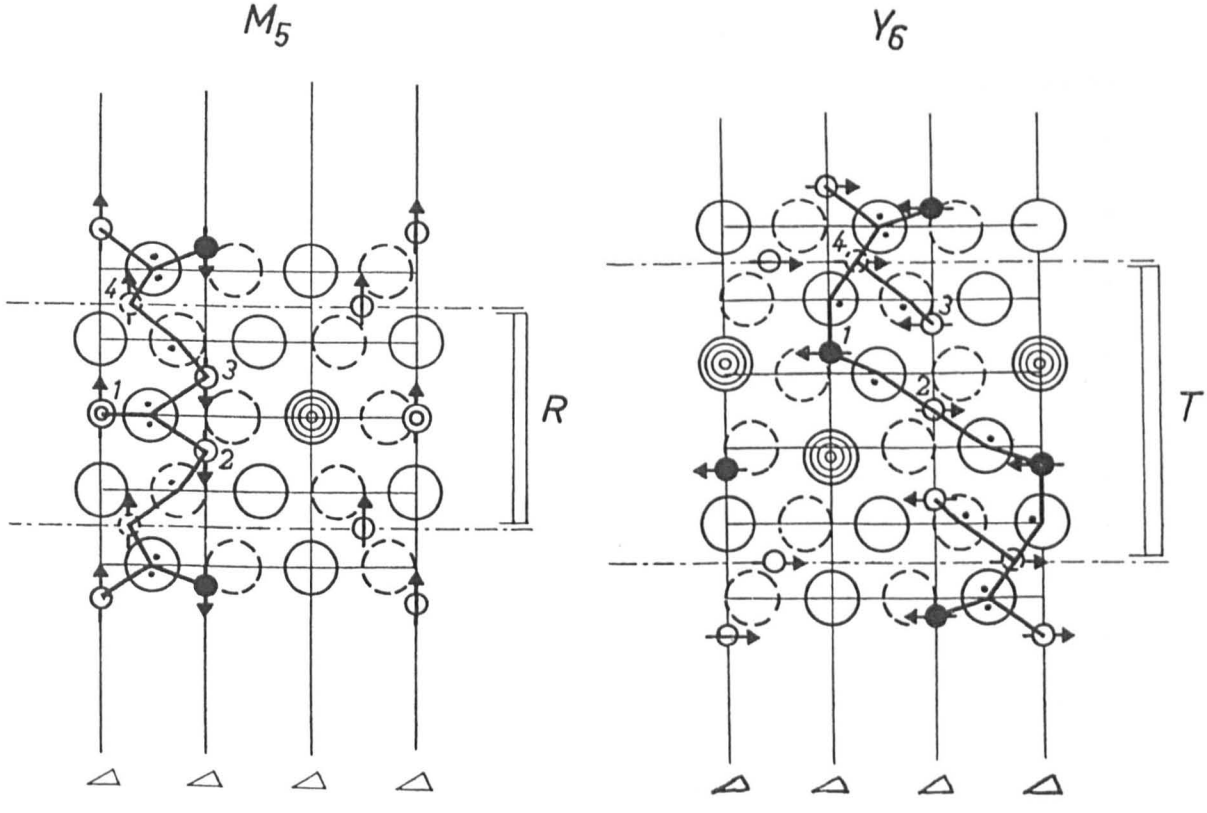

Fig. 182 The superexchange interactions of the R and T blocks of hexagonal ferrites. The dots represent the angles of the interactions as they go through the oxygen atom [7].

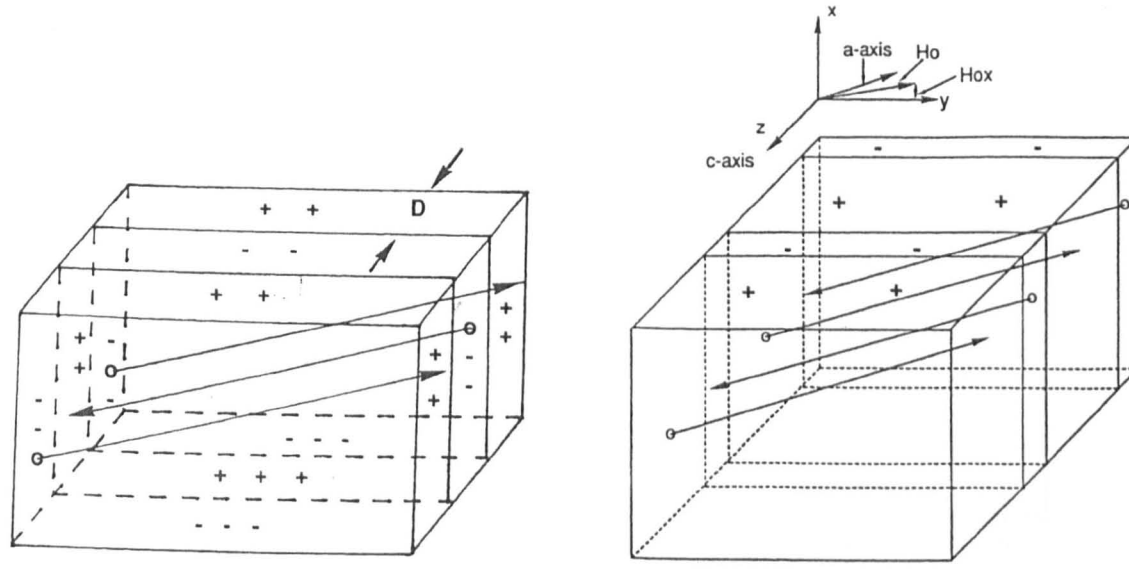

Fig. 183 The domain structure of Co_2Y and Co_2Z, showing domains of equal width separated by 180 ° domain walls [12;353].

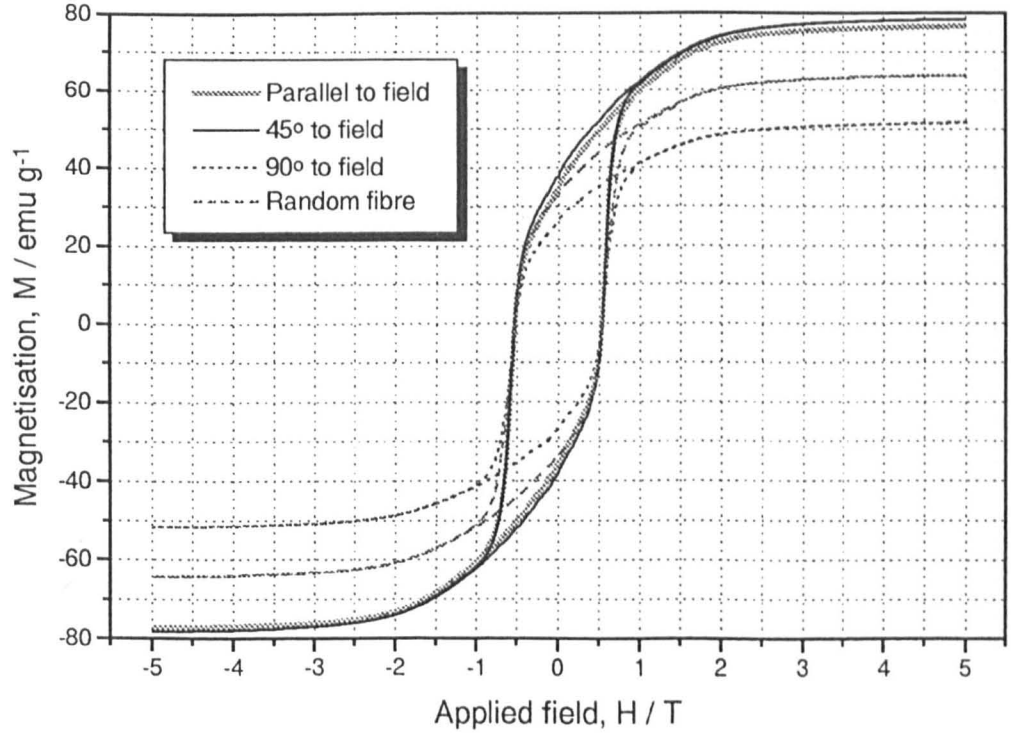

Fig. 184 The hysteresis loops for BaM fibres, both random and aligned, fired to 1000 °C / 3hr immediately after drying.

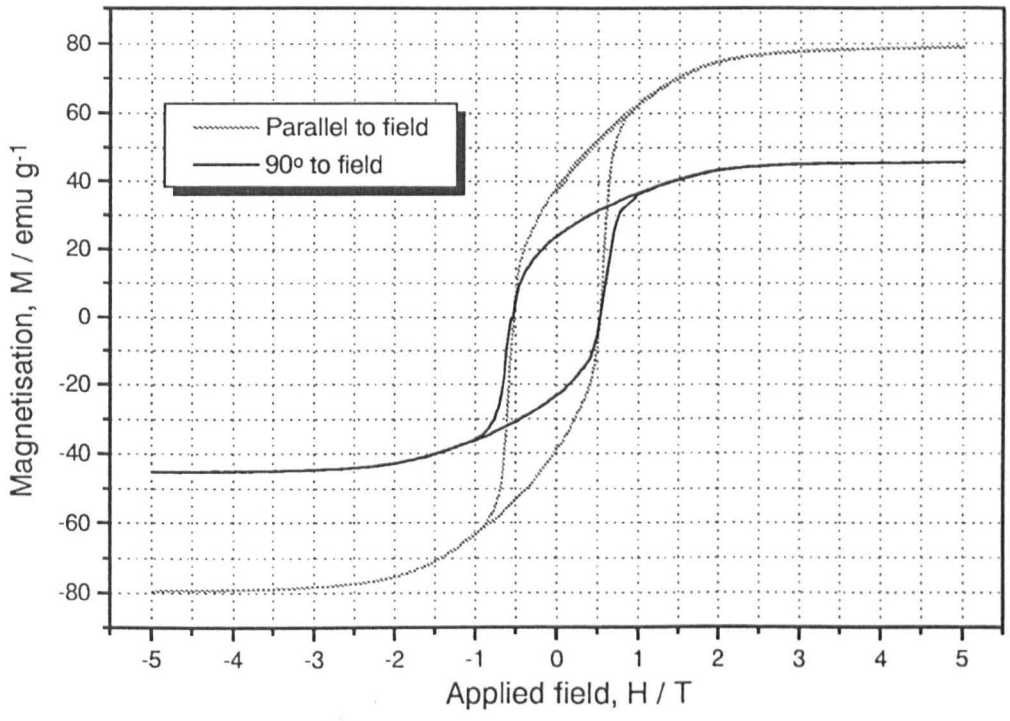

Fig. 185 The hysteresis loops for aligned BaM fibres fired to 1000 °C / 3hr after 2 yr storage.

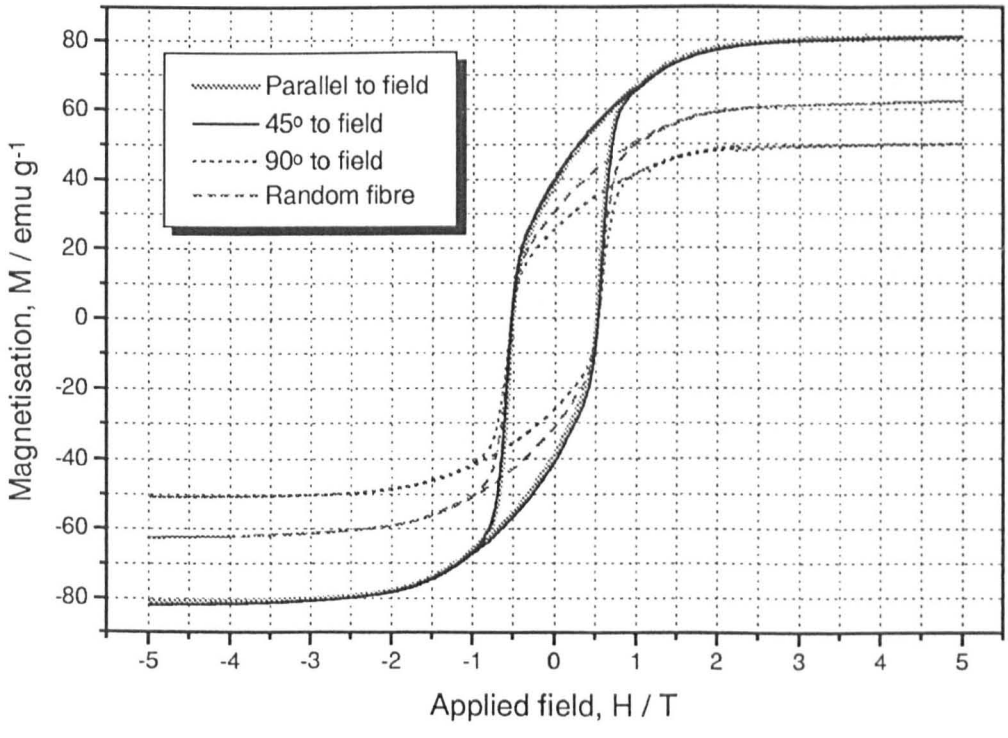

Fig. 186 The hysteresis loops for BaM fibres, both random and aligned, fired to 1000 °C / 3hr after 3 yr storage.

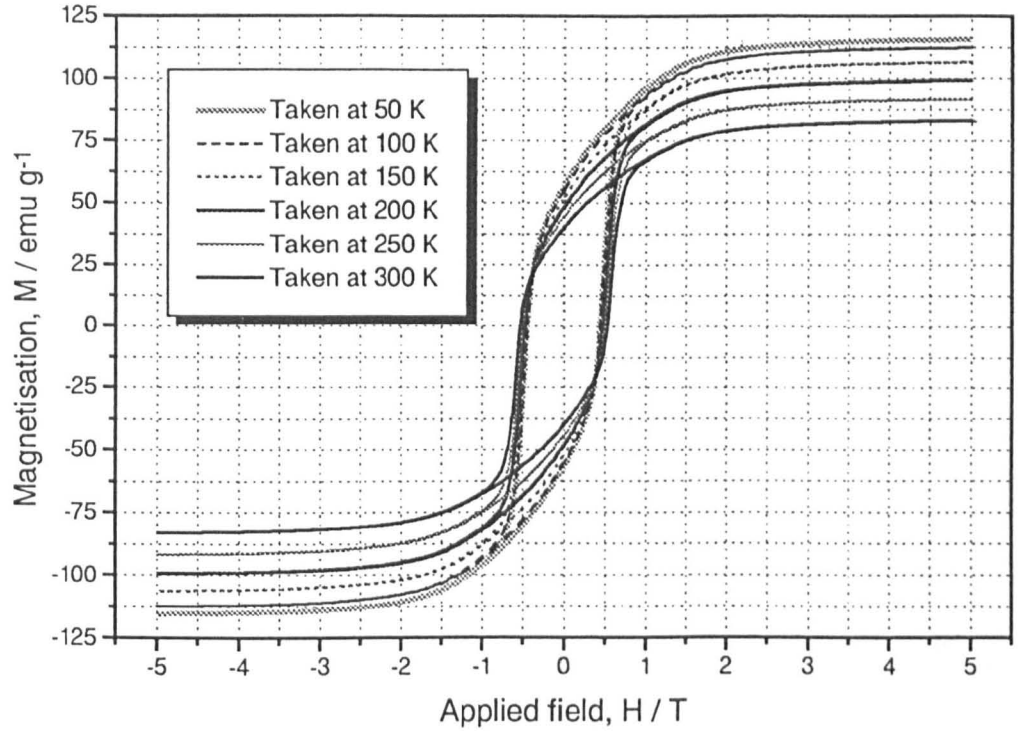

Fig. 187 Change in the hysteresis loops for BaM fibres, aligned ‖ to H and fired to 1000 °C / 3hr after 3 yr storage, with measurement temperature.

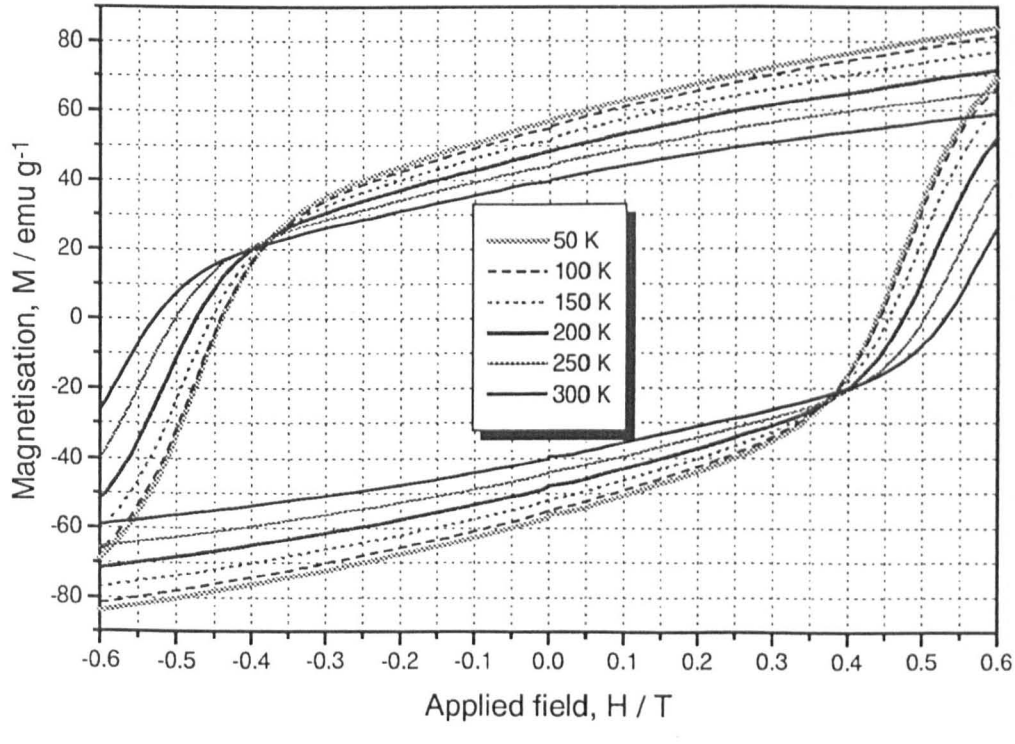

Fig. 188 Detail of the hysteresis loops from figure 187, showing change in H_c and M_r.

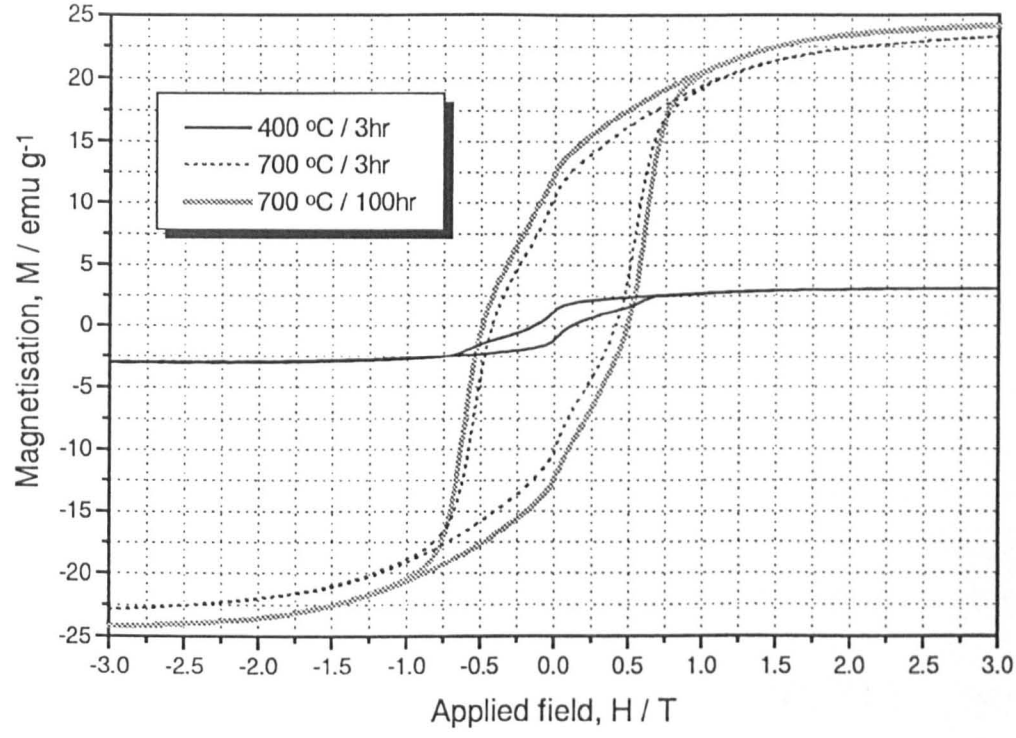

Fig. 189 The hysteresis loops for BaM fibres, aligned || to H and after 3 yr storage, fired to 400 °C / 3hr and 700 °C / 3hr and 100 hr.

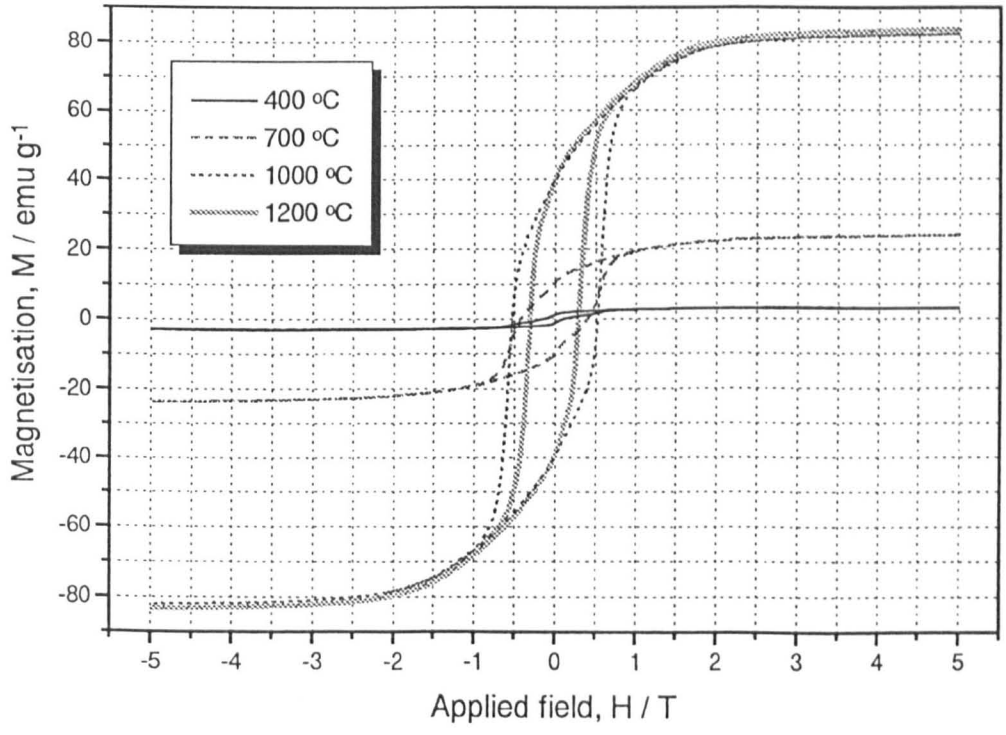

Fig. 190 The hysteresis loops for BaM fibres, aligned || to H and after 3 yr storage, fired to 400 °C, 700 °C, 1000 °C and 1200 °C / 3hr.

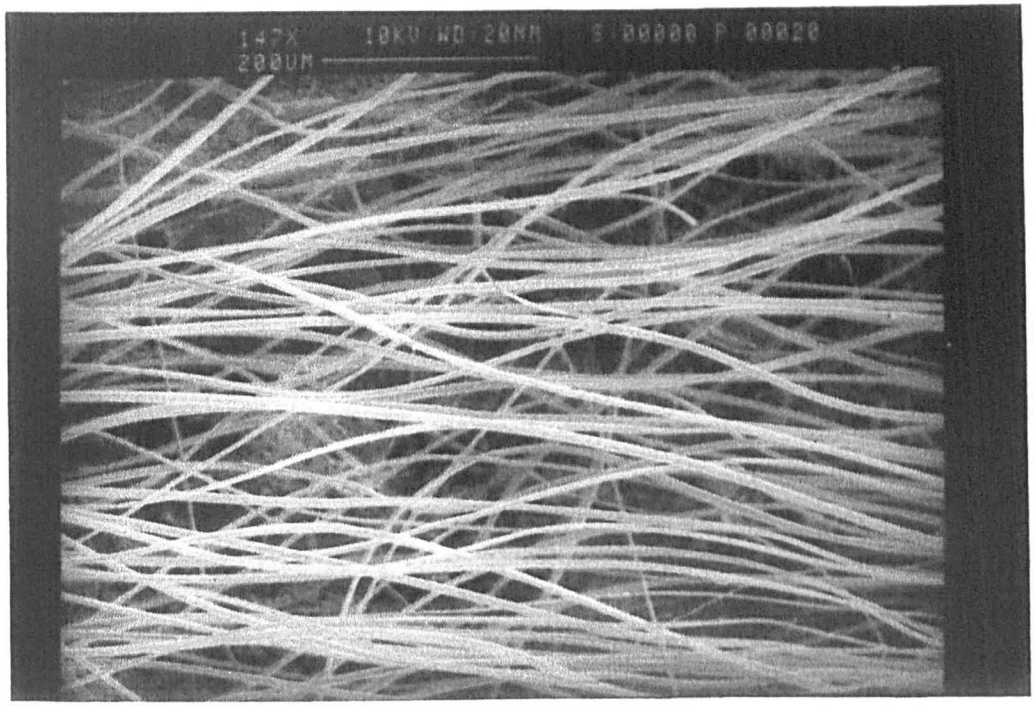

Fig. 191 SEM demonstrating the loss of alignment following the steaming process.

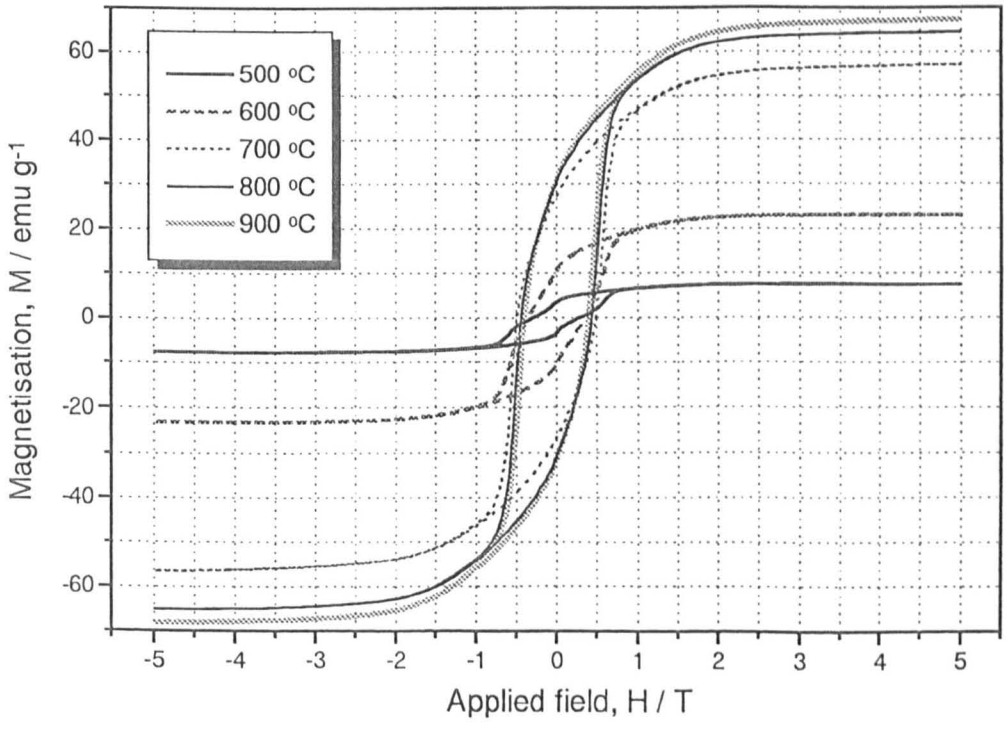

Fig.192 Hysteresis loops of BaM fibres, aligned || to H and after 3 yr storage, steamed at 500, 600, 700, 800 and 900 °C / 3hr.

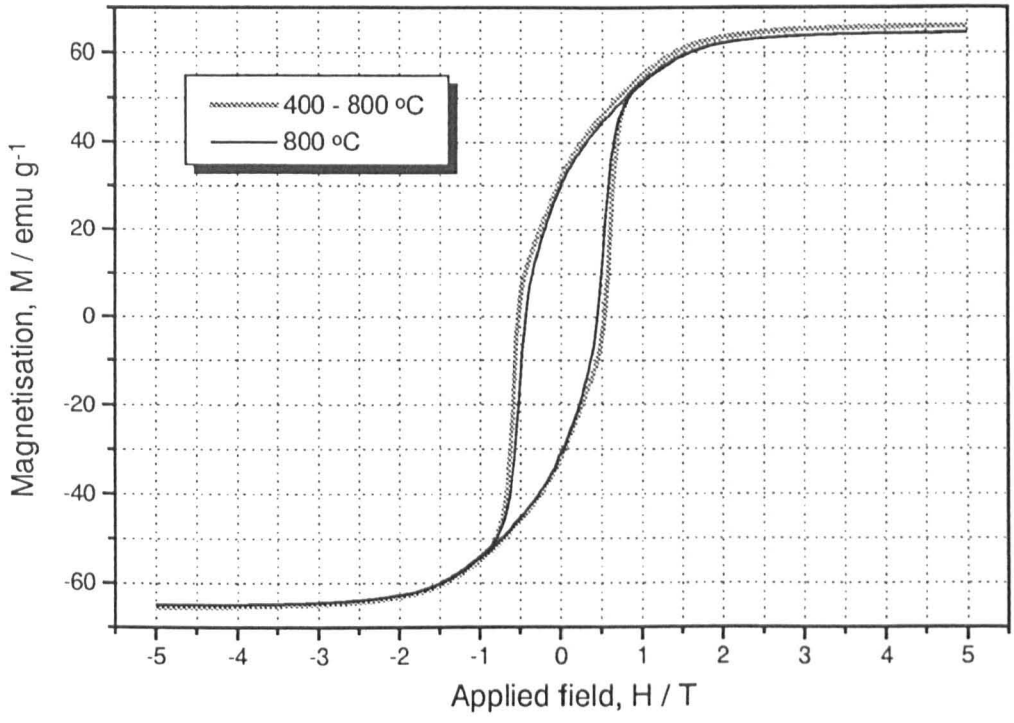

Fig. 193 Hysteresis loops of BaM fibres, aligned || to H and after 3 yr storage, steamed at 400 - 800 and 800 °C / 3hr.

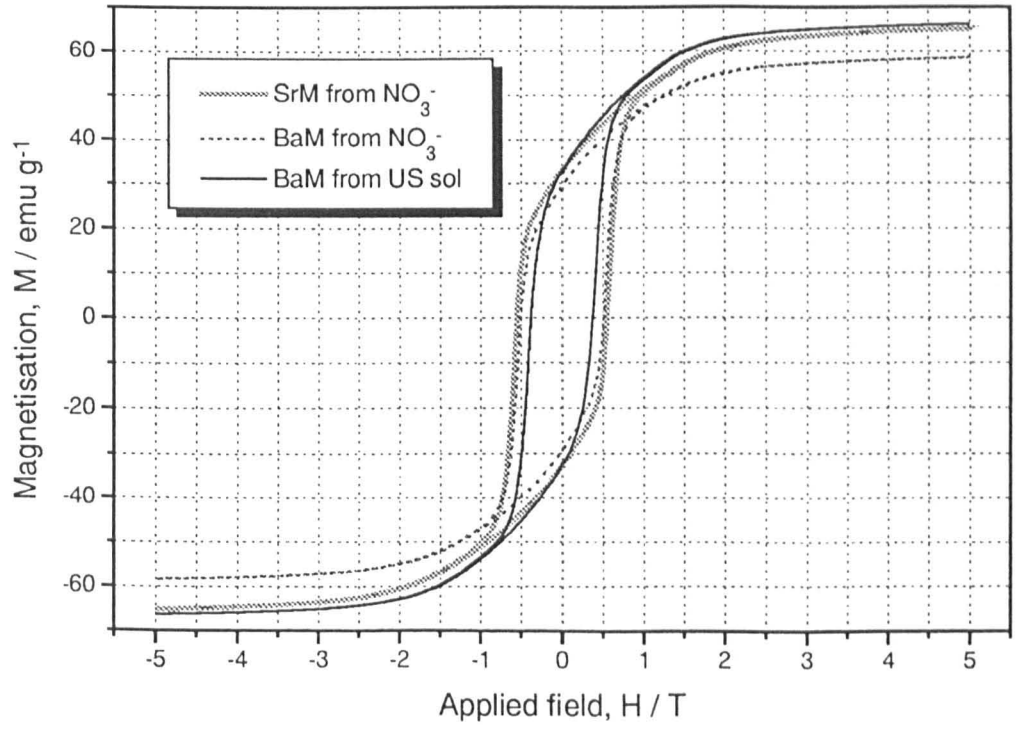

Fig. 194 Hysteresis loops of random BaM and SrM fibres made from Fe/NO_3 sols and BaM fibres from an ultrasonically peptised sol, all fired to 1000 °C / 3hr.

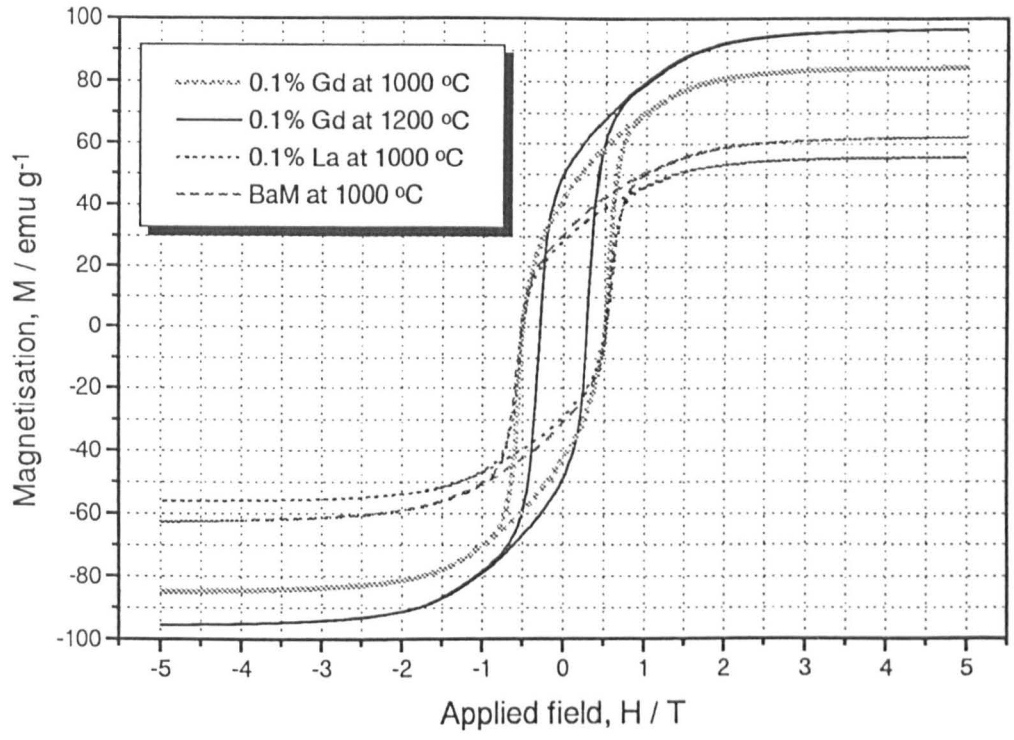

Fig. 195 Hysteresis loops of random BaM fibres doped with 1% La_2O_3 fired to 1000 °C / 3hr and Gd_2O_3 fired to 1000 °C and 1200 °C / 3hr, compared to BaM at 1000 °C / 3hr.

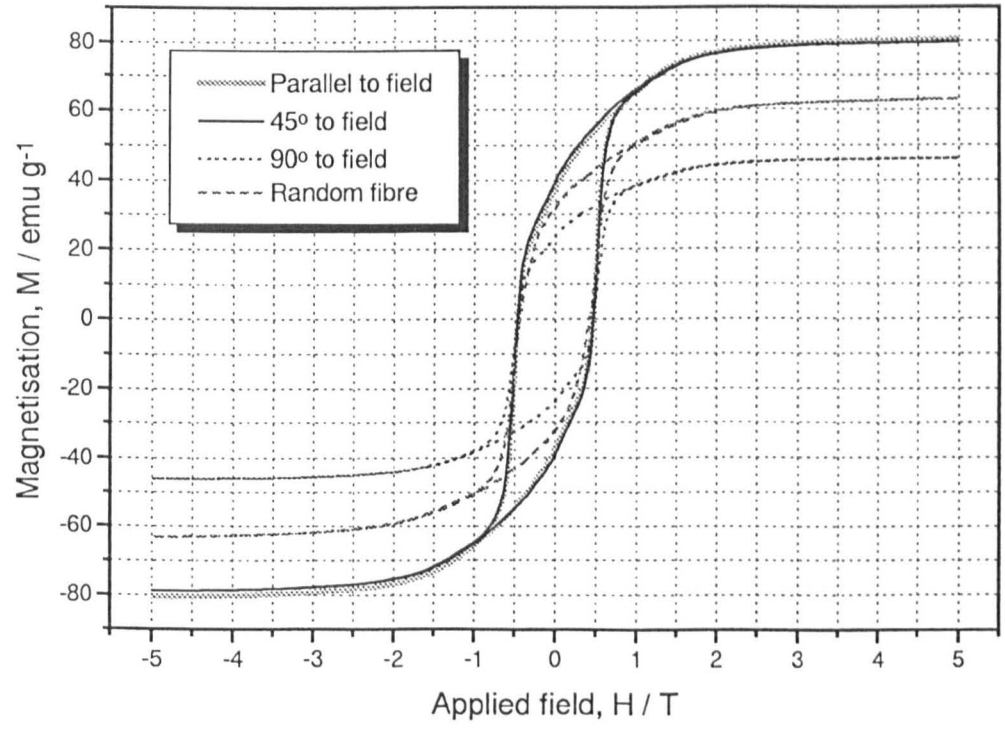

Fig. 196 The hysteresis loops for SrM fibres, both random and aligned, fired to 1000 °C / 3hr immediately after drying.

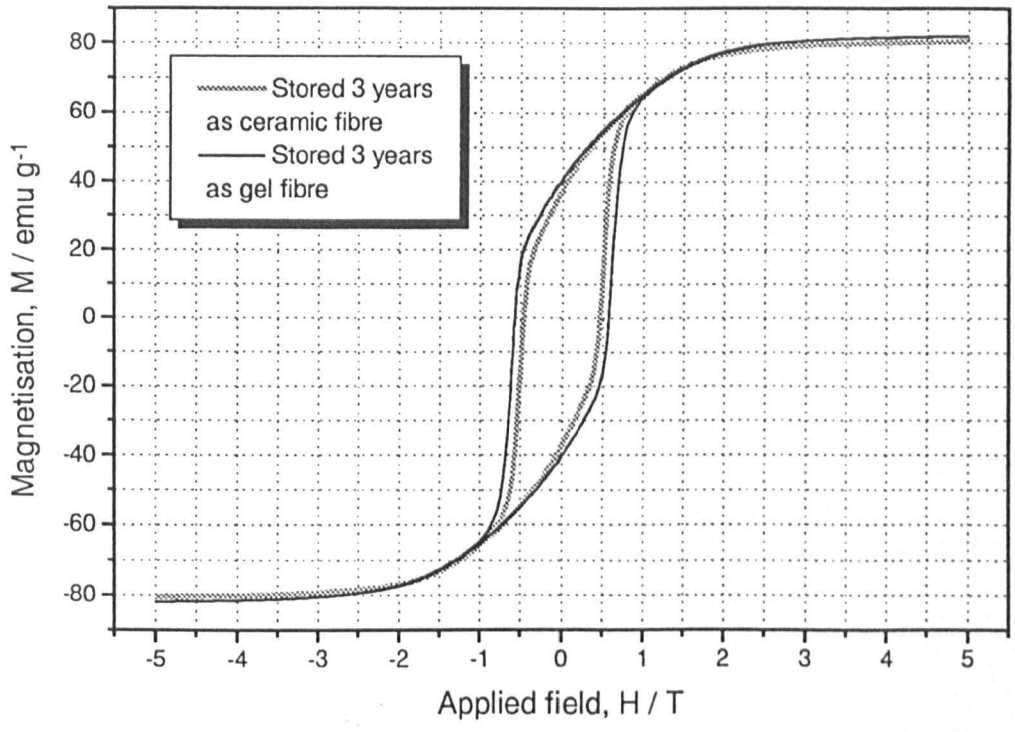

Fig. 197 The hysteresis loops for SrM fibres, fired immediately after drying and after storage for 3 yr, both aligned || to H and fired to 1000 °C / 3hr.

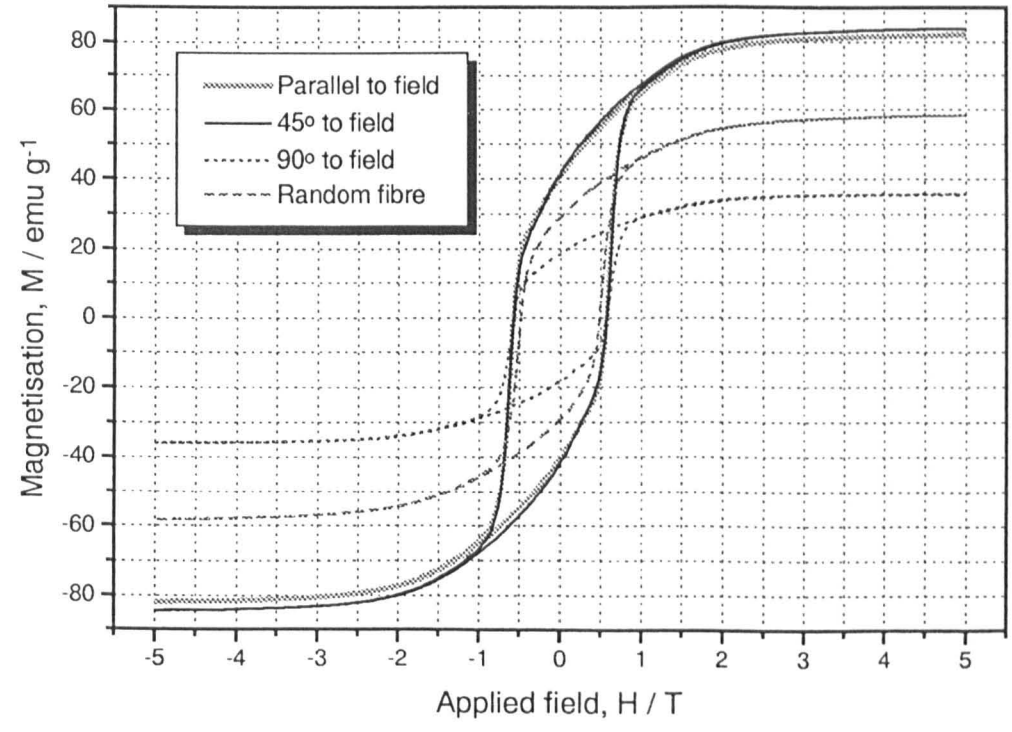

Fig. 198 The hysteresis loops for SrM fibres, both random and aligned, fired to 1000 °C / 3hr after 3 yr storage.

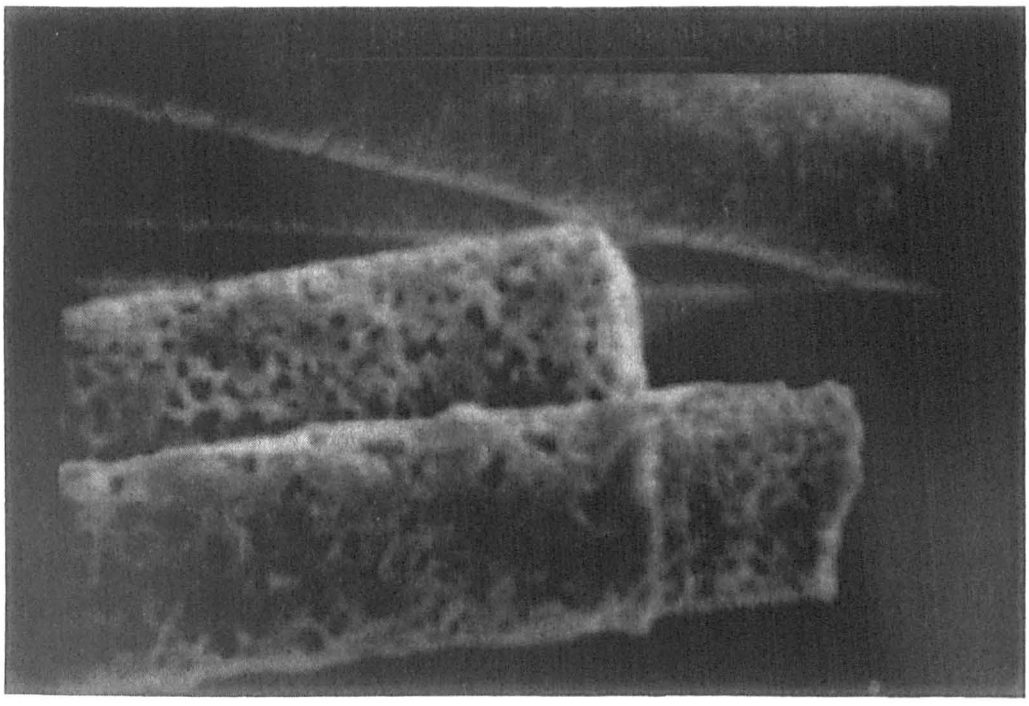

Fig. 199 SEM of aligned SrM fibre, stored for 3 yr before firing to 1000 °c / 3hr.

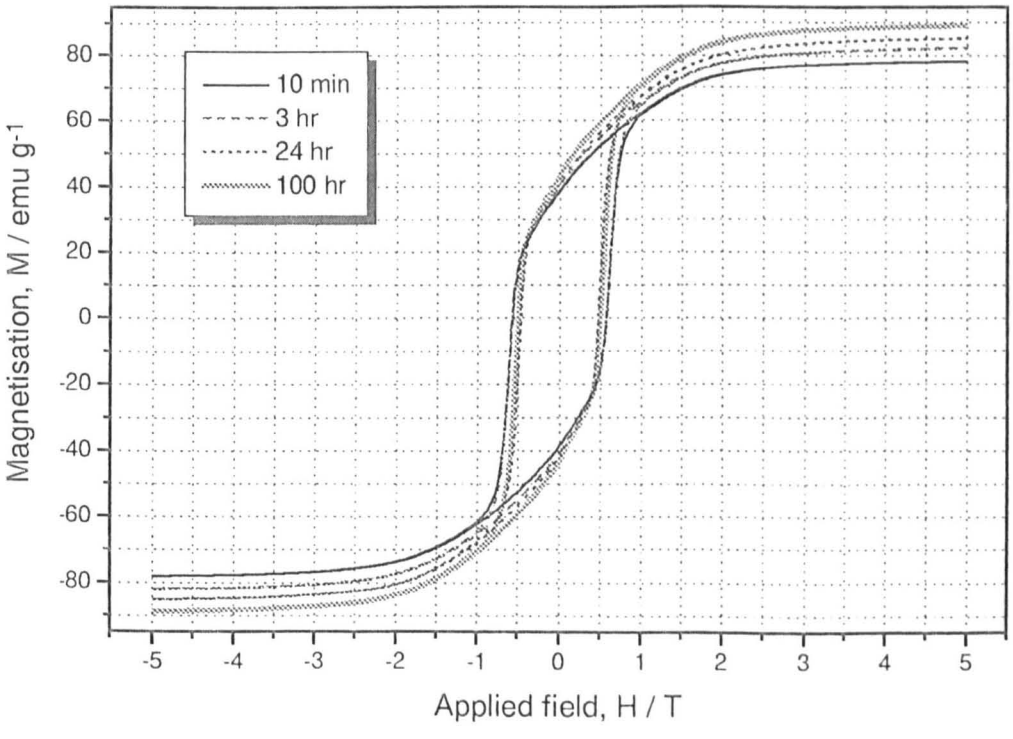

Fig. 200 The hysteresis loops for SrM fibres, fired after storage for 3 yr and aligned || to H, fired to 1000 °C for 10 min, 3hr, 24 hr and 100 hr.

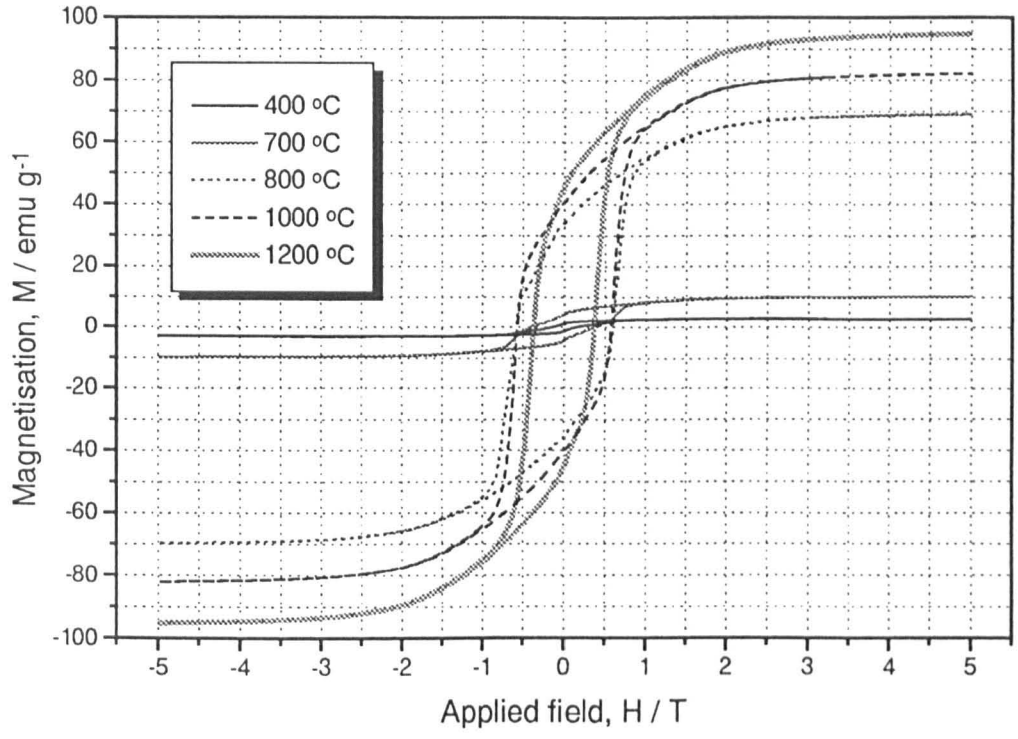

Fig. 201 The hysteresis loops for SrM fibres, aligned || to H and after 3 yr storage, fired to 400 °C, 700 °C, 800 °C, 1000 °C and 1200 °C / 3hr.

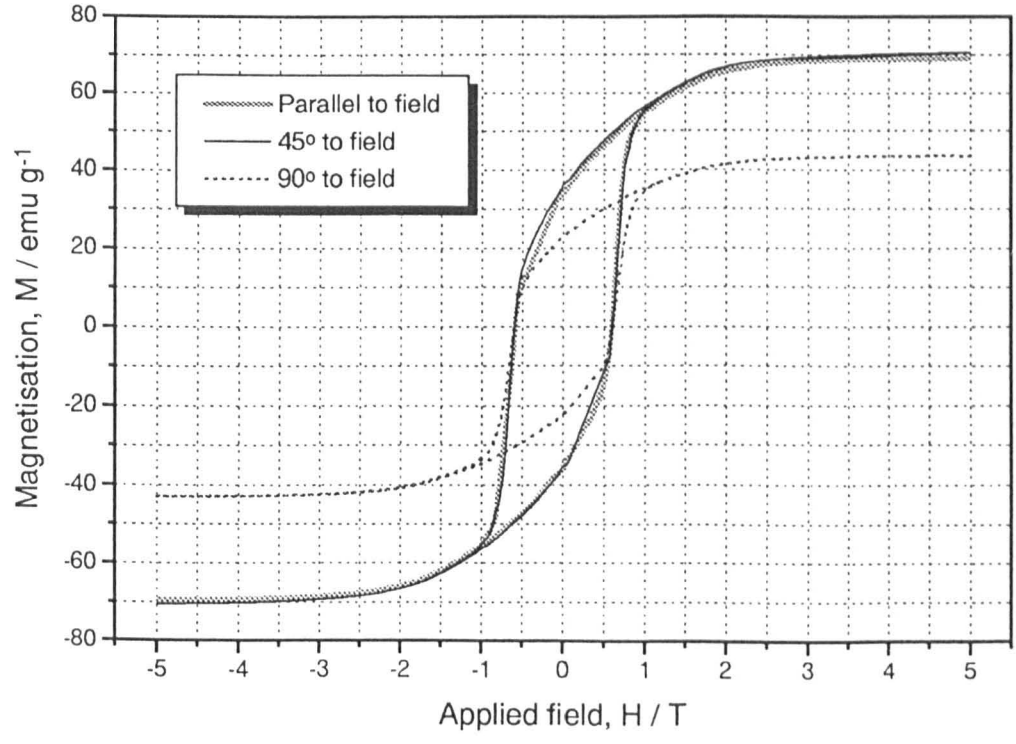

Fig. 202 The hysteresis loops for aligned SrM fibres fired to 800 °C / 3hr after 3 yr storage.

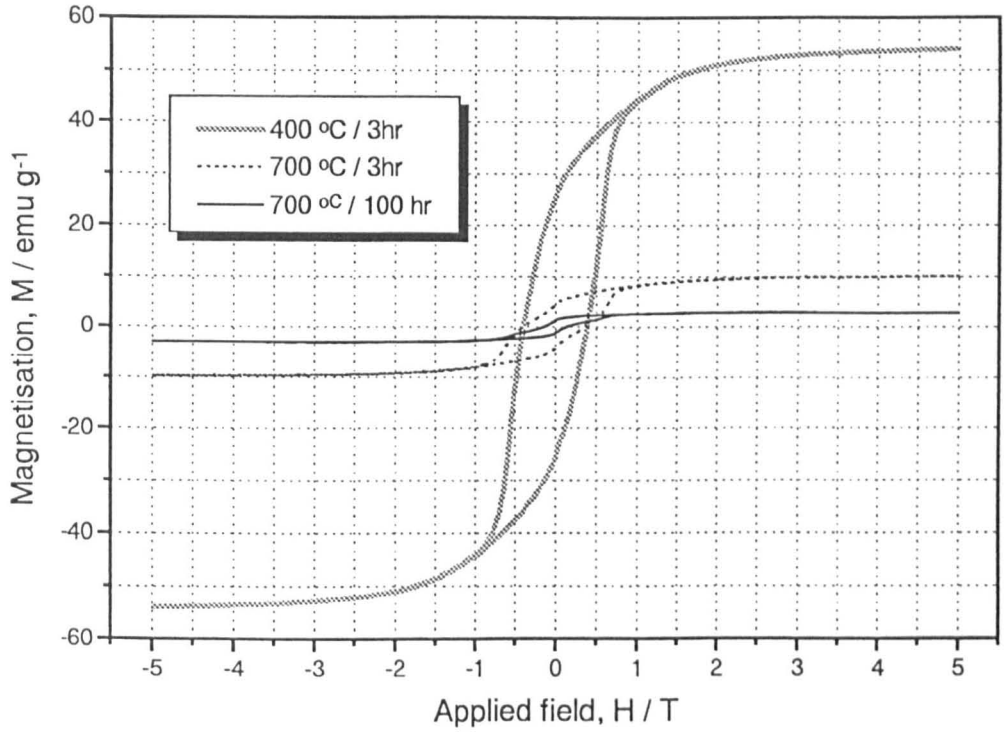

Fig. 203 The hysteresis loops for SrM fibres, aligned || to H and after 3 yr storage, fired to 400 °C and 700 °C/ 3hr and 700 °C / 100 hr.

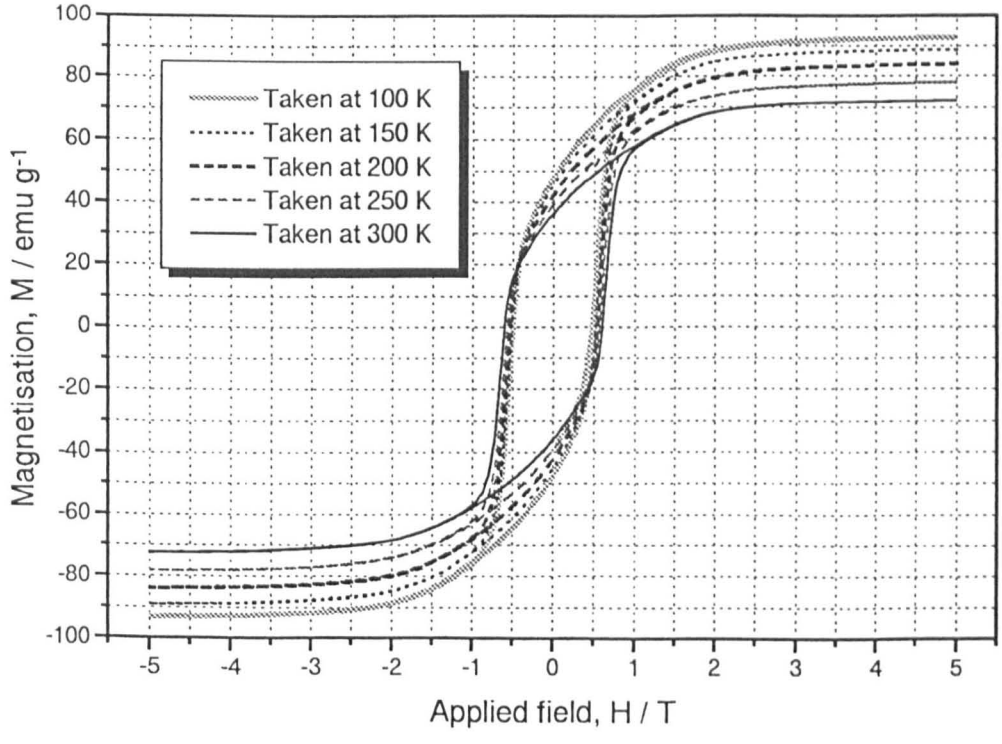

Fig. 204 Change in the hysteresis loops for SrM fibres, aligned || to H and fired to 800 °C / 3hr after 3 yr storage, with measurement temperature.

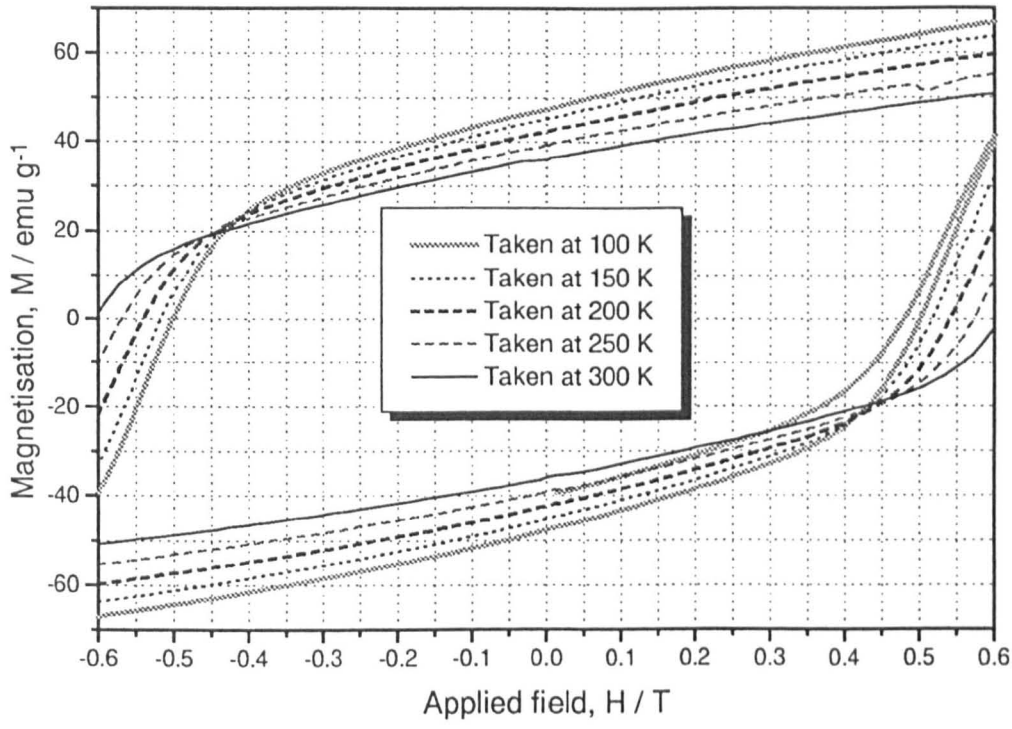

Fig. 205 Detail of the hysteresis loops from figure 204, showing change in H_c and M_r.

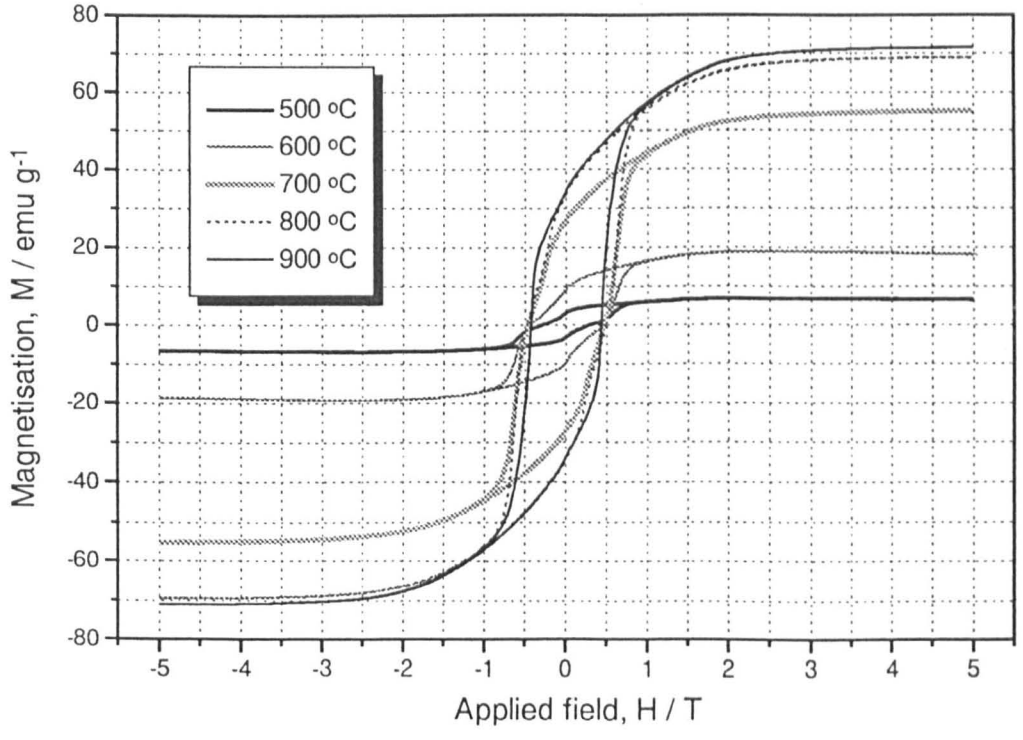

Fig. 206 Hysteresis loops of SrM fibres, aligned || to H and after 3 yr storage, steamed at 500, 600, 700, 800 and 900 °C / 3hr.

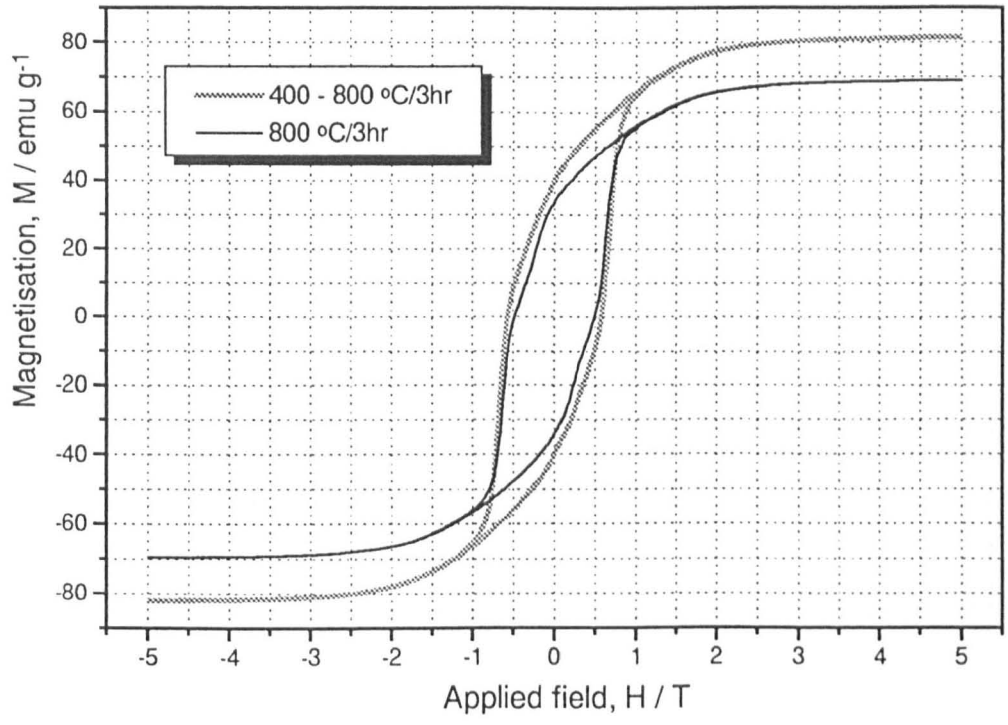

Fig. 207 Hysteresis loops of SrM fibres, aligned || to H and after 3 yr storage, steamed at 400 - 800 and 800 °C / 3hr.

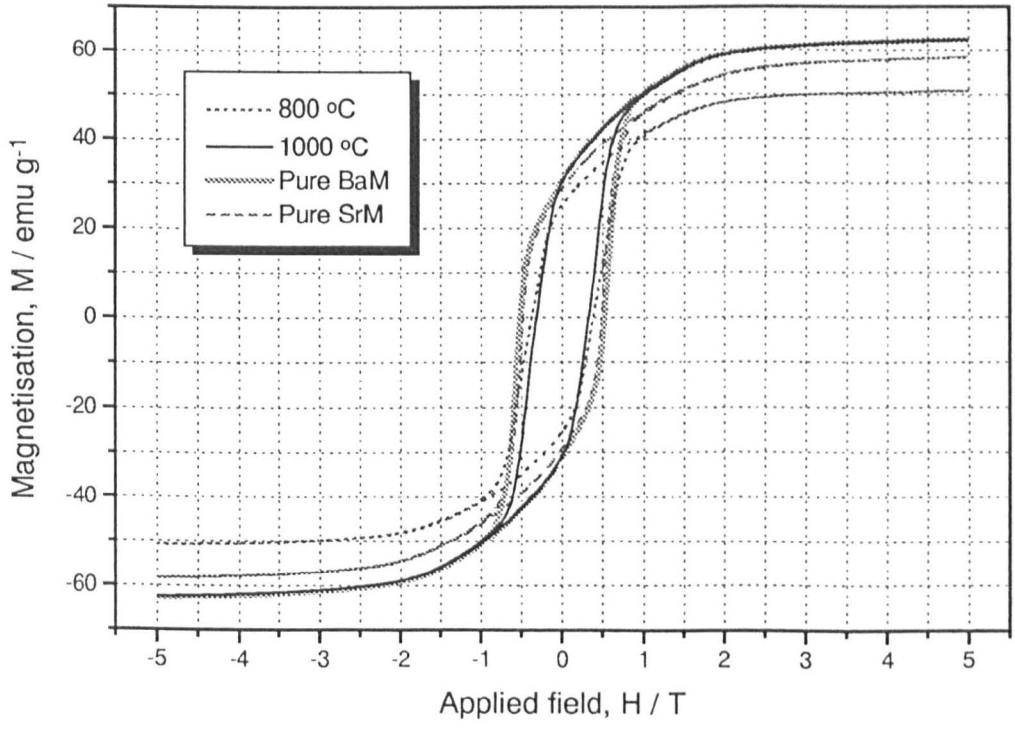

Fig. 208 Hysteresis loops of $Ba_{0.5}Sr_{0.5}M$ random fibre fired to 800 °C and 1000 °C / 3hr, compared to BaM and SrM at 1000 °C / 3hr.

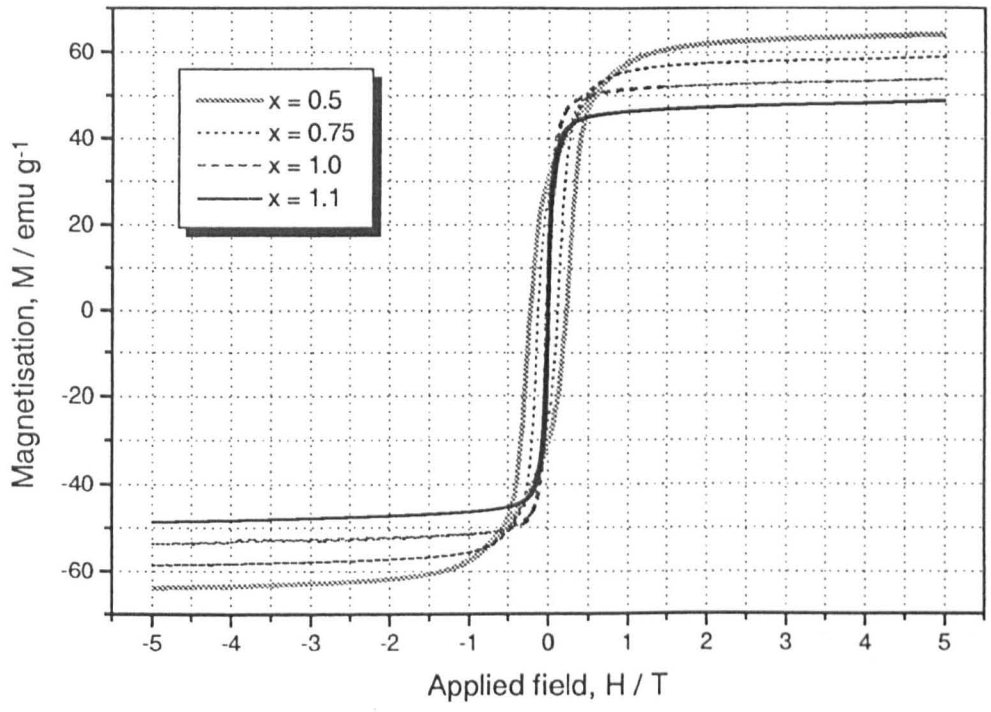

Fig. 209 Hysteresis loops of random $BaCo_xTi_xFe_{12-x}O_{19}$ fibres for x = 0.5, 0.75, 1.0 and 1.1, fired to 1000 °C

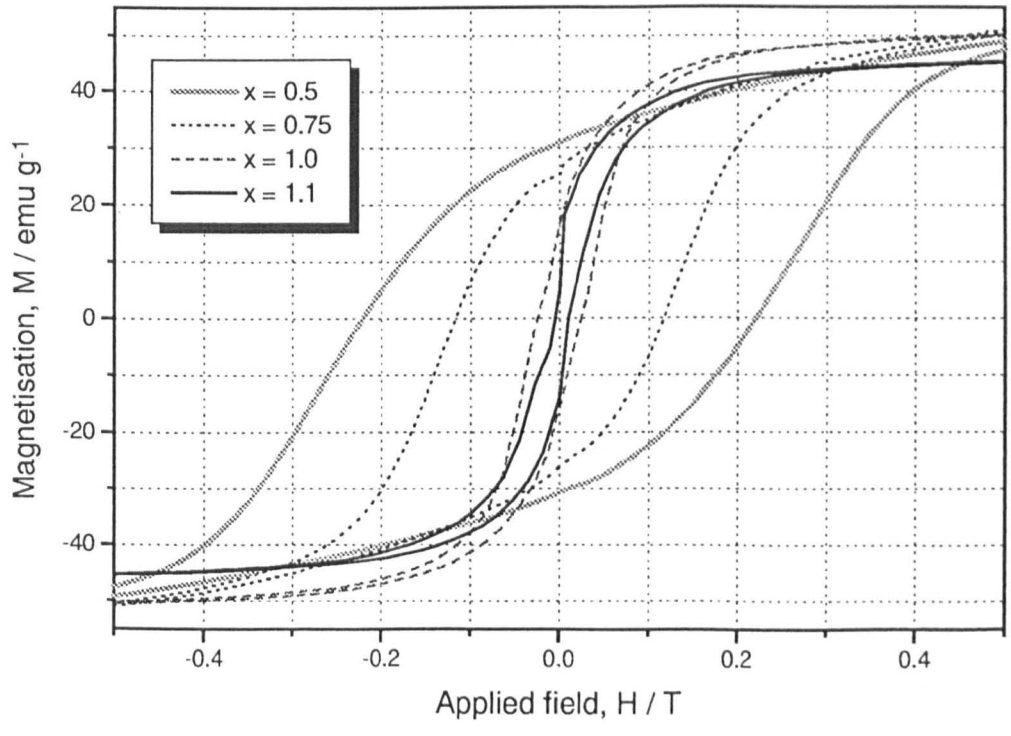

Fig. 210 Detail of the hysteresis loops from figure 209, showing change in H_c and M_r

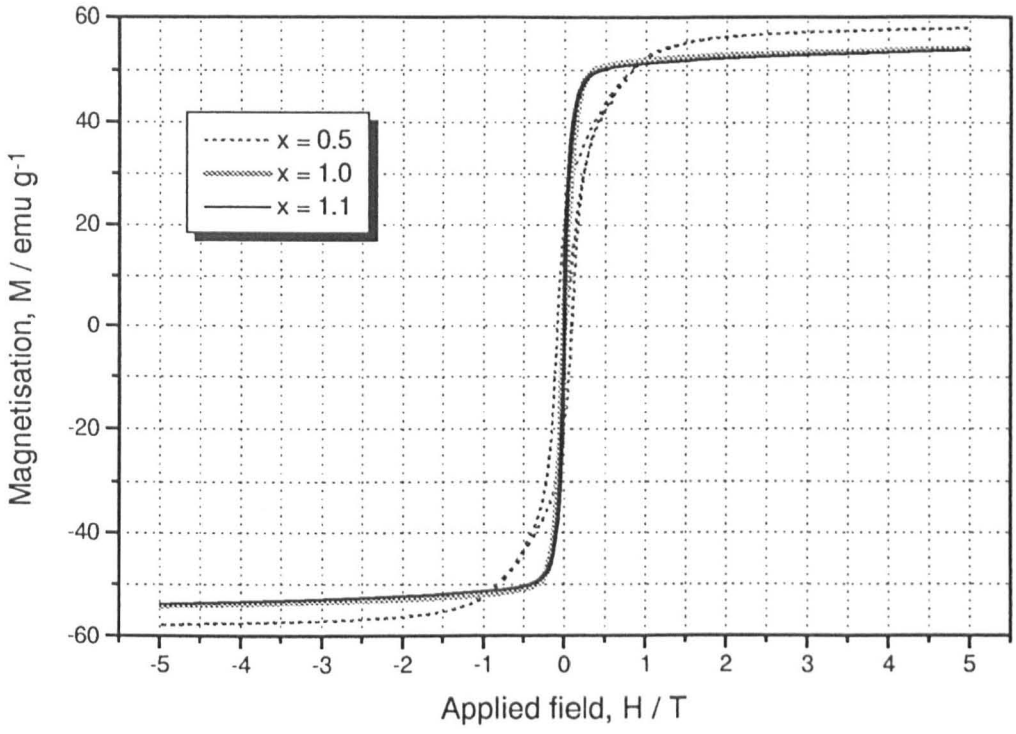

Fig. 211 Hysteresis loops of random $BaCo_xTi_xFe_{12-x}O_{19}$ fibres for x = 0.5, 1.0 and 1.1, fired to 1200 °C

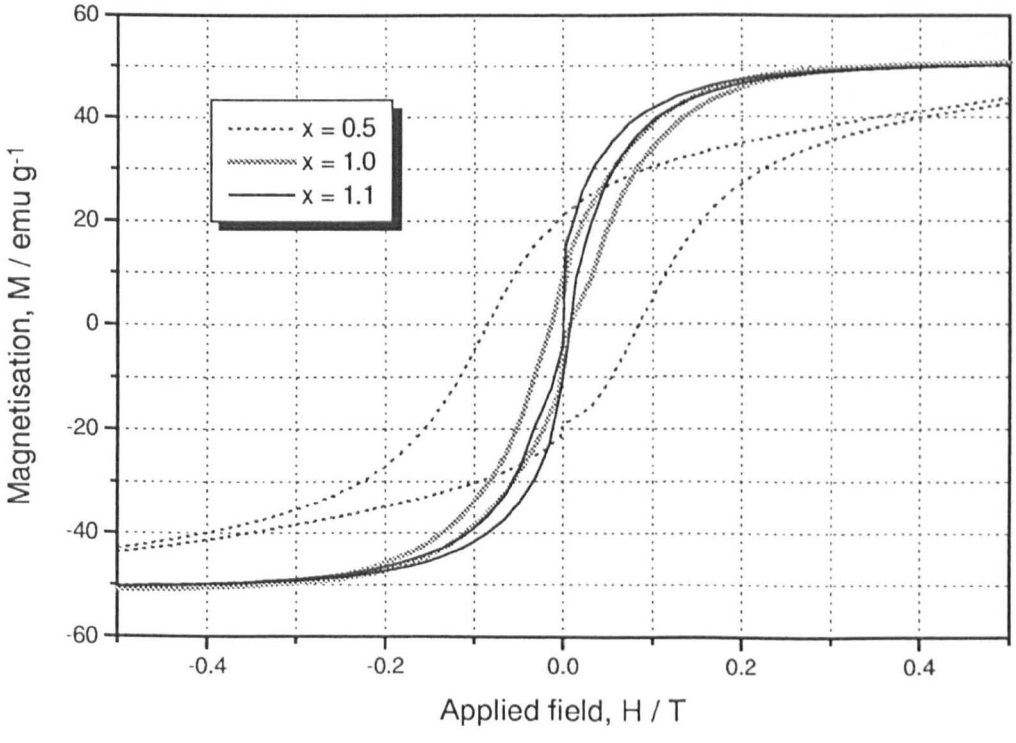

Fig. 212 Detail of the hysteresis loops from figure 211, showing change in H_c and M_r.

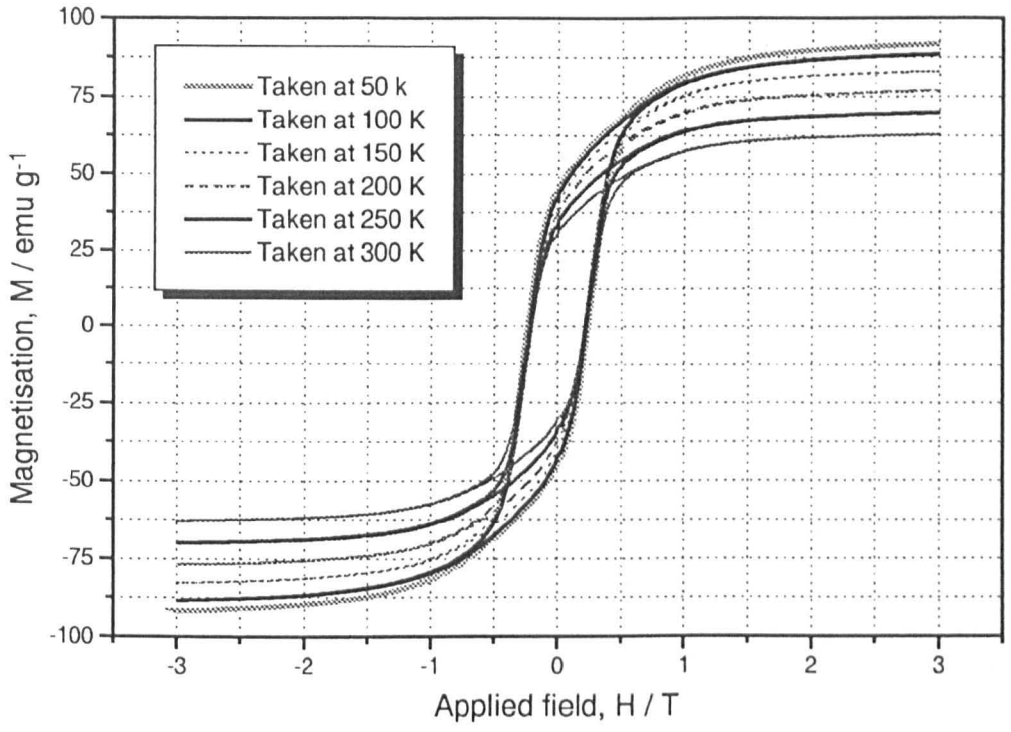

Fig. 213 Change in the hysteresis loops for random $BaCo_{0.5}Ti_{0.5}Fe_{11}O_{19}$ fibres fired to 1000 °C / 3hr with measurement temperature

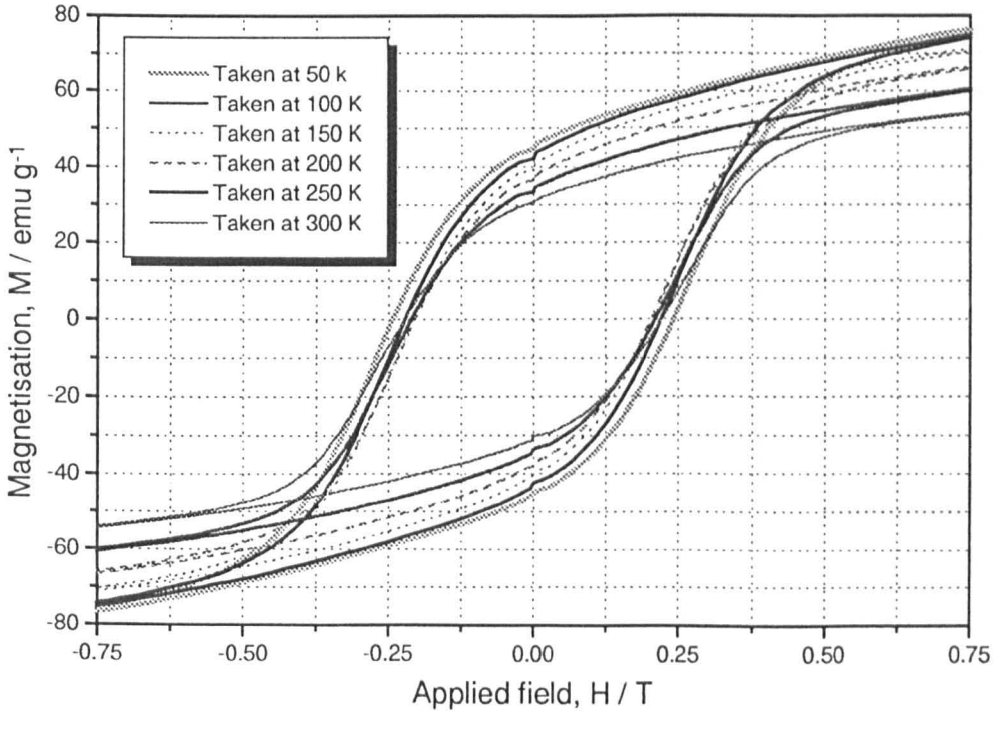

Fig. 214 Detail of the hysteresis loops from figure 213, showing change in H_c and M_r.

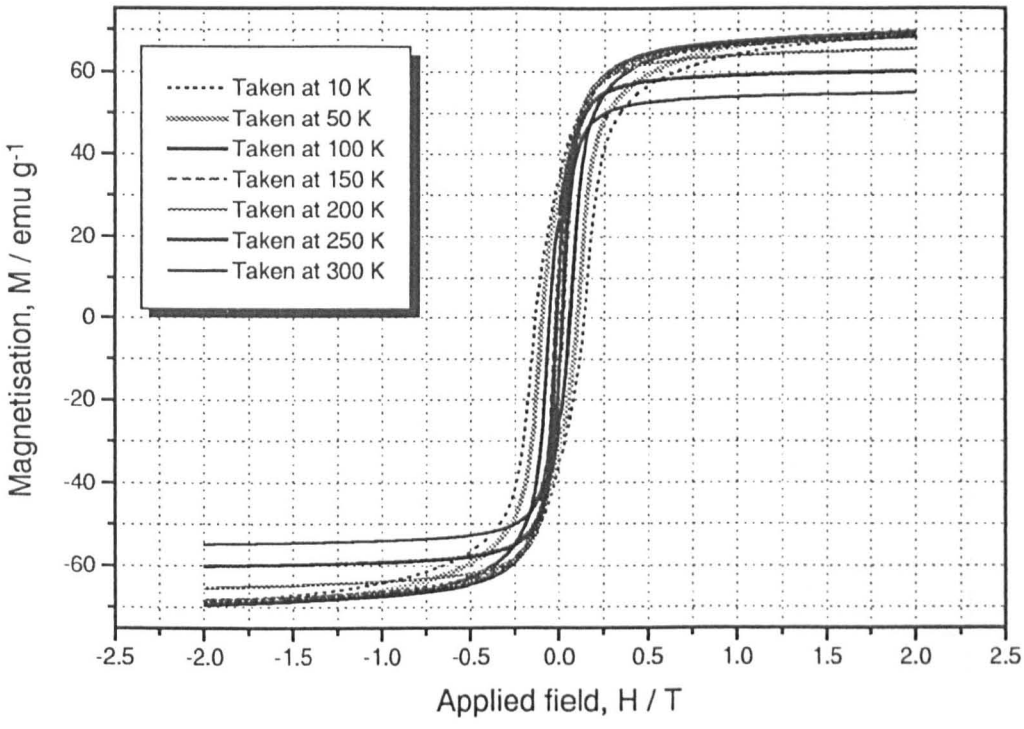

Fig. 215 Change in the hysteresis loops for random $BaCoTiFe_{10}O_{19}$ fibres fired to 1000 °C / 3hr with measurement temperature

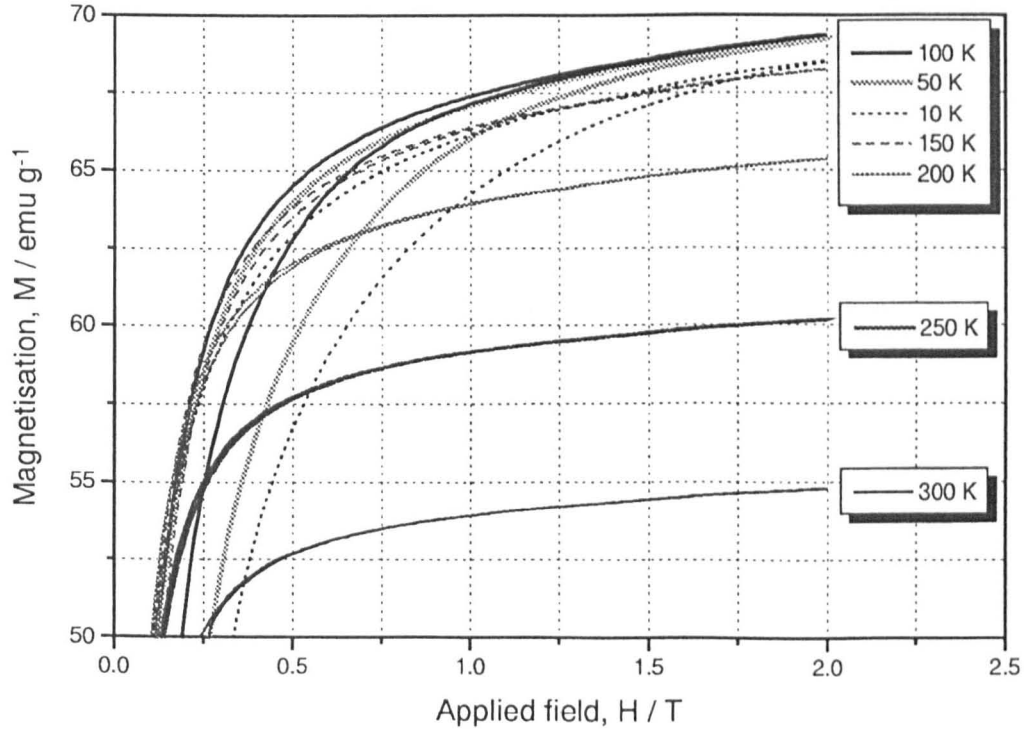

Fig. 216 Detail of the hysteresis loops from figure 215, showing change in M_s.

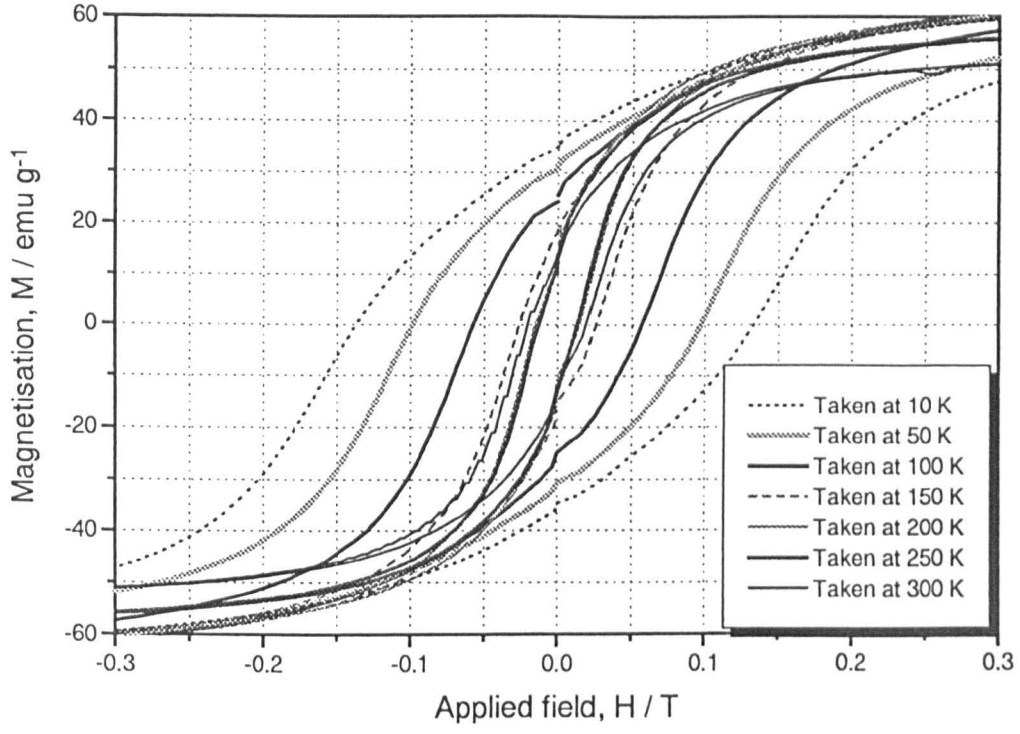

Fig. 217 Detail of the hysteresis loops from figure 215, showing change in H_c and M_r.

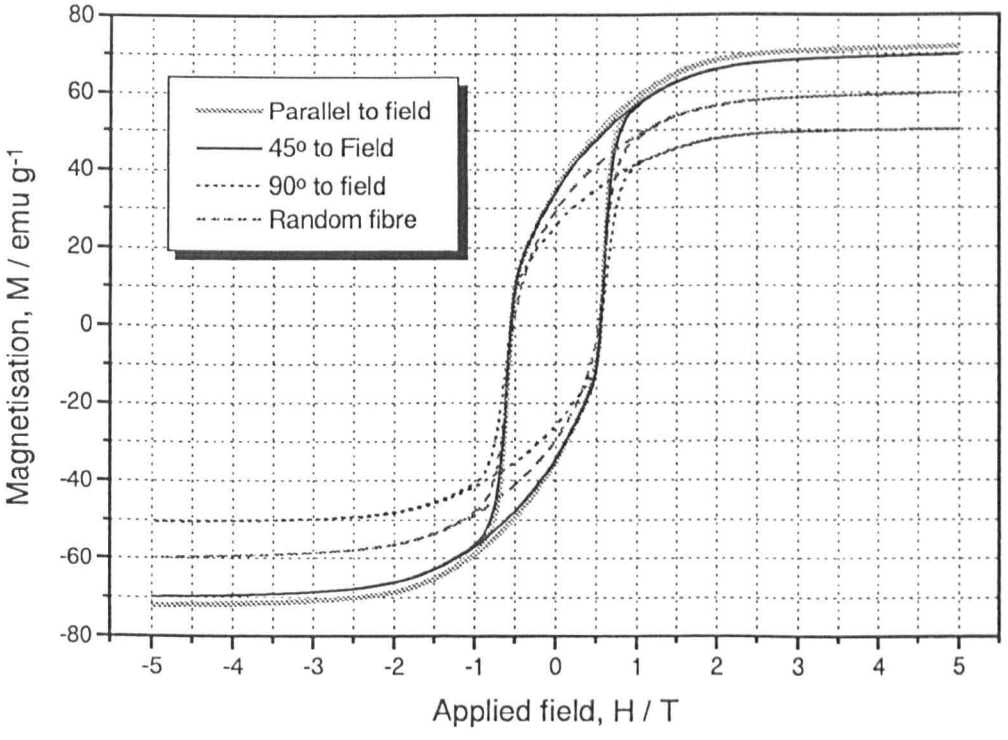

Fig. 218 The hysteresis loops for aligned and random $SrCo_{0.5}Ti_{0.5}Fe_{11}O_{19}$ fibres fired to 1000 °C / 3hr after 1 yr storage.

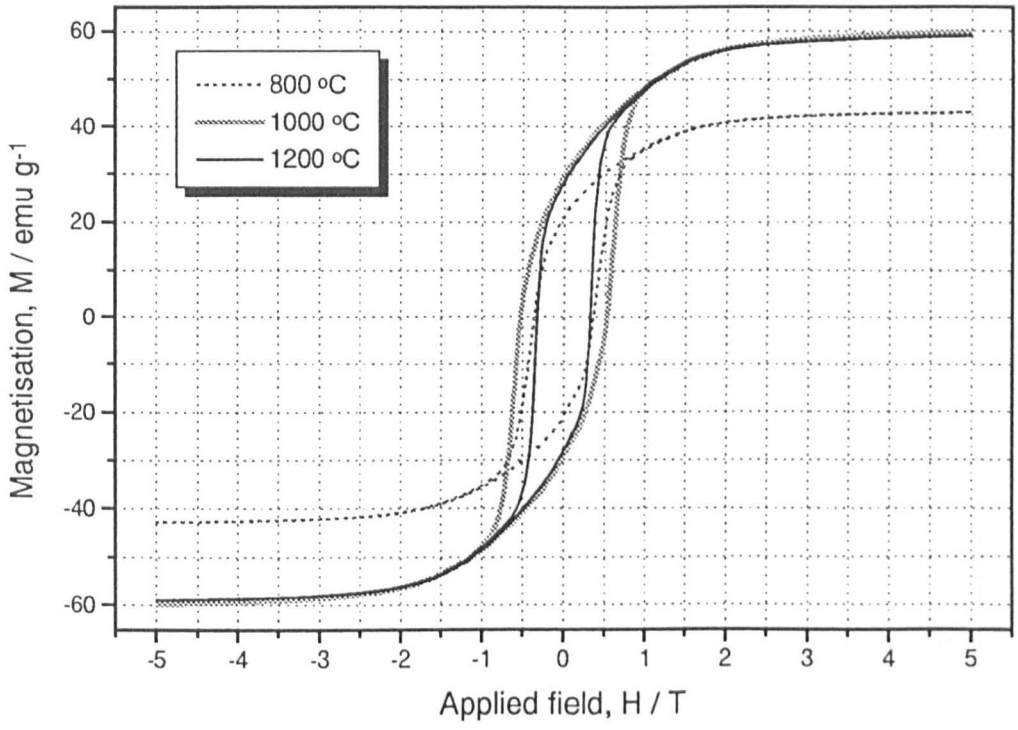

Fig. 219 The hysteresis loops for random $SrCo_{0.5}Ti_{0.5}Fe_{11}O_{19}$ fibres fired to 800 °C, 1000 °C and 1200 °C / 3hr after 1 yr storage.

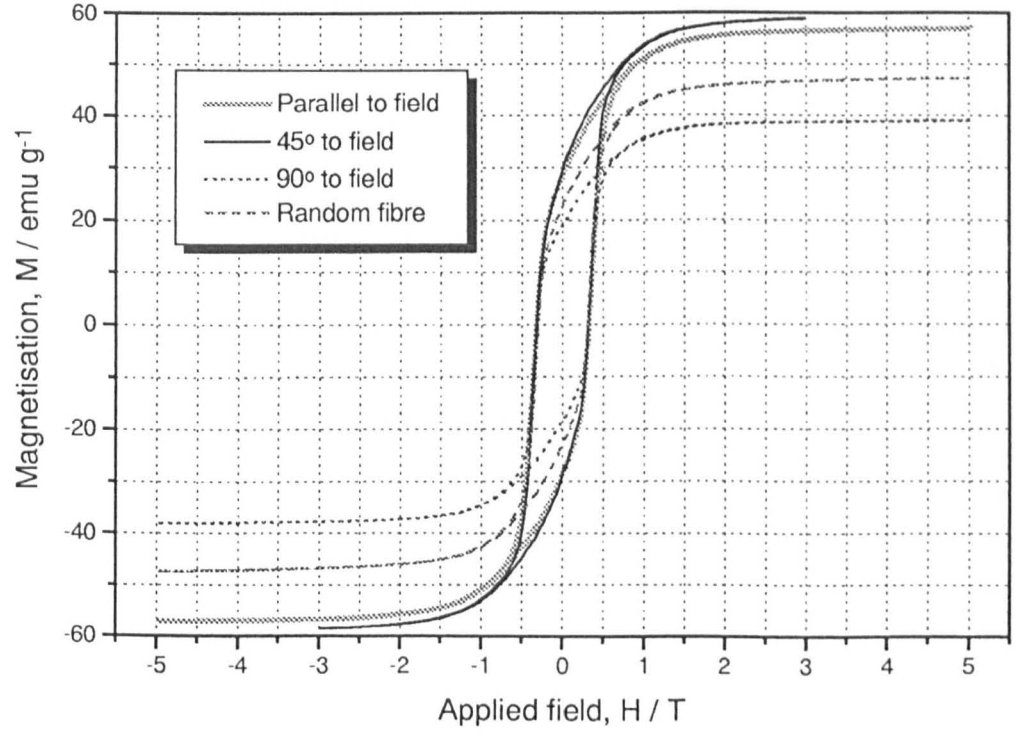

Fig. 220 The hysteresis loops for aligned and random $SrCoTiFe_{10}O_{19}$ fibres fired to 1000 °C / 3hr after 1 yr storage.

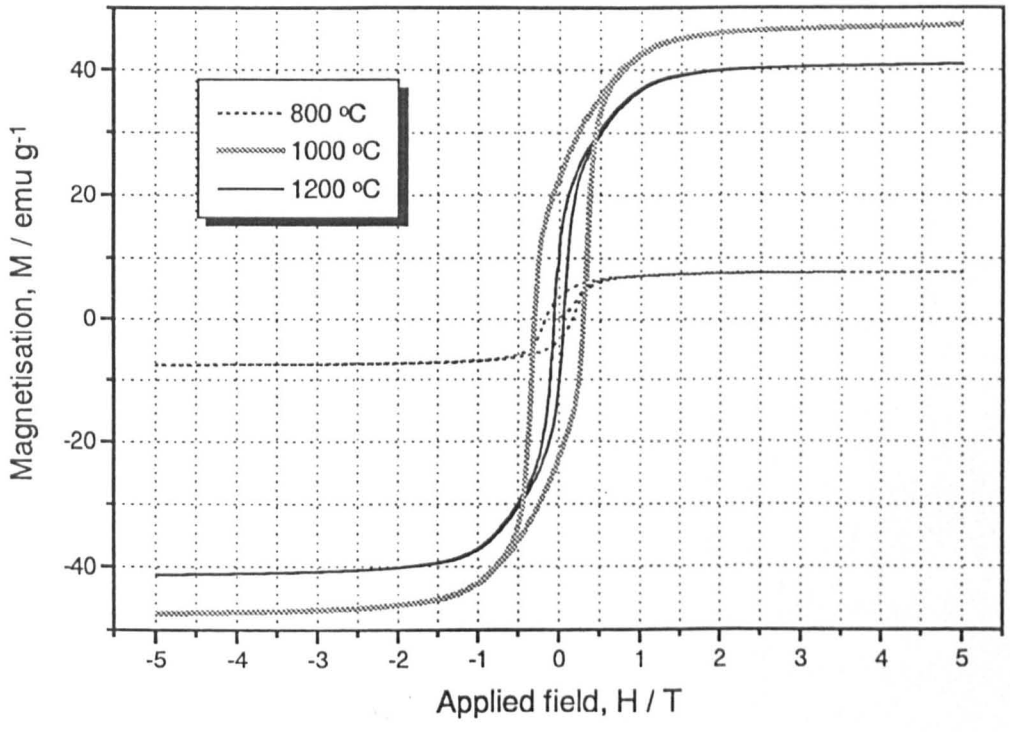

Fig. 221 The hysteresis loops for random $SrCoTiFe_{10}O_{19}$ fibres fired to 800 °C, 1000 °C and 1200 °C / 3hr after 1 yr storage.

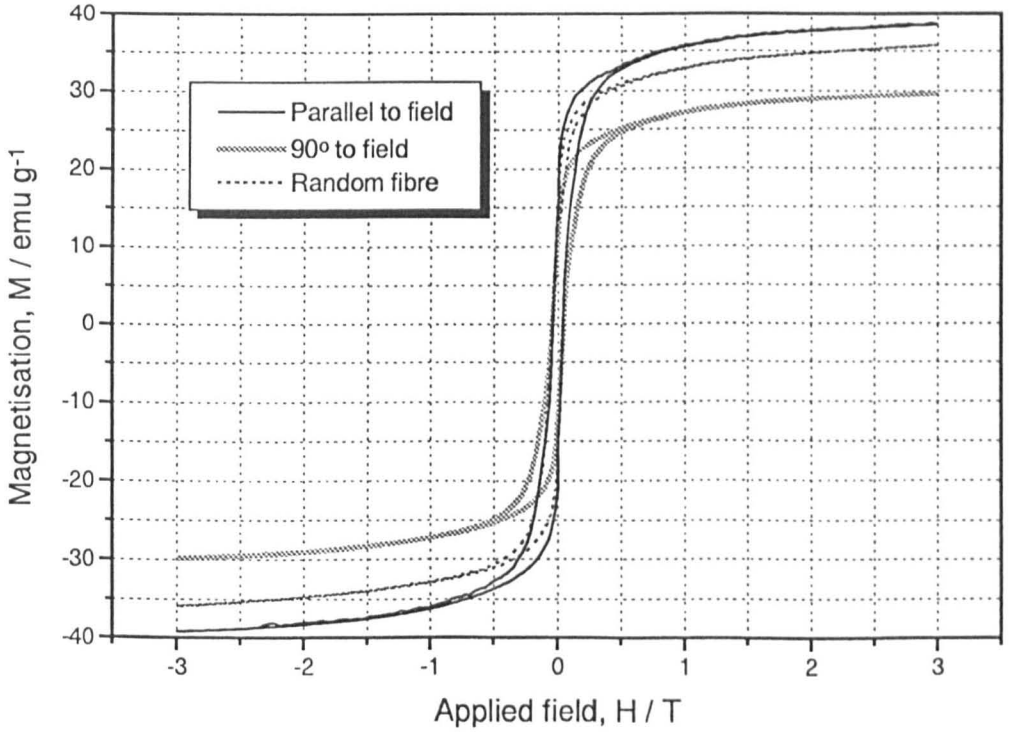

Fig. 222 The hysteresis loops for aligned Co_2Y fibres fired to 1000 °C / 3hr immediately after drying.

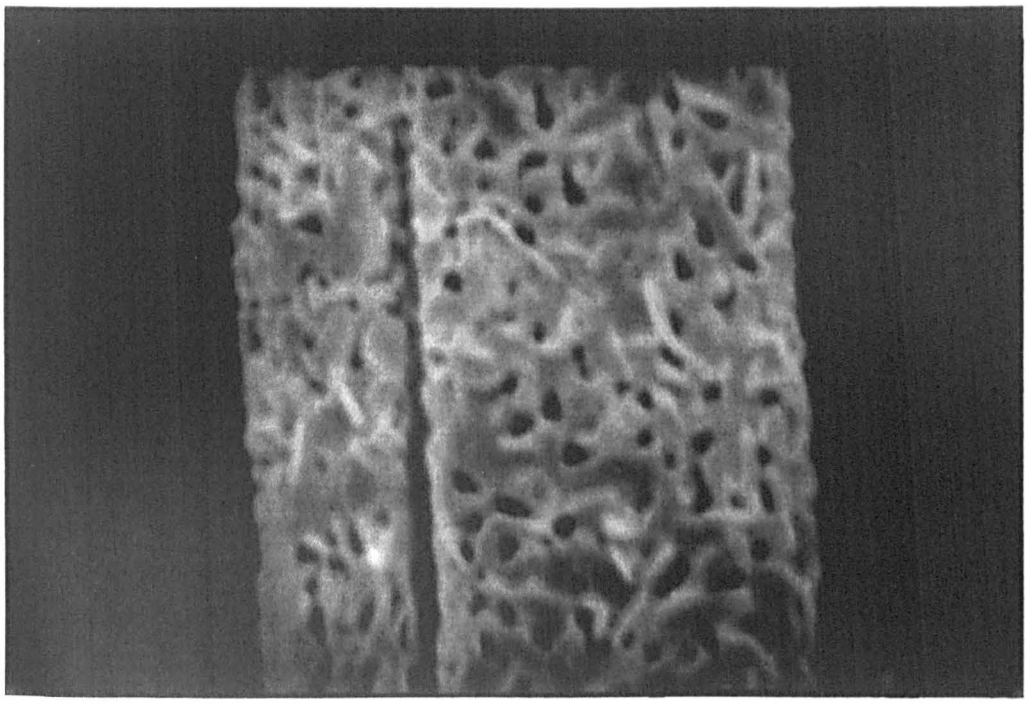

Fig. 223 SEM micrograph of Co_2Y fibres stored for 3 yr and fired to 1000 °C / 3hr.

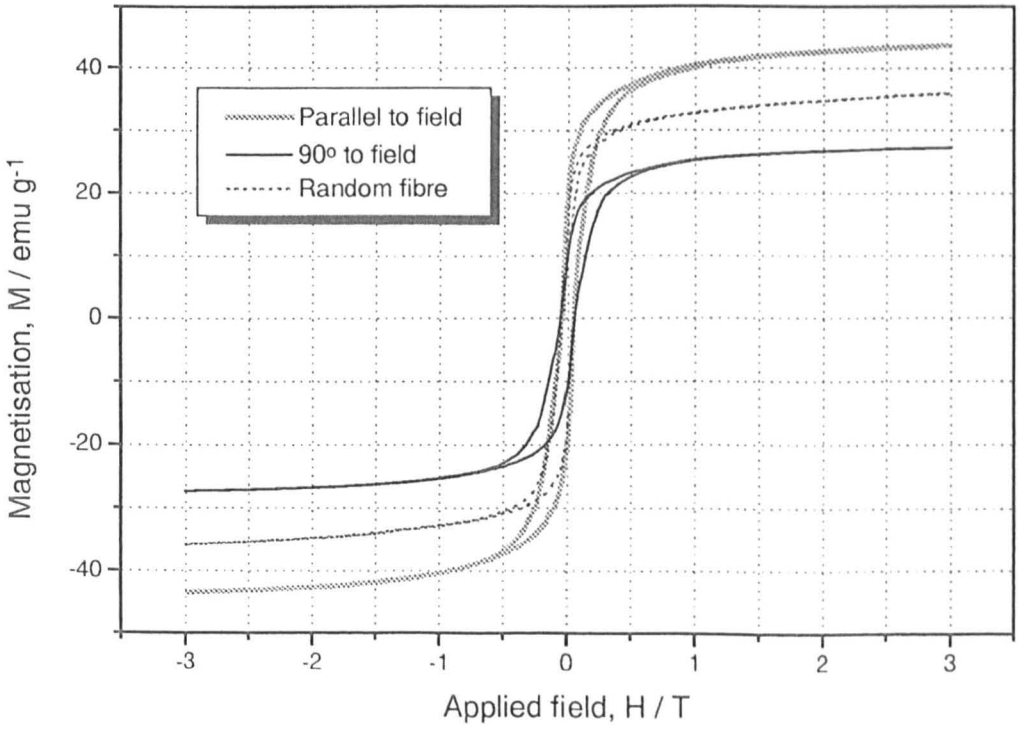

Fig. 224 The hysteresis loops for aligned and random Co_2Y fibres fired to 1000 °C / 3hr after 3 yr storage.

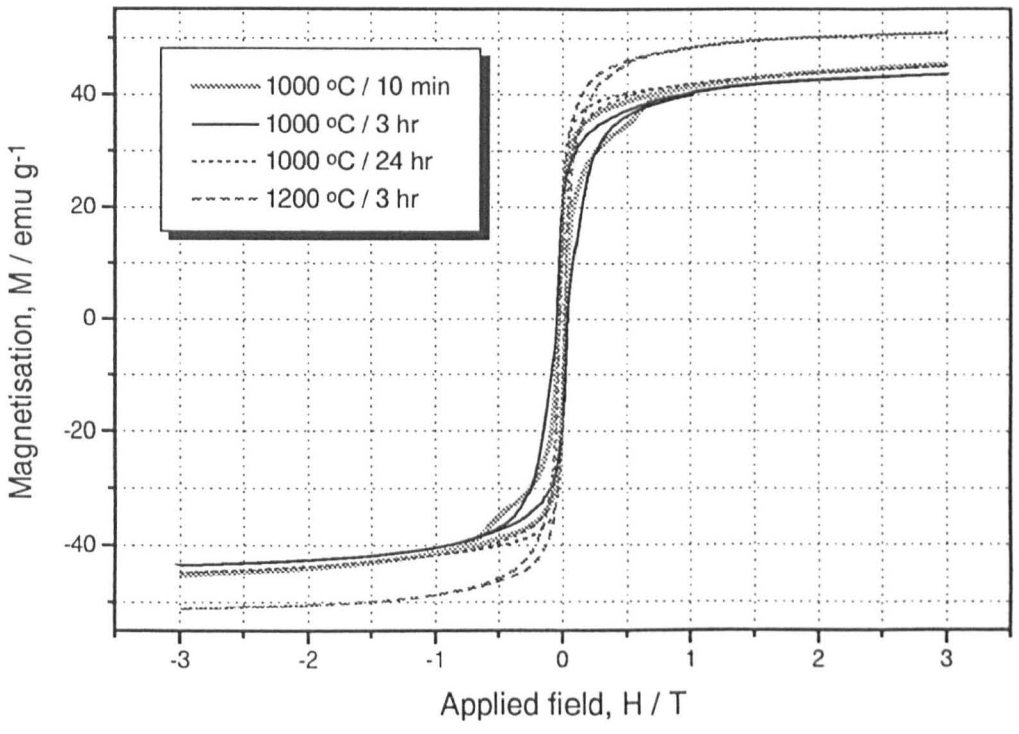

Fig. 225 The hysteresis loops for Co_2Y fibres, stored for 3 yr and aligned || to H, and fired to 1000 °C / 10 min, 3hr and 24 hr, and 1200 °C / 3hr.

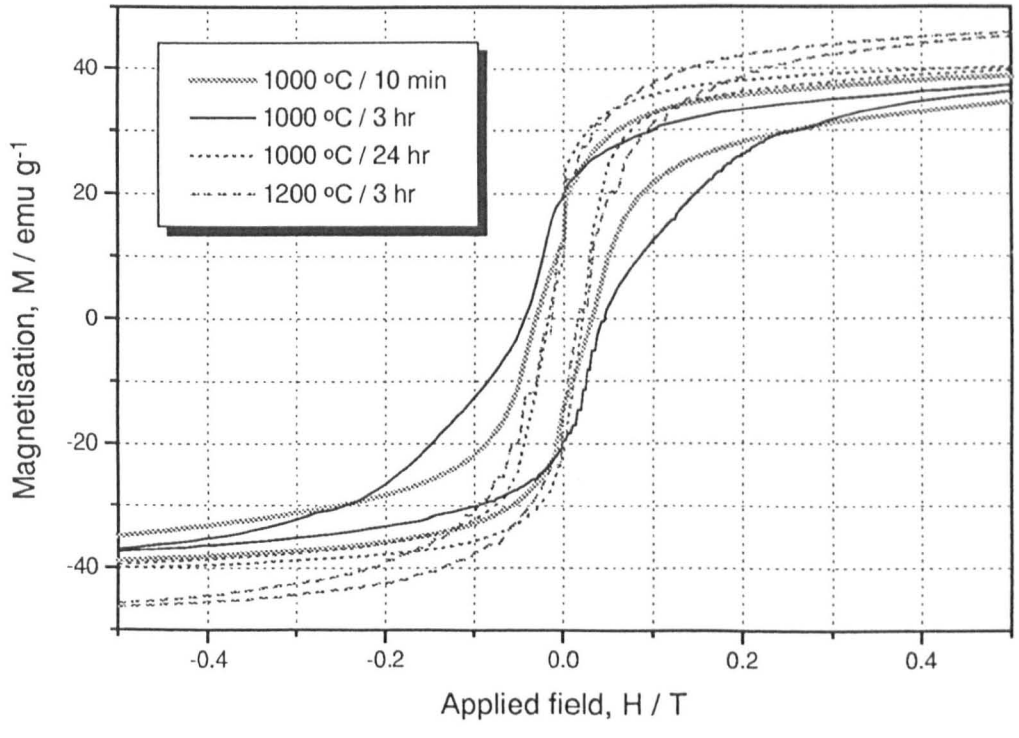

Fig. 226 Detail of the hysteresis loops from figure 225, showing change in H_c and loop shape.

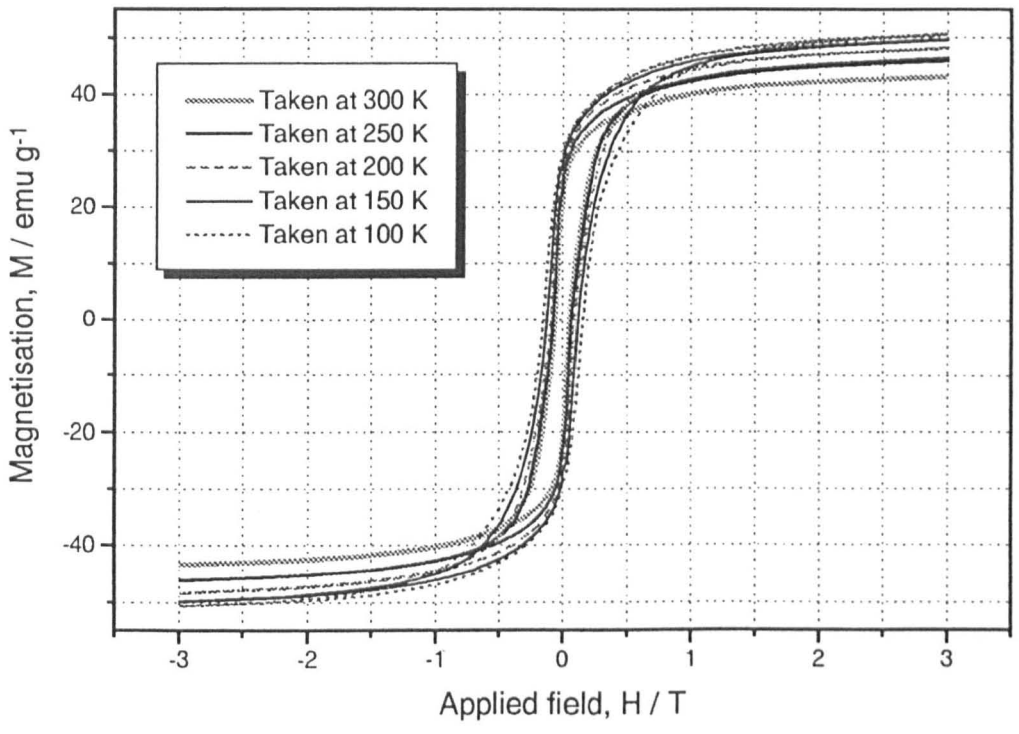

Fig. 227 Change in the hysteresis loops for Co_2Y fibres, aligned || to H and fired to 1000 °C / 3hr, with measurement temperature.

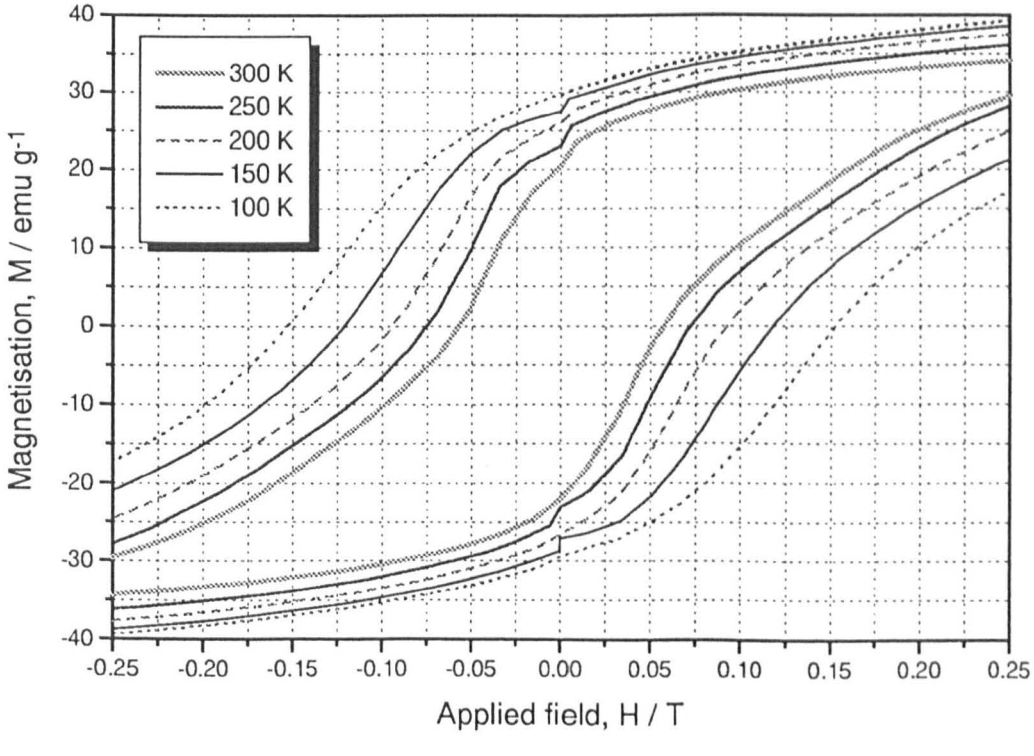

Fig. 228 Detail of the hysteresis loops from figure 227, showing change in H_c and M_r.

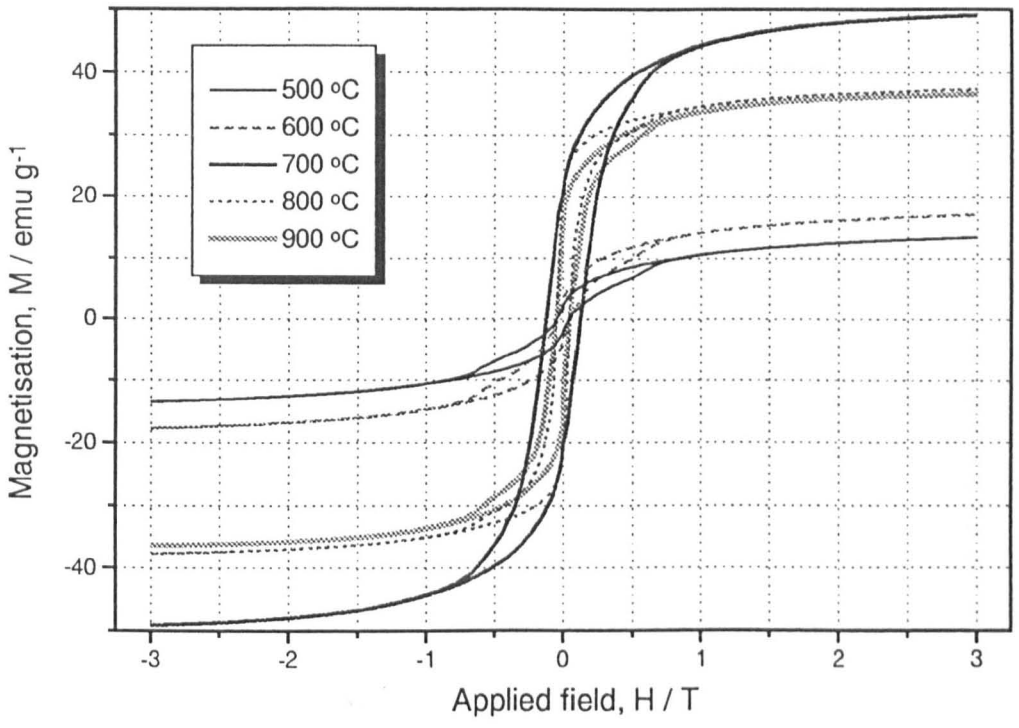

Fig. 229 Hysteresis loops of Co_2Y fibres, aligned || to H and after 3 yr storage, steamed at 500, 600, 700, 800 and 900 °C / 3hr.

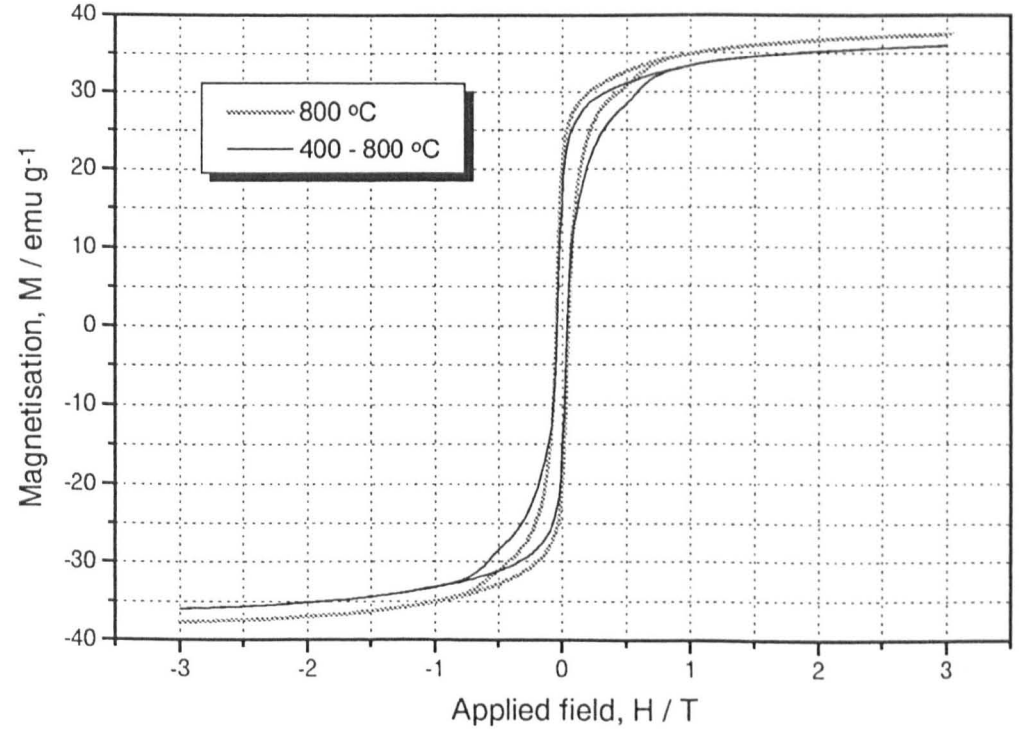

Fig. 230 Hysteresis loops of Co_2Y fibres, aligned || to H and after 3 yr storage, steamed at 400 - 800 and 800 °C / 3hr.

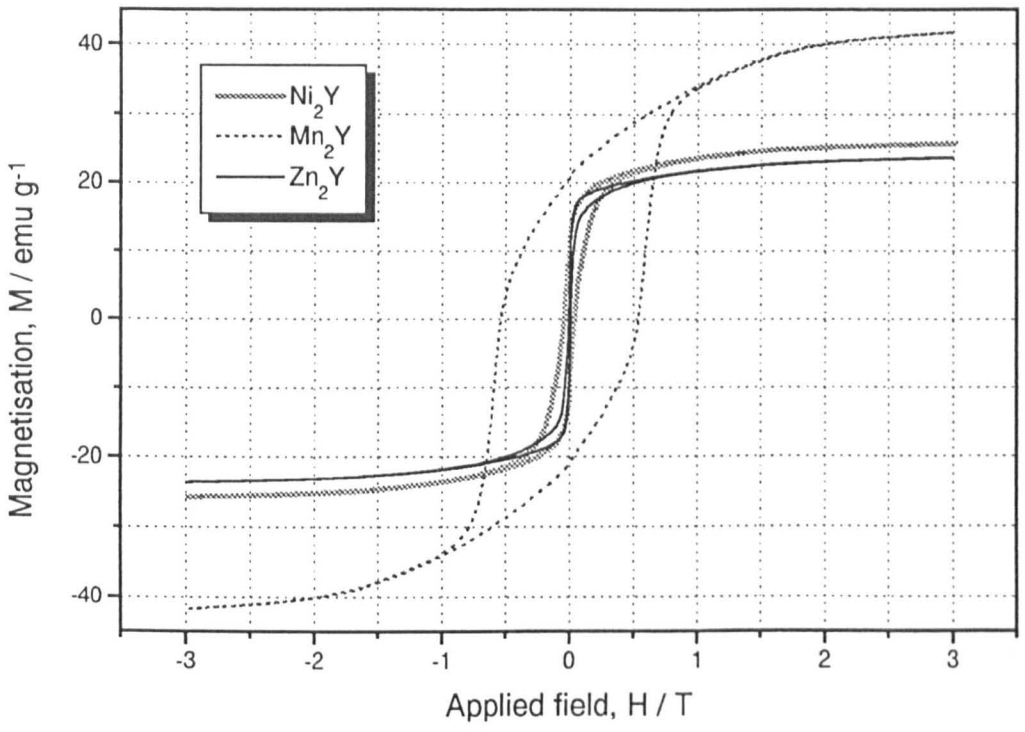

Fig. 231 Hysteresis loops of random Ni_2Y, Mn_2Y and Zn_2Y fibres fired to 1000 °C / 3hr.

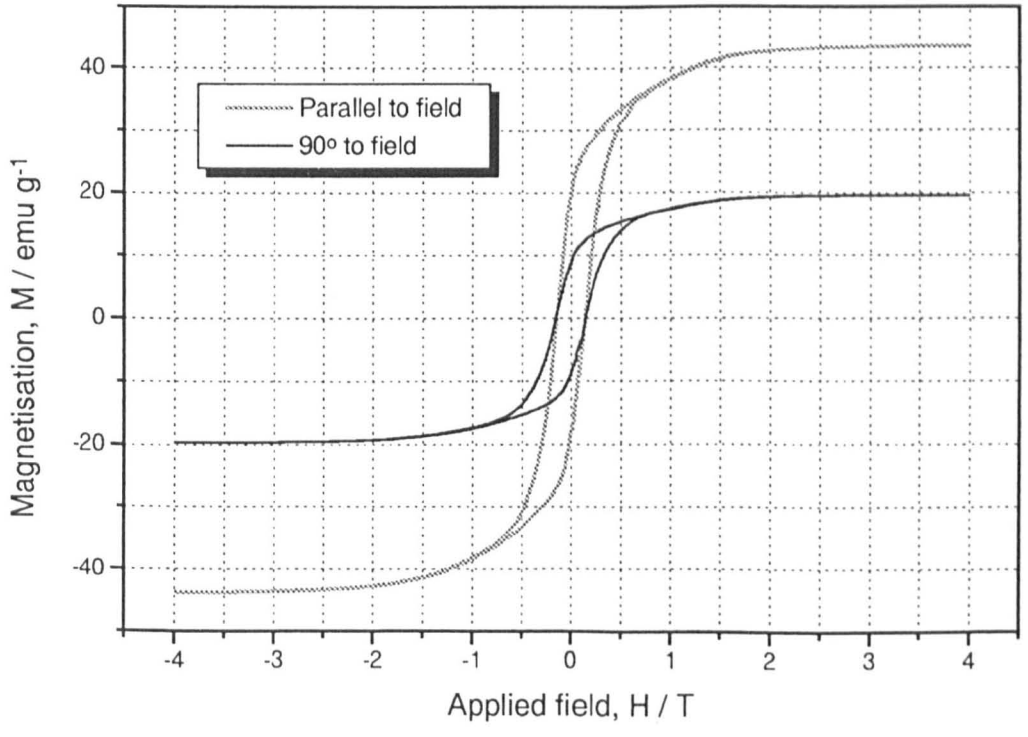

Fig. 232 Hysteresis loops of Co_2Z fibre aligned || to H and fired at 1000 °C / 3hr.

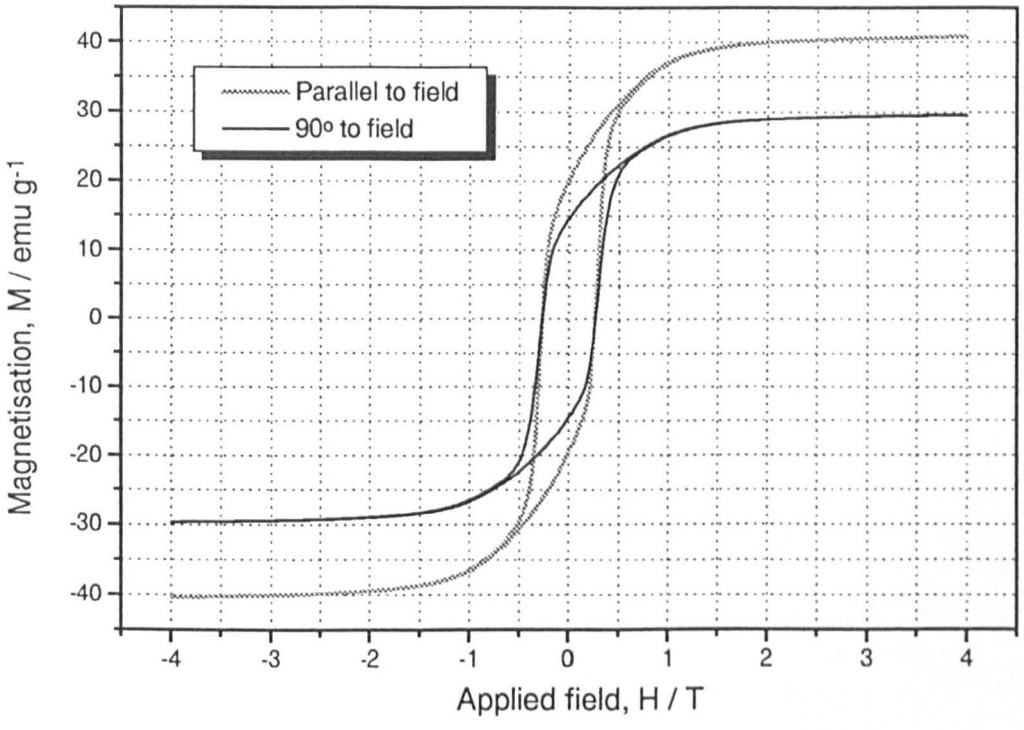

Fig. 233 Hysteresis loops of Co_2Z fibre aligned || to H and fired at 1000 °C / 100 hr.

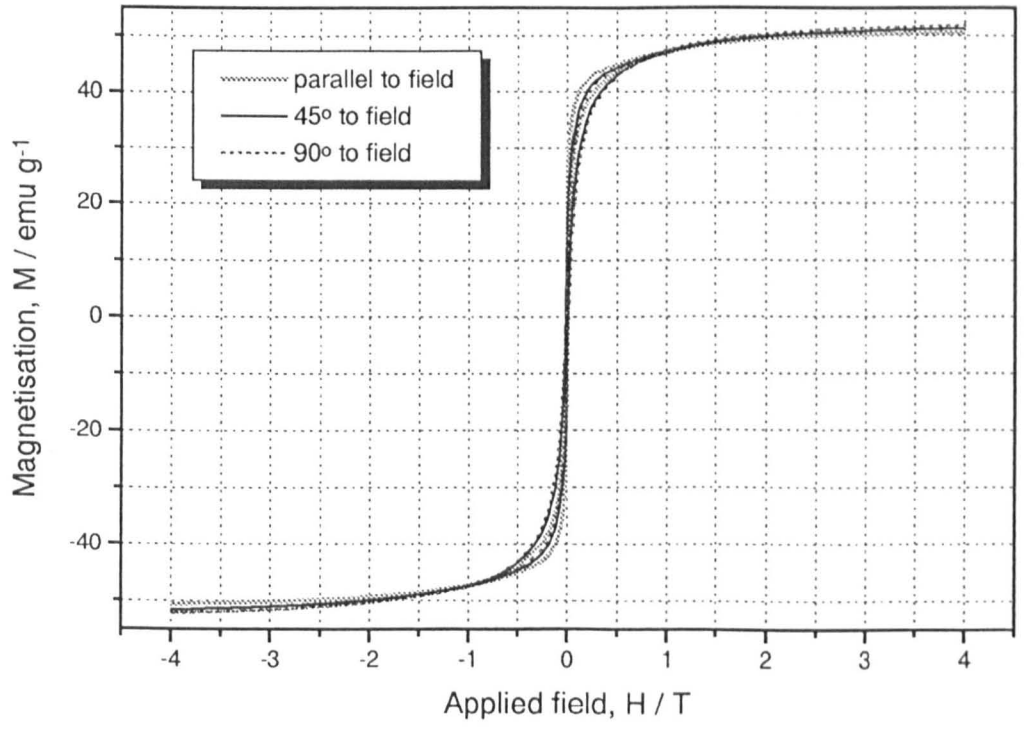

Fig. 234 Hysteresis loops of old aligned Co_2Z fibre fired at 1250 °C / 3hr.

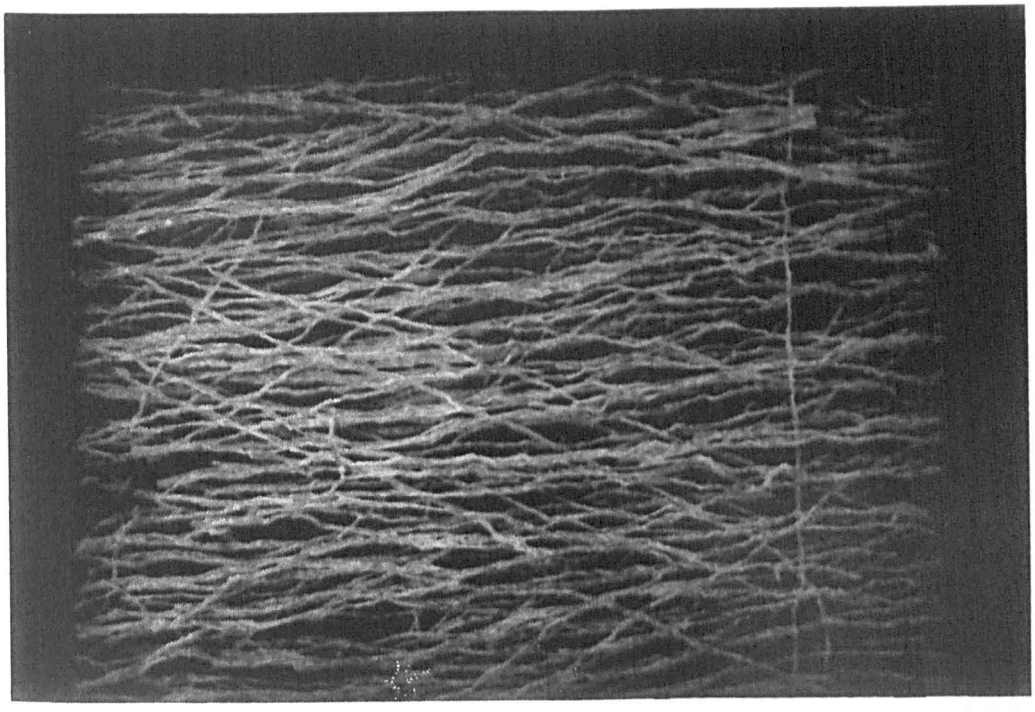

Fig. 235 SEM micrograph of the wavy, twig-like nature of the ostensibly well aligned Co_2Z fibre, as a result of DGG at 1250 °C / 3hr.

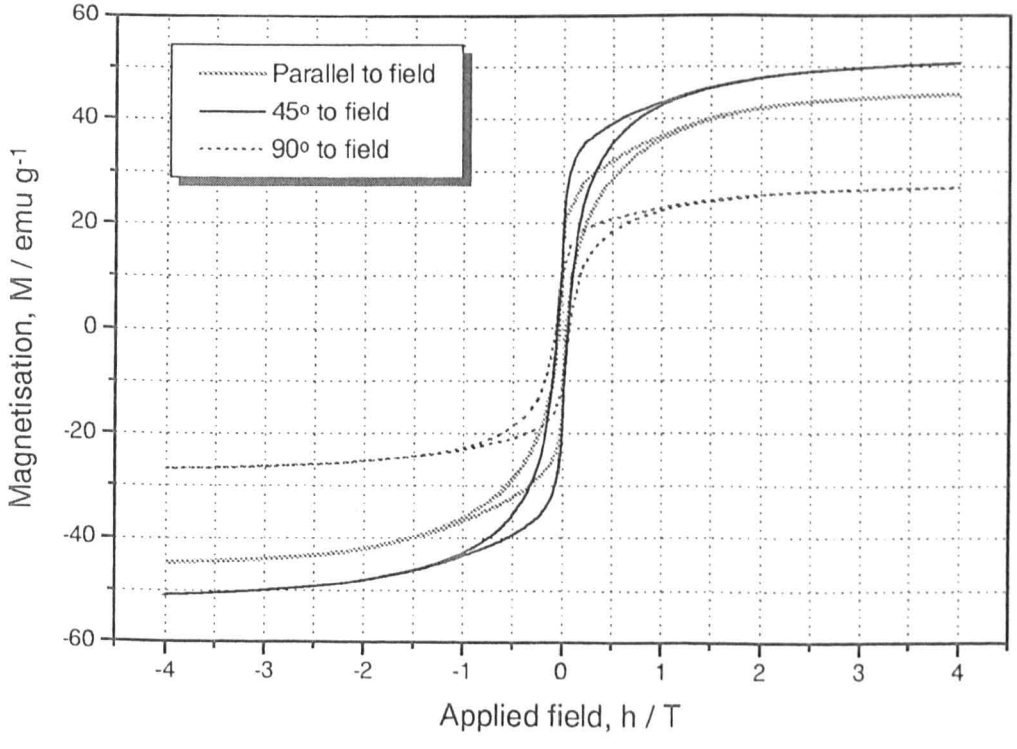

Fig. 236 Hysteresis loop of aligned poor Co_2Z fibre, with high Cl^- content, fired at 1250 °C / 3hr.

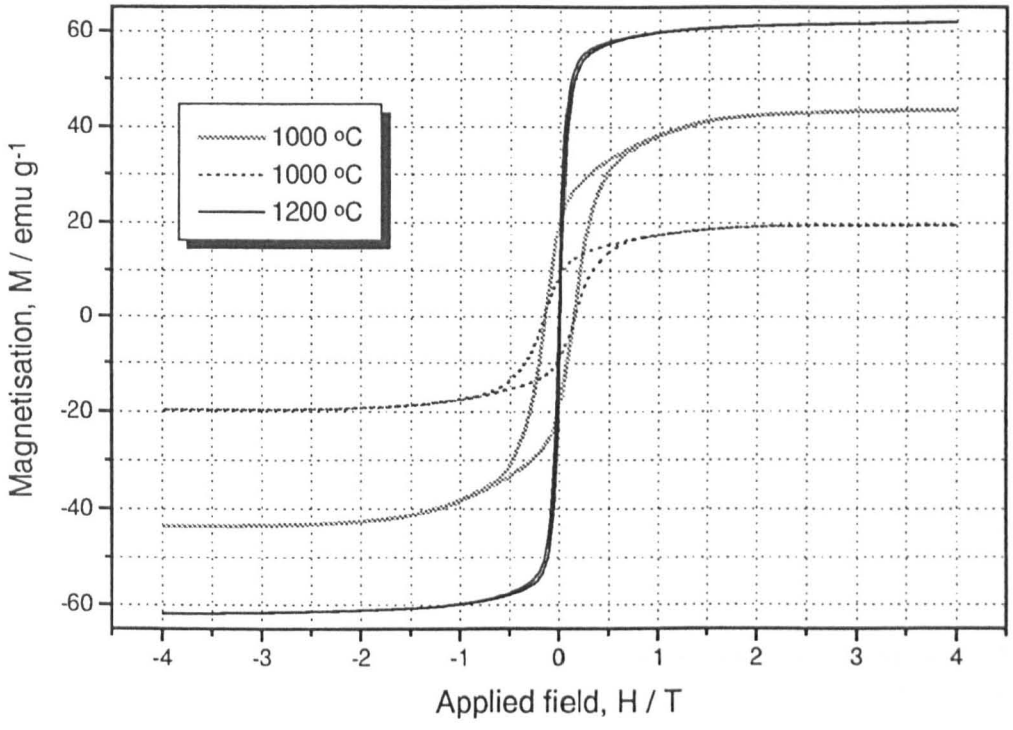

Fig. 237 Hysteresis loops of aligned pure Co_2Z fibre, with low Cl^- content, fired at 1000 °C and 1250 °C / 3hr.

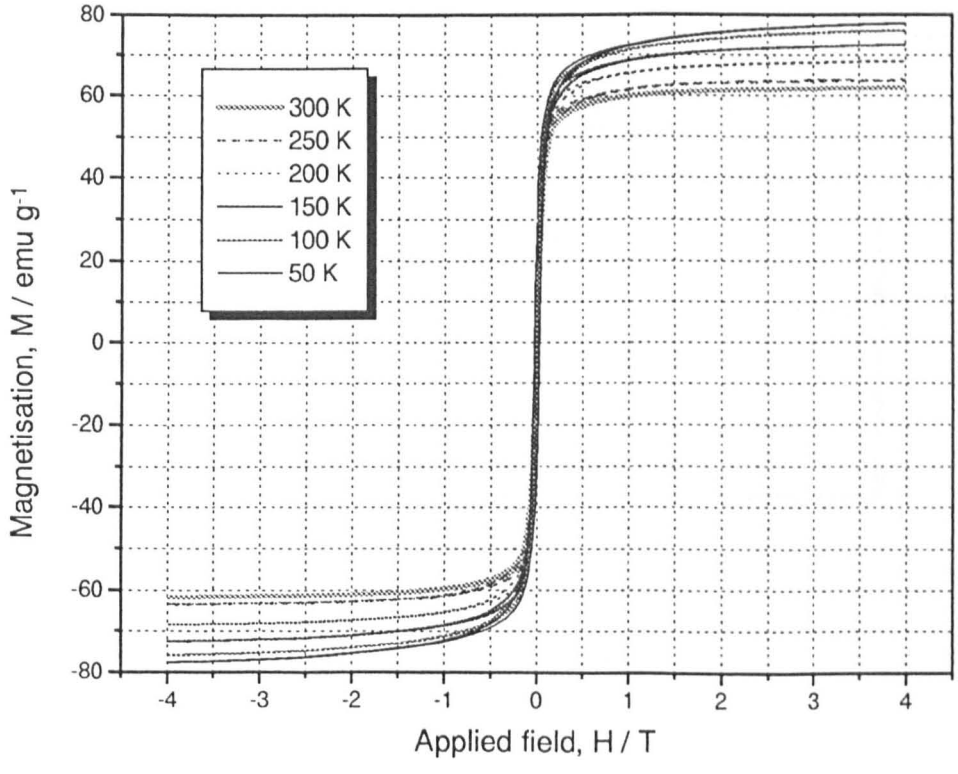

Fig. 238 Change in the hysteresis loops for pure Co_2Z fibres, fired to 1250 °C / 3hr, with measurement temperature.

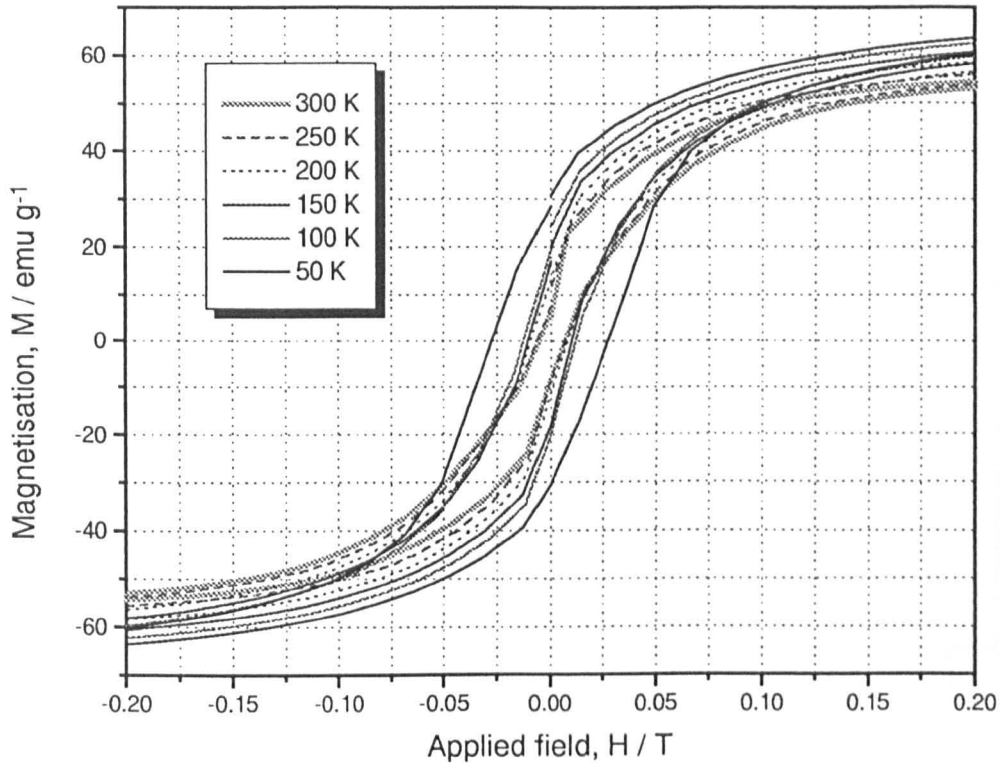

Fig. 239 Detail of the hysteresis loops from figure 238, showing change in H_c, M_r and lobe width.

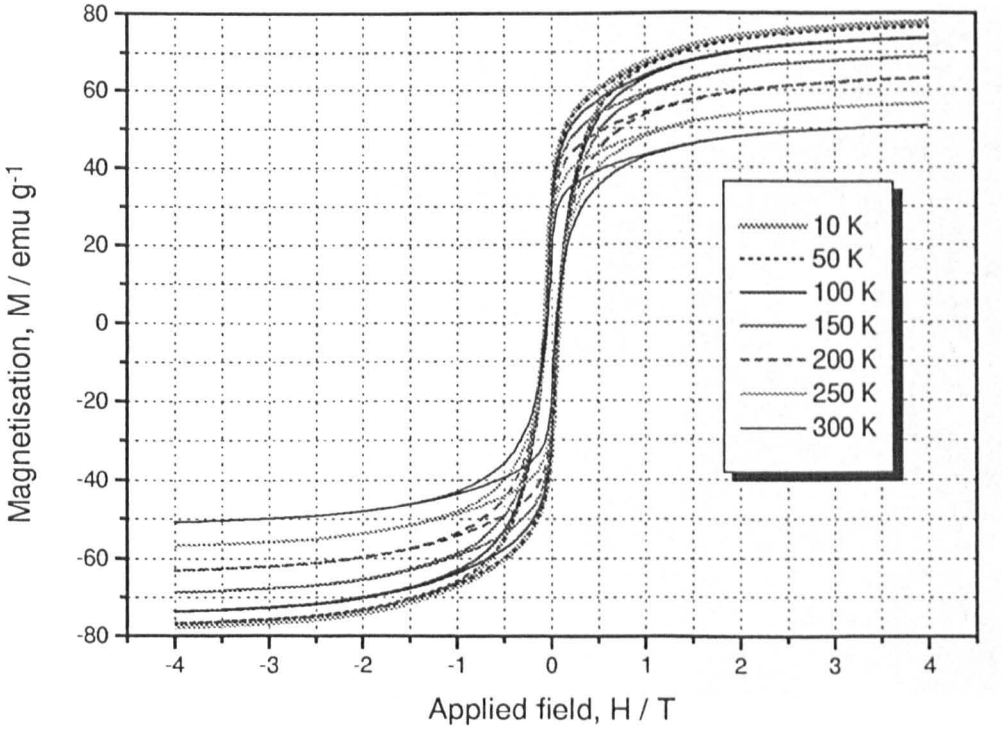

Fig. 240 Change in the hysteresis loops for poor Co_2Z fibres, fired to 1250 °C / 3hr, with measurement temperature.

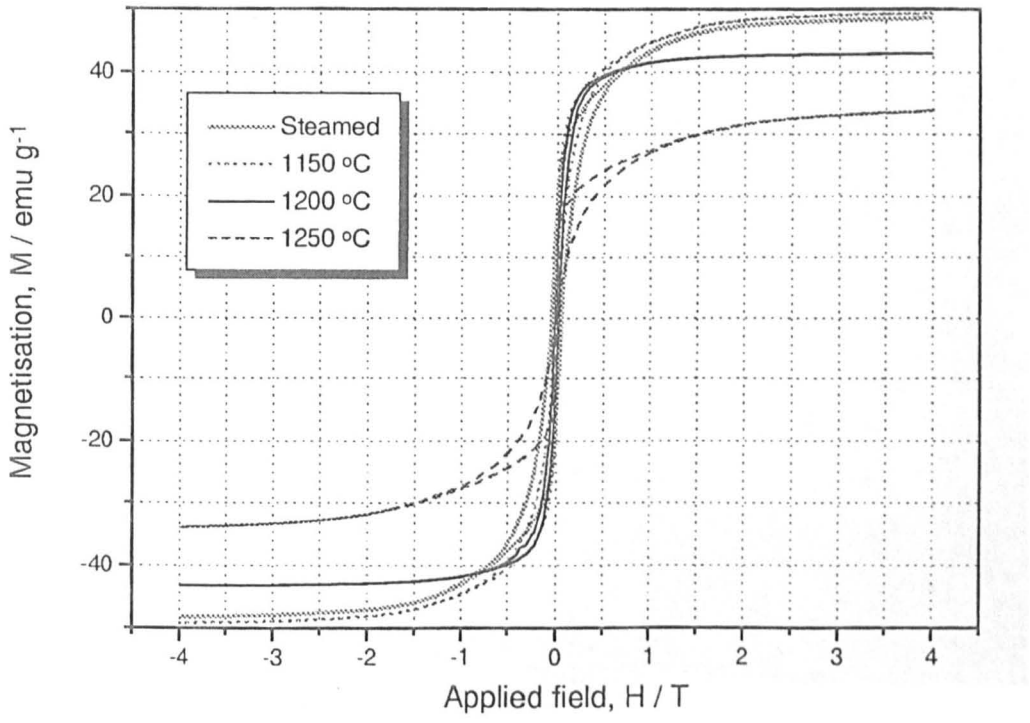

Fig. 241 Hysteresis loops of Co_2Z fibres aligned || to H, steamed at 900 °C / 3hr and then fired to 1150, 1200 and 1250 °C / 3hr.

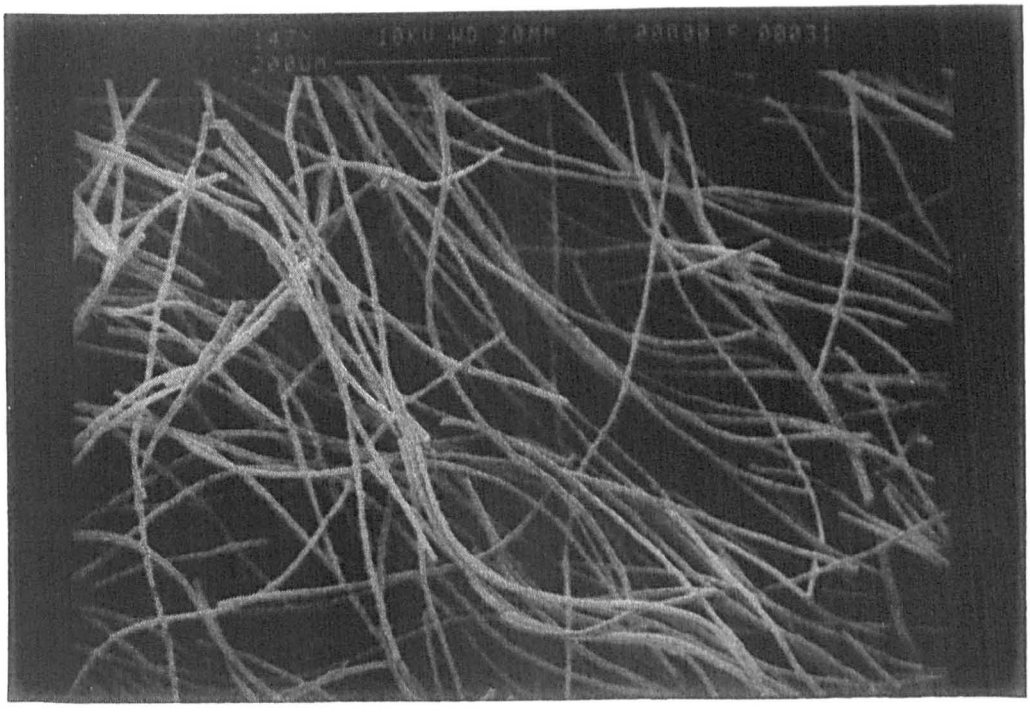

Fig. 242 SEM micrograph showing the loss of alignment in Co_2Z fibres steamed at 900 °C / hr.

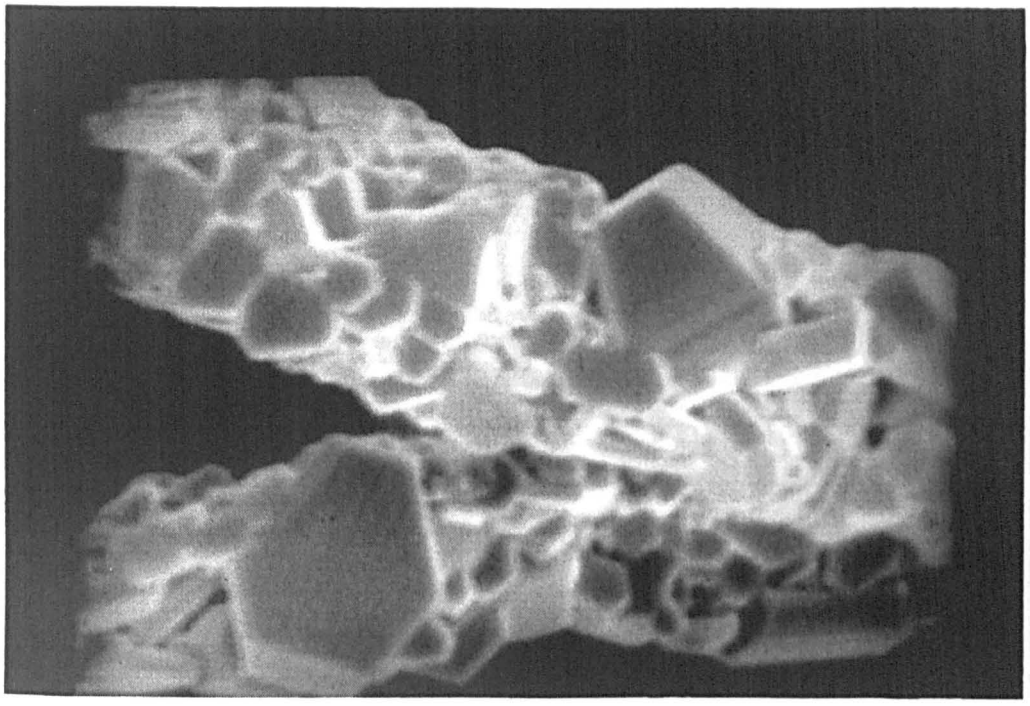

Fig. 243 SEM micrograph showing the microstructure of Co_2Z fibres steamed at 900 °C / 3hr and then fired to 1150 °C / 3hr.

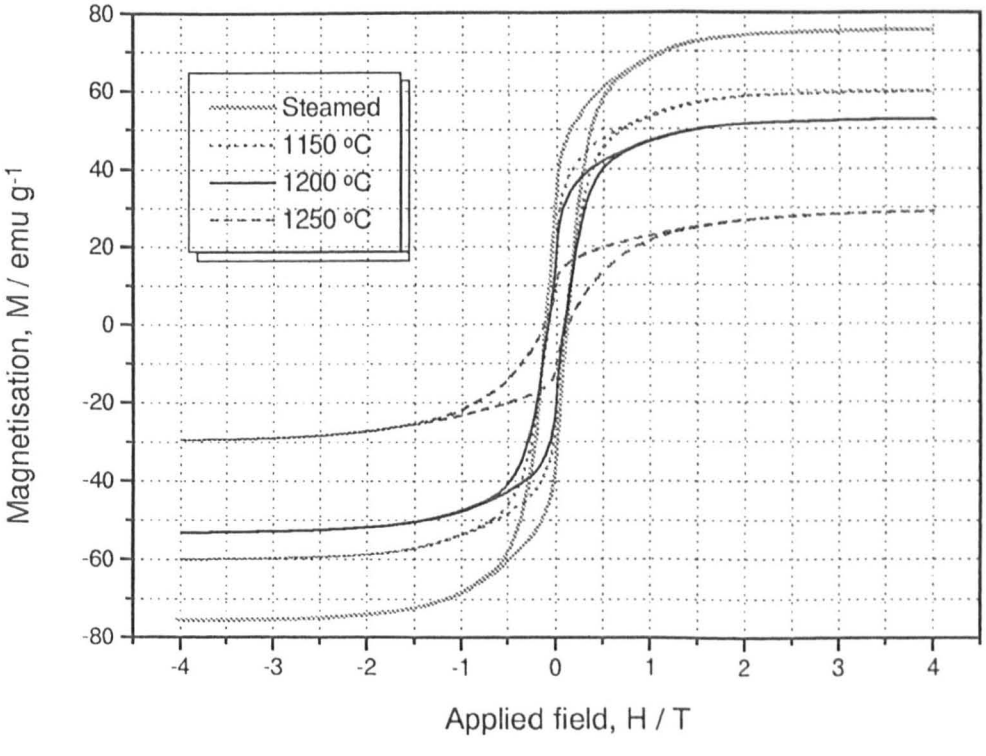

Fig. 244 Hysteresis loops of Co_2Z fibres aligned || to H, steamed from 400 - 900 °C / 3hr and then fired to 1150, 1200 and 1250 °C / 3hr.

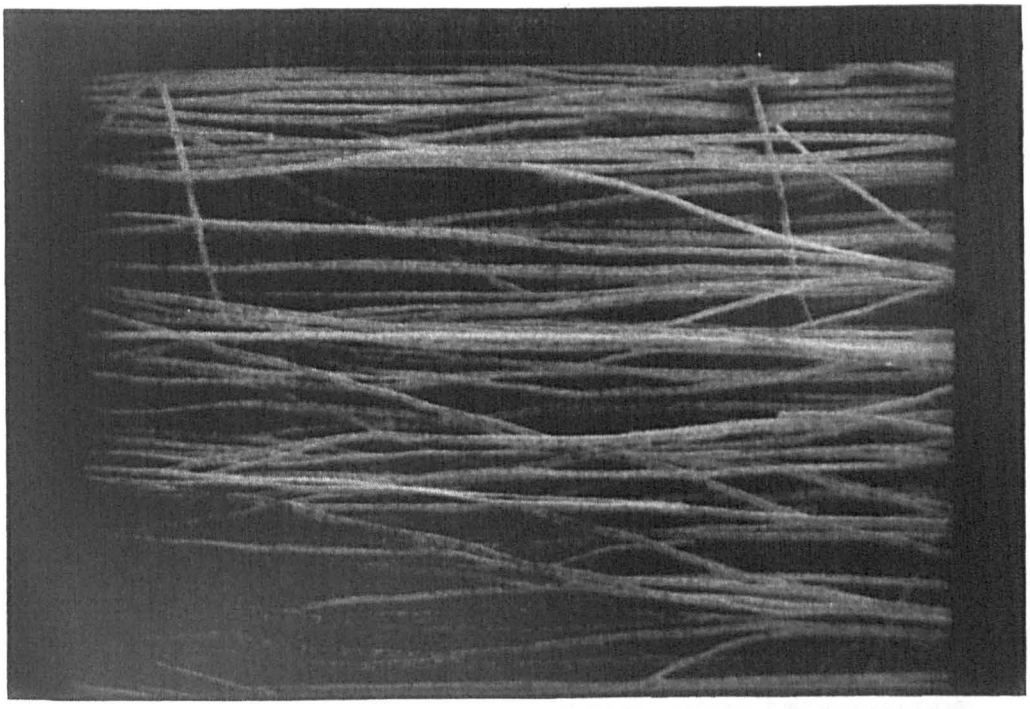

Fig. 245 SEM micrograph showing the alignment of Co_2Z fibres steamed at 900 °C / 3hr after prefiring to 1000 °C / 3hr in air.

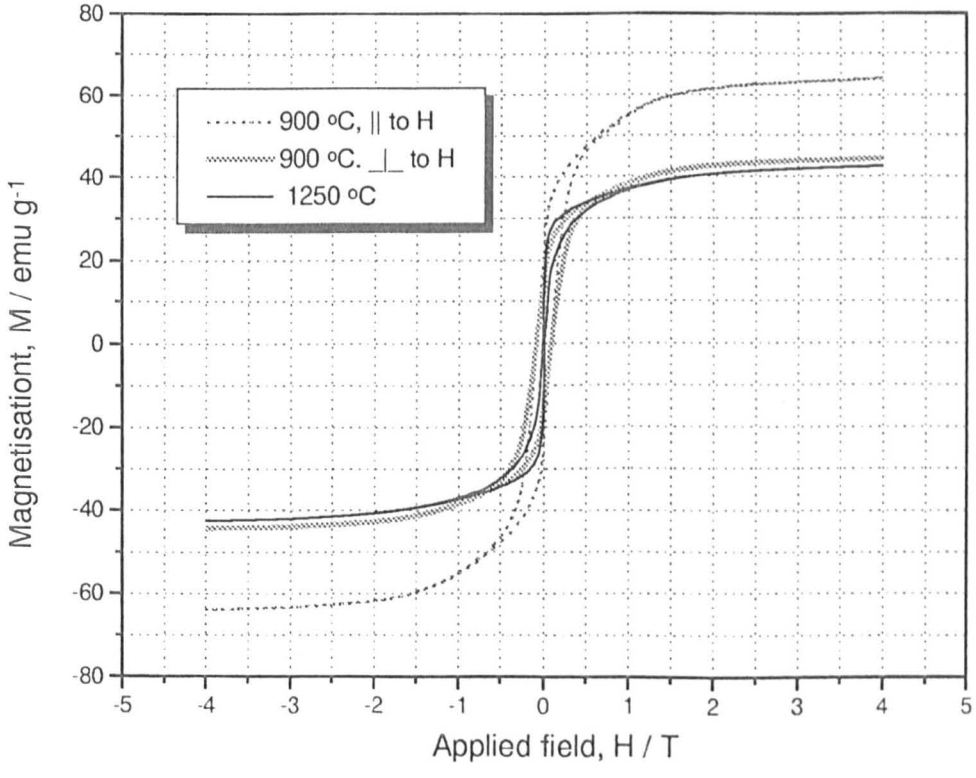

Fig. 246 Hysteresis loops of Co_2Z fibres, prefired to 1000 °C / 3hr and steamed at 900 °C / 3hr aligned || and _|_ to H, and then fired to 1250 °C / 3hr.

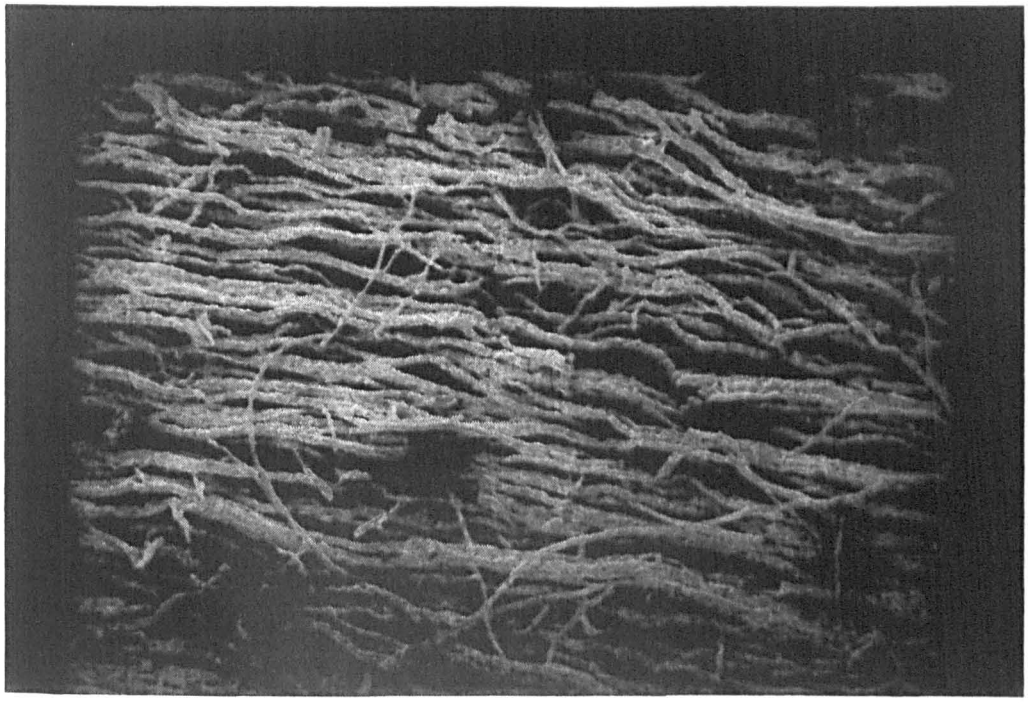

Fig. 247 SEM micrograph showing the alignment of Co_2Z fibres, steamed at 900 °C / 3hr after prefiring to 1000 °C / 3hr in air, fired to 1250 °C / 3hr.

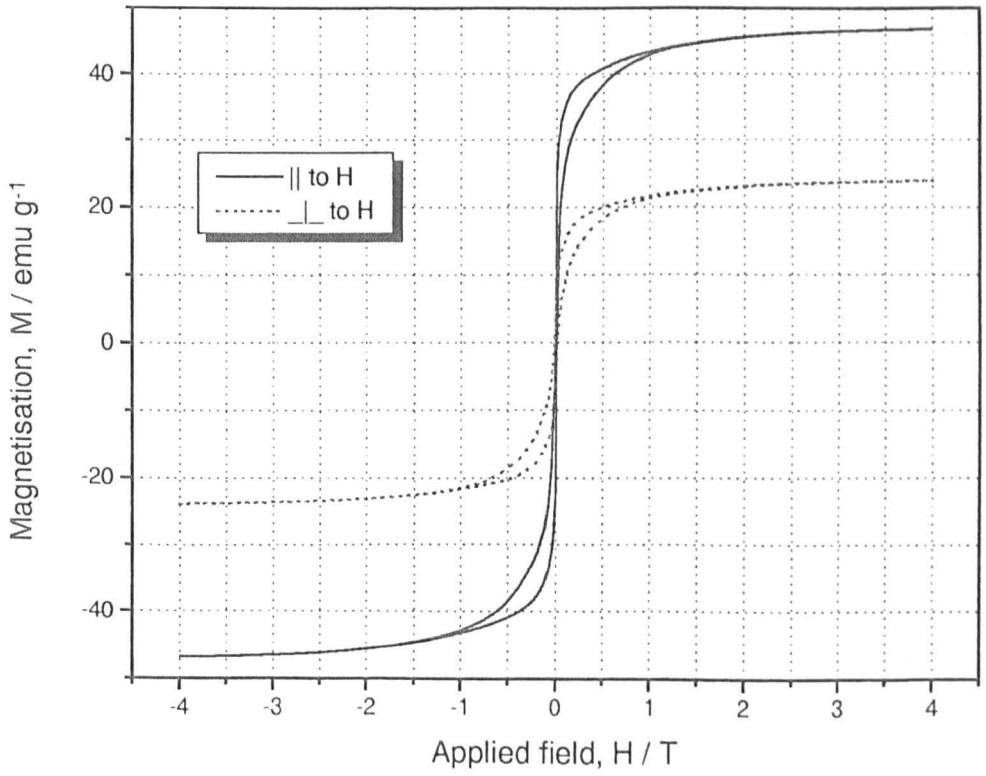

Fig. 248 Hysteresis loops of aligned 0.67% CaO doped Co_2Z fibre fired at 1175 °C / 3hr.

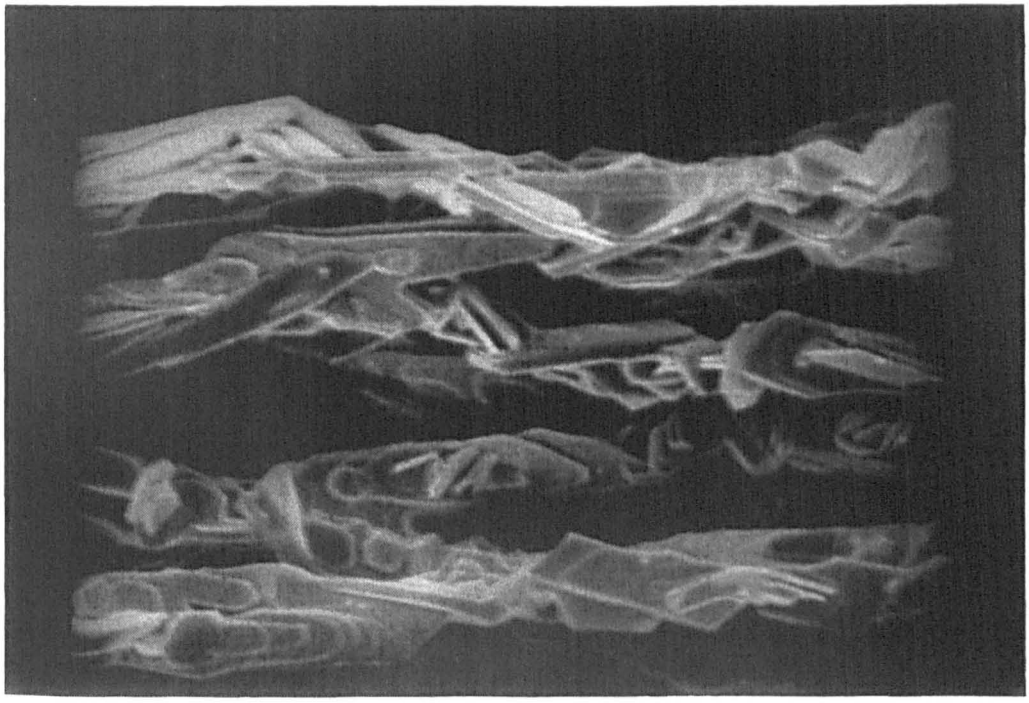

Fig. 249 SEM micrograph of 0.67% CaO doped Co_2Z fibre fired at 1200 °C / 3hr, demonstrating better alignment than undoped Co_2Z.

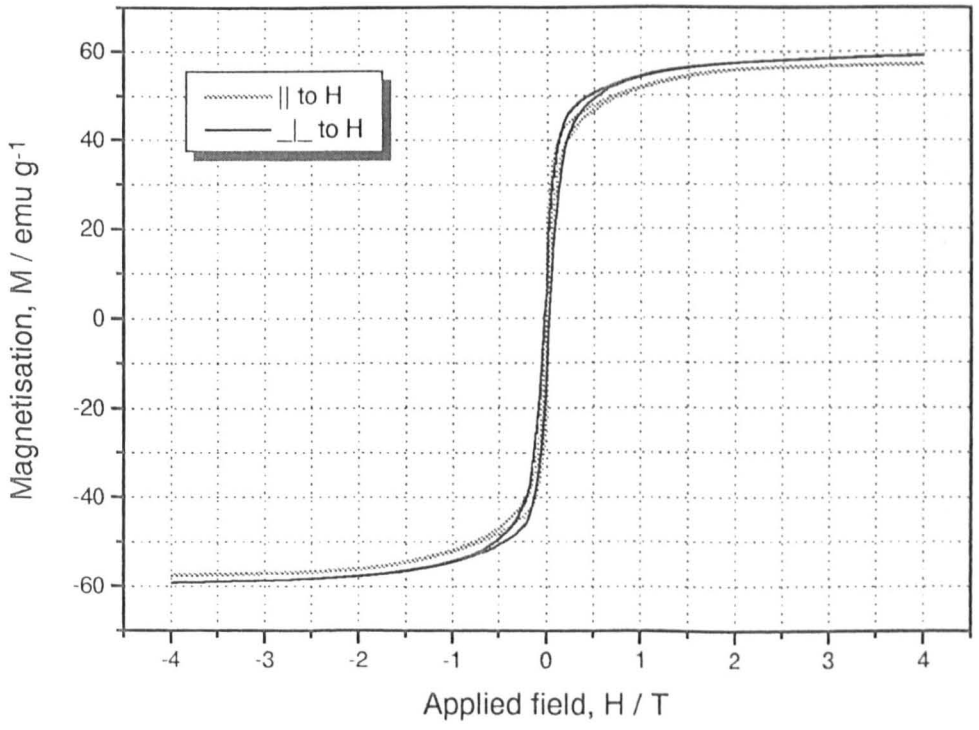

Fig. 250 Hysteresis loops of aligned 0.67% CaO doped Co_2Z fibre fired at 1200 °C / 3hr.

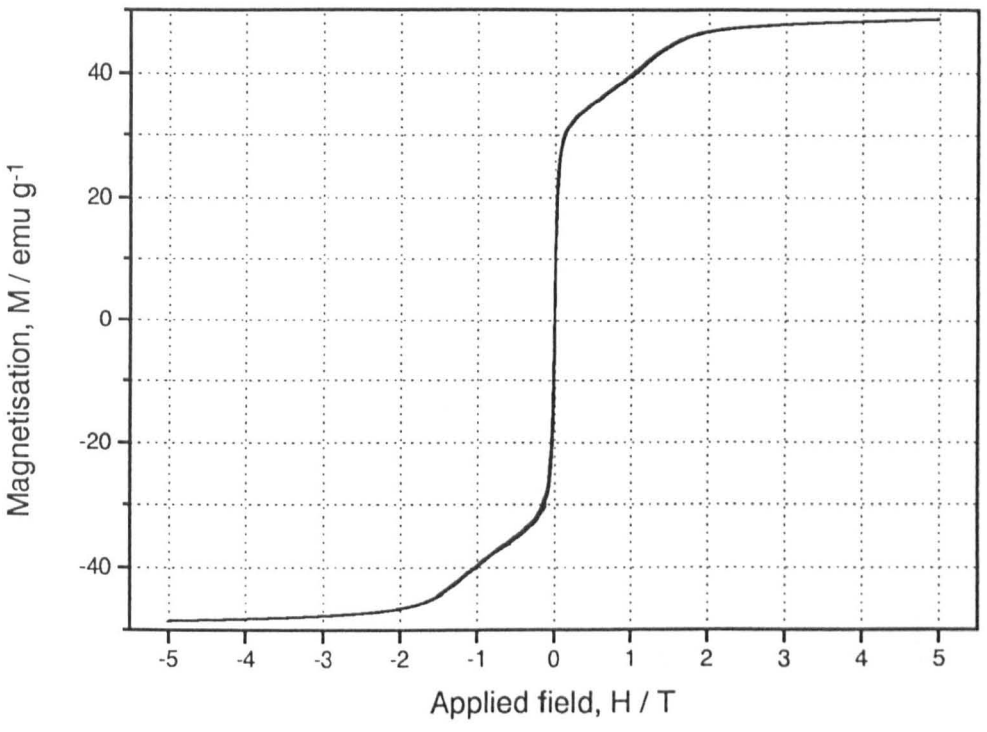

Fig. 251 Hysteresis loop of random Sr_3Co_2Z fibre fired at 1250 °C / 3hr.

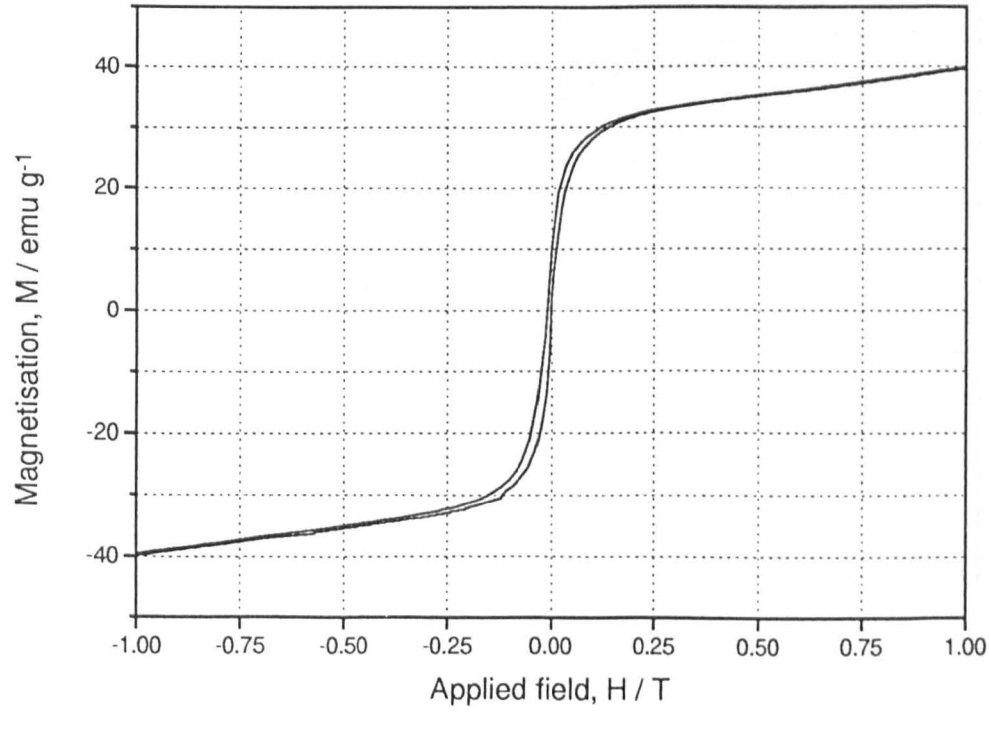

Fig. 252 Expanded view of the hysteresis loop from figure 251.

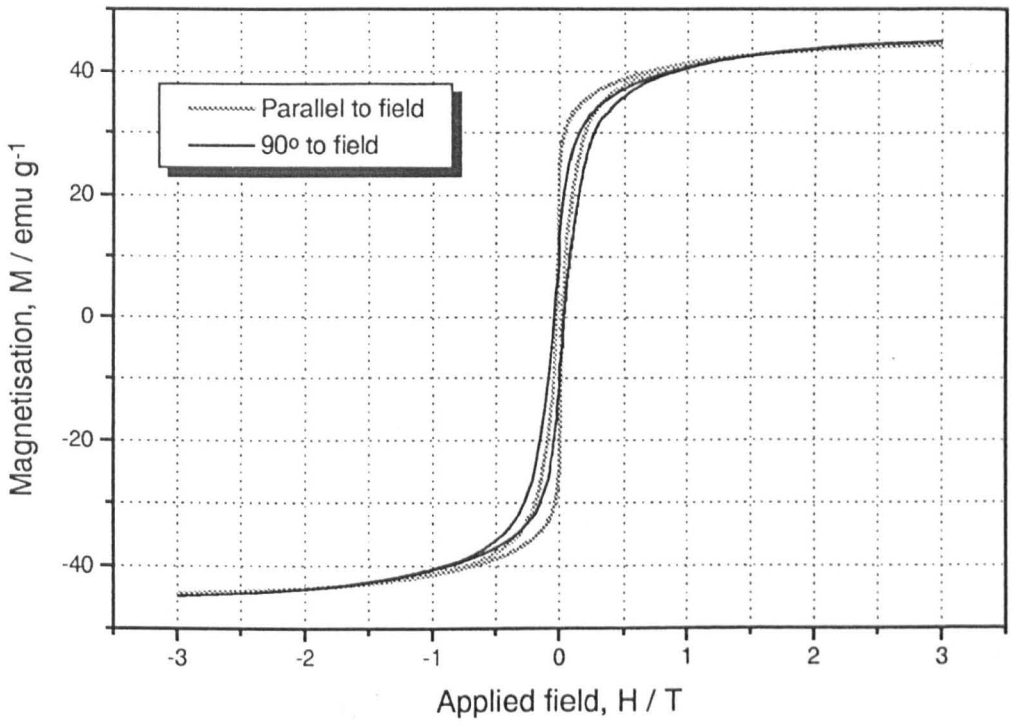

Fig. 253 Hysteresis loops of aligned Co_2W fibre fired at 1250 °C / 3hr.

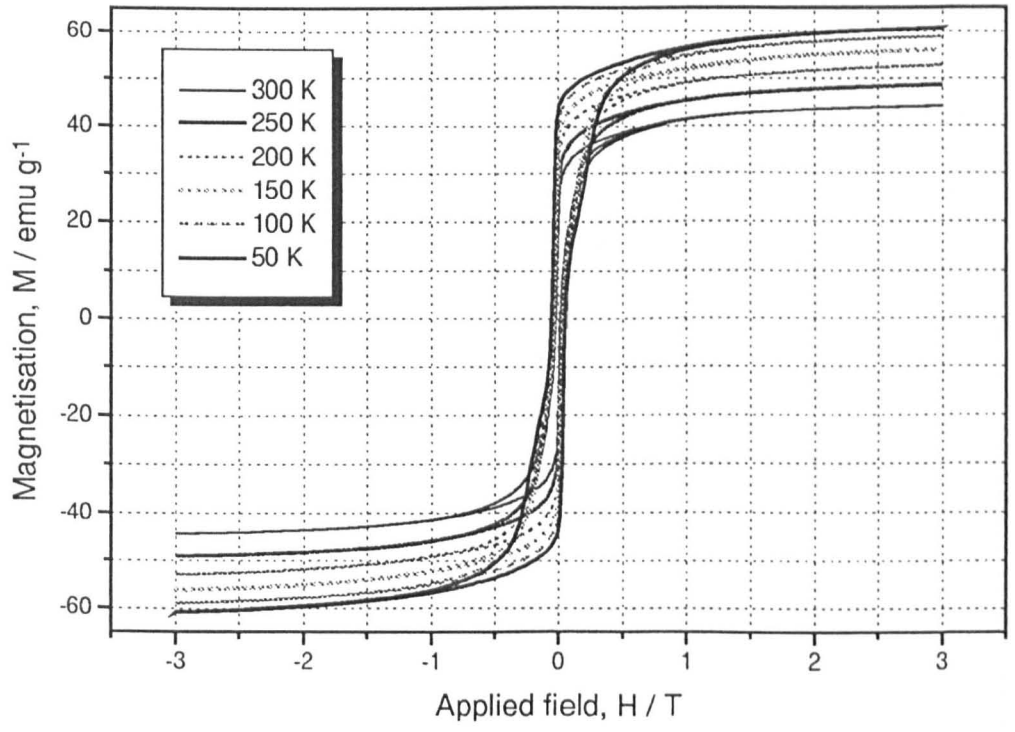

Fig. 254 Change in the hysteresis loops for Co_2W fibres, aligned || to H and fired to 1250 °C / 3hr, with measurement temperature

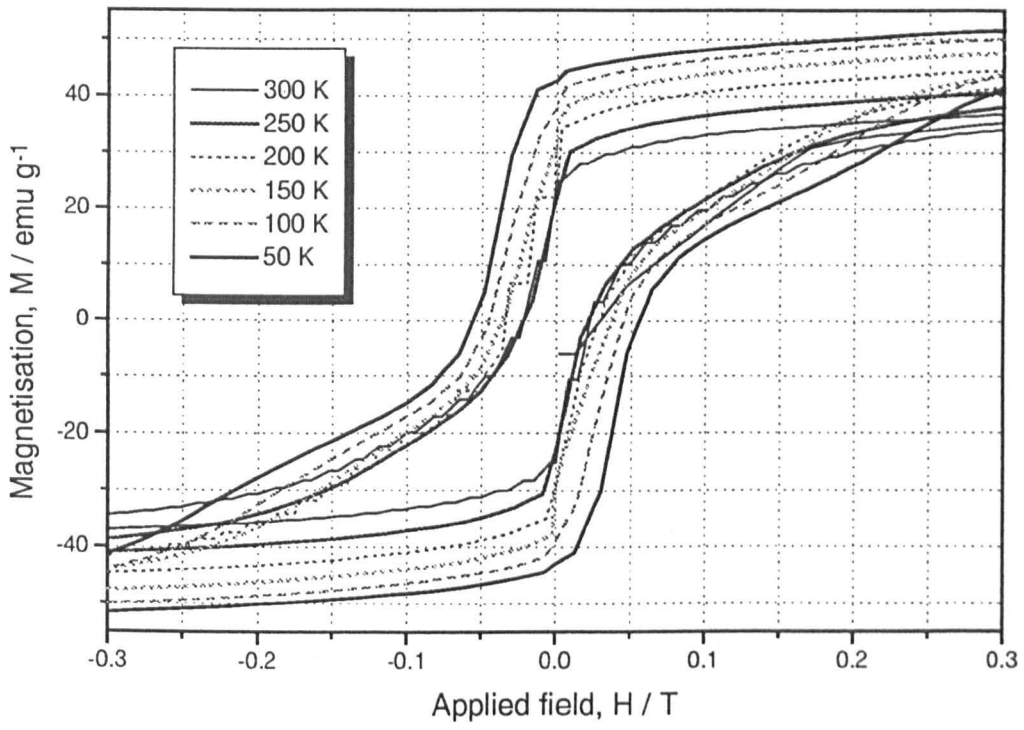

Fig. 255 Detail of the hysteresis loops from figure 254, showing change in H_c, M_r and lobe width.

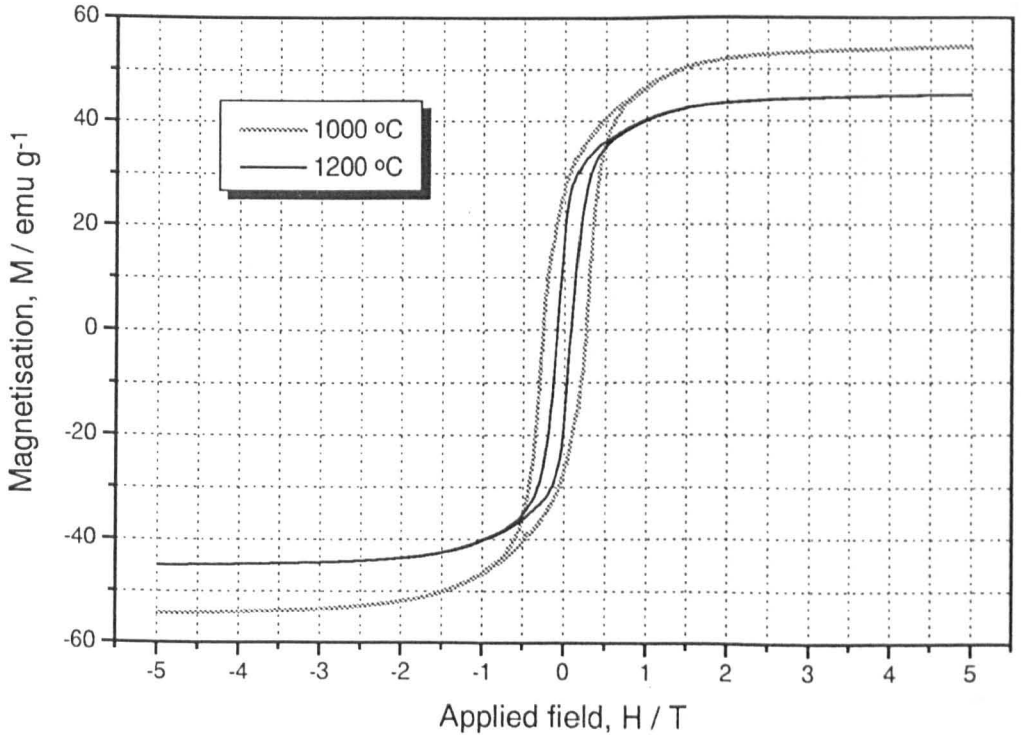

Fig. 256 Hysteresis loops of random Co_2X fibres fired at 1000 and 1200 °C / 3hr.

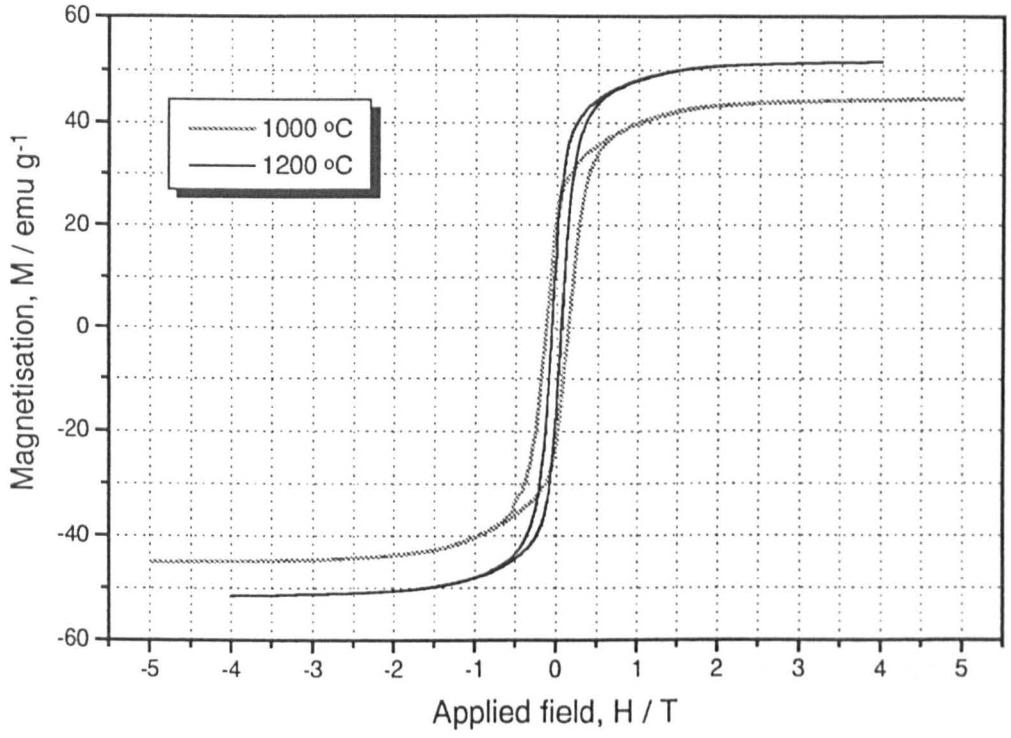

Fig. 257 Hysteresis loops of random Co_2U fibres fired at 1000 and 1200 °C / 3hr.

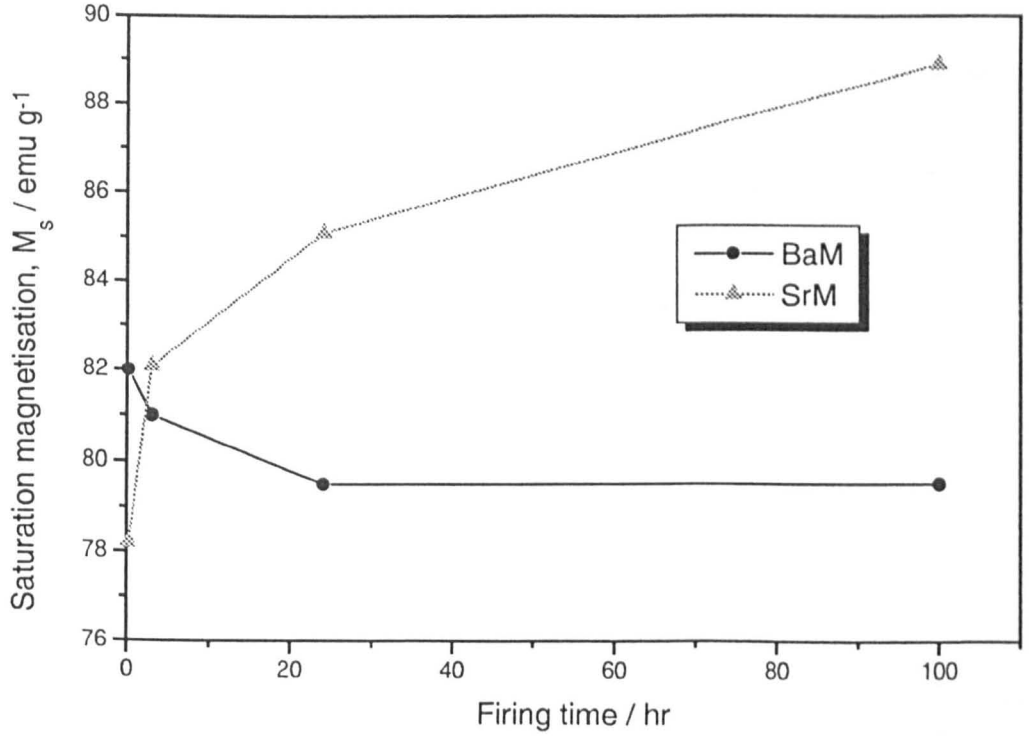

Fig. 258 Change in M_s with firing time at 1000 °C for 3 yr stored BaM (●) and SrM (▲) samples aligned || to H.

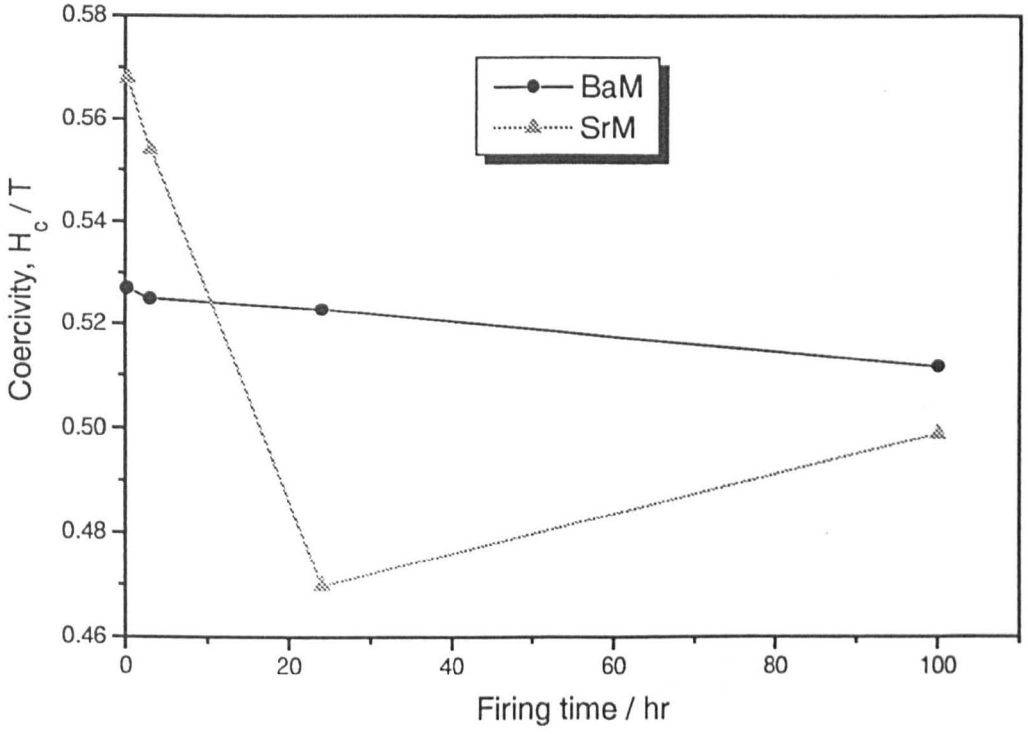

Fig. 259 Change in H_c with firing time at 1000 °C for 3 yr stored BaM (●) and SrM (▲) samples aligned || to H.

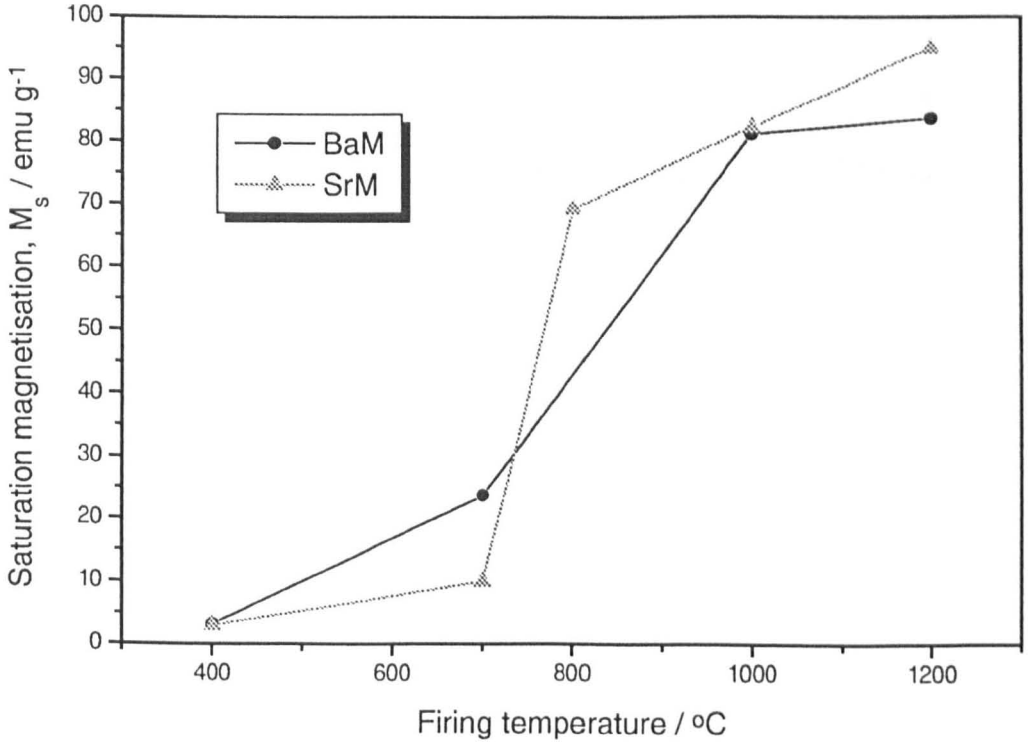

Fig. 260 Change in M_s with firing temperature for 3 yr stored BaM (●) and SrM (▲) samples aligned || to H.

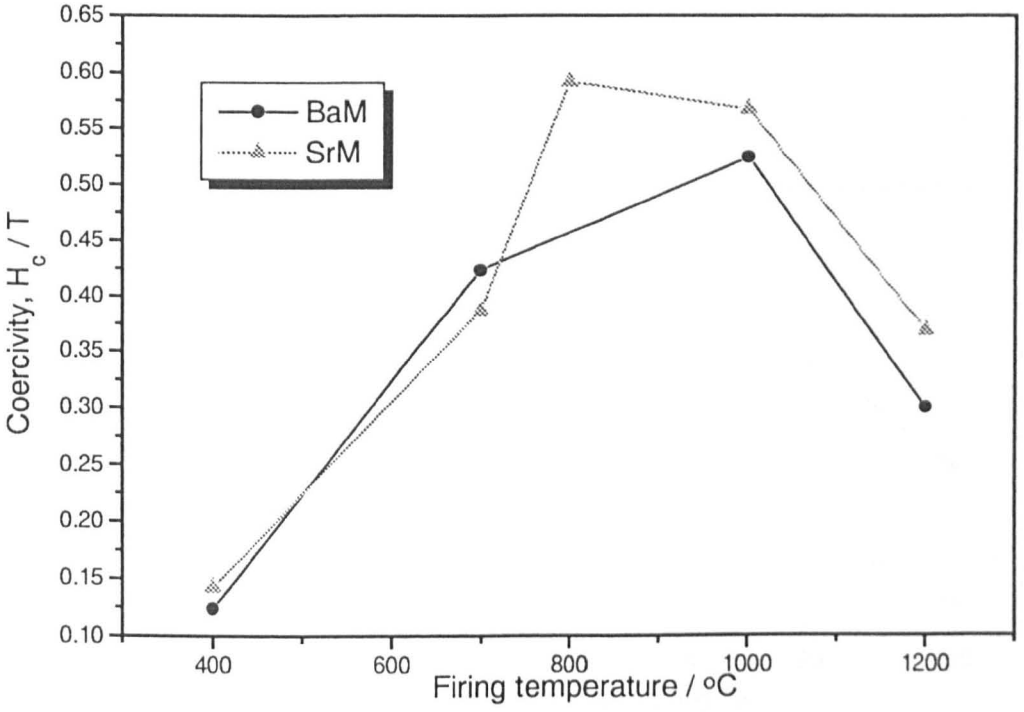

Fig. 261 Change in H_c with firing temperature for 3 yr stored BaM (●) and SrM (▲) samples aligned || to H.

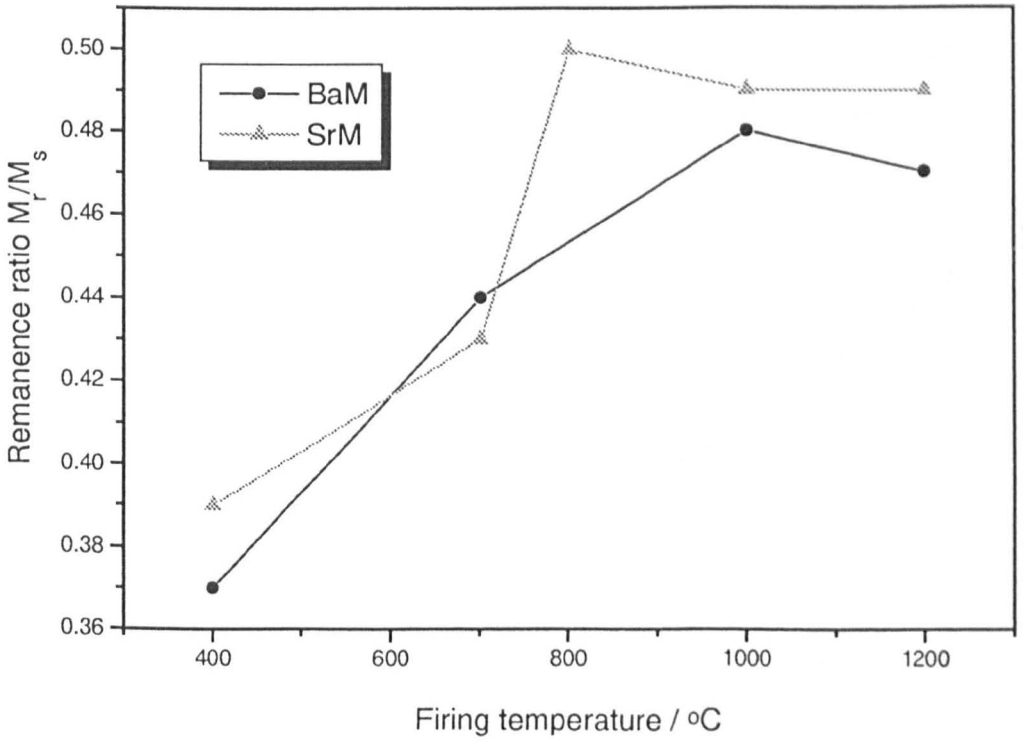

Fig. 262 Change in M_r/M_s with firing temperature for 3 yr stored BaM (●) and SrM (▲) samples aligned || to H.

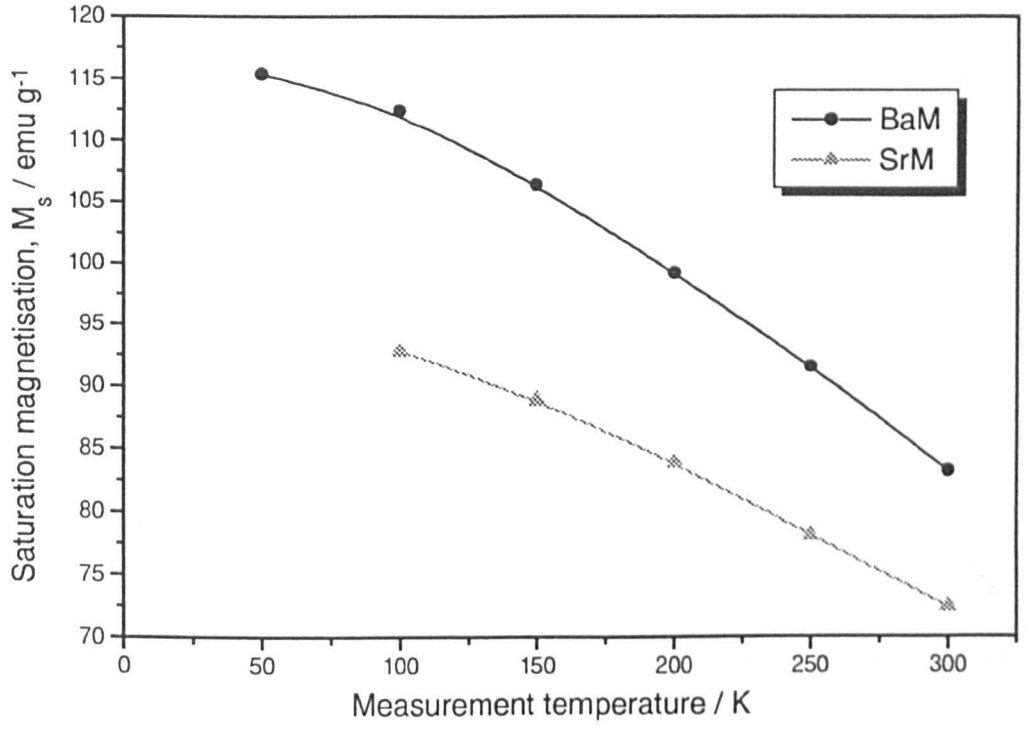

Fig. 263 Change in M_s with measurement temperature for 3 yr stored BaM (●) and SrM (▲) samples aligned || to H, and fired to 1000 °C / 3hr and 800 °C / 3hr respectively.

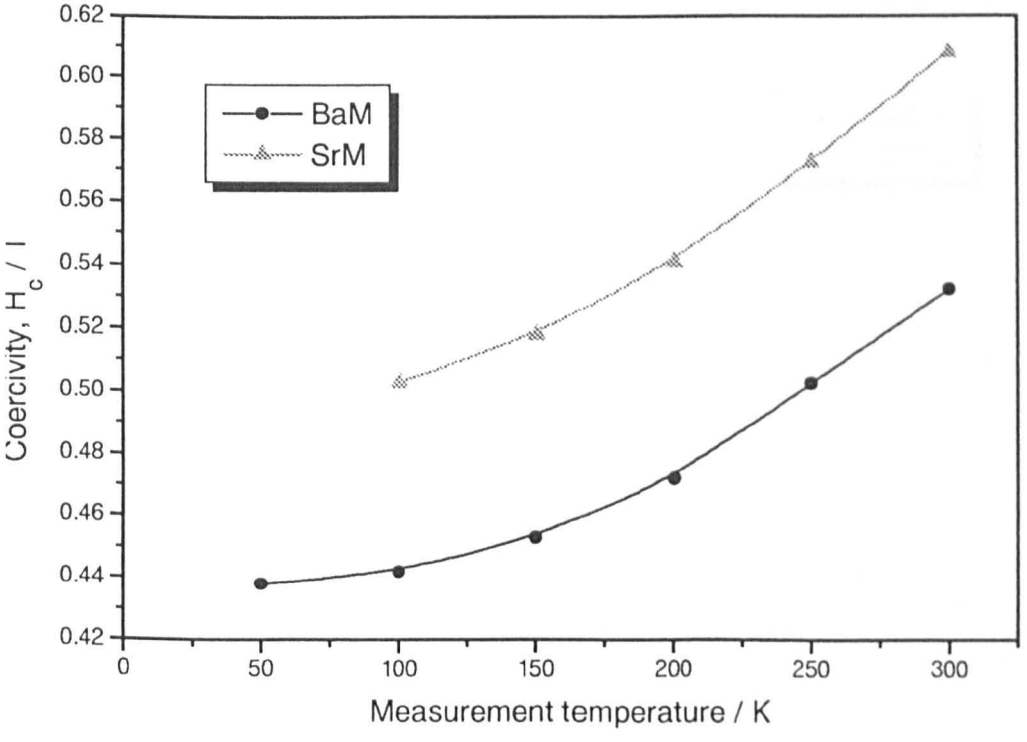

Fig. 264 Change in H_c with firing temperature for 3 yr stored BaM (●) and SrM (▲) samples aligned || to H, and fired to 1000 °C / 3hr and 800 °C / 3hr respectively.

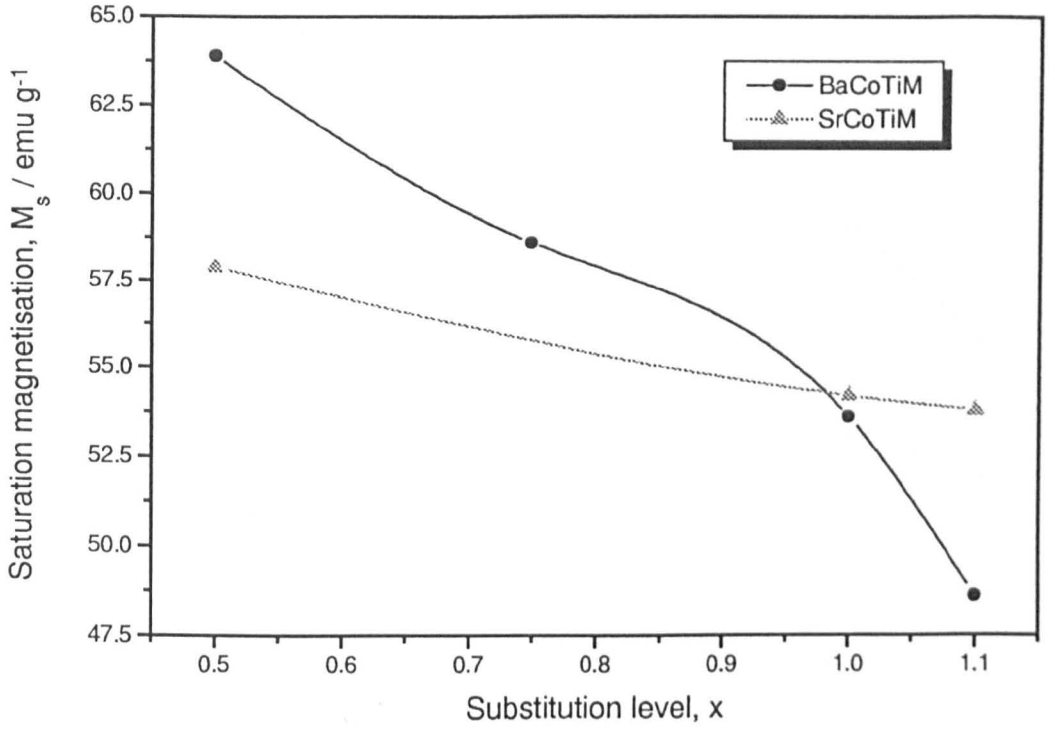

Fig. 265 Change in M_s with substitution for random $BaCo_xTi_xFe_{12-2x}O_{19}$ fibres fired to 1000 °C / 3hr (●) and 1200 °c / 3hr (▲).

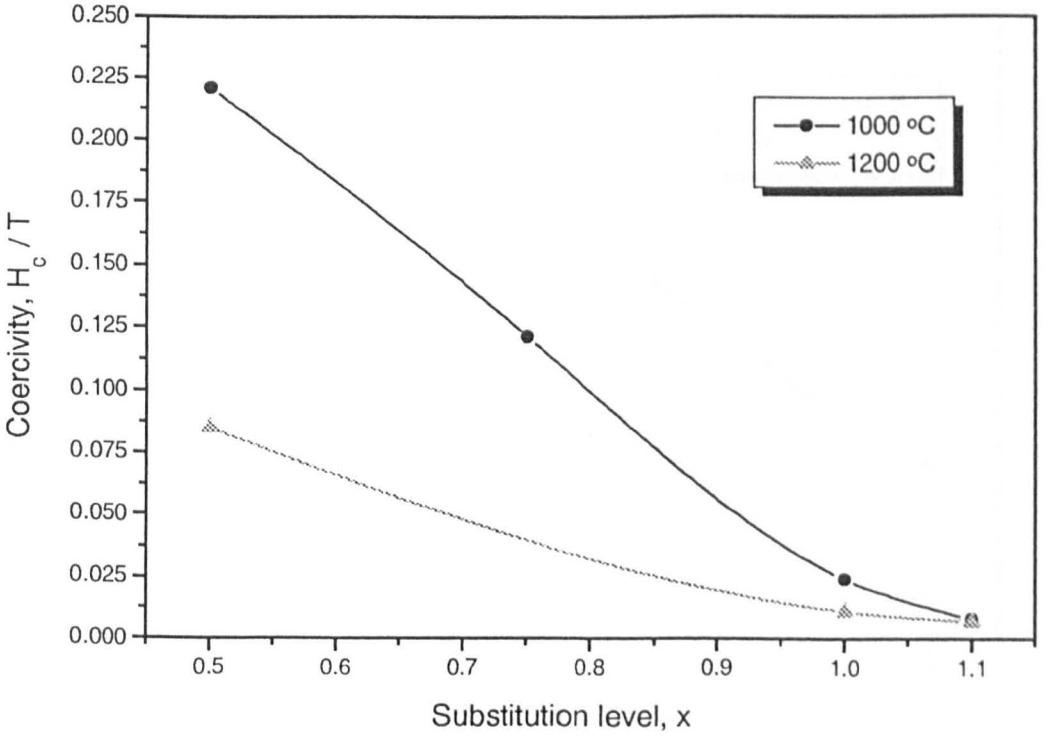

Fig. 266 Change in H_c with substitution for random $BaCo_xTi_xFe_{12-2x}O_{19}$ fibres fired to 1000 °C / 3hr (●) and 1200 °c / 3hr (▲).

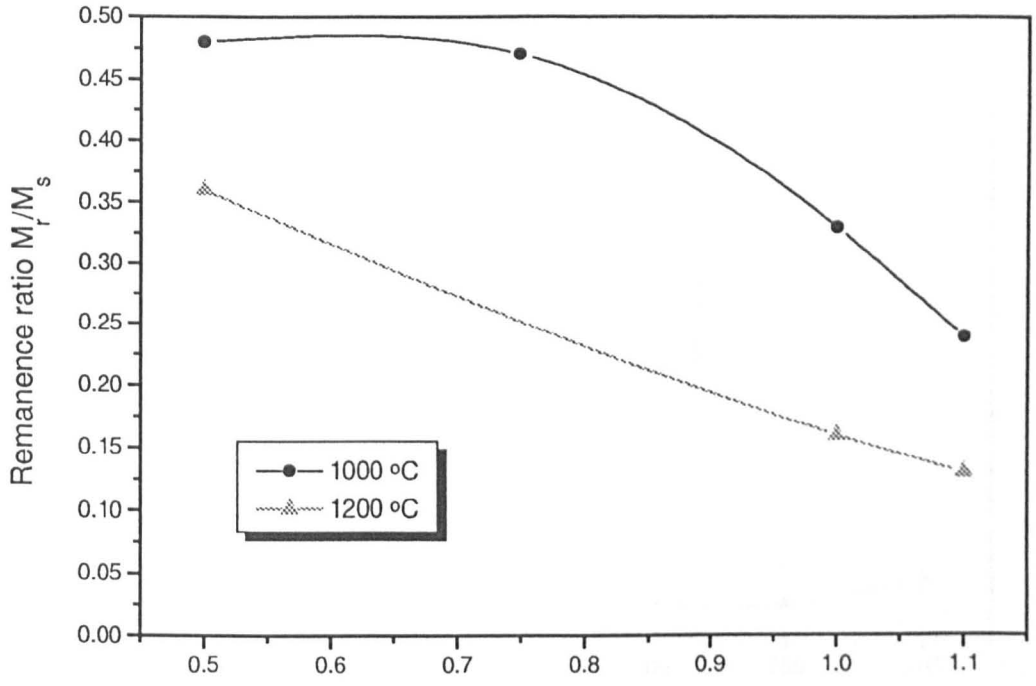

Fig. 267 Change in M_r/M_s with substitution for random $BaCo_xTi_xFe_{12-2x}O_{19}$ fibres fired to 1000 °C / 3hr (●) and 1200 °c / 3hr (▲).

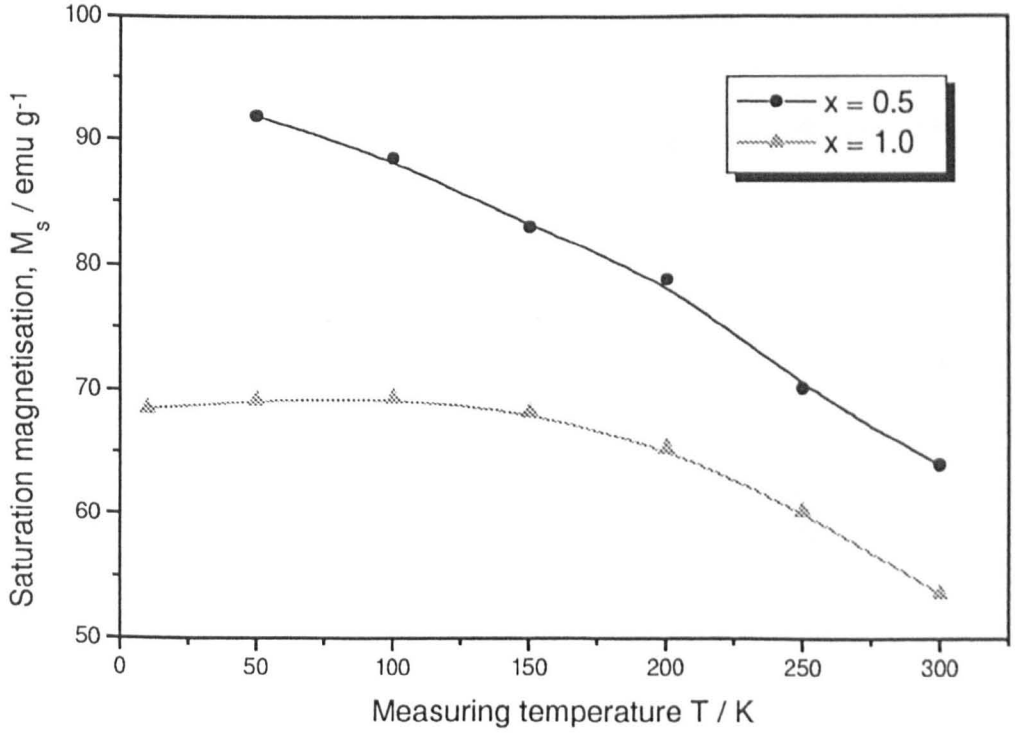

Fig. 268 Variation in M_s with measuring temperature for random $BaCo_xTi_xFe_{12-2x}O_{19}$ fibres, fired to 1000 °C / 3hr, at x = 0.5 (●) and 1.0 (▲).

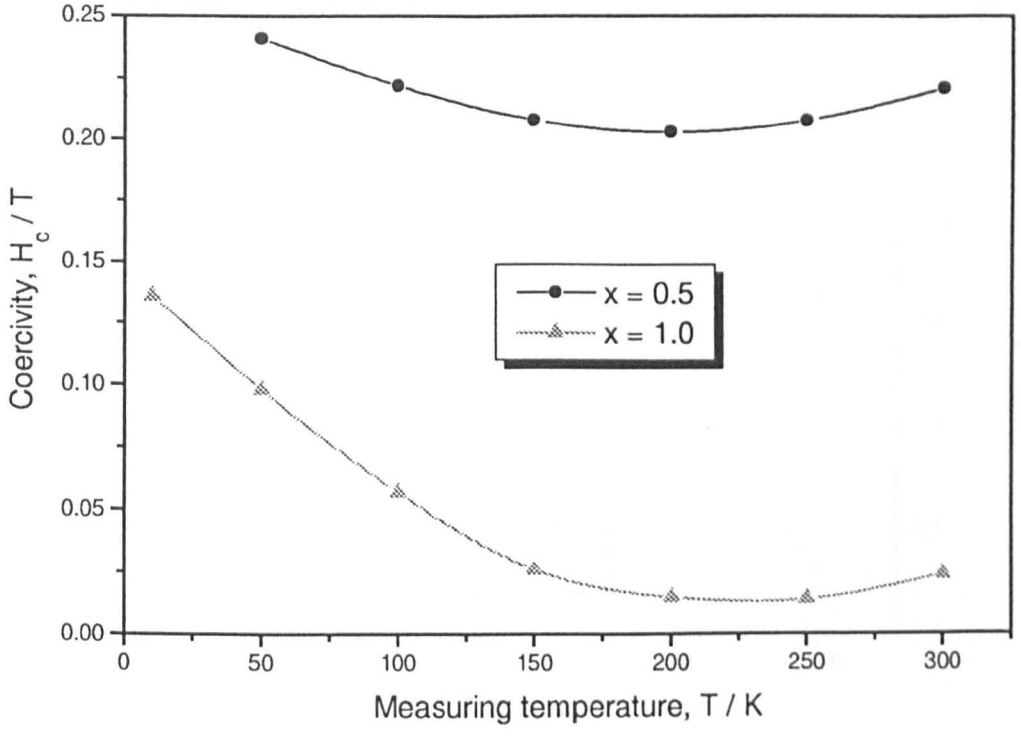

Fig. 269 Variation in H_c with measuring temperature for random $BaCo_xTi_xFe_{12-2x}O_{19}$ fibres, fired to 1000 °C / 3hr (●) and 1200 °c / 3hr (▲).

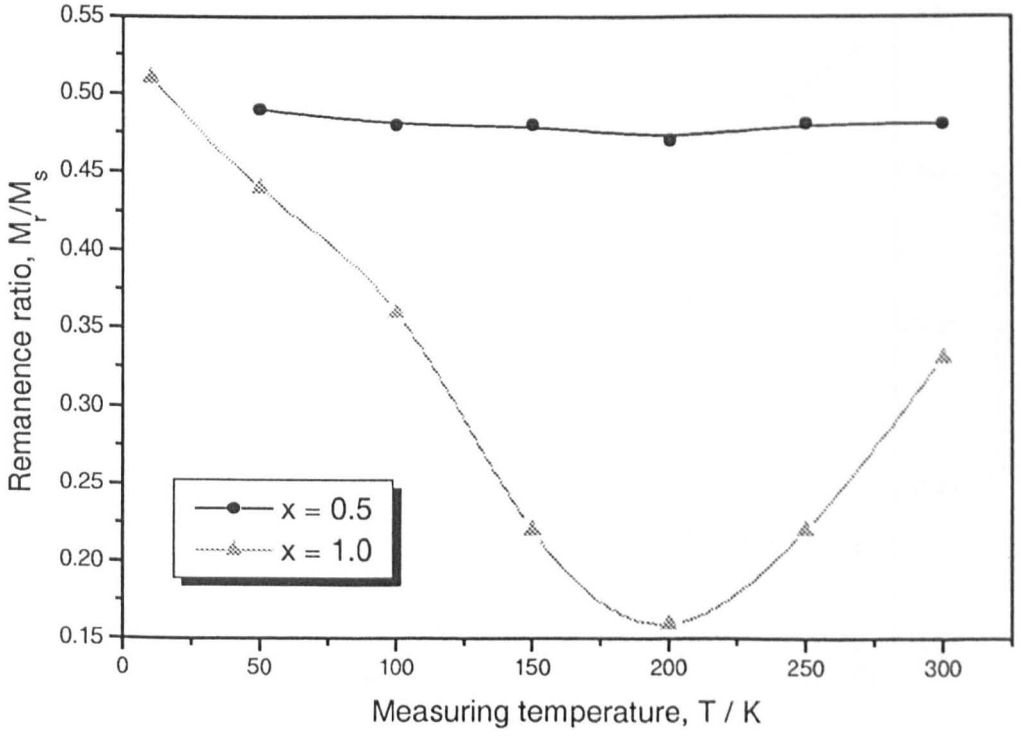

Fig. 270 Variation in M_r/M_s with measuring temperature for random $BaCo_xTi_xFe_{12-2x}O_{19}$ fibres, fired to 1000 °C / 3hr (●) and 1200 °c / 3hr (▲).

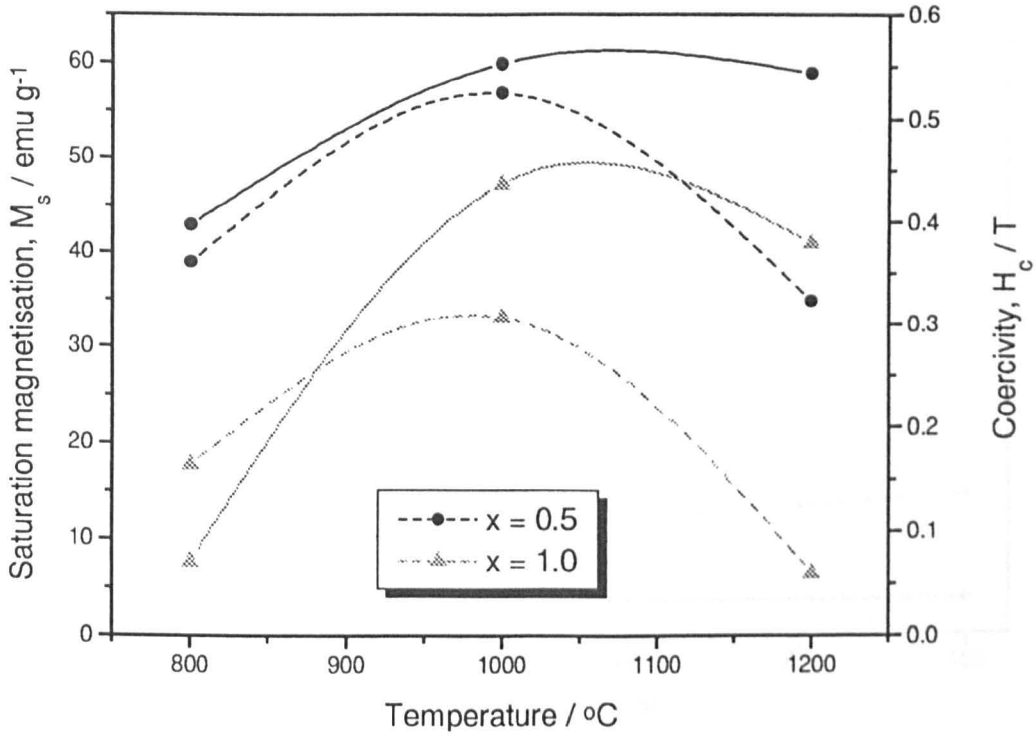

Fig. 271 Variation in M_s (solid lines) and H_c (dashed lines) with firing temperature for random $BaCo_xTi_xFe_{12-2x}O_{19}$ fibres, at x = 0.5 (●) and 1.0 (▲).

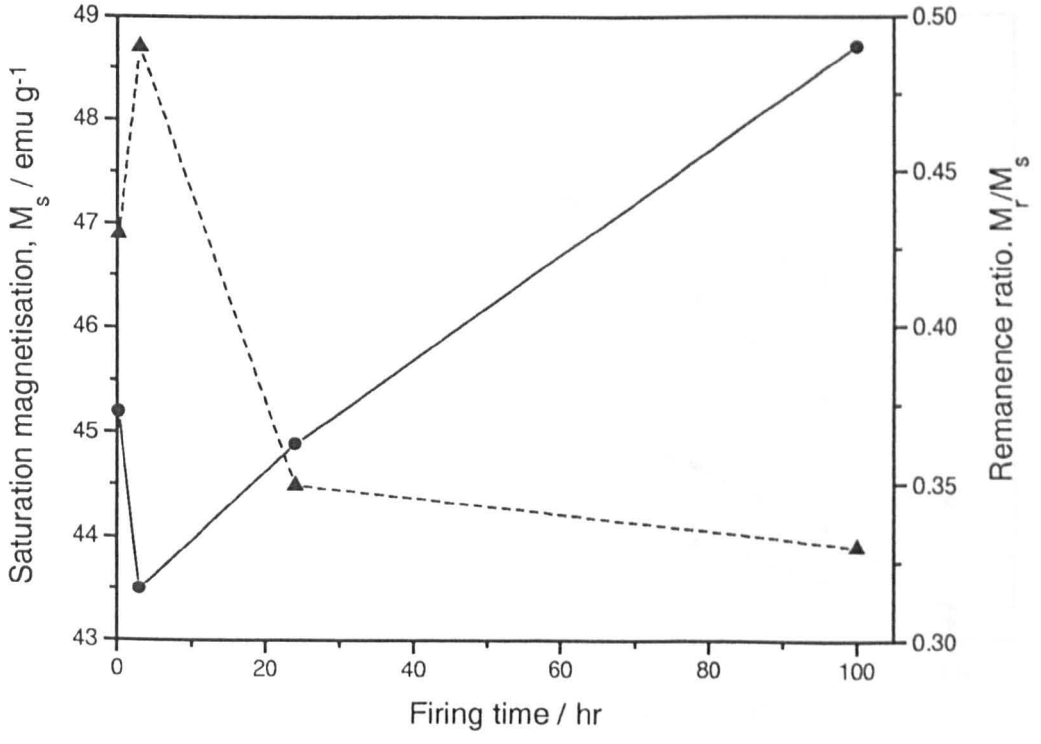

Fig. 272 Changes in M_s (●) and M_r/M_s (▲) with firing time, for Co_2Y fibres aligned || to H, at 1000 ^{0}C.

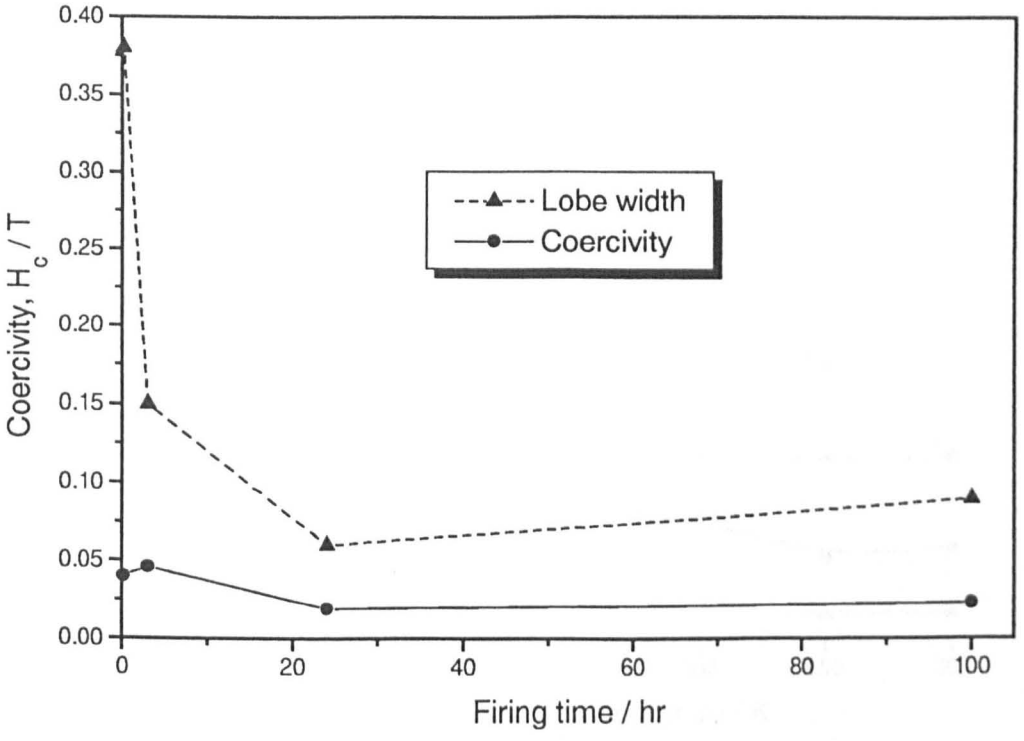

Fig. 273 Changes in H_c (●) and lobe width (▲) with firing time, for Co_2Y fibres aligned || to H, at 1000 ^{0}C.

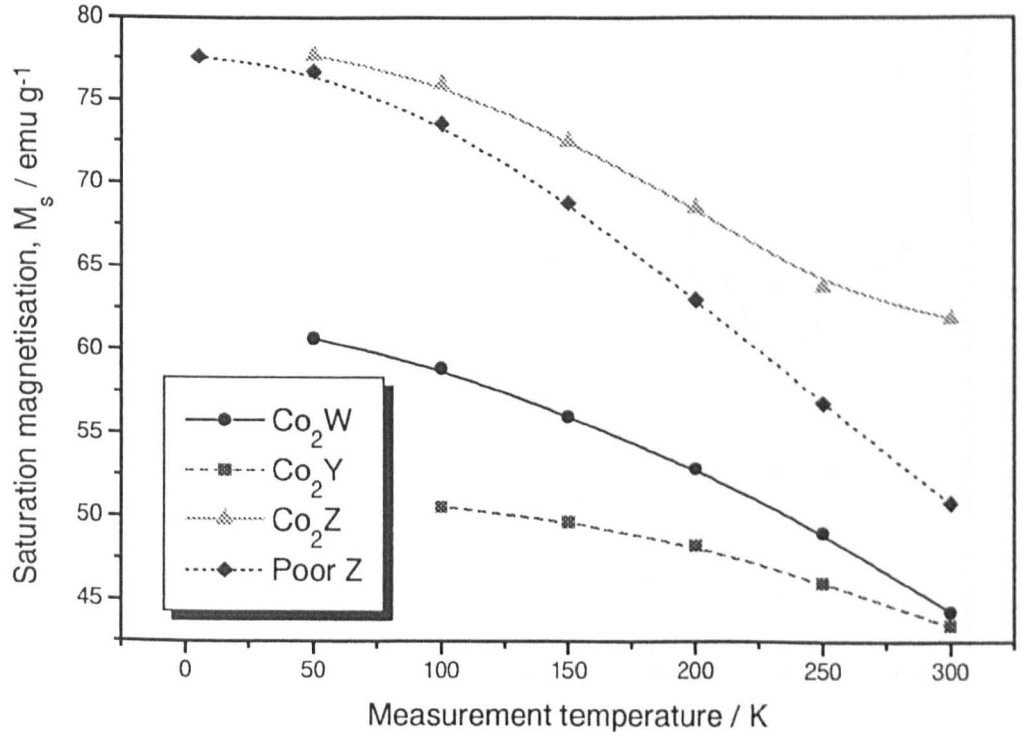

Fig. 274 Variation in M_s with measuring temperature for Co_2Y, Co_2Z and Co_2W fibres aligned || to H.

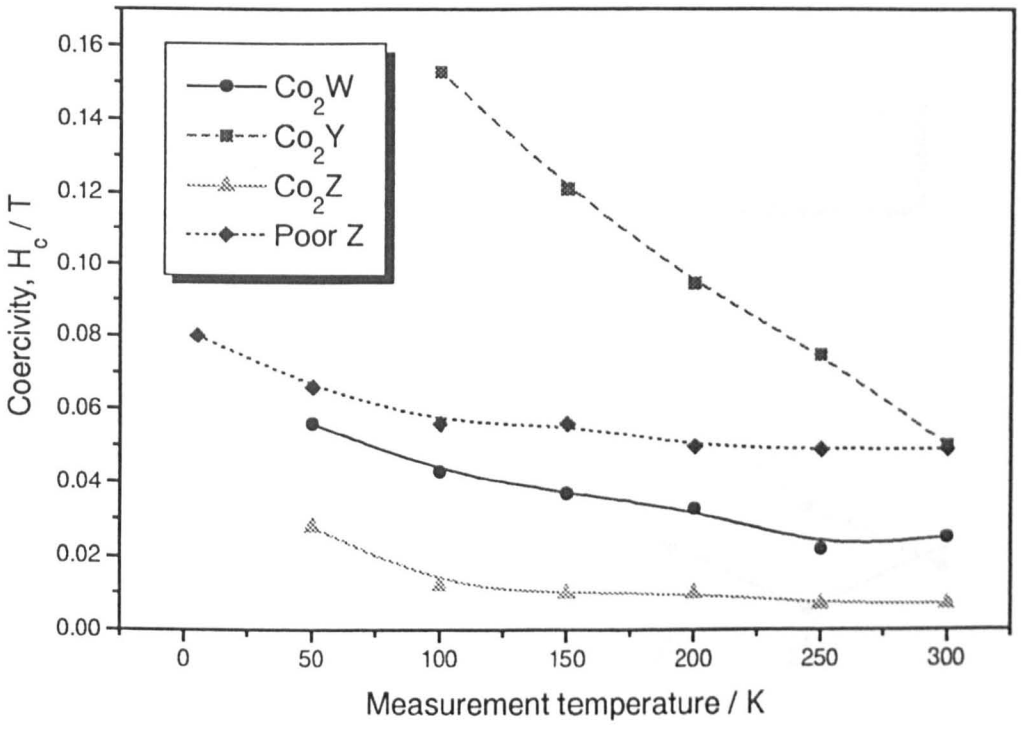

Fig. 275 Variation in H_c with measuring temperature for Co_2Y, Co_2Z and Co_2W fibres aligned || to H.

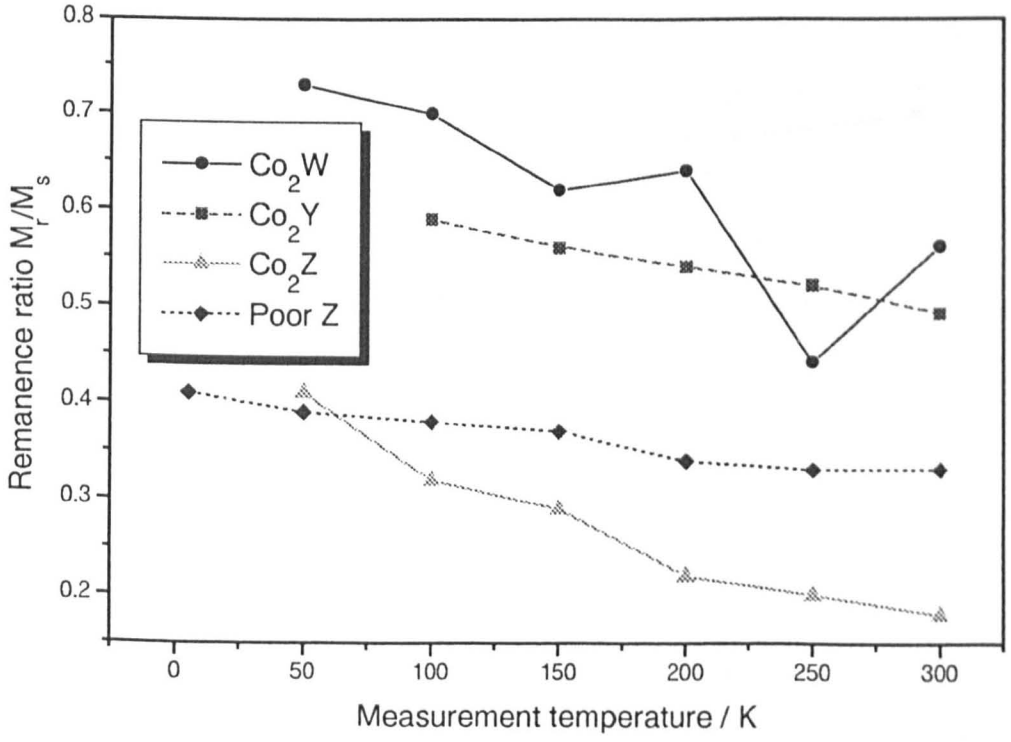

Fig. 276 Variation in M_r/M_s with measuring temperature for Co_2Y, Co_2Z and Co_2W fibres aligned || to H.

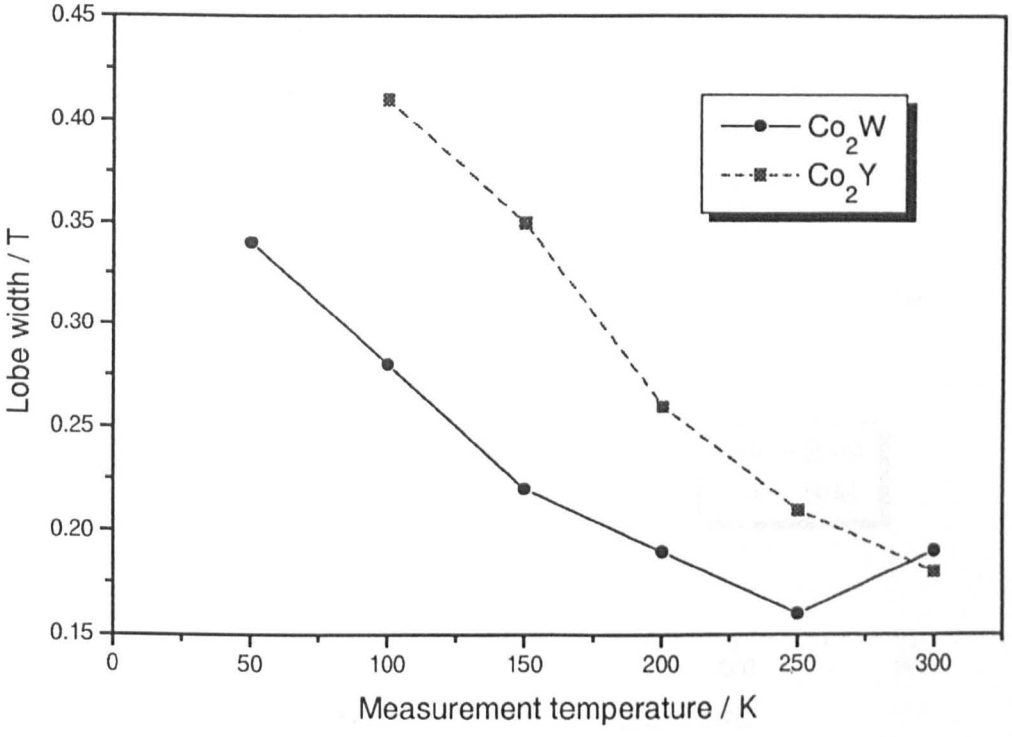

Fig. 277 Variation in lobe width with measuring temperature for Co_2Y and Co_2W fibres aligned || to H.

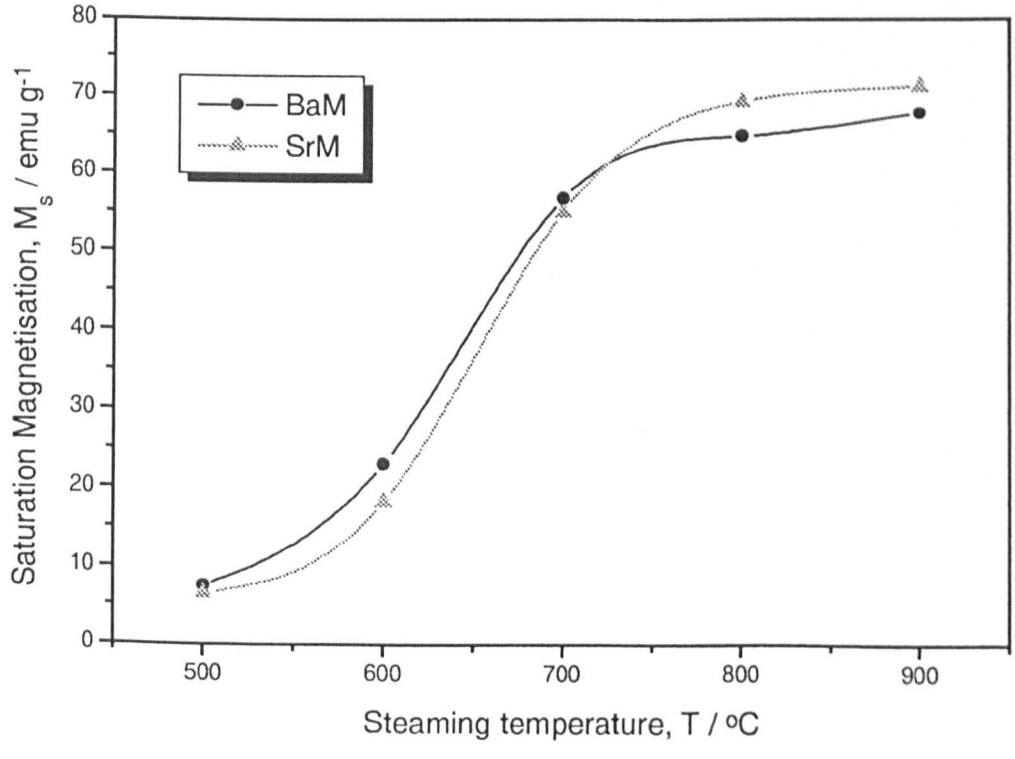

Fig. 278 Change in M_s with steaming temperature for BaM and SrM.

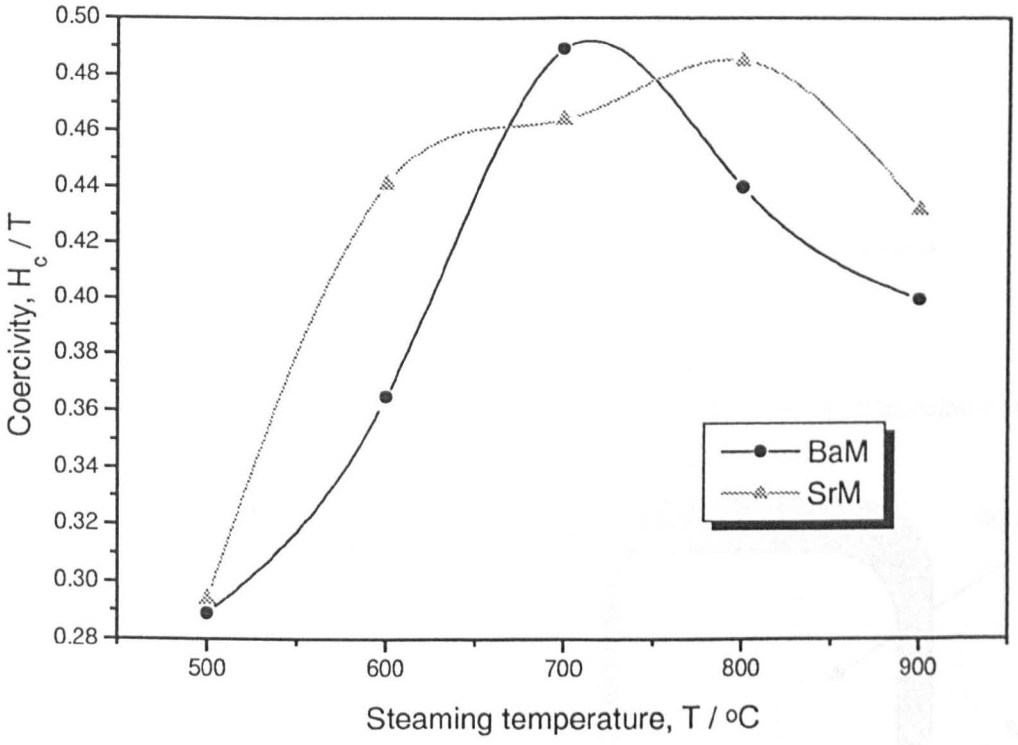

Fig. 279 Change in H_c with steaming temperature for BaM and SrM.

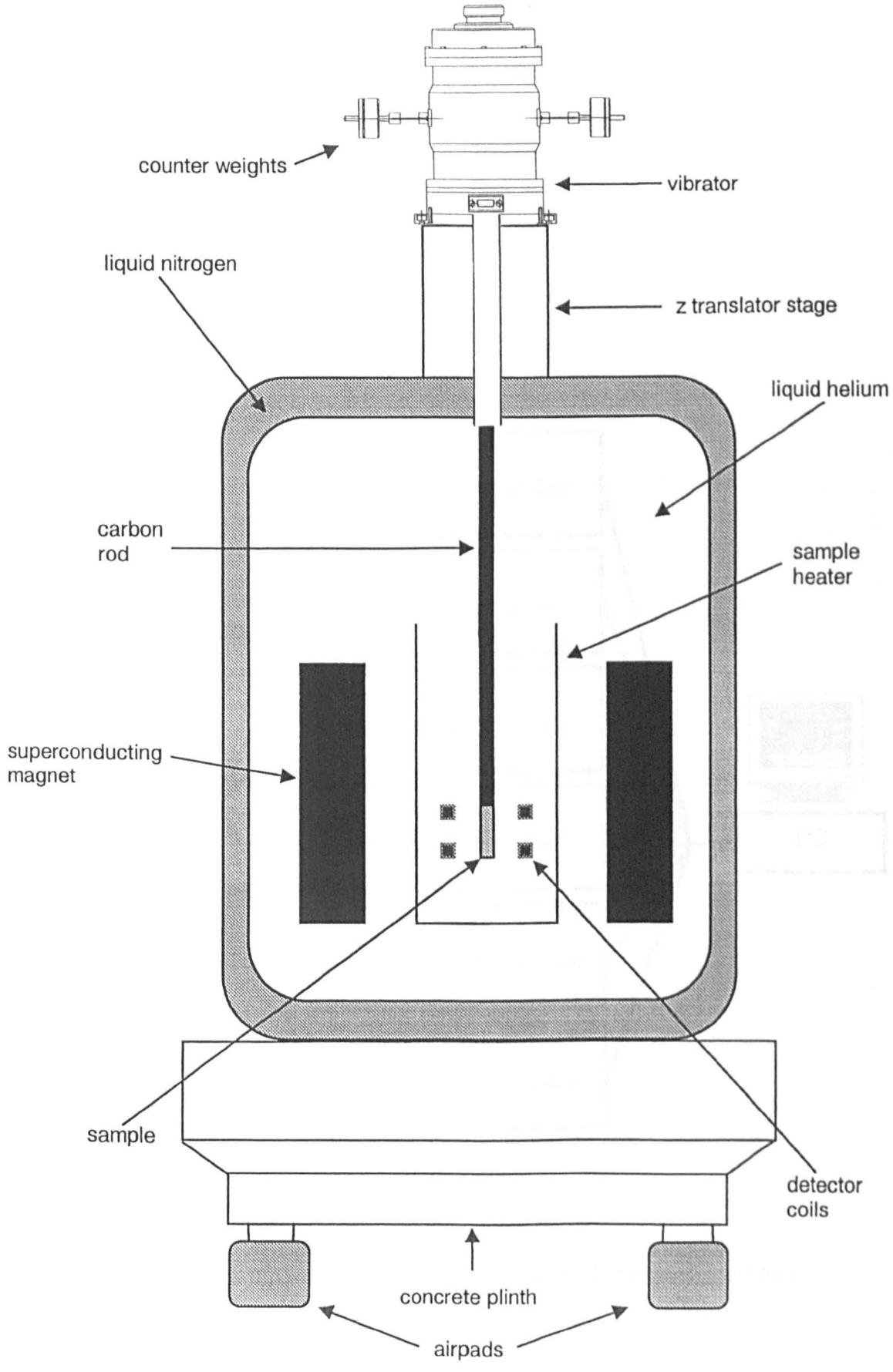

Fig. 280 Diagram of the VSM apparatus used to measure the fibres

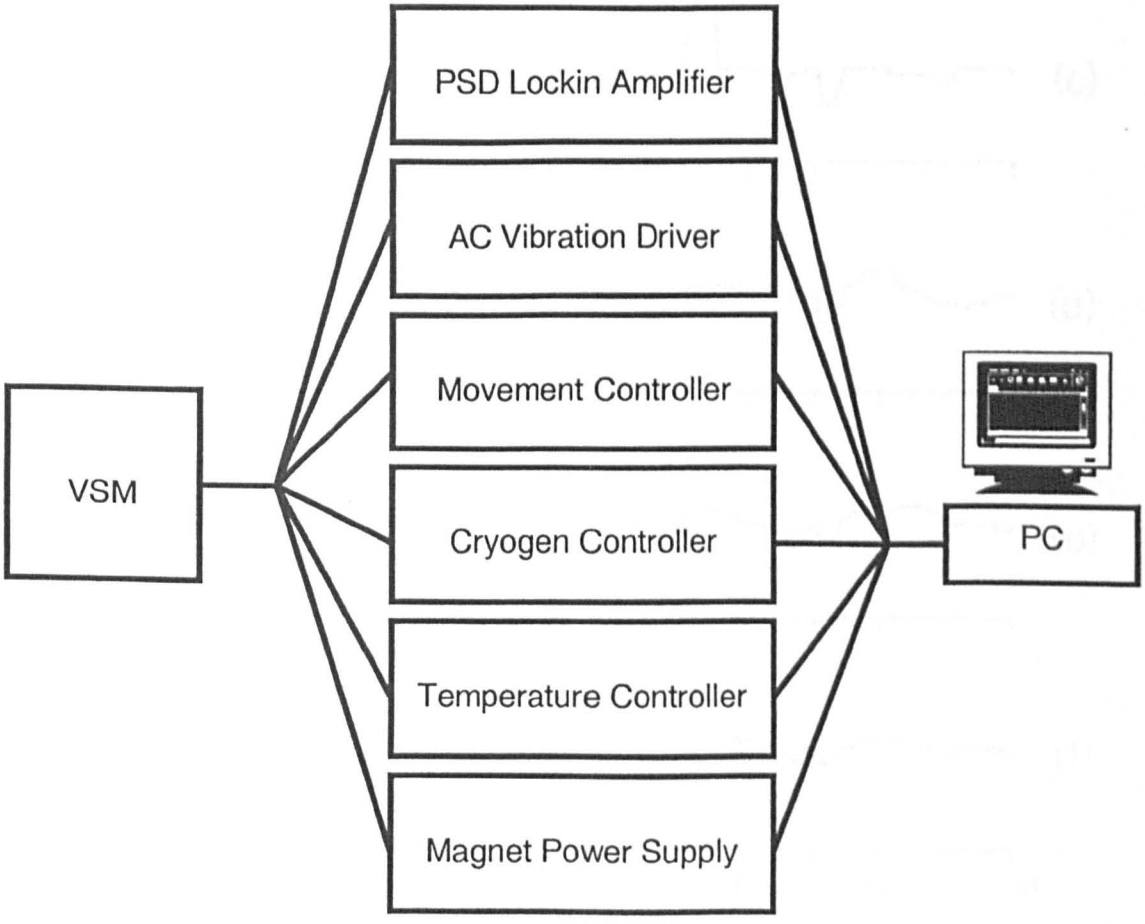

Fig. 281 Schematic of the set-up of the equipment used to control the VSM

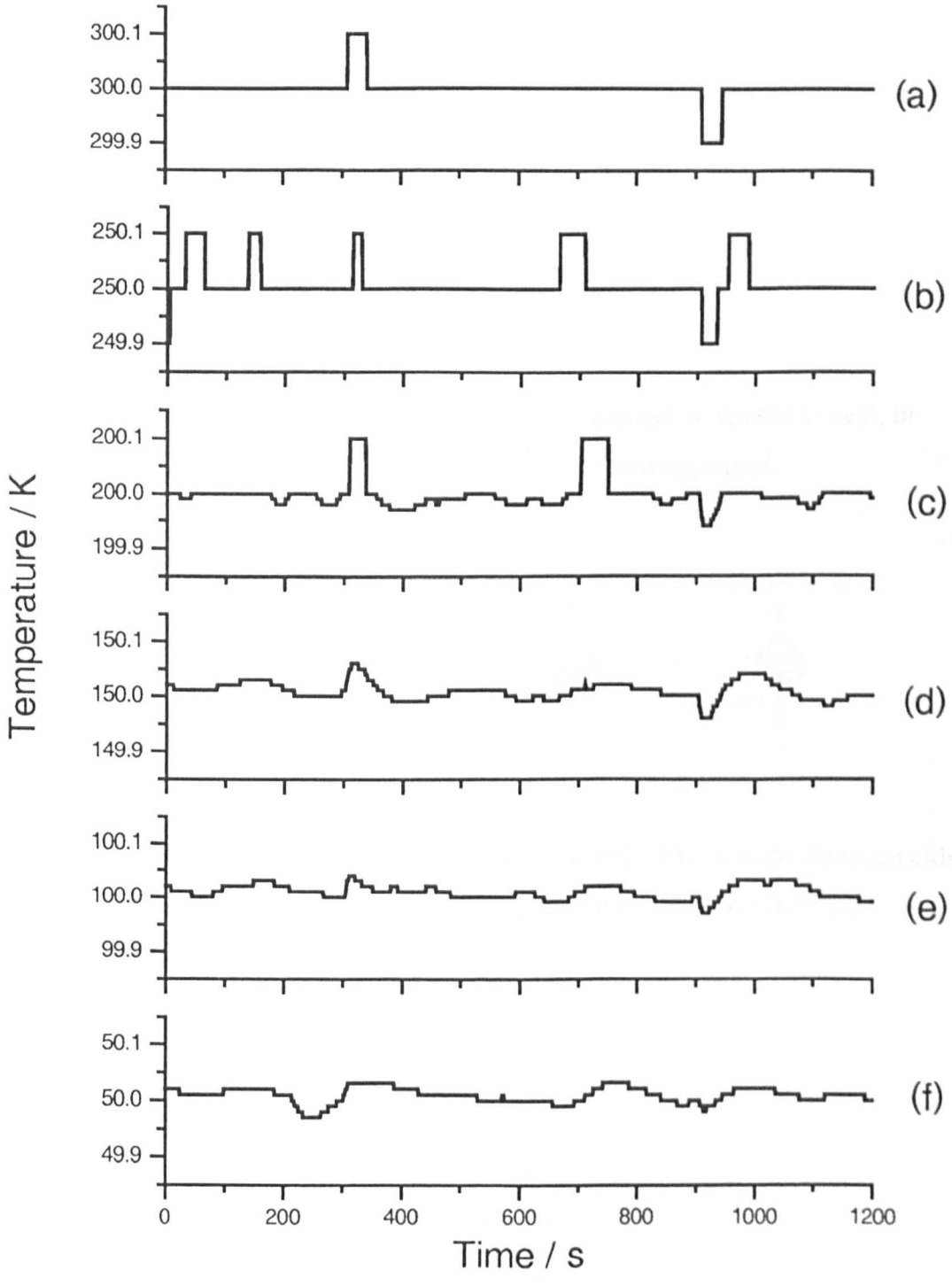

Fig. 282 VSMTEMP Variation in temperature during a 20 minute loop up to 5 T, after the samples were allowed to stabilise at the measuring temperature for 15 minutes for a) 300 K, b) 250 K, c) 200 K, d) 150 K, e) 100 K and f) 50 K.

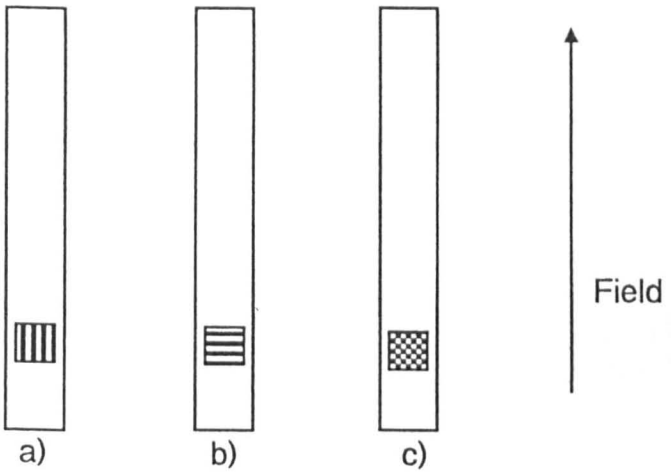

Fig. 283 The mounting of VSM samples where a) alignment is parallel to field, b) alignment is perpendicular to field and c) random alignment.

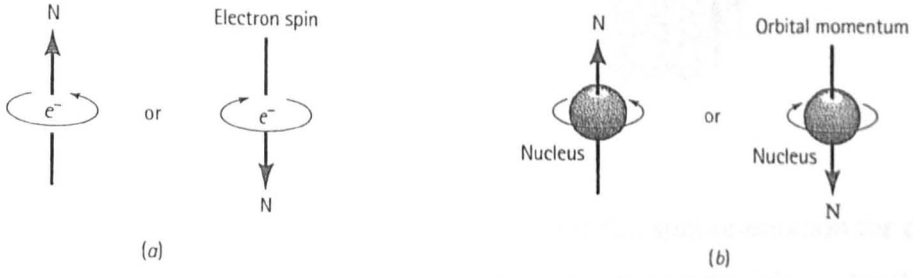

Fig. 284 The spin of the electron (a) produces a magnetic field with the direction either up or down, and the electrons orbiting around the nucleus (b) create a magnetic field around the atom [105].

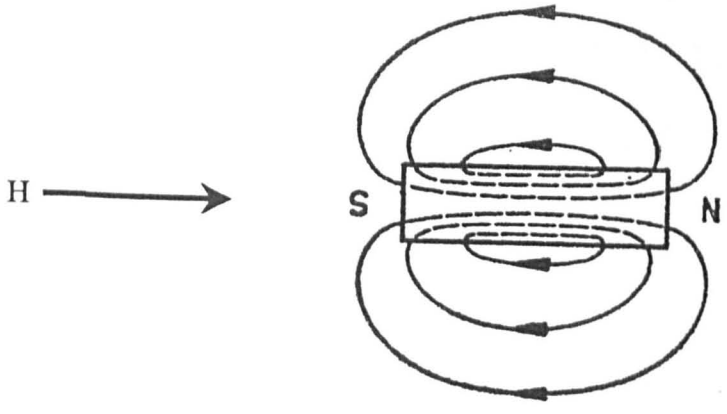

Fig. 285 The field set up by a magnetic material opposing an applied South - North field [391].

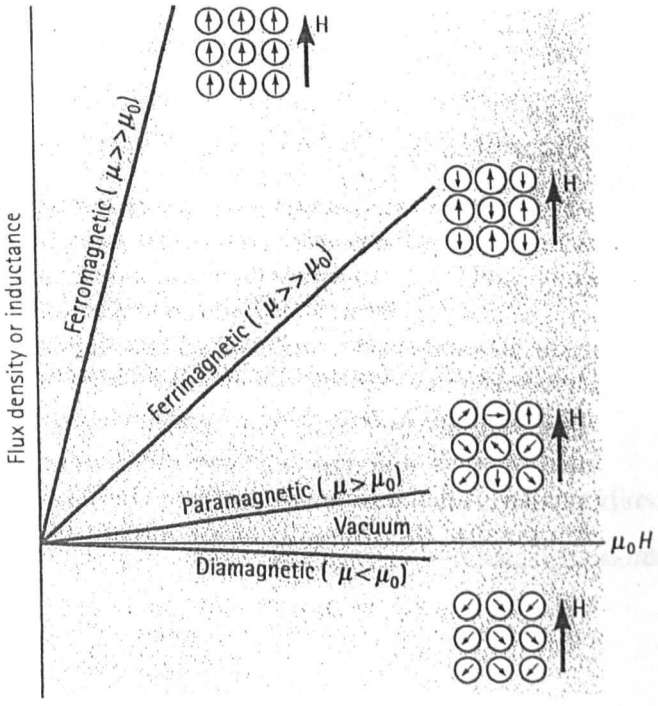

Fig. 286 A comparison of the inductance and electron spin orientation for diamagnetic, paramagnetic, ferrimagnetic and ferromagnetic materials, under the same applied field [105].

a) b) c)

Fig. 287 Comparison of the spins of the magnetic moments in a) ferromagnetic, b) antiferromagnetic and c) ferrimagnetic materials.

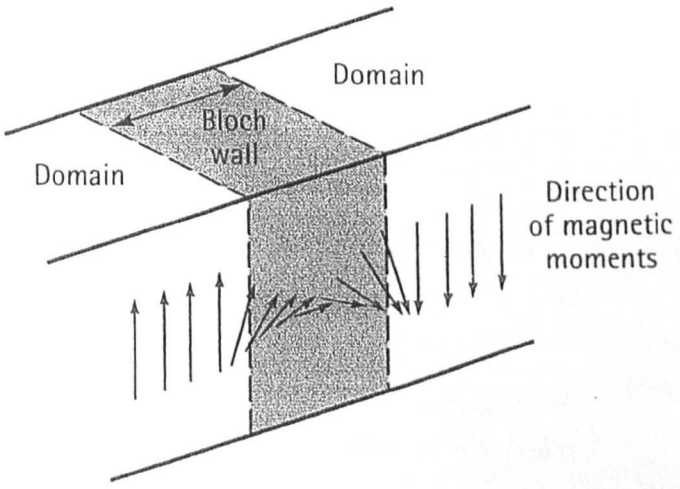

Fig. 288 A diagram showing the magnetic moments changing direction continuously throughout the boundary wall between two magnetic domains [105].

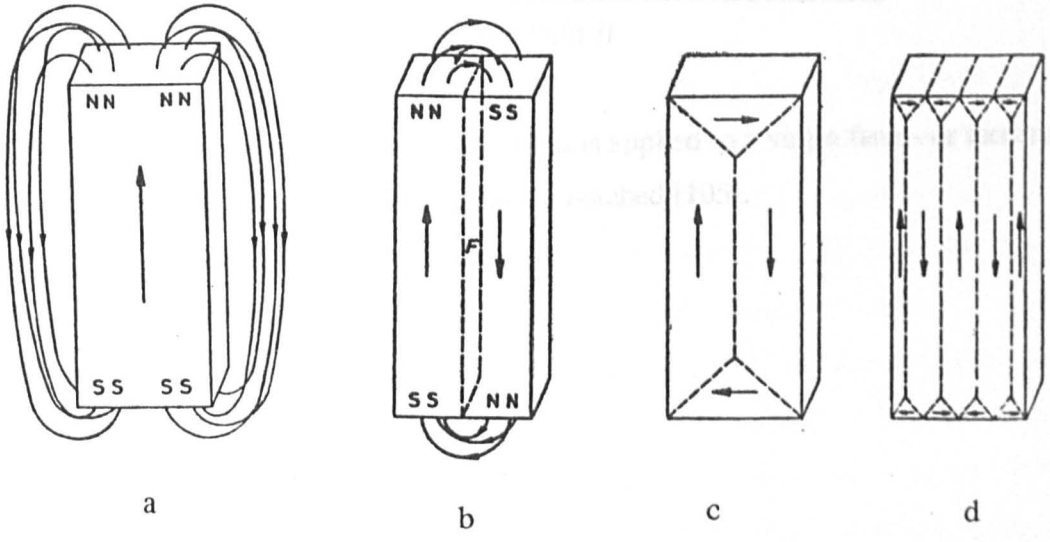

Fig. 289 The minimisation of magnetostatic energy by domain division. A single domain grain aligned in the preferred axis acts a tiny bar magnet with lines of magnetic flux flowing from north to south (a). If the grain is split into two opposing domains they share the flux and the energy is minimised (b). If the north and south poles are capped by another two perpendicular grains the flux is entirely contained within the grain and the energy is at a minimum (c). However, further division parallel to the preferred axis can lead to an increase in energy as the volume of the closure domains is reduced (d) [391].

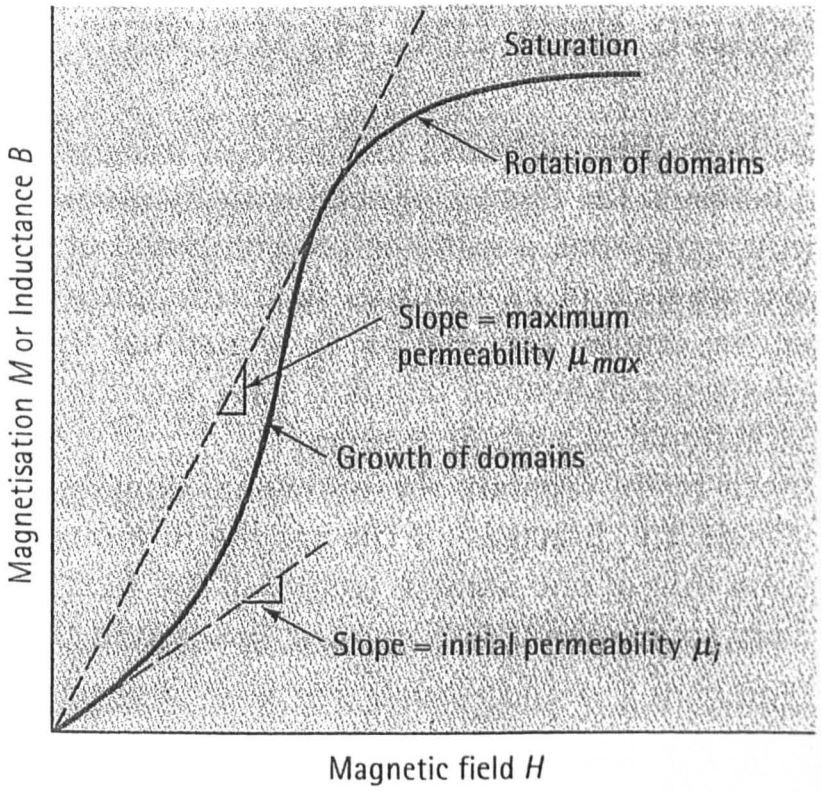

Fig. 290 The magnetisation curve when a field is applied to a virgin ferro- or ferrimagnetic material, until magnetic saturation is reached [105].

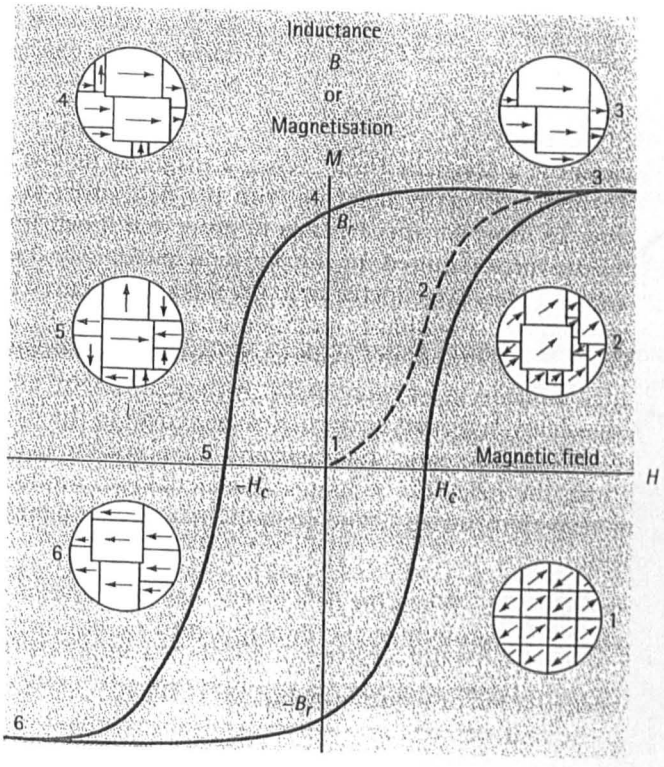

Fig. 291 The magnetic hysteresis loop and virgin magnetisation curve (dotted line), formed when induced magnetisation, B, is plotted against applied field, H for a ferro- or ferrimagnet. The material goes from virgin (zero) magnetisation to initial permeability, μ_i (1), then maximum permeability μ_{max} (2) and magnetic saturation M_s (3) with increasing applied field and consequent domain orientation. As the field is removed the magnetisation falls to the remnant value, M_r (B_r in this diagram) (4), at zero field, and with a field applied in the reverse direction the magnetisation will fall as the domains are randomised again by the opposing field. At the coercive field, H_c (5), the net magnetisation will again equal zero as all the domains are randomly oriented one more, and the magnetisation will then increase again with increasing field to an equal but opposite saturation magnetisation (6). Once fully magnetised, the material will follow the same cycle ad-infinitum, forming the hysteresis loop [105].

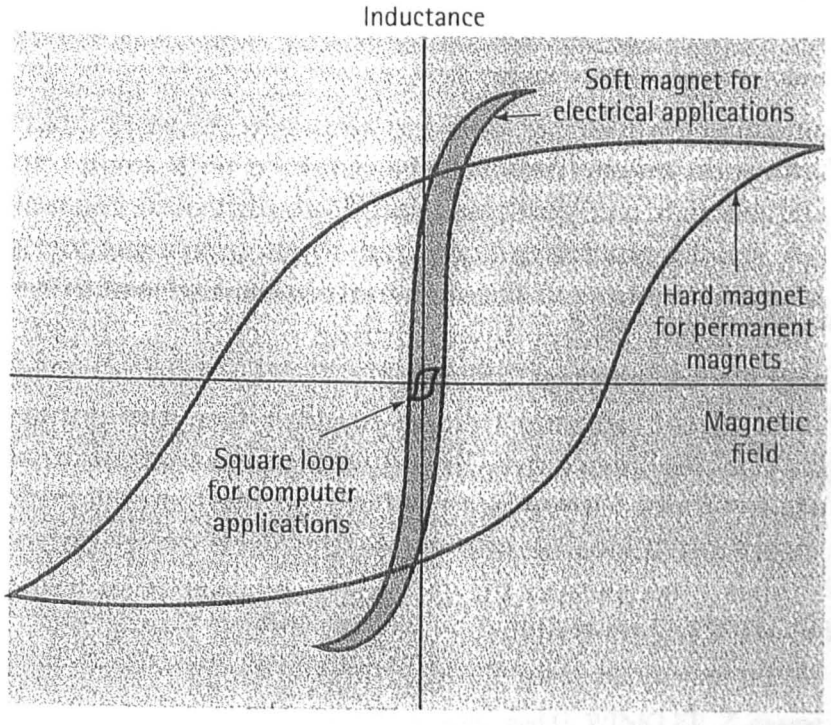

Fig. 292 Comparison of the hysteresis loop shapes for a hard ferrite, suitable for use as a permanent magnet, and a soft ferrite, more suited for electrical applications. The small, square ferrite in the centre is more typical of materials used for computer memory applications [105].

References

1. G. AMINOFF, *Geol. Foren. Stockh. Forh.* **47** (1925) 283
2. V. ADELSKOLD, *Arkiv. Kemi., Min. Geol.* **12A** (1938) 1
3. J. J. WENT, G. W. RATHENAU, E. W. GORTER and G. W. van OOSTERHOUT, *Phil. Tech. Rev.* **13** (1952) 194
4. G. H. JONKER, H. P. J. WIJN and P. B. BRAUN, *Phil. Tech. Rev.* **18** (1956) 145
5. A. E. van ARKEL, E. J. W. VERWEY and M. G. van BRUGGEN, *Rev. Trv. Chim.* **55** (1936) 331
6. J. L. SNOEK, *Phil. Tech. Rev.* 8 (1946) 353
7. J. SMIT and H. P. J. WIJN, in "Ferrites", Philips Technical Library, Eindhoven, (1959)
8. W. H. von AULOK, in "Handbook of Microwave Ferrites", Academic Press, New York (1965)
9. S. RAM, D. BAHADUR and D. CHAKRAVORTY, *J, Non-Cryst. Sol.* **101** (1988) 227
10. D. SAMARAS, A COLLOMB, S. HADJIVASILIOU, C. ACHILLEOS, J. TSOUKALA, J. PANNETIER and J. RODRIGUEZ, *J. Magn. Mag. Mat.* **79** (1989) 193
11. P. B. BRAUN, *Phil. Res. Rep.* **12** (1957) 491
12. G. A. JONES, S. F. H. PARKER, J. G. BOOTH and D. S. SIMKIN, *IEEE Trans. Mag.* **MAGN-26** (1990) 2804
13. A. TAUBER, J. S. MEGILL and J. R. SHAPPIRIO, *J. Appl. Phys.* **41** (1970) 1353
14. L. M. CASTELLIZ, K. M. KIM and P. S. BOUCHER, *J. Canadian Ceram. Soc.* **38** (1969) 57
15. G. ALBANESE, A. DERIU and S. RINALDI, *Appl. Phys.* **7** (1975) 1313
16. A. J. KERECMAN, A. TAUBER, T. R. AVLON and R. O. SAVAGE, *J. Appl. Phys.* **39** (1968) 726
17. J. A. KOHN, D. W. ECKART and C. F. COOK Jr., *Science* **172** (May 7, 1971, No. 3983) 519
18. C. G. KOOP, *Phys. Rev.* **83** (1951) 121
19. L. G. van UITERT, *Proc. IRE* **44** (1956) 1294
20. L. G van UITERT, *Proc. Comf. Mag. Magn. Mat. AIEE* **44** (1955) 299
21. R. M. CORNELL and U. SCHWERTMANN, in "The Iron Oxides", VCH, Weinheim, Germany (1996)
22. G. A. WAYCHUNAS, *Rev. in Mineral.* **25** (1991) 11
23. W. FEITNECHT, *Rev. Pure Appl. Chem.* (1964) 423
24. E. NECKENBURGER, H. SEVERIN, J. K. VOGEL and G. WINKLER, *Z. Angew. Phys.* **18** (1964) 65
25. W. ROOS, *J. Amer. Ceram. Soc.* **63** (1980) 601
26. C. D. MEE and J. C. JESCHKE, *J. Appl. Phys.* **34** (1963) 1271
27. K. HANEDA, C. MIYAKAWA and H. KOJIMA, *J. Amer. Ceram. Soc.* **57** (1974) 354
28. H. YAMAMOTO, H. KUMEHARA, R. TAKEUCHI and N. NISHIO, *J. de Phys. IV* **7** (1997) C1-535
29. A. G. BAGUL, J. J. SHROTRI, S. D. KULKARNI, C. E. DESHPANDE and S. K. DATE, in "Ferrites", *Proc. ICF6*, Kyoto and Tokyo (1992) 109
30. T. TAKADAS and M. KIYAMA, *Proc. Int. Conf. Ferrites*, Japan (1970) 96
31. S. OKAMOTO, *J. Amer. Ceram. Soc.* **51** (1968) 594
32. K. TABARU, K. YAMAUCHI and Z. IGARASHI, *Jap. Pat.* **32,497**, March 1975
33. R. H. ARENDT and C. E. van BUREN, *US Pat.* **3810937** (1974)
34. R. H. ARENDT, *US Pat.* **3793443** (1974)
35. T.-S. CHIN, S. L. HSU and M. C. DENG, *J. Magn. Mag. Mat.* **120** (1993) 63
36. C. H. LIN, M. J. HUANG, T. S. CHIN and S. K. GONG, in "Ferrites", *Proc. ICF6*, Tokyo and Kyoto (1992) 173
37. N. M. BORISOVA, Z. V. GOLUBENKO, T. G. KUZ'MICHEVA, L. P. OL'KHOVIK and V. P. SHABATIN, *J. Magn. Mag. Mat.* **114** (1992) 317
38. L. P. OL'KHOVIK, N. M. BORISOVA, A. S. KAMZIN and O. G. FISENKO, *J. Magn. Mag. Mat.* **154** (1996) 365
39. G. LITSARDAKIS, A. C. STERGIOU, J. GIORGIOU, S. SKLAVOUNOS, D. SAMARAS, M. PERNET and P. GERMI, *J. Magn. Mag. Mat,* **120** (1993) 58
40. G. LITSARDARKIS, J. GEORGIOU, A. C. STERGIOU and D. SAMARAS, *J. de Phys. IV* **7** (1997) C1-533
41. T. KAGOTANI, H. TAKAMURA, M. OKADA and M. HOMMA, in "Ferrites", *Proc. ICF6*, Tokyo and Kyoto (1992) 1137
42. E. MATIJEVIC, *J. Coll. Interface Sci.* **117** (1987) 593
43. C. SURIG, D. BONNENBERG, K. A. HEMPEL, P. K. KERDUCK, H. J. KLAAR and C. SAUER, *J. de Phys. IV* **7** (1997) C1-315
44. C. SURIG, K. A. HEMPEL and C. SAUER, *J. Magn. Mag. Mat.* **157-8** (1996) 268
45. W. ZHONG, W. DING, N. ZHANG, J. HONG, Q. YAN and Y. DU, *J. Magn. Mag. Mat.* **168** (1997) 196
46. M. MEDARDE, J. RODRIGUEZ, M. VALLET, M. PERNET, X. OBRADORS and J. PANNETIER, *Phys. B* **157-7** (1989) 36
47. M. CHIBA, C. UEMURA and Y. KOIZUMI, in "Ferrites", *Proc. ICF6*, Kyoto and Tokyo (1992) 89
48. E. OTSUKI and TH. MATSUZAWA, *J. de Phys. IV* **7** (1997) C1-323
49. X. WANG, D. LI, L. LU and X. WANG, *J. Alloys Compounds* **237** (196) 45

50. V. K. S. SANKARANARAYANAN, Q. A. PANKHURST, D. P. E. DICKSON and C. E. JOHNSON, *J. Magn. Mag. Mat,* **125** (1993) 199
51. V. K. S. SANKARANARAYANAN, Q. A. PANKHURST, D. P. E. DICKSON and C. E. JOHNSON, *J. Magn. Mag. Mat,* **120** (1993) 73
52. J.-H. LEE, T.-B. BYEON, H.-J. LEE, C.-G. KIM and T.-O. KIM, *J. de Phys. IV* **7** (1997) C1-751
53. B. T. SHIRK and W. R. BUESEM, *J. Amer. Ceram. Soc.* **53** (1970) 192
54. H. SATO and T. UMEDA, in "Ferrites", *Proc. ICF6*, Kyoto and Tokyo (1992) 1122
55. S. KURISU and O. KUBO, in "Ferrites", *Proc. ICF6*, Tokyo and Kyoto (1992) 1398
56. W. ZHONG, W. DING, Y. JIANG, N. ZHANG, J. ZHANG, Y. DU and Q. YAN, *J. Amer. Ceram. Soc.* **80** (1997) 3258
57. S. K. MISHRA, L. C. PATHAK and V. RAO, *Mat. Let.* **32** (1997) 3258
58. S. CASTRO, M. GAYASO, J. RIVAS, J. M. GRENECHE, J. MIRA and C. RODRIGUEZ, *J. Magn. Mag. Mat.* **152** (1996) 61
59. G. ELWIN, I. P. PARKIN, Q. T. BUI, L. FERNANDEZ BARQUIN, Q. A. PANKHURST, A. V. KOMAROV and Y. G. MOROZOV, *J. Mat. Sci. Let.* **16** (1997) 1237
60. R. J. MILLER, Thesis, Ohio State University (1970)
61. Z. X. TANG, S. NAFIS, C. M. SORENSON and G. C. H. HADJIPANAYIS, *IEEE Trans. Magn.* **MAG-25** (1974) 354
62. W. A. KACZMAREK, A. CALKA and B. W. NINHAM, *Mat. Chem. Phys.* **32** (1992) 43
63. V. PILLAI, P. KUMER, M. HOU, P. AYYUB and D. SHAH, *Adv. Coll. Interface Sci.* **55** (1995) 241
64. D. A. RAWLINSON and P. A. SERMON, *J. de Phys. IV* **7** (1997) C1-755
65. B. RAMAMURTHY ACHARYA, N. VENKATRAMANI, S. PRASAD, S. N. SHRINGI, R. KRISHNAN, M. TESSIER and Y. DUMOND, *IEEE Trans. Magn.* **MAGN-29** (1993) 3370
66. T. FUJI, H. KATO, Y. MIURA and J. TAKADA, *J. de Phys. IV* **7** (1997) C1-485
67. R. GERBER, R. ATKINSON and Z. SIMSA, *J. Magn. Mag. Mat.* **175** (1997) 79
68. W.-D. CHO, T.-B. BYEON, A. HEMPEL, D. BONNENBERG, C. SURIG and T.-O. KIM, *J. de Phys. IV* **7** (1997) C1-499
69. A. ISHIKAWA, K. TANAHASHI and M. FUTAMOTO, *J. Appl. Phys.* **79** (1996) 7080
70. T. L. HYLTON, M. A. PARKER, M. ULLAH, K. R. COFFEY, R. UMPHRESS and J. K. HOWARD, *J. Appl. Phys.* **75** (1994) 5960
71. B. Y. WONG, X. SUI, D. E. LAUGHLIN and M. H. KRYDER, *J. Appl. Phys.* **75** (1994) 5966
72. J. BURSIK, Z. SIMSA, L. STICHAUER and R. TESAC, *J. Magn. Mag. Mat.* **157-8** (1996) 311
73. E. BRANDO, H. VINCENT, J. L. SOUBEYROUX and P. WOLPERS, *J. Magn. Mag. Mat.* **157-8** (1996) 465
74. M. GOMI, J. CHO and M. ABE, *J. Appl. Phys.* **82** (1997) 5126
75. S. PIGNARD, J. P. SENATEUR, H. VINCENT, J. KREISEL and A. ABRUTIS, *J. de Phys. IV* **7** (1997) C1-483
76. M. ABE and Y. TAMURA, *J. Appl. Phys.* **22** (1983) L511
77. K. EGUSA, K. MARUGAME, M. ABE and T. ITOH, in "Ferrites", Proc ICF6, Tokyo and Kyoto (1992) 11
78. J. DUFOR, L. LOPEZ, A. FORMOSO,C. NEGRO, R. LATORRE, and F. LOPEZ-MATEOS, *Chem. Eng. J.* **59** (199) 287
79. J. DUFOR, R. LATORRE, C. NEGRO, E. M. ALCALA, A. FORMOSO, and F. LOPEZ-MATEOS, *J. Magn. Mag. Mat.* **172** (1997) 308
80. J. DUFOR, R. LATORRE, E. M. ALCALA, C. NEGRO, A. FORMOSO, and F. LOPEZ-MATEOS, *J. Magn. Mag. Mat.* **157-8** (1996) 125
81. H. STABLEIN, in "Ferromagnetic Materials" vol. 3, ed. E. P. WOHLFARTH, North-Holland Physics Publishing, Amsterdam (1982), p. 441-602
82. W. A. KACZMAREK and B. W. NINHAM, *J. de Phys. IV* **7** (1997) C1-47
83. O. ABE and M. NARITA, *Solid State Ionics* **101-3** (1997) 103
84. H. M. DURR, *J. de Phys. IV* **7** (1997) C1-57
85. M. SAGAWA, H. NAGATA, T. WATANABE and O. ITATANI, *J. de Phys. IV* **7** (1997) C1-307
86. N. HORIISHI and S. YAMAMOTO, in "Ferrites", *Proc. ICF6*, Tokyo and Kyoto (1992) 1041
87. J. DING, T. TSUZUKI and P. G. McCORMICK, *J. Magn. Mag. Mat.* **177-81** (1998) 931
88. G. F. AUSTIN and G. D. McTAGGART, in "Treatise on Materials Science and technology" vol. 9, ed. F. F. Y. WANG, Academic Press, New York (1976), p. 35
89. H. G. RICHTER and H. VOLLER, *DEW-T Ber.* 8 (1968) 214
90. J. S. REED and R. B. RUNK, in "Treatise on Materials Science and Technology" vol. 9, ed. F. F. Y. WANG, Academic Press, New York (1976), p. 71
91. C. A. M. van der BROEK and A. L. STUIJTS, *Phil. Tech. Rev.* **37** (1977) 157
92. A. MORISAKO, M. MATSUMOTO and M. NAOE, *IEEE Trans. Magn.* **MAG-23** (1987) 2358
93. T. SUZUKI, *J. Mag. Soc. Jpn.* **15** (1991) 833
94. R. GERBER, R. ATKINSON, and Z. SIMSA, *J. Magn. Mag. Mat.* **175** (1997) 79
95. O. KUBO, T. IDO and H. YOKOYAMA, *IEEE Trans. Magn.* **MAG-18** (19982) 1122
96. M. FUJITA, K. KAKIZAKI, N. H. RATSUKA and K. HANEDA, in "Ferrites", *Proc. ICF6*, Tokyo and Kyoto (1992) 968

97. C. KOOY and U. ENZ, *Phil. res. Rept.* **15** (1966) 7
98. A. S. VAINGANKAR, S. G. KULKRNI and M. S. SAGARE, *J. de Phys. IV* **7** (1997) C1-155
99. A. MATSUSHITA, T. IKENAG and S. ABE, *J. de Phys. IV* **7** (1997) C1-163
100. A. FAVRE, N. GUILHAUME and A. PIERRE, *J. de Phys. IV* **7** (1997) C1-675
101. H. A. GOLDBERG (Hoechst Celanese Corp., New Jersey), *US Pat.* **4725490**, February 1988
102. Y. HIRATA, T. NUMAZAWA and H. TAKADA, *Jap. J, Appl. Phys, Pt. 1* **36** (1997) 6062
103. C. M. LESCA, J. A. CORNIE, J. B. FRILER and A. S. ARGON, *J. Mat. Sci.* **28** (1993) 4391
104. L. R. McCREIGHT. H. W. RAUNCH Snr and W. H. SUTTON, in "Ceramic and Graphite Fibres and Whiskers", Academic Press, New York (1965), p. 48-55
105. D. R. ASKELAND, "The Science and Engineering of Materials", 3rd S. I. edition, Chapman and Hall, London (1996)
106. F. O. ANDEREGG, *Ind. Eng. Chem.* **31** (1939) 290
107. R. F. CAROSELI, in "Man Made Fibers, Science and Technology" vol. 3, editors H. F. MARK, S. M. ATLAS and E. CERNIA, Wiley Interscience, New York (1968), p. 432
108. S. EHLERS, *Des. Eng.* **59** (1964) 88
109. M. D. TAYLOR, in "Fine Ceramic Fibres", editors A. R. BUNSELL and M-H. BERGER, Marcel Dekker Inc, New York (1999)
110. A. R. BUNSELL, M-H. BERGER and A. KELLY, in "Fine Ceramic Fibres", Marcel Dekker Inc, New York (1999)
111. G. S. CORMAN, *Ceram, Eng. Sci. Proc.* **12** (1991) 1745
112. S. DENG, *J. Mat. Sci.* **31** (1996) 6077
113. S. DENG and R. WARREN, *J. Eur. Ceram. Soc.* **15** (1995) 513
114. M. F. STANTON, M. LAYARD, M. MILLER, M. MAY and E. KENT, *J. Natl. Cancer Inst.* **58** (1977) 587
115. "Safety in the Use of Mineral and Synthetic Fibres", International Labour Office, Geneva, Switzerland, *Occupational Safety and Health Series* **64** (1990)
116. P. ENGLE, *US Pat.* **2020403**, November 1935
117. Owens Corning Fibreglass Corp, *US Pat.* **2234986**, March 1941
118. F. T. WALLENBERGER, N. E. WESTON and K. MOTZFELDT, *Ceram. Eng. Sci. Proc.* **12** (1991) 1039
119. W. H. OTTO and R. F. VIDANOFF, (Narmco Industries Inc., San Diego), BuWeps, Cont. **N600(19) 59607**, Final summary rpt., January 1964
120. L. R. McCREIGHT, in "Ceramic and Graphite Fibres and Whiskers", Academic Press, New York (1965), p. 123-4
121. V. A. WENTE, *Ind. Eng. Chem.* **48** (1956) 1342
122. T. FURUYA, Y. UCHIYAMA, A. KOUDA (Denki Kagaku Kogyo Kabushi Kaisha), *UK Pat. App.* **2028788**, March 1980
123. K. A. KARST and H. G. SOWMAN (Minnesota Mining and Manufactruring Co.), *US Pat.* **4047963** September 1977
124. M. J. MORTON, J. D. BIRCHALL and J. E. CASSIDY, *UK Pat.* **1360197**, July 1974
125. M. H. STACEY and M. D. TAYLOR, (ICI), *Eur. Pat.* **318203**, 1987
126. J. D. FRENCH, G. E. WEITZ, E. J. LUKE, R. B. CASS, B. JADDIAN, P. BHARGAVA and A. SAFARI, *Proc. SPIE - Int. Soc. Opt. Eng.* **3044** (1997) 406
127. "A New Contender In Speciality Glass Fiber", *Chem. Week* **13**, April 22 (1987)
128. Horizons Inc, *US Pat*. **3110545**, November 1963
129. I. J. McCOLM and N. J. CLARK, in "High Performance Ceramics", Blackie, London (1988)
130. Massachusetts Institute of Technology, *US Pat.* **2048651**, July 1936
131. I. D. COCKSHOTT (ICI), unpublished work, 1974
132. Babcock and Wlicox Co., *Br. Pat* **1098595**, January 1968
133. T. F. COOK, *J. Amer. Ceram. Soc.* **74** (1991) 2959
134. S. W. TSAI and H. T. HAHN, in "Introduction to Composite Materials", Technomic Publishing Co., Westport, CONN, USA (1980), p. 1-5
135. D. K. HALE, *J. Mat, Sci.* **11**(1976) 2105
136. W. F. BROWN, *J, Chem. Phys.* **23** (1955) 1514
137. S. W. TSAI and H. T. HAHN, in "Introduction to Composite Materials", Technomic Publishing Co., Westport, CONN, USA (1980), p. 383-90
138. W. E. A. DAVIES, *J. Phys. D* **7** (1974) 120
139. H. L. Cox, *J. Appl. Phys.* **3** (1952) 72
140. J. AVESTON, G. COOPER and A. KELLY, in "Properties of Fibre Composites", *Conf. Proc. National Physical Laboratory*, IPC, London, p. 15
141. J. V. MILEWSKI, *Adv. Ceram. Mat.* **1** (1986) 36
142. Johns-Manville Corp., *US Pat.* **3118807**, January 1964
143. The Carborundum Company, *US Pat.* **2731359**, January 1956
144. A. R. BUNSELL (ed.), in "Fiber Reinforcements for Composite materials", Elsevier, Amsterdam (1988), p. 3

145. Toyota Motor Co. Ltd., Isolite Babcock refractories Co, Ltd and Japan Kokai Tokyo Koho, *Jap. Pat.* **59113139**, June 1984
146. R. C. PULLAR, D. R. PYKE, M. D. TAYLOR, and A. K. BHATTACHARYA, *J. Mat. Sci.* **33** (1998) 5229
147. H. Z. HUANG, H. KOZUKA and S. SAKA, *Jpn. J. Appl. Phys.* **28** (1989) 1805
148. G. A. LESIETRE, S. Y. ARLAGADD, S. K. KURTZ and S. YOSHIKAWA, "Inorganic Materials Symposium 1992", Materials Park, Ohio, USA, editor R. B. BHAGAT, p. 151-7
149. J. D. FRENCH, G. E. WEITZ, E. J. LUKE, R. B. CASS, B. JADDIAN, P. BHARGAVA and A. SAFARI, *Proc. SPIE - Int. Soc. Opt. Eng.* **3044** (1997) 406
150. J. M. RULE (duPont and Company), Uk Pat. **3007878**, November 1953
151. R. ROY, *J. Amer. Ceram. Soc.* **39** (1956) 145
152. D. H. NAPPER in "Polymeric Stabilization of Colloidal Dispersions", Academic Press, New York (1983)
153. C. J. BRINKER and G. W. SCHERER, in "Sol Gel Science", Academic Press, New York (1990)
154. J. Th. OVERBEEK, *J. Colloid Sci.* **58** (1977) 408
155. G. A. PARKS,*Chem. Rev.* **65** (1965) 177
156. R. J. HUNTER, in "Zeta Potential in Colloid Science", Academic Press, New York (1981)
157. E. MATEJEVIC, in "Principles and Applications of Water Chemistry, editors S. D. FAUST and J. V. HUNTER, Wiley, New York (1967)
158. D. NICHOLS in "Complexes and First Row Transition Elements", Macmillan, London (1974)
159. S. GITS-LEON, F. LEFAUCHEUX and M. C. ROBERT, *J. Cryst. Growth* **84** (1987) 155
160. P. J. FLORY, in "Principles of Polymer Chemistry", Cornell University Press, New York (1953)
161. R. ZALLEN in "The Physics of Amorphous Solids", Wiley-Interscience, New York (1983)
162. H. D. GESSER and P. C. GOSWAMI, *Chem. Rev.* **89** (1989) 765
163. P. J. FLORY, *Faraday Disc. Chem. Soc.* **57** (1974) 7
164. L. L. HENCH and J. K. WEST, *Chem. Rev.* **90** (1990) 33
165. Y. P. KLIMENTOVA, L. F. KIRICHEKO and Z. Z. VYSOTSKII, *Ubr. Khim. Zh.* **26** (1970) 49
166. J. M. FLETCHER and C. J. HARDY, *Chem. Ind.* **18** (1968) 48
167. J. D. MACKENZIE, *J. Non-Cryst. Solids* **100** (1988) 162
168. J. C. BERNIER, *Mat. Sci. Eng.* **A109** (1989) 233
169. E. MATEIJIVIC, in "The Science of Ceramic Chemical Processing", eds. L. L. HENCH and D. R. ULRICH, Wiley, New York (1986
170. J. L. and D. L. SEGAL, *Proc. Br. Ceram. Soc.* **36** (1985) 123
171. D. W. JOHNSON, Jr., *Ceram. Bull.* **60** (1981) 221
172. U. SCHWERTMANN and R. M. CORNELL, in "Iron Oxides in the Laboratory", VCH, Weinheim, Germany (1991)
173. M. D. TAYLOR and M. H. STACEY, personal communication (1996)
174. J. H. A. van der WOUDE and P. L. de BRUYN, *Coll. Surf.* **12** (1984) 179
175. M.-L. LAY, H.-M. WU and C.-H. HUANG, *J. Mat. Sci.* **30** (1995) 5473
176. M. H. STACEY, personal communication (1995)
177. P. N. PUSEY, "Some Effects of Polydispersity on the scattering of Radiation by Colloids", Symposium on the Polydispersity Problem in Colloid Science, University of Nottingham (1987)
178. D. R. PYKE and M. D. TAYLOR, private communication regarding unpublished research for ICI plc
179. A. L. HORVATH, in "Handbook of Aqueous Electrolyte Solutions", Ellis Horwood Ltd., Chichester, UK (1985)
180. S. ROHRSETZER and F. CSEMPESZ, *Colloid Polymer Sci.* **257** (1979) 85
181. "Stability Constants", Special Publication No. 17, Supplement No. 1, London Chemical Society (1964)
182. R. S. YOUNG, in "Cobalt", Reinhold Publishing Corp., New York (1948)
183. J. J. CHRISTENSEN, D. J. EATOUGH and R. M. IZATT, *Chem. Rev.* **74** (1974) 353
184. M. HIRAOKA, in "Crown Compounds, Their Characteristics and Applications. Studies in Organic Chemistry" vol. 12", Elsevier, Amsterdam (1982)
185. P. B. METZ, D. MORAS and R. WEISS, *Acta Cryst.* **B29** (1973) 1382
186. D. G. PARSONS and J. N. WINGFIELD, *Inorg. Chim. Acta.* **18** (1976) 263
187. P. C. JUNK and J. W. STEED, *J. Chem. Soc., Dalton Trans.* (1999) 407
188. "Gmelins Handbuch der Anorganischen Chemie" vol. 58 – Kobalt, Verlag Chemie, Weinheim (1963)
189. J. WOODHEAD, personal communication (1997)
190. C. F. BOHREN and D. R. HUFFMAN, in "Absorption and Scattering of Light from Small Particles, Wiley Interscience, London (1983)
191. C. J. BRINKER and R. A. ASSINK, *J. Non-cryst. Solids* **111** (1989) 48
192. M. D. TAYLOR, D. R. PYKE and M. H. STACEY, ICI and University of Warwick, unpublished work and personal communications 1994-99
193. K. GOSLINS, W. J. SIME, U. J. MULLEY and M. J. BALDOCK (Unilever Ltd.), *Eur. Pat. App.* **79301204**, January 1980
194. D. L. TEAGARDEN, J. F. RADAVICH, J. L. WHITE and S. L. HEM, *J. Pharm. Sci.* **70** (1989) 762
195. T. ASSIH, A. AYRAH, M. ABENOLA and J. PHILIPPOU, *J. Mat. Sci.* **23** (1988) 3326
196. S. SAKKA and H. KOZUKA, *J. Non-Cryst. solids* **100** (1988) 142

197. D-Y. SHIN and S-M. HAN, *J. Sol-gel Sci. Tech.* **1** (1994) 267
198. Y. ABE, S. HORIKIRI, K. FUJIMURA and E. ICHIKI, *Proc. 4th Int. Conf. Comp. Mat.* (Tokyo, 1981) 1427
199. S. SCHONHERR, H. GORZ, D. MULLAR and W. GESSNER, *Z. Anorg. Alleg. Chem.* **47** (1984) 188
200. J. C. W. CHEN, Y. YANG, J. R. MARTINEZ, S. DONG, V. TELLURI and C. JAKUS, *J. Polymer Sci. Pt. A: Polymer Chem.* **29** (1991) 495
201. W. GLAUBIT, D. SPORN and R. JAHN, *J. Sol-Gel Sci. Tech.* **2** (1994) 525
202. S. SAKKA and K. KAMIYA, *J. Non-Cryst. Solids* **48** (1982) 31
203. G. WINTER, M. MANSMANN, N. SCHON and H. SCHNORING (Bayer AG), *UK Pat.* **1313677**, April 1973
204. M. D. TAYLOR, ICI, personal communication (1996)
205. M. von SMOLUCHOWSKI, *Z. Phys. Chem.* **92** (1917) 129
206. "General Properties of Polyox Water Soluble Resins", Union Carbide (1981)
207. "Polyox: Forming Association Compounds", Union Carbide Bulletin **F-43272** (1971)
208. J. J. STRATTA, Union Carbide Technical Bulletin **45-T-2** (1969)
209. "Crown Ethers and Phase Transfer Catalysis in Polymer Science", vol. 5, ed. L. J. MATHIAS and C. E. CARRAHER, Plenum Press, New York (1984)
210. L. H. AHRENS, *Geochim. Cosmochim. Acta* **2** (1952) 155
211. L. PAULING, in "The Nature of the Chemical Bond", Cornell University Press, Ithaca, NY (1960)
212. "CRC Handbook of Chemistry and Physics, 69th edition", ed. R. C. WEAST, M. J. ASTLE and W. H. BEYER, CRC Press Inc., Boca Raton, Florida (1988)
213. Sumitomo Chemical Co. Ltd., *UK Pat.* **1457801**, December 1976
214. R. L. COBLE, *J. Appl. Phys.* **32** (1961) 787
215. M. P. HARMER, H. M. CHAN and D. M. SMYTH, in "Compositional Control of Ceramic Microstructures - an Overview", *Mat. Res. Soc. Symp. Proc., Defect Prop. Process, High Tech. Non-metal. Mat.* (1986) 125
216. M. HILLERT, *Acta Metal.* **13** (1965) 227
217. C. WAGNER, *Z. Elektrochem.* **65** (1961) 581
218. D. J. SROLVITZ, M. P. ANDERSON, G. S. GREST and P. S. SAHNI, *Scripta Metal.* **17** (1983) 241
219. V. TIKARE and J. D. CAWLEY, *J. Amer. Ceram. Soc.* **81** (1998) 485
220. K. W. MAHIS, K. HANSON and J. W. MORRID Jr., *Acta Metal.* **28** (1980) 443
221. M. A. FORTES and A. C. FERRO, *Acta Metal.* **33** (1985) 1697
222. Z. NIKOLIC and W HUPPMANN, *Acta Metal.* **28** (1980) 475
223. M. A. VINNIK, *Russ. J. Inorg. Chem.* **10** (1965) 1164
224. A. TAUBER, S. DIXON Jr. and R. O. SAVAGE Jr., *J. Appl. Phys.* **41** (1964) 1008 Jr., *J. Appl. Phys.* **41** (1964) 1008
225. H. SEVERIN, J. K. VOGEL and G. WINKLER, *Z. Ang. Phys.* **18** (1964) 65
226. B. MASON, *Geol For.* **65** (1943) 97
227. M. ERCHAK Jr., I. FUNKUCHEN and R. WARD, *J. Amer. Ceram. Soc.* **28** (1946) 2085
228. M. ERCHAK Jr., I. FUNKUCHEN and R. WARD, *J. Amer. Ceram. Soc.* **28** (1946) 2093
229. H. J. van HOOK, *J. Amer. Ceram. Soc.* **47** (1964) 579
230. B. T. SHIRK, *Mat. Res. Bull.* **5** (1970) 771
231. Y. GOTO and T. TAKADA, *J. Amer. Ceram. Soc.* **43** (1960) 150
232. G. SLOCARI, *J. Amer. Ceram. Soc.* **56** (1973) 489
233. A. G. SADLER, *J. Canadian Ceram. Soc.* **34** (1965) 155
234. P. BATTI, *Ann. Chim. (Rome)* **50** (1960) 1461
235. H. STABLEIN and W. MAY, *Ber. Deut. Keram. Geselschaft* **46** (1969) 69
236. J. S. REED and R. M. FULRATH, *J. Amer. Ceram. Soc.* **56** (1973) 207
237. B. DURRANT and J. M. PARIS, *J. Mat. Sci. Lett.* **16** (1981) 274
238. H. WULLKOPF, *Int. J. Mag.* **3** (1972) 179
239. H. NEUMANN and H. P. J. WIJN, *J. Amer. Ceram. Soc.* **51** (1968) 536
240. V. V. GRISHAEV, A. P. ERASTOVA, M. N. KUROTOVA, B. M. LEBED and J. G. SAKSONOV, *Electon. Tech. Series* **6**, *Mat.* **7** (1984) 24
241. J. H. OH, T. NAMIKAWA and M. SATOU, *J. Jap. Chem. Soc.* (1978) 636
242. K. HANAWA, H. SAKAI and A. SIMIZU, in "Ferrites", *Proc. ICF6*, Tokyo and Kyoto (1992) 1395
243. V. K. S. SANKARANARAYANAN and D. C. KHAN, *J. Magn. Mag. Mat,* **153** (1996) 337
244. K. NOMA, N. MATSUSHITA, S. NAKAGAWA and M. NAOE, *J. Appl. Phys.* **79** (1996) 5970
245. Y. GOTO and K. TAKAHASHI, *J. Jap. Soc. Powd. Powd. Metall.* **17** (1971) 193
246. K.GOTO, *J. Jap. Soc. Powd. Powd. Metall.* **18** (1972) 209
247. Y. GOTO, M. HIGASHIMOTO and K. TAKAHASHI, *J. Jap. Soc. Powd. Powd. Metall.* **21** (1974) 21
248. S. A. SEYYED EBRAHIMI, A. J. WILLIAMS, N. MARTINEZ, A. ATAIE, A. KIANVASH, C. B. PONTON and I. R. HARRIS, *J. de Phys. IV* **7** (1997) C1-325
249. H. KOJIMA and C. MIYAKAWA, *Bull. Res. Inst. Sci. Meas., Tokohu University* **13** (1965) 105
250. H. KOJIMA, in "Ferromagnetic Materials" vol. 3, ed. E. P. WOHLFARTH, North-Holland Physics Publishing, Amsterdam (1982), p. 305 – 91
251. W. BERGER and F. PAWLEK, *Arch. Eisenhuttenwesen* **28** (1957) 101

252. L. G. van UITERT, *J. Appl. Phys.* **28** (1957) 317
253. Y. J. CHEN and M. H. KRYDER, *J. Appl. Phys.* **79** (1996) 4878
254. P. BATTI, *Univ. Triest, Fac. Ingegneria* **11** (1969)
255. P. BATTI and G. SLOCCARI, *Ann. Chim.* **57** (1967) 777
256. A. DESCHAMPS and F. BERTAUT, *C. R. Acad. Sci.* **244** (1957) 3069
257. J. M. P. J. VERSTEGEN, *J. Sol. State Chem.* **7** (1973) 468
258. T. M. PERAKALINA, M. A. VINNIK, R. I. ZEVEREVA and A. P. SCHUROVA, *Zh. Eksp. Teor. Fiz.* **59** (1970) 1490
259. T. M. PERAKALINA and V. P. CHEPARIN, *Fiz. Tverd. Tela.* **9** (1967) 217
260. K. WATANABE and J. KAWABE, *J. Mat. Chem.* **7** (1997) 1797
261. X. BATLLE, M. GARCIA del MURO and A. LABARTA, *Phys. Rev. B* **55** (1997) 6440
262. T. O. KIM, S. J. KIM, P. GROHS, D. BONNENBERG and K. A. HEMPEL, in "Ferrites", Proc. ICF6, Tokyo and Kyoto, (1992) 75
263. W. GRUNBERGER, B. SPRINGMANN, M. BRUSBERG, M. SCHMIDT and R. JANKE, *J. Magn. Mag. Mat.* **101** (1991) 173
264. S. I. KUZNETSOVA, E. P. NAIDEN and T. N. STEPANOVA, *Inorg. Mat.* **24** (1988) 856
265. A. L. STUIJTS, in "Ceramic Microstructures", John Wiley, New York (1968), p. 443
266. E. M. C. HUIJSER-GERITS and G. D. RIECK, *J. Appl. Cryst.* **9** (1976) 18
267. J. DROBEK, W. C. BIGELOW and R. G. WELLS, *J. Amer. Ceram. Soc.* **44** (1961) 262
268. C. JAQUIOD and D. AUTISSIER, *J. Magn. Mag. mat.* **104-7** (1992) 419
269. T. M. PEREKALINA, A. D. SHCHVROVA, S. S. FONTON and D. G. ANNIKOV, *Soviet Phys.* **JETP-31** (1970) 440
270. M. A. VINNIK, A. I. AGRANOVSKAYA and N. N. SEMENOVA, *Russ. J. Inorg. Chem.* **12** (1967) 18
271. G. SLOKAR and E. LUCCHINI, *J. Magn. Mag. Mat.* **8** (1978) 237
272. H. NISHIO and H. YAMAMOTO, *J. de Phys. IV,* **7** (1997) C1-317
273. L. M. SILBER and E. TSANTES, *IEEE Trans. Magn.* **MAGN-5** (1969) 600
274. G. U. BEN-XI, L. U. HUAI-XIAN and D. U. YOU-WEI, *J. Magn. Mag. Mat.* **31-4** (1983) 803
275. T.-T. FANG, J. B. HWANG and F. S. SHIAU, *J. Mat. Sci. Let.* **8** (1989) 1386
276. F. HABEREY, R. LECKEBUSCH, M. ROSENBERG and K. SAHL, *Mat. Res. Bull.* **15** (1980) 493
277. H. TAGUCHI, *J. de Phys. IV* **7** (1997) C1-299]
278. O. T. OZKAN and H. ERKALFA, *J. Eur. Ceram. Soc.* **14** (1994) 351
279. M. TOKAR, *J. Amer. Ceram. Soc.* **52** (1969) 302
280. F. KOOLS, *Ber. Dt. Keram. Ges.* **55** (1978) 301
281. Y. CHEN, D. E. LAUGHLIN, X. MA and M. H. KRYDER, *J. Appl. Phys.* **81** (1997) 4380
282. S. RAM, *J. Magn. Mag. Mat.* **82** (1989) 129
283. H. STABLEIN, *Tech. Mit. Krupp., Forsch. Ber.* **26** (1968) 81
284. M. J. RUTHNER, in "Ferrites", *Proc. ICF6*, Tokyo and Kyoto (1992) 40
285. Sumitomo Chemical Co. Ltd., *Jpn. Pat. Appl.* **4871058**, June 1973
286. H. TAGUCHI, T. TAKEISHI, K. SUWA, K. MASUZAWA and Y. MINACHI, *J. de Phys. IV* **7** (1997) C1-311
287. T. K. KUNDU and D. CHAKRAVORTY, *J. Mat. Res.* **14** (1999) 395
288. F. HABEREY and F. KOOLS, *Proc. ICF4.*, Japan, (1980) 356
289. J.-H. SEOK, J.-H. KIM and S.-H. CHO, in "Ferrites", *Proc. ICF6*, Tokyo and Kyoto (1992) 1126
290. F. J. A. den BROEDER and P. E. C. FRANKEN, in "Grain Boundary Phenomena in Electronic ceramics, ed. L. M. LEVINSON, The American Ceramic Society, Columbus, Ohio (1981) 494
291. L. ARMELAO, G. GRANOZZI, E. TONDELLO, P. COLOMBO, G. PRINCIPI, P. P. LOTTICI and G. ANTONIOLI, *J. Non-Cryst. Solids* **192** (1995) 435
292. M. D. TAYLOR, personal communication (1997)
293. E. M. C. HUIJSER-GERITS, G. D. RIECK and D. L. VOGEL, *J. Appl. Cryst.* **3** (1970) 243
294. T. AKASHI, *Jap. J. Appl. Phys* **30** (1961) 708
295. M. PAULUS, *Phys. Status. Solidi.* 2(1962) 1181 & 1325
296. C. SURIG and K. A. HEMPEL, *IEEE Trans.* **MAG-30** (1994) 997
297. V. DEVENDER REDDY and P. VENUGOPAL REDDY, *Phys. Stat. Sol. A* **142** (1994) 451
298. J. NICOLAS, in "Ferromagnetic Materials" vol. 2, ed. E. P. WOHFARTH, North-Holland Physics Publishing, Amsterdam (1980) p. 291
299. J. F. MOULDER, W. F. STCKLE, P. E. SOBOL and K. D. BOMBEN, in "The Handbook of X-ray Photoelectron Spectroscopy", ed. J. CHASTAIN and R. C. KING, Jr., Physical Electronics Inc., Eden Prairie, Minnesota (1995)
300. V. K. S. SANKARANARAYANAN, Q. A. PANKHURST, D. P. E. DICKSON and C. E. JOHNSON, *J. Magn. Mag. Mat,* **120** (1993) 73
301. W. ZHONG, W. DING, N. ZHANG, J. HONG, Q. YAN and Y. DU, *J. Magn. Mag. Mat.* **168** (1997) 196
302. M. D. TAYLOR, personal communication, (1998)
303. R. C. PULLAR and A. K. BHATTACHARYA, *Mat. Lett.* **39** (1999) 173
304. W. B. HILLIG, *Bull. Amer. Ceram. Soc.* **66** (1987) 373

305. K. P. BELOV, L. I. KOROLEVA, R. Z. LEVITIN, Y. V. JERGIN and A. V. PEDKO, *Phys. Staus Solidi* **12** (1965) 219
306. H. B. G. CASIMIR, J. SMIT, U. ENZ, J. F. FAST, H. P. J. WIJN, E. W. GORTER, A. J. W. DUINESTEIN, J. D. FAST and J. J. JONG, *J. Phys. Rad.* **20** (1959) 360
307. M. TAKAHASHI, *J. Appl. Phys.* **33** (1962) 1101
308. L. NEEL, *Ann. Phys.* **3** (1948) 137
309. P. W. ANDERSON, *Phys. Rev.* **79** (1950) 705
310. H. G. RICHTER, *IEEE Trans. Magn.* **MAGN-4** (1968) 263
311. R. F. FISCHER and H. KRONMULLER, *J. Appl. Phys.* **83** (1998) 3271
312. K. J. SIXTUS, K. J. KRONENBERG and R. K. TENZER, *J. Appl. Phys.* **27** (1956) 1051
313. D. J. CRAIK and E. H. HILL, *J. Phys. Colloque* **38** (1977) C1-39
314. M. VELET, P. RODRIGUEZ, X. OBRADORS and A. ISALGUE, *J. de Phys. IV* **7** (1997) C1-335
315. J. DUFOR, R. LATORRE, C. NEGRO, E. M. ALCALA, A. FORMOSO, and F. LOPEZ-MATEOS, *J. Magn. Mag. Mat.*, **172** (1997) 308
316. W. A. KALZMAREK and B. W. NINHAM, *J. Appl. Phys.* **76** (1994) 6065
317. W. ROOS, H. HAAK, C. VOIGHT and K. A. HEMPEL, *J. Phys. Colloque* **38** (1977) C1-35
318. H. S. SHIN and S.-J. KWON, in "Ferrites", *Proc. ICF6*, Tokyo and Kyoto (1992) 1402
319. C. S. WANG, F. L. WEI, M. LU, D. H. HAN and Z. YANG, *J. Magn. Mag. Mat.* **183** (1998) 241
320. K. HANEDA and A. H. MORRISH, *Phase Trans.* **24-6** (1990) 66
321. H. FAHLENBRACH, *Werkst. U. Betr.* **90** (1957) 735
322. A. L. STUIJTS, G. W. RATHENAU and G. H. WEBER., *Phil. Tech. Rev.* **16** (1954/5) 141
323. H. L. GLASS, *Proc. IEEE* **76** (1988) 151
324. I.-C. TUNG, L. H. PERNG, S. W. WANE and T. S. CHIN, *J. de Phys. IV* **7** (1997) C1-743
325. I.-C. TUNG, L. H. PERNG, T. S. CHIN and C. H. LIN, *J. de Phys. IV* **7** (1997) C1-745
326. S. KITAHATA and M. KISHIMOTO, in "Ferrites", *Proc. ICF6*, Tokyo and Kyoto (1992) 972
327. S.-I. KITAHATA, *Jpn. J. Appl. Phys.* **36** (1997) 676
328. H. YOKOYAMA, T. MAEDA, T. NOMURA, O. KUBO and T. IDO, in "Ferrites", *Proc. ICF6*, Tokyo and Kyoto (1992) 1418
329. L. JAHN and H. G. MULLER, *Phys. Status Solidi* **35** (1969) 723
330. B. T. SHIRK and W. R. BUESSM, *J. Appl. Phys.* **40** (1969) 1294
331. A. COCHARDT, *J. Appl. Phys.* **34** (1963) 1273
332. W. A. KACZMAREK, B. IDZIKOWSKI and K.-H. MULLER, *J. Magn. Mag. Mat.* **177-81** (1998) 921
333. C. TANASOIU, P. NICOLAU, C. MICEA, *IEEE Trans. Magn.* **MAGN-12** (1976) 980
334. J.-H. SEOK, J.-J. KIM., B.-K. LEE and S.-H. CHO, in "Ferrites", *Proc. ICF6*, Tokyo and Kyoto (1992) 180
335. E. WU, S. J. CAMPBELL and W. A. KACZMAREK, *J. Magn. Mag. Mat.* **177-81** (1998) 255
336. V. V. PANKOV, M. PERNET, P. GERMI and P. MOLLARD, *J. Magn. Mag. Mat.* **120** (1993) 69
337. A. YAZAKI, D. ENDO, T. UCHIDA, Y. NAGATA and K. OHTA, in "Ferrites", *Proc. ICF6*, Tokyo and Kyoto (1992) 385
338. H. TAGUCHI, F. HIRATA, T. TAKESHI and T. MORI, in "Ferrites", *Proc. ICF*, Tokyo and Kyoto (1992) 1118
339. B. RAMAMURTHY ACHARYA, S. PRASAD, N. VENKATARAMANI and S. N. SHRINGI, *J. de Phys. IV* **7** (1997) C1-147
340. S. DIAZ, N. SUAREZ, J. C. FALOH, J. C. SANCHEZ, F. LECCABUE, B. E. WATTS and G. ALBANESE, *J. de Phys. IV.* **7** (1997) C1-333
341. J. SMIT, F. K. LOTGERING and U. ENZ, *J. Appl. Phys. Suppl.* **31** (1960) 137 S
342. X. SUI and M. H. KRYDER, *IEEE Trans. Magn.* **MAG-30** (1994) 4044
343. A. TAUBER, J. A. KOHN and R. O. SAVAGE, *J. Appl. Phys.* **14** (1963) 1265
344. M. V. CABANAS, J. M. GONZALEZ-CALBET, J. RODRIGUEZ-CARJAVAL and M. VALLET-REGI, *J. Solid State Chem.* **111** (1994) 229
345. K. HANEDA, X. Z. ZHOU and A. H. MORRISH, in "Ferrites", *Proc. ICF6*, Tokyo and Kyoto(1992) 1406
346. F. K. LOTGERING, U. ENZ and J, SMIT, *Phil. Res. Rept.* **16** (1961) 441
347. K. SUETO, H. SAKUMOTO, A. SUZUKI and M. SUGIMOTO, in "Ferrites", *Proc. ICF6*, Tokyo and Kyoto (1992) 964
348. D. AUTISSIER, A. PODEMBSKI and C. JACQUIOD, *J. de Phys. IV* **7** (1997) C1-409
349. X. WANG, G. XIONG, X. WANG, Y. LIU and L. ZHANG, *J. Mat. Sci. Let.* **16** (1997) 1606
350. R. SLOWAK, C. VOIGHT, K. A. HEMPEL and A. KYPRIAMIDIS, *Appl. Phys.* **14** (1977) 197
351. G. ALBANESE, M. CARBICICCHIO, A. DERIU, G. ASTI and S. RINALDI, *Appl. Phys.* **7** (1975) 227
352. J. VERWEEL, *J. Appl. Phys.* **38** (1967) 1111
353. G. A. JONES, *J. Magn. Mag. Mat.* **127** (1993) 195
354. A. P. LIPLOT, A. GERARD and F. GRANDJEAN, *IEEE Trans. Mag.* **MAGN-18** (1982) 1463
355. R. MULLER, *J. Magn. Mag. Mat.* **120** (1993) 61
356. A. COLLOMB, B LAMBERT-ANDRON, J. X. BOUCHERLE and D. SAMARAS, *Physica Status Solidi A* **96** (1986) 385

357. C. GUILLAUD, *Proc IEEE* **104B** (1957) 165
358. M. PAULUS and C. GUILLAUD, *J. Phys. Soc. Jpn.* **17** (1962) 632
359. Y. LESCROEL and A. PIERROT, *Cables Transm.* **14** (1960) 220
360. E. W. GORTER, *Phil. Res. Rep.* **9** (1954) 403
361. E. OGAWA and O. KUBO, in "Ferrites", *Proc. ICF 6*, Tokyo and Kyoto (1992) 1410
362. A. H. MONES and E. BANKS, *J. Phys. Chem. Solids* **4** (1958) 217
363. U. N. MULAY, A. P. B. SINHA, *Indian J. Pure Appl. Phys.* **8** (1970) 412
364. N. K. DUNG, D. L. MINH, B. T. CONG, N. CHAU and N. X. PHUC, *J. de Phys. IV* **7** (1997) C1-313
365. M. MARYSKO, Z. FRAIT and S. KRUPICKA, *J. de Phys. IV* **7** (1997) C1-347
366. C. HASHIMOTO, T. KIMURA, K. HASHIMOTO, H. KIMURA and K. HANEDA, in "Ferrites", *Proc. ICF6*, Tokyo and Kyoto (1992) 1414
367. P. BRAHMA, A. K. GIRI, D. CHAKRAVORTY, M. ROY and D. BAHADUR, *J. Magn. Mag. Mat.* **117** (1992) 163
368. Z. SIMSA, R. GERBER, V. LEWIS and V. A. M. BRABERS, *J. de Phys.* **7** (1997) C1-197
369. Y. KANEKO, S. ANAMOTO and A. HAMAMURA, *J. Jpn. Inst. Powder Powder Metal.* **34** (1987) 169
370. M. V. RANE, D. BAHADUR, S. K. MANDAL and M. J. PATNI, *J. Magn. Mag. Mat.* **153** (1996) L1
371. N. NAGAI, N. S. UGITA and M. MAEKAWA, *J. Magn. Mag. Mat.* **120** (1993) 33
372. X. Z. ZHOU, A. H. MORRISH, Z. YANG and H.-X. ZENG, *J. Appl. Phys.* **75** (1994) 5556
373. E. BRANDO, H. VINCENT and J. RODRIGUEZ-CARJAVAL, *J. de Phys. IV* **7** (1997) C1-303
374. S. DIAZ, J. L. SANCHEZ, F. LECCABUE, B. E. WATTS, G. BOCELLI and G. ALBANESE, *J. de Phys. IV* **7** (1997) C1-331
375. S. G. LEE and S. J. KWON, *J. Magn. Mag. Mat.* **153** (1996) 279
376. S. RAM and J. C. JOUBERT, *J. Magn. Mag. Mat.* **99** (1991) 133
377. G. ALBANESE, M. CARBUCCHIO and G. ASTI, *Appl. Phys.* **11** (1976) 81
378. H. YAMAMOTO, T. MAKI and T. TAKAHASHI, in "Ferrites", *Proc. ICF6*, Tokyo and Kyoto (1992) 113
379. S. RAM and J. C. JOUBERT, *IEEE Trans. Mag.* **MAGN-28** (1992) 15
380. M. V. CABANAS, J. M. GONZALEZ-CALBET and M.VALLET-REGI, *J. Solid State Chem.* **115** (1995) 347
381. O. KUBO, T. IDO, H. YOKOYAMA and Y. KOIKE, *J. Appl. Phys.* **57** (1985) 4280
382. W. H. GERLING, *IEEE Trans. Magn.* **MAGN-6** (1970) 737
383. S. FONER, *Rev. Sci. Instr.* **30** (1959) 548
384. J. MALLINSON, *J. Appl. Phys.* **37** (1966) 251
385. M. SPRINGFORD, J. R. STOCKTON and W. R. WAMPLER, *J. Phys.* **E4** (1972) 1036
386. R. PAUTHERNET, *J. Appl. Phys.* **53** (1982) 2029
387. C. D. GRAHAM, *J. Appl. Phys.* **53** (1982) 2032
388. M. SUGIMOTO, *J. Amer. Ceram. Soc.* **82** (1999) 269
389. M. SUGIMOTO, in "Ferromagnetic Materials" vol. 3, ed. E. P. WOHFARTH, North-Holland Physics Publishing, Amsterdam (1980) p. 392 – 440
390. Y. IKEDA and Y. BRANDO, *J. de Phys.* **7** (1997) C1-343
391. C. HECK , in "Magnetic Materials and their Applications", Butterworths, London (1974).
392. J. P. JOULE, *Ann. Elect. Magn. Chem.* **8** (1842) 219
393. D. NICHOLLS, in "Complexes and First-Row Transition Elements", Macmillan Education Ltd., London (1974)
394. F. BLOCH, *Z. Phys.* **74** (1932) 295
395. J. KACZER, *Czech. J. Phys.* **B12** (1962) 354
396. H. J. WILLIAMS, *Elec. Eng.* **69** (1950) 817
397. J. D. LIVINGSTONE, *J. Appl. Phys.* **41** (1970) 197
398. H. P. WIJN, E. GORTER, C. J. ESVELDT and P. GELDERMANS, *Phil. Tech. Res.* **16** (1954) 124
399. O. ECKERT, *Proc. IEEE* **104B** (1957) 428
400. E. A. NESBIT and R. D. HEIDENREICH, *J. Appl. Phys.* **30** (1959) 1000
401. H. P. J. WIJN, H. van der HEIDE and J. F. FAST, *Proc IEEE* **104B** (1957) 412
402. E. W. GORTER and C. J. ESVELDT, *Proc IEEE* **104B** (1957) 419
403. F. FRAUNBERGER, *Ann. Phys.* **6** (1948) 178
404. J. SMIT, *J. Phys. Rad.* **20** (1959) 370
405. F. K. LOTGERING, *J. Phys. Chem. Solids* **35** (1974) 1633
406. J. C. SLOVCZEWSKI, *J. Appl. Phys. Let.* **32** (1961) 2535
407. W. H. MEIKLEJOHN and C. P. BEAN, *Phys. Rev.* **105** (1957) 904
408. F. E. WAWNER, in "Fiber Reinforcements for Composite Materials", ed. A. R. BUNSELL, Elsevier, Amsterdam (1988), p. 371-3
409. S. YAJIMA, X. HASEGAWA, J. HAYASHI and M. IIUMA, *J. Mat. Sci.* **13** (1978) 2569
410. G. SIMON and A. R. BUNSELL, *J. Mat. Sci.* **19** (1984) 349
411. S. YAJIMA, T. IWAI, T. YAMAMURA, K. OKAMURA and Y. HASEGAWA, *J. Mat. Sci.* **16** (1981) 1349

412. T. YAMAMURA, T. ISHIKAWA, M. SHIBUYA, T. HISAYUKY and K. OKAMURA, *J. Mat. Sci.* **23** (1988) 2589
413. T. SEGUCHI, M. SUGIMOTO and K. OKAMURA, in "High Temperature Ceramic Matrix Composites, Woodhead, Cambridge, UK (1993), p.51
414. J. LIPOWITZ, H. A. FREEMAN, R. T. CHEN and E. R. PRACK, *Adv. Ceram. Mat.* **2** (1987) 121
415. G. E. LEGROW, T. F. LIM, J. LIPOWITZ and R. S. R. REAOCH, *J. Amer. Ceram. Soc. Bull.* **6** (1987) 363
416. W. VERBEEK, *Ger. Offen.* **2218960**, 1973
417. H. P. BALDUS, G. PASSING, D. SPORN and A. THIERAUF, in "High Temperature Ceramic Matrix Composites, Vol. 2, Ceramic Transformations", ed. R. NASLAN and A. G. EVANS, ACS Westerville, USA (1995), p. 75
418. R. Y. LIN, J. ECONOMY, H. H. MURTY and R. OHNSORG, *Appl. Polymer Symp.* **29** (1976) 175
419. "Speciality Inorganic Fibres", Chemical Economics Handbook, SRI International (1992)
420. I. HARTER, C. C. NORTON Jr and C. D. Christie (Babcock and Wilson Co.), *US Pat.* **2467889**, April 1949
421. du Pont, *US Pat.* **3104943**, September 1963
422. Babcock and Wilcox Co., *BR Pat.* **1098595**, January 1968
423. M. H. STACEY, M. D. TAYLOR and A. M. WALKER, *Proc of ICCM6/ECCM2, Vol. 5*, Elsevier, London (1987), p. 371-81
424. D. M. WILSON, S. L. LIEDER and D. C. LUENBERG, *Ceram. Sci. Proc.* **8** (1995) 1005
425. Y. ABE, A. R. BUNSELL, G. SIMON and M. AKIYAMA, in "Fiber Reinforcements for Composite materials", ed. A. R. BUNSELL, Elsevier, Amsterdam (1988), p. 427
426. W. R. CANNON and T. G. LANDON, *J. Mat. Sci.* **18** (1983) 683
427. A. K. BHATTACHARYA, A. HARTRIDGE, K. K. MALLICK and D. M. TAYLOR, *J. Mat. Sci.* **15** (1996) 1654
428. H. SHIN (du Pont Co.), *UK Pat.* **1414854**, November 1975
429. A. K. DHINGRA, *Phil. Trans. Roy. Soc. Ldn*, **A294** (1980) 411
430. J. C. ROMINE, *Ceram. Eng. Sci.* **8** (1987) 755
431. K .KOBA, T. UTSUNOMIYA, Y. SAITOW, K. IWANAGA, M. MATSUE and N. NISHITARI (Mitsui Mining Co. Ltd.), *Eur. Pat. App.* **260868**, March 1988; *Jpn. Pat. App.* **217183**, September 1986
432. T. E. WOOD, D. M. WILSON and H. G. SOWMAN (Minnesota Mining and Manufacturing Co.), *Eur. Pat. App.* **294208**, December 1988
433. W. GLAUBITT, D. SPORN and R. JAHN, *J. Sol-Gel Sci. Tech.* **2** (1994) 525
434. T. MAKI and S. SAKKA, *J. Mat. Sci. Lett.* **5** (1986) 28
435. G. W. RITTER, *US Pat.* **4545924**, October 1983
436. W. ZHOU and T. D. McGEE, *J. Mat. Sci. Lett.* **17** (1998) 673
437. Q.-G. CHEN and J. T. DAVIES, *Brit. Ceram. Trans.* **96** (1997) 170
438. T. A. PARTHASARATHY, T. MAH and K. KELLER, *J. Amer. Ceram. Soc* **75** (1992) 1756
439. T. A. PARTHASARATHY, T. MAH and K. KELLER, *Ceram. Eng. Sci, Proc.* **12** (1991) 1767
440. K. D. BUDD and D. M. WILSON (Minnesota Mining and Manufacturing Co.), *US Pat. App.* **709377** September 1991
441. G. N. MORSCHER, K. C. CHEN and K. S. MAZDIYAZNI, *Ceram. Eng. Sci, Proc.* **15** (1994) 181
442. D. POPOVICH, J. L. LOMBARDI and B. H. KING, *Ceram. Eng. Sci, Proc* **18** (1997) 65
443. W. GLAUBITT, W. WATZKA, H. SCHUTZ and D. SPORN, *J. Sol-Gel Sci. Tech.* **8** (1997) 29
444. Y. LIU, Z. ZHANG, B. KING, J. HALLORAN and R. M. LAINE, *J. Amer. Ceram. Soc* **81** (1998) 629
445. B. H. KING and J. W. HALLORAN, *J. Amer. Ceram. Soc.* **78** (1995) 2141
446. R. C. PULLAR, M. D. TAYLOR and A. K. BHATTACHARYA, *J. Eur. Ceram. Soc.* **18** (1998) 1759
447. R. C. PULLAR, M. D. TAYLOR and A. K. BHATTACHARYA, *J. Eur. Ceram. Soc.* **19** (1999) 1747
448. B. H. KING and J. W. HALLORAN, *J. Amer. Ceram. Soc.* **78** (1995) 2141
449. S. C. FARMER, A. SAYIR, P. O. DICKERSON and S. L. DRAPER, *Ceram. Eng. Sci. Proc.* **16** (1995) 969
450. P. A. DOLEMAN and E. G. BUTLER, *Key Eng. Mat.* **127-131** (1997) 193
451. *Ceram. Bull* **70**, No.4 (1991) 673
452. A. W. NAUMANN and F. P. GORTSENA (Union Carbide Corp.), *Ger. Offen.* **2007209**, September 1970
453. H. SHOZO, T. KOZO, A. YASUAKI and F. AKIO (Sumitomo Chemical Co.), *Jpn. Pat.* **741 34928**, December 1974
454. R. C. GARVIE, R. H. HANNINK and R. T. PASCOE, *Nature* **258** (1975) 703
455. H. TSUBAKINO, R. HAMAMOTO and R. NOZATO, *J. Mat. Sci.* **26** (1991) 5521
456. D. B. MARSHAL, F. L. LANGE and P. D. MORGAN, *J. Amer. Ceram. Soc.* **70** (1987) C-187
457. T. YOGO, *J, Mat. Sci.* **25** (1990) 2394
458. Y. ABE, T. KUDO, H. TOMIOKA, T. GUNJI, Y. NAGAO and T. MISONO, *J. Mat. Sci.* **33** (1998) 1863
459. G. DE, A. CHATTERJEE and D. GANGULI, *J. Mat. Sci. Lett.* **9** (1990) 845
460. R. C. PULLAR, M. D. TAYLOR and A. K. BHATTACHARYA, to be submitted to *J. Eur. Ceram. Soc.*

461. R. C. PULLAR, M. D. TAYLOR and A. K. BHATTACHARYA, *J. Mat. Sci.* **33** (1998) 3229
462. K. KAMIYA, S. SAKKA and Y. TATEMICHI, *J. Mat. Sci.* **15** (1980) 1765
463. Horizons Inc., *US Pat.* **3096144**, July 1963
464. du Pont, *US Pat.* **3129105**, April 1964
465. H. SCHOLZ. W. WATZKA and P. VIERHAUS, *Ger Offen* **19635748**, March 1998
466. K. KAMIYA, K. TANMOTO and T. YUKO, *J. Mat. Sci. Lett.* **5** (1986) 40
467. R. MEYER Jr, T. SSHRONT and S. YOSHIKAWA, *J. Amer. Ceram. Soc.* **81** (1998) 861
468. J. D. FRENCH, G. E. WEITZ, E. J. LUKE, R. B. CASS, B. JADDIAN, P. BHARGAVA and A. SAFARI, *Proc. SPIE - Int. Soc. Opt. Eng.* **3044** (1997) 406
469. S. FORSTER and M. D. TAYLOR, University of Warwick (1996), unpublished work
470. A. K. BHATTACHARYA, A. HARTRIDGE, K. K. MALLICK and M. D. TAYLOR, *J. Mat. Sci.* **31** (1996) 558
471. Owens-Corning Fibre Glass Corp., *US Pat.* **2968622**, January 1961
472. Horizons Inc., *US Pat.* **3082699**, March 1963
473. K. ISHINO, Y. NARUMIYA and Y. HASHIMOTO (TDK Ltd, Tokyo), *Jpn. Pat App.* **204617**, November 1982
474. R. M. ARONS (Celanese Corp., New York), *US Pat.* **4559191**, December 1985
475. Horizons Inc, *US Pat.* **3077380**, February 1963
476. Owens Corning Fibreglass Corp., *US Pat,* **3065091**, November 1962
477. J. T. A. POLLOCK, *J. Mat. Sci.* **7** (1972) 631
478. G. N. MORSCHNER, S. FARMER and A. SAYER, *Ceram. Sci. Proc.* **16** (1995) 959

Bibliography

The following books have been used as general reference books and for background reading, in addition to the specific references listed above.

"Ferrites" by J. SMIT and H. P. J. WIJN, Philips Technical Library, Eindhoven (1959).

"Ferromagnetic Materials" vol. 2, edited by E. P WOHLFARTH, North-Holland Physics Publishing, Amsterdam (1980).

"Ferromagnetic Materials" vol. 3, edited by E. P WOHLFARTH, North-Holland Physics Publishing, Amsterdam (1982).

"Ferrites" by E. E. RICHES, Mills and Boon Technical Library, London (1972).

"Magnetic Materials and their Applications" by C. HECK, Butterworths, London (1974).

"Magnetism and Magnetic Materials" by J. P. JAKUBOVICS, The Institute of Materials, Cambridge University Press (1994).

"Structure and Properties of Magnetic Materials" by D. J. CRAIK, Pion Ltd., London (1971).

"Sol Gel Science" by C. J. BRINKER and G. W. SCHERER, Academic Press, New York (1990).

"The Physics of Amorphous Solids" by R. ZALLEN, Wiley-Interscience, New York (1983).

"Advanced Inorganic Chemistry" by F. A. COTTON and G. WILKINSON, John Wiley and Sons, Inc., New York (1980).

"Comprehensive Inorganic Chemistry", Volume 3, edited by J. C. BAILAR Jr., H. J. EMELEUS, R. NYHOLM and A. F. TROTMAN-DICKENSON, Pergamon Press, Oxford (1973).

"Complexes and First Row Transition Elements" by D. NICHOLS, Macmillan, London (1974).

"Polymeric Stabilization of Colloidal Dispersions" by D. H. NAPPER, Academic Press, New York (1983).

"Dynamic Light Scattering" by B. J. BERNE and R. PECCORA, Wiley Interscience, New York (1976).

"Fine Ceramic Fibres" edited by A. R. BUNSELL and M-H. BERGER, Marcel Dekker Inc, New York (1999).

"High temperature mechanical Behaviour of Ceramic Composites" edited by S. V. NAIR and K. JAKUS, Butterworth-Heinemann, London (1995).

"Composite Materials: Science and Engineering" by K. K. CHAWLA, Springer-Verlag Inc., New York (1987).

"Materials Science and Technology", Volumes 3B, 11 and 13, edited by R. W. CAHN, P. HAASEM and E. J. KRAMER, VCH, Weinheim (1993 and 1994).

"Ceramic Microstructures" edited by R. M. FULRATH and J. A. PASK, John Wiley and Sons, Inc., New York (1968).

"Strong Solids" by A. KELLY, Clarendon Press, Oxford (1973).

"Materials Science and Engineering: An Introduction" by W. D. CALLISTER, Jr., John Wiley and Sons, Inc., Toronto (1997).

"Linear Ferrite Devices for Microwave Applications" by W. H. VON AULOCK and C. E. FAY, Academic Press, New York (1968).

Appendix A

Theory of Magnetism

Although lodestone has been known since prehistory, the science of magnetics only began 150 years ago, as metallurgy developed. The first magnetic property to be investigated scientifically was the Joule Effect, in which a piece of magnetic iron in an electrical field elongates in the direction of the field and contracts transversely to the field [392]. The effect is now known as magnetorestriction, and it clearly demonstrates the relationship between electric and magnetic fields.

Most materials interact with magnetic fields, as dielectric materials interact with electric fields. The electronic structure of a material forms magnetic dipoles, and it is the interactions between these dipoles which determines the magnetic behaviour, although this can be modified by composition, microstructure and processing methods.

1.1 Magnetic moment

Each electron has two magnetic moments, which generate the strength of the field associated with the electron. The moment, called the Bohr magnetron or μ_B, is defined as:

$$\mu_B = \frac{q\,h}{4\pi\, m_e} = 9.27 \times 10^{-24}\ A\,m^2 \qquad \text{Eqn. A.1}$$

where q = the charge of the electron, h = Planck's constant and m_e = the mass of the electron. These moments are caused by the orbital momentum of the electron around the nucleus and the spin of the electron around it's own axis, the direction of which is determined by the quantum number (fig. 284). Each discrete energy level in an atom can contain one or two electrons, and if the electrons are a pair then the spins are always opposite and cancel each other out; therefore full energy levels always have a net magnetic moment of zero.

This should mean that all atoms with an odd atomic number should have a net magnetic moment, but often the lone electron is a valence electron, which pairs with the valence electron of another atom, thus cancelling out their spins. However, some elements such as transition metals and rare earth metals have inner energy levels which are not full. For example, in the first row transition metals the five 3d energy levels fill up with one electron at a time, not forming pairs with opposing spins until they all contain one electron first, and the outer 4s level is full with a pair of electrons. There are two exceptions to this; chromium has just one electron in each 3d and 4s level ($3d^5\ 4s^1$) and these are cancelled out by interactions with other atoms, and copper has a completely full 3d shell with a lone

electron in the 4s level ($3d^{10}\ 4s^1$) which is again cancelled out by other atoms [393]. Zinc has totally full 3d and 4s levels ($3d^{10}\ 4s^2$). In the other transition metals scandium ($3d^1\ 4s^2$), titanium ($3d^2\ 4s^2$), vanadium ($3d^3\ 4s^2$), manganese ($3d^5\ 4s^2$), iron ($3d^6\ 4s^2$), cobalt ($3d^7\ 4s^2$) and nickel ($3d^8\ 4s^2$), there is a permanent magnetic moment, related to the number of unpaired electrons, which acts as a magnetic dipole. The response of the atom to an applied magnetic field depends upon how this dipole reacts to the field, and in most transition metals the sum of the individual unaligned moments of the atoms is zero. However, in the magnetic metals iron, cobalt and nickel an exchange interaction occurs, in which the orientation of the dipole in one atom influences the surrounding atoms to adopt the same orientation, aligning the magnetic moments and amplifying the effect of the magnetic field [105]. The ions of these metals are formed by losing the 4s electrons first, so The M^{2+} ions will have the same the same number of Bohr magnetons as the metal. Therefore Fe and Fe^{2+} both have 4 μ_B, but Fe^{3+} loses an electron from the only pair in the 3d level, leaving 5 lone electrons = 5 μ_B.

1.2 Magnetisation and magnetic permeability

If an electric current I is passed through a coil of n turns and of length l, a magnetic field, H, results with a strength of

$$H = \frac{n\,I}{l} \qquad \text{Eqn. A.2}$$

where the units of H are A m^{-1}. Magnetic field is also measured in Oersteds, where 1 A m^{-1} = 4p x 10^{-3} Oe. When a magnetic field is applied in a vacuum lines of magnetic flux are induced, and the number of these lines is called the inductance or flux density, B. For an applied field H this is given by

$$B = \mu_o H \qquad \text{Eqn. A.3}$$

where μ_o = the permeability of free space, a constant with the value of 4π x 10^{-7} T m A^{-1}, which = 1 Oe. The units of inductance are Tesla, T, or Gauss, G, where 1 T = 1 x 10^4 G, and 1 G = 1 Oe.

If a magnetic material is placed in a magnetic field, the magnetic inductance is determined by the way in which the induced and permanent dipoles of that material interact with the applied field. In this case

$$B = \mu H, \qquad \text{Eqn. A.4}$$

where μ = the permeability of the material in that field. The influence of the magnetic material on the field is described by the relative permeability, μ_r, where

$$\mu_r = \frac{\mu}{\mu_o} \qquad \text{Eqn. A.5}$$

and a large value for μ_r indicates that the material amplifies the effect of the magnetic field. Magnetisation occurs when the magnetic dipoles are oriented by an applied magnetic field, permitting larger magnetic energies to be stored than if the field were absent. This increased energy can be stored temporarily or permanently, and the magnetisation, M can be seen as an increase in the inductance, B, so that:

$$B = \mu_o H + \mu_o M \qquad \text{Eqn. A.6}$$

If the material is a good magnet, μ_o M is much, much greater than μ_o H, so it can be said that:

$$B \cong \mu_o M \qquad \text{Eqn. A.7}$$

The magnetic susceptibility, χ, is then defined as the ratio between the magnetisation of the material and the applied field:

$$\chi = \frac{M}{H} \qquad \text{Eqn. A.8}$$

Therefore, it can be seen from equations A.4 and A.5 that to get a high inductance, B, a material with a high relative permeability, μ_r, is needed, and from equation A.8 that to get a strong magnetisation, M, a high magnetic susceptibility, χ, is required.

1.3 Demagnetising factors

When a specimen becomes a magnet in an applied field, magnetic poles form within it and the magnetic flux flows from south to north. This sets up a field in the sample opposing the uniform applied field of the inducing coil (fig. 285). If M = magnetisation of the sample, the field H is reduced by a value proportional to M, so the effective field H_{eff} is given by

$$H_{eff} = H - NM \qquad \text{Eqn. A.9}$$

and the real permeability, μ', is given by

$$\mu' = \mu_r - N \qquad \text{Eqn. A.10}$$

where N = the demagnetising factor [391]. N depends upon the shape of the sample, and its precise calculation is only possible for an ellipsoid, being non-uniform in rectangular sheets, cylinders, and other polyhedra. It can be approximated That $N = {}^1/_3$ for a sphere and N = 0 for a rod of infinite length, for example a continuous fibre with a very large aspect ratio. The demagnetising factor determines the ratio of the length to cross sectional area of commercial permanent magnets.

1.4 Classes of magnetic material

When a magnetic field is applied to a group of atoms, several kinds of magnetic behaviour result from the interactions between the magnetic dipoles and that field, as shown in figure 286.

1.4.1 Diamagnetism

All substances possess diamagnetism, produced by the full energy levels of the substance, and diamagnetic materials are repelled by a magnetic field as an induced magnetic moment is set up in opposition to the applied magnetic field. This causes the magnetisation to be less than zero, with a negative susceptibility and a relative permeability, μ_r, of around 0.99995. Copper, alumina, silica and gold are all diamagnetic at room temperature, and superconductors must become diamagnetic to have zero resistance. For all practical purposes χ is independent of temperature, the exception being graphite. The diamagnetic effect is very weak, and is usually masked if the material also simultaneously possess another form of magnetism, but when a material is referred to as non-magnetic it is still diamagnetic.

1.4.2 Paramagnetism

Paramagnetism derives from the spin and orbital angular momentum of unpaired electrons in atoms, resulting in a weak net magnetic moment in an applied field. The dipoles align with the magnetic field resulting in a positive magnetisation, but there is no interaction between the dipoles so extremely large fields are required to align all of them, and the effect is lost as soon as the field is removed. Nevertheless the effect is around 1000 times greater in

magnitude than the diamagnetic effect, with μ_r = 1.0 - 1.01. The decrease in χ is inversely proportional to the rise in temperature, according to the Curie Law. Metals such as aluminium and titanium, alloys of copper and many transition metal complexes are paramagnetic.

1.4.3 Superparamagnetism

Extremely finely divided ferro- or ferrimagnetic materials with nanosized particles, such as colloids or some fine precipitates, exhibit superparamagnetic behaviour. The atoms form in non-magnetic matrices, causing the magnetic hysteresis loop to collapse (zero coercivity) and drastically reducing the magnetisation compared to the standard material.

1.4.4 Ferromagnetism

This is caused by the unfilled 3d energy levels of the magnetic metals iron, cobalt, nickel, and a few other elements such as gadolinium. The permanent dipoles easily line up with an applied field due to exchange interactions that act as a form of mutual reinforcement, resulting in large magnetisations with relatively small magnetic fields. This results in a large magnetic permeability of the order 1 x 10^6, and some of the effect remains after the withdrawal of the field (fig. 287). The inductance, B, depends upon the field strength, H, so B-H plots are a useful way of measuring the properties of ferromagnets, and the magnetic susceptibility also depends upon the applied field strength. Ferromagnets include the metals iron, cobalt, nickel, their alloys, and some rare earth metals such as erbium, dysprosium and gadolinium and their alloys. Ferromagnetic compounds can also exist which do not contain any individual ferromagnetic elements, such as the intermetallic compounds $ZrZn_2$ and Au_4V, and some alloys of manganese with copper and aluminium [391].

1.4.5 Antiferromagnetism

In some materials the magnetic moments in neighbouring dipoles align in opposition to one another in an applied magnetic field. Even though the strength of each individual dipole is high, the equal and opposite moments cancel each other out resulting in zero magnetisation (fig. 287). The magnetic susceptibility increases with temperature to a maximum at the Néel temperature, and then falls again with further temperature increases. This occurs in materials such as manganese and chromium metals and many divalent metal oxides such as FeO, MnO and NiO.

1.4.6 Ferrimagnetism

This is a special case of uncompensated antiferromagnetism, which occurs in many ceramic materials composed of mixtures of ions with differing magnetic moments. The dipoles of one ion may align with the field while another aligns against it, but as the opposing moments are not equal a net magnetisation results (fig. 287). Ferrimagnetic materials also retain some magnetisation after the removal of the field, and they have a moderately large magnetisation between that of paramagnetic and ferromagnetic materials, and they resemble the ferromagnets in their behaviour. This is the type of magnetisation usually found in spinel, hexagonal and garnet ferrites.

2. Magnetisation in ferro- and ferrimagnetic materials

In solid crystalline structures the electron spin moment dominates the orbital momentum moment, and an interaction between the atoms of the lattice leads to a parallel alignment of the electron spins in ferro- and ferrimagnetic compounds. The electrostatic forces that align some or all of the spins are called exchange forces. However, a condition for this to occur is that the ratio of crystal spacing to the radius of the energy level containing a lone inner electron must be greater than three. This is only true for three of the 3d transition elements, the ferromagnetic metals iron, cobalt and nickel. Therefore, to form a ferro- or ferrimagnetic compound three conditions must be met:

- There must be unfilled inner electron levels such as the 3d level in at least some of the atoms, uninvolved in bonding, which contain unpaired electrons.

- The alignments of the electron spins must be either all parallel or not fully compensated, resulting in a net magnetic moment or dipole.

- The atoms must form a crystalline lattice, with a lattice constant at least three times greater than the radius of the unfilled electron levels

From this it can be seen how some alloys of other, non magnetic metals could satisfy these conditions and become ferro- or ferrimagnetic.

2.1 Magnetic domains and saturation magnetisation

Within the grain structure of ferro- and ferrimagnetic materials there exists a substructure of magnetic regions, or Weiss domains, even in the absence of an external applied field.

Domains are regions where all the magnetic dipoles are aligned with one another, and vary in size from 50 μm down to tens of nm, depending upon the substance. Boundaries called Bloch walls separate these domains [394], which are not true walls but narrow zones of 100 nm or less, in which the direction of the magnetic moment continuously changes from that of one domain to the next (fig. 288). The magnetisation within a wall doesn't have to rotate through 180°, but there are also 90° walls in cubic structures and 120° and 60° walls in hexagonal structures [395]. Each domain is spontaneously magnetised to saturation, but the particles of a polycrystalline material will contain many domains which cancel each other out, giving a net particle magnetisation approaching zero, unless the particle size is near or below the domain size for that material.

Each domain behaves as a tiny bar magnet, with loops of magnetic flux running from north to south (fig. 289). If two parallel but opposed domains are neighbours they share their opposing flux paths, minimising the energy, so a two domain crystal has a lower energy than a single domain crystal of the same size (fig. 289). If the north and south poles are also capped by two opposing domains perpendicular to the original domain the magnetostatic energy is lowered even more, as the lines of flux are now entirely contained within the particle by this end closure (fig. 289). However, there is an optimum number of domains with the lowest energy, after which any further division into smaller domains increases the energy as the volume of the end closure domains becomes too small (fig. 289). This results in there being an optimum domain size, which is dictated by the structure of the material [396]. The domain size can be affected by magnetorestriction or changes in the crystal energy or internal structure of the material, but it is not known if there is a theoretical minimum or maximum domain size.

In a virgin material the domains are unaligned with respect to one another, and this lack of orientation results in a net magnetisation of zero. When a magnetic field is applied, domains close to the orientation grow at the expense of unaligned domains, through movement of the Bloch walls. Initially most of the wall shifts are reversible, so domains grow with difficulty, and large increases in applied field are required to get any magnetisation - this shallow slope, as shown in figure 290, defines the initial permeability of the material, μ_i. This cannot be measured directly, but only extrapolated to zero from measurements at very low field strengths of only a few A m^{-1} (10 A m^{-1} = 1.25 x 10^{-6} T). As the field increases the favourably oriented grains grow more easily, the permeability growing to a maximum until all the unaligned domains have been swallowed by their better aligned neighbours, and the magnetisation increases rapidly with the applied field. The rate of increase then drops off again as those domains which are favourably oriented with, but not aligned exactly along, the direction of field rotate, until all are perfectly aligned and the saturation magnetisation, M_s, is

reached. At this point, no further increase in magnetisation is possible for the material with further increase in field strength.

If a particle is domain sized, the walls cannot move, and so the magnetisation must rotate within the domain, even if it must rotate up to 180° to align with the applied field. As long as the particle is fixed in place this process occurs during the μ_{max} section of the initial curve, and not in the final section where the rotations of < 90° occur. Fibres can act as elongated single domains, and in cobalt metal rods as the diameter decreases from 1 μm to 70 nm, the coercivity along the filament axis increases from 30 to 330 Oe [397].

2.2 Remanence, coercivity and the hysteresis loop

When the magnetic field is then removed, the domain walls stay in the nearest favourable energy configuration, even if it is higher than their original one. The resistance offered by these irreversible domain wall shifts prevents the regrowth of the domains into random orientations, and therefore many domains retain their orientation near the direction of the original field. Those domains which rotated to align with the field will relax back into their old positions when the field is removed, by a process called reversible rotation. If any domains have rotated through an angle θ which is more than 90° however, for example in a single domain sized material, the domains relax back to face a direction opposite their original orientation at an angle of θ - 90°, in an irreversible rotation process. They will now contribute towards the magnetisation in the direction of the applied field.

The residual magnetisation thus present in a magnetised ferro- or ferrimagnet is called the remnant magnetisation, or remanence, M_r. Such materials form permanent magnets with a permanent magnetic moment without an applied field, although the domains may relax back into random orientations with time, changes in temperature or stoichiometry, or through physical shocks and impacts. A sample with domains already oriented with the field will retain a higher magnetisation when the field is withdrawn, as less magnetisation will be lost to the reversible rotation process.

If an opposite magnetic field is now applied, the few domains which posses an alignment favouring the opposing field will grow, until the domains have been forced to become randomly oriented again and cancel one another out, resulting in a net magnetisation of zero again. The reverse field required to achieve this is called the coercive field, or coercivity, H_c. With a further increase in reverse field all the domains will eventually become reoriented in the opposite direction with the same magnitude of saturation magnetisation as before, albeit of the opposite sign.

If this field is also then removed, the magnetisation will fall to a remanence equal but opposite the value of that found previously, and an identical coercive force will be needed in

the original field direction to randomise the domains again and obtain a net magnetisation value of zero. However often alternating fields are now applied to this material it will always follow the same path, forming an "S" shaped hysteresis loop if inductance, B, is plotted against applied field, H, as shown in figure 291, and the virgin magnetisation curve is lost forever, unless the domains are re-randomised at zero applied field. Even if the field is removed before the point at which the loop closes, it will still from a closed hysteresis loop.

Hysteresis will occur between the two quantities B and H if a cyclical change in H leads to cyclical variations in B, and those changes in B lag behind the changes in H. Therefore the value of B at any point in the loop relies not just on the instantaneous value of H but also on prior changes. The area of the hysteresis loop is proportional to the energy consumed in one cycle, this energy then being lost resulting in a loss of magnetisation, and a smooth loop is an indication of a large number of domains in the sample.

2.3 Magnetic losses

Losses of magnetic permeability can occur through two mechanisms. When a magnetic material is cycled through a series of applied fields in alternating directions forming a hysteresis loop, this causes a harmonic distortion which in turn gives flux excursions and reduces μ by the permeability loss factor, δ, to give an effective permeability, μ_{eff}. As this loss is related to the energy product of the loop, a material with a smaller hysteresis loop will suffer less losses. The loss factor has a frequency dependent component, so at high frequencies of alternating field, an extra loss occurs, small at first but which increases rapidly with rising frequency. The rate of increase and the frequency at which it becomes critical varies with the material. These losses are called anomalous eddy current losses, and although their mechanism is uncertain, it is known to involve the movement of electrons within the material, and increases with electrical conductivity. Eddy currents also increase exponentially with temperature, but they are negligible at room temperature in materials with a good resistance. The component of loss of the real permeability, μ', is called the imaginary permeability, μ'', and the reciprocal of permeability, μ^{-1}, is called the reluctivity.

Magnetic losses can also occur through ohmic resistance of a coil, in which case the energy is lost as heat, and the loss is proportional to a square of the frequency. However, the permeability can only be measured accurately for a toroidal shaped device. A lossy, or disipative coil can be regarded as an inductive permeability, μ', and a resistive permeability, μ'', which are equivalent to the real and imaginary permeabilities.

This gives rise to the complex permeability of the material or device, μ_{eff}, so called because it involves a constant which is a complex number, $j = \sqrt{-1}$. The complex permeability is given as [391].

$$\mu_{eff} = \mu' - j\mu'' \qquad \text{Eqn. A.11}$$

or

$$\frac{1}{\mu_{eff}} = \frac{1}{\mu'} - \frac{1}{j\mu''} \qquad \text{Eqn. A.12}$$

2.4 Hard and soft ferrites, square ferrites and perminvars

The magnetic hardness of a material is unrelated to it's mechanical strength, and refers purely to the coercivity of the magnet. A hard ferrite has a high coercivity and a broad hysteresis loop, and is therefore hard to demagnetise to zero. Soft ferrites have a low coercivity and a narrow hysteresis loop, and are therefore easier to demagnetise. Hard magnets also usually, but not always, have higher saturation and remnant magnetisations than related soft ferrites, and soft ferrites need less energy to travel through the hysteresis cycle, as shown by the smaller area of their hysteresis loops (Fig. 292).

Also sometimes of importance is the squareness of the loop. A ferrite is square when it has a high remanence (M_r / M_s > 0.8) which persists for some time after the field is reversed, with a sudden decrease of magnetisation with increasing field near the coercivity. Increasing the squareness of the loop also increases it's area, and therefore the energy associated with it. The squareness of a ferrite is usually described by it's energy product, the maximum product of induced magnetisation B and applied field H, which is also described by the largest rectangle that can be drawn in the second and fourth quadrants of the loop. This makes the ferrite hard to demagnetise accidentally, as it can withstand small reverse fields with out losing much magnetisation, until it nears the coercive field value. Square loops do occur naturally with some compounds such as magnesium-manganese spinel ferrites, but they usually have to be induced through a structural anisotropy, through magnetorestriction by applying a stress, or orienting the particles with a thermomagnetic treatment [398].

The opposite of a square ferrite is an isoperm, in which the permeability changes very little with increasing applied field, giving a soft ferrite shape with a low coercively and saturation magnetisation. These materials, such as manganese-zinc spinel ferrite, have a very low remanence and hence a very steep curve through zero applied field, with M_r / M_s = 0.1 - 0.2, and a high initial permeability. They can also be found in induced oriented square ferrites when the field is perpendicular to the easy axis. They are thought to be caused by a large number of highly mobile domain walls, or a few very wide domains with large closure domain volumes [391].

Another kind of hysteresis loop shows a constant permeability at low fields, giving a loop than is almost or fully closed in the centre but which then opens up at slightly higher fields, in a figure of eight shape. These are named permeability invariant, or perminvar materials. As the magnitude of the applied field is increased, the constriction in the centre becomes less pronounced, disappearing completely at high fields. The effect was first seen in iron rich alloys containing cobalt and an excess of oxygen, slowly cooled down from the Curie point [399]. It is thought to occur because the Bloch walls lie in deep energy troughs, and at low fields they cannot escape these so only reversible processes occur, resulting in a low and constant permeability until the energy threshold is passed and irreversible processes can take place. The mechanism is suggested to be a relaxation process involving diffusion of electrons, holes or ions, stabilised by a slight excess of oxygen during cooling [400]. A perminvar magnetite has been made by doping it with cobalt [401], and a perminvar ferrite can be converted to a square ferrite with a higher energy product and coercivity than that found in spontaneous square ferrites, through thermomagnetic cooling [402].

2.5 Dependence of magnetisation with temperature

As the temperature increases from 0 K the magnetic permeability, and therefore the magnetisation, of ferro- and ferrimagnetic materials generally decreases constantly and slowly until it falls rapidly at a point known as the Hopkinson temperature. It then decreases until $\mu = 1$, at which point the spontaneous magnetisation of the material vanishes, and this point of zero magnetisation is known as the Curie point or temperature, T_c. With rising temperature thermal agitation works against the electrostatic exchange forces ordering the spins, resulting in the loss of ferro- or ferrimagnetism at the Curie point. Obviously if a material has a Curie point below room temperature it is no longer ferro- or ferrimagnetic at room temperature, and if a material is heated above T_c and allowed to cool down in the absence of a magnetic field all of the domains will become truly randomised and the virgin state can be regained. As the temperature increases over T_c the material begins to gain magnetisation slowly again, but of a much smaller magnitude, as the material becomes paramagnetic. It has been suggested that there may be no definite T_c, but rather a transition range over which the domains disappear, and this transition from ferro- or ferrimagnetic to paramagnetic is sharper for a more homogenous material [403].

2.6 Magnetic anisotropy

Magnetic anisotropy is an effect when the magnetic properties of a substance are seen to differ from one orientation of the material to the other, and the material does not behave as an

isotropic magnet. These anisotropies can be beneficial for many applications, and originate from a variety of sources.

The most important type of magnetic anisotropy in hexagonal ferrites is magnetocrystalline anisotropy (MCA), which is dependent upon the crystal lattice structure, and in which the magnetisation is dependent on the direction relative to that structure. MCA is connected to the energy needed to turn a magnetisation vector from the preferred low energy, or easy direction, to a difficult, higher energy orientation, represented by the anisotropy constants K_1 and K_2. For single hexagonal crystals the total anisotropy energy is given by the sum

$$\sum_K = K_o + K_1 \sin^2\phi + K_2 \sin^4\phi + \ldots \qquad \text{Eqn. A.13}$$

where K_0 = the energy to magnetise the easy axis, and ϕ = the angle between the direction of magnetisation and the c-axis [391]. The higher order terms are not usually necessary, K_o has a low value as the easy axis is a low energy orientation, and often even the second order term is not required. A high crystalline anisotropy is a prerequisite for a high coercivity, for example the anisotropy constants (measured in 10^3 erg cm^{-3}) for magnetite are K_1= -120 and K_2 = 28, for manganese zinc spinel K_1 = 15 and K_2 = 0, and for BaM K_1 = 3000 and K_2 = 0. BaM is a very magnetically hard material suitable for permanent magnets, and all of the spinel ferrites are soft magnets except for $CoFe_2O_4$ which is a hard magnet, and has the high anisotropy constants K_1 = 3800 and K_2 = 0 [7].

The MCA in ferrites originates from dipole-dipole interactions, which can be calculated from the net magnetic moment of the lattice, and spin-orbit coupling in which the spin direction of an ion is coupled to the lattice via the orbital momentum of the ion. This is difficult to calculate for BaM as although the ground state Fe^{3+} ions have known orbital moments, there are also exited states mixed into the ground state created by perturbations such as the unusual five-fold symmetry of the trigonal bipyramidal site, and these must be major contributors to the anisotropy constants [404]. If the La^{3+} ion is substituted for barium to make LaM, one of the iron ions must become Fe^{2+} to compensate for the trivalent ion, and Fe^{2+} has a large orbital moment and therefore larger spin orbit coupling. because of this, the anisotropy constant for LaM is greater than for BaM [405]. Co^{2+} ions also cause large increases of anisotropy in spinels due to increased spin-orbit coupling, and this explains why the anisotropy constants of $CoFe_2O_4$ and the Co_2 ferrites are so large [406].

There are other kinds of magnetic anisotropy, such as form anisotropy, determined by the morphology of the magnetic particles, material or component, but this can only be calculated accurately for an ellipsoidal shape. The Joule effect shows that tensile or

compressive stress can effect the magnetisation, resulting in stress anisotropy, and this can be important in materials with a low MCA. Stress anisotropy is used to form some magnetic steels, and it applies to thin films less than 300 nm thick which acquire an anisotropic stress in they are deposited obliquely onto a substrate. The interaction between a ferromagnetic substrate and a ferrimagnetic oxide film can also produce asymmetrical shifts of the hysteresis loop up or down in an applied field, caused by a magnetic exchange anisotropy [407]. However perhaps the most important secondary form of magnetic anisotropy for hexagonal ferrites is induced uniaxial anisotropy, achieved by applying a field to a randomly oriented polycrystalline material as it cools down through the Curie point. A material with a high T_c is needed to allow ion or hole diffusion, and this process is often used to manufacture oriented perminvar and ferrite products.

2.7 Uses of ferro- and ferrimagnetic materials

Pure metals are too conductive and their large loops suffer power losses too high for use in electrical devices, whereas their poor energy product and low remanence make them unsuitable for permanent magnets. However, iron-nickel alloys make soft magnets with a high magnetic permeability suitable for use as magnetic recording heads. An addition of 3 - 5% silicon to iron produces an alloy suitable for use as motor and generator cores. To reduce eddy current losses thin silicon-iron sheets are laminated with alternating layers of a dielectric material to increase the resistivity of the composite. Such devices are of use at low and medium frequencies, although at high frequencies magnetic losses become more significant due to the speed of realignment of the domains.

This can be solved by mounting domain-sized particles in a resistive polymer composite, so the particles can rotate easily in the soft matrix. If the grain size can be made equal to or smaller than the domain size, the domains can change orientation only by rotation, as there as no Bloch walls to move. This rotation requires more energy than the domain growth process, so coercivities are raised and such materials make better permanent magnets. Complex metal alloys can be made with much improved saturation magnetisations and energy products, such as Alnico made by a phase transition on cooling to give a phase rich in iron and cobalt precipitates. Better still are permanent alloy magnets made from powder metallurgy, and compacted in a magnetic field, such as Co_5Sm and $Nd_2Fe_{14}B$.

Permanent magnets made from hard ferrites are not as good as these alloys, but they are cheaper and easier to make, and hexagonal ferrites are used in all three of the applications mentioned above. Magnetic tapes and discs are also made from coating a tape with a layer of γ-Fe_2O_3, or embedding these sub-domain-sized particles into a polymer film. Dust magnets, made of BaM in an elastic or plastic binder to make a plastoferrite RMC which is easily

workable and can be cut into any shape, are familiar to all of us as fridge magnets, both on and inside the door.

Appendix B

Survey of polycrystalline ceramic fibres

1. Non-oxide based polycrystalline fibres

1.1 Fibres manufactured by chemical vapour deposition (CVD)

The earliest non-oxide ceramic fibres were silicon carbide or boron fibres, produced from chemical vapour deposition (CVD) with a filament core made of metal or carbon in the early 1960's. The resulting fibres had diameters of 100 –140 μm, and were therefore inflexible and could not be woven or shaped. The process is inherently costly, but titanium cored fibres remain the only way of reinforcing titanium MMCs.

The first fibres manufactured by this method were boron fibres 100 μm thick, deposited on 20 μm diameter tungsten filaments from a mixture of H_2 and BCl_3, although other substrate cores have been used since. A coating of B_4C or SiC is sometimes added to limit fibre degradation during processing, but even so these fibres are not usable over 1000 °C due to interface reactions. The grain size is only 3 nm so the fibre is virtually amorphous. Boron nitride fibres have also been made by heating the CVD boron fibres to 1400 °C in a stream of ammonia gas [133].

140 μm SiC fibres were made using chlorosilanes such as CH_3SiCl on a carbon or titanium core. With a titanium core pure SiC is obtained, but with a carbon core there are often carbon impurities in the fibre, and carbon can also migrate to the fibre surface. To prevent loss of fibre properties during composite manufacture a coating is added to the surface, such as with *Textron* SCS_n fibre, where n = the depth of the coating in μm. Commercially manufactured CVD fibres include *Textron* SCS_6, with a titanium core, which is used in titanium MMCs and there is also a *Textron* boron fibre with a tungsten core. DERA have produced a SiC fibre with a tungsten core, and all fibres of this type have an elastic modulus of ~400 Gpa and a tensile strength of 3 – 4 GPa [408].

1.2 Fibres from pyrolysis of an organic precursor

A group of fibres have been developed, based on silicon carbide, produced from the pyrolysis of organosilicon precursor filaments, analogous to the manufacture of carbon fibres from polyacrylonitrile filaments. SiC was the first such fibre, produced by Nippon Carbon, and their *Nicalon* range, used widely in CMCs, are the most successful fine ceramic fibres world-wide.

A polycarbosilane precursor fibre is produced with a structure similar to the 6 atom

ring of β-SiC, the low molecular weight of the precursor making the drawing of the fibre awkward [409]. The fibre is heated at 200 °C in air to crosslink the structure, but this also introduces oxygen into the structure, which remains after pyrolysis. The methyl groups in the polymer are not in the Si-C-Si chain, so during subsequent pyrolysis when the hydrogen is driven off a carbon residue is left behind. The ceramic is made by slow heating to 1200 °C in an inert atmosphere, and the resulting fibre is mostly β-SiC with a grain size of 2 nm, but there is also some free carbon less than 1 nm and an excess silicon/oxygen/carbon intergranular phase. The most popular SiC fibres are *Nicalon NLM-202* which are 56.6% Si, 31.7% C, 11.7% O and 14 μm in diameter. They possess an elastic modulus of 190 GPa and a strain to break of 1.05%, but over 1000 °C the mechanical properties fall and the fibre creeps due to this oxygen rich intergranular phase [410].

A mixed SiC-TiC fibre was first produced in 1981 from a polytitano-carbosilane precursor, made by crosslinking a polycarbosilane with a titanium alkoxide, which was then pyrolised between 1400 - 1700 °C under nitrogen [411]. *Tyrano LOX-M* is commercially manufactured from a similar precursor by Ube Industries, but it has less titanium added to give a final composition of 54.0% Si, 31.6% C, 12.4% O and 2.0% Ti. In this process the precursor fibre is pyrolysed at 180 °C to condense Si-H bonds and crosslink titanium compounds, and then converted to the ceramic at 1000 °C in a nitrogen atmosphere [412]. The 2% titanium in the ceramic fibre is said to inhibit crystallisation and resist oxidation of carbon by forming Ti-C bonds, but the fibre is still of no use over 1000 °C due to the even higher oxygen content. The fibres are however finer and stronger than *Nicalon*, with a diameter of 8.5 μm, an elastic modulus of 180 GPa and a strain to break of 1.4%.

The latest generation of *Nicalon* and *Tyrano* fibres are produced by the crosslinking of precursors using electron irradiation, avoiding the introduction of oxygen at this stage [413]. *Hi-Nicalon* is a 14 μm fibre produced from this new method, with the composition of 62.4% Si, 37.1% C and 0.5% O; obviously a much reduced oxygen content. It has a similar strain to break as the old *Nicalon* fibres, but an increased elastic modulus of 263 Gpa and improved creep resistance to over 1200 °C. *Tyrano LOX-E*, produced by a similar process shows little improvement over the previous *Tyrano* fibres as it still retains 5.8% oxygen from the use of titanium alkoxides to make the precursor. Recently the use of polyzirconocarbosilane has allowed the replacement of 2% titanium with 1% zirconium, reducing the oxygen content to 1.7% in *Tyrano ZE* fibre. This 11 mm fibre has a strain to break of 1.5%, an elastic modulus of 233 Gpa and increased creep resistance and high temperature stability [110]. Stoichiometric SiC fibres are currently under development by different manufacturers, theoretically possessing better creep properties. However, they will still suffer from oxidation over 1200 °C in oxidising conditions as a layer of silica forms,

modifying the properties of the SiC-matrix interface and limiting the future improvements possible in these materials.

A group of fibres studied but not commercially manufactured so far are based on the silicon carbide – silicon nitride system, made from the pyrolysis of polycarbosilazane precursors polymerised at 520 °C and then converted to the ceramic at 1200 – 1500 °C [414]. A weight loss of 35% occurs during pyrolysis to give black fibres with good dielectric properties (1000 times more resistive than graphite) and good mechanical properties. Dow-Corning *HPZ* fibre has the composition 59% Si, 28% N, 10% C and 3% and is 10 -12 μm in diameter with a good strain to break of 1% and an elastic modulus of 200 GPa.[415], and amorphous Si_3N_4 fibres with a diameter of 10 μm have been formed at 1200 °C in a nitrogen atmosphere [416].

Tonen have manufactured a 10 μm silicon nitride fibre with the composition 58.6% Si, 38.2% N, 2.7% O and 0.5% C, which has a strain to break of 1% and an elastic modulus of 250 GPa. However, this ceramic fibre is amorphous, retaining 90% of it's strength at 1300 °C and it still has 55% at 1500 °C. After reaching 1400 °C Si_3N_4 crystallises on the surface, causing the fibre to loose strength [110].

Bayer have reported a new amorphous single phase carbon nitride ceramic spun from a polymer precursor which is stable in an oxidising atmosphere to 1600 °C. This is said to be due to the formation of a protective double layer of SiO_2 on BNO, preventing the penetration of oxygen to the fibre within, although this fibre is still very much in the developmental stage [417]. Boron nitride fibres have also been made from a totally inorganic polymer route. B_2O_3 is blow spun or melt extruded in a dry environment and then heated in an ammonia stream at 800 °C to give BN fibres, which are then stretched at 2000 °C to give a fine fibre [418].

2. Oxide based ceramic fibres

2.1 Alumina-based fibres

Alumina based fibres, mostly containing silica as a second component, have been produced since the second world war. Aluminosilicate fibres are used mainly as refractory linings in kilns and as reinforcing fibres in MMCs, and now world production of these fibres is around 100, 000 tonnes / year [419]. α-Alumina fibres are stiffer, denser and less strong than carbon or boron fibres, and are therefore inferior reinforcing fibres at low temperatures, but they have greater creep resistance as continuous fibres. Therefore they are used mainly as reinforcements in niche applications demanding superior resistance to aggressive, high temperature oxidising environments, although continuous fibres are also used in furnace linings, fire retardent materials and other high temperature applications. Consequently they

are produced on a smaller scale of about 1000 tonnes / year [419]. Alumina based fibres are the only continuous polycrystalline oxide ceramic fibres currently available on the market.

2.1.2 Aluminosilicate fibres

Many fibres have been produced based on phases of alumina other than α-alumina, usually with added silica. More silica means greater strength, rendering the fibres more flexible and easier to handle, but at the cost of reducing the elastic modulus and creep resistance.

Alumino silicate fibres blown from a kaolin melt appeared after 1945, and were first manufactured by Babcock and Wilcox in the USA [420]. The replacement of silica with alumina improved the refractory performance but reduced spinnability of the melt, and the 47% Al_2O_3 in these kaolin derived fibres was near the maximum achievable by this process. They also had shot levels of over 50% of the mass of product. A process for making mullite Taylor wires 13 μm in diameter and 1 mm long was patented by du Pont in 1963 [421].

Most alumina based fibres are now manufactured by a sol-gel process, again first developed by Babcock and Wilcox to make fibres with a lower silica content [422]. In this sol-gel process a low temperature precursor is spun to give a gel fibre, which is then calcined to yield a ceramic fibre, a process which can be fine tuned to improve the product.

Following the asbestos scares in the late 1960's ICI developed *Saffil* fibre in 1972 as a possible replacement, but it was soon commercially produced as a high temperature insulating material. *Saffil* is a refractory insulation material, consisting of short discontinuous fibres of 96% δ-alumina and 4% silica with a diameter of 3 μm [124]. The fibre has a good strain to break of 67% and an elastic modulus of 300 GPa, and when the fibre is blended with aluminosilicates it extends the usable range from 1200 °C to 1600 °C [109]. The resulting fibres blankets are less dense and give an improved thermal response than ceramic insulating bricks, and are also more thermally and physically shock resistant. ICI later investigated a process for producing aligned alumina fibres called *Safimax*, a continuous aligned blanket version of *Saffil*, which was never developed commercially [125]. Two products were produced, one of which was a 3.6 μm, low density fibre of 2.1 g cm^{-3} which had an excellent strain to break of 1.0% and an elastic modulus of 200 GPa named *Saffil LD*. The denser fibre, named *Saffil SD* and with a smaller diameter of 3 μm and a density of 3.3 g cm^{-3}, had a higher elastic modulus of 300 GPa and a lower strain to break of 0.67% [423]. However, these two products are the most flexible polycrystalline alumina based fibres yet produced, both with a flexibility eight times greater than that of E-glass fibre, whereas all other similar fibres have a flexibility much less than that of E-glass. This flexibility was attributed to a combination of the low diameter and silica content.

Shortly after the commercialisation of *Saffil* 3M produced the *Nextel* range of

continuous aluminosilicate fibres, mostly based on mullite ($3Al_2O_3.2SiO_2$) with up to 28% silica added, and some with B_2O_3 also added as a grain growth inhibitor. These fibres were oval in cross section due to the solvent evaporation and drying stages in their fabrication from a sol-gel process, with an average diameter of 11 μm. *Nextel-312* was the first continuous alumina based fibre, consisting of amorphous mullite with B_2O_3 added to give the composition of 62% Al_2O_3, 24% SiO_2 and 14% B_2O_3 [123]. The boria additive is both to reduce grain size and to render the fibre more glassy, lowering the elastic modulus but increasing flexibility. As a result it has an extremely high strain to break of 1.12% but an elastic modulus of only 152 GPA, and above 1000 °C boria compounds become volatile, inducing severe shrinkage above 1200 °C. However, *Nextel-312* conserves 75% of it's mechanical properties up to 1000 °C, and does not creep below this temperature. Apart from the below mentioned *Nextel-610* α-alumina fibre, the exception of the *Nextel* range of fibres is *Nextel-720*, richer in alumina and without any boria, with the composition of 85% Al_2O_3 and 15 % SiO_2. This is actually a mixed phase fibre consisting of 55% mullite and 45% α-alumina, the resulting microstructure giving an elastic modulus of 260 Gpa and improved creep properties up to 1200 °C. There is a loss of strength due to stress induced crack growth between the mixed phases, but the lower strain to break of 0.81% is still very good for a polycrystalline ceramic fibre, and the creep performance is superior to all other polycrystalline alumina based fibres [424].

Sumitomo manufactured a 15% silica, 85% γ-alumina fibre with a diameter of 18 μm, produced from an organic aluminium-silicon precursor, named *Altex* [213]. This had a low elastic modulus of only 210 Gpa but a high strain to break of 0.86%, giving a material which was very easy to handle [425]. The crystalline γ-alumina phase has a very low grain size and density, and changes phase to mullite at 1127 °C. Amorphous silica stabilises γ-alumina up to this point, and consequently *Altex* has very good tensile properties up to 1000 °C, but the fibre deforms plastically over 1100 °C and creeps badly, the process accelerated by the large amount of silica. [426] Sumitomo have also claimed to have made 10 μm alumina silica fibres, 15 μm alumina boria fibres, and 10 μm titania-, magnesia- and chromia alumina fibres from polymeric precursors, requiring temperatures up to 1800 °C to form the ceramic [285].

Recently the Inorganic Fibres Group at the University of Warwick has produced mullite fibres from a non-organic sol-gel precursor with diameters of 4 - 7 μm, using an adapted version of the ICI *Safimax* process. The aqueous spinning solution was synthesised from aluminium nitrate and *Synton 30* silica sol, to give ceramic mullite fibres at a low temperature of 930 C, compared to the 1000 C usually required to form the ceramic from polymeric precursors [427].

2.1.2 α-Alumina fibres

In the late 1970's du Pont produced a small diameter continuous fibre of almost pure (99.9%) α-alumina named *Fiber FP* [428]. This was produced by blending powdered alumina with an alumina rich precursor solution which was then extruded through spinnerets, drawn and fired in air at 1300 °C . An added silica surface layer increased fibre strength by healing surface flaws and increased the fibre's wettability with light alloys when forming a MMC [429]. The fibre was difficult to handle due to it's low strain to break of 0.28%, and was withdrawn from the market for this reason. However it had a high elastic modulus of 440 Gpa and maintained strength up to 1000 °C, after which point creep and grain growth weakened the fibre drastically. Du Pont later produced, on a pilot scale, *PRD-166*, an 18 μm α-alumina fibre with 15% partially stabilised zirconia added. In this microcrystalline fibre the largest alumina grains were 0.3 μm and the zirconia grains were all below 0.1 μm, giving an improved strain to break of 0.4% and an elastic modulus of 330 Gpa, and creep resistance up to 1100 °C [430].

Mitsui Mining produced the 99.5% α-alumina *Almax* fibre, which was weavable due to it's small diameter of 10 μm. Unfortunately the fibre was also porous making it weak with a strain to break of only 0.3%, and an elastic modulus of 330 Gpa. This lowered creep resistance, and consequently the material was withdrawn from commercial manufacture [431].

3M also manufactured a 10 μm diameter, 99% α-alumina fibre as part of the *Nextel* range, *Nextel-610*, adding 0.67% α-Fe_2O_3 as a nucleating agent and 0.33% silica as a grain growth inhibitor [432]. This was rather more successful with a grain size below 0.1 mm resulting in a fibre with an elastic modulus of 373 Gpa, a relatively high strain to break of 0.67% and creep resistance equal to that of the weaker du Pont *Fiber FP*.

Recently a pure alumina fibre has been produced from a viscous organic sol. Gel fibres 10-14 μm in diameter and several km long were drawn directly from the sol at a rate of 200 m min^{-1} without the addition of a spinning aid, which proceeded to form a-alumina at 1150 °C [433]. 10 mm long alumina fibres have also been produced from the unidirectional freezing of a hydrogel, which produced porous α-alumina fibres suitable for use as a catalyst support [434].

There is a little developmental work reported on the synthesis of alumina based spinel fibres, and short $MgAl_2O_4$ fibres have been pulled from a chlorohydrate based system [435], although several researchers have reported that it is more difficult to produce a spinnable spinel precursor solution [436]. Barium hexaaluminate, a refractory material with a melting point of 1900 °C and a hexagonal structure analogous to that of BaM ferrite, has also been

made in fibrous form from a sol-gel route [437].

2.2 Yttrium aluminium garnet (YAG) fibres

Of all the ceramic materials currently investigated, single crystal YAG demonstrates superior creep properties [111] Furthermore, the creep in YAG is very weakly dependent upon orientation, unlike the strongly anisotropic creep in alumina, and the large size of the cubic unit cell of the garnet dramatically reduces the dislocation creep mechanism [438]. In polycrystalline YAG boundary diffusion will become an important process and reduce the creep resistance of the material, but never-the-less at 1400 °C polycrystalline YAG with a grain size of 3 μm is three times better than polycrystalline alumina of the same grain size [439].

The commercial attractions of YAG fibres were first recognised by 3M [440], and subsequently YAG fibres have almost entirely been either spun from organometallic precursors [441], or extruded from a melt [442]. Continuously spinnable YAG fibres have been produced from an alkoxide precursor [443], and fibres as fine as 20 μm have been extruded from an organic precursor, which crystallised to form single phase YAG at 1000 °C [444].

It was supposed that organic precursors were needed to make a high strength product of textile dimensions. YAG fibres produced from aqueous sols have largely been unsuccessful, requiring the addition of up to 20% organic polymer to stabilise the sol precursor, and giving discontinuous fibres with a very large diameter of 120 μm and a grain size of 3 μm [445]. Due to segregation in the precursor these fibres also did not form the YAG phase below temperatures of 1300 °C. It would be preferable to manufacture continuous fine fibres of less than 20 μm diameter for optimum strength, flexibility and weavability [133], and to collect these fibres in a dried form on a winding mechanism.

Such fibres have recently been manufactured recently by the author [446], blow spun from an aqueous sol using a modified *Saffil* process and collected as a blanket of gel fibre with an alignment of 90% within 20°, comparable to commercially available aligned alumina fibres. These gel fibres underwent a subsequent crystallisation to form single phase YAG fibres of 5.5 μm diameter between 700-800 °C, the lowest reported crystallisation temperature for this material, and this indicated that the sol was extremely homogenous. After optimisation of the process [447] the fibres fired to 1200 °C had a high strain to break of 0.92% - 0.73%, which fell to 0.51% - 0.43% at 1550 °C, comparing well with fine YAG fibres produced from organic precursors [444]. The grain size was only 1 μm even at the high temperature of 1550 °C. The creep resistance was found to be worse than that of the large diameter fibres made from aqueous sols [448], but this can be largely attributed to the 20 fold

difference in fibre diameter and a grain size three times smaller, an apparently unavoidable feature of fine fibres. To balance the requirements of creep resistance against mechanical strength a grain size of 0.5-2 μm is claimed to be ideal [444], and these fibres clearly satisfy this requirement.

Other non sol-gel based methods include the production of Al_2O_3-YAG eutectic filaments using an edge-defined film-fed growth technique [449] and a laser heated floating zone method [450], and the manufacture of a composite fibre consisting of a melt extruded thermoplastic polymer fibres containing YAG powder [442].

2.3 Zirconia fibres

Continuous zirconia fibres are of interest as high strength reinforcement materials, with a higher melting point of over 2700 °C and better chemical resistance to reactive environments than alumina. Zirconia fibre is also being developed for it's dielectric properties, as an electrode in fuel cells and as a substrate for superconducting oxides amongst others [451], and for these high performance applications the degree of control over microstructure achieved from the sol-gel process is required. The only commercially available zirconia fibres are short discontinuous *Zircar* fibres produced by Union Carbide from a rudimentary process, in which cellulosic fibres are impregnated with zirconium salts, and the organic matrix then burnt off [452]. Patents have also been made for zirconia fibres made by a sol-gel process from either aqueous [124] or organic precursors [453].

To produce a high strength zirconia fibre a small grain structure below 0.5 μm must be obtained by the addition of 1.5 - 5 mol% magnesia, calcia, ceria or yttria, so the crystal structure is partially stabilised in the tetragonal phase at room temperature. With dopants below this level; a much larger grain size forms, giving the usually higher temperature monoclinic phase also at room temperature. When stressed the tetragonal material reverts back to the monoclinic phase, the transformation resulting in microcracking which weakens the fibre's tensile strength but allows it to absorb fracture energy [454]. The tetragonal phase is stable up to 1600 °C but it is degraded by ageing in a moist environment at much lower temperatures [455], so for use at very high temperature or in reactive environments the cubic phase may be more suitable. This can be achieved at room temperature by doping the zirconia with 8 mol% yttria, to form fully stabilised cubic zirconia.

In 1987 a 2 - 5 μm diameter fibre was hand drawn from an acetate solution, and heated to 1000 °C to give the tetragonal phase, which was maintained until it changed phase at 1600 °C. This tetragonal phase resulted in a strength of up to 2.6 GPa in 3 μm fibres, higher than any alumina based fibre [456]. Continuous stabilised zirconia fibres can be produced from the either the pyrolysis of an organic precursor fibre [457] or the extrusion of

a precursor polymer [458], but these processes typically result in a thicker fibre of around 20 μm which does not form the tetragonal phase until over 1100 °C, resulting in a larger grain size and a lower tensile strength comparable to alumina fibres.

The spinning or drawing of an organometallic sol-gel precursor can yield a fibre of tetragonal zirconia at a much lower temperature of 500 °C which should produce a stronger fibre [459]. Recently the author has manufactured continuous aligned blankets of partially and fully yttria-stabilised zirconia blow spun from an aqueous sol-gel precursor, to give zirconia fibres with a fine diameter of 5 μm, and which are currently under investigation [460.]. The author has also produced strontium zirconate fibres with a diameter of 6 - 10 μm from a hydrolysed alkoxide precursor, which formed the single phase ceramic at 800 °C with a grain size of only 28 nm [461]. Discontinuous glass fibres with 33% zirconia have been produced from a mixed silica-zirconia alkoxide sol-gel process, to give fibres with a higher chemical resistance than pure glass. The gel fibres were pulled by hand during the hydrolysis and gelation of the mixed alkoxides, and the resulting silane based fibres heated to produce the vitreous form at 700 °C [462].

2.4 Titania based polycrystalline fibres

Horizons Inc. have evaporated a colloid to produce polycrystalline filaments of barium zirconate and titanate [463], and fine metal titanate fibres with the formula $M_2O.TiO_2$ (where M = alkali metal) were produced from a hydrothermal process followed by melt extrusion, to give a fibre which remained flexible up to 1000 °C [464]. A process for extruding mono- and multi-filament lead titanate fibres from an organic sol has been reported, the perovskite phase being seeded with up to 5% crystals and the fibre collected on winding apparatus [465]. Pure titania fibres have also been produced by a sol-gel method, the gel fibre pulled from an alkoxide precursor and fired to give the ceramic fibre [466].

Many titania based ceramic compounds are piezoelectric, the most famous being lead zirconium titanate (PZT); fibres have been produced of this material but the production methods employed so far have tended to be rather crude. Fibres of PZT are usually made by extruding an alkoxide precursor to give fibres anywhere between 10 - 70 μm in diameter, which form the ceramic at temperatures over 1200 °C and with a grain size over 1 μm [467]. However a viscous suspension spinning process has been used to make continuous fine filaments of PZT fibre 10 - 25 μm in diameter, collected in tows over 1700 m in length, and of moderate flexibility [468]. PZT fibres have been produced at the University of Warwick from an aqueous sol [469], as have zirconium titanate fibres with a diameter of 5 μm and which crystallised at only 750 °C [470].

2.5 Iron based polycrystalline fibres

The first continuous ferrite filaments were manufactured from the extrusion of a melt to make spinel ferrites containing iron, manganese, cobalt, nickel, copper, zinc, magnesium and cadmium. These ferrimagnetic fibres were also passed through a magnetic fields during processing to orient the crystallites as they formed during cooling [471]. Horizons Inc produced polycrystalline filaments of iron oxide and nickel spinel ferrite using their very basic colloidal evaporation technique in the early 1960's [472]. Since then progress has been very slow to manufacture a magnetic ferrite fibre, despite the many possible benefits and applications of such a material.

In 1982 TDK proposed a process for the manufacture of composite manganese-zinc and nickel-zinc spinel ferrite fibres from the core-sheath method, for possible weaving into an EM wave absorbing cloth [473]. A hollow organic fibre precursor would be filled with a 0.5 - 10 μm ferrite powder and then heated to produced the ceramic, a carbon or silicon nitride fibre filled with ferrite. If the ferrite loading was over 20% too much flexibility of the fibre was lost, and some ferrite compositions reacted with the carbon fibre precursor during the heating process. A similar process was suggested for producing extremely short spinel ferrite fibres with an aspect ratio of less than 30 for use in a sintered monolithic composite in EM shielding applications [474]. In this case a ceramic filled hollow organic fibre would be isostatically pressed, pyrolysed and sintered to produce a composite fibre 130 μm in diameter and up to 1 mm long. B_2O_3 filaments doped with BaM and SrM ferrites have also been melt spun and heated between 700 - 1000 °C to form the ferrite composite filament [54].

2.6 Single crystal fibres and whiskers

Some mention should be made of single crystal fibres, which have different properties to their polycrystalline cousins.

Whiskers are usually monocrystals grown in the form of filaments, whose aspect ratios can equal those of discontinuous fibres, being 20 –1000 μm in length. Their very small diameters of 0.5 – 1.5 μm mean that they contain few defects and consequently have very high strengths approaching the theoretical maximum. However, this very small diameter is within the range for suspect carcinogen fibres, and they are hard to align in a composite matrix, although they could provide transverse reinforcement to a conventionally aligned reinforcing fibre. Sapphire whiskers measuring 2.5 to 180 μm in diameter by 2 - 75 mm long were grown from a molten aluminium metal by Horizons Inc [475], and titania, zirconia and zircon whiskers were grown from a melt of the oxides at the same time [476].

Continuous monocrystalline α-alumina filaments have been developed by Saphikon,

grown slowly from molten alumina. These filaments are very expensive, with a diameter of over 100 μm, but by careful orientation of the seed crystal and with the absence of grain boundaries they should be able to withstand temperatures of around 1600 °C [477]. The Saphikon fibre is not without defects however, as bubbles can form from convection during the fibre growth, but never the less it has better creep resistance than any polycrystalline alumina fibres. The same process is also used by Saphikon to produce a eutectic fibre consisting of interpenetrating dual phases of α-alumina and yttrium aluminium garnet (YAG). These laminas are oriented parallel to the fibre axis resulting in creep resistance superior to that of pure polycrystalline α-alumina fibres, but the material still relaxes at temperatures over 1100° C [478].